TU Delft

Delft University of Technology

Document Version
Final published version

Citation (APA)
Raghavan, V. (2026). *Mixed wave energy arrays: Going beyond the status quo: An exploration of the hydrodynamics and techno-economics*. [Dissertation (TU Delft), Delft University of Technology]. https://doi.org/10.4233/uuid:521f43da-2de5-4690-9524-836060a5f1bf

Important note
To cite this publication, please use the final published version (if applicable).
Please check the document version above.

Copyright
In case the licence states “Dutch Copyright Act (Article 25fa)”, this publication was made available Green Open Access via the TU Delft Institutional Repository pursuant to Dutch Copyright Act (Article 25fa, the Taverne amendment). This provision does not affect copyright ownership.
Unless copyright is transferred by contract or statute, it remains with the copyright holder.

Sharing and reuse
Other than for strictly personal use, it is not permitted to download, forward or distribute the text or part of it, without the consent of the author(s) and/or copyright holder(s), unless the work is under an open content license such as Creative Commons.

Takedown policy
Please contact us and provide details if you believe this document breaches copyrights.
We will remove access to the work immediately and investigate your claim.

*This work is downloaded from Delft University of Technology.*

# MIXED WAVE ENERGY ARRAYS: GOING BEYOND THE STATUS QUO

## AN EXPLORATION OF THE HYDRODYNAMICS & TECHNO-ECONOMICS



VAIBHAV RAGHAVAN

**Mixed wave energy arrays: Going beyond the status quo**

An exploration of the hydrodynamics and techno-economics

# Mixed wave energy arrays: Going beyond the status quo

An exploration of the hydrodynamics and techno-economics

**Dissertation**

for the purpose of obtaining the degree of doctor
at Delft University of Technology
by the authority of the Rector Magnificus,
prof. dr. ir. H. Bijl,
chair of the Board for Doctorates
to be defended publicly on
Friday, 03 July 2026 at 12.30

by

**Vaibhav RAGHAVAN**

This dissertation has been approved by the promoter and the copromotor.

Composition of the doctoral committee:

| | |
|---|---|
| Rector Magnificus, | chairperson |
| Prof. dr. A.V. Metrikine, | Delft University of Technology, *promotor* |
| Dr. G. Lavidas, | Delft University of Technology, *copromotor* |
| *Independent members:* | |
| Prof. dr. B.J.H. van de Wiel, | Delft University of Technology |
| Prof. dr. E. Loukogeorgaki, | Aristotle University of Thessaloniki, Greece |
| Prof. dr. V. Venugopal, | University of Edinburgh, U.K. |
| Prof. dr. A. Vakis, | University of Groningen, Netherlands |
| Prof. dr. ir. M. van Koningsveld, | Delft University of Technology, *reserve member* |

This work has been fully financed by the TU Delft.




*Keywords:* Wave energy arrays, mixed arrays, mono arrays, Point absorbers, flaps, attenuators, BIEM, BEM, HAMS-MREL, Hydrodynamics, techno-economics, q-factor, M-factor

*Printed by:* Proefschriftspecialist

*Cover by:* Durga Santhoshi Ammu

*Copyright:* 2026, Vaibhav Raghavan

*ISBN:* 978-94-6518-334-3

An electronic copy of this dissertation is available at
https://repository.tudelft.nl/.

*Become capable, and success will run behind you on its own*

Ranchoddas Shamaldas Chanchad (3 Idiots)

# CONTENTS

**Summary** xi

**Samenvatting** xiii

**Nomenclature** xv

**1. Introduction** 1
1.1. Wave Energy Converters . . . 2
1.2. Research background and Motivation . . . 7
1.3. Thesis objectives . . . 12
1.4. Thesis outline . . . 13
1.5. Novel Contributions of the thesis . . . 14

**2. Theory and Validation of HAMS-MREL** 15
2.1. Formulation of the fundamental multi-body interaction problems in HAMS-MREL 16
2.2. Discretization of the integral equations and solution of the linear algebraic system . . . 18
2.3. Advanced solver features . . . 19
2.3.1. Wave fields - pressure and free surface elevation . . . 20
2.3.2. Global symmetry . . . 20
2.3.3. Suppression of irregular frequencies . . . 21
2.3.4. Generalized modes approach . . . 22
2.4. Validation of HAMS-MREL and the advanced solver features . . . 23
2.4.1. Frequency domain numerical validation of HAMS-MREL . . . 23
2.4.2. Computational resources utilized - Comparing HAMS-MREL and WAMIT . . . 39
2.4.3. Computational resources utilised and advanced features . . . 41
2.5. Experimental validation of HAMS-MREL - fixed bottom detached OWC device . . . 43
2.5.1. Experimental setup . . . 43
2.5.2. Experimental procedure . . . 43
2.5.3. Numerical Methodology . . . 44
2.5.4. Comparitive results . . . 50
2.6. Experimental validation of HAMS-MREL for an array of point absorbers . . . 56
2.6.1. Experimental dataset and physical setup . . . 56
2.6.2. Time domain modelling with WEC-Sim . . . 56
2.6.3. Numerical setup for SWELL . . . 58
2.6.4. Validation against Experimental Data . . . 59
2.7. Differentiating HAMS-MREL from HAMS . . . 63
2.8. Conclusions . . . 63

**3. Analysis of Mono and Mixed arrays in shallow water** 65
3.1. Scatter diagram . . . 66
3.2. Assumptions . . . 66
3.3. Hydrodynamic model implemented for single devices . . . 69
3.3.1. Convergence study for the mesh . . . 70
3.3.2. Calculation of the natural frequency of the devices . . . 71
3.4. Hydrodynamic model implemented for arrays . . . 78
3.4.1. Active control . . . 79
3.5. Considered configurations . . . 81
3.6. Metrics for comparing mixed and mono arrays . . . 83

3.7. Results and Discussion . . . 84
3.7.1. Power absorption for single devices . . . 84
3.7.2. A global view of the array q-factors . . . 86
3.7.3. Comparing mono and mixed arrays – Directional variation . . . 87
3.7.4. Average $q$-factor - Variation with number of devices . . . 89
3.7.5. Average $q$-factor - Variation with spacing . . . 98
3.7.6. Variation of average $M$-factors . . . 101
3.7.7. Choosing the best configurations . . . 108
3.8. Summary and Conclusions . . . 111

**4. Analysis of Mixed and Mono arrays in deep waters** **113**
4.1. Scatter diagram . . . 114
4.2. Assumptions . . . 114
4.3. Hydrodynamic model implemented for the single devices . . . 115
4.3.1. Calculation of the natural frequency of the devices . . . 116
4.3.2. Incorporating control and viscous drag under regular waves - Passive control strategy under no constraints . . . 118
4.3.3. Incorporating control and viscous drag under irregular waves - Passive control strategy under no constraints . . . 120
4.4. Considered configurations . . . 120
4.5. Hydrodynamic model implemented for arrays with passive control and no constraints . . . 122
4.6. Results and Discussion . . . 123
4.6.1. Comparing mono and mixed arrays - Directional variation . . . 128
4.6.2. Variation with the number of devices . . . 128
4.6.3. Variation with spacing . . . 136
4.6.4. Choosing the best configurations . . . 142
4.7. Conclusions . . . 142

**5. Comparing the Hydrodynamics of mixed and mono-arrays** **145**
5.1. Shallow water - Analysis in regular waves . . . 146
5.1.1. Performance based on q- and M-factors . . . 151
5.2. Shallow water - Analysis in irregular waves . . . 159
5.3. Deep water - Analysis in regular waves . . . 163
5.3.1. Performance based on q- and M-factors . . . 167
5.4. Deep water - Analysis in irregular waves . . . 174
5.5. Limitations of the $q$- and $M$ factors . . . 184
5.6. Conclusions . . . 184

**6. Economics of wave energy arrays** **187**
6.1. Scatter diagram and dominant direction plot in shallow and deep waters . . . 188
6.2. Cost and performance evaluation of single devices . . . 189
6.3. Practical considerations for choosing arrays . . . 192
6.4. Description of the array configurations . . . 193
6.5. Wave array economics . . . 196
6.6. Conclusions . . . 198

**7. Conclusions** **201**
7.1. Limitations and Future work . . . 202

**A. Additional validation cases for HAMS-MREL** **221**
A.1. Case 1 - Three semi-submerged cylinders compared with semi-analytical solutions and WAMIT . . . 221
A.2. Case 2 - Floating OWC compared with semi-analytical solutions and WAMIT . . . 224
A.2.1. Computational resources comparing HAMS-MREL and WAMIT . . . 224

**B. Flap - BIEM Shape function, rotational inertia and viscous damping coefficient** **229**
B.1. Implementation of the generalized modes to obtain the shape functions . . . . . 229
B.1.1. Body boundary condition for the first order boundary value problem . . . 229
B.1.2. Derivation of the shape function for a flap . . . . . 229
B.2. Derivation of the moment of inertia of the flap . . . . . 231
B.3. Derivation of the linearized viscous damping coefficient for the flap . . . . . 233

**C. Attenuator - Deriving the mass, stiffness and viscous damping matrices** **235**
C.1. Deriving the mass and stiffness matrices . . . . . 235
C.1.1. Kinematics . . . . . 236
C.1.2. Kinetic energy . . . . . 237
C.1.3. Potential energy . . . . . 237
C.1.4. Euler–Lagrange formulation . . . . . 237
C.1.5. Mass and stiffness matrices . . . . . 238
C.2. Deriving the viscous damping coefficient matrix . . . . . 238

**D. Additional results for shallow-water mixed arrays** **241**

**E. Additional results for deep-water mixed arrays** **277**

**Acknowledgements** **289**

**List of Publications, awards and Open-Source contributions** **291**

**Curriculum Vitæ** **295**

# SUMMARY

Wave energy represents a highly predictable and energy-dense renewable resource with the potential to contribute significantly to future low-carbon energy systems. Despite decades of research and the existence of numerous Wave Energy Converter (WEC) concepts, large-scale commercial deployment remains limited. This is primarily due to high capital costs, deployment in adverse offshore conditions, technological uncertainty, and challenges associated with scaling from single devices to array-level deployments. Most existing wave energy arrays are deployed as mono-arrays, consisting of identical devices operating in the same degree of freedom. While this approach simplifies design and control, it may limit flexibility in array design and constrain overall hydrodynamic and economic performance.

This dissertation introduces and systematically investigates the concept of mixed wave energy arrays, in which different types of WECs operating in distinct degrees of freedom are deployed within the same array. The central hypothesis is that combining devices with complementary hydrodynamic characteristics can influence array-level power absorption, directional behaviour, and techno-economic performance relative to conventional mono-arrays. By exploiting differences in resonance behaviour, radiation characteristics, and wave–structure interaction mechanisms, mixed arrays may offer alternative pathways for improving energy capture while balancing spatial and economic constraints.

The thesis begins by introducing an accurate and computationally efficient numerical framework for analysing the hydrodynamic behaviour of both mono and mixed WEC arrays. To this end, the HAMS–MREL solver is formulated, extended, and validated for multi-body and multi-degree-of-freedom systems. The model explicitly accounts for wave–structure interactions, array effects, and directional wave incidence, enabling consistent and systematic assessment of single devices and arrays of increasing complexity. Validation against analytical solutions, experimental data, and established numerical tools, together with parallelised implementations, demonstrates the suitability of the framework for array-scale investigations.

This modelling framework is then applied to examine and compare the hydrodynamic behaviour of mono and mixed arrays in both shallow- and deep-water environments. A broad range of array configurations is considered under regular and irregular wave conditions, allowing the influence of device type, spacing, layout, and wave directionality to be assessed. The analyses provide insight into how hydrodynamic interactions and directional effects differ between mono and mixed arrays, and how these differences influence array-level behaviour across a range of operating conditions.

Finally, the hydrodynamic analyses are integrated with a techno-economic assessment of wave energy arrays. Using representative cost models and site-independent assumptions, the levelised cost of energy of mono and mixed arrays is evaluated alongside spatial performance indicators such as array footprint. This combined assessment enables a consistent comparison of alternative array concepts, highlighting the trade-offs between energy production, spatial efficiency, and economic performance in different deployment contexts.

Overall, the findings of this thesis demonstrate that mixed wave energy arrays constitute a viable alternative to conventional mono-technology deployments and merit consideration in future wave energy farm design. By jointly examining hydrodynamic behaviour, spatial characteristics, and techno-economic implications at the array scale, this work provides a structured framework for evaluating next-generation wave energy arrays. The modelling tools and insights developed in this thesis form a foundation for future optimisation studies, control integration, and site-specific assessments aimed at advancing the commercial viability of wave energy systems.

# SAMENVATTING

Wave energy vormt een hoogst voorspelbare en energierijke hernieuwbare energiebron met het potentieel om een belangrijke bijdrage te leveren aan toekomstige koolstofarme energiesystemen. Ondanks decennia van onderzoek en het bestaan van een groot aantal concepten voor wave energy converters (Wave Energy Converters, WEC's), blijft grootschalige commerciële toepassing beperkt. Dit is voornamelijk te wijten aan hoge investeringskosten, inzet onder zware offshore omstandigheden, technologische onzekerheid en de uitdagingen die gepaard gaan met de opschaling van individuele apparaten naar array-niveau. De meeste bestaande wave energy arrays worden gerealiseerd als mono-arrays, bestaande uit identieke apparaten die in dezelfde vrijheidsgraad opereren. Hoewel deze benadering ontwerp en besturing vereenvoudigt, kan zij de flexibiliteit in array-ontwerp beperken en de hydrodynamische en economische prestaties op arrayschaal beperken.

Dit proefschrift introduceert en onderzoekt systematisch het concept van gemengde wave energy arrays, waarin verschillende typen WEC's, die in uiteenlopende vrijheidsgraden opereren, binnen één array worden gecombineerd. De centrale hypothese is dat het combineren van apparaten met complementaire hydrodynamische eigenschappen invloed kan hebben op de energieopname op arrayschaal, het richtingsafhankelijke gedrag en de techno-economische prestaties ten opzichte van conventionele mono-arrays. Door verschillen in resonantiegedrag, stralingskarakteristieken en golf–structuurinteracties te benutten, kunnen gemengde arrays alternatieve ontwerproutes bieden waarbij energieopbrengst, ruimtegebruik en kosten in samenhang worden beschouwd.

Het proefschrift start met de ontwikkeling van een nauwkeurig en rekenkundig efficiënt numeriek raamwerk voor de analyse van het hydrodynamische gedrag van zowel mono- als gemengde WEC-arrays. Hiertoe wordt de HAMS–MREL-oplosser geformuleerd, uitgebreid en gevalideerd voor multi-body systemen met meerdere vrijheidsgraden. Het model houdt expliciet rekening met golf–structuurinteracties, array-effecten en richtingsafhankelijke golfbelasting, waardoor een consistente en systematische analyse mogelijk is van zowel individuele apparaten als arrays met toenemende complexiteit. Validatie aan de hand van analytische oplossingen, experimentele data en gevestigde numerieke modellen, in combinatie met parallelle implementaties, toont de geschiktheid van het raamwerk voor analyses op arrayschaal aan.

Vervolgens wordt dit modelraamwerk toegepast om het hydrodynamische gedrag van mono- en gemengde arrays te onderzoeken en te vergelijken in zowel ondiep als diep water. Een breed scala aan arrayconfiguraties wordt beschouwd onder regelmatige en onregelmatige golfcondities, waardoor de invloed van apparaattype, onderlinge afstand, lay-out en golfinvalshoek kan worden geanalyseerd. Deze studies bieden inzicht in hoe hydrodynamische interacties en richtingsafhankelijke effecten verschillen tussen mono- en gemengde arrays en hoe deze verschillen het gedrag op arrayschaal beïnvloeden onder uiteenlopende operationele omstandigheden.

Ten slotte worden de hydrodynamische analyses geïntegreerd met een techno-economische beoordeling van wave energy arrays. Op basis van representatieve kostenmodellen en locatie-onafhankelijke aannames wordt de levelised cost of energy van mono- en gemengde arrays geëvalueerd, samen met ruimtelijke prestatie-indicatoren zoals de benodigde oppervlakte van de array. Deze gecombineerde benadering maakt een consistente vergelijking mogelijk van verschillende arrayconcepten en belicht de afwegingen tussen energieproductie, ruimtelijke efficiëntie en economische prestaties in diverse inzetcontexten.

In het geheel tonen de bevindingen van dit proefschrift aan dat gemengde wave energy arrays een levensvatbaar alternatief vormen voor conventionele mono-technologie-implementaties en relevante aandacht verdienen bij het ontwerp van toekomstige wave energy parken. Door hydrodynamisch gedrag, ruimtelijke kenmerken en techno-economische implicaties gezamenlijk op arrayschaal te beschouwen, biedt dit werk een gestructureerd

raamwerk voor de evaluatie van wave energy arrays van de volgende generatie. De ontwikkelde modelleringsinstrumenten en inzichten vormen een basis voor toekomstig onderzoek naar optimalisatie, integratie van besturing en locatie-specifieke beoordelingen gericht op het bevorderen van de commerciële haalbaarheid van wave energy.

# NOMENCLATURE

The following nomenclature is used throughout this dissertation. Symbols are grouped by category for clarity.

## ROMAN SYMBOLS

| Symbol | Description | Units |
|---|---|---|
| $a_0$ | Diameter | m |
| $A$ | Wave amplitude; cross-sectional area | m; $m^2$ |
| $A_D$ | Projected area for drag calculation | $m^2$ |
| $A_0$ | Horizontal area of free surface (waterplane) | $m^2$ |
| $A_{\text{arr}}$ | Total array spatial footprint | $km^2$ |
| $A_{js}^{(k)(q)}$ | Added mass: $j$-th DOF of body $k$ due to motion $s$ of body $q$ | Varies |
| $b_a(\omega)$ | Radiation damping coefficient (heave) | N s/m |
| $b_v$ | Linearised viscous damping coefficient (heave) | N s/m |
| $b_{\text{PTO}}(\omega)$ | PTO damping coefficient (heave) | N s/m |
| $B_a(\omega)$ | Radiation damping coefficient (pitch) | N m s/rad |
| $B_v$ | Linearised viscous damping coefficient (pitch) | N m s/rad |
| $B_{\text{PTO}}(\omega)$ | PTO damping coefficient (pitch) | N m s/rad |
| $B_{js}^{(k)(q)}$ | Radiation damping: $j$-th DOF of body $k$ due to motion $s$ of body $q$ | Varies |
| $C$ | Characteristic device dimension (mixed arrays) | m |
| $c_h$ | Hydrostatic stiffness coefficient (heave) | N/m |
| $C_h$ | Hydrostatic stiffness coefficient (pitch) | N m/rad |
| $C_{33}$ | Hydrostatic restoring coefficient (heave) | N/m |
| $C_D$ | Drag coefficient | – |
| $C_{NL}$ | Nonlinear (quadratic) damping coefficient | N m $s^2$/$rad^2$ |
| $D$ | Device diameter | m |
| $d$ | Real part of intrinsic impedance; water depth | N s/m; m |
| $e$ | Imaginary part of intrinsic impedance | N s/m |
| $E_j^{(k)}$ | Wave excitation force on $j$-th DOF of body $k$ | N |
| $f_e(\omega)$ | Heave excitation force | N |
| $F_B(t)$ | Buoyancy force (time domain) | N |
| $F_{\text{exc}}(t)$ | Wave excitation force (time domain) | N |
| $F_{\text{PTO}}(\omega)$ | PTO force | N |
| $F_{\text{rad}}(t)$ | Radiation force (time domain) | N |
| $g$ | Gravitational acceleration ($= 9.81$) | $m/s^2$ |
| $G(\xi; \mathbf{x})$ | Green's function | Varies |
| $h$ | Water depth | m |
| $H$ | Wave height; hybrid factor (H-factor) | m; – |
| $H_s$ | Significant wave height | m |
| $I$ | Moment of inertia | kg $m^2$ |
| $I_a(\omega)$ | Frequency-dependent added moment of inertia (pitch) | kg $m^2$ |
| $I_d$ | Dry (structural) moment of inertia | kg $m^2$ |
| $J_5$ | Second moment of waterplane area (pitch, mode 5) | $m^4$ |
| $J_7$ | Second moment of waterplane area (pitch, mode 7) | $m^4$ |

| Symbol | Description | Units |
|---|---|---|
| $K$ | Stiffness; stiffness matrix | N/m;Varies |
| $K_d$ | Disturbance coefficient ($= \lvert\eta_{\text{total}}\rvert / \lvert\eta_{\text{inc}}\rvert$) | – |
| $k_p$ | Complex pressure–velocity coefficient | – |
| $L$ | Wavelength; characteristic device length (attenuator) | m |
| $L_s$ | Submergence depth (flap) | m |
| $L_{AE}$ | Lever arm from hinge to force application point | m |
| $m$ | Body mass; number of PA devices in farm | kg; – |
| $m_a(\omega)$ | Frequency-dependent added mass (heave) | kg |
| $m_d$ | Dry (structural) mass | kg |
| $m_{-1}$, $m_0$ | Spectral moments of order $-1$ and 0 | Varies |
| $M$ | Number of bodies; M-factor | – |
| $M_e(\omega)$ | Pitch excitation moment | N m |
| $M_{\text{PTO}}(\omega)$ | PTO moment (pitch) | N m |
| $n$ | Number of devices; project lifetime; outward normal | –; yr; – |
| $N$ | Number of DOFs; number of frequencies | – |
| $N_p^T$ | Total number of panels (mesh) | – |
| $N_{\text{PA}}$ | Number of Point Absorber devices | – |
| $N_{\text{fl}}$ | Number of flap devices | – |
| $N_{\text{att}}$ | Number of attenuator devices | – |
| $P(\omega)$ | Absorbed power at frequency $\omega$ | W |
| $P_{\text{abs}}$ | Average mechanical power absorbed | W |
| $P_{\text{inc}}$ | Incident wave power per unit crest width | kW/m |
| $P_{\text{inst}}$ | Installed capacity | MW |
| $P_{\text{irr}}$ | Power absorbed under irregular waves | W |
| $P_{\text{net},\eta}$ | Net electrical power (with PTO efficiency $\eta$) | W |
| $P_{\text{rated}}$ | Rated (maximum) power | kW |
| $\bar{P}_{\text{BOX}}$ | Period-averaged hydrodynamic power extracted | W |
| $\bar{P}_w$ | Period-averaged incident wave power | W |
| $P_{\text{OWC}}$ | Air pressure inside OWC chamber | Pa |
| $q$ | Interaction factor (q-factor) | – |
| $r$ | Discount rate; radial distance; lever arm | –; m; m |
| $R$ | Distance between source and field point | m |
| $S(\omega)$ | Wave spectral density | $\text{m}^2\,\text{s}$ |
| $S_B^{(k)}$ | Immersed (wetted) surface of body $k$ | $\text{m}^2$ |
| $S_j^{(k)}$ | Shape function for $j$-th DOF of body $k$ | – |
| $S_{\text{WP}}^{(k)}$ | Waterplane surface of body $k$ | $\text{m}^2$ |
| $T$ | Wave period; kinetic energy | s; J |
| $T_d$ | Damped natural period | s |
| $T_e$ | Energy period | s |
| $T_n$ | Natural (undamped) period | s |
| $T_p$ | Peak spectral period | s |
| $u_j$, $v_j$, $w_j$ | Cartesian components of shape function | – |
| $V$ | Potential energy | J |
| $W$ | Device width (flap/attenuator) | m |
| $x$, $y$, $z$ | Cartesian coordinates (global) | m |
| $x_l$, $y_l$, $z_l$ | Cartesian coordinates (local, body-fixed) | m |
| $x_d$, $y_d$, $z_d$ | Cartesian coordinates (deformed frame) | m |
| $\mathbf{x}$ | Position vector | m |
| $\mathbf{n}^{(k)}$ | Outward unit normal to body $k$ | – |

## GREEK SYMBOLS

| Symbol | Description | Units |
|---|---|---|
| $\alpha$ | PTO damping control variable | – |
| $\beta$ | Wave incidence angle (relative to $x$-axis) | rad or ° |
| $\gamma$ | Spectral peaking factor; symmetry transformation factor | – |
| $\zeta$ | Complex displacement amplitude (generalised coordinate) | m or rad |
| $\zeta_1$ | Surge displacement | m |
| $\zeta_3$ | Heave displacement | m |
| $\zeta_5$ | Pitch rotation (global or forearm) | rad |
| $\zeta_7$ | Rear-arm pitch rotation (flex DOF) | rad |
| $\zeta_{\max}$ | Maximum displacement constraint | m |
| $\zeta_j^{(k)}$ | Complex amplitude for $j$-th DOF of body $k$ | m or rad |
| $\eta$ | Free-surface elevation; PTO conversion efficiency | m; – |
| $\eta_D$ | Free-surface elevation due to diffraction | m |
| $\eta_{\text{mixed}}$ | Capture-width ratio (mixed array) | m |
| $\theta$ | Rotation/pitch angle; wave direction | rad or ° |
| $\bar{\theta}$ | Normalised flap rotation amplitude (RAO) | – |
| $\lambda$ | Wavelength; eigenvalue | m; rad$^2$/s$^2$ |
| $\lambda_r$ | Real part of complex eigenvalue | – |
| $\lambda_i$ | Imaginary part of complex eigenvalue | – |
| $\mu$ | Deep-water wavenumber ($= \omega^2/g$) | 1/m |
| $\nu$ | Wavenumber (real positive root of dispersion equation) | 1/m |
| $\rho$ | Fluid (water) density | kg/m$^3$ |
| $\sigma_u$ | Standard deviation of velocity | m/s |
| $\tau$ | Wave period (alternative notation) | s |
| $\tau_A$ | Excitation torque about hinge point $A$ | N m |
| $\phi$ | Velocity potential; eigenmode shape | m$^2$/s; – |
| $\phi_D$ | Diffraction potential | m$^2$/s |
| $\phi_I$ | Incident wave potential | m$^2$/s |
| $\phi_R$ | Radiation potential | m$^2$/s |
| $\phi_S$ | Scattered potential | m$^2$/s |
| $\phi_j^{(k)}$ | Radiation potential for $j$-th DOF of body $k$ | m$^2$/s |
| $\hat{\phi}$ | Normalised eigenvector | – |
| $\varphi$ | Phase angle; velocity potential (alternative notation) | rad; m$^2$/s |
| $\omega$ | Angular (radial) frequency | rad/s |
| $\omega_d$ | Damped angular frequency | rad/s |
| $\omega_n$ | Natural angular frequency | rad/s |

## MATRICES AND VECTORS

| Symbol | Description | Units |
|---|---|---|
| $\mathbf{M}_d$ | Structural (dry) mass matrix | kg |
| $\mathbf{M}_a(\omega)$ | Added-mass matrix | kg |
| $\mathbf{B}_a(\omega)$ | Radiation-damping matrix | N s/m |
| $\mathbf{B}_v$ | Linearised viscous-damping matrix (diagonal) | N s/m |
| $\mathbf{B}_{\text{PTO}}(\omega)$ | PTO-damping matrix | N s/m |
| $\mathbf{C}_h$ | Hydrostatic stiffness matrix | N/m |
| $\mathbf{F}_e(\omega)$ | Excitation force/moment vector | N or N m |

*Matrices and Vectors (continued)*

| Symbol | Description | Units |
|---|---|---|
| $\boldsymbol{\zeta}(\omega)$ | Response-amplitude (RAO) vector | m or rad |
| $\mathbf{Z}(\omega)$ | Intrinsic impedance matrix | Varies |
| $\mathbf{Z}_{\text{PTO}}(\omega)$ | PTO impedance matrix | Varies |
| $\mathbf{H}$ | Total impedance matrix | Varies |
| $[\widehat{A}]$ | Symmetry-transformed system matrix | – |
| $[R]$ | Symmetry transformation matrix | – |

## OPERATORS AND SPECIAL NOTATION

| Symbol | Description |
|---|---|
| $\nabla^2$ | Laplacian operator ($\partial^2/\partial x^2 + \partial^2/\partial y^2 + \partial^2/\partial z^2$) |
| $\partial/\partial n$ | Normal derivative at body surface |
| $\text{Re}(\cdot)$ | Real part of a complex quantity |
| $(\cdot)^*$ | Complex conjugate |
| $\lvert\cdot\rvert$ | Absolute value / magnitude |
| $i$ (or $j$) | Imaginary unit ($\sqrt{-1}$) |
| $\mathcal{L}$ | Lagrangian |
| $\mathbb{R}$ | Set of real numbers |

## SUBSCRIPTS AND SUPERSCRIPTS

| Notation | Description |
|---|---|
| $(\cdot)_j$ | $j$-th degree of freedom ($j = 1, \ldots, 6$ for rigid-body modes) |
| $(\cdot)^{(k)}$ | Quantity associated with body $k$ |
| $(\cdot)_D$ | Diffraction component |
| $(\cdot)_I$ | Incident-wave component |
| $(\cdot)_R$ | Radiation component |
| $(\cdot)_S$ | Scattered component |
| $(\cdot)_a$ | Added (hydrodynamic) quantity |
| $(\cdot)_d$ | Dry (structural) quantity; damped quantity |
| $(\cdot)_h$ | Hydrostatic quantity |
| $(\cdot)_n$ | Natural (undamped) quantity |
| $(\cdot)_{\text{exc}}$ | Excitation quantity |
| $(\cdot)_{\text{rad}}$ | Radiation quantity |
| $(\cdot)_{\text{PTO}}$ | Power Take-Off quantity |
| $(\cdot)_{\text{arr}}$ | Array quantity |
| $(\cdot)_T$ | Total (summed over all bodies/panels) |
| $(\cdot)_{\text{WP}}$ | Waterplane quantity |

## DIMENSIONLESS PERFORMANCE METRICS

| Symbol | Description |
|---|---|
| $q$ | Interaction factor (q-factor): ratio of array power to the sum of isolated-device powers; $q > 1$ indicates constructive interaction |

| | |
|---|---|
| $H$ | Hybrid factor (H-factor): ratio of mixed-array power to the best-performing mono-array power |
| $M$ | Mixed factor (M-factor): geometry-normalised capture-width efficiency metric; $M > 1$ indicates more power per unit width than devices in mono-arrays |
| CWR | Capture Width Ratio: ratio of absorbed power to incident power per unit crest width |
| $K_d$ | Disturbance coefficient: ratio of total to incident free-surface elevation |

## ECONOMIC PARAMETERS

| Symbol | Description | Units |
|---|---|---|
| LCOE | Levelised Cost of Energy | €/MWh |
| CAPEX | Capital Expenditure | M€/MW |
| OPEX | Operational Expenditure | % of CAPEX/yr |
| AEP | Annual Energy Production | MWh/yr |
| CF | Capacity Factor | % |
| CRF | Capital Recovery Factor $= r(1+r)^n/[(1+r)^n - 1]$ | – |
| FoM | Figure of Merit (packing density / LCOE) | MWhrkm$^2$/€ |
| $r$ | Discount rate | – |
| $n$ | Project lifetime | yr |

## ABBREVIATIONS AND ACRONYMS

| Abbreviation | Description |
|---|---|
| BEM / BIEM | Boundary Element Method / Boundary Integral Equation Method |
| BIE | Boundary Integral Equation |
| CAPEX | Capital Expenditure |
| CCC | Complex Conjugate Control |
| CFD | Computational Fluid Dynamics |
| CWR | Capture Width Ratio |
| DOF | Degree(s) of Freedom |
| EKF | Extended Kalman Filter |
| GCS | Global Coordinate System |
| GMRES | Generalised Minimal Residual (iterative linear solver) |
| HAMS | Hydrodynamic Analysis of Marine Structures (open-source BEM solver) |
| HAMS-MREL | HAMS-Marine Renewable Energies Lab |
| IR | Irregular Frequency |
| KC | Keulegan–Carpenter number |
| LCOE | Levelised Cost of Energy |
| LCS | Local Coordinate System |
| LU | LU decomposition (direct linear solver) |
| MPC | Model Predictive Control |
| MSE | Mean Square Error |
| NLFK | Nonlinear Froude–Krylov (force) |
| NLH | Nonlinear Hydrostatics |
| NRMSE | Normalised Root Mean Square Error |
| OpenMP | Open Multi-Processing (parallelisation framework) |

| Abbreviation | Description |
|---|---|
| OPEX | Operational Expenditure |
| OWC | Oscillating Water Column |
| OWSC | Oscillating Wave Surge Converter |
| PA | Point Absorber |
| PTO | Power Take-Off |
| RAO | Response Amplitude Operator |
| RSS | Regular Sea State |
| SAE | Simple And Effective |
| ASAE | Array SAE (array-level extension of SAE) |
| SPH | Smooth Particle Hydrodynamics |
| TRL | Technology Readiness Level |
| WEC | Wave Energy Converter |

# 1

# INTRODUCTION

*Wave energy represents a highly predictable and largely untapped renewable resource with the potential to contribute significantly to future low-carbon electricity systems, particularly in coastal and island regions. Realising this potential at utility scale requires wave energy converters to be deployed in arrays, where hydrodynamic interactions between devices play a critical role in determining power production, spatial footprint, and overall economic performance. This chapter presents the research background and motivation for the thesis, which focuses on the numerical modelling of wave energy arrays, with a particular emphasis on the transition from conventional mono-type arrays to mixed arrays. The state of the art in wave energy array modelling is first reviewed, followed by a clear definition of the scope of the work, the research methodology adopted in this thesis and its novel contributions.*

1

The global population has increased from 2.5 billion people in 1950 to over 8 billion by the end of 2022, wherein3 billion of these have been added were since 1998. The world's population is expected to rise to 9.7 billion in 2050 [1]. With the world's population growing rapidly, dependence only on fossil fuels is no longer a viable option. Therefore, development of more renewable forms of energy, particularly marine renewables has gained traction in the last two decades.

Wave energy has immense potential and could theoretically provide at least twice the amount of electricity currently being produced globally, owing to its high energy density [2, 3]. Compared to other dominant renewable energy sources such as wind and solar, wave energy exhibits a substantially higher power density, typically in the range of 2–3 kW/m$^2$, compared to approximately 0.4–0.6 kW/m$^2$ for wind and 0.1–0.2 kW/m$^2$ for solar energy [4, 5] (the usage of kW/m$^2$ is to be able to compare different renewable energy sources). In addition to the abundance of the resource, ocean waves are more predictable and exhibit greater temporal availability throughout the year than many other renewable sources. These characteristics have motivated ambitious policy initiatives, with the European Union setting deployment targets of 1 GW of wave energy capacity by 2030 and 40 GW by 2050 [6].

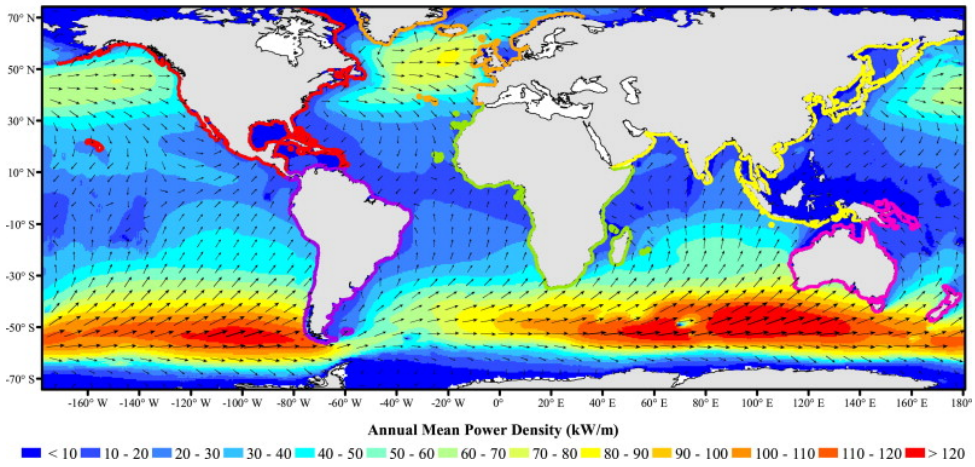



Figure 1.1.: The global wave energy potential across the globe [7]

Figure 1.1 shows the global wave energy potential across the globe [7]. The UK leads in wave energy potential, followed by United States, Chile, Australia, and Portugal. In order to attain these capacities, the technological advances need to accelerate, and policy developments need to be conducive.

## 1.1. WAVE ENERGY CONVERTERS

While there are many ways of classifying WECs, the primary energy conversion principle is used here to showcase different types of WECs [8]. The devices can be hence classified as potential energy, kinetic energy or mechanical energy-based devices.

### OVERTOPPING DEVICES (POTENTIAL ENERGY)

Overtopping wave energy converters extract energy from the potential energy of waves by allowing them to run up a sloped structure and spill into one or more elevated reservoirs. The collected water creates a hydraulic head that drives low-head turbines as it is released back to the sea. These devices are typically floating or shore-mounted and rely largely on mature hydropower technologies, resulting in reduced technical

risk and relatively smooth power output due to the buffering effect of the reservoir. However, their large structural footprint, high material requirements, and sensitivity to wave climate can limit efficiency and deployment flexibility.

An example of this WEC includes the Wave Dragon (see Figure 1.2), which is floating type overtopping structure.

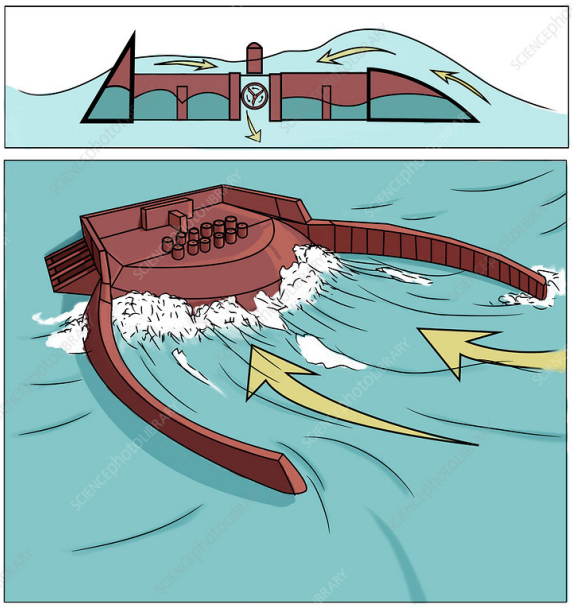


Figure 1.2.: WaveDragon Overtopping WEC (Credit: Spencer Sutton)

### OSCILLATING WATER COLUMN DEVICES (KINETIC ENERGY)

Oscillating Water Column (OWC) devices convert wave-induced pressure and kinetic energy using a partially submerged chamber that is open below the free surface. Incoming waves cause the internal water column to oscillate, compressing and decompressing the air trapped above it, which is forced through an air turbine connected to a generator. OWCs benefit from having only one moving component, the turbine, which is not in direct contact with seawater, simplifying maintenance and improving survivability. Their main limitations arise from relatively low time-averaged turbine efficiency and strong sensitivity to chamber geometry and wave frequency.

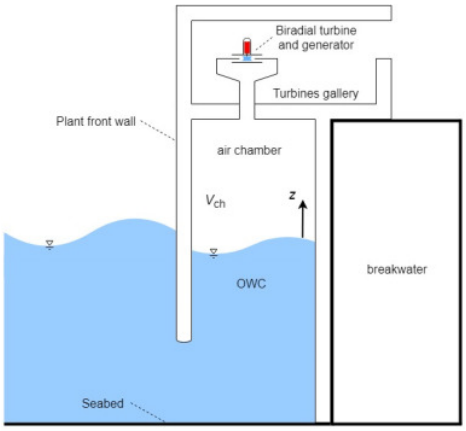
An example of this is the Mutriku OWC multi-chamber WEC (see Figure 1.3) integrated with the breakwater located in Bay of Biscay, Mutriku, Spanish Basque Country.

### FLEXIBLE MEMBRANE DEVICES(KINETIC ENERGY)

Flexible membrane WECs extract energy through the deformation of lightweight elastic structures subjected to wave-induced pressure variations. Changes in shape or volume of the membrane are converted into useful power via an associated power take-off system. These devices offer potential advantages in terms of reduced structural loads, improved survivability, and lower transportation and installation costs. However, uncertainties related to long-term material durability and limited operational experience mean that flexible membrane concepts remain at an early stage of technological development.



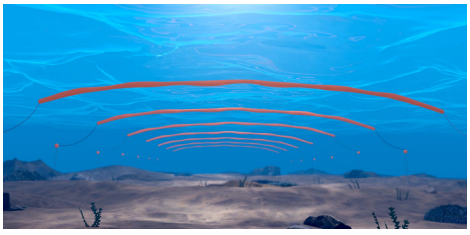

(a) Mutriku breakwater-integrated OWC wave energy plant.



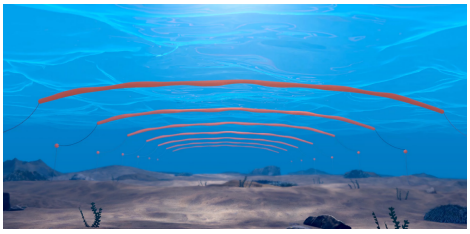

(b) Schematic of the Mutriku OWC showing the air chamber and bidirectional turbine [9]

Figure 1.3.: Mutriku Oscillating Water Column (OWC) wave energy converter: (a) breakwater-integrated installation and (b) schematic representation of the operating principle.

An example of this is the S3 WEC from SBM Offshore (see Figure 1.4). The SBM S3 WEC is a fully submerged, flexible membrane device that extracts energy from wave-induced pressure variations below the free surface. Incident waves deform the compliant structure, inducing motion of the fluid in the flexible membrane, that is converted into electricity via an internal power take-off system, while the submerged configuration enhances survivability and eliminates visual impact.



(a) Illustration of a S3 WEC [10]



(b) Laboratory-scale experimental model of a S3 WEC expanding under wave excitation

Figure 1.4.: S3 WEC

### POINT ABSORBERS (MECHANICAL ENERGY)

A point absorber is a type of WEC characterised by its small horizontal dimensions relative to the wavelength of the incoming waves. Typically resembling a large buoy, this device floats on the ocean surface or is submerged just below it, capturing energy from the vertical rise and fall (heave) of the waves. As the buoy moves relative to a stationary base or a secondary floating component, it drives a power take-off system—such as a hydraulic piston or a linear generator—to convert mechanical motion into electricity. Because they are "point" sources, they can capture energy from waves approaching from any direction, making them highly versatile, though they often require robust mooring systems to withstand extreme storm conditions.



Figure 1.5.: Corpower C4 PA device [11]

An example of this is Corpower C4 device (see Figure 1.5).

### PRESSURE-DIFFERENTIAL DEVICES (MECHANICAL ENERGY)

Pressure-differential devices harness energy from wave-induced pressure variations below the free surface by driving the motion of submerged or near-bottom floaters. Their fully or partially submerged configuration enhances survivability and eliminates visual impact, making them attractive for environmentally sensitive areas. However, installation, inspection, and maintenance operations are more complex and costly due to limited accessibility, which can offset some of the operational advantages.

An example of this is the Symphony WEC (see Figure 1.6).

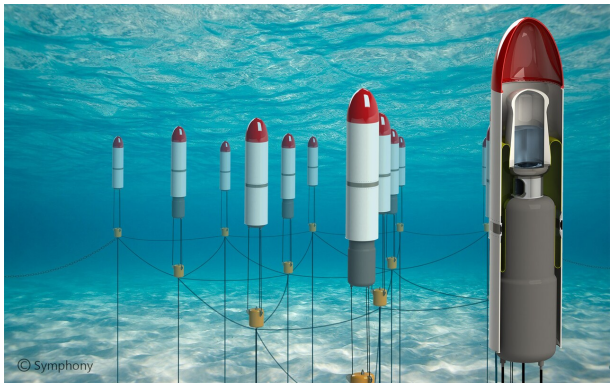



Figure 1.6.: Symphony pressure differential WEC

1

### OSCILLATING WAVE SURGE CONVERTERS (MECHANICAL ENERGY)

Oscillating Wave Surge Converters (OWSCs) or flaps consist of pitching flaps mounted on the seabed in shallow water, where they are driven by the horizontal surge motion of water particles. Anchored and hinged at the bottom, these devices exploit nearshore wave energy while experiencing lower loads than offshore systems. Their proximity to shore simplifies installation and maintenance, although reduced wave energy levels and potential conflicts with other coastal activities can restrict suitable deployment sites.

An example of this is the Waveroller WEC (see Figure 1.7).



Figure 1.7.: Waveroller flap WEC

### ATTENUATOR DEVICES (MECHANICAL ENERGY)

Attenuators are long, floating, multi-segment devices aligned parallel to the dominant wave direction. Energy is extracted from the relative pitch motion between hinged sections as waves propagate along the device. This configuration reduces wave loading compared to terminator devices such as flaps and provides inherent power limiting under extreme sea states, improving survivability. Attenuators are well suited for offshore deployment, although their mechanical complexity and joint reliability are important design considerations.

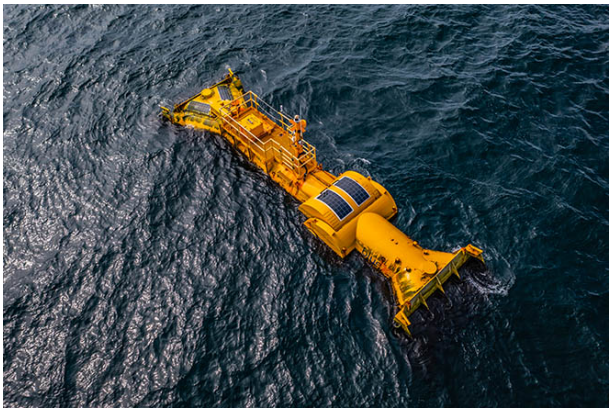


Figure 1.8.: Mocean Blue-X attenuator

An example of this is the Mocean Blue-X WEC (see Figure 1.8), which is a two-body attenuator.

## 1.2. RESEARCH BACKGROUND AND MOTIVATION

Despite the diversity of concepts outlined above, wave energy has yet to reach commercial maturity. The challenges that continue to impede widespread deployment are discussed in the following section, and form the motivation for the work presented in this thesis.

### CURRENT ECONOMIC STATUS OF WAVE ENERGY DEVICES

The current economic landscape for WECs is characterised by high capital intensity and a wide range of Levelised Cost of Energy (LCOE) estimates, reflecting the technology's pre-commercial status relative to mature renewables [12, 13]. Initial Capital Expenditure (CAPEX) for WECs varies significantly by depth and device type, generally estimated between €2.5 million and €6.0 million per MW [13]. Recent energy system modelling specifically assigns initial costs of €5 million/MW for far-shore devices, €4 million/MW for nearshore, and €3 million/MW for shallow water applications [14]. Consequently, the LCOE for wave energy device remains high, typically spanning €180 in high resource regions such as Ireland to €1600/MWh in the US [15].

When compared to proven offshore technologies such as offshore wind, wave energy is still significantly more expensive, primarily due to the lack of convergence on a dominant design and economies of scale. Studies place the LCOE of offshore wind at approximately €101/MWh [13, 16] in high energy seas. In comparison to floating solar, which has an estimated installation cost of €10 million/MW (ranging €6–16 million/MW depending on wave exposure) [14], wave energy is a viable option. In medium to low resource regions such as the North Sea, offshore solar is estimated to have an LCOE between €203 - €407/MWh [17].

In order to achieve these set EU targets with low LCOE, WECs need to be deployed in large numbers (arrays). Utilising arrays of WEC devices, the LCOE can be lowered to the range of €160/MWh to €400/MWh [13]. Optimal device selection in moderate resources could potentially further lower this to between €60 and €150/MWh under favourable financial discount rates [12].

### CURRENT CHALLENGES FOR THE WAVE ENERGY INDUSTRY

The high LCOE of WECs is attributable to by a number of challenges which the industry is currently facing:

- The design of WECs requires an accurate understanding of the complex physics of wave-structure interaction which tends to make the design overly conservative. With highly variable and non-linear loads (Hydrostatic, viscous, mooring etc) acting on WECs particularly in medium to high sea states, WECs need to have a broad bandwidth of absorption while being able to withstand storm conditions.

- Over a thousand WEC concepts currently exist [18] with a majority of them being far from pre-commercialization. Research and Development usually requires rigorous testing for a few years before commercial deployability is possible. Full-scale prototypes are expensive, with a number of projects failing at the testing/initial deployment phase [19].

- WECs must survive in harsh seawater environments for prolonged periods of time, which imposes stringent requirements on structural integrity, materials, and system reliability. Continuous exposure to corrosion, biofouling, cyclic wave loading, and extreme weather events can significantly degrade performance and accelerate fatigue damage. As a result, conservative design margins are often adopted to ensure survivability, leading to increased structural mass and higher

capital expenditure. In addition, the need for robust mooring systems, corrosion protection, and regular inspection and maintenance further increases complexity and operational costs, particularly for devices deployed in remote or offshore locations.

### MONO TO MIXED ARRAYS

Many WEC devices including the Corpower C4 point absorber device [11] and AW WaveRoller oscillating surge device [20], alongside others, are on their way to commercial deployment with arrays. The HiWave-5 project from Corpower is set to test a 4 WEC array (One C4 and three C5 WECs) off the coast of Agucadoura, Northern Portugal [21]. The Ondas de Peniche (ONDEP) project aims to deploy a 2 MW wave energy array featuring four Waveroller WECs off the coast of Peniche, Portugal in the next five years [22]. Therefore, research focused on the study of such devices, particularly in wave arrays has become highly relevant. This requires computationally efficient tools that can capture wave-structure hydrodynamic interactions considering multiple bodies.

Mono-arrays refer to arrays of the same device with the same geometry, size and structural properties deployed in multiple numbers (>1). These are currently the most commonly studied arrays, whether it is academic research or commercial deployment (Some examples were given earlier). There are a number of experimental and numerical studies focused on the hydrodynamics, power production and optimization of mono-arrays with PAs ([23–41]), flaps ([42, 43]), attenuators ([27, 44]) and OWCs [45]. The employed hydrodynamic models for the WECs vary from low fidelity frequency domain models with Boundary Integral Equation Method (BIEM) to high fidelity Computational Fluid Dynamics (CFD) models such as Smooth Particle Hydrodynamics (SPH).

Going a step further, being able to derive more power from the same number of devices over a range of periods will increase the energy density per unit area obtained from WECs, thus making wave energy more efficient. Therefore, numerical investigations have also been extended to 'heterogeneous' and 'hybrid' wave arrays.

Heterogeneous wave arrays employ the same type of wave energy converter while changing the size, or draft or a combination of both. Goteman [46] studied arrays with cylindrical PAs, with varying diameters with and without moonpools. The analytical method based on multiple scattering method utilizing the hydrodynamic coefficients from WAMIT was used for assessing the hydrodynamics. When studying arrays of four devices, it was found that considering two cylinders with moonpool and two without (varying the inner/outer radius) gave 2.9% more power than mono arrays with one type of device. Furthermore, arrays of 12 devices were investigated with different diameters with 1000 different layouts. The difference in power absorption between the best and worst layout was found to be 23 %. Ermakov et al. [47] investigated the optimization of heterogeneous arrays using a control co-design approach, utilizing the enforcement of displacement constraints in the frequency domain. The methodology was utilized for 3 to 5 cylindrical point absorber devices considering multi-directional wind and ocean waves. Results showed that the improvements in power production could be up to 37% to 72.2% from 3 to 5 WECs. Abdulkadir et al. [48] performed a frequency domain based optimization of heterogeneous arrays (varying diameter) of cylindrical devices using a time domain model with Power-Constrained Bang-Singular-Bang (PCBSB) control. Detailed simulation of homogeneous and heterogeneous arrays showed an average performance improvement of 6.6%, 20.02% and 9.71% for 3,5 and 7 devices for a representative wave period of 6 s and wave height of 0.82 m.

'Hybrid' arrays were investigated in the work of Zheng et al. [45], which analyses the performance of arrays comprising of cylindrical PAs and cylindrical OWCs with varying diameters/drafts. Hybrid arrays of 4 devices with 2 PA and 2 OWCs were investigated and evaluated using the *H*-factor, that shows if the hybrid array is more constructive or destructive compared to the mono-array by taking the ratio of the power produced by a hybrid array to a mono-array. For some wave periods, *H*-factor as high as 1.6 were obtained for the hybrid arrays. The *H*-factor is also used later in the current study.

This thesis thus introduces mixed arrays, a concept that is entirely new, in which different types of wave energy converters operating in distinct degrees of freedom are deployed within the same array. Wolgamot et al. [26] briefly investigated an optimised array of three devices (an ellipsoid, an elliptical cylinder, and a hemisphere) operating in heave, surge, and sway, respectively, under regular waves. Their study focused on the influence of wave directionality on array power production; however, performance gains relative to equivalent mono-type arrays were not quantified. Particular emphasis is placed on closely spaced configurations, reflecting the practical importance of maximising energy yield while minimising spatial footprint.

### NUMERICAL MODELLING OF WEC ARRAYS

The methods currently used to analyse the hydrodynamics of WEC arrays include analytical, semi-analytical and numerical methods. Analytical methods, though accurate, suffer from a major drawback of being applicable to only the simplest of geometries [49].

Semi-analytical methods involve a combination of numerical and analytical techniques and have been widely used in literature. Child et al. [36] used direct matrix analytical method to optimize array of cylinders, where the hydrodynamics of the individual WECs could be determined numerically. Mcnatt et al. [27] utilized the multiple scattering wave theory developed by Kagemoto and Yue to the diffraction transfer matrix method. This method utilizes the hydrodynamic coefficients from a BIEM solver to obtain the wave fields from a single device and extends this to an array.

Renzi and Dias [50] develop a semi-analytical linear potential-flow model for an infinite periodic array of flap-type wave energy converters and derive closed-form relations between reflection, transmission, radiation coefficients, and power absorption. The study shows that, unlike heaving point absorbers, flap-type arrays can exploit transverse-mode resonance to achieve high capture factors, with optimal performance occurring when transverse modes are fully trapped by appropriate device spacing. Zheng et al. [45] developed a novel semi-analytical technique to study the interaction of combinations of PAs and OWCs. While these semi-analytical methods are very computationally efficient for arrays with large spacings, it can become inefficient for closely spaced arrays when the evanescent wave modes become important, which these methods neglect (since the computational resources required for this are very high [27]).

Over the last 20 years though, numerical models have become more popular due to availability of large computational resources. These enable the calculation of large number of WECs considering various parameters such as location, sea states, spatial constraints etc. Frequency domain models (BIEM), Time domain models (based on integro-differential Cummins equation), CFD (FEM), Phase averaged wave propagation models (SWAN, MIKE21SW) and Phase-resolving wave propagation models (MILDwave, REFDIF, SWASH) are some of the available numerical methods.

Considering time-domain models based on integro-differential Cummins equation, these are more accurate than the frequency domain models such as BIEM particularly when considering non-linear forces, however when evaluating large arrays, these can be very computationally expensive [51].

Since modelling the hydrodynamic interactions including the influence of radiated waves between structures is very important for understanding array effects, Phase-averaged and Phase-resolving models can be ruled out due to the following limitations [3]. With phase-averaged models when modelling WEC arrays and capturing array effects, the limitation arises due to their coarse mesh and phase independence. Furthermore, the modelled WECs are either assigned specific degree of reflection and transmission or simulated based on a wave-structure solver which makes them more applicable for far-field effects, thus not capturing the complete hydrodynamics of the WECs.

Phase resolving models such as MILDWave or REFDIF can go one step ahead and offer the possibility of coupling with BIEM solvers to capture near-field effects (mainly capturing radiated waves in addition to diffracted waves) which can be used to

evaluate the far-field effects through the phase resolving models. However, WECs are modelled not as physical bodies but as regions of prescribed reflection, transmission and absorption. Hence, device motions, PTO dynamics etc cannot be implemented [52].

CFD solvers such as OpenFOAM, REEF3D and Gerris have been utilized for studying wave-structure interactions [53]. Though highly accurate, they demand much larger computational resources when compared to frequency domain solvers based on BIEM. Hence, it's also seen in literature that CFD methods are only applied to WEC arrays with a few identical WECs. Therefore, frequency domain method based on BIEM form the right balance between accuracy and computational effort even when modelling large arrays.

### CHOICE OF BIEM SOLVER

Frequency-domain numerical tools are widely used in offshore renewable energy research for array-scale analyses due to several key advantages: (a) they provide accurate and reliable predictions at the preliminary design stage, (b) their frequency-dependent hydrodynamic outputs are directly required for coupled time-domain simulations, and (c) they exhibit significantly lower computational cost compared to high-fidelity approaches such as Computational Fluid Dynamics (CFD) [54–56]. Among these methods, Boundary Integral Equation Methods (BIEMs) based on linear potential flow theory have become a standard choice.

A number of well-established commercial BIEM solvers are available, including WAMIT [57], WADAM [58], OrcaWave [59], Hydrostar [60], and ANSYS AQWA [61]. These tools have been extensively validated through code-to-code comparisons, analytical benchmarks, and experimental wave tank studies [62], and are routinely employed for both single-device and array-level hydrodynamic analyses.

In parallel, several non-commercial, in-house BIEM solvers have been developed and applied extensively to wave energy converter (WEC) research. One such solver is DIFFRACT [63], which, although neither commercial nor open source, has played a significant role in advancing multi-body BIEM formulations. Sun et al. [64] employed DIFFRACT to model the three-float M4 WEC as a two-body system and demonstrated accurate predictions of motions and power output under regular waves for small wave heights. The solver was further applied to small linear arrays of three to five M4 devices, where power gains of up to 10% were observed for certain combinations of wave period and direction.

Wolgamot et al. [26] used DIFFRACT to investigate arrays of three axisymmetric WECs in the frequency domain under optimal control assumptions. Their analysis showed that configurations optimized for peak absorption in a given wave direction inevitably experience reduced absorption for other headings. In a subsequent study, Wolgamot et al. [65] extended the application of DIFFRACT to second-order hydrodynamic effects in a square array of four truncated cylinders subjected to monochromatic waves. By exploiting near-trapped modes in shallow water and accounting for both first- and second-order excitation forces, they demonstrated that additional power gains of up to 30% could be achieved.

Another in-house solver is OREGEN-BEM, which incorporates OpenMP parallelization and was introduced by Li and Stansby [66]. The solver was applied to both single- and multi-body systems and validated through cross-comparisons with commercial solvers such as OrcaWave, WAMIT, and WADAM, as well as the open-source solver HAMS [67]. For single-body cases, OREGEN-BEM showed comparable computational performance to WAMIT and HAMS, while for two- and three-body problems it was at least 1.3 times faster than the commercial solvers considered. Li and Stansby [62] further applied OREGEN-BEM to the five-body M4 WEC using analytical constraint equations to represent inter-body connections, demonstrating good agreement with OrcaWave and experimental results across a range of wave periods and array configurations.

OREGEN-BEM has also been coupled with the non-potential flow solver OceanWave3D to form a hybrid linear–nonlinear framework [68]. This approach was used to analyse the dynamics of a single floating buoy, including mooring line effects and mechanical

constraints. Comparisons with experiments showed that linear OREGEN-BEM predictions were sufficiently accurate for moderate wave steepness, while the hybrid framework improved accuracy under more nonlinear conditions.

Alongside commercial and in-house tools, substantial effort has been devoted to the development of open-source BIEM solvers. For multi-body and array-scale simulations, widely used open-source codes include Nemoh 2.x, Nemoh 3.0, and Capytaine. These solvers can compute diffraction and radiation solutions for multiple interacting bodies, providing hydrodynamic coefficients, excitation forces, and wave field quantities such as free-surface elevation and pressure.

Nemoh 2.x [69], developed at École Centrale de Nantes and released in 2014, was the first open-source linear potential flow solver and has since been applied extensively to array studies with experimental and cross-model validation [69–75]. It solves the diffraction and radiation problems using a source distribution formulation and allows computation of first-order hydrodynamic coefficients with a single global symmetry plane. However, Nemoh 2.x does not suppress irregular frequencies and suffers from high computational cost, limited documentation, and the absence of parallelization [76].

Irregular frequencies are numerical artefacts arising from ill-conditioning of the boundary integral equations [77]. They coincide with eigenfrequencies of hypothetical internal sloshing modes obtained from the interior Dirichlet problem [78] and are associated with the interaction between the body waterplane and the free surface [79]. In Nemoh 2.x, additional limitations arise from the use of interpolated Green's function tables, which can require between 64,000 and 200,000 entries depending on the problem size [80], as well as difficulties in modelling thin structures and overlapping panels [80, 81].

Nemoh 3.0 [76], released in 2023, introduced several improvements, including the extended boundary integral method for irregular frequency suppression, enhanced linear solvers (Gauss elimination, LU decomposition, and GMRES), and the computation of second-order loads. Improved interpolation and integration schemes increased accuracy relative to Nemoh 2.x, and validation against the commercial solver Hydrostar demonstrated good agreement. Although Nemoh 3.0 performs better for thin structures, discrepancies remain when compared with WAMIT, and difficulties persist for geometries involving overlapping elements, such as Oscillating Water Columns (OWCs). Additionally, parallelization is not yet implemented.

Capytaine [82] is a Python-based BIEM solver initially derived from Nemoh 2.x. It supports both source and potential formulations and offers multiple linear solvers, including LU-based direct solvers and GMRES-based iterative solvers, with OpenMP parallelization. Recent developments include the implementation of irregular frequency suppression [83]. While Capytaine has been validated for certain multi-body applications, array-scale validation remains limited. Studies within the WECfarm project [84, 85] demonstrated good agreement with experiments for two-WEC arrays, while Herdayanditya et al. [83] validated hydrodynamic coefficients, excitation forces, and pressure wave fields against ANSYS AQWA. Nevertheless, similar to Nemoh, Capytaine still faces challenges when modelling overlapping geometries typical of OWCs.

HAMS [67, 79] is a recently developed open-source BIEM solver that employs Green's function approximations similar to those proposed by Newman. Several studies have demonstrated its high computational efficiency and accuracy. Raghavan et al. [86] showed that HAMS is approximately 2–3 times faster than WAMIT v6.x, twice as fast as Capytaine v1.4, and 10–20 times faster than Nemoh 2.x for representative WEC geometries, while maintaining accuracy comparable to WAMIT. Sheng et al. [80] further showed that HAMS outperforms Nemoh in both accuracy and computational speed, particularly for thin structures and configurations involving overlapping panels, where Nemoh fails to converge.

Additional validation studies, such as those by Uzunoglu et al. [87], demonstrated near-identical hydrodynamic coefficients and RAOs between HAMS and WAMIT for complex geometries including moonpool openings, with similarly close agreement observed in time-domain simulations.

Despite these advantages, HAMS currently lacks several features essential for

comprehensive array-scale analyses, including multi-body hydrodynamic interactions, wave field computations, RAOs, global symmetry planes, irregular frequency suppression, and generalized modes [67, 79, 80]. The inclusion of these capabilities would enable detailed studies of wave interference, shielding effects, array layout optimisation, coupled load and motion prediction, and fatigue analysis. Generalized modes are particularly important for modelling constrained or articulated WECs, such as bottom-hinged flaps and multi-body attenuators, and for hydroelastic analyses of slender structures [88, 89].

With the integration of these features, HAMS would offer a powerful and efficient framework for detailed array-scale analysis and optimisation of wave energy farms and other offshore renewable energy systems.

## 1.3. THESIS OBJECTIVES

Based on the preceding discussion, a systematic evaluation of mixed wave energy converter (WEC) arrays is required, considering power performance, hydrodynamic behaviour, and levelised cost of energy (LCOE), and benchmarking these against equivalent mono-array configurations. Particular emphasis is placed on closely spaced arrays, reflecting the practical need to maximise energy yield while minimising spatial footprint. Since WECs can be deployed in both shallow and deep-water environments, it is essential to investigate combinations of devices that may complement each other hydrodynamically across these depth regimes.

This leads to the primary research objective of this thesis:

**How do mixed WEC arrays perform relative to mono arrays in terms of power absorption, hydrodynamic behaviour, and LCOE in shallow and deep waters?**

Addressing this question requires a numerical modelling framework that is both accurate and computationally efficient for simulations ranging from small to large arrays. Based on the assessment of existing numerical approaches, frequency-domain Boundary Integral Equation Methods (BIEMs) offer the most suitable balance between accuracy and computational efficiency for array-scale analyses. Among the available open-source BIEM solvers, HAMS has demonstrated particularly strong performance, achieving high computational efficiency while maintaining accuracy comparable to the commercial solver WAMIT.

However, to enable detailed array-level studies, HAMS must be extended to incorporate a computationally efficient multi-body interaction framework. In addition, several advanced modelling features are required to fully characterise array behaviour. These include wave field computations to analyse device interactions and shielding effects, suppression of irregular frequencies to improve numerical robustness, global symmetry to further reduce computational cost, and the inclusion of generalised modes to enable the modelling of constrained or articulated devices such as bottom-hinged flaps in shallow water and multi-body attenuators in deep water. These capabilities are particularly important for assessing the performance of mixed arrays composed of different device types.

This motivates the second research question of the thesis:

**Can a multi-body interaction framework be implemented within HAMS that maintains high accuracy while remaining computationally efficient, and can advanced modelling features be incorporated within this extended framework?**

Accordingly, the overarching aim of this thesis is to develop and validate a multi-body extension of HAMS and to apply this framework to a comprehensive assessment of mono and mixed WEC arrays in both shallow and deep-water environments. The performance of these arrays is evaluated in terms of power absorption, hydrodynamic interactions, and LCOE, with the objective of demonstrating under which conditions mixed arrays can outperform mono arrays when all relevant physical and economic factors are considered.

## 1.4. THESIS OUTLINE



The outline of the Thesis is as follows

**Chapter 2: Theory and validation of HAMS-MREL-** Chapter 2 presents the theoretical formulation, numerical implementation, and validation of the HAMS-MREL (Marine Renewable Energies Lab) boundary integral equation solver for multi-body hydrodynamic interaction problems. The chapter introduces the governing equations, boundary conditions, and discretisation strategy for modelling diffraction and radiation effects in arrays of floating bodies. Advanced solver features, including symmetry exploitation, suppression of irregular frequencies, and efficient computation of wave fields and generalized modes, are described. The solver is validated through systematic comparisons against semi-analytical solutions, commercial BIEM and CFD solvers, and experimental measurements, demonstrating its accuracy, robustness, and computational efficiency for array-scale applications.

**Chapter 3: Analysis of mono and mixed arrays in shallow water-** Chapter 3 investigates the hydrodynamic performance of mono and mixed wave energy converter arrays deployed in shallow-water environments. A weakly non-linear frequency-domain framework is employed to model PAs and flap devices under both passive and active control strategies. The chapter analyses the influence of array layout, spacing, wave direction, and control strategy on power absorption, using interaction-based metrics ($q$- and $M$-factors) to quantify constructive and destructive effects. The results highlight the performance advantages of mixed arrays in shallow water, particularly in terms of enhanced energy capture and directional robustness compared to mono arrays.

**Chapter 4: Analysis of mono and mixed arrays in deep water-** Chapter 4 extends the hydrodynamic analysis to deep-water conditions, focusing on arrays composed of point absorbers and attenuator devices. The chapter evaluates the performance of mono and mixed arrays under regular and irregular wave conditions, accounting for spacing, array size, and wave directionality. Device-level and array-level responses are analysed to assess the impact of hydrodynamic interactions on power absorption. The findings demonstrate that mixed arrays retain favourable interaction characteristics in deep water, achieving improved robustness and competitive performance relative to mono arrays across a broad range of operating conditions.

**Chapter 5: Comparative hydrodynamic analysis of mixed and mono arrays-** Chapter 5 provides an in-depth comparative assessment of the hydrodynamic mechanisms governing the performance of mixed and mono arrays in both shallow and deep water. The chapter examines natural frequencies, eigenmodes, cross-coupling strengths between different types of devices,wave-field characteristics and power absorption from individual devices to elucidate the physical origins of constructive and destructive interactions. Wave field visualisations and cross-coupling analyses are used to distinguish interaction regimes across array configurations. This chapter establishes a clear physical interpretation of why mixed arrays outperform mono arrays under specific geometric and wave conditions.

**Chapter 6: Economics of wave energy arrays-** Chapter 6 presents a techno-economic comparison of mono and mixed wave energy arrays, integrating hydrodynamic performance with cost and spatial considerations. Capital and operational expenditures are estimated using depth-dependent cost models, while annual energy production is derived from array-level hydrodynamic simulations. The chapter evaluates levelised cost of energy, capacity factor, packing density, and spatial footprint for shallow- and deep-water deployments. The results demonstrate that mixed arrays offer a favourable balance between energy yield, cost, and spatial efficiency, leading to lower LCOE and improved deployment feasibility compared to mono arrays under realistic constraints.

1

**Chapter 7: Conclusions-** Chapter 7 presents the main findings of the thesis along with the limitations and future work.

## 1.5. NOVEL CONTRIBUTIONS OF THE THESIS

The thesis has the following novel contributions:

- Development and release of HAMS-MREL, an open-source multi-body BIEM solver extending HAMS with multi-body hydrodynamic coupling, free-surface elevation and pressure fields, irregular frequency suppression, global symmetry, generalised modes, WEC-Sim integration, and OpenMP parallelisation (speed-ups of up to 47× on 32 cores), validated against experiments, semi-analytical solutions and WAMIT.
- Introduction and systematic evaluation of the mixed-array concept (arrays combining WECs of different geometries operating in distinct degrees of freedom) as a pathway to exploit complementary hydrodynamic interactions in both shallow and deep water.
- Extensive comparative analysis of mixed and mono arrays of point absorbers, flaps, and attenuators across array layout, spacing, wave direction, number of devices, and control strategy, for two contrasting sites representative of Dutch shallow and Irish deep-water conditions.
- Formulation and application of the Array Simple and Effective (ASAE) active control strategy for mixed arrays, enabling frequency-domain assessment of active control without the computational cost of time-domain co-simulation.
- Proposal of the $M$-factor as a geometry-normalised metric complementary to the $q$-factor, enabling fair comparison of array performance across mixed and mono configurations with devices of different characteristic dimensions.
- In-depth analysis of the underlying hydrodynamic mechanisms (radiation coupling, directional scattering, and multi-modal response) that explain why mixed arrays outperform or underperform mono-device farms.
- First-of-its-kind techno-economic assessment of mixed wave energy arrays, translating hydrodynamic performance into LCOE and packing density at equivalent array capacity and equivalent spatial footprint, and establishing mixed arrays as a spatially efficient, cost-competitive pathway for wave energy deployment.

# 2

# THEORY AND VALIDATION OF HAMS-MREL

*In theory, there is no difference between theory and practice. In practice, there is.*

Yogi Berra

*This chapter presents the formulation, implementation, and validation of HAMS-MREL, a multi-body extension of the open-source HAMS Boundary Integral Equation Method solver for offshore renewable energy applications. The solver enables the analysis of hydrodynamic interactions among multiple floating and fixed bodies in both finite and infinite water depths, and incorporates advanced numerical features including wave-field reconstruction, suppression of irregular frequencies, global symmetry exploitation, and generalized modes for constrained motions. Validation is performed using semi-analytical solutions, cross-model comparisons with the commercial BIEM solver WAMIT and CFD results, and experimental datasets in both the frequency and time domains. Numerical results show close agreement with reference solutions, with mean square errors in computed wave fields below 2% and hydrodynamic coefficients generally within 5% of benchmark values. Experimental comparisons demonstrate good reproduction of measured free-surface elevations, pressures, and device motions, with amplitude deviations typically below 10%. Parallelization and symmetry significantly improve computational efficiency, yielding speed-up factors of up to 47.2 relative to serial, non-symmetric simulations. Overall, the results establish HAMS-MREL as a validated, accurate, and computationally scalable tool for multi-body hydrodynamic analysis of wave energy devices and arrays.*

section 2.1 introduces the numerical formulation leading up to the boundary integral equations governing the multi-body interaction problem, section 2.2 presents the discretization of these integral equations and the solution strategy for the resulting linear algebraic system, section 2.3 describes the advanced solver features implemented in HAMS-MREL, section 2.4 discusses the numerical validation of HAMS-MREL and its advanced features in the frequency domain through semi-analytical solutions and cross-model comparisons with WAMIT across five test cases, together with an assessment of the associated computational resources, section 2.5 presents the experimental validation of HAMS-MREL alongside cross-model validation against the CFD solver OpenFOAM for the case of a rectangular fixed-bottom detached OWC, section 2.6 covers the time-domain validation of HAMS-MREL against experiments by means of WEC-Sim for an array of point absorbers, section 2.7 highlights the main differences between HAMS-MREL and the original HAMS solver. Finally, section 2.8 highlights the main conclusions of this chapter.

## 2.1. FORMULATION OF THE FUNDAMENTAL MULTI-BODY INTERACTION PROBLEMS IN HAMS-MREL

The flow considering multiple bodies with variable geometries within the linear potential flow theory is assumed to be inviscid, irrotational, incompressible and free of flow-separation effects. This is a fluid-structure interaction problem with $M$ bodies (body can be floating or submerged) where the fluid in this case is water (this is shown in Figure 2.1). The flow is described through a total complex spatial velocity potential $\phi(\mathbf{x})$, with $\mathbf{x} : x, y, z$ for all bodies which can be expressed as a combination of three parts: the complex spatial incident wave potential $\phi_I(\mathbf{x})$, the complex spatial scattered potential $\phi_S(\mathbf{x})$ and the complex spatial radiated potential $\phi_R(\mathbf{x})$. $(\mathbf{x})$ refers to the Cartesian coordinates. This is shown in the following equation:

$$\phi = \phi_I + \phi_S + \phi_R = \phi_D + \phi_R \tag{2.1}$$

The potential, within the fluid domain, satisfies the Laplace equation given as:

$$\nabla^2 \phi = 0 \tag{2.2}$$

In Equation 2.1, $\phi_D$ is the complex spatial diffraction potential. The considered potentials are used for both finite and infinite depth conditions.

To obtain the hydrodynamic coefficients and excitation forces, the diffraction and radiation potentials need to be computed by solving the diffraction and radiation boundary integral equation problem respectively.

The formulation of the diffraction problem for a single floating body within HAMS is provided in the work of Liu [79]. The single body diffraction problem can be extended to incorporate interaction due to the presence of $M$ bodies by building upon the single body fluid interaction.

The boundary conditions to be satisfied by the total diffraction potential, are on the free surface (Equation 2.3), on the body surface (Equation 2.4), at the sea bottom (Equation 2.5), and in the far field (Equation 2.6 shows Sommerfeld's radiation condition). The boundary conditions are shown as follows.

$$\frac{\partial \phi_D}{\partial z} = \frac{\omega^2}{g} \phi_D, z = 0 \tag{2.3}$$

$$\frac{\partial \phi_D}{\partial n} = 0, \text{on } S_B^{(k)} \tag{2.4}$$

where $S_B^{(k)}$ is the body surface of the $k^{th}$ body. This boundary condition applies to all bodies.

$$\frac{\partial \phi_D}{\partial z} = 0, z = -h, \text{or } z \to \infty \text{ depending on the depth condition} \tag{2.5}$$

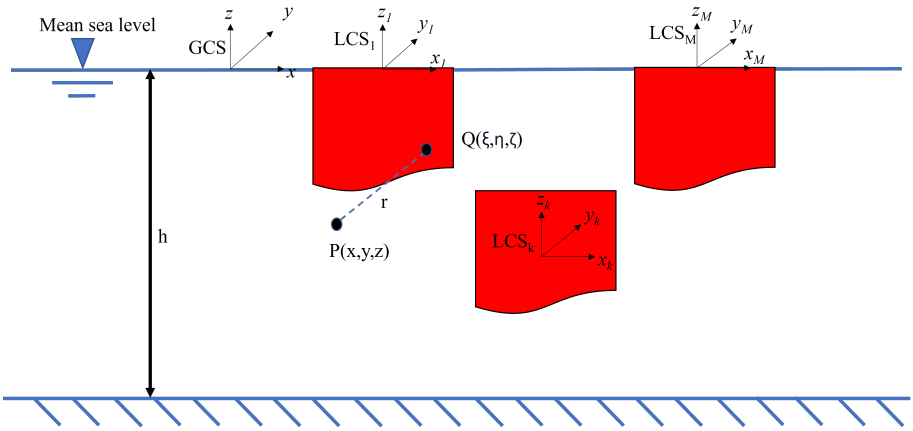



Figure 2.1.: Definition of the coordinate system for the multiple body interaction problem. *GCS* refers to the global coordinate system and *LCS* refers to the local coordinate system per body. *Q* denotes the source point on the immersed body surface and *P* denotes the field point anywhere in the fluid domain.

$$\lim_{R\to\infty}[\sqrt{\mu R}(\frac{\partial\phi_D}{\partial R}-i\mu\phi_D)]=0 \tag{2.6}$$

where $\mu=\omega^2/g$ is the deepwater wave number, $g$ is the acceleration due to gravity, $h$ denotes the water depth considering finite depth, $R$ is the horizontal distance from any of the bodies and '$i$' refers to the imaginary unit with its coefficient referring to the imaginary part of a complex number. Within this formulation, the Sommerfeld's radiation condition should be satisfied at large distances from the group of bodies.

To derive the boundary integral equations for the diffraction problem with the Green's function approach as an extension of the fluid-body interaction with HAMS, mixed source/dipole boundary integral equations are derived. The scattered potential for body $k$, $k=1,...,M$, should consider the contribution from all bodies including itself. The boundary integral equation considering this with $S_B^T=S_B^{(1)}+S_B^{(2)}+...+S_B^{(M)}$ can then be given as follows:

$$2\pi\phi_S(\mathbf{x})+\iint_{S_B^T}\phi_S(\xi)\left(\frac{\partial G(\xi;\mathbf{x})}{\partial n_\xi}\right)dS_\xi=-\iint_{S_B^T}\left(\frac{\partial\phi_I}{\partial n}\right)G(\xi;\mathbf{x})dS_\xi \tag{2.7}$$

Here $x$ refers to the field point, $\xi$ refers to the source point, $G$ is the Green's function and the subscript '$I$' indicating the incident wave. The Green's function for the shallow and deep water conditions are explained in detail in the work of Liu [79] and Liang et al.[90] respectively. The velocity potential for the incident wave can be specified based on the complex wave amplitude and the wave frequency. In deep water, the velocity potential of the incoming plane harmonic wave can be defined as:

$$\phi_I=-\frac{igA}{\omega}e^{\mu z}e^{i\mu(xcos\beta+ysin\beta)} \tag{2.8}$$

and for shallow depth as:

$$\phi_I=-\frac{igA}{\omega}\frac{cosh\nu(z+h)}{cosh\nu h}e^{i\nu(xcos\beta+ysin\beta)} \tag{2.9}$$

where $\beta$ is the angle between the direction of propagation of the incident wave and the positive $x$-axis, and $\nu$ is the wavenumber, defined as the real positive root of the respective water wave dispersion equation.

The radiation problem can be formulated in a similar way to that of the diffraction problem. It is assumed that the considered body is in motion with all the remaining bodies being stationary. This is obtained from the body surface boundary condition. Together with this boundary condition, all the boundary conditions are given(Equation 2.10 - Equation 2.13).

$$\frac{\partial \phi_j^{(k)}}{\partial z} = \mu \phi_j^{(k)}, z = 0 \tag{2.10}$$

$$\frac{\partial \phi_j^{(k)}}{\partial n} = n_j^{(k)}, \text{on } S_B^{(k)} \tag{2.11}$$

Here $\phi_j^{(k)}$ refers to the radiation potential of the fluid velocity field generated by the $j^{th}$ degree of freedom (dof) for the $k^{th}$ body. $j$ = 1,...,6 and $k$ = 1,...,$M$. $n_j^{(k)}$ is the normal vector in the $j^{th}$ dof for the $k^{th}$ body. As stated previously, when the $k^{th}$ body is in motion, all the other bodies are assumed to be stationary.

$$\frac{\partial \phi_j^{(k)}}{\partial z} = 0, z = -h, \text{or } z \to \infty \text{ depending on the depth condition} \tag{2.12}$$

Finally, the Sommerfield's radiation condition:

$$\lim_{R \to \infty} [\sqrt{\mu R}(\frac{\partial \phi_j^{(k)}}{\partial R} - i\mu \phi_j^{(k)})] = 0 \tag{2.13}$$

Similar to the diffraction problem, the boundary integral equation for the complete radiation problem can be given as follows:

$$2\pi \phi_j^{(k)}(\mathbf{x}) + \iint_{S_B^T} \phi_j^{(k)}(\xi) \left( \frac{\partial G(\xi; \mathbf{x})}{\partial n_\xi} \right) dS_\xi = \iint_{S_B^T} G(\xi; \mathbf{x}) \frac{\partial \phi_j^{(k)}}{\partial n} dS_\xi \tag{2.14}$$

Considering the boundary condition on the body surface (Equation 2.11), this can be reduced to the following equation:

$$2\pi \phi_j^{(k)}(\mathbf{x}) + \iint_{S_B^T} \phi_j^{(k)}(\xi) \left( \frac{\partial G(\xi; \mathbf{x})}{\partial n_\xi} \right) dS_\xi = \iint_{S_B^{(k)}} G(\xi; \mathbf{x}) n_j^{(k)} dS_\xi \tag{2.15}$$

## 2.2. DISCRETIZATION OF THE INTEGRAL EQUATIONS AND SOLUTION OF THE LINEAR ALGEBRAIC SYSTEM

The boundary surfaces are discretized into a set of quadrilateral or triangular plane panels to approximate the exact geometry of the bodies. The radiation and diffraction velocity potentials are represented by piecewise constant functions over each panel, as in the existing HAMS formulation [79]. By extending the existing 'collection' method wherein the centroids of the panels represent the collection points, the boundary integral equation for the diffraction problem (Equation 2.7) is discretized into:

$$2\pi \phi_S(\mathbf{x}_i) + \sum_{l=1}^{N_p^T} D_{il} \phi_S(\mathbf{x}_l) = \sum_{l=1}^{N_p^T} S_{il} V_I(\mathbf{x}_l), (i = 1, 2, \ldots, N_p^T) \tag{2.16}$$

Here $N_p^T$ is the summation of panels over all bodies. The integrations of the sources and dipoles within the mixed source/dipole formulation over each panel for the scattering problem is given as follows:

$$D_{il} = \iint_{S_{B,l}} \frac{\partial G(\xi; \mathbf{x}_i)}{\partial n_\xi} dS_\xi \tag{2.17}$$

$$S_{il} = \iint_{S_{B,l}} G(\xi; \mathbf{x}_i) dS_\xi \tag{2.18}$$

and

$$V_I(\mathbf{x}_l) = -\frac{\partial \phi_I}{\partial n}(\mathbf{x}_l) \tag{2.19}$$

Similarly, the collection method can be applied to the radiation problem and is given as:

$$2\pi\phi_j^{(k)}(\mathbf{x}_i) + \sum_{l=1}^{N_p^T} D_{il}\phi_j^{(k)}(\mathbf{x}_l) = \sum_{m=1}^{N_p^k} S_{im} n_j^{(k)}(\mathbf{x}_m) \tag{2.20}$$

with $i = 1, 2, \ldots, N_p^{(M)}, j = 1, 2, \ldots, 6$ and

$$n_j^{(k)}(\mathbf{x}_l) = \frac{\partial \phi_j^{(k)}}{\partial n}(\mathbf{x}_l) \tag{2.21}$$

This assembly for the radiation problem is done for all $M$ bodies to obtain the final set of linear algebraic equations for all $M$ bodies.

For both the diffraction and radiation problem, $N_p^T$ number of linear equations are obtained which need to be solved simultaneously. The LU decomposition solver currently available in the HAMS package is adapted to solve the set of linear algebraic equations for both the diffraction and radiation problem.

Once the velocity potentials on the body surfaces are obtained, the hydrodynamic coefficients and excitation forces can be computed based on [91]. By integrating the pressure multiplied by the $j^{th}$ component of the normal vector over the $k^{th}$ body, the hydrodynamic forces acting in the $j^{th}$ dof of the $k^{th}$ body can be computed. These are as follows:

$$E_j^{(k)} = i\omega\rho \iint_{S_B^k} \phi_D n_j^{(k)} dS \tag{2.22}$$

$$A_{js}^{(k)(q)} + (i/\omega) B_{js}^{(k)(q)} = \rho \iint_{S_B^k} \phi_j^{(q)} n_s^{(k)} dS \tag{2.23}$$

where $E_j^{(k)}$ is the wave excitation force in the $j^{th}$ dof of the $k^{th}$ body, and $A_{js}^{(k)(q)}$ and $B_{js}^{(k)(q)}$ are the added mass and radiation damping coefficients, respectively, in the $s^{th}$ dof of the $k^{th}$ body due to the $j^{th}$ mode of motion of the $q^{th}$ body.

## 2.3. ADVANCED SOLVER FEATURES

This section discusses the theoretical background of some advanced features in HAMS-MREL, that were utilized for the array studies later. These features utilize the framework discussed in the last two sections.

### 2.3.1. WAVE FIELDS - PRESSURE AND FREE SURFACE ELEVATION

The complex-valued hydrodynamic pressure on the body boundary or fluid domain is related to the velocity potential by the linearized Bernoulli equation:

$$p(\mathbf{x}) = i\omega\rho\phi(\mathbf{x}) \tag{2.24}$$

The total velocity potential in HAMS-MREL is defined by:

$$\phi(\mathbf{x}) = \phi_D(\mathbf{x}) - i\omega \sum_{j=1}^{6M} \zeta_j \phi_j(\mathbf{x}) \tag{2.25}$$

where the radiation and diffraction potentials have been explained in the previous section. $\zeta_j$ refers to the amplitude of motion in the $j^{th}$ dof. The body can be evaluated separately for the diffraction and radiation problems and then combined.

Similar to the complex-valued hydrodynamic pressure, the free-surface elevation $\eta(\mathbf{x})$ at any field point $\mathbf{x}$ can also be obtained from the total velocity potential. This is obtained from the dynamic free-surface condition as:

$$\eta(\mathbf{x}) = \frac{i\omega}{g}\phi(\mathbf{x})_{z=0} \tag{2.26}$$

### 2.3.2. GLOBAL SYMMETRY

The computational efficiency of the solution from HAMS-MREL can be significantly improved by utilizing symmetry. With the current implementation, a single global plane of symmetry (either along $x$ or $y$) can be utilized [67, 92]. The discretized form of the boundary integral equations (diffraction or radiation) can be expressed as:

$$[A]\{\phi\} = \{B\} \tag{2.27}$$

Considering a single plane of symmetry, it is possible to partition the matrix $A$, vector $\phi$ and matrix $B$ (see Figure 2.2, where the partition is made about $y$=0. This indicates that for the panels in $+y$, the vector with the potential is given as $\phi_2$. For the panels in $-y$, the vector with the potential is given as $\phi_1$ ).

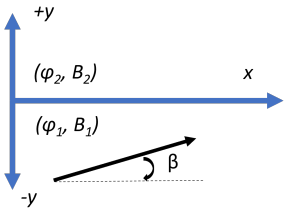



Figure 2.2.: Symmetry partitioning - symmetry plane $y$=0

This can be expressed as:

$$[A] = \begin{bmatrix} A_{11} & A_{12} \\ A_{21} & A_{22} \end{bmatrix} \tag{2.28}$$

$$\{\phi\} = \{ \ \phi_1 \quad \phi_2 \ \}^T \tag{2.29}$$

$$\{B\} = \{ \ B_1 \quad B_2 \ \}^T \tag{2.30}$$

where $A_{11}$ is the submatrix of the coefficients associated with the discretization of boundary region 1, while $A_{12}$ is the corresponding submatrix from the coupling

between the boundaries 1 and 2. $\phi_1$ and $\phi_2$ are the components of the velocity potential corresponding to elements in boundaries 1 and 2 respectively. Similarly $B_1$ and $B_2$ are the right-hand side vectors associated with boundaries 1 and 2 respectively. Furthermore, the following relations can be employed in the calculation:

$$A_{11} = A_{22}, A_{12} = A_{21} \tag{2.31}$$



In order to reduce the number of linear equations to be solved, an orthogonal transformation matrix $[R]$ can be utilized such that:

$$[\widehat{A}] = \frac{1}{\gamma}[R][A][R] \tag{2.32}$$

$$\{\widehat{\phi}\} = [R]\{\phi\} \tag{2.33}$$

$$\{\widehat{B}\} = [R]\{B\} \tag{2.34}$$

with $\gamma = 2$, since there are two regions due to a single plane of symmetry. The transformation matrix is taken from [93].

$$R = \begin{bmatrix} 1 & 1 \\ 1 & -1 \end{bmatrix} \tag{2.35}$$

The transformation enables the linear system into a simplified diagonal form:

$$\begin{bmatrix} \widehat{A}^{(1)} & 0 \\ 0 & \widehat{A}^{(2)} \end{bmatrix} \begin{bmatrix} \widehat{\phi}^{(1)} \\ \widehat{\phi}^{(2)} \end{bmatrix} = \begin{bmatrix} \widehat{B}^{(1)} \\ \widehat{B}^{(2)} \end{bmatrix} \tag{2.36}$$

From this $\{\widehat{\phi}\}$ can be obtained.

### 2.3.3. SUPPRESSION OF IRREGULAR FREQUENCIES

When solving mixed source-dipole BIE in HAMS-MREL, substantial errors can occur at 'irregular frequencies'. This is observed as a significant jump or dip in the hydrodynamic coefficients and excitation forces, and can result in unrealistic estimations of the response of floating structures.

Irregular frequencies are purely numerical and arise from ill-conditioning of the boundary integral problems [77]. These coincide with the eigen frequencies of the hypothetical sloshing modes (flow that fills the interior of the structure), which are obtained from the internal Dirichlet problem [78] and are numerically caused by the interaction of the water-plane section of floating bodies intersecting with the free-water surface [79].

An extended BIE which adapts the method from HAMS and incorporates the body boundary condition wherein when one body is in motion in a certain degree of freedom, the other bodies are stationary, is developed and utilized, which assumes the potentials on the interior of the water plane are zero. This is only performed for bodies where the input waterplane mesh is provided. By applying the Green's equation in the interior of the floating body, additional BIE are introduced which are combined with the conventional BIEs. The extended equation to obtain the scattered potential for body $k$, $k = 1,...,M$, should consider the contribution from all the available waterplane meshes ($S_{WP}$). The boundary integral equation considering this with $S_B^T = S_B^{(1)} + S_B^{(2)} + ... + S_B^{(M)}$ can then be given as follows:

$$\iint_{S_B^T} \phi_S(\mathbf{x}) \left( \frac{\partial G(\xi;\mathbf{x})}{\partial n_\xi} \right) dS_\xi = -\iint_{S_B^T} \left( \frac{\partial \phi_I(\xi)}{\partial n} \right) G(\xi;\mathbf{x}) dS_\xi \tag{2.37}$$

Here $\mathbf{x}$ refers to the field point and belongs to the water plane meshes ($S_{WP}^T = S_{WP}^{(1)} + S_{WP}^{(2)} + ... + S_{WP}^{(M)}$), $\xi$ refers to the source point and belongs to $S_B^T$. $G$ is the

Green's function. The Green's function for the shallow and deep water conditions are explained in detail in the work of Liu [79].

Similar to the diffraction problem, the boundary integral equation for the complete radiation problem can be given as follows:

$$\iint_{S_B^T} \phi_j^{(k)}(\mathbf{x}) \left( \frac{\partial G(\xi;\mathbf{x})}{\partial n_\xi} \right) dS_\xi = \iint_{S_B^T} G(\xi;\mathbf{x}) n_j^{(k)} dS_\xi \tag{2.38}$$

Considering the boundary condition on the body surface (where only a single body $k$ is moving in a certain degree of freedom $j$), this can be reduced to the following equation:

$$\iint_{S_B^T} \phi_j^{(k)}(\mathbf{x}) \left( \frac{\partial G(\xi;\mathbf{x})}{\partial n_\xi} \right) dS_\xi = \iint_{S_B^{(k)}} G(\xi;\mathbf{x}) n_j^{(k)} dS_\xi \tag{2.39}$$

When the $k^{th}$ body is in motion, all the other bodies are assumed to be stationary.

Considering the total number of elements as $N_{WP}^T$ for all the water plane meshes and $N_P^T$ for all the considered bodies, a set of overdetermined linear algebraic equations can be obtained as follows:

$$[A]_{(N_{WP}^T + N_P^T) X N_P^T} \{\phi\}_{N_P^T} = [B]_{(N_{WP}^T + N_P^T) X N_P^T} \tag{2.40}$$

The least squares method implemented for solving the set of linear algebraic equations is implemented here.

### 2.3.4. GENERALIZED MODES APPROACH

The generalized modes approach can be used to model flexible structures or structures with kinematic constraints, an example of such bodies are flap WECs, and/or large floating bodies with several hinged components such as attenuators. This is done by introducing specified motion of the structure based on its mode shapes considering constraints, for example hinges. In order to incorporate any generic motion of the structure, the body boundary condition in the BIEM problem needs to be modified. This is based on the approach introduced in [94].

The body boundary condition can be expressed as a general expression:

$$\frac{\partial \phi_j^{(k)}}{\partial n} = \mathbf{S_j^{(k)}} . \mathbf{n^{(k)}} \tag{2.41}$$

where $\mathbf{S_j^{(k)}}$ is a 3D vector shape function of the $k^{th}$ body, with cartesian components $u_j^{(k)}, v_j^{(k)}, w_j^{(k)}$ and $\mathbf{n^{(k)}} = (n_x^{(k)}, n_y^{(k)}, n_z^{(k)})$ is the normal vector projecting from the $k^{th}$ body towards the fluid [94]. In general, for the rigid body translational degrees of freedom ($j$ = 1,2,3), the shape function is unit vector in the corresponding direction, and for the rigid body rotations (j=4,5,6), $\mathbf{S_j} = \mathbf{S_{j-3}} \times \mathbf{r}$, where $\mathbf{r}$ is the lever arm vector with respect to a rotation center[94, 95].

The projection of the normal vector can then be written as:

$$\mathbf{S_j^{(k)}} . \mathbf{n^{(k)}} = u_j^{(k)} n_x^{(k)} + v_j^{(k)} n_j^{(k)} + w_j^{(k)} n_z^{(k)} \tag{2.42}$$

Therefore, by deriving this vector shape function for any additional mode/degree of freedom, the radiation and diffraction problem can also be solved considering this degree of freedom in HAMS-MREL. The vector shape function can represent general mode shapes corresponding to structural deflections, the motions of the interior free surfaces inside moonpools, or multiple bodies with constraints [57].

## 2.4. VALIDATION OF HAMS-MREL AND THE ADVANCED SOLVER FEATURES

This section focuses on the validation of HAMS-MREL and its advanced features. It is broken into three parts. The first part considers numerical validation with semi-analytical solutions from literature and cross-model validation for the core framework and the advanced features. The second part focuses on the experimental validation of HAMS-MREL considering frequency results and the third part focuses on the experimental validation of HAMS-MREL considering time-domain results. Most geometries utilized in the wave energy sector were considered to showcase the robustness and range of the solver.



### 2.4.1. FREQUENCY DOMAIN NUMERICAL VALIDATION OF HAMS-MREL

This section focuses on the validation of HAMS-MREL considering the availability of semi-analytical solutions by other investigators found in literature and cross-model results with commercial BIEM solver WAMIT, for five cases. Two out of the four cases published in [54] are shown here for validating the framework considering floating structures in finite and deep waters (The other cases are added in Appendix A). The other three cases are the validation studies on the advanced features taken from [96]. A case for the Global symmetry is not shown, since the results match exactly. However, the computational resource with parallelization are discussed later in subsection 2.4.3. For all the cases, with regard to the HAMS meshes, the normal vector of the panels points from the body towards the fluid.

#### CASE 1: TWO SEMI-IMMERSED CYLINDERS IN SHALLOW WATERS- COMPARISON WITH SEMI-ANALYTICAL SOLUTIONS AND WAMIT IN SHALLOW WATERS

The solutions for the hydrodynamic coefficients and excitation forces from interaction theory proposed by Kagemoto and Yue in [49] for two semi-immersed floating cylinder were used for validation here.

The theory considers plane wave diffraction and radiation within the formulation of the linear potential flow for multiple bodies. The propagating and evanescent wave fields (also referred to as local waves) are decomposed into cylindrical waves in terms of Henkel and modified Bessel functions. To account for the interactions among the bodies when solving the diffraction problem, the scattered potential $\phi_i^S$ for the $i^{th}$ body is represented through the incident potentials $\phi_j^I$ of body $j$, $j \neq i$ based on addition theorems for Bessel functions. Furthermore, the authors use the diffraction characteristics of an isolated body through “diffraction transfer matrices" that relate to the incident and diffracted cylindrical partial waves. The derivation of the radiation problem follows closely with the development here (see [97] and [98]). The radiation coefficients are derived from the culmination of radiation coefficients of a body in isolation in combination with the partial cylindrical wave contributions (both propagating and evanescent) from the scattering and incident potentials. In addition to the aforementioned semi-analytical method, a cross-model comparison is also carried out here with WAMIT.

The two-cylinder case is shown in Figure 2.3, 1200 panels were used for the mesh (shown in Figure 2.4) for both WAMIT and HAMS-MREL in this comparison. 1200 panels for the mesh was decided based on a convergence study. Figure 2.5a, Figure 2.5b and Figure 2.5c show the convergence of the added mass, radiation damping and excitation forces respectively for the heave-heave of cylinder 1 as an example. Similar studies were performed for all the cases mentioned in this chapter, with the results shown in the appendix. It can be observed that the radiation damping and excitation forces already begin to converge with 400/800 panels, while the added mass converges around 1200 panels. The increased number of panels comes from the dependency of the added mass on the near field velocity potentials while both the radiation damping and excitation forces depend on the far field wave patterns, making the added mass more susceptible to the panel distribution on the geometry [69, 99, 100].

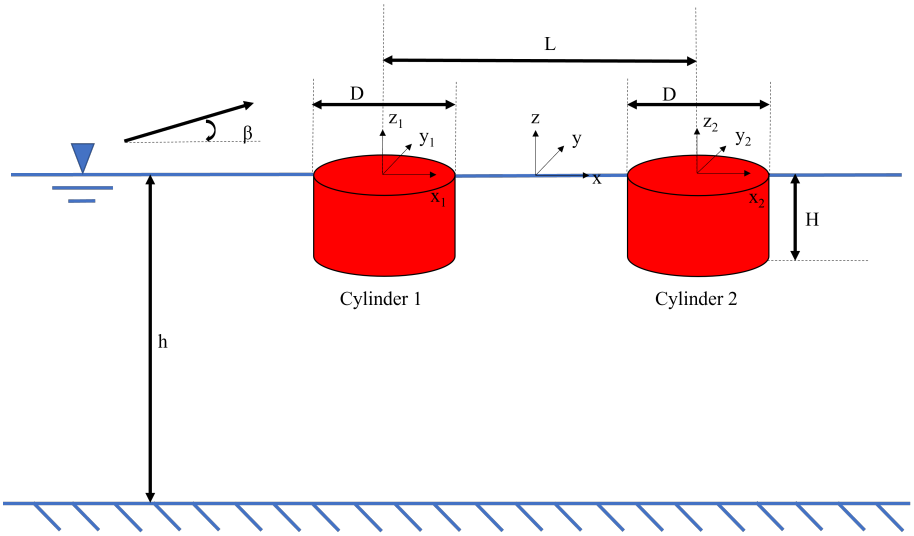



Figure 2.3.: Two semi-immersed cylinders (Case 1)

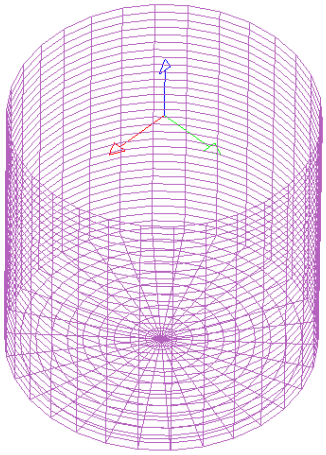
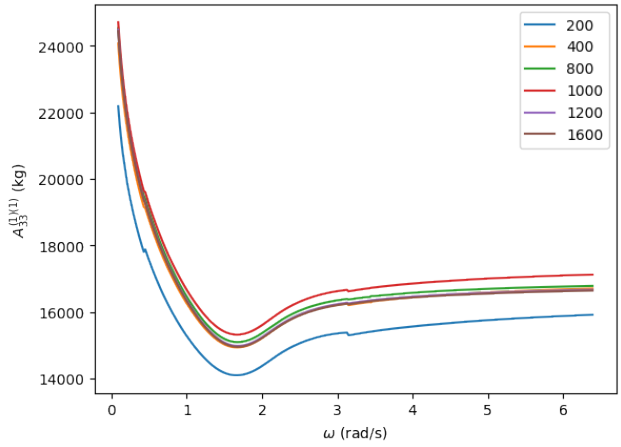


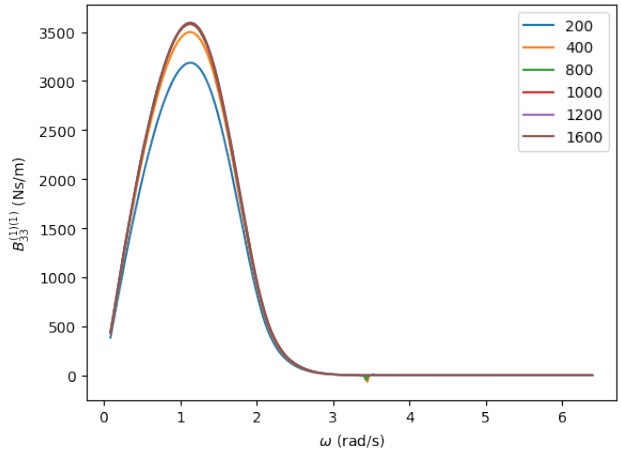
Figure 2.4.: Cylindrical mesh with 1200 panels used in Case 1

Table 2.1.: Properties used for the simulation in HAMS-MREL and WAMIT for Case 1

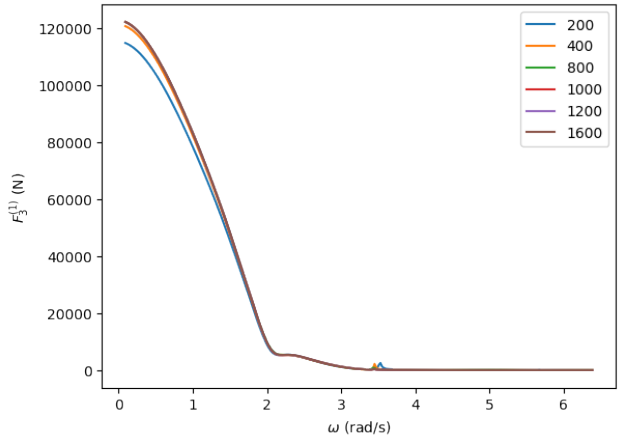
| Property | Unit | Value |
|---|---|---|
| Diameter, $D$ | $m$ | 4 |
| Spacing, $L$ | $m$ | 5.2 |
| Water Depth, $h$ | $m$ | 8 |
| Draft, $H$ | $m$ | 4 |
| Angle of incidence, $\beta$ | $deg$ | 0 |




(a) Added mass




(b) Radiation damping




(c) Excitation force

Figure 2.5.: Convergence of hydrodynamic coefficients for the heave-heave mode for Cylinder 1: (a) added mass, (b) radiation damping, and (c) excitation force

$$A_{total,surge} = A_{11}^{(1)(1)} + A_{11}^{(1)(2)} + A_{11}^{(2)(1)} + A_{11}^{(2)(2)} \tag{2.43}$$

$$B_{total,surge} = B_{11}^{(1)(1)} + B_{11}^{(1)(2)} + B_{11}^{(2)(1)} + B_{11}^{(2)(2)} \tag{2.44}$$

$$E_{total,surge} = |E_1^{(1)} + E_1^{(2)}| \tag{2.45}$$

$$A_{total,heave} = A_{33}^{(1)(1)} + A_{33}^{(1)(2)} + A_{33}^{(2)(1)} + A_{33}^{(2)(2)} \tag{2.46}$$

The properties selected for the two-cylinder case have been shown in Table 2.1. The number of panels were based on a convergence study that was carried out, and the mesh discretisation is exactly the same in HAMS-MREL and WAMIT to minimise discrepancies. Figure 2.6a shows the total surge added mass (Equation 2.43), Figure 2.6b shows the total surge radiation damping (Equation 2.44), Figure 2.6c shows the total surge excitation forces (Equation 2.45) and Figure 2.6d shows the total heave added mass (Eq. Equation 2.46) for the two cylinders together. The quantities are made dimensionless as indicated in the figures. $\nu$ refers to the wave number, $D = 2a$ with $a$ is the radius of the cylinder and $a_0$ is the wave amplitude. Refer to Equation 2.22 and Equation 2.23 for the definitions of the excitation force and hydrodynamic coefficients respectively.

As seen from the results, HAMS-MREL is close to both WAMIT as well as the semi-analytical method. For the total surge added mass, HAMS-MREL slightly under-predicts the results as compared to the semi-analytical solution, particularly for $\nu D > 2$. However, it can also be seen that WAMIT slightly over-predicts the values as compared to the semi-analytical solution in the same regime.

### CASE 2: TWO SUBMERGED SPHERES IN DEEP WATERS - COMPARED WITH SEMI-ANALYTICAL SOLUTIONS AND WAMIT

The semi-analytical solution for two interacting submerged spheres is used for validation from the work of Wu [101]. This case was chosen to highlight the capability of HAMS-MREL for modelling submerged bodies, as this would be crucial to model devices such as the submerged pressure differential WEC among others. A spherical geometry is chosen to showcase a different geometry as compared to Case 1.

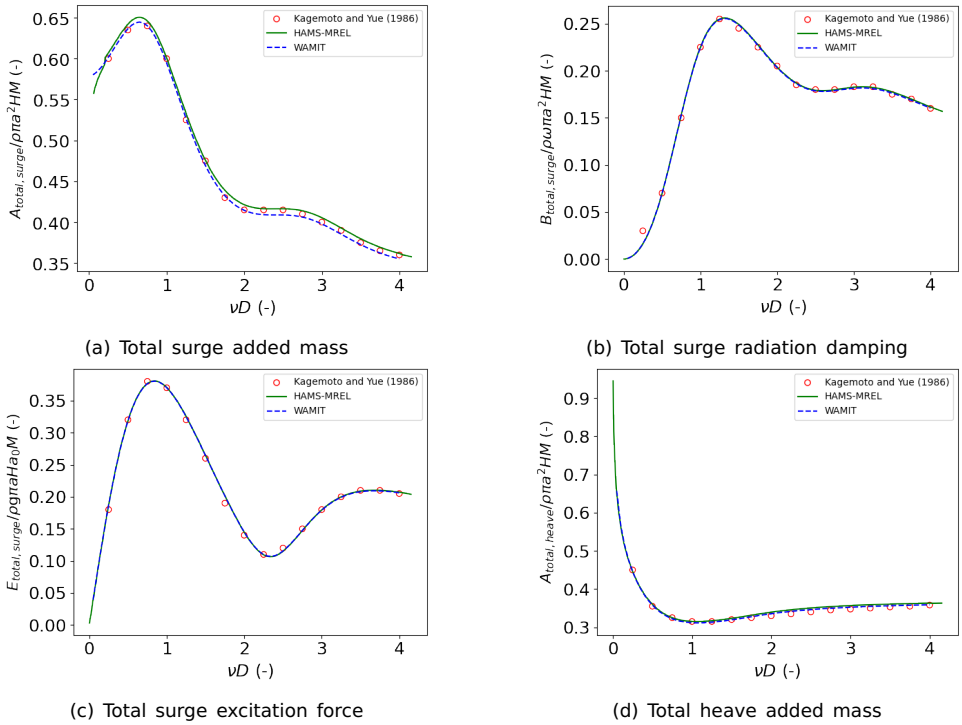
Wu's work extends on the multipole expansion theory proposed by Thorne [102] for a single sphere using the linear potential flow theory. The theory proposed by Thorne expresses the velocity potential through a series of singularities placed within the considered body. With the extension of this theory, Wu proposes an interaction theory that is applicable for any number of spheres with arbitrary radii and submergences.

Table 2.2.: Properties used for the simulation in HAMS-MREL and WAMIT for Case 2

| Property | Unit | Value |
|---|---|---|
| Diameter, $D$ | $m$ | 6 |
| Spacing, $L = 4a$ | $m$ | 12 |
| Water Depth, $h$ | $m$ | Infinite |
| Submergence, $S$ | $m$ | 9 |
| Angle of incidence, $\beta$ | *degrees* | 45 |

The two submerged sphere case is shown in Figure 2.7. The properties considered are shown in Table 2.2. The mesh used within HAMS-MREL and WAMIT is shown in Figure 2.8.

The semi-analytical solution for the hydrodynamic coefficients and excitation forces from Wu[101] were compared with HAMS-MREL and WAMIT for Sphere 2. The comparisons are presented for surge, sway, and heave motions in Figure 2.9, Figure 2.10 and Figure 2.11 respectively.




(a) Total surge added mass

(b) Total surge radiation damping

(c) Total surge excitation force

(d) Total heave added mass

Figure 2.6.: Hydrodynamic coefficients and excitation forces for both cylinders in Case 1

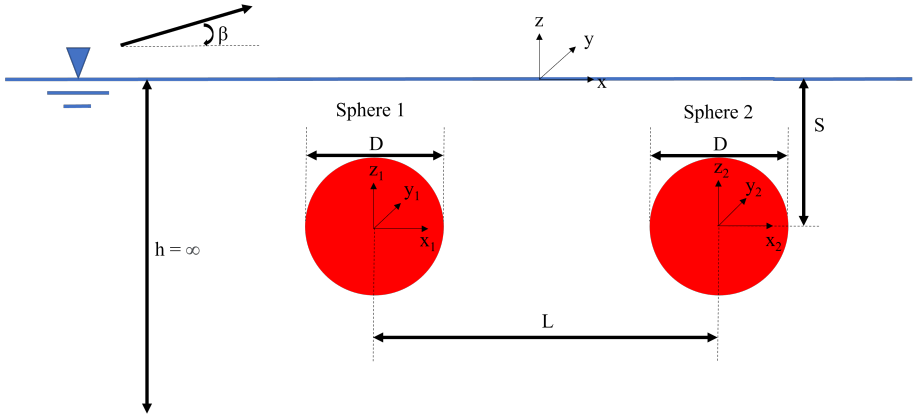



Figure 2.7.: Two submerged sphere interaction problem (Case 2)

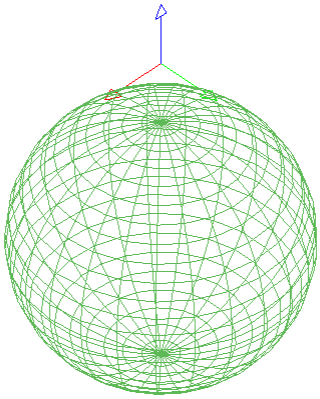
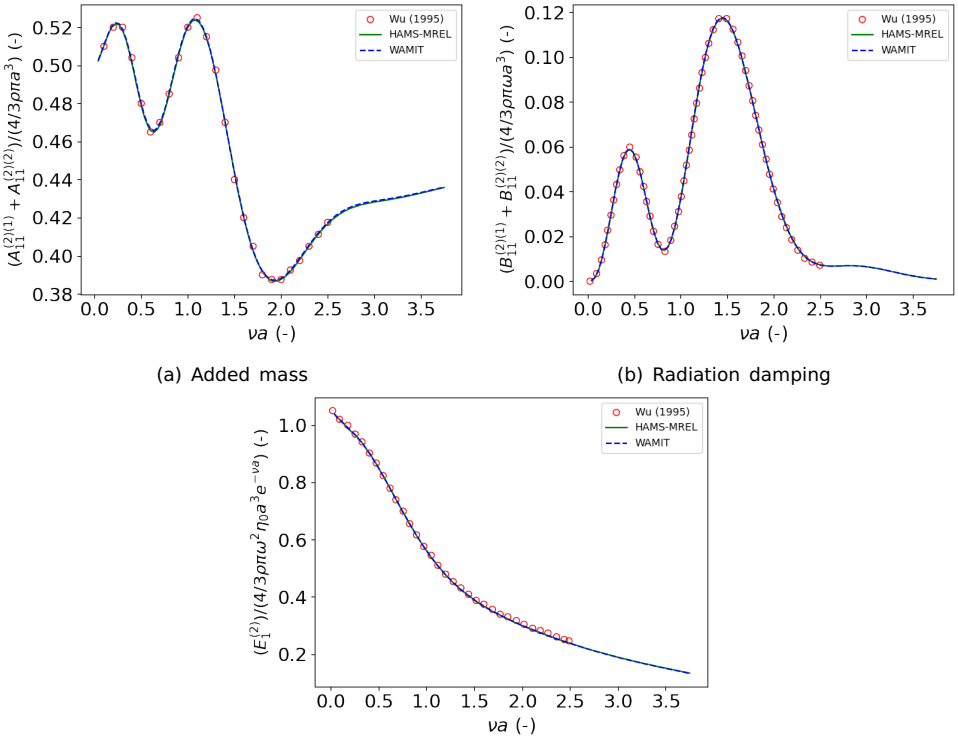


Figure 2.8.: Spherical mesh with 625 panels used in Case 2



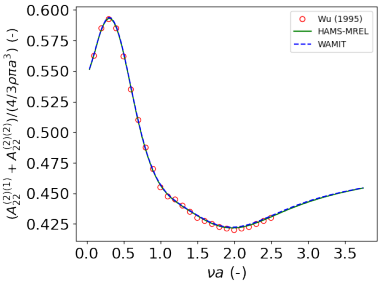

(a) Added mass

(b) Radiation damping

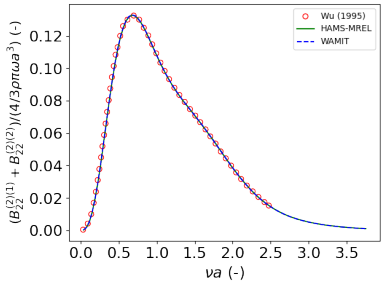
(c) Excitation force

Figure 2.9.: Hydrodynamic coefficients and excitation force for surge of Sphere 2.

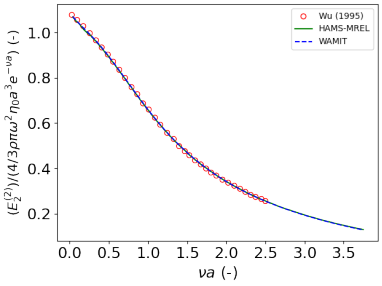
It can be observed that the results from HAMS-MREL exactly match to both the semi-analytical solution from Wu [101] as well as WAMIT for all three dofs.




(a) Added mass

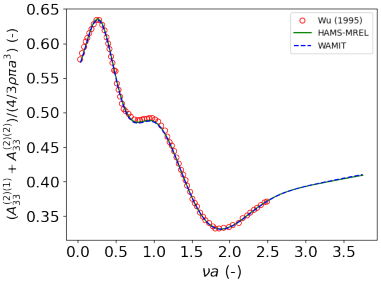



(b) Radiation damping

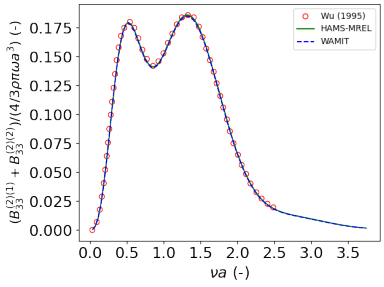



(c) Excitation force

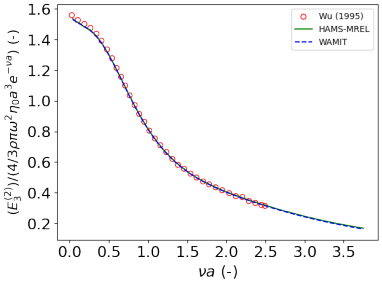
Figure 2.10.: Hydrodynamic coefficients and excitation force for sway of Sphere 2.




(a) Added mass




(b) Radiation damping




(c) Excitation force

Figure 2.11.: Hydrodynamic coefficients and excitation force for heave of Sphere 2.

2

### CASE 3: THREE CYLINDER CASE IN DEEP WATERS - VALIDATION OF WAVE FIELDS WITH WAMIT

To validate the wave fields in HAMS-MREL, a simulation of a three cylinder case was run and compared with WAMIT. The free-surface elevation for diffraction and radiation are individually considered here. The case is taken from the work of Raghavan et al. [54]. The case is shown in Figure 2.12 and the mesh is shown in Figure 2.13. The properties of the case are shown in Table 2.3.

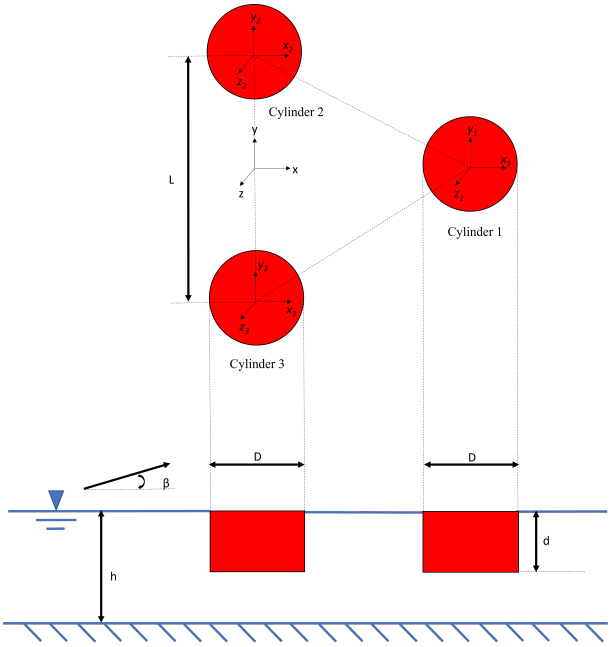



Figure 2.12.: Three cylinder case - wave fields (This figure is taken from [54])

Table 2.3.: Properties of the three cylinder case for obtaining wave fields

| Property | Value |
|---|---|
| Diameter, $D$ (m) | 6 |
| Draft, $d$ (m) | 10.95 |
| Water depth, $h$ (m) | 120 |
| Spacing, $L$ (m) | 15 |
| Incident wave angle, $\beta$ (deg) | 0 |
| Number of frequencies, $N_\omega$ (-) | 100 |
| Amplitude of wave, $A$ (m) | 1 |

The non-dimensional diffraction and radiation free-surface elevation validation is shown in Figure 2.14 and Figure 2.15 respectively. The diffraction and radiation fields have been made non-dimensional based on WAMIT manual [100] as shown in Equation 2.47

$$\frac{\eta_D}{A} = \frac{-\phi_D}{igA/\omega} \tag{2.47}$$

$$\frac{\eta_j^{(k)}}{A} = \frac{\mu\phi_j^{(k)}}{L^n} \tag{2.48}$$

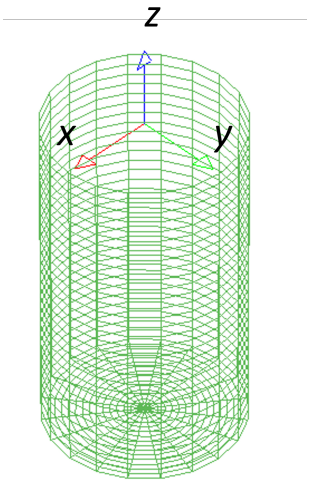



Figure 2.13.: Cylindrical mesh with 900 panels used in Case 3

where $\eta_D$ and $\eta_j^{(k)}$ are the free-surface elevation for the diffraction and $j^{th}$ mode, $k^{th}$ body radiation respectively. $L$ is the length scale, taken as 1.0 in this case. $n$=0 for $j$=1,2,3 and $n$=1 for $j$=4,5,6.

As seen in Figure 2.14 and Figure 2.15, the Mean Squared Error (MSE) was less than 2 % across the considered domain. For the considered case, 10000 field points ($N_f$) were considered as field points for the computation of the free surface elevation field for each of the 100 frequencies ($N_\omega$).

### CASE 4: THREE CYLINDER CASE IN DEEP WATERS - VALIDATION OF THE SUPPRESSION OF IRREGULAR FREQUENCIES

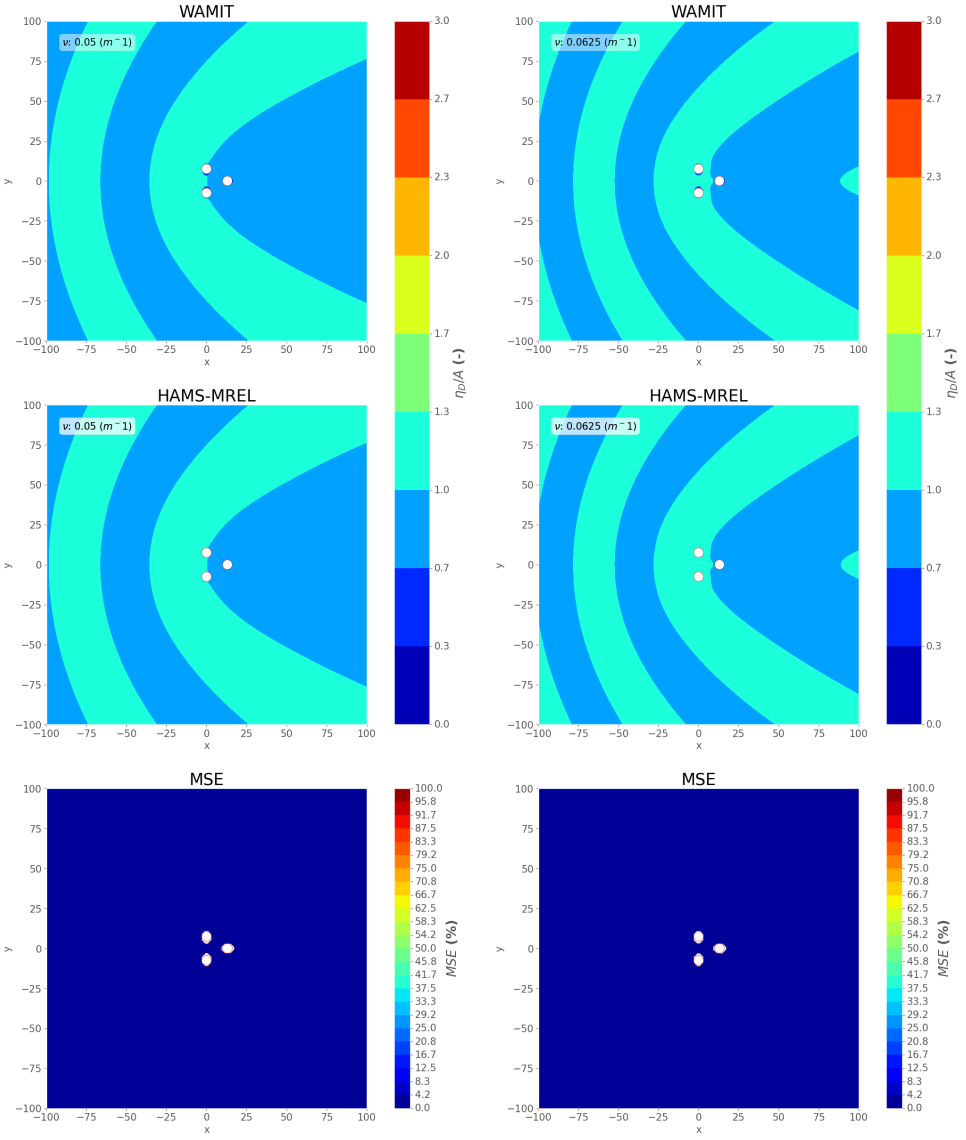
The case of a single row of point absorber cylindrical devices considered. This is shown in Figure 2.16, where three cylinders are considered. The mesh for one of the cylinders is shown in Figure 2.17a. The properties for the case are given in Table 2.4.

Table 2.4.: Properties of the Three cylinder case for symmetry

| Property | Value |
|---|---|
| Diameter, $D$ (m) | 6 |
| Draft, $d$ (m) | 1.5 |
| Water depth, $h$ (m) | 120 |
| Spacing, $L$ (m) | 18 |
| Incident wave angle, $\beta$ (deg) | 0 |
| Number of frequencies, $N_\omega$ (-) | 300 |

The waterplane mesh utilized for each cylindrical mesh is shown in Figure 2.17b.To make a comparison with and without the suppression of irregular frequencies, three different simulations were preformed:

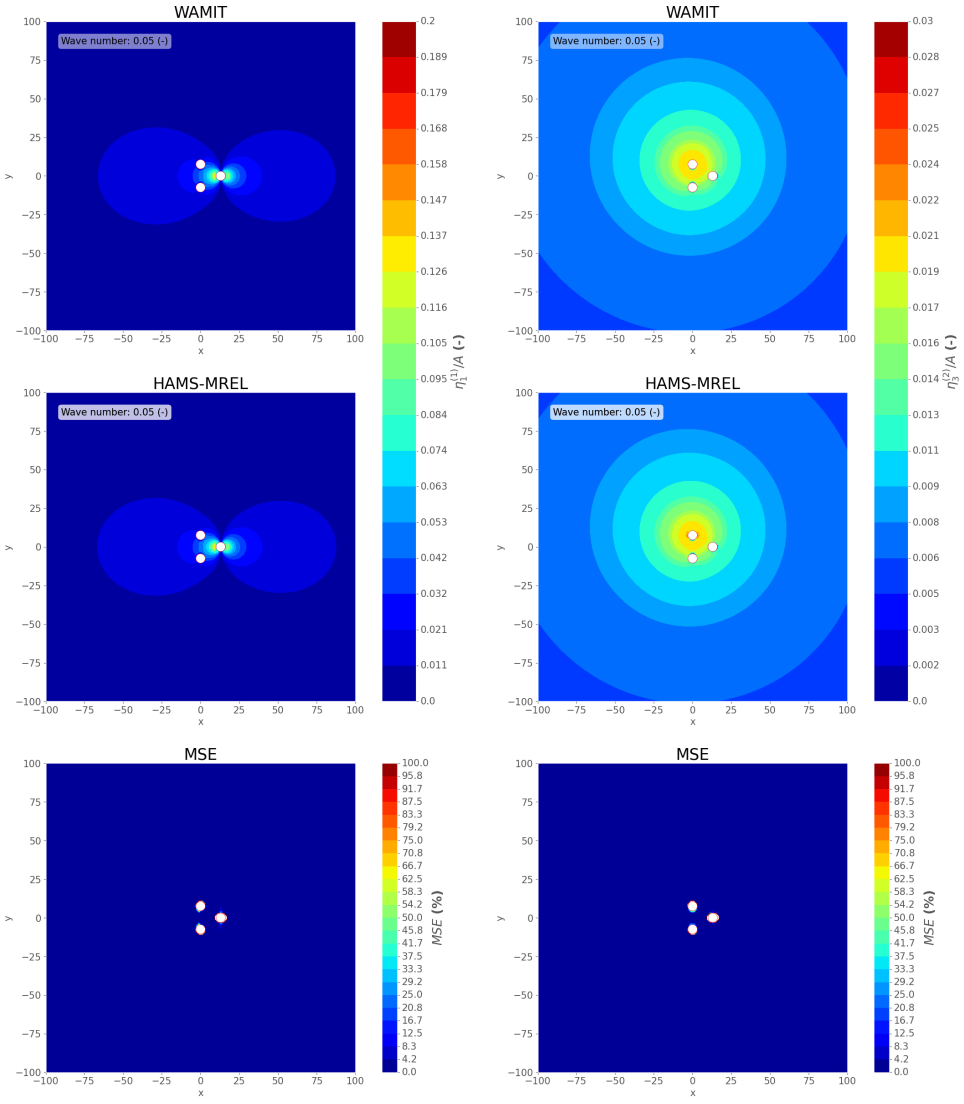
- Simulation 1 - No suppression of irregular frequencies (No-IR)
- Simulation 2 - Suppression of irregular frequencies for Cylinder 1 and 2 (IR-2)




(a) Non-dimensional Diffraction free surface elevation $\eta_D/A$ for wavenumber $\nu$=0.05

(b) Non-dimensional Diffraction free surface elevation $\eta_D/A$ for wavenumber $\nu$=0.0625

Figure 2.14.: Validation of the non-dimensional diffraction free surface elevation, the first row shows the WAMIT results, second row the HAMS-MREL, and the third row the Mean Square Errors (MSE) between the models




(a) Non-dimensional Radiation free surface elevation $\eta_1^{(1)}/A$ for wavenumber $\nu$=0.05

(b) Non-dimensional radiation free surface elevation $\eta_3^{(2)}/A$ for wavenumber $\nu$=0.5

Figure 2.15.: Validation of the non-dimensional Radiation free surface elevation, the first row shows the WAMIT results, second row the HAMS-MREL, and the third row the Mean Square Errors (MSE) between the models

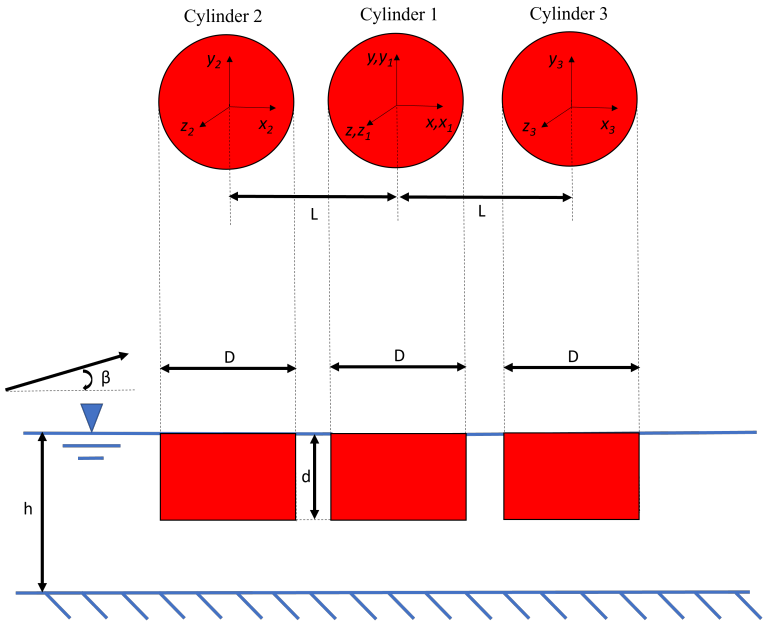
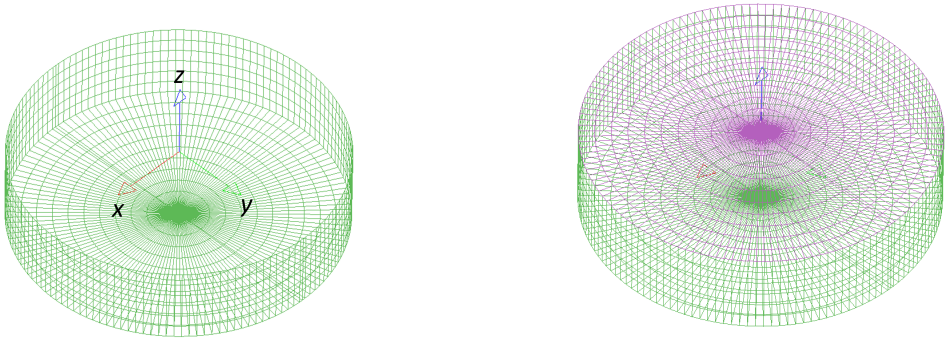



Figure 2.16.: Three cylinder case

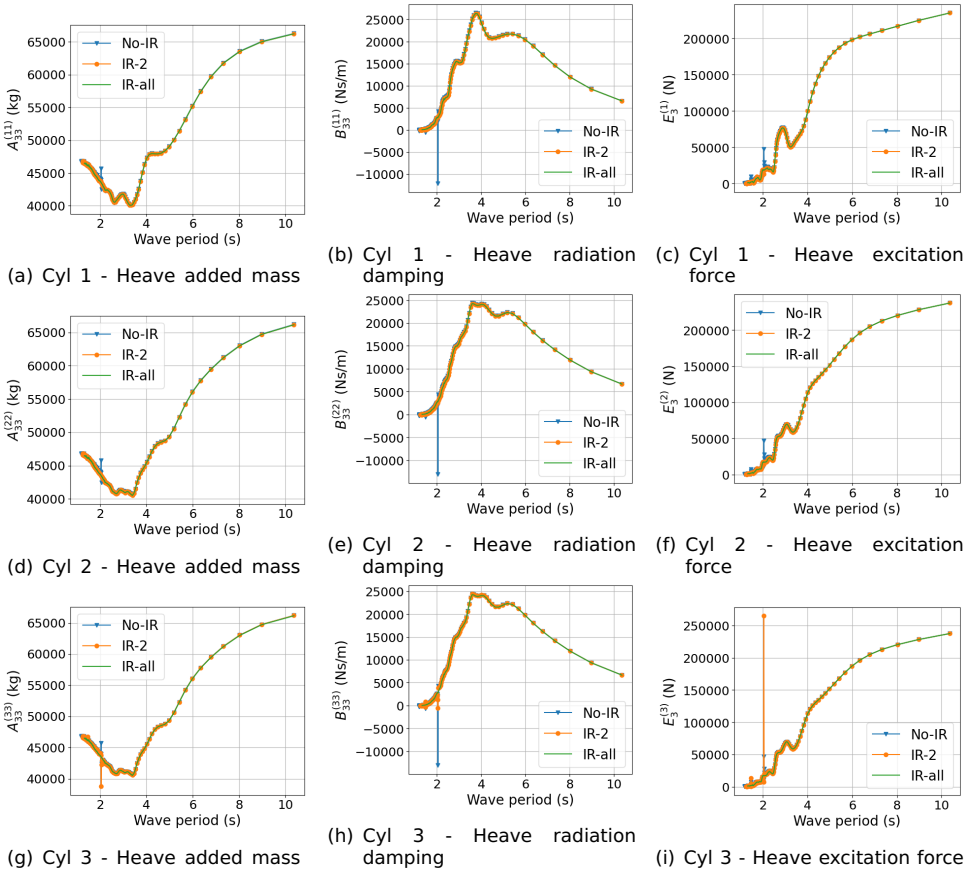



(a) Whole cylinder mesh

(b) Cylinder mesh with the Waterplane mesh

Figure 2.17.: Cylinder mesh with and without water plane mesh

- Simulation 3 - Suppression of irregular frequencies for all cylinders (IR-all)




(a) Cyl 1 - Heave added mass

(b) Cyl 1 - Heave radiation damping

(c) Cyl 1 - Heave excitation force

(d) Cyl 2 - Heave added mass

(e) Cyl 2 - Heave radiation damping

(f) Cyl 2 - Heave excitation force

(g) Cyl 3 - Heave added mass

(h) Cyl 3 - Heave radiation damping

(i) Cyl 3 - Heave excitation force

Figure 2.18.: Hydrodynamic coefficients and excitation forces for heave for the three cylinder case

The results are shown in Figure 2.18. When considering the three cylinder case with no irregular frequency suppression, it is observed that the spike due to the irregular frequency occurs at the period of around 2 s for all the cylinders. This can be seen in the 'No-IR' simulation in Figure 2.18 (a)-(i). When considering Simulation 2, wherein the waterplanes are only utilized for Cylinder 1 and 2, it is observed that the irregular frequency is suppressed (see Figure 2.18 (a)-(f)) while it is not suppressed for Cylinder 3 (see Figure 2.18 (g)-(i)). Furthermore, it can be observed that when the waterplane mesh is used in all cylinders, the irregular frequency for each cylinder is suppressed. The computational time utilized by HAMS-MREL for the simulations is shown in Table 2.9. 300 frequencies were considered for each simulation. $N^T$ is the total number of panels in each simulation.

### CASE 5: FLAP IN SHALLOW WATERS - VALIDATION OF THE GENERALIZED MODES APPROACH WITH WAMIT

In order to demonstrate this approach in HAMS-MREL, the rigid flap from the work of Van 'T Hoff [103] is taken, which has been validated with scaled experiments. The

derivation of the shape function has been done in Raghavan et al. [104] and is added in the appendix (see Appendix B). Therefore, the shape function is summarized.

The flap is modelled as a two body problem, where the top and bottom are two different bodies. The geometry of the flap is shown in Figure B.1. The flap top combines two geometries, a rectangular box and a triangular box, while the flap bottom, which is rigidly fixed to the sea bottom, is composed of a rectangular box. The dimensions of these parts is shown in Table 2.5. The hinge is located at $L_s = 8.9$ m from the free surface. The water depth is 10.9 m, thus the hinge being at 2 m above the sea bottom.

Table 2.5.: Properties of the flap(all dimensions in m)

| Part | Dimension ($W \times T \times H$) |
|---|---|
| **Flap top** | |
| Rectangular box | 18 × 1.8 × 8.5 |
| Triangular box | 18 × 0 - 1.8 × 0.9 |
| **Flap bottom** | |
| Rectangular box | 18 × 1.8 × 1.5 |

$xyz$ is the global coordinate system. $x_l y_l z_l$ is the local coordinate system located at the top of the flap and coincides with the global coordinate system, $x_d y_d z_d$ is the deformed coordinate system due to the flap's unit rotation $\theta$. The flap is aligned such that the width ($W$) is along the $Y$ axis. The surface of the flap is discretized into panels.

The shape function for the additional degree of freedom/mode shape for the flap top is given as:

$$\mathbf{S_7^{(1)}} = (L_s + z, 0, -x) \tag{2.49}$$

Since the flap bottom is stationary, the shape function for the bottom is a null vector.

$$\mathbf{S_7^{(2)}} = (0, 0, 0) \tag{2.50}$$

Using this as the body boundary condition for the additional pitch motion about the hinge, the radiation and diffraction problems can be solved to obtain the hydrodynamic coefficients and excitation forces.

A cross-model validation with WAMIT was conducted. As previously mentioned, the geometry and results for the hydrodynamic coefficients and excitation force for the flap were adopted from the study by Van 'T Hoff [103], as they have been experimentally validated. It is important to note that Van 'T Hoff used a slightly lower mesh resolution compared to the converged mesh resolution recommended by WAMIT, due to the minimal impact of mesh resolution on the final results. For this initial comparison, the same mesh resolution (518 panels for both flap top and bottom) utilized by WAMIT was also implemented in HAMS-MREL.

In the WAMIT model, the flap was represented as a two-body problem. The flap top (see Figure B.1) was assigned a single degree of freedom in pitch with its rotation center located at the hinge ($z$ = -8.9 m), while the flap bottom was treated as stationary, thus only diffraction effects were considered. Lower-order panels were utilized for all simulations to solve both diffraction and radiation problems.

The resulting hydrodynamic coefficients, specifically the added mass coefficient and radiation damping coefficient, are illustrated in Figure 2.21a and Figure 2.21b, respectively. Comparing the added mass coefficient ($A_{77}^{(11)}$) computed by both solvers, results are very close within the range of 1 to 6 seconds. Below 1 s, HAMS-MREL slightly overestimates the coefficient. Between 6 s and 14 s, HAMS-MREL shows a minor overestimation of approximately 5%, but aligns closely with WAMIT beyond 14 s.

For the radiation damping coefficient ($B_{77}^{(11)}$), the results from both solvers are generally in good agreement, although HAMS-MREL slightly overestimates the coefficient near the peak at around 5 s.

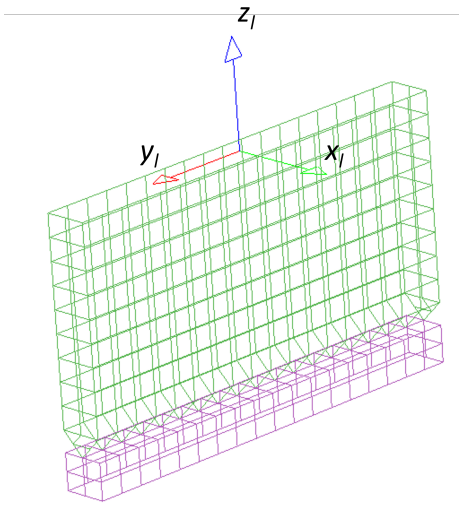



Figure 2.19.: Mesh of the flap in HAMS-MREL with 518 panels - top (green) and bottom (pink) - from [104]

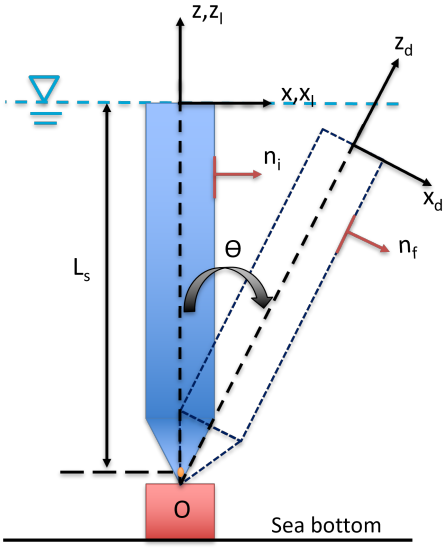
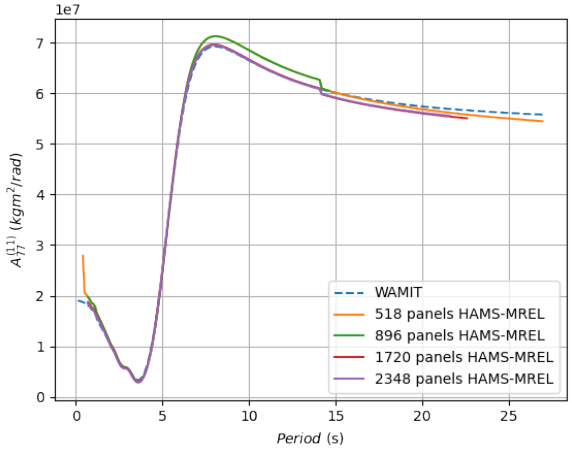
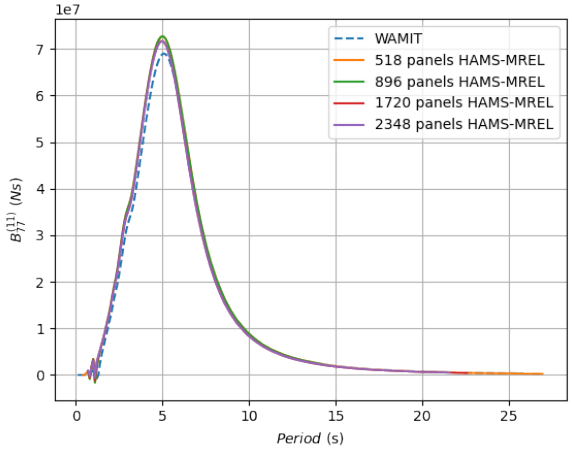


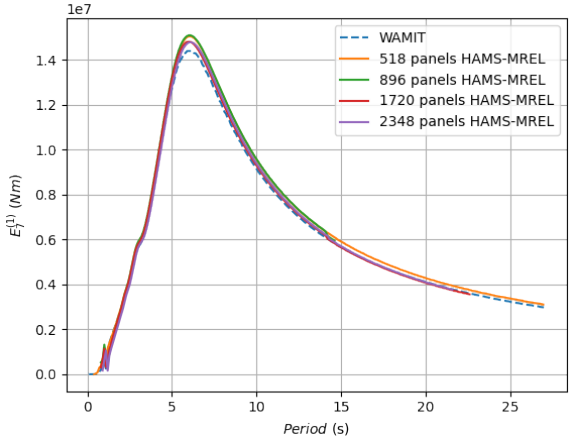

Figure 2.20.: Schematic representation of rotation of the flap (from [104])




(a) Added mass $A_{77}^{(11)}$




(b) Radiation damping $B_{77}^{(11)}$




(c) Excitation force $E_7^{(1)}$

Figure 2.21.: Hydrodynamic coefficients and excitation force for the flap rotational degree of freedom.

Excitation force results ($E_7^{(1)}$) are presented in Figure 2.21c. Both solvers yield closely matched results, with HAMS-MREL slightly overestimating by approximately 5% near the peak occurring at around 6 s.

An unusual peak is observed at the short period of 1 s in both the radiation damping coefficient and excitation force, although it is less prominent in the added mass coefficient. This anomaly can be attributed to an irregular frequency effect, typically observed at high wave frequencies. Such effects can be mitigated by employing a waterplane mesh alongside the hull mesh and solving the extended boundary value problem, as discussed in the previous validation case. However, addressing this is beyond the scope of the current section.

A mesh convergence study for the flap top was conducted to examine potential improvements in the added mass estimates from HAMS-MREL, with the outcomes also depicted in Figure 2.21a, Figure 2.21b, and Figure 2.21c. The results demonstrate that increasing mesh resolution significantly enhances the agreement between HAMS-MREL and WAMIT, notably for the added mass coefficient $A_{77}^{(11)}$. With 1720 panels, the results from both solvers align closely up to 14 s, with HAMS-MREL showing only a slight underestimation (less than 3%) beyond this range. It should again be emphasized that WAMIT's mesh resolution used here is lower than the converged resolution, thus minor discrepancies when using higher-resolution meshes are expected.

### 2.4.2. COMPUTATIONAL RESOURCES UTILIZED - COMPARING HAMS-MREL AND WAMIT

This section focuses on comparing the computation time between WAMIT and HAMS-MREL for the some of the validation cases. Furthermore, the parallelization capabilities of HAMS-MREL for multiple bodies are investigated with varying number of cores for all the features.

Comparison is done between WAMIT and HAMS-MREL in terms of the analysis time for the first two cases. The analyses were carried out in a 4 core, 8 GB RAM PC with a Intel Core i5-4440 CPU processor (3.10 GHz). The computation times for the analyses are shown in Table. A.3. Since WAMIT v6.1 was used for these analyses, no parallelization was available in WAMIT. Accordingly, for this comparison, no parallelization was used in HAMS-MREL.

Table 2.6.: Simulation times for the first two validation cases with HAMS-MREL and WAMIT (Time in min)

| Case | $N_p^T$ | $N_\omega$ | WAMIT | HAMS-MREL |
|---|---|---|---|---|
| Case 1 | 2400 | 80 | 18.00 | 131.50 |
| Case 2 | 1250 | 100 | 6.00 | 3.05 |

In Table A.3, $N_p^T$ is the total number of panels and $N_\omega$ is the number of frequencies used in the analysis. From Table. A.3, it can be observed that for the considered infinite depth case, HAMS-MREL is generally 2 times faster than WAMIT, whereas for the considered finite depth case, it is 7 times slower than WAMIT. HAMS-MREL does employ parallelization, which can speed up the calculations. This feature was added in WAMIT for v7 or higher [80].

To explore parallelization in HAMS-MREL for the calculation of the hydrodynamic coefficients and excitation forces within the core framework, the analyses were carried on the Snellius High Performance Computer (SURF Netherlands) for Cases 1 and 2. All the analyses were carried out in a 64 GB node with AMD Rome 7H12 processor (3.3 GHz). The number of cores for the calculations were varied from 1 core to 32 cores. The computation ratio (Percentage ratio of the speed in $p$ cores to the speed with one core, where $p$ varies from 1 to 32) with the number of cores and the speed-up ratio (ratio of the speed in 1 core to the speed with $n$ core, where $n$ varies from 1 to 32) with the number of cores is shown in Fig. 2.22. As seen, the computations can be speeded up

as much as 14 times for the finite depth case as compared to the infinite depth case, where the ratio is a little over 2.

This also shows the effectiveness of the OpenMP parallelization in HAMS-MREL with regard to the finite depth cases, where it also takes the most time. Comparing the finite depth and infinite depth cases, the finite depth cases are 3 times slower than the infinite depth cases with increasing number of cores.

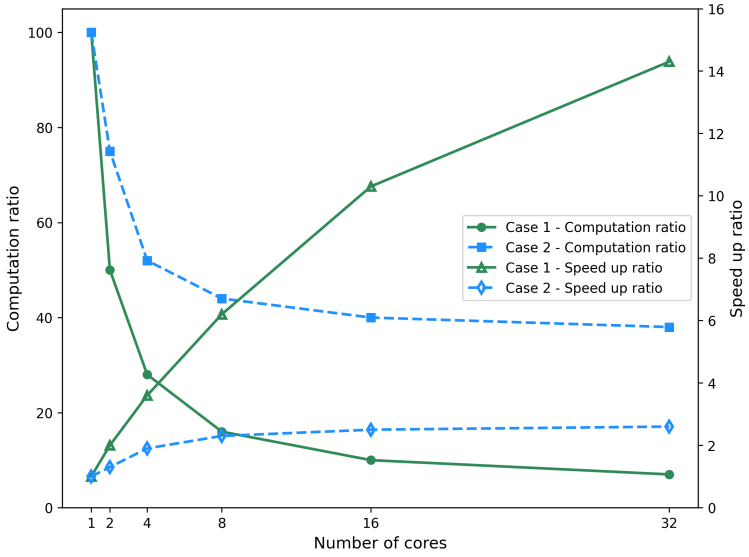



Figure 2.22.: Computation ratio and Speed up ratio with number of cores for Case 1 and 2 - Finite and Deep waters

## DISCUSSION

For the infinite depth cases, the results from WAMIT and HAMS-MREL are very close to each other. When solving for the infinite depth free-surface Green's function, WAMIT breaks down the entire flow domain into four sub-domains based on parameters $X = \nu R$ and $Y = \nu|z+h|$ ($\nu$ is the deepwater wave number, $R$ is the distance between the source and field point and $h$ is the water depth). Different semi-analytical expansions are used to approximate the Green's function in each sub-domain as proposed by Newman [105]. In HAMS-MREL, a different approach is used with a global approximation algorithm utilised which is valid within the entire flow region, that is used to compute the infinite depth Green's function which is accurate up to the second order, as proposed by Liang et al. [90]. Liang et al mentions that Newman's algorithms, as well as the proposed global approximation algorithms within HAMS-MREL have an accuracy of up to $10^{-6}$. This could explain why HAMS-MREL and WAMIT are very close for the infinite depth cases.

When considering Cases 1 and 3, which have the finite depth condition, some differences are observed. These are observed at $\nu a > 1.5$ particularly for the added mass in surge and pitch-surge degrees of freedom and slightly for the radiation damping for the same degrees of freedom for Case 3. There could be two potential reasons for this:

1. The algorithms used for the computations of the finite depth Green's functions: Similar to WAMIT, HAMS-MREL decomposes the flow domain into four sub-domains

based on the ratio $R/h$ to evaluate the finite depth free-surface Green's function; Here $R$ is the distance between the source point and the target point, and $h$ is the water depth. HAMS-MREL employs different semi-analytical expansions in different regimes including one in the vicinity of the logarithmic singularity[67]. To make the algorithm computationally efficient, expressions are derived to calculate the number of terms for these semi-analytical solutions, which are based on performing meticulous convergence studies [67]. In WAMIT, the polynomial expansions in different domains are computed based on evaluating the converging solution of the Green's function, as part of the algorithm itself.

2. The solver used for solving the set of linear algebraic equations: WAMIT offers three different solvers (i) A special iterative solver, (ii) a direct solver, and a (iii) block iterative solver. For the considered finite depth cases, the special iterative solver was utilized, based on generalized minimum residual, that obtains the lowest residual error. This solver is highly recommended for lower order panels (in this we work with the constant panel method), and doesn't require temporary storage which makes it computationally efficient [100]. For both case 1 and 3, convergence was obtained with a maximum of 22 iterations. In HAMS-MREL, a direct solver based on LU decomposition is the only currently available option. This was incorporated in the original HAMS tool as it only requires the left side of the matrix (for both the diffraction and radiation problem) to be evaluated once even for multiple wave headings, making the solver computationally efficient when calculating the hydrodynamic coefficients and excitation forces in a variety of sea states and incident wave angles [67]. The usage of two different solvers between HAMS-MREL and WAMIT could also be contributing to the differences observed the results of Case 1 and 3.

Comparing the differences in computational resources between finite and infinite depth cases for the two solvers, it is observed that HAMS-MREL is generally faster than WAMIT for the considered infinite depth cases, while WAMIT is faster than HAMS-MREL for the considered finite depth cases. The parts of the code that are expected to take the most time is the computation of the Green's function [67], followed by the solution to the set of linear algebraic equations. While the computational time of the iterative solver in WAMIT is proportional to $(N_p^T)^2$, the computation time for the direct solver with LU decomposition in HAMS-MREL is proportional to $(N_p^T)^3$ [106]. Therefore, for the infinite depth cases it is possible that the calculation of the Green's function in HAMS-MREL compensates for the lower speed of its direct solver, thus making it faster than WAMIT. However, in the finite depth cases, the increased computation time due to the direct solver in HAMS-MREL is not compensated by the computation of the finite depth Green's function. This is hard to confirm in WAMIT, since it is commercial and its code is not accessible. It should be noted, that all comparisons are drawn when the same number of panels are considered in both HAMS-MREL and WAMIT. WAMIT offers the possibility of symmetry, which could significantly make it faster. However, this is not within the scope of this research, since the focus is on comparing HAMS-MREL with its current capabilities as an open-source solver.

### 2.4.3. COMPUTATIONAL RESOURCES UTILISED AND ADVANCED FEATURES

To quantify the computational performance of HAMS–MREL and assess the benefits of its advanced features, a series of benchmark simulations were conducted considering wave-field reconstruction, symmetry exploitation, suppression of irregular frequencies, and generalized modes.

**Wave-field computation and parallelization:** For Case 3, used to validate the computed wave fields, $N_f = 10{,}000$ field points were considered for each of $N_\omega = 100$ wave frequencies when evaluating the free-surface elevation. Table 2.7 compares the computational time per frequency with and without parallelization. By employing

32 computational cores, a speed-up factor of 23 is achieved relative to the serial (single-core) case, highlighting the efficiency of the parallel wave-field solver.

Table 2.7.: Computation time for wave-field simulations

| Simulation | $N_\omega$ | $N_f$ | Time/frequency (s) | Computation gain (-) |
|---|---|---|---|---|
| No par (1 core) | 100 | 10,000 | 2700 | 1.0 |
| Par (32 cores) | 100 | 10,000 | 124 | 23.0 |

**Effect of global symmetry:** The influence of global symmetry on computational performance was evaluated using the same array configuration as Case 4. Four scenarios were considered to isolate the effects of symmetry and parallelization:

- *No sym, no par*: no symmetry and no parallelization (base case),
- *No sym, par*: no symmetry with parallelization,
- *Sym, no par*: symmetry with no parallelization,
- *Sym, par*: symmetry with parallelization.

The resulting computation times, summarized in Table 2.8, demonstrate that both symmetry exploitation and parallelization independently yield substantial reductions in computational cost. When combined, these techniques result in a maximum speed-up factor of 47.2 relative to the base case. All parallel simulations employed 32 cores.

Table 2.8.: Computation time for simulations considering symmetry

| Simulation | $N_P^T$ | $N_\omega$ | Time/frequency (s) | Computation gain (-) |
|---|---|---|---|---|
| No sym, no par | 7344 | 300 | 2405 | 1.0 |
| No sym, par | 7344 | 300 | 185 | 13.0 |
| Sym, no par | 3672 | 300 | 852 | 2.9 |
| Sym, par | 3672 | 300 | 51 | 47.2 |

**Suppression of irregular frequencies:** The parallelization efficiency was further assessed for simulations employing a water-plane mesh on all three cylinders to suppress irregular frequencies, as described in Case 4. Table 2.9 presents the computational time per frequency for the three considered mesh configurations, both with and without parallelization.

Using 32 cores, a computational gain of approximately 13.5 is obtained, which is consistent with previously reported results for HAMS–MREL [54], where a speed-up factor of about 14 was observed for finite-depth cases. This confirms that the inclusion of additional water-plane panels does not significantly degrade parallel efficiency.

Table 2.9.: Computation time for simulations with suppression of irregular frequencies

| Simulation | $N_P^T$ | $N_{WP}^T$ | $N^T$ | $N_\omega$ | Parallelization | Time/frequency (s) |
|---|---|---|---|---|---|---|
| Simulation 1 | 7344 | 0 | 7344 | 300 | Yes | 185 |
| Simulation 2 | 7344 | 3168 | 10512 | 300 | Yes | 209 |
| Simulation 3 | 7344 | 4572 | 11916 | 300 | Yes | 233 |
| Simulation 3 | 7344 | 4572 | 11916 | 300 | No | 3150 |

**Generalized modes:** Finally, the computational performance associated with generalized modes was evaluated for a bottom-mounted oscillating flap. A mesh comprising 1,720 panels was considered, together with 270 frequencies and seven degrees of freedom describing the motion of the flap top. The results, reported in Table 2.10, show that parallelization across 32 cores yields a speed-up factor of 16.9 relative to the serial computation, demonstrating the robustness of the parallel implementation even when additional degrees of freedom are introduced.



Table 2.10.: Computation time for simulations with generalized modes

| Simulation | $N_p^T$ | $N_\omega$ | Time/frequency (s) | Computation gain (-) |
|---|---|---|---|---|
| No par (1 core) | 1720 | 270 | 49.6 | 1.0 |
| Par (32 cores) | 1720 | 270 | 2.93 | 16.9 |

## 2.5. Experimental validation of HAMS-MREL - fixed bottom detached OWC device

This section focuses on the experimental and cross-model validation of HAMS-MREL in case of excitation under regular waves for a rectangular fixed bottom detached OWC device. This was adapted from the research paper, [56], which was a collaborative effort between TU Delft and University of Florence.

### 2.5.1. Experimental setup

The experimental model was installed in the Wave-Current flume One (LABIMA-WCF1) located at LABIMA, University of Florence, Italy. The LABIMA-WCF1 is a structure built entirely from steel and glass side walls, with a total length of 37.0 m and width and height of 0.8 m. The piston type wave generator is installed at one end of the wave flume, and it has a stroke equal to 1.5 m, driven by an electromechanical system with an absolute encoder of 0.01 cm accuracy of piston ([107]).

The model has a height of 0.527 m, length (orthogonal the wave direction) of 0.795 m, and width (along the wave direction) of 0.256 m. The plan and elevation of the model are shown in Figure 2.23a and the device as placed in the wave tank is shown in Figure 2.23b. The details of the OWC device and the experimental setup is given in [56].

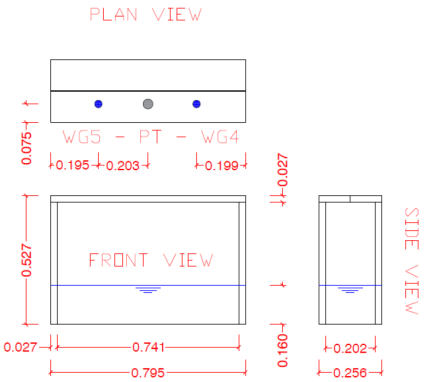
The model was firmly fixed to the side walls such that the internal draft was 0.16 m. In Figure 2.23a, WG4 and WG5 refer to the wave gauges used to measure the displacement of the internal free surface with respect to the still water level inside, and PT is the pressure sensor used to measure the pressure fluctuations in the air pocket above the internal free surface. Two wave gauges were chosen to be used for the model to ensure there was no sloshing of the internal water column.

Two test configurations were utilized. The first configuration was without the OWC model. This configuration was used to measure the testing wave conditions at the model location, in the absence of wave-structure interaction, which would later be used to test the OWC model. The second configuration was with the device installed.

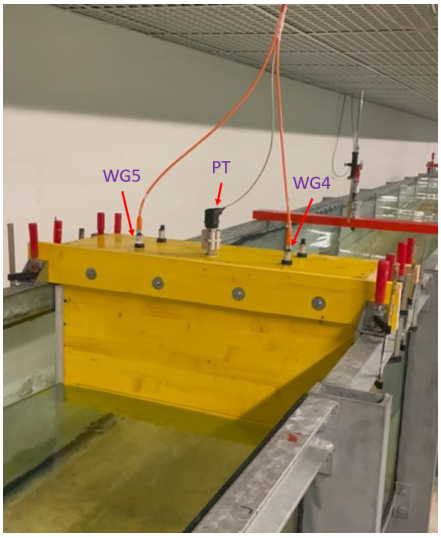
### 2.5.2. Experimental procedure

The test cases selected for the experiment were based on the Le Méhauté diagram (shown in Figure 2.24), which shows the regions of applicability of the various wave conditions (i.e. linear and non-linear) for regular waves based on the water depth ($h$), wave height($H$), wave length($\lambda$) and time period ($\tau$) of the wave.

10 regular wave cases were considered for this (see Table. 2.11). The first four tests H01-H04 were performed to compare how BEM and CFD performed with various wave theories (Airy wave theory, Stoke's $2^{nd}$ order and Stoke's $3^{rd}$ order) and cases H03, H05-10 were done keeping the wave height almost constant and varying the time period




(a) OWC device plan and elevations




(b) OWC placed in tank - WG4 and WG5 are wave gauge designated by orange wires and PT is the pressure gauge depicted by the black wire

Figure 2.23.: OWC device [108]

of the incident waves. This was to determine the Response Amplitude Operator (RAO) for the water column in the device under different wave steepness.

Table 2.11.: Test Matrix - effective values measured at the model position by means of tests in absence of the model (water depth is 0.5m)

| Case name | Wave height, $H$ (cm) | Wave period measured, $\tau$ (s) | Wave frequency, $\omega$ (rad/s) | Water steepness, $H/L$ (-) | Wave theory |
|---|---|---|---|---|---|
| H01 | 2.50 | 2.34 | 2.68 | 0.050 | Airy linear |
| H02 | 1.10 | 1.43 | 4.39 | 0.022 | Airy linear |
| H03 | 6.60 | 1.43 | 4.39 | 0.132 | Stokes $2^{nd}$ order |
| H04 | 9.30 | 1.43 | 4.39 | 0.186 | Stokes $3^{rd}$ order |
| H05 | 6.30 | 1.00 | 6.28 | 0.126 | Stokes $3^{rd}$ order |
| H06 | 6.40 | 1.20 | 5.23 | 0.128 | Stokes $3^{rd}$ order |
| H07 | 6.50 | 1.60 | 3.93 | 0.130 | Stokes $3^{rd}$ order |
| H08 | 6.00 | 1.80 | 3.49 | 0.120 | Stokes $2^{nd}$ order |
| H09 | 6.10 | 2.00 | 3.14 | 0.122 | Stokes $2^{nd}$ order |
| H10 | 6.10 | 2.20 | 2.85 | 0.122 | Stokes $2^{nd}$ order |

The details of the experimental procedure are explained in detail in [56].

### 2.5.3. NUMERICAL METHODOLOGY

This subsection provides a description of the CFD-NWT and numerical BEM model of the OWC device, followed by the framework that combines both these methodologies. The obtained results from this framework are validated with experimental data.

#### CFD MODEL DESCRIPTION

The CFD model was developed and implemented by Dr. Irene Simonetti from the University of Florence, who was a co-author in the publication [56]. The details of the model can be found in the publication. The mesh for the model is shown in Figure 2.25.

The validation of the CFD-NWT with data from laboratory experiments has been shown and discussed in [110], showing relative errors for the height of free surface oscillation

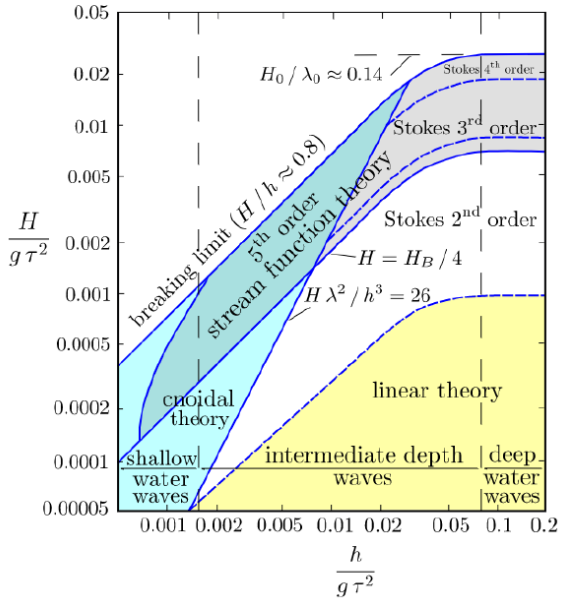



Figure 2.24.: Le Méhauté diagram [109]

and height of the pressure oscillation inside the OWC chamber lower than 15% for all the tested wave conditions. The validation errors are also reported in Table 2.12 for the sake of completeness.

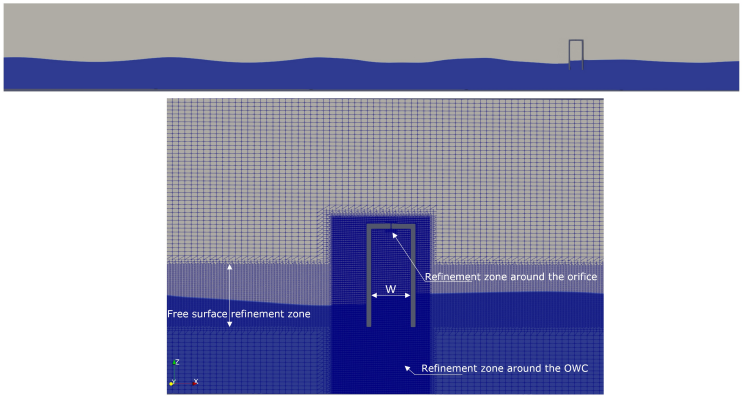



Figure 2.25.: Overview of the CFD-NWT (top) and of the computational mesh in the near field of the OWC (bottom) [54]

Table 2.12.: Relative error between Experimental tests and CFD-NWT for the height of free surface oscillation ($H_{OWC}$) and height of the pressure oscillation inside the OWC chamber ($\nabla P_{OWC}$)

| Case name | Relative Error $H_{OWC}$[-] | Relative Error $\nabla P_{OWC}$[-] |
|---|---|---|
| H01 | −0.06 | 0.13 |
| H02 | −0.07 | 0.04 |
| H03 | −0.07 | 0.04 |
| H04 | −0.05 | 0.03 |
| H05 | −0.02 | 0.02 |
| H06 | −0.05 | −0.03 |
| H07 | −0.01 | 0.03 |
| H08 | 0.03 | 0.08 |
| H09 | 0.00 | 0.07 |
| H10 | −0.07 | 0.14 |

### NUMERICAL BEM MODEL DESCRIPTION

The numerical BEM model for the OWC device was created based on the two-body system approach, where the submerged device hull was modelled as a fixed body (Body 1) and the imaginary piston in place of the water column (Body 2) was modelled as a second body. The dimensions of the model are chosen in correspondence with the experiment. The left and right side walls of the hull were not considered since this is where the box is connected to the wave tank and is not in contact with water. There is no gap between the piston surface and the hull surface. The in-house BEM solver HAMS-MREL provides accurate results when the source and target points overlap as seen in the previous section. The imaginary piston is modelled to the length of the water column. The model is shown in Figure 2.26. The hull of the body was modelled without a base, since the experimental model does not have a base as well. The piston was modelled with a base surface that is in contact with water. The input wave frequencies were considered from 2 to 5 rad/s, with the selection based on the experiments.

In order to decide on the number of elements required for discretizing the model, a convergence study was performed. The BEM solver HAMS-MREL provides the added mass coefficient, radiation damping coefficient (together the hydrodynamic coefficients) and excitation forces as the output. These parameters were utilized to perform the sensitivity analysis. A convergence study was performed similar to the one shown in Figure 2.5a-Figure 2.5c. Based on the results of the convergence study, 1800 elements were selected since the difference with further increase in elements was negligible (convergence is reached) for all the parameters.

After obtaining the hydrodynamic coefficients and excitation forces, the dynamic equation of motion for the model can be solved to obtain the displacement of the free surface. It should be noted, that since the BEM model only considers the part of the body that is submerged in the water, the force due to the pressure above the internal free surface needs to be accounted for in another way. Therefore an additional pressure based forcing term is introduced into the final dynamic equation of motion for the device which results in (Equation 2.51).

$$[i\omega(M_{33} + A_{33}^{(2)(2)}) + B_{33}^{(2)(2)} + \frac{C_{33}}{i\omega}]v_3^{(2)} = F_3^{(2)} - A_0 P \tag{2.51}$$

where $\omega$ is the radial frequency ($rad/s$), $M_{33}$ is the mass of the piston ($kg$) which here is equal to the mass of the water column, $A_{33}^{(2)(2)}$ is the added mass of the piston ($kg$) obtained from HAMS-MREL, $B_{33}^{(2)(2)}$ is the radiation damping ($Ns/m$) obtained from HAMS-MREL, $C_{33}$ is the hydrostatic restoring coefficient ($N/m$) (in this case for a box in

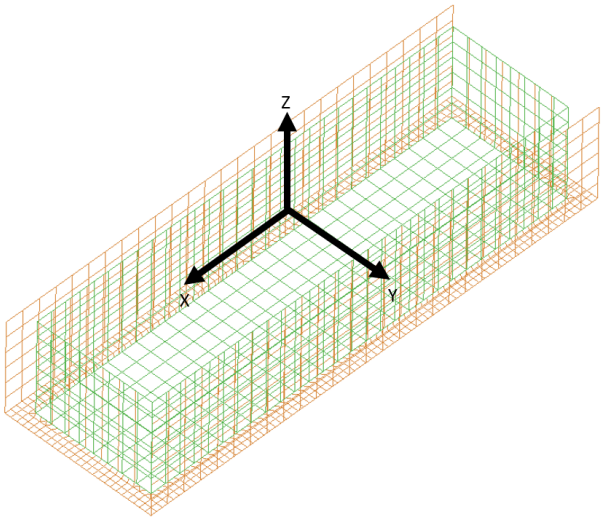



Figure 2.26.: HAMS-MREL model box OWC device: Hull (Body 1 in orange) and imaginary piston (Body 2 in green). The reference global axis is XYZ

heaving motion), $v_3^{(2)}$ is the complex amplitude of the velocity of the free surface (m/s), $F_3^{(2)}$ is the excitation force ($N$) obtained from HAMS-MREL and $A_0P$ is the force due to the pressure above the free surface where $A_0$ is the horizontal area of the free surface ($m^2$) and $P$ is the complex amplitude of the pressure ($N/m^2$) above the water column.

From the CFD-NWT results [111], it can be observed that the pressure above the free surface and discharge through the orifice have a non-linear relationship. However, since we are currently focusing on a linear formulation, the complex pressure amplitude $P$ and complex heave piston velocity $v_3^{(2)}$ are related using a damping coefficient $k$ [112]. It is assumed that the damping coefficient is real-valued and this relationship will exist only if the phase difference between the pressure and velocity is 0 or $\pi$ radians. This can be written as follows:

$$P = kA_0 v_3^{(2)} \tag{2.52}$$

In order to derive the damping coefficient relating pressure above the water column and the discharge through the orifice, two approaches are adopted based on a framework combining BEM and CFD. These are highlighted in the following section.

The framework is presented in Figure A.1. Using the time series of the pressure above the water column and the velocity/displacement of the free surface from the CFD analysis, the coefficient $k$ can be derived. To illustrate the use of the coefficient relating pressure and discharge, two methods are used.

#### BEM model with coefficient considering the phase difference between pressure and discharge

As the first step to calculate the coefficient $k$, the time series of the pressure above the water column and displacement of the free surface obtained from the CFD simulation were used. A curve fitting was performed on the CFD free surface displacement time series (see Figure A.4a) using a sine curve. The derivative of this curve was used to identify the velocity, and hence the discharge. A similar curve fitting was also performed

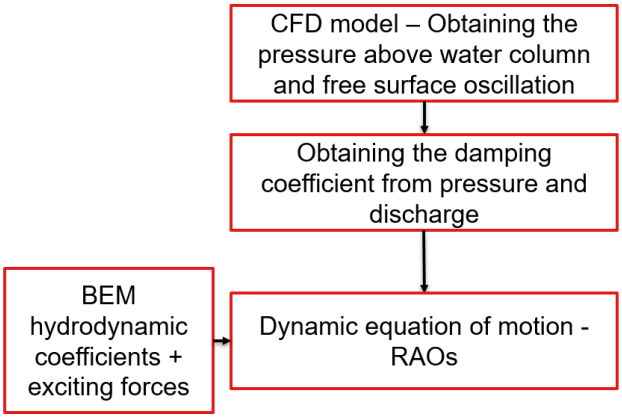



Figure 2.27.: Framework for combining BEM and CFD

for the CFD pressure time series (see Figure A.3b). Using this, the amplitude of the pressure and velocity along with the phase difference between the two were measured.

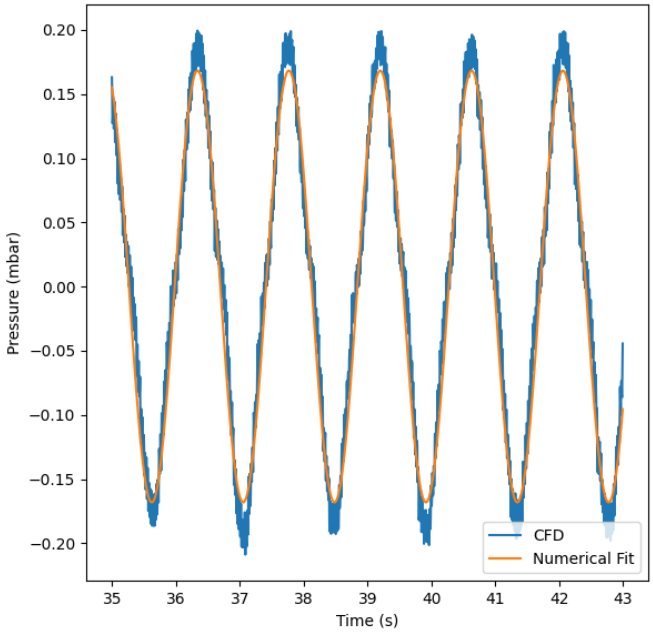



Figure 2.28.: Curve fitting for pressure above the free surface using CFD time series

The obtained phase difference for the 10 cases is summarized in Table 2.13. As observed from the table, the phase difference between the pressure and discharge is different from $0/\pi$ radians indicating that the coefficient $k$ must be complex valued and hence characterizes stiffness and/or inertia in addition to damping (similar to [113–116]).

The obtained phase difference between the pressure and discharge is introduced into Eqn.2.52 to calculate the coefficient $k$. The parameter $\phi$ is introduced to represent the

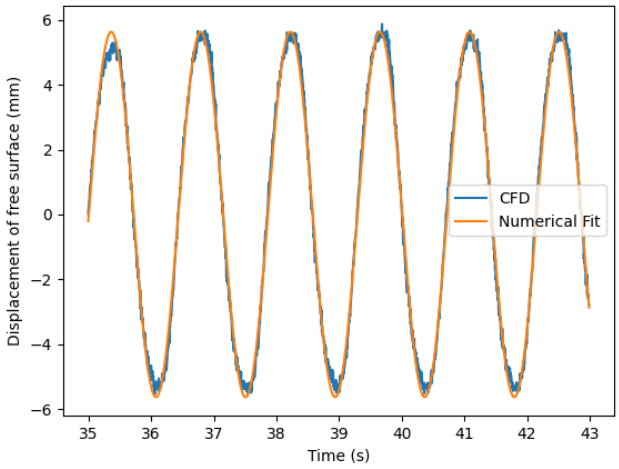



Figure 2.29.: Curve fitting for displacement of the free surface using CFD time series

Table 2.13.: Phase difference between pressure above the water column and velocity of the free surface for all 10 cases

| Case name | Phase difference $\phi$[radians] |
|---|---|
| H01 | 0.43 |
| H02 | 0.25 |
| H03 | 0.27 |
| H04 | 3.39 |
| H05 | 3.47 |
| H06 | 0.32 |
| H07 | 3.38 |
| H08 | 3.36 |
| H09 | 0.22 |
| H10 | 3.33 |

pressure-discharge phase difference. Then Eqn.2.52 thus becomes

$$k_p = \frac{P}{A_0 v_3^{(2)}} * \exp(i\phi) \tag{2.53}$$



where $k_p$ is the complex valued coefficient that accounts for the phase difference. It should be noted that the peak pressure and velocity values are obtained from the curve fitting process. Eqn. 2.53 can then be substituted in Eqn.2.51, which will enable us to solve the dynamic equation of motion of the box OWC water column.

#### BEM MODEL WITH SEMI-EMPIRICAL FREQUENCY DEPENDENT COEFFICIENT

The second method for obtaining the coefficient $k$ is to derive a semi-empirical frequency dependent coefficient based on curve fitting. This will be referred to as $k_i$ to differentiate it from $k_p$. This was done in the following steps:

1. Based on the parameters of the BEM model i.e. the added mass coefficient ($A_{33}^{(2)(2)}$), radiation damping coefficient ($B_{33}^{(2)(2)}$), excitation forces ($F_3^{(2)}$), mass of the piston ($M_{33}$), restoring piston coefficient ($C_{33}$), and the numerical velocity ($v_3^{(2)}$) of the piston obtained from the CFD NWT, the complex value of $k_i$ was obtained in terms of these parameters. This is shown in Eqn. 2.54.

$$k_i = [F_3^{(2)} - [i\omega(M_{33} + A_{33}^{(2)(2)}) + B_{33}^{(2)(2)} + \frac{C_{33}}{i\omega}]v_3^{(2)}]/A_0^2 v_3^{(2)} \tag{2.54}$$

2. A complex frequency dependent semi-empirical coefficient is derived. The real and imaginary parts of the complex coefficient were fitted. A curve fitting is performed with a second order polynomial of the following form:

$$k_i(\omega) = (a_1 + ia_2)\omega^2 + (b_1 + ib_2)\omega + (c_1 + ic_2) \tag{2.55}$$

3. The real and imaginary parts of the semi-empirical frequency dependent coefficient are shown in Fig. 2.30 and Fig. 2.31. The CFD $k_i$ refers to the coefficient derived in step 1 using the CFD-NWT results, while the semi-empirical $k_i$ refers to the coefficient as obtained from the curve fitting performed in step 2.

### 2.5.4. COMPARITIVE RESULTS

This experimental results are compared with the developed CFD–BEM framework for all tested wave cases. The comparison focuses on (i) relative differences in the peak free-surface oscillation inside the OWC ($H_{OWC}$), (ii) pressure oscillations in the OWC chamber ($\nabla P_{OWC}$), (iii) response amplitude operators (RAOs), and (iv) capture width ratio (CWR). Results are evaluated for the CFD–BEM model using coefficient $k_p$, the CFD–BEM model using $k_i$, and against CFD–NWT and experimental data.

Table 2.14 shows that the relative error in $H_{OWC}$ can reach up to 0.21 for the CFD–BEM model with $k_p$, while the error in $\nabla P_{OWC}$ ranges between 0.11 and 0.20. These differences are primarily attributed to the sinusoidal curve fitting inherent to the frequency-domain formulation. As a linear model, CFD–BEM cannot capture non-linear effects observed in experiments, which directly influence the response amplitudes.

A direct comparison of Table 2.12 and Table 2.14 quantifies the accuracy gap between the time-domain CFD–NWT and the linear, frequency-domain CFD–BEM model using $k_p$. For the free-surface oscillation inside the chamber ($H_{OWC}$), the CFD–NWT relative errors remain small across all ten test cases, rangingbetween $-0.07$ and $0.03$ , whereas the CFD–BEM model with $k_p$ shows systematically larger and predominantly negative deviations, reaching a maximum magnitude of $-0.21$ for case H04 and $-0.11$ for H02. A similar trend is observed for the pressure oscillation above the water column ($\nabla P_{OWC}$): the CFD–NWT errors are confined to the interval $[-0.03, 0.14]$, while the CFD–BEM with

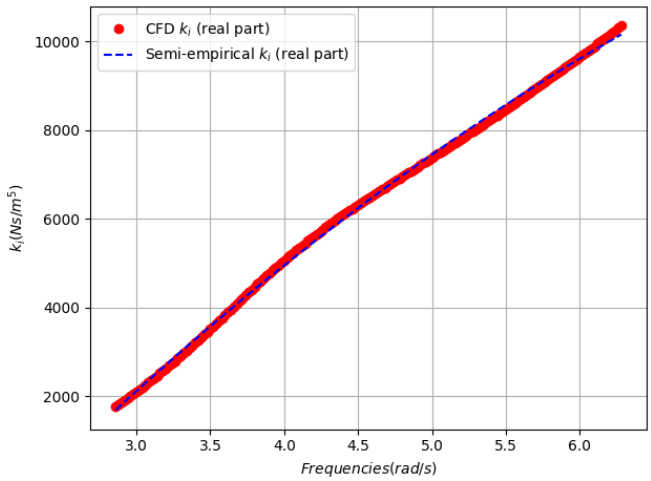



Figure 2.30.: Real part of the frequency dependent instantaneous coefficient $k_i$

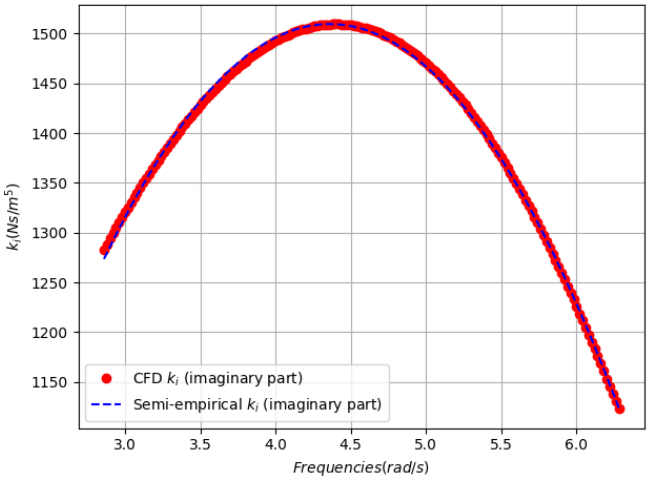



Figure 2.31.: Imaginary part of the frequency dependent instantaneous coefficient $k_i$

Table 2.14.: Relative error between experimental tests and CFD–BEM model results ($k_p$) for the height of free-surface oscillation ($H_{OWC}$) and the pressure oscillation inside the OWC chamber ($\nabla P_{OWC}$).

| Case name | Relative error $H_{OWC}$ [-] | Relative error $\nabla P_{OWC}$ [-] |
|---|---|---|
| H01 | −0.04 | 0.15 |
| H02 | −0.11 | 0.17 |
| H03 | −0.10 | 0.15 |
| H04 | −0.21 | 0.16 |
| H05 | −0.02 | 0.20 |
| H06 | −0.01 | 0.16 |
| H07 | −0.06 | 0.16 |
| H08 | −0.05 | 0.14 |
| H09 | −0.04 | 0.11 |
| H10 | −0.02 | 0.12 |

$k_p$ consistently overestimates the pressure amplitude, with errors in the range 0.11–0.20 for every case and a peak of 0.20 at H05. The widening of the gap is most pronounced for the steeper, more non-linear waves (H03 and H04, Stokes 2$^{nd}$ and 3$^{rd}$ order), where CFD–NWT still reproduces the experiment within 7% on $H_{OWC}$ and 4% on $\nabla P_{OWC}$, while the CFD–BEM model with $k_p$ deteriorates to 21% and 16% respectively. This behaviour is consistent with the linear nature of the BEM formulation combined with the sinusoidal curve fit embedded in $k_p$, which by construction cannot represent the crest–trough asymmetry and higher-order Stokes contributions resolved by the CFD–NWT.

The RAO $\zeta_3^{(2)}$ is computed using

$$\zeta_3^{(2)} = \frac{v_3^{(2)}}{Hi\omega}, \tag{2.56}$$

and compared with CFD–NWT and experimental results in Figure A.2. The CFD–BEM model with $k_p$ reproduces the overall experimental trend but consistently overestimates the response.

In contrast, the CFD–BEM model with $k_i$ shows excellent agreement with experiments across the tested wave periods. This outcome is at first glance surprising, since $k_i$ is itself derived from the CFD–NWT results, whose own agreement with experiment is less tight. The explanation lies in how the RAO is extracted from each model. For the CFD–NWT, the RAO is obtained by averaging peak amplitudes of the time series over a 10 s window. As shown in Figure A.4a, the CFD signal exhibits rapid, high-frequency fluctuations in the vicinity of each peak, and these fluctuations carry through into the peak-averaged amplitude and contribute to the observed error. The CFD–BEM formulation, by contrast, represents the response as a pure sinusoid, so the peak is unambiguous by construction.

The OWC hydrodynamic efficiency is quantified using the capture width ratio (CWR),

$$CWR = \frac{\bar{P}_{BOX}}{\bar{P}_w}, \tag{2.57}$$

where $\bar{P}_w$ is the period-averaged incident wave power and $\bar{P}_{BOX}$ is the average hydrodynamic power extracted by the OWC. The incident wave power is evaluated using Stokes second-order wave theory,

$$\bar{P}_w = \frac{1}{16}\rho g H^2 \frac{\omega}{k}\left(1 + \frac{2kh}{\sinh(2kh)}\right)\left(1 + \frac{9H^2}{64k^4h^6}\right), \tag{2.58}$$

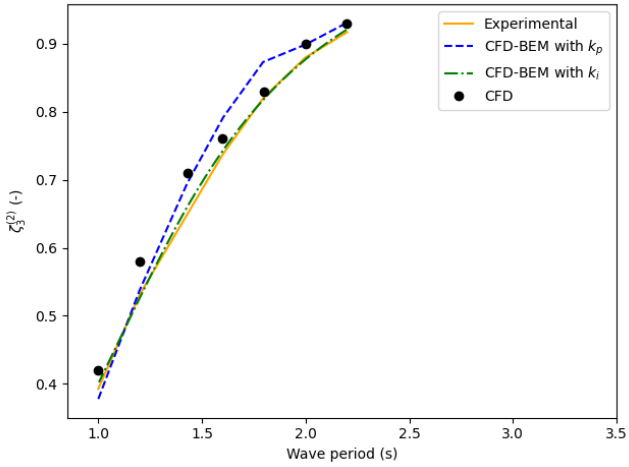



Figure 2.32.: Response amplitude operator ($\zeta_3^{(2)}$) obtained from experiments, CFD–BEM, and CFD modelling.

while $\bar{P}_{BOX}$ is obtained from

$$\bar{P}_{BOX} = \frac{1}{T_{OWC}} \int_0^{T_{OWC}} \left| P_t \frac{d\eta_t}{dt} \right|_{OWC} A_{OWC}\, dt. \tag{2.59}$$

The CWR comparison shown in Figure A.4b indicates good agreement between experiments, CFD, and the CFD–BEM model with $k_i$, although the latter slightly underestimates CWR due to its linear pressure representation.

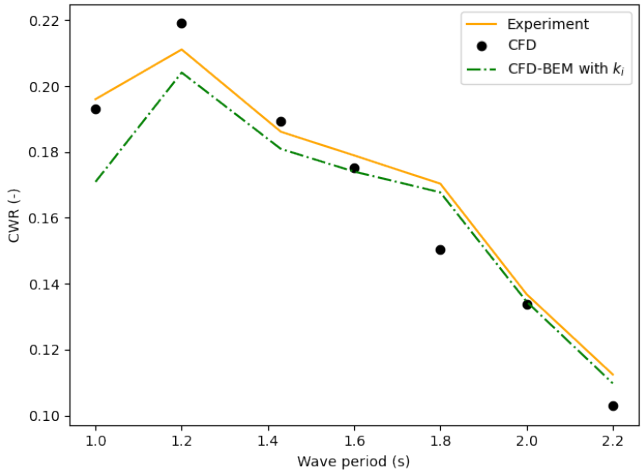



Figure 2.33.: Comparison of capture width ratio (CWR).

Figure A.3a compares the coefficients $k_p$ and $k_i$. Both coefficients are complex-valued, with the real part representing damping and the imaginary part representing a restoring

(stiffness) effect. Since the imaginary component remains positive, it contributes to the system stiffness. Given the small-scale experimental setup, air compressibility effects are assumed negligible, and the observed stiffness contribution is attributed to non-linear orifice effects captured by the coefficients.

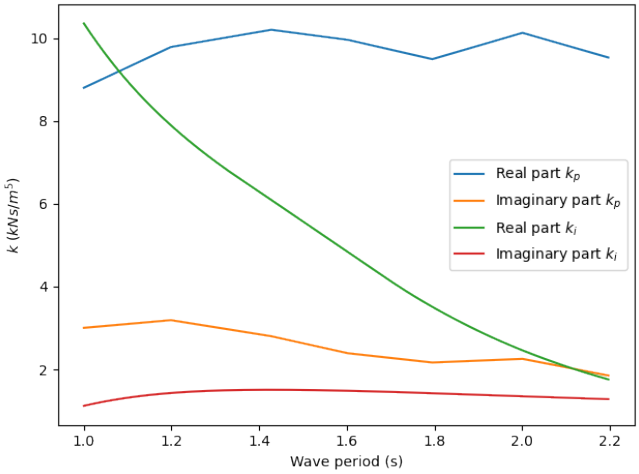
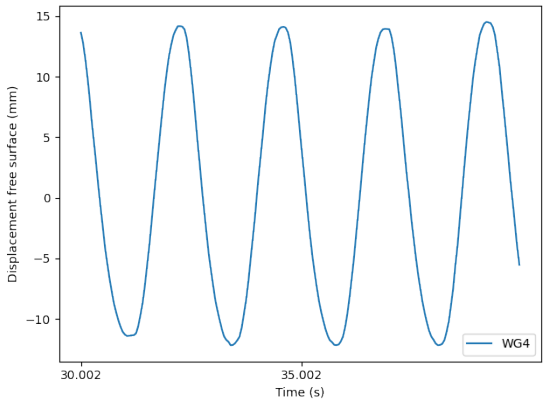



Figure 2.34.: Comparison of coefficients $k_p$ and $k_i$.

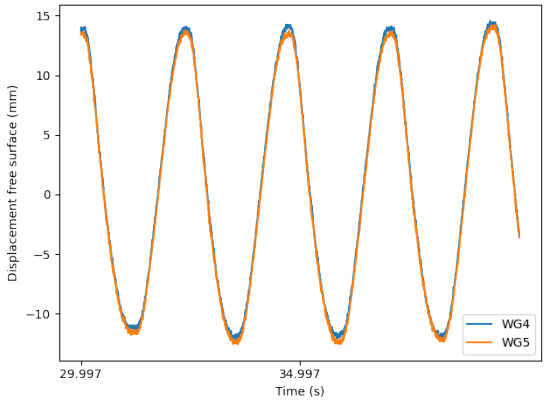
For the CFD–BEM model with $k_p$, both damping and stiffness are increasingly overestimated with wave period. In contrast, the $k_i$ model—derived via curve fitting from CFD simulations—effectively captures non-linear effects associated with second- and third-order Stokes waves, which are absent in the purely linear BEM formulation.

Non-linear wave asymmetry further explains the observed discrepancies. As illustrated for case H02 in Figure 2.35a, incident waves exhibit asymmetric crest and trough amplitudes, characteristic of shallow-water wave propagation. This asymmetry intensifies with increasing wave period and is reflected in both the internal free-surface motion (Figure 2.35b) and chamber pressure variations (Figure 2.35c). These effects lead to asymmetric air injection and ejection processes, contributing to the deviation between experiments and the CFD–BEM model with $k_p$.

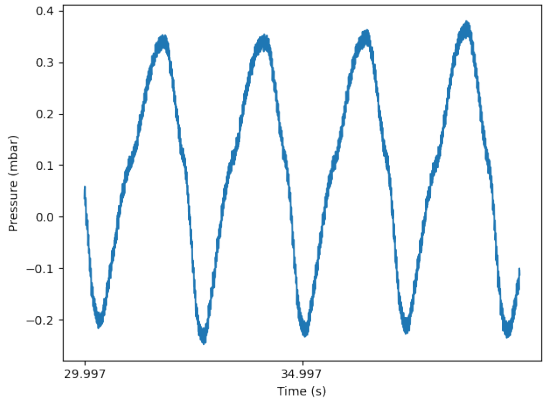
Overall, while both CFD–BEM approaches are suitable for preliminary OWC analysis, the model using $k_p$ provides a first-order response estimate, whereas the CFD–BEM model with $k_i$ offers improved predictive accuracy by partially accounting for non-linear effects within a linear frequency-domain framework.




(a) H02 – Incident wave (experiment).




(b) H02 – Displacement of the free surface inside the OWC (experiment).




(c) H02 – Pressure variation inside the OWC chamber (experiment).

Figure 2.35.: Experimental time histories for case H02 illustrating wave asymmetry and its influence on the internal OWC response.

## 2.6. EXPERIMENTAL VALIDATION OF HAMS-MREL FOR AN ARRAY OF POINT ABSORBERS

This section presents a time-domain validation of HAMS-MREL combined with WEC-SIM for a five-device Point Absorber (PA) array, with the Standardized Wave Energy Converter Array Learning Library (SWELL) dataset [41]. The validation is based on the work of Asikkis et al. [117], conducted as a collaboration between TU Delft and the University of Groningen, led by the University of Groningen. The focus of the study is to validate the workflow, wherein the hydrodynamic coefficients and excitation forces from HAMS-MREL are fed into WEC-Sim, and the obtained results for there responses and forces are compared against experiments.

### 2.6.1. EXPERIMENTAL DATASET AND PHYSICAL SETUP

The SWELL dataset comprises a series of wave basin experiments conducted at Aalborg University, Denmark, and is specifically designed to investigate the hydrodynamic behaviour of wave energy converter (WEC) arrays. Owing to its open-access nature, detailed documentation, and wide range of layouts and wave conditions, SWELL has become a reference benchmark for validating numerical WEC models.

The array configuration considered corresponds to Layout 7 in the SWELL dataset and consists of four floaters arranged in a row, with a fifth floater positioned downstream. All floaters were 1:20 scale models of the Wavestar WEC, a well-established point absorber concept.

Two experimental test types are considered in this study. Test 1 provides free-surface elevation measurements without the presence of floaters and is used to define the wave input in the numerical simulations. Test 2 provides the hydrodynamic loads acting on fixed WECs, enabling direct validation of excitation predictions independent of PTO effects. While the publication goes beyond the validation of WEC-Sim with HAMS-MREL into comparing linear and non-linear effects, for the purposes of this validation only Test 2 was utilized.

Five regular wave conditions (RSS1–RSS5) were considered, spanning a range of wave periods and steepness values relevant to WEC operation. These conditions are summarized in Table 2.15. Here, $T_L$ denotes the duration of each experiment and $H/\lambda$ represents the wave steepness.

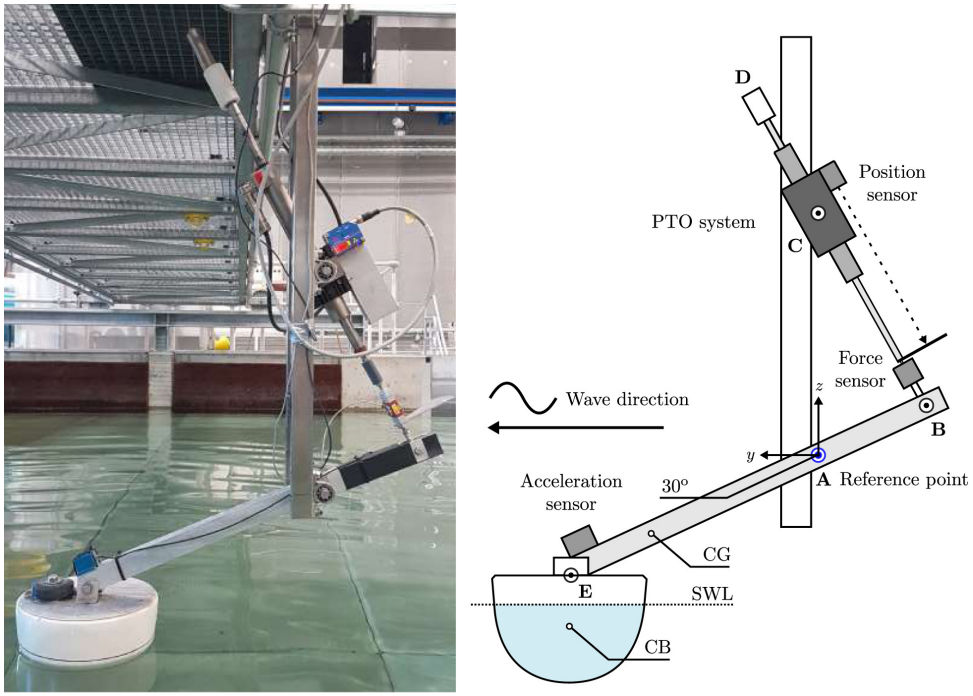
Table 2.15.: Regular wave conditions used in Test 1 of the SWELL experiments. All tests were conducted with an approximately constant wave height of $\sim 0.05$ m and varying wave periods, with each run lasting 60 s [41].

| ID | Type | $H$ [m] | $\lambda$ [m] | $H/\lambda$ [-] | $T$ [s] | $T_L$ [s] |
|---|---|---|---|---|---|---|
| RSS1 | Regular | 0.052 | 1.00 | 0.052 | 0.80 | 60 |
| RSS2 | Regular | 0.053 | 1.27 | 0.042 | 0.90 | 60 |
| RSS3 | Regular | 0.043 | 1.57 | 0.028 | 1.00 | 60 |
| RSS4 | Regular | 0.045 | 3.57 | 0.013 | 1.20 | 60 |
| RSS5 | Regular | 0.052 | 4.46 | 0.012 | 1.50 | 60 |

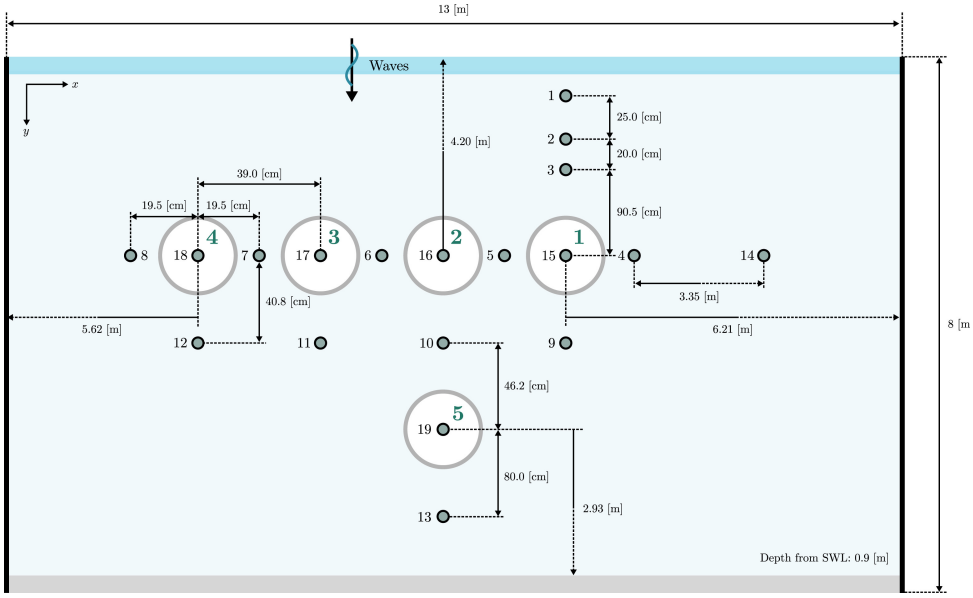
All measurements were acquired at a sampling frequency of 200 Hz. The instrumentation used and their associated uncertainties are detailed in [117]. While the dataset variable `ExcitationForce-WE` is labelled as an excitation force, it corresponds to the force measured at point B along the arm rather than at the floater centre of mass. Consequently, the experimentally derived excitation torque about the hinge point A, provided as `ExcitationTorque-WE`, is used for validation.

### 2.6.2. TIME DOMAIN MODELLING WITH WEC-SIM

WEC-Sim [118] was utilized for the time domain modelling. WEC-Sim utilizes hydrodynamic parameters computed externally by frequency-domain BEM solvers, such as WAMIT, Nemoh, Ansys Aqwa and Capytaine. Once obtained, WEC-Sim calculates




(a) The test facility showing one of the five Wavestar floaters equipped with instrumentation, along with a schematic of the floater setup illustrating the location of sensors and reference points.




(b) Top view layout of the five-floater array within the wave basin, including inter-device spacing.

Figure 2.36.: Experimental setup of the SWELL benchmark case (Layout 7, adapted from [41]).

the time domain response of the system by solving Newton's second law for rigid body dynamics, considering only the significant hydrodynamic and mechanical forces relevant to the analysis. The hydrodynamic model in WEC-Sim is based on the Cummins equation, which accounts for radiation memory effects through a convolution integral of the radiation impulse response function. For this study, the equation of motion of the floating bodies is expressed as:

$$m\ddot{X}(t) = F_{\text{exc}}(t) + F_{\text{rad}}(t) + F_B(t) + F_{\text{pto}}(t) \tag{2.60}$$

- $m$ is the mass of the floating body,
- $\ddot{X}(t)$ is the acceleration vector of the body,
- $F_{\text{exc}}(t)$ is the wave excitation force,
- $F_{\text{rad}}(t)$ is the radiation force, which in the full Cummins formulation includes the added mass at infinite frequency and a convolution integral of the radiation impulse response function,
- $F_B(t)$ is the buoyancy force, and
- $F_{\text{pto}}(t)$ is the reaction force from the hydraulic Power Take-Off (PTO) system (described later).

HAMS-MREL is integrated with WEC-Sim enabling time-domain simulations of WECs and WEC arrays based on hydrodynamic coefficients computed by this solver. The integration is performed by feeding appropriately formatted input containing the hydrodynamic coefficients and excitation forces into BEMIO.

A more detailed description of the WEC-Sim formulation can be found in [119, 120].

### 2.6.3. NUMERICAL SETUP FOR SWELL

To solve the boundary integral equation (BIE), HAMS-MREL requires the wetted geometry of each floating body to be discretized into surface panels. In this study, the number of panels in the mesh for the Wavestar floaters was based on a convergence study based on the evaluation of Normalized Root Mean Square Error (NMRSE). The detailed study on the mesh convergence can be found in [117]. Based on this analysis, the 727-panel mesh is selected for all subsequent simulations, as it provides a suitable compromise between computational cost and numerical accuracy.

The key input parameters adopted for the HAMS-MREL simulations are summarized in Table 2.16. A wave heading of 0° was imposed throughout, consistent with the experimental configuration. The frequency range was extended up to 15 rad/s to ensure that the high-frequency hydrodynamic response was adequately captured.

For the time-domain simulations performed using WEC-Sim, the wave input was derived from Test 1 of the SWELL experimental dataset, in which wave elevation measurements were obtained in the absence of floaters. Each floater in the array was modelled as a fixed body, consistent with the experimental setup, as illustrated by the Simulink model shown in Figure 2.37. A fixed time step of 0.005 s was employed using the WEC-Sim solver `ode4`. This choice ensures sufficient temporal resolution to match the experimental sampling frequency and satisfies the WEC-Sim recommendation of resolving each wave period using approximately 100–200 time steps [119].

The primary hydrodynamic output obtained from WEC-Sim is the wave excitation force acting on each floater. However, the experimental data used for validation are reported in terms of the wave excitation torque $\tau_A$ about the hinge point $A$. To enable direct comparison, the numerical excitation forces were post-processed to compute the corresponding torque using

$$\tau_A = F_{\text{exc},z}\, L_{AE} \sin(\theta) + F_{\text{exc},x}\, L_{AE} \cos(\theta), \tag{2.61}$$

where $\theta = 30°$ is the angle between the arm and the horizontal, $F_{exc,z}$ and $F_{exc,x}$ are the vertical and horizontal components of the wave excitation force, respectively, and $L_{AE}$ denotes the distance from the hinge point $A$ to the force application point $E$ on the floater (see Figure 2.36).



Table 2.16.: Input parameters used in the HAMS-MREL simulations for the SWELL case, including environmental conditions, wave characteristics, and mesh resolutions.

| Parameters | Value | Units |
|---|---|---|
| Wave heading | 0 | ° |
| Wave frequency | 0.2:0.187:15 | rad/s |
| Depth | 0.9 | m |
| Density | 1000 | kg/m$^3$ |
| Number of panels | 48 | [-] |
| | 453 | [-] |
| | 727 | [-] |
| | 1481 | [-] |

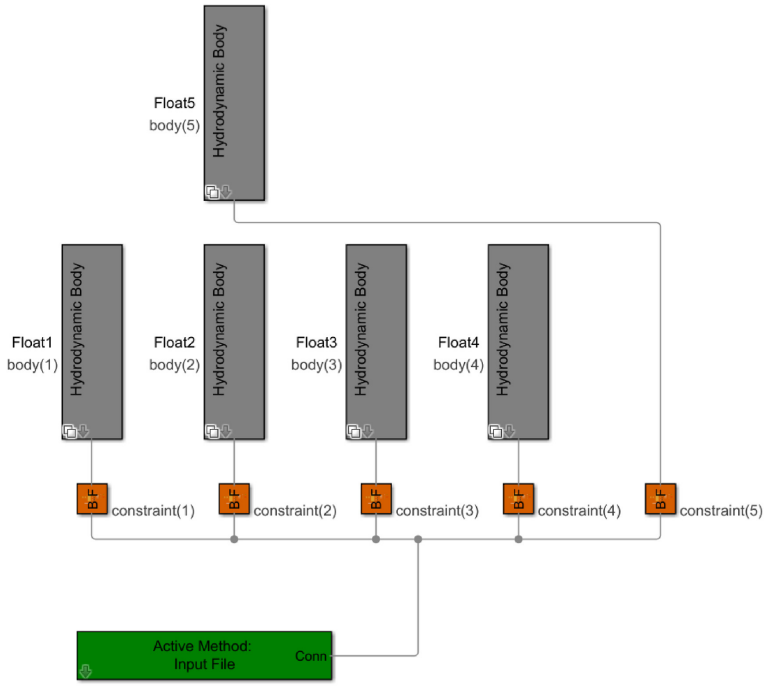



Figure 2.37.: Simulink model in WEC-Sim representing the five-floater array for the SWELL test case. Each floater is modelled with a fixed constraint [117].

### 2.6.4. VALIDATION AGAINST EXPERIMENTAL DATA

The wave excitation torque predictions (Test 2) obtained using HAMS-MREL were validated against experimental measurements from the SWELL dataset for five regular wave conditions (RSS1–RSS5). The primary objective of this validation was to evaluate

the solver's predictive capability across a range of wave steepness conditions, while also addressing the limited validation available in the literature for excitation force predictions within dense WEC arrays.

Figure 2.38 presents the phase-averaged excitation torque signals obtained from numerical simulations and experiments for each floater and wave condition. Phase averaging was performed by extracting complete wave cycles after the ramp-up period, aligning them by phase, and averaging the corresponding time samples within each cycle. This procedure yields a representative steady-state response under regular wave forcing. Overall, good agreement is observed for most floaters and wave conditions, indicating that HAMS-MREL effectively captures the dominant wave–body interaction mechanisms within the array.

To quantify the accuracy of the predictions, the Normalized Root Mean Square Error (NRMSE) was computed for each excitation torque signal across all floaters and wave conditions, as shown in Figure 2.39. The NRMSE values range from approximately 2–21%, with the largest discrepancies consistently observed for the downstream floater (Floater 5). In particular, Floater 5 exhibits elevated NRMSE values of approximately 17–19% under higher wave steepness conditions (RSS1–RSS3), highlighting the increased difficulty of accurately modelling downstream hydrodynamic interactions at greater steepness levels. In contrast, the remaining floaters generally show good agreement, with NRMSE values typically below 10%, aside from isolated cases such as Floater 3 under the RSS2 condition.

Part of the observed discrepancies may also be attributed to experimental uncertainties. Specifically, the wave input used in the simulations is derived from Test 1 of the SWELL dataset, in which no floaters are present, whereas the excitation torque measurements correspond to Test 2, where the floaters are installed. Variations between these experimental runs, arising from wavemaker repeatability or active absorption effects, may introduce inconsistencies between the simulated and actual wave fields. Furthermore, the linear potential flow formulation assumes inviscid, irrotational flow and a constant wetted surface area, assumptions that become increasingly violated under higher wave steepness conditions.

Further insight into solver performance is provided by the analysis of excitation torque signal characteristics shown in Figure 2.40. Differences in predicted and measured maxima, minima, and amplitudes range from negligible values (approximately 1%) to deviations as large as 56%. These variations highlight the sensitivity of local hydrodynamics to the position within the array, with the downstream floater again exhibiting the largest discrepancies. For Floater 5, improved agreement is observed under lower wave steepness conditions (RSS4 and RSS5). In contrast, for floaters 1–4, larger discrepancies occur under the lowest steepness condition (RSS5), where numerical predictions consistently overestimate the excitation torque.

These trends can be attributed to several factors. Lower-frequency waves associated with RSS5 correspond to longer wavelengths and higher wave-induced pressures acting on the array. Conversely, under higher-frequency conditions (RSS1–RSS4), shorter wavelengths of approximately 1–1.5 m become comparable to the floater spacing (0.6–1.1 m), potentially inducing stronger non-linearities in the form of local diffraction, scattering, and interference effects that are not fully captured by linear theory. Additionally, higher wave steepness conditions introduce nonlinear Froude–Krylov forces due to significant variations in the wetted surface area, further contributing to the observed discrepancies.

Overall, this validation study demonstrates that HAMS-MREL reliably predicts wave excitation torques across a broad range of wave conditions, with particularly strong performance under moderate wave steepness where linear assumptions remain valid. For higher steepness scenarios, the results should be interpreted with appropriate caution, as increased nonlinear effects inherently limit the predictive capability of linear potential flow-based models.

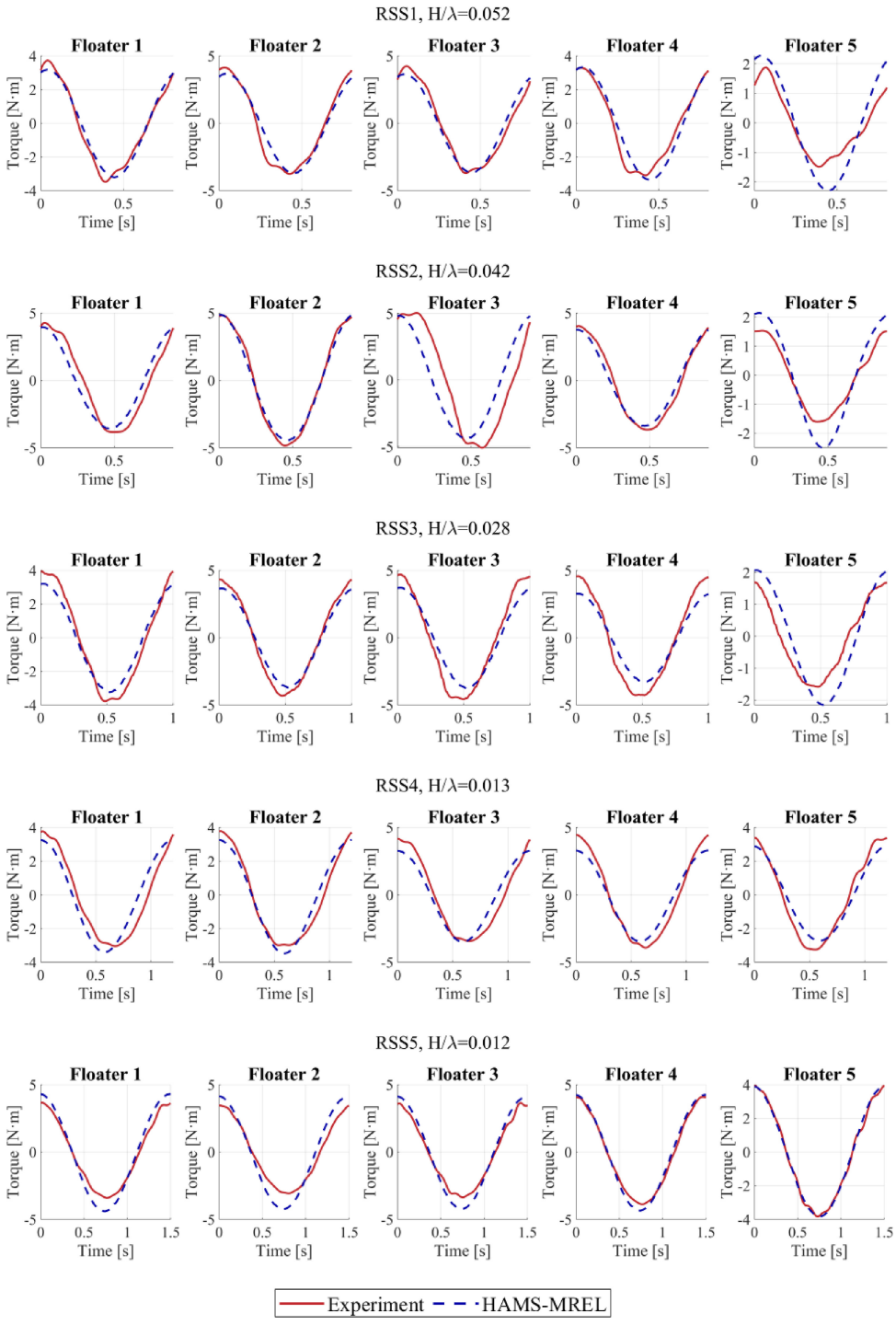



Figure 2.38.: Comparison of phase-averaged wave excitation torque signals between HAMS-MREL simulations (dashed blue) and experimental measurements (solid red) for all five floaters under five regular wave conditions (RSS1–RSS5) [117].

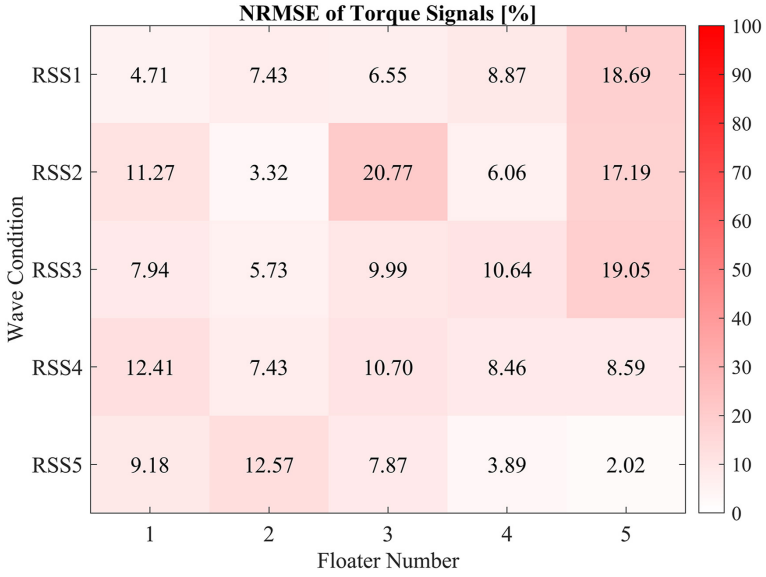



Figure 2.39.: Normalized Root Mean Square Error (NRMSE, %) of excitation torque signals across all floaters and wave conditions [117].

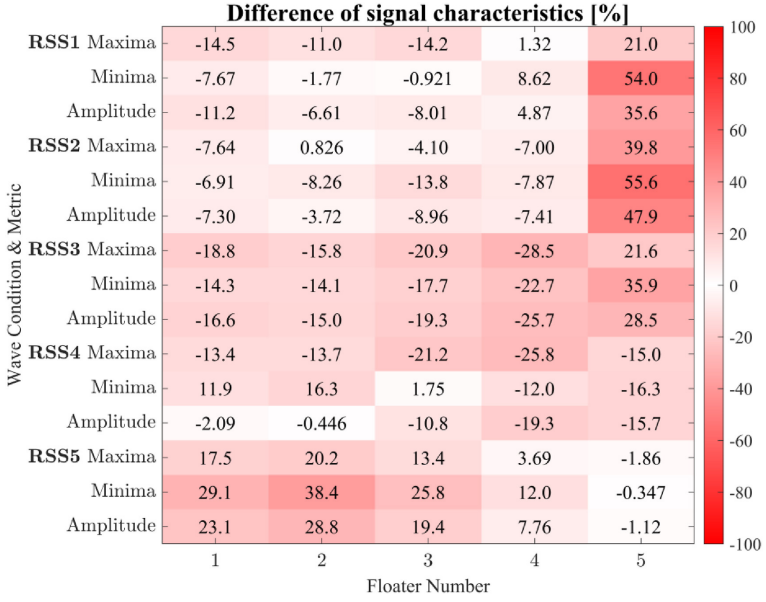



Figure 2.40.: Percentage difference in signal characteristics (maxima, minima, amplitude) of the excitation torque between HAMS-MREL simulations and experiments across all floaters and wave conditions [117].

## 2.7. DIFFERENTIATING HAMS-MREL FROM HAMS

Having presented the theoretical formulation of HAMS-MREL and demonstrated its performance across a range of numerical benchmarks, cross-model comparisons, and experimental validation campaigns, it is useful to consolidate the specific ways in which the solver departs from its parent code, HAMS. This synthesis clarifies the scope of the developments carried out in this thesis and provides a concise reference for users familiar with HAMS or with other open-source BIEM solvers.



The principal differences between HAMS and HAMS-MREL can be summarised as follows. The boundary integral formulation has been extended to handle an arbitrary number of interacting bodies with independent local coordinate systems, enabling full hydrodynamic cross-coupling between floaters and fixed structures in an array (Section 1.1; validated against semi-analytical solutions and WAMIT in Cases 1 and 2 of Section 1.4). Free-surface elevation and pressure-field computations for both diffraction and radiation problems have been added to support the study of wave interference and shielding effects, with validation against WAMIT presented for the three-cylinder configuration in Case 3. A waterplane-mesh treatment has been incorporated to suppress irregular frequencies (Case 4), and a global symmetry option has been introduced to further reduce computational cost for symmetric layouts (Section 1.3.2). Support for generalised (dry) modes allows the modelling of constrained and articulated devices, such as bottom-hinged flaps and multi-body attenuators, within the same framework, as demonstrated in Case 5 for a bottom-hinged flap. Finally, OpenMP parallelisation has been implemented across the core solver and the new features, and the solver output has been aligned with WEC-Sim, which enabled the experimental time-domain validation against the five-floater SWELL array presented in Section 1.6.

Together, these extensions transform HAMS from a single-body frequency-domain solver into a general-purpose multi-body framework suited for array-scale analyses of marine renewable energy systems, while preserving the computational efficiency and accuracy that motivated its selection in the first place.

## 2.8. CONCLUSIONS

This chapter presented the formulation, implementation, and validation of HAMS-MREL, a multi-body extension of the HAMS solver, with emphasis on numerical accuracy, experimental fidelity, and computational efficiency. Validation was conducted using semi-analytical benchmarks, cross-model comparisons with WAMIT and CFD, and experimental datasets in both the frequency and time domains.

For the frequency-domain numerical validation, HAMS-MREL demonstrated excellent agreement with established reference solutions. In the two semi-immersed cylinder case in finite depth, the added mass, radiation damping, and excitation forces closely followed semi-analytical interaction theory and WAMIT results across the investigated frequency range. Minor deviations were observed at higher nondimensional wavenumbers ($\nu D > 2$), where HAMS-MREL slightly under-predicted the total surge added mass, while WAMIT exhibited a small over-prediction relative to the semi-analytical solution. For the submerged sphere case in deep water, the surge, sway, and heave hydrodynamic coefficients and excitation forces computed by HAMS-MREL matched exactly with both Wu's semi-analytical solution and WAMIT, confirming the robustness of the solver for submerged and pressure-differential type devices.

The wave-field validation for a three-cylinder configuration in deep water further confirmed solver accuracy. Diffraction and radiation free-surface elevations were computed over $N_f = 10{,}000$ field points for $N_\omega = 100$ wave frequencies. The mean square error between HAMS-MREL and WAMIT remained below 2 % across the entire computational domain for both diffraction and radiation cases, demonstrating accurate resolution of near-field interaction effects and far-field wave propagation relevant to array-scale analyses.

The suppression of irregular frequencies was validated using a three-cylinder point-absorber configuration. Pronounced irregular-frequency spikes observed at wave periods of approximately 2 s in the added mass, radiation damping, and excitation force

responses were fully eliminated when water-plane meshes were applied to all bodies. Partial suppression was observed when water-plane meshes were applied to only a subset of bodies, confirming the consistency and locality of the implemented approach.

The generalized modes formulation was validated using a bottom-mounted oscillating flap in shallow water. Cross-comparison with WAMIT showed very good agreement for the rotational added mass, radiation damping, and excitation force. Differences were generally within ±5 % at wave periods of 5–6 s, and reduced to below 3 % after mesh refinement (from 518 to 1720 panels). These results confirm that HAMS-MREL can accurately represent constrained and articulated motions relevant to oscillating wave surge converters.

Experimental validation provided further confidence in the solver. For the experimental validation of the fixed-bottom detached OWC considering the frequency domain formulation, HAMS-MREL reproduced the incident wave elevation, internal free-surface displacement, and chamber pressure variations with good accuracy. Across the tested wave periods, discrepancies in free-surface elevation amplitude were typically below 5 %, while pressure amplitudes inside the OWC chamber were predicted within 5–10 % of the measured values.

For the experimental validation of a PA array considering the time-domain formulation, hydrodynamic coefficients generated by HAMS-MREL and coupled with WEC-Sim reproduced measured motions with good accuracy. Predicted heave response amplitudes deviated typically by 5–8 % from experimental measurements, while peak responses were captured within ±10 % across the tested sea states (higher wave steepness). Time histories showed good phase agreement, and the root-mean-square error of the simulated responses remained low relative to the measured signal amplitudes. These results confirm that the frequency-domain hydrodynamics obtained from HAMS-MREL provide a reliable basis for time-domain simulations of interacting WEC arrays even with increased wave steepness.

From a computational performance standpoint, HAMS-MREL proved to be scalable and efficient. For infinite-depth cases, HAMS-MREL was up to 2× faster than WAMIT in serial computations, while for finite-depth cases it was approximately 7× slower due to the use of a direct LU solver. The implementation of OpenMP parallelization substantially mitigated this limitation. Speed-up factors of approximately 14× were achieved for finite-depth cases when increasing the core count from 1 to 32, while infinite-depth cases showed speed-ups of around 2×.

For wave-field computations, parallelization led to a 23× speed-up. The exploitation of global symmetry further reduced computational cost, and when combined with parallelization yielded a maximum speed-up factor of 47.2×. Importantly, the inclusion of water-plane meshes for irregular-frequency suppression did not significantly degrade parallel efficiency, with speed-ups remaining around 13–14×.

Overall, the numerical, experimental, and computational results demonstrate that HAMS-MREL is a validated, accurate, and scalable multi-body BIEM solver across a range of geometries. It reliably captures hydrodynamic interactions, wave fields, constrained motions, and array effects across shallow and deep-water regimes. These validated capabilities form a robust foundation for the array-level hydrodynamic performance assessments and techno-economic analyses of mono and mixed wave energy farms presented in the subsequent chapters.

# 3

# ANALYSIS OF MONO AND MIXED ARRAYS IN SHALLOW WATER

*If at first the idea is not absurd, then there is no hope for it*

Albert Einstein

*This chapter introduces for the first time in scientific literature, mixed arrays defined as arrays of WECs of different geometries operating in different degrees of freedom. A systematic hydrodynamic assessment of mixed WEC arrays operating in shallow-water conditions is performed and compared with mono arrays, defined as arrays of the same device. Mono arrays composed of point absorbers (PAs) and flaps are compared against mixed PA–flap arrays using a weakly non-linear frequency-domain framework that accounts for viscous losses and both passive and active control strategies. Array performance is evaluated across variations in device count, spacing, layout, and incident wave direction using interaction-based (q-factor) and geometry-normalised (M-factor) metrics. The results demonstrate that mixed arrays consistently outperform flap mono arrays and, in some configurations and directions, match or exceed the performance of PA mono arrays as well. The enhanced performance of mixed arrays is attributed to hydrodynamic synergy arising from complementary device dynamics, leading to improved directional robustness and more stable behaviour with increasing array size. While mixed arrays introduce additional configuration and control complexity, the findings indicate that they offer a robust and efficient pathway for wave energy extraction in shallow-water coastal regions.*

This chapter introduces the hydrodynamic modelling framework used to evaluate the performance of mono and mixed WEC arrays in shallow-water conditions. Two wave energy converters are considered in this study. The first is a point absorber (PA), whose geometry is inspired by the state-of-the-art CorPower C4 device [11]. Two variations of this geometry are considered here. The second is a bottom-fixed oscillating flap, modelled after the commercial WaveRoller concept [22]. The chapter begins by describing the wave climate and key modelling assumptions, followed by a detailed presentation of the weakly non-linear hydrodynamic models developed for both the PA and the flap, for single devices as well as array configurations. The results first examine the global behaviour of mono and mixed arrays, before analysing the influence of incident wave direction, number of devices, and inter-device spacing. The chapter concludes by identifying the optimal mixed-array configuration for in-depth performance assessment.



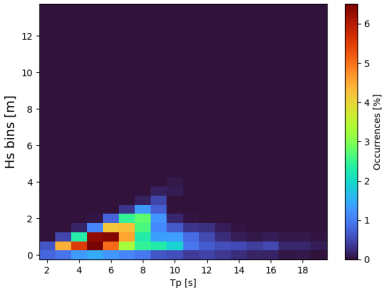
## 3.1. SCATTER DIAGRAM

A location off the north coast of the Netherlands was selected for this study. The Dutch coast offers several benefits for wave-energy deployment: (a) favourable coastal characteristics with smoother depth variation [121], (b) a significant resource of ≥ 7 kW/m available at shallow depths of 15 to 20 m [122], (c) high vessel accessibility due to milder mean conditions of ≥ 90% [122, 123], and (d) accelerated proof-of-concept testing of WECs due to shared grid-connection hubs [121], (e) smaller extreme waves reducing the cost of required infrastructure [12].

The selected location at Lat 53.6°, Lon 6.3° lies 7.3 km off the coast of Schiermonnikoog, one of the northern islands of the Netherlands (see Figure 3.1a). The scatter diagram for this location is shown in Figure 3.1b. The site lies in a low- to mid-resource region, with peak occurrences at $H_s$ = 0.5–1 m and $T_p$ = 5 s. The scatter diagram further indicates that the largest share of occurrences (approximately 32%) for a given significant wave-height bin occurs at $H_s$ = 0.5–1 m. Therefore, this wave height is used to study the directional variation of the $q$-factors in section 3.7.




(a) Considered location at Lat 53.6°, Lon 6.3° off the coast of the Netherlands




(b) Scatter diagram at Lat 53.6°, Lon 6.3° off the coast of the Netherlands

Figure 3.1.: Selected offshore location and corresponding wave climate off the coast of the Netherlands.

## 3.2. ASSUMPTIONS

Hydrodynamic models based on a weakly non-linear frequency-domain framework are used to simulate both single devices and arrays. This section summarises the underlying assumptions.

### GEOMETRY OF THE PA FOR SHALLOW WATERS

The reference device in this study is the CorPower C4 point absorber, which has a diameter of 9 m and a draft of 5.42 m and is predominantly designed for deep-water applications [124]. To investigate its suitability for shallower sites and mixed-array configurations, two modified geometries are considered: a scaled-down device and a scaled-up device, both sharing the same draft as the smaller point absorber (PA).

The smaller PA is introduced for three main reasons. First, point absorbers are most effective when their characteristic dimension is small relative to the incident wavelength. In shallow water, wavelengths corresponding to a given wave period are shorter; consequently, a reduced-diameter PA can still operate efficiently. Second, the reduced draft limits the vertical variation of orbital velocity, allowing viscous drag to be reasonably estimated using the body's structural velocity alone, thereby improving the validity of the weakly non-linear formulation. Third, a shallower draft provides increased seabed clearance, improving the practical feasibility of nearshore deployment.

In parallel, a larger PA is considered while maintaining a reduced draft, in order to isolate the influence of device size on mixed-array interactions. For the larger PA, the natural period lies close to 4.5 s, which is close to the most frequently occurring peak period in the site-specific scatter diagram. This makes the larger PA more geometrically tuned to the prevailing wave climate. Owing to the increased device dimensions, wavelengths at shorter periods (around 3–4 s) become comparable to the device diameter, suggesting that nonlinear effects may be more pronounced. However, since the site represents a relatively low-energy wave climate, the resulting responses are still expected to be captured adequately using a weakly non-linear modelling approach.

At the selected 15 m water depth, the dominant sea states are characterised by peak periods of approximately 5–6 s and significant wave heights around 1 m (see Figure 3.1b). Although the natural period of the 6 m PA (approximately 3.6 s) lies below the spectral peak, the combined effects of hydrodynamic radiation damping and PTO control broaden the operational bandwidth, enabling effective energy absorption across the dominant 3–12 s period range. As such, the adapted PA configurations provide a practical representation of nearshore-scaled CorPower-type devices, balancing hydrodynamic performance, geometric tuning, and deployment feasibility in shallow-water mixed arrays.

According to the Le Méhauté diagram [125], regular waves with periods of 3–12 s at a depth of 15 m fall close to second-order Stokes theory at $T = 3$ s and shift toward linear Airy theory at $T = 12$ s. A weakly non-linear model is therefore adopted here.

### VISCOUS LOSSES

Viscous drag effects are incorporated into the hydrodynamic models under both passive and active control strategies. The motivation for including viscous drag differs depending on the WEC type.

For the flap device, viscous drag can be highly significant. Da Silva et al. [126] performed a statistical linearization of Morison's equation to account for viscous drag in shallow-water conditions under irregular sea states. When comparing frequency-domain simulations without viscous losses to time-domain simulations that included them, differences of up to 33% in absorbed power were observed for peak periods $T_p$ ranging from 8 to 15 s and a significant wave height $H_s$ of 1.5 m. Furthermore, for $T_p = 12$ s and $H_s$ varying from 0 to 5 m, the difference in absorbed power reached up to 100% at higher wave heights.

For the PA, viscous effects generally become relevant only at larger $H_s$ values, since the drag force is nonlinear and scales with the square of the relative velocity between the structure and the surrounding flow (particularly in deep-water conditions). This is not typically the case in shallow water for the present study, where the maximum $H_s$ is 2–2.5 m. However, given the curved geometries of the PAs considered, nonlinear Froude–Krylov (NLFK) forces can be important even at small displacements. Including viscous drag within the frequency-domain model therefore supports more robust power

estimates under the conditions considered. Hence, viscous drag is also included for the PA [127].

### NON-LINEAR HYDROSTATICS AND NON-LINEAR FROUDE–KRYLOV FORCES

Non-linear hydrostatics (NLH) and NLFK forces can be important for PAs, especially those with near-hemispherical geometries (such as the CorPower C4-inspired device) operating in medium to high sea states [128–130]. In the present study, however, only low sea states up to $H_s = 2$–$2.5$ m are considered.

Regarding NLH, in addition to the relatively low sea states, motion constraints are applied under the active control strategy to limit the heave displacement to 1.2 m (approximately 30% of the draft). This ensures that the change in the submerged cross-sectional area $\Delta A$ remains within approximately 7% (see Figure 3.2) for the smaller PA and within 9% for the large PA (Figure 3.3). Therefore, NLH effects are neglected here.

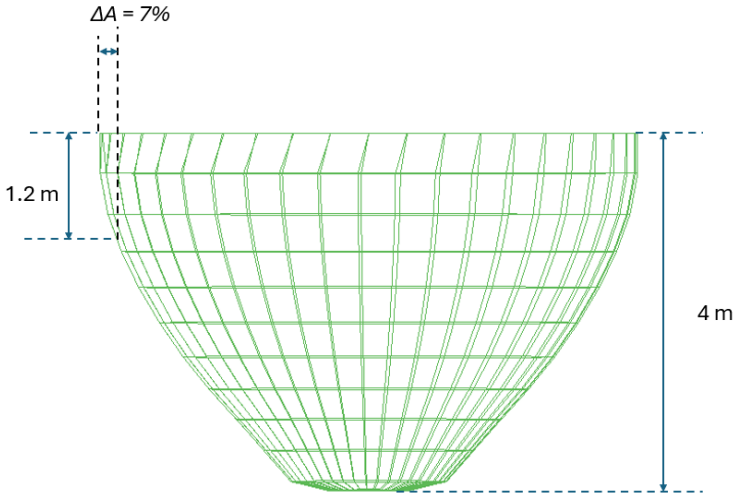



Figure 3.2.: Variation in submerged area with maximum displacement for the small PA

For NLFK forces on the PA, although these can become relevant even for small displacements, their accurate representation typically requires medium- to high-fidelity modelling approaches. Nonetheless, including viscous drag within the hydrodynamic model provides sufficiently improved power estimates under the conditions considered, without explicitly modelling NLFK effects.

### MOORING SYSTEM FOR PA

Taut mooring is assumed for the PAs. The primary role of the mooring system is to counteract drift and current forces; therefore, the weight of moorings and anchors is expected to be small [131]. For heaving WEC arrays, Meyer et al. [132] showed that a taut mooring system at a scaled depth of 15 m has a small influence on the heave response across the considered wavelength ranges (where the wavelength range was defined as the ratio of incident wavelength to array length). Consequently, the mooring system is not explicitly modelled here, since its influence is assumed negligible.

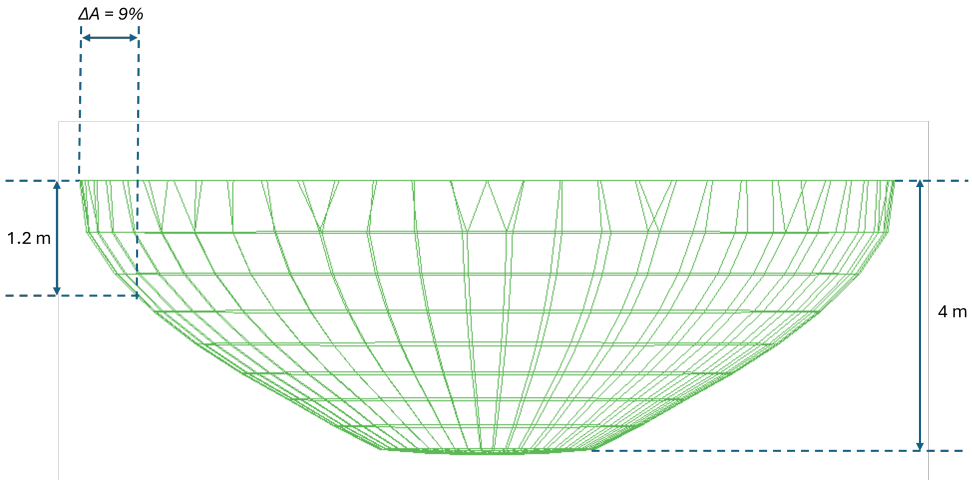



Figure 3.3.: Variation in submerged area with maximum displacement for the large PA



#### SPACING OF THE WECS IN THE ARRAY

A minimum spacing of $4L$, where $L$ is the characteristic dimension of the WEC in the array, is used for two reasons: (a) to avoid direct near-field interactions that could lead to unrealistic surge interference and/or impractical layouts, and (b) because boundary element methods may produce inaccurate or overestimated results when devices are very closely spaced, where higher-order asymptotic approximations may be required [133, 134].

## 3.3. HYDRODYNAMIC MODEL IMPLEMENTED FOR SINGLE DEVICES

This section describes the hydrodynamic model for the single PA and flap devices. The formulation is later extended to arrays.

#### DEVICE DESCRIPTION

The geometry and mass properties of the small PA are given in Table 3.1a, and those of the large PA in Table 3.1b. The geometry and mass properties of the flap device are given in Table 3.1c and are taken from [135].

(a) Properties of the small PA device

| Property | Value | Unit |
|---|---|---|
| Diameter | 6 | $m$ |
| Weight | 70 | $T$ |
| Draft | 4 | $m$ |

(b) Properties of the large PA device

| Property | Value | Unit |
|---|---|---|
| Diameter | 12 | $m$ |
| Weight | 272 | $T$ |
| Draft | 4 | $m$ |

(c) Properties of the flap device

| Property | Value | Unit |
|---|---|---|
| Width | 17.7 | $m$ |
| Height | 10.6 | $m$ |
| Peak thickness | 3 | $m$ |
| Moment of inertia | $8.8 \times 10^6$ | $kg\,m^2$ |
| Draft | 9 | $m$ |

Table 3.1.: Geometric and inertial properties of the wave energy converters considered in the shallow-water array studies (For the flap the peak thickness is at 7.1 m from the top of the foundation block)

### 3.3.1. CONVERGENCE STUDY FOR THE MESH

Convergence studies was performed for the PA and flap meshes. The minimum panel size per device was estimated as $\lambda/6$ [43, 136], where $\lambda$ is the wavelength corresponding to the smallest wave period considered. Based on the scatter diagram, a minimum period of $T = 3$ s was selected for both regular and irregular-wave calculations. At a depth of 14.5 m and $T = 3$ s, this yields a minimum required panel size of 2.34 m.

While the number of panels in BEM depends primarily on the incident wavelength, a mesh that is sufficient for a single device is generally sufficient for multiple devices [137]. The key caveat is interaction accuracy at narrower spacings [138]. Based on the convergence study for the individual PA (both small and large), 234 panels are sufficient for the hull. For the flap, 633 panels are sufficient for the hull and concrete foundation together. Since the number of devices varies from 2 to 10 with a minimum spacing of 4×characteristic dimension, higher-resolution meshes were adopted to better capture interaction effects: 715 panels for the small PA and 724 panels for the large PA. Similarly, for the flap, 1074 panels were used for the hull and concrete foundation per device in the array. Computational efficiency was also an important factor, since in HAMS-MREL the computation time scales approximately with $N_p^3$ [54]. A waterplane mesh was used for the PA to suppress irregular frequencies in the considered frequency range.

The final meshes for the small PA, large PA, and flap used in all calculations are shown in Figure 3.4, Figure 3.5, and Figure 3.6, respectively.

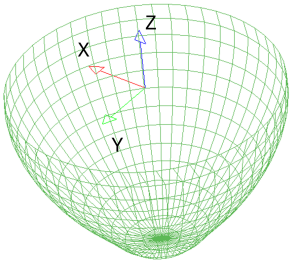



Figure 3.4.: Mesh for the small PA with 715 panels

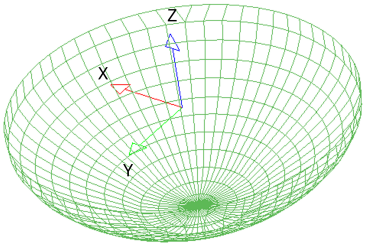



Figure 3.5.: Mesh for the large PA with 724 panels

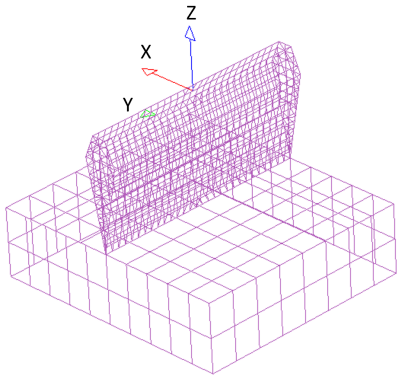



Figure 3.6.: Mesh for the flap with 1074 panels in the hull and foundation



### 3.3.2. CALCULATION OF THE NATURAL FREQUENCY OF THE DEVICES

The equation of motion for a single PA (small or large), for a given angular frequency $\omega_i$ and neglecting PTO and viscous drag effects, is:

$$[-\omega_i^2(m_d + m_a(\omega_i)) + i\omega_i b_a(\omega_i) + c_h]\,\zeta(\omega_i) = f_e(\omega_i) \tag{3.1}$$

where $m_d$ is the dry mass and $m_a$ is the frequency-dependent added-mass coefficient in heave. The term $b_a$ is the radiation-damping coefficient in heave, $c_h$ is the hydrostatic stiffness coefficient in heave, $f_e$ is the heave excitation force, and $\zeta$ is the displacement amplitude (body excursion). For a wave amplitude of 1 m, the excursion corresponds to the Response Amplitude Operator (RAO), which can be written as $\bar{\zeta} = \zeta/a$, where $a$ is the wave amplitude.

Similarly, the equation of motion for the flap in pitch is:

$$[-\omega_i^2(I_d + I_a(\omega_i)) + i\omega_i B_a(\omega_i) + C_h]theta(\omega_i) = M_e(\omega_i) \tag{3.2}$$

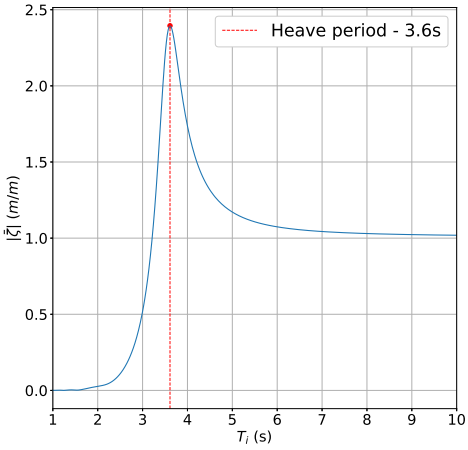
where $I_d$ is the dry moment of inertia and $I_a$ is the frequency-dependent added moment of inertia in pitch. The term $B_a$ is the radiation-damping coefficient in pitch, $C_h$ is the hydrostatic stiffness coefficient in pitch, $M_e$ is the pitch excitation moment, and $\theta$ is the rotation amplitude. The flap RAO is $\bar{\theta} = \theta/a$.

A straightforward way to estimate the natural period for these single-DOF devices is to plot the RAO versus wave period $T_i = 2\pi/\omega_i$ and identify the period corresponding to the peak response. The RAO plots $\bar{\zeta}$ versus $T_i$ for the small and large PA are shown in Figure 3.7a and Figure 3.7b, respectively, while $\bar{\theta}$ versus $T_i$ for the flap is shown in Figure 3.7c. The natural periods of the small and large PA are 3.6 s and 4.5 s, respectively, and that of the flap is 17.5 s.

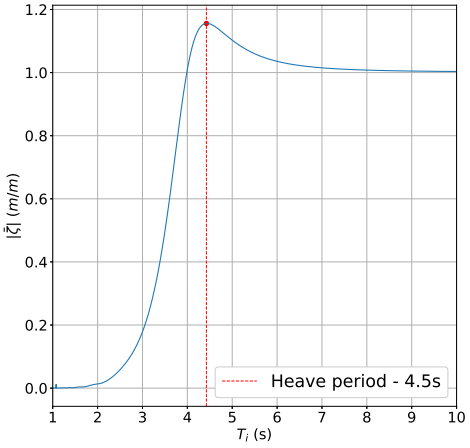
The frequency-dependent hydrodynamic coefficients and excitation forces are obtained using the frequency-domain boundary element method (BEM) solver HAMS-MREL [54]. For the flap, the generalized modes approach based on our previous work [104] is used to determine the hydrodynamic coefficients and excitation forces (added in Appendix B).

#### PASSIVE CONTROL STRATEGY CONSIDERING VISCOUS DRAG UNDER REGULAR WAVES

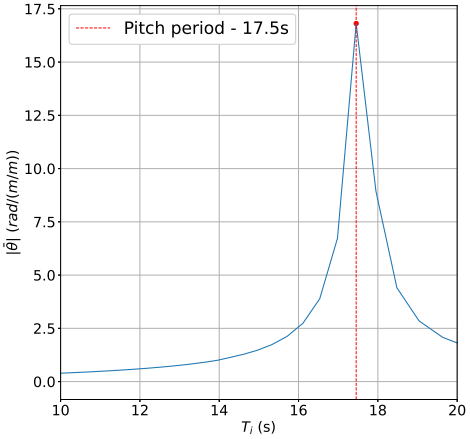
A passive control strategy is commonly used for power take-off (PTO) systems, with the objective of maximizing absorbed power by tuning the response velocity amplitude




(a) RAO $\bar{\zeta}$ vs period $T_i$ for small PA




(b) RAO $\bar{\zeta}$ vs period $T_i$ for large PA




(c) RAO $\bar{\theta}$ vs period $T_i$ for flap

Figure 3.7.: Response of single WECs

[139]. This is achieved by introducing a frequency-dependent damping coefficient for the PTO into the equation of motion, which relates the PTO force to the body velocity. No constraints are imposed on displacement or PTO forces. For a PA, the relevant velocity is the heave velocity, whereas for a flap-type device it is the rotational pitch velocity. In the frequency domain, the PTO force and moment for the PA and flap, respectively, can be expressed as:

$$F_{PTO}(\omega_i) = i\omega_i b_{PTO}(\omega_i)\zeta(\omega_i), \quad M_{PTO}(\omega_i) = i\omega_i B_{PTO}(\omega_i)\theta(\omega_i) \tag{3.3}$$

The frequency-dependent PTO damping coefficient that maximizes absorbed power for the PA can be obtained following Hals et al. [139] as:

$$b_{PTO}(\omega_i) = \sqrt{R(\omega_i)^2 + X(\omega_i)^2} \tag{3.4}$$

where the real and imaginary components are defined as:

$$R(\omega_i) = b_a(\omega_i) + b_v \tag{3.5}$$

$$X(\omega_i) = i\omega_i[m_d + m_a(\omega_i)] + \frac{c_h}{i\omega_i} \tag{3.6}$$

Here, $b_a(\omega_i)$ is the radiation damping, $b_v$ the viscous damping, $m_d$ the dry mass, $m_a(\omega_i)$ the added mass, and $c_h$ the hydrostatic restoring coefficient.

For incident regular waves, the viscous damping is estimated using the Lorentz linearization approach [140]:

$$b_v = \frac{4}{3\pi} C_D \rho A_D \tag{3.7}$$

where $C_D$ is the drag coefficient in heave, $\rho$ the fluid density, and $A_D$ the projected area in heave. A similar formulation is adopted for the flap-type WEC, accounting for PTO and viscous drag in pitch.

Including both PTO damping and viscous drag yields the frequency-domain formulation for regular waves:

$$[-\omega_i^2(m_d + m_a(\omega_i)) + i\omega_i(b_a(\omega_i) + b_{PTO}(\omega_i) + b_v) + c_h]\,\zeta(\omega_i) = f_e(\omega_i) \tag{3.8}$$

For the flap, a drag coefficient of $C_D = 1.7$ is adopted based on [135]. For the PAs, the original CorPower C4 geometry has a heave drag coefficient of $C_D = 0.25$ [124]. Since the PAs considered here are scaled versions of this device, the drag coefficient is adjusted using the Keulegan–Carpenter (KC) number, a dimensionless parameter comparing fluid particle excursion to the device characteristic length. The KC number for a given frequency [141] is:

$$KC(\omega_i) = \frac{2\pi\zeta(\omega_i)}{D} \tag{3.9}$$

where $\zeta(\omega_i)$ is the heave displacement amplitude and $D$ is the device diameter. The variation of the KC number for wave heights between 0.5 m and 2 m is shown in Figure 3.8 for the small PA.

It can be observed that even for $H = 2$ m, the KC number remains between 1 and 3. A similar range is obtained for the large PA. Based on this, a viscous drag coefficient of $C_D = 0.5$ to 1 can be considered [126, 141]. A value of 0.5 is used here for both PAs. This is used for all frequencies (regular waves) and sea states (irregular waves).

The power for each discrete frequency $\omega_i$ is then:

$$P(\omega_i) = \frac{1}{2} b_{PTO}(\omega_i)\,\omega_i^2\,|\zeta_i|^2. \tag{3.10}$$

A PTO conversion efficiency $\eta$ is assumed to compute the uni-directional electrical power delivered to the grid. An efficiency of 80–90% is achievable for PTO actuators [142, 143]; here, $\eta = 0.9$ is adopted, giving $\eta P(\omega_i)$.

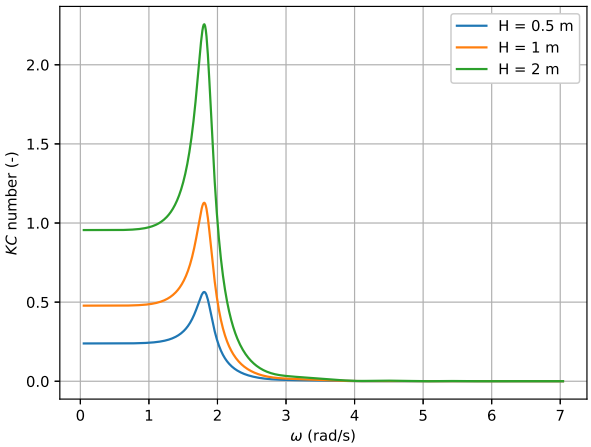



Figure 3.8.: Variation of the Keulegan–Carpenter (KC) number for wave heights from 0.5 m to 2 m for the small PA

### PASSIVE CONTROL STRATEGY CONSIDERING VISCOUS DRAG UNDER IRREGULAR WAVES

The modelling for the single devices with passive control under irregular sea states follows our previous work [144].

For irregular sea states, a weakly non-linear frequency-domain formulation is used to estimate the WEC response including viscous losses. This begins by considering the response at discrete frequencies, which is analogous to regular-wave conditions. The equation of motion at each discrete frequency $\omega_i$ follows from Equation 3.8. The optimal PTO coefficient is tuned to the energy period, since the energy period represents the average energy distribution across the spectrum [145]. The viscous damping coefficient is evaluated using the spectral-domain method [146, 147], which has been shown to capture viscous drag accurately up to $H_s = 5.5$ m [148] for spherical point absorbers.

For each time step of the irregular sea-state time series, the energy period $T_e$ is used to compute an equivalent regular-wave condition for estimating $b_{PTO}$:

$$T_e = \frac{m_{-1}}{m_0}, \tag{3.11}$$

where $m_{-1}$ and $m_0$ are the spectral moments of order $-1$ and 0, respectively. The corresponding $b_{PTO}$ is computed using Equation 3.4–Equation 3.6.

Because both passive PTO damping and viscous losses depend on the response, an iterative scheme is required:

1. Initial estimate using Lorentz linearisation [140]:

$$b_v^{(0)} = \frac{4}{3\pi} C_D \rho A_D, \tag{3.12}$$

   where $\rho$ is water density, $C_D$ is the constant drag coefficient, and $A_D$ is a characteristic area of the WEC.

2. Solve Equation 3.8 for all $\omega_i$ to compute the velocity amplitudes and the standard deviation of the velocity, $\sigma_u$.

3. Update $b_v$ using the spectral-domain formulation:

$$b_v = \frac{1}{2}\rho C_D A_D \sigma_u \sqrt{\frac{8}{\pi}}, \tag{3.13}$$

4. Update $b_{PTO}$ using Equation 3.4 and repeat until convergence. Convergence is defined when the mean squared error (MSE) between consecutive response vectors is below the tolerance:

$$\text{MSE} = \frac{1}{N}\sum_{i=1}^{N}\left(S_i^{(n)} - S_i^{(n-1)}\right)^2 < 10^{-6}, \tag{3.14}$$

where $S_i^{(n)}$ is the response at iteration $n$ and $N$ is the number of frequencies.



Once convergence is achieved, the absorbed power is computed as

$$P_{\text{irr}} = \eta \int_0^\infty 2P(\omega)\, S(\omega)\, \mathrm{d}\omega, \tag{3.15}$$

where $S(\omega)$ is the variance spectrum (based on Goda-type spectra with $\gamma$ based on [144]), and the spectral power is

$$P(\omega_i) = \frac{1}{2} b_{PTO}\, \omega_i^2\, |\zeta_i|^2. \tag{3.16}$$

The same procedure is applied to the flap. As noted earlier, viscous drag is particularly significant for flap-type devices. Da Silva et al. [126] performed a statistical linearization of Morison's equation to account for viscous drag in shallow-water conditions under irregular sea states.

Two cases were considered: one using only the structural velocity to compute viscous force, and another using the relative velocity (difference between structural and fluid velocities across depth). For $H_s$ ranging from 1 to 2 m and $T_p$ between 5 and 12 s (consistent with the present study), the mean difference in absorbed power between the two approaches for the flap was approximately 5–10%, with the structural-velocity-only approach yielding an underestimation.

While relative-velocity formulations can improve accuracy, they require depth discretisation and additional iteration. For arrays of up to 10 devices, this would substantially increase computational complexity and runtime. Therefore, for the present analysis, the structural-velocity-based statistical linearisation is adopted for the flap, consistent with the approach used for the PA.

#### ACTIVE CONTROL CONSIDERING VISCOUS DRAG

Under an active control strategy, both the amplitude and phase of the response velocity are targeted. The PTO impedance is varied so that the response velocity is in phase with the excitation force, which theoretically maximises absorbed power [139]. This can place the device near continuous resonance; therefore, displacement constraints are imposed to obtain realistic power estimates. For active control, the method proposed by Fusco and Ringwood [149] and extended by Ermakov et al. [47] is adopted.

The method provides a simple causal approximation of active control, requiring only one tunable parameter and no optimisation. A broadband control problem is reformulated as a sequence of monochromatic control problems, requiring estimators for the time-varying wave frequency and excitation force. For brevity, the formulation is presented for a 1-DOF heaving PA; the same procedure is applied to the flap.

The linear frequency-domain force–displacement relationship is

$$\zeta(\omega_i) = \frac{f_{\text{ex}}(\omega_i) + f_{\text{PTO}}(\omega_i)}{i\omega_i Z(\omega_i)} \tag{3.17}$$

where $\zeta(\omega_i)$ is the heave displacement, $f_{ex}$ is the excitation force, $f_{PTO}$ is the control force, and $Z(\omega_i)$ is the intrinsic impedance.

The intrinsic impedance [150], including viscous effects, is

$$Z(\omega_i) = b_a(\omega_i) + b_v + i\omega_i\left(m_d + m_a(\omega_i) - \frac{c_h}{\omega_i}\right) \tag{3.18}$$

where the parameters are defined in section 3.3.2.

The theoretical maximum power extraction occurs when the PTO applies the complex conjugate of the intrinsic impedance:

$$F_{PTO}(\omega_i) = i\omega_i Z^*(\omega_i)\zeta(\omega_i). \tag{3.19}$$

Substituting this into Equation 3.3.2 yields the optimum velocity condition:

$$V(\omega) = \frac{1}{2(b_a(\omega_i) + b_v)} F_{exc}(\omega). \tag{3.20}$$

This control law is non-causal and would require perfect prediction of future wave forces, since all frequencies can in principle be present simultaneously. In practice, however, the excitation force is concentrated within a restricted band, largely within the flat region of $1/2B(\omega_i)$, as shown in Figure 3.9.

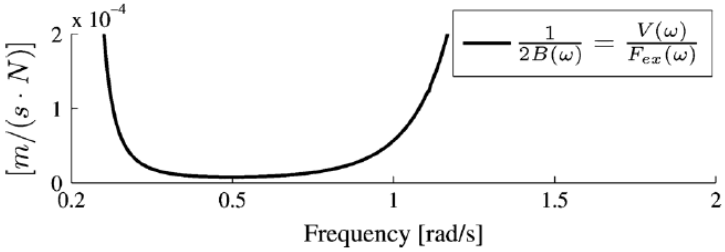



Figure 3.9.: Optimal relation between excitation force and heave velocity. The phase is zero [149]

Accordingly, the excitation force is assumed to be a narrow-banded harmonic process (a reasonable assumption for the considered location in the North Sea off the coast of the Netherlands), defined by the time-varying amplitude $A(t)$, frequency $\omega(t)$, and phase $\varphi(t)$:

$$f_{ex}(t) = A(t)\cos(\omega t + \varphi(t)). \tag{3.21}$$

The reference displacement can then be related to the excitation force based on real-time estimation of the peak frequency. The Extended Kalman Filter (EKF) has been shown to estimate the instantaneous peak frequency and amplitude from wave-elevation measurements [151].

Active control without constraints can lead to unrealistically large motions, since the device is maintained near resonance. Therefore, to obtain realistic absorbed power, a displacement constraint is applied, following Ermakov et al. [47]. A parameter $\alpha$ is introduced as the PTO damping control variable enforcing motion limits. The PTO impedance $Z_{PTO}$ for Complex Conjugate Control (CCC) at frequency $\omega_i$ is defined as:

$$Z_{PTO} = (2\alpha - 1)d - ie \tag{3.22}$$

where $d$ is the real part and $e$ is the imaginary part of the intrinsic impedance. The displacement then follows as

$$\zeta = \frac{f_{ex}}{2i\omega_i \alpha x}. \tag{3.23}$$

To satisfy the displacement constraint, $\alpha$ is adjusted as

$$\text{If } |\zeta| > \zeta_{max}, \text{then } \alpha = \frac{|\zeta|}{\zeta_{max}}. \tag{3.24}$$

This updated value of $\alpha$ is then used to recompute $Z_{PTO}$, and the absorbed power in regular waves is obtained as

$$P(\omega_i) = \frac{1}{2} Z_{PTO}\, \omega_i^2\, |\zeta_i|^2. \tag{3.25}$$

This procedure preserves the in-phase velocity condition while limiting the maximum displacement through a simple adjustment of $\alpha$. The maximum displacement for the PAs is chosen as 0.3×draft based on Figure 3.2/Figure 3.3, and for the flap as 15°, to remain within the linear motion regime.

Under irregular waves, the power $P_{\text{irr}}$ is computed as

$$P_{\text{irr}} = \int_0^\infty P(\omega) p_{ss}(\omega)\, d\omega, \tag{3.26}$$

where $p_{ss}(\omega)$ is the probability distribution function of wave frequencies, obtained from the wave spectral density $S(\omega)$ as

$$p_{ss}(\omega) = \frac{S(\omega)}{\int_0^\infty S(\omega) d\omega}. \tag{3.27}$$

When considering irregular waves, the EKF requires approximately one to two dominant wave cycles to estimate the instantaneous amplitude and frequency of the excitation force. These EKF-based estimates are then used to update the PTO impedance for CCC. As a result, unlike the regular-wave case, the PTO impedance becomes time-varying, but it does not change instantaneously; instead, it can be treated as quasi-constant over each dominant wave cycle and updated gradually as the EKF tracks evolving wave characteristics.

Under these quasi-stationary conditions, the intrinsic reactive terms representing stiffness and inertia remain almost constant within each wave cycle. In the regular-wave case, the time-averaged work done by these reactive components is zero over each interval; they only contribute to temporary energy storage and release. Following up on the quasi-static condition and the work done in the regular-wave case, the mean absorbed (useful) power is assumed to be governed solely by the resistive (damping) component of the PTO impedance, with negligible work done to change the stiffness and inertia components. For exact power calculations, these should also be considered. However, this is not quantified within this thesis.

For constrained WEC motion, approximately 10–40% of the PTO power is temporarily injected back into the system by the controller [149], under both regular and irregular waves. For an ideal bidirectional PTO with 100% efficiency, this reversible exchange does not affect the mean absorbed power, since injected energy is fully recovered later. In practice, however, hydraulic or electrical PTOs designed for bidirectional power flow have a finite efficiency, typically $\eta \approx 0.8$–$0.9$ [142, 143], and reversed power flow introduces an additional penalty on net electrical output. This effect can be quantified as follows.

Let $P_{\text{abs}}$ denote the average mechanical power absorbed by the PTO (i.e. the cycle-averaged positive part of the PTO power time series), and let $P_{\text{rev}}$ denote the average *reversed* power (i.e. the cycle-averaged negative part, where energy flows from the PTO back into the device). Define the ratio of reversed to absorbed power as

$$Q = \frac{P_{\text{rev}}}{P_{\text{abs}}}. \tag{3.28}$$

For an ideal, lossless PTO with 100% efficiency, the net mechanical power delivered by the PTO is

$$P_{\text{net},100} = P_{\text{abs}} - P_{\text{rev}} = P_{\text{abs}}(1-Q). \tag{3.29}$$

When the PTO has a finite efficiency $\eta$, power flowing from the WEC into the electrical system is reduced by the factor $\eta$, whereas reversed power flowing from the electrical system back into the WEC must be supplied at a rate $P_{\text{rev}}/\eta$. The net electrical power is therefore

$$P_{\text{net},\eta} = \eta P_{\text{abs}} - \frac{P_{\text{rev}}}{\eta} = P_{\text{abs}}\left(\eta - \frac{Q}{\eta}\right). \tag{3.30}$$



Eliminating $P_{\text{abs}}$ using the 100% efficient expression above yields

$$\boxed{\frac{P_{\text{net},\eta}}{P_{\text{net},100}} = \frac{\eta - Q/\eta}{1-Q}}. \tag{3.31}$$

This expression relates the achievable net electrical power under a realistic PTO efficiency $\eta$ to the ideal net mechanical power and the reversed-power fraction $R$. Here, taking $\eta = 0.9$ and $R = 0.2$ gives

$$\frac{P_{\text{net},0.9}}{P_{\text{net},100}} = \frac{0.9 - 0.2/0.9}{1-0.2} = \frac{0.6778}{0.8} \approx 0.847, \tag{3.32}$$

so that with 20% reversed power and 90% PTO efficiency, the device delivers approximately $0.847\,P_{\text{net},100}$, i.e. about 85% of the ideal net power.

Thus, when considering a causal CCC implementation, the useful absorbed power remains determined by the damping term of the PTO impedance, while the reactive stiffness and inertia terms mediate reversible energy exchanges. This factor of 0.847 is used as the effective efficiency when deriving the power obtained under active control for both single devices and arrays.

## 3.4. HYDRODYNAMIC MODEL IMPLEMENTED FOR ARRAYS

The hydrodynamic models for single devices under passive and active control, in both regular and irregular waves, are extended to arrays in this section. The formulation applies to arrays of any number of WECs, either mono or mixed.

### PASSIVE CONTROL

The weakly non-linear frequency-domain model developed for individual devices (section 3.3.2 and section 3.3.2) is extended to account for hydrodynamic interactions within wave farms. The full multi-body equation of motion for a farm of $n$ devices (mono or mixed) at frequency $\omega_i$ is given in Eq. (10) of the paper:

$$\left[-\omega_i^2\left(\mathbf{M}_d + \mathbf{M}_a(\omega_i)\right) + i\omega_i\left(\mathbf{B}_a(\omega_i) + \mathbf{B}_{\text{PTO}}(\omega_i) + \mathbf{B}_v\right) + \mathbf{C}_h\right]\boldsymbol{\zeta}(\omega_i) = \mathbf{F}_e(\omega_i), \tag{3.33}$$

where each term is now a matrix or vector describing the hydrodynamics of all devices in the array:

- $\mathbf{M}_d \in \mathbb{R}^{n\times n}$ is the diagonal mass matrix,
- $\mathbf{M}_a(\omega_i) \in \mathbb{R}^{n\times n}$ is the fully populated added-mass matrix,
- $\mathbf{B}_a(\omega_i) \in \mathbb{R}^{n\times n}$ is the fully populated radiation-damping matrix,
- $\mathbf{B}_{PTO}(\omega_i) \in \mathbb{R}^{n\times n}$ is the fully populated optimised PTO-damping matrix,
- $\mathbf{B}_v \in \mathbb{R}^{n\times n}$ is the diagonal linearised viscous-damping matrix,

- $\mathbf{C}_h \in \mathbb{R}^{n\times n}$ is the global hydrostatic stiffness matrix, built by combining the single-body hydrostatic terms along the diagonal of the global matrix,
- $\mathbf{F}_e(\omega_i) \in \mathbb{R}^{n\times 1}$ is the excitation force/moment vector,
- $\boldsymbol{\zeta}(\omega_i) \in \mathbb{R}^{n\times 1}$ is the response-amplitude (RAO) vector. This contains the heave RAO for PAs and the pitch rotation amplitude for flaps.

For an incident wave amplitude of 1 m, $\boldsymbol{\zeta}(\omega_i)$ corresponds to the RAO vector for all devices.

To determine the optimised PTO damping for a farm, the single-device procedure is extended following Falnes [152] and Vervaet et al. [85]. The optimised frequency-dependent PTO-damping matrix is

$$\mathbf{B}_{PTO}(\omega_i) = \left[ \left(\mathbf{B}_a(\omega_i) + \mathbf{B}_v\right)^2 + \left( \omega_i\left(\mathbf{M}_d + \mathbf{M}_a(\omega_i)\right) - \frac{\mathbf{C}_h}{\omega_i} \right)^2 \right]^{1/2}. \tag{3.34}$$

This optimised PTO coefficient has been experimentally validated in [85].

For regular waves, $\mathbf{B}_v$ is diagonal, with viscous coefficients computed using Lorentz linearisation (Equation 3.7). For irregular waves, the spectral-domain iterative method introduced for the single device is applied to compute viscous damping for the whole farm, following section 3.3.2, with one key difference: the response of each device is used to determine its viscous coefficient via the spectral-domain formulation, after which the global viscous damping vector is reconstructed from all devices. The same convergence criterion (MSE $= 10^{-6}$) is used.

For regular waves, the absorbed power of the array at frequency $\omega_i$ is

$$P_{\text{array}}(\omega_i) = \frac{1}{2}\eta\,\omega_i^2\,\boldsymbol{\zeta}^*(\omega_i)\,\mathbf{B}_{PTO}(\omega_i)\,\boldsymbol{\zeta}(\omega_i), \tag{3.35}$$

where $^*$ denotes the complex conjugate.

For irregular waves, the total power is

$$P_{\text{irr}} = \int_0^\infty 2\,P(\omega)\,S(\omega)\,d\omega, \tag{3.36}$$

where $P(\omega)$ is obtained from Equation 4.6, and $S(\omega)$ is the spectral density.

### 3.4.1. ACTIVE CONTROL

This implementation follows Ermakov et al. [47], who applied the SAE method and extended it to arrays (Array SAE). The approach was validated against Model Predictive Control (MPC) in the same reference for mono arrays.

The resulting displacement vector $\boldsymbol{\zeta}(\omega_i) \in \mathbb{R}^n \times 1$ for a wave of angular frequency $\omega_i$ is given by [150]:

$$\boldsymbol{\zeta}(\omega_i) = \frac{1}{i\omega_i}\,\mathbf{Z}^{-1}(\omega_i)\cdot\left[\mathbf{F}_{ex}(\omega_i) + \mathbf{F}_{PTO}(\omega_i)\right] \tag{3.37}$$

where the intrinsic impedance matrix $\mathbf{Z}(\omega_i)$ is defined as

$$\mathbf{Z}(\omega_i) = \mathbf{B}_a(\omega_i) + \mathbf{B}_v + i\omega_i\left[\mathbf{M}_d + \mathbf{M}_a(\omega_i) - \frac{\mathbf{C}_h}{\omega}\right] \tag{3.38}$$

For an array of $n$ WECs, the impedance matrix $\mathbf{Z}$ contains all hydrodynamic interaction terms:

$$\mathbf{Z} = \begin{pmatrix} z_{1,1} & \dots & z_{1,n} \\ \vdots & \ddots & \vdots \\ z_{n,1} & \dots & z_{n,n} \end{pmatrix} = \begin{pmatrix} d_{1,1} + je_{1,1} & \dots & d_{1,n} + je_{1,n} \\ \vdots & \ddots & \vdots \\ d_{n,1} + je_{n,1} & \dots & d_{n,n} + je_{n,n} \end{pmatrix}, \tag{3.39}$$

where $z_{1,1}$ denotes the intrinsic impedance of the first WEC, and $z_{n,1}$ estimates the influence of the first WEC on the $n$-th device. The real part $d_{i,j}$ corresponds to the combined radiation and viscous damping, while the imaginary part $e_{i,j}$ represents the combined contributions from added mass and hydrostatic stiffness.

The implementation of the ASAE controller in the WEC array requires the evaluation of the global intrinsic impedance of the PTO systems, represented by $\mathbf{Z}_{PTO}(\omega)$, based on the current system state $\mathbf{Z}(\omega)$:

$$\mathbf{Z}_{pto} = \begin{pmatrix} (2\alpha_1 - 1)d_{1,1} - je_{1,1} & \dots & (2\alpha_n - 1)d_{1,n} - je_{1,n} \\ \vdots & \ddots & \vdots \\ (2\alpha_1 - 1)d_{n,1} - je_{n,1} & \dots & (2\alpha_n - 1)d_{n,n} - je_{n,n} \end{pmatrix} \tag{3.40}$$

where $\alpha_i$ denotes the PTO damping control variable for the $i^{\text{th}}$ WEC, tuned so as to enforce motion limits on that device (heave translation for the PA and pitch rotation for the flap). In each column of (3.40), the real part is scaled by the same factor $(2\alpha_i - 1)$, reflecting the assumption of linear hydrodynamic interactions between devices. Consequently, the coupling in the radiation damping of one WEC influences all other devices in the array.

The total intrinsic impedance $\mathbf{H}$ for the centrally controlled mixed array is obtained as

$$\mathbf{H} = \mathbf{Z} + \mathbf{Z}_{pto} = \begin{pmatrix} 2\alpha_1 d_{1,1} & \dots & 2\alpha_n d_{1,n} \\ \vdots & \ddots & \vdots \\ 2\alpha_1 d_{n,1} & \dots & 2\alpha_n d_{n,n} \end{pmatrix}. \tag{3.41}$$

For each WEC in the array, the displacements can be evaluated as $\zeta = (1/i\omega)\mathbf{H}^{-1}F_{ex}$, or equivalently

$$\zeta = \begin{pmatrix} \zeta_1 \\ \vdots \\ \zeta_n \end{pmatrix} = \begin{pmatrix} 2\alpha_1 d_{1,1} & \dots & 2\alpha_n d_{1,n} \\ \vdots & \ddots & \vdots \\ 2\alpha_1 d_{n,1} & \dots & 2\alpha_n d_{n,n} \end{pmatrix}^{-1} \begin{pmatrix} F_1 \\ \vdots \\ F_n \end{pmatrix}. \tag{3.42}$$

The required inverse system matrix $\mathbf{H}^{-1}$ is

$$\mathbf{H}^{-1} = \begin{pmatrix} \frac{C_{1,1}}{2\alpha_1|\mathbf{H}|} & \dots & \frac{C_{n,1}}{2\alpha_1|\mathbf{H}|} \\ \vdots & \ddots & \vdots \\ \frac{C_{1,n}}{2\alpha_n|\mathbf{H}|} & \dots & \frac{C_{n,n}}{2\alpha_n|\mathbf{H}|} \end{pmatrix}, \tag{3.43}$$

where $C_{i,j}$ are the cofactors of the elements $x_{i,j}$, and $|\mathbf{H}|$ is the determinant of $\mathbf{H}$.

Thus, the displacements for each WEC can be written as

$$\zeta = \begin{pmatrix} \zeta_1 \\ \vdots \\ \zeta_n \end{pmatrix} = \begin{pmatrix} \frac{1}{2i\omega\alpha_1}\left(\sum_{i=1}^{n} \frac{C_{i,1}F_i}{|\mathbf{H}|}\right) \\ \vdots \\ \frac{1}{2i\omega\alpha_n}\left(\sum_{i=1}^{n} \frac{C_{i,1}F_i}{|\mathbf{H}|}\right) \end{pmatrix}. \tag{3.44}$$

To satisfy displacement constraints and remain within linear hydrodynamic assumptions [150], $\alpha_i$ is adjusted and applied. If the displacement required for CCC exceeds realistic limits (i.e., $|\zeta_i| > \zeta_{\text{Max}}$), the PTO parameter is adjusted and implemented as

$$\text{If} \quad |\zeta_i| > \zeta_{Max} \quad \rightarrow \quad \alpha_i = \frac{|\zeta_i|}{\zeta_{Max}}. \tag{3.45}$$

The time-averaged power production $\mathbf{P} \in \mathbb{R}^n$ for any $\omega_i$ is computed as:

$$\mathbf{P}(\omega_i) = \begin{pmatrix} P_1(\omega_i) \\ \vdots \\ P_n(\omega_i) \end{pmatrix} = \frac{1}{2}\,\mathrm{Re}\big(\mathbf{Z}_{\mathrm{pto}}(\omega_i)\big)\,\omega_i^2 |\boldsymbol{\zeta}(\omega_i)|^2$$
$$= \frac{1}{2}\begin{pmatrix} (2\alpha_1-1)d_{1,1}(\omega_i) & \dots & (2\alpha_n-1)d_{1,n}(\omega_i) \\ \vdots & \ddots & \vdots \\ (2\alpha_1-1)d_{n,1}(\omega_i) & \dots & (2\alpha_n-1)d_{n,n}(\omega_i) \end{pmatrix} \omega_i^2 \begin{pmatrix} |\zeta_1(\omega_i)|^2 \\ \vdots \\ |\zeta_n(\omega_i)|^2 \end{pmatrix}. \tag{3.46}$$

The proposed ASAE method is simple considering both control implementation and performance evaluation, enabling rapid assessment. Unlike time-domain methods, the approach is fast for control calculations at each time step, ensuring that no convergence checks for power values are required.

## 3.5. CONSIDERED CONFIGURATIONS

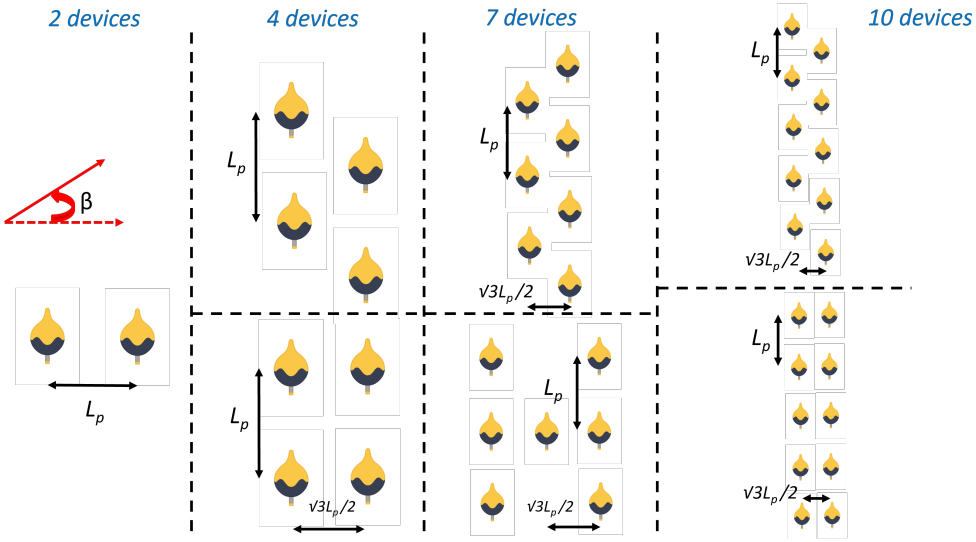



Figure 3.10.: PA configurations (large or small PA)

Two sets of arrays are considered. The first includes mono and mixed arrays comprising the small PA and the flap, while the second includes mono and mixed arrays comprising the large PA and the flap. Across all three array types—PA arrays, flap arrays, and mixed PA–flap arrays—the configurations follow a consistent geometric logic based on array size (2, 4, 7, and 10 devices), spatial arrangement, and directional exposure. For arrays with four or more devices, two layouts are considered: a rectangular configuration (bottom row in each panel) and a staggered configuration (top row). The rectangular arrangement places devices on a regular grid, whereas the staggered pattern offsets alternate rows by half a spacing to resemble diamond-like packing. All arrays are evaluated for four normalised spacings of $4C$, $6C$, $8C$, and $10C$, where $C$ is the characteristic dimension of the device (device diameter $D$ for the PA, flap width $W$ or an equivalent characteristic span for the flap, and an averaged dimension for the mixed case). This systematic spacing variation enables investigation of near-field and far-field hydrodynamic interactions across compact to loosely spaced layouts.

Each array is subjected to 12 incident-wave directions, spaced at 30° intervals, covering the full 360° directional range. For flap devices, 0° is defined as the

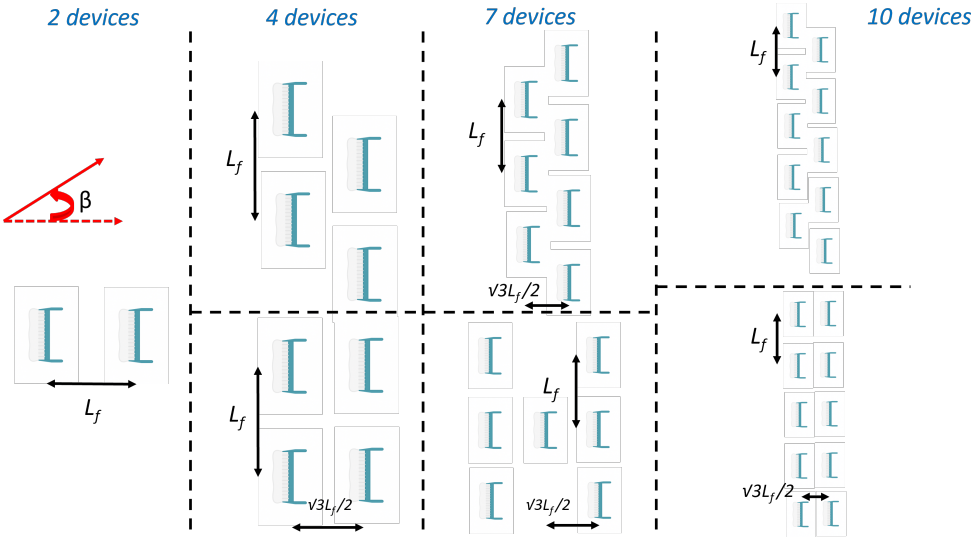



Figure 3.11.: FL configurations

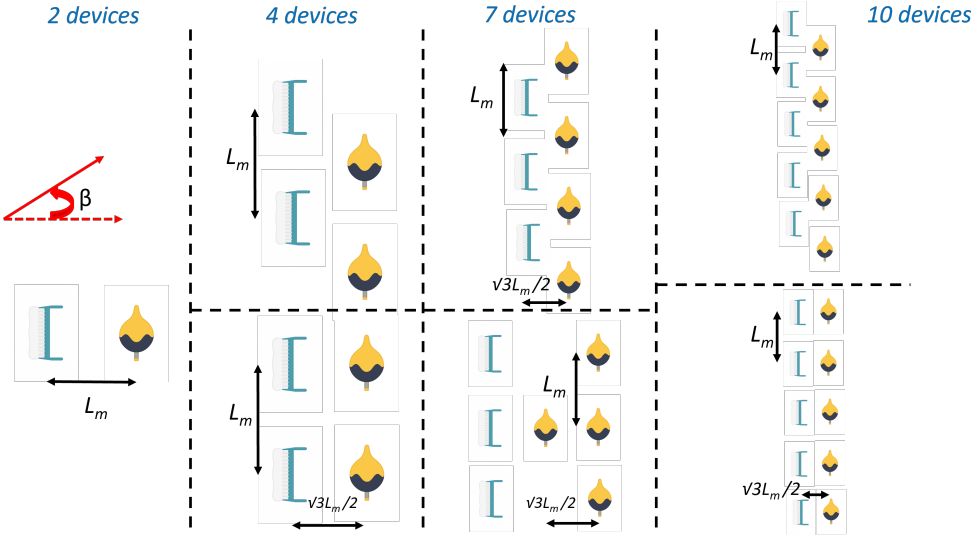



Figure 3.12.: Mixed array configurations (with large or small PA)

direction perpendicular to the flap length, i.e. broadside incidence. This orientation is hydrodynamically significant because flap devices exhibit strongly direction-dependent excitation forces and radiation patterns. In contrast, PAs are axisymmetric in heave and are therefore directionally insensitive in isolation; however, in arrays, hydrodynamic interactions introduce directional variability in power absorption. Mixed arrays combine these characteristics: the directional response is governed by both the orientation-dependent behaviour of the flaps and the intrinsic symmetry of the PAs,

often producing more asymmetric and, in some cases, more constructive interaction patterns than mono farms.

The 2-device case represents the simplest interaction scenario and serves as a baseline for understanding pairwise constructive and destructive interference. The 4-device arrays extend this into first-order grid and staggered motifs, enabling cross-row interactions. The 7-device arrays adopt a hexagonal-like cluster around a central device in the staggered layout and a compact 3-3-1 pattern in the rectangular version, capturing the transition from small to mid-scale arrays. Finally, the 10-device arrays form elongated multi-row structures where long-range diffraction and radiation effects become more pronounced. These consistent geometric patterns across PA, flap, and mixed arrays allow direct comparison not only between configurations but also across device types, highlighting how device geometry and orientation influence overall farm-level hydrodynamic performance.

Considering all variations, a total of (3 (number of device counts) ×4 (number of spacings) ×12 (incident directions) ×2 (layouts) +4 × 12 (for the 2-device case)) ×2 (passive and active control) results in 672 cases per array type. Therefore, across the two PAs, flaps, and the two mixed arrays, a total of 3360 cases are analysed.



## 3.6. METRICS FOR COMPARING MIXED AND MONO ARRAYS

To analyse farm performance under both regular and irregular waves, three metrics are considered:

- $q$-factor - The $q$-factor is defined as the ratio of the power absorbed by the farm to that of the devices in isolation. It indicates whether a given farm configuration is destructive (<1) or constructive (>1), based on hydrodynamic interactions between WECs:

$$q = \frac{P_{farm}}{m * P_p + n * P_f} \tag{3.47}$$

  where $m$ is the number of PA devices and $n$ is the number of flap devices in the farm. $P_p$ and $P_f$ denote the power absorbed by a PA and flap, respectively, in isolation. $P_{farm}$ may refer to a mono or mixed farm. For the flap, the isolated-device power is taken in the most favourable direction (0° or 180°).

- $H$-factor - The hybrid factor, introduced by Zheng et al. [45], indicates whether the mixed farm performs equivalently to or better than the mono farms:

$$H = \frac{P_{mixed}}{m * q_p * P_p + n * q_f * P_f} \tag{3.48}$$

  This metric directly evaluates whether the mixed farm is more constructive ($H > 1$) or destructive ($H < 1$) relative to the mono farms, accounting for farm effects in both cases.

- $M$-factor - Given the differences in device dimensions, it is also informative to assess power absorbed per unit device width, and compare mixed and mono farms accordingly. This is expressed using the capture-width ratio:

$$M = \frac{\eta_{mixed}}{\left(\frac{m}{m+n} * \eta_p + \frac{n}{m+n} * \eta_f\right)} \tag{3.49}$$

  where $\eta_p$ and $\eta_f$ are the capture-width ratios of the PA and flap mono farms, respectively. The relevant capture-width ratios are

$$\eta_{mixed} = \frac{P_{mixed}}{(m * D + n * W) * P_{inc}} \tag{3.50}$$

$$\eta_p = \frac{q_p * P_p}{D * P_{inc}} \tag{3.51}$$

$$\eta_f = \frac{q_f * P_f}{W * P_{inc}} \tag{3.52}$$

where $P_{inc}$ is the incident wave power in kW/m. This metric normalises the differences in power production due to device size, thereby capturing both hydrodynamic interactions and geometric efficiency. This factor will be referred to as the $M$-factor (or mixed factor).



The $H$-factor provides a useful comparison of mixed-farm performance relative to mono farms by measuring whether the combined array produces more or less power than its single-type counterparts. However, $H$ does not explicitly account for differing characteristic dimensions and, therefore, differences in intercepted wavefront. In mixed farms containing both PAs and flaps—whose diameters and widths can differ substantially—absolute power alone is not a geometry-normalised measure of performance. As a result, two configurations can appear similar in terms of $H$ even when one extracts wave energy more efficiently per unit device width.

The $M$-factor resolves this limitation by normalising performance using the capture-width ratio. By evaluating absorbed power per unit characteristic width, $M$ separates geometric effects from interaction effects. This is especially informative in heterogeneous arrays, where device size is as important as device response. In practice, the $M$-factor can exceed the $H$-factor, indicating that mixed farms not only produce more total power but also use device width more efficiently. For this reason, the final analysis focuses on the $q$-factor and the $M$-factor, which together capture interaction-driven behaviour and geometry-normalised efficiency.

Hence, to evaluate mono and mixed arrays, $q$ and $M$ are utilised.

## 3.7. RESULTS AND DISCUSSION

This section discusses the main results considering both the single devices and the arrays. Both mono and mixed arrays are evaluated for power performance ($q$-factor) and capture width performance ($M$-factor), and compared with each other. The hydrodynamics of the best configurations are discussed towards the end.

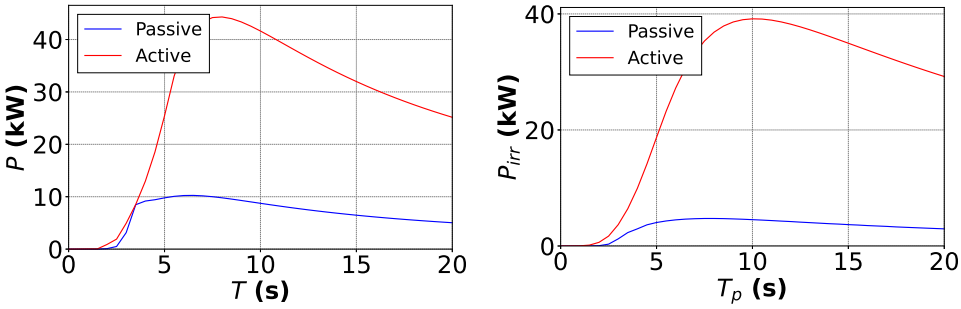
### 3.7.1. POWER ABSORPTION FOR SINGLE DEVICES

Figure 3.13a presents the absorbed power of a single small PA operating under active and passive control in regular waves, accounting for PTO efficiency. Under active control, the peak absorbed power is approximately 4.5 times higher than that achieved with passive control, with consistently enhanced performance across the full range of wave periods. This highlights the importance of enforcing a phase alignment between the device velocity and the excitation force—an essential feature of active control that enables maximized power extraction. Near the natural period of the PA (3.6 s), the performance gap narrows, as both control strategies inherently drive the system close to resonance, where conditions approximate complex conjugate control even without an actively tuned PTO.

For irregular waves, Figure 3.13b shows that the PA achieves nearly eight times the peak power under active control compared to passive control. This amplified difference can be partly attributed to the treatment of viscous effects under passive control: in irregular waves, a spectral-domain viscous damping formulation is employed, providing a broadband representation of dissipation across all contributing frequencies. In contrast, regular-wave simulations rely on a Lorentz-linearized viscous term, which approximates linear drag at a single frequency. The spectral approach therefore captures a more representative range of dissipative mechanisms across the range of frequencies per sea state, contributing to a more realistic estimation of the power absorbed in irregular sea states. Furthermore, when considering the passive control under irregular waves, the

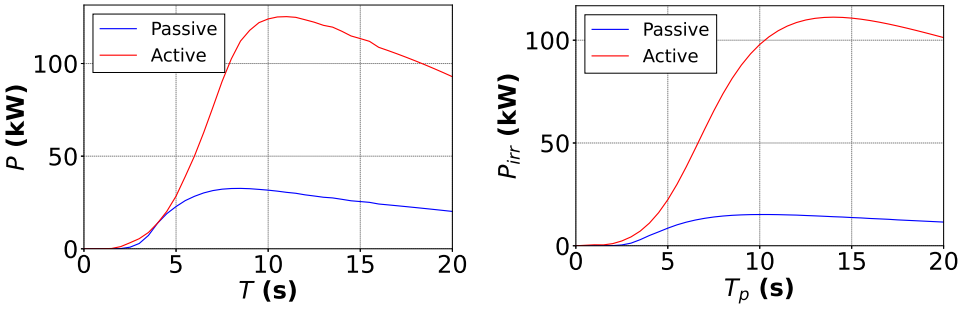
PTO is tuned to the energy period per sea state, which is therefore not optimized for all frequencies that are considered in the spectra for any given sea state.

A similar behavior is observed for the larger PA (see Figure 3.14), hence this is not explained for brevity.



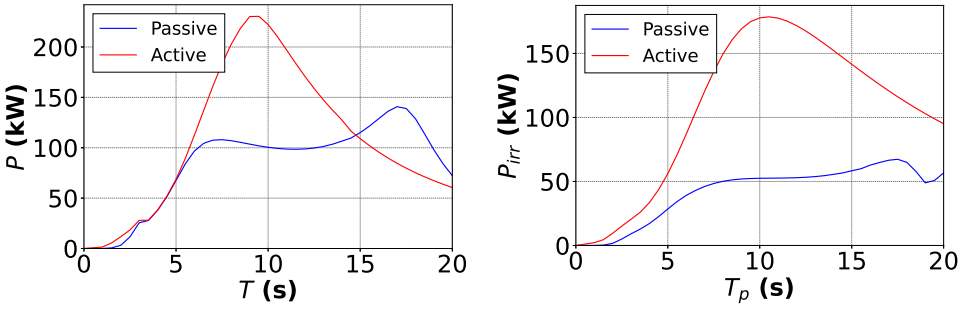

(a) Regular waves (b) Irregular waves

Figure 3.13.: Smaller PA single device power output




(a) Regular waves (b) Irregular waves

Figure 3.14.: Bigger PA single device power output




(a) Regular waves (b) Irregular waves

Figure 3.15.: Flap single device power output

Figure 3.15a presents the absorbed power of the flap device with active and passive control under regular waves. Unlike the PA, both control strategies do not yield nearly identical power absorption near the flap's natural period of 17.5 s, since the displacement constraint imposed in the active control strategy limits the power. Similar to the behaviour observed for the PA, the combination of energy-period–based optimization of the PTO and the use of spectral-domain viscous damping in irregular waves results in reduced absorbed power compared to regular-wave conditions. This reduction reflects the dissipation captured through the spectral viscous formulation, which distributes energy across multiple frequencies rather than concentrating it at the peak period.



Comparing the PA and flap, it can be observed that under passive control, the small PA produces almost $1/10^{th}$ the power produced by the flap owing to the differences in sizes of the WECs as well as the shallow water condition, which is more beneficial for the flap. This difference is reduced to about $1/4^{th}$ with larger PA due to its larger size. When considering active control, the smaller PA produces almost $1/5^{th}$ as much as flap and the larger PA almost half, showing larger benefits of the control strategy for the PAs as compared to the flap. This difference in power produced under passive/active control is also reflected in the mono and mixed arrays, which will be discussed later.

### 3.7.2. A GLOBAL VIEW OF THE ARRAY Q-FACTORS

Only the results for irregular waves active control for small and big PA are shown here. The rest can be found in Appendix D for brevity.

Figure D.1 shows the variation of the mean $q$-factor over the 3–12 s wave-period range, computed across all configurations (i.e., all directions, array sizes, and spacings) under passive control in regular waves, for mixed arrays using the small PA and the large PA. This period band is selected based on the scatter diagram for $H_s = 1\,\text{m}$, where most sea-state occurrences fall between 3 and 12 s. Although the scatter diagram represents irregular conditions, this range is used solely to provide a consistent and representative basis for comparing array performance in regular waves.

Across both PA sizes, mono PA arrays exhibit near-unity behaviour with a relatively narrow spread, indicating robust and largely directionally insensitive interactions. Mono flap arrays show a much broader spread, ranging from fully destructive cases ($q = 0$) to mildly constructive values, with the lowest values occurring when waves approach from 90° or 270° where flap excitation is minimal. For the mixed arrays, increasing the PA size primarily shifts the lower bound upward: while the small-PA mixed arrays can approach weakly destructive values, the large-PA mixed arrays remain more robust under passive control by maintaining consistently non-negligible mean $q$-factors, while achieving comparable upper values.

Figure D.2 presents the corresponding results for irregular waves under passive control. Mono PA arrays remain tightly clustered around unity for both PA sizes, confirming stable performance across wave directions and configurations. Mono flap arrays again exhibit the widest spread, including fully destructive cases ($q = 0$) associated with perpendicular wave incidence. Mixed arrays display intermediate behaviour between the two mono configurations; however, the effect of PA size is more evident in irregular seas, where the large-PA mixed arrays show a clear upward shift of the performance envelope, particularly through an increased lower bound, indicating reduced susceptibility to strongly destructive interactions compared to the small-PA mixed arrays.

Figure D.3 illustrates the variation of the mean $q$-factor averaged over the 3–12 s wave-period range for all mono and mixed configurations operating under active control in regular waves. For both PA sizes, mono PA arrays remain relatively stable and close to unity, while mono flap arrays continue to show strong directional dependence with fully destructive cases when waves approach perpendicularly. The mixed arrays exhibit the largest sensitivity to configuration under active control, and increasing the PA size shifts the mixed-array envelope upward, most clearly through a higher lower bound and an increased upper range, indicating that the larger PA strengthens the baseline absorbed-power contribution while enabling stronger constructive interference

when favourable hydrodynamic coupling occurs.

Figure 3.16 shows the mean $q$-factor variation under active control in irregular waves. Mono PA arrays maintain near-unity behaviour for both PA sizes, whereas mono flap arrays again span from fully destructive to moderately constructive cases due to their strong directional dependence. Mixed arrays demonstrate the broadest performance envelope under active control, and the influence of PA size remains consistent: large-PA mixed arrays exhibit an upward shift relative to the small-PA case, with higher minimum mean $q$-factors and an increased constructive ceiling. Overall, combining active control with a larger PA reduces the occurrence of strongly destructive mixed-array configurations while preserving the ability to access constructive interaction regimes.

Under irregular waves, the peak mean $q$-factor of the large-PA mixed array is higher under passive control ($q \approx 1.19$) than under active control ($q \approx 1.08$) because the $q$-factor normalises array power by the isolated-device power, and this denominator is substantially smaller under passive control. Since the optimal PTO damping is tuned to the energy period $T_e$ via the spectral-domain scheme, the isolated PA and flap operate well below their constrained active-control ceiling in irregular seas, leaving considerable headroom for constructive hydrodynamic interactions to amplify the ratio. In contrast, the active control strategy already drives each isolated device close to its displacement-constrained limit, so the same constraint that ensures realistic motions also clips the upside of constructive interference within the array.

To summarize, Mono PA arrays stay tightly clustered around unity regardless of PA size or sea state, confirming they are robust and direction-insensitive by construction. Mono flap arrays display the widest spread, ranging from amost fully destructive ($q \approx 0$) at transverse incidence to mildly constructive elsewhere. Mixed arrays sit between the two, and the single clearest design lever is PA size: moving from the small to the large PA shifts the lower bound of the mixed-array envelope upward, so large-PA mixed arrays avoid the strongly destructive regime that small-PA mixed arrays can still fall into. This trend is preserved under both passive and active control, with active control broadening the envelope further.

### 3.7.3. Comparing Mono and Mixed Arrays – Directional Variation

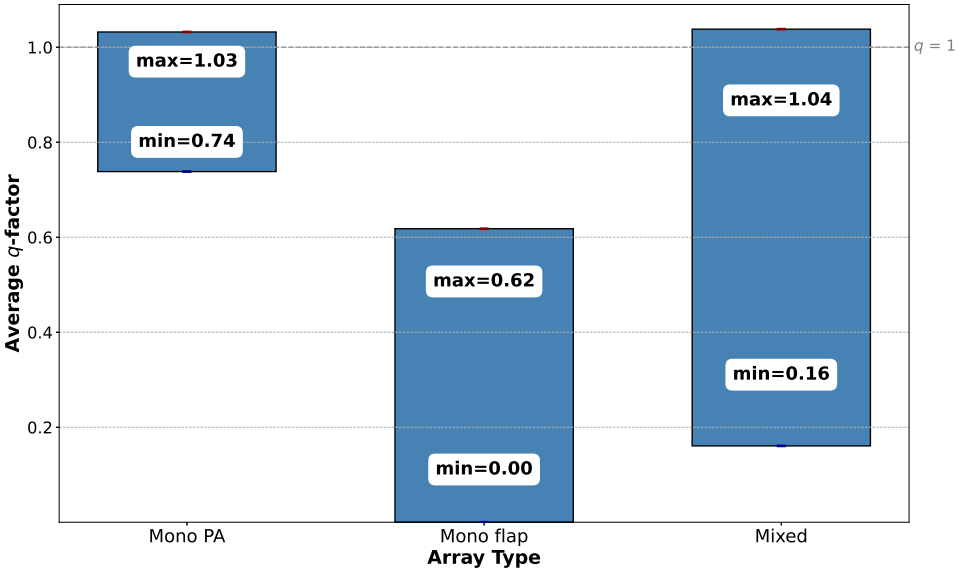
The directional dependence of the mean $q$-factor for mono and mixed arrays is examined for both passive and active control under regular and irregular wave conditions. Results are shown separately for arrays incorporating the small PA and the large PA to isolate the influence of PA size on directional performance as well.

Only the results for irregular waves active control for small and big PA are shown here. The rest can be found in Appendix D for brevity.

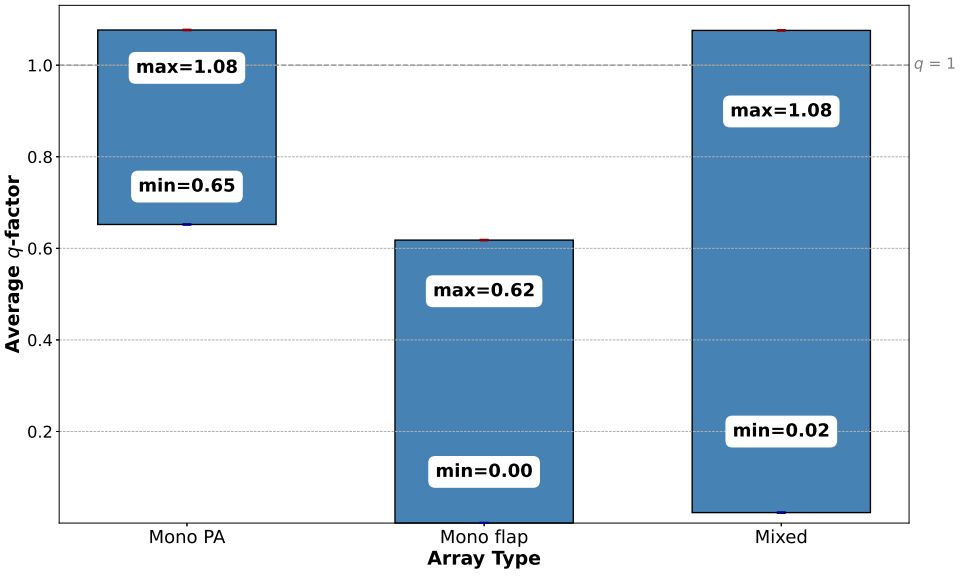
Figure D.4 and Figure D.5 show the directional variation of the mean $q$-factor under passive control in regular waves for the small and large PA, respectively. For both PA sizes, mono PA arrays exhibit the most directionally robust behaviour, with mean $q$-factors remaining close to unity across all directions and only mild reductions at oblique incidence. In contrast, mono flap arrays display strong directional sensitivity, with performance deteriorating rapidly as the incident wave direction approaches 90° and 270°, where the mean $q$-factor collapses to zero due to minimal flap excitation.

Mixed arrays consistently outperform the mono flap configuration for all directions. For the small PA, mixed-array performance generally lies between that of the mono PA and mono flap arrays, with pronounced reductions near 90° and 270°, but without fully destructive behaviour. When the large PA is used, the mixed arrays show a clear upward shift in performance across all directions, with higher minimum $q$-factors and improved robustness at oblique incidence. This indicates that increasing the PA size strengthens the baseline energy capture and reduces directional vulnerability under passive control. This is also observed from the increased power absorption from the large PA, which is now closer to the flap as compared to the small PA.

Figure D.6 and Figure D.7 present the corresponding results for irregular waves under passive control for the small and large PA, respectively. The overall trends remain consistent with the regular-wave case, but with reduced directional contrast due to




(a) Small PA




(b) Large PA

Figure 3.16.: Overall comparison of mono and mixed arrays considering mean $q$-factors under irregular waves and active control, shown for mixed arrays using (a) a small PA and (b) a large PA.

spectral averaging. Mono PA arrays maintain near-unity performance across all directions for both PA sizes. Mono flap arrays again exhibit the strongest directional dependence, with complete loss of performance at 90° and 270°.

Mixed arrays show intermediate behaviour, with mean $q$-factors that remain non-zero for all directions. The use of the large PA leads to a systematic increase in mixed-array performance across the full directional range, particularly at oblique and perpendicular incidence, where the minimum $q$-factors are significantly higher than those observed for the small PA. This demonstrates that PA size plays a more prominent role in stabilising mixed-array performance under irregular seas.

When active control is applied, the directional behaviour changes markedly, as shown in Figure D.8 and Figure D.9 for the small and large PA, respectively. Mono PA arrays remain relatively insensitive to wave direction, with mean $q$-factors clustered close to unity for both PA sizes. Mono flap arrays continue to show strong directional dependence, although their peak performance improves slightly compared to passive control.



Mixed arrays benefit most from active control. For the small PA, mixed arrays outperform both mono configurations over a few directions, particularly around 0° and 180°. With the large PA, this effect is amplified, and mixed arrays achieve the highest mean $q$-factors observed in the directional analysis. The enhanced response reflects stronger hydrodynamic coupling enabled by active phase and amplitude control, combined with the increased energy contribution from the larger PA.

Figure 3.17 and Figure 3.18 show the directional variation under active control in irregular waves for the small and large PA, respectively. Mono PA arrays again demonstrate stable, near-unity behaviour with limited directional sensitivity. Mono flap arrays retain strong directional dependence, with near-zero performance at perpendicular incidence.

Mixed arrays exhibit the widest performance envelope under these conditions. For the small PA, mixed-array $q$-factors remain significantly above those of the mono flap arrays for all directions. The introduction of the large PA leads to a substantial increase in both the minimum and maximum mixed-array $q$-factors, particularly at 0° and 180°. The asymmetry between these two directions is consistently observed, with higher performance at 180°, where the PAs encounter the incident wave field first and induce less severe wave-field distortion before interaction with the downstream flaps.

To summarize, Mono PA arrays remain near-unity across all 12 headings, while mono flap arrays collapse to zero at 90° and 270° as expected. Mixed arrays consistently beat the mono flap at every direction and, once the large PA is used, shift uniformly upward over the full 360°, raising both minimum and maximum q-factors. A persistent 0°/180° asymmetry shows that PAs encountering the incident field first (180°) distort the wavefield less before it reaches the downstream flaps, giving higher q-factors than the reverse heading. Active control amplifies the mixed-array advantage: the large-PA mixed configuration under active control achieves the highest q-factors seen anywhere in the directional analysis.

### 3.7.4. AVERAGE $q$-FACTOR - VARIATION WITH NUMBER OF DEVICES

This section examines how the mean $q$-factor (averaged over $T = 3$–12 s) varies with the number of devices for all considered cases. Note that for the two-device farms, the rectangular and staggered layouts are geometrically equivalent and therefore produce identical results. Also, plots for the different arrays might be shown with different spacings, this is since the behavior with other spacings is very similar.

Only the results for irregular waves active control for small and big PA are shown here. The rest can be found in Appendix D for brevity.

#### REGULAR WAVES PASSIVE CONTROL

**PA mono arrays:** Under regular waves with passive control, mono arrays of small PAs exhibit a clear dependence of the mean $q$-factor on both array size and spacing. At the tightest spacing ($4D$ - see Figure D.10a), the mean $q$-factor tends to decrease as additional devices are added, indicating increasingly destructive hydrodynamic interactions in denser farms. This degradation is strongest for oblique and transverse headings, where wave shadowing and radiated-wave interference accumulate along

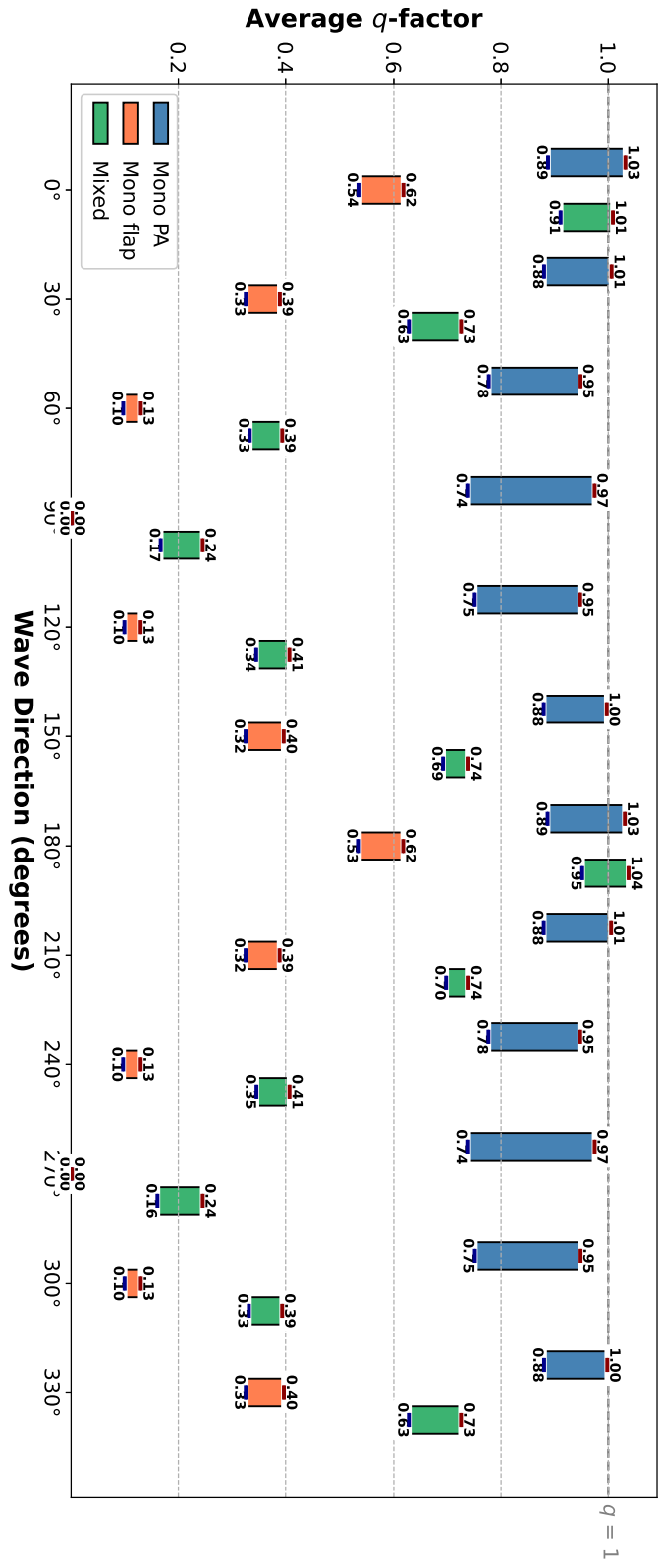



Figure 3.17.: Directional comparison of mono and mixed arrays under irregular waves and active control: small PA.

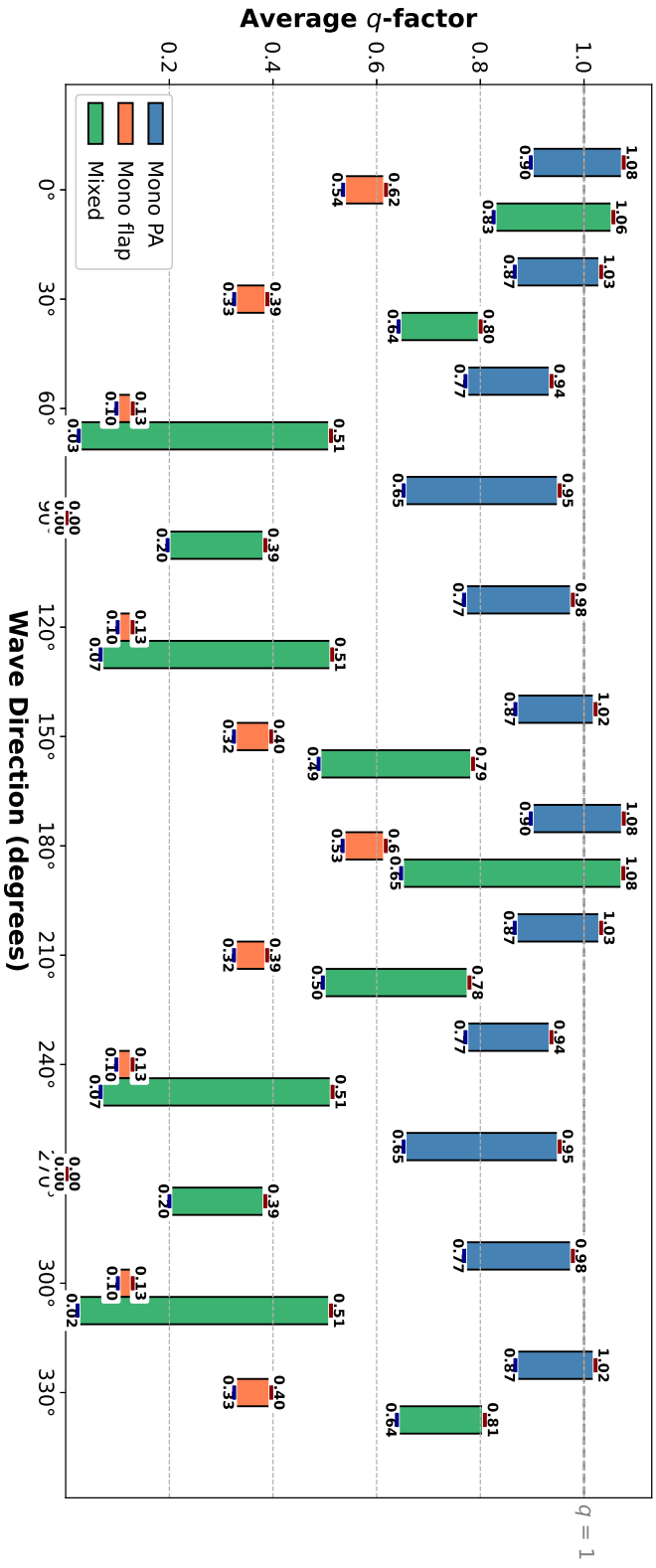



Figure 3.18.: Directional comparison of mono and mixed arrays under irregular waves and active control: large PA.

the array as it grows from 2 to 10 devices. Increasing the spacing to 6$D$ and 8$D$ reduces these penalties, with mean $q$-factors remaining closer to unity over a broader range of array sizes, particularly for head-on and near-head-on incidence. At 10$D$ (see Figure D.10b), interaction effects are weak and the mean $q$-factor stays close to (or slightly above) unity even for the largest farms, suggesting behaviour approaching isolated-device performance.

Layout effects are most pronounced at small spacings. Across 4$D$–8$D$, staggered farms consistently outperform rectangular farms, especially as the number of devices increases. The staggered arrangement reduces direct downstream shadowing and distributes interactions more evenly, which limits the monotonic decline in $q$ observed for rectangular layouts at 4$D$. As spacing increases, the gap between layouts narrows as interactions become negligible. Overall, for small PA mono arrays, increasing spacing and adopting a staggered layout are effective strategies to preserve performance as the farm scales.

For mono arrays of large PAs (see Figure D.10c), the predominantly destructive trends are observed, with the sensitivity to array growth being stronger. Small farms typically remain close to unity across most headings, with occasional mild amplification for certain oblique/following-wave cases. As the array grows, the mean $q$-factor decreases more clearly for several directions, reflecting the cumulative influence of radiated-wave interactions. The reduction is more pronounced than for small PAs, consistent with the larger hydrodynamic footprint of the devices. Increasing the spacing mitigates these effects, maintaining mean $q$-factors closer to unity even for larger farms, although large-PA arrays remain more interaction-sensitive than the small-PA case.

**Flap mono arrays:** For mono flap arrays under regular waves with passive control, the mean $q$-factor is dominated by wave direction rather than by spacing, layout, or array size (see Figure D.10d). For aligned headings (0° and 180°), the mean $q$-factor remains relatively high and varies only weakly as the farm grows from 2 to 10 devices. In contrast, for transverse headings (around 90° and 270°), the mean $q$-factor collapses to approximately zero for all array sizes, reflecting the weak excitation of flap motion under perpendicular incidence. Intermediate (oblique) directions exhibit lower $q$-factors and may show a mild reduction with increasing array size, consistent with progressive upstream modification of the wave field. Differences between rectangular and staggered layouts are minor, indicating that for mono flap farms under passive control the directional excitation characteristics dominate over geometric interaction tuning.

**Mixed arrays:** For mixed arrays combining small PAs and flaps under passive control in regular waves, the mean $q$-factor generally remains near unity for head-on and following wave directions and retains a measurable dependence wave heading as compared to spacing (see Figure D.10e). At intermediate spacings (6$D$–8$D$), aligned conditions often yield the strongest constructive interactions, with $q$ increasing modestly as the farm grows. Off-axis and beam-like headings show weaker performance and may exhibit mild attenuation, with the largest reductions occurring for the most unfavourable directions. As spacing increases toward 10$D$, both amplification and attenuation are reduced slightly and the response becomes more uniform with respect to both array size and direction. Overall, 6$D$–8$D$ provides a favourable compromise between constructive interactions in aligned seas and robustness to less favourable headings.

When the PA size is increased, mixed farms with large PAs and flaps show a stronger dependence on array size at small spacings (see Figure D.10f). Relative to the small-PA mixed case, the mean $q$-factor is typically slightly lower - particularly for aligned and near-aligned headings - consistent with stronger scattering and shadowing associated with the larger absorber diameter. Increasing the spacing reduces this sensitivity and the trends approach those of the small-PA mixed farms. Nevertheless, even at larger spacings, large-PAs can retain slightly stronger interaction-driven variability, indicating that their footprint continues to modify the surrounding wave field beyond the near-field.

### REGULAR WAVES ACTIVE CONTROL

**Mono PA arrays:** With active control in regular waves, mono arrays of small PAs become more sensitive to array size than under passive control (see Figure D.11a and Figure D.11b). Across all spacings, head-on and near-head-on headings maintain mean $q$-factors close to unity as the farm grows from 2 to 10 devices. Considering the spacing of $4D$, similar to passive control which produced clear performance degradation with increasing farm size, active control also shows similar behavior. Consequently, the dependence on layout is also weaker, with only modest differences between rectangular and staggered farms, especially at intermediate and large spacings ($6D$–$10D$).

Large-PA mono arrays on the other hand, under active control, retain a less clearer dependence on spacing and array size, but generally show a better performance as compared to passive control (see Figure D.11c). Aligned headings often remain near unity (and can occasionally exceed it) for small farms, while oblique and transverse headings show a gradual reduction as additional devices are added, particularly at tighter spacings. This reflects the stronger wave-field modification induced by the larger absorbers, which cannot be fully suppressed by control. Increasing the spacing mitigates these effects, and staggered layouts tend to maintain slightly higher mean $q$-factors for larger farms. Overall, active control improves robustness for both PA scales, but large-PAs remain more sensitive to farm density than small-PAs.



**Mono flap arrays:** For mono flap arrays under active control in regular waves, the mean $q$-factor remains primarily governed by wave direction (see Figure D.11d). Aligned headings (0° and 180°) form a near-constant plateau as array size increases, with negligible sensitivity to spacing. Oblique headings remain substantially lower with minimal variation across spacings and farm sizes. Transverse incidence (90° and 270°) continues to yield near-zero mean $q$-factors, indicating that active control cannot overcome the kinematic incompatibility between flap motion and perpendicular wave forcing. Layout effects are negligible, reinforcing that directionality dominates flap-farm behaviour.

**Mixed arrays:** Mixed farms under active control exhibit a smoother and more balanced response than either mono configuration (see Figure D.11e). For small-PA mixed arrays, mean $q$-factors cluster around unity for the head-on and following directions (adapted from the flap array behavior). Off-axis headings show only modest reductions, and the variations with array size are generally weaker than under passive control. Intermediate spacings again provide a favourable compromise, enabling interaction benefits without amplifying directional penalties.

Mixed farms with large PAs show stronger interaction signatures and a clearer dependence on farm density, particularly at tight spacings (see Figure D.11f). While aligned headings remain close to unity (and can show mild amplification), off-axis headings exhibit larger deviations as the farm grows due to stronger radiated-wave interactions from the large PAs. Increasing spacing smooths these trends and brings mean $q$-factors closer to unity across directions (see Figure D.11g). In summary, active control improves robustness for both mixed configurations, but large-PAs amplify both constructive gains in aligned seas and performance variability under less favourable headings.

### IRREGULAR WAVE PASSIVE CONTROL

**Mono PA arrays:** Under irregular waves with passive control, mono arrays of both small and large PAs show a clear dependence of mean $q$-factor on farm size and wave heading, with substantially different sensitivity between scales. For small PAs (see Figure D.12a and Figure D.12b), the mean $q$-factor decreases gradually as the number of devices increases, but remains relatively close to unity for aligned incidence (0° and 180°) even for large farms. Oblique headings exhibit a stronger decline with increasing $N_t$, while transverse headings (90° and 270°) consistently yield the lowest mean $q$-factors, indicating limited constructive interaction under broadband forcing.

Large-PA arrays display the same directional ordering but with stronger scaling effects (see Figure D.12c). Near-unity performance can be retained for aligned incidence in small farms, yet a clearer degradation emerges as $N_t$ increases, particularly for oblique and transverse directions where shadowing and destructive interference accumulate more rapidly. This stronger size sensitivity reflects the larger hydrodynamic footprint of the devices. Overall, in irregular seas and with passive control, small-PA farms are more robust to scaling, whereas large-PA farms require more careful spacing and layout choices to limit interaction-driven losses.



**Mono flap arrays:** For flap-only farms under irregular waves with passive control, the mean $q$-factor is largely set by directional excitation and varies only weakly with array size (see Figure D.12d). Aligned incidence (0° and 180°) maintains near-unity performance across all farm sizes, while oblique headings show substantially lower $q$-factors with only mild additional reductions as $N_t$ increases. Transverse headings again yield negligible $q$-factors for all configurations due to weak excitation under perpendicular incidence. Hence, spacing and layout remain secondary for mono flap farms relative to wave direction.

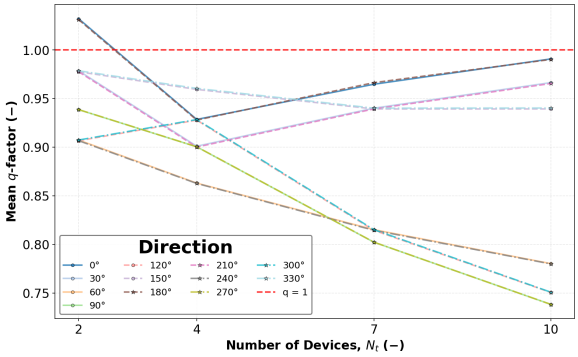
**Mixed arrays:** Under irregular waves with passive control, mixed arrays moderate the dependence of mean $q$-factor on farm size relative to mono configurations, with clear differences between small-PA and large-PA mixed farms. For small-PA mixed arrays (see Figure D.12e), mean $q$-factors remain clustered near unity for aligned incidence and vary only weakly as the array grows to $N_t = 10$. Oblique headings are lower, but the trends with $N_t$ are relatively stable, consistent with complementary radiation characteristics reducing cumulative interaction penalties coming from the PA mono arrays. Transverse headings remain least favourable, dominated by limited flap excitation, but do not exhibit the abrupt “collapse” characteristic of flap-only farms due to the PA mono arrays.

Mixed arrays with large PAs (see Figure D.12f and Figure D.12g) show a stronger dependence on both array size and wave direction. Although aligned headings remain comparatively stable, a slight increase with increasing $N_t$ emerges in oblique and opposing directions is observed, reflecting the stronger wave-field modification and radiated-wave interactions associated with the larger absorbers. Consequently, large-PA mixed farms exhibit a broader directional spread and a more pronounced scaling than the small-PA mixed case, particularly at smaller spacings. Overall, large-PA mixed farms provide greater robustness in irregular seas.

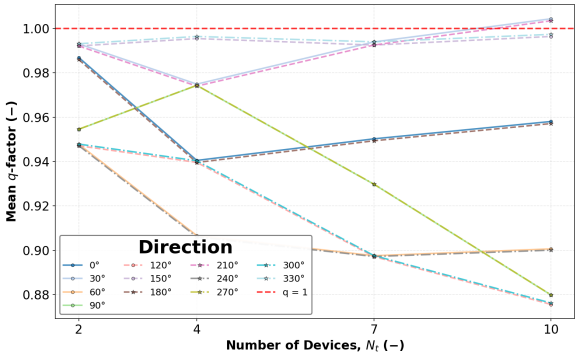
#### IRREGULAR WAVE ACTIVE CONTROL

**Mono PA arrays:** For small-PA mono arrays under irregular waves with active control, the mean $q$-factor moves closer to isolated-device behaviour relative to passive control, but remains mildly direction dependent. At $4D$ (see Figure 3.19a), aligned and near-aligned headings (0°, 30°, 180°) remain near neutral as the array grows, whereas oblique and transverse headings (approximately 60°-120° and 270°) show a systematic reduction with increasing $N_t$. Increasing the spacing toward $10D$ (see Figure 3.19b) progressively weakens these interaction effects and brings the mean $q$-factor closer to unity across headings. Thus, active control reduces the sensitivity to farm density but does not remove the need for appropriate spacing and orientation in irregular seas.

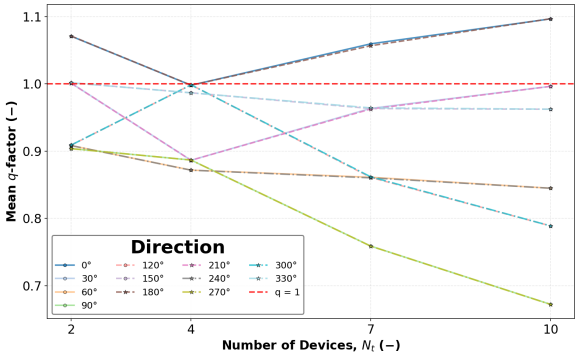
Large-PA mono arrays under active control show stronger interaction signatures than the small-PA case. For aligned and near-aligned headings (0°, 30°, 180°, 210°), mean $q$-factors are often at or slightly above unity for small farms and remain close to unity as $N_t$ increases, indicating that active control can sustain constructive interactions for favourable incidence. However, oblique and transverse headings exhibit larger reductions with increasing $N_t$, particularly at tight spacings (see Figure 3.19c), due to the stronger radiated-wave field and scattering from the large absorbers. Increasing spacing (see Figure 3.19d) mitigates these penalties and yields convergence toward isolated performance.




(a) Small PA mono: spacing 4$D$, staggered configuration

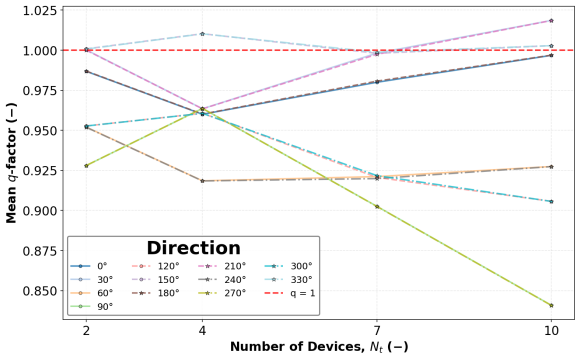



(b) Small PA mono: spacing 10$D$, staggered configuration

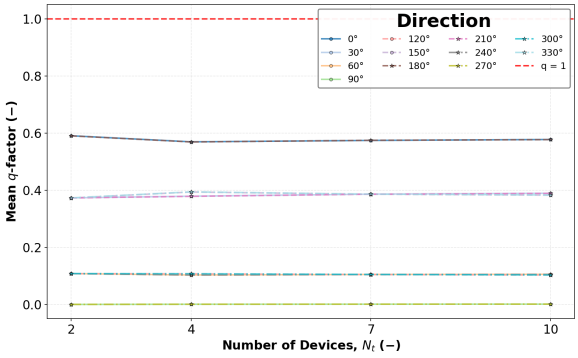



(c) Big PA mono: spacing 4$D$, staggered configuration

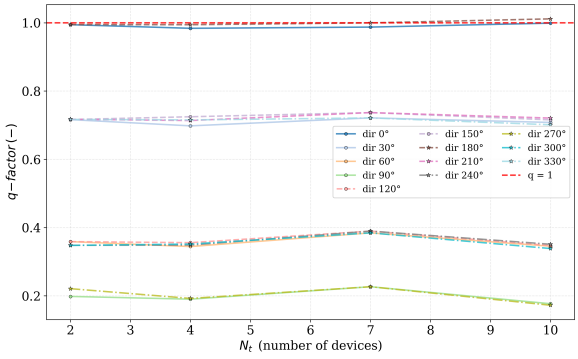
Figure 3.19.: Variation of mean $q$-factor (averaged over $T = 3$–12 s) with the number of devices $N_b$ for mono and mixed arrays under irregular waves with active control. Spacing and configuration for each case are indicated in the subcaptions.




(d) Big PA mono: spacing 10$D$, staggered configuration

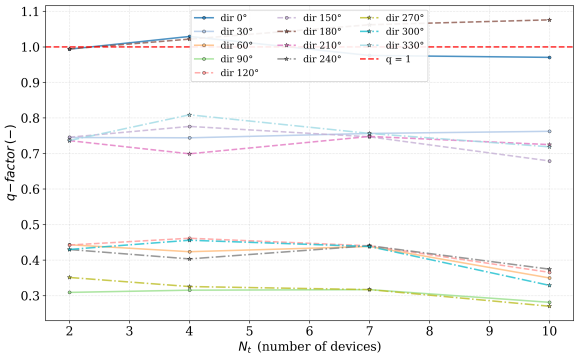



(e) Flap mono: spacing 6$D$, staggered configuration

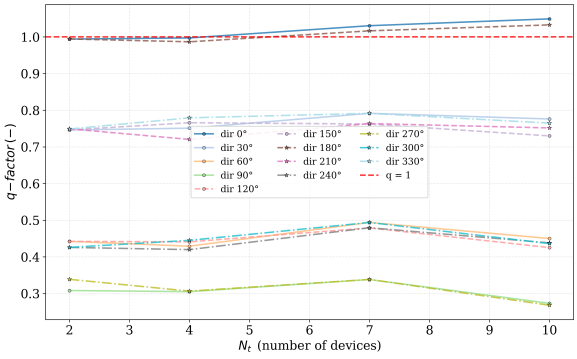



(f) Mixed (small PA + flap): spacing 8$D$, staggered configuration

Figure 3.19.: (continued).




(g) Mixed (big PA + flap): spacing $4D$, staggered configuration




(h) Mixed (big PA + flap): spacing $8D$, staggered configuration

Figure 3.19.: (continued).

Comparing scales, active control benefits both configurations, but large-PAs remain more sensitive to farm density: they can achieve higher gains for aligned incidence, yet incur larger penalties for off-axis headings in dense layouts. Small-PAs provide a more predictable efficiency profile across spacings and array sizes, whereas large-PAs demand more strategic spacing to manage their amplified interaction effects.

**Mono flap arrays:** For flap-only farms (see Figure 3.19e) under irregular waves with active control, the mean $q$-factor is again dominated by directional excitation, with negligible dependence on spacing or farm size. Aligned headings maintain a stable plateau near isolated performance across $4D$–$10D$, oblique headings remain substantially lower with minimal sensitivity to spacing, and transverse headings yield near-zero performance regardless of configuration. This confirms that control cannot overcome the underlying kinematic mismatch under perpendicular incidence.

**Mixed arrays:** For mixed arrays with small PAs and flaps (see Figure 3.19f) under irregular waves and active control, mean $q$-factors remain close to unity for aligned headings over all array sizes, indicating that active control helps suppress cumulative interaction penalties as the farm grows. Off-axis headings can show severe reductions and often exhibit a weak non-monotonic dependence on $N_t$, with performance sometimes peaking at intermediate farm sizes before decreasing slightly for the largest arrays, suggesting a balance between constructive interactions and cumulative shadowing. Transverse headings remain least favourable, but the PA component prevents a complete collapse of performance, yielding a smoother directional response than flap-only farms.

For mixed arrays with large PAs and flaps, the directional spread is wider and spacing effects are more evident (see Figure 3.19g and Figure 3.19h), especially in dense layouts. Aligned incidence maintains $q$ close to unity across spacings, whereas off-axis headings form an intermediate performance band and show clearer reductions at tight spacing due to cumulative shadowing and radiated-wave interactions from the large PAs. Increasing spacing reduces these penalties and smooths the trends with array size. Overall, active control improves robustness for both mixed configurations, but the large-PA mixed farms remain more sensitive to density and heading, while the small-PA mixed farms provide more consistent performance across a broader range of conditions.

### 3.7.5. AVERAGE $q$-FACTOR - VARIATION WITH SPACING

This section examines how the mean $q$-factor (averaged over $T = 3$–$12$ s) varies with inter-device spacing for all cases. Results are reported for spacings from $4D$ to $10D$ and for multiple farm sizes. Note that for the two-device farms, the rectangular and staggered layouts are geometrically equivalent and therefore yield identical results. Also, plots for the different arrays might be shown with varying number of devices, this is since the behavior for the arrays with different WEC numbers is very similar.

Only the results for irregular waves active control for small and big PA are shown here. The rest can be found in Appendix D for brevity.

#### REGULAR WAVES PASSIVE CONTROL

**PA mono arrays:** For mono arrays of small PAs, the mean $q$-factor shows a clear spacing dependence that becomes stronger as the farm grows. For small farms ($N_b = 2$, see Figure D.13a), interactions are typically mild and often constructive, with aligned headings occasionally peaking at intermediate spacings ($6D$–$8D$). As the farm size increases (e.g. $N_b = 7$–$10$), tight spacing ($4D$) becomes increasingly detrimental for off-axis and transverse headings, where destructive interference and shadowing reduce the mean $q$-factor (see Figure D.13b). Increasing the spacing progressively weakens these interactions, and by $10D$ the mean $q$-factor generally approaches unity across most headings, indicating near-isolated behaviour. At small spacings, staggered layouts tend to outperform rectangular layouts by reducing direct downstream shadowing and

smoothing the directional response; this advantage diminishes as spacing increases and interactions weaken.

Large-PA mono arrays exhibit a stronger spacing sensitivity, consistent with their larger hydrodynamic footprint. While $N_b = 2$ (see Figure D.13c) farms remain close to unity across all spacings, larger farms (see Figure D.13d) show pronounced variations that depend on both heading and layout. In aligned seas, constructive interactions can emerge at intermediate spacings, with staggered layouts typically reaching their peak performance at smaller spacings than rectangular layouts (e.g. around $6D$ versus $8D$). Conversely, at tight spacing ($4D$), transverse directions remain the most penalised, with mean $q$-factors dropping noticeably for the largest farms due to strong radiated-wave interference. Increasing spacing toward $10D$ reduces both amplification and attenuation, bringing the response closer to unity, although large-PAs may retain slightly more variability than small-PAs even at the largest separations.

Overall, the key difference between PA scales is the amplitude of interaction effects: large-PAs can yield higher constructive gains at optimal spacing and layout, but they are also more vulnerable to performance losses at tight spacing and unfavourable. Small-PAs are generally more stable and converge more smoothly toward $q \approx 1$ as spacing increases, across most directions.

**Mono flap arrays:** For flap-only arrays (see Figure D.13e), spacing plays a secondary role compared to wave direction. Aligned headings (0°, 180°) maintain nearly constant mean $q$-factors across the full spacing range, with only minor changes as spacing increases. Oblique headings remain substantially lower and similarly insensitive to spacing, while transverse headings (90°, 270°) yield near-zero mean $q$-factors for all spacings due to weak excitation under perpendicular incidence. Differences between rectangular and staggered layouts are minimal, confirming that the flap response is governed primarily by directional excitation rather than by interaction tuning through spacing.

**Mixed arrays:** For mixed arrays combining small PAs and flaps (see Figure D.13f), the spacing dependence is moderate and reflects a balance between PA-driven interactions and the directional selectivity of the flap. At $4C$, the largest farms show the least directional spread, with aligned headings remaining relatively robust while off-axis headings experience interaction-driven reductions. Increasing the spacing to $6C$–$8C$ typically improves performance across most headings and can yield mild amplification for aligned seas, particularly in staggered layouts. By $10C$, mean $q$-factors cluster closer to unity across headings, indicating weakened coupling and more uniform farm behaviour. Importantly, the presence of PAs prevents the complete collapse in transverse seas characteristic of flap-only farms, producing a smoother directional response even at small spacings.

Mixed arrays with large PAs and flaps (see Figure D.13g) show the slightly stronger spacing sensitivity among the mixed cases. In aligned seas, these arrays can achieve their highest mean $q$-factors at intermediate spacing (often around $6C$ in staggered layouts), but they also exhibit lower mean $q$ at $4C$ for off-axis headings due to stronger scattering and radiated-wave interference from the large PAs. Increasing spacing reduces these penalties and drives convergence toward $q \approx 1$ for aligned arrays, though large-PAs may retain slightly stronger residual interaction signatures than small-PAs. In summary, small-PA mixed arrays provide more consistent performance across spacings, whereas large-PA mixed arrays offer higher peak gains but require more careful spacing tuning to avoid interference losses.

#### REGULAR WAVES ACTIVE CONTROL

**PA mono arrays:** With active control, spacing remains an important driver of array interactions, but performance becomes more robust compared to passive control. For small-PA farms (see Figure D.14a and Figure D.14b), the mean $q$-factor for aligned headings is generally near or above unity across the spacing range, while off-axis headings improve steadily with increasing spacing, approaching unity at $10D$. In larger

farms, the penalty at 4$D$ for transverse headings can still be noticeable, but it is reduced relative to passive control; staggered layouts often retain slightly higher $q$-factors at tight to intermediate spacings by limiting direct shadowing.

Large-PA farms remain more spacing-sensitive under active control (see Figure D.14c and Figure D.14d). Aligned and near-aligned headings can show constructive peaks at intermediate spacings, whereas off-axis headings experience clearer penalties at tight spacing in large farms. Increasing spacing mitigates these effects and yields smoother behaviour across headings, but large-PAs still exhibit broader directional spread than small-PAs at comparable spacing due to their stronger wave-field modification.



**Mono flap arrays:** Active control does not materially change the spacing dependence of flap-only farms (see Figure D.14e). Mean $q$-factors remain primarily governed by wave direction: aligned headings form a stable plateau across spacings, oblique headings remain lower with minimal spacing sensitivity, and transverse headings remain near zero regardless of spacing or layout.

**Mixed arrays:** Mixed farms with small PA and flaps (see Figure D.14f) under active control show a stable response over spacing, with mean $q$-factors generally clustered around unity and modest constructive peaks for aligned incidence at intermediate spacings. Off-axis penalties at tight spacing are reduced relative to passive control, and performance converges toward unity as spacing increases. Large-PA mixed farms (see Figure D.14g) still display slightly stronger spacing sensitivity and a wider directional spread than small-PA mixed farms, particularly at 4$C$, but active control limits severe degradations and accelerates convergence toward isolated behaviour at 10$C$ for aligned direction. For the other direction the value is lower, since the power utilized for the single flap is in the dominant direction.

#### IRREGULAR WAVE PASSIVE CONTROL

**PA mono arrays:** Under irregular waves with passive control, small-PA mono arrays show a clear directional trend: mean $q$-factors converge toward unity as spacing increases from 4$D$ to 10$D$ in aligned and near aligned directions cosidering 2 devices (see Figure D.15a). At 4$D$, directional sensitivity is strongest and transverse headings are most penalised, especially as farm size increases (see Figure D.15b). Increasing spacing progressively weakens radiated-wave coupling and shadowing, leading to clustering of $q$ near unity by 10$D$ particularly observed as the number of devices increases.

Large-PA mono arrays (see Figure D.15c and Figure D.15d) follow the same trend but with stronger variability at intermediate spacings (6$D$–8$D$). Their larger footprint produces deeper interaction troughs at 4$D$ and maintains a broader directional spread until spacing approaches 10$D$, where the behaviour gets closer to the isolated performance. Large PA array show consistently destructive behavior throughout the considered regimes, suggesting spectral normalization lowers the peak while broadening the spatial response of the arrays.

**Mono flap arrays:** For flap-only farms (see Figure D.15e), spacing has negligible influence in irregular seas. Aligned headings remain near a constant mean $q$ across 4$W$–10$W$, oblique headings remain lower, and transverse headings collapse to near zero for all spacings.

**Mixed arrays:** Small-PA mixed farms (see Figure D.15f) show steady improvement with spacing particularly for aligned and following directions, with the widest directional spread at 4$C$ and convergence toward $q \approx 1$ by 10$C$. Large-PA mixed farms (see Figure D.15g) display slightly stronger spacing sensitivity: tight spacing yields the largest penalties for off-axis headings, while intermediate spacings reduce these losses and aligned headings remain comparatively robust. At 10$C$, both mixed configurations cluster

near unity for the aligned directions, though large-PAs can retain slightly improved performance compared to the small PA mixed arrays.

#### IRREGULAR WAVE ACTIVE CONTROL

**PA mono arrays:** Active control increases robustness but does not remove spacing effects. For small-PAs (see Figure 3.20a and Figure 3.20b), the main penalty at tight spacing is confined to off-axis headings in large farms; increasing spacing reduces these penalties and yields convergence toward unity across headings. For large-PAs (see Figure 3.20c and Figure 3.20d), spacing is more critical: tight spacing sustains broader directional spread and larger penalties for oblique headings in large farms, while increasing spacing markedly improves uniformity and brings mean $q$-factors closer to isolated behaviour. Certain angles such as 210 ° give mean $q$-factors consistently greater than 1 for large PA arrays while for small arrays, the interactions are predominantly destructive.



**Mono flap arrays:** Flap-only farms (see Figure 3.20e) remain insensitive to spacing under active control, with performance dictated by heading and persistent near-zero response for transverse incidence.

**Mixed arrays:** Mixed farms under active control converge more rapidly toward unity with spacing than under passive control. Small-PA mixed (see Figure 3.20f) farms show the smoothest behaviour across $4C$–$10C$, while large-PA mixed farms Figure 3.20g retain slightly stronger spacing sensitivity at $4C$ but approach a stable behaviour as spacing increases.

### 3.7.6. VARIATION OF AVERAGE $M$-FACTORS

This section focuses on the variation of the mean $M$-factors with number of devices and spacing. Similar to the variation of the mean $q$-factors, only figures representative of the behavior of the arrays is shown here.

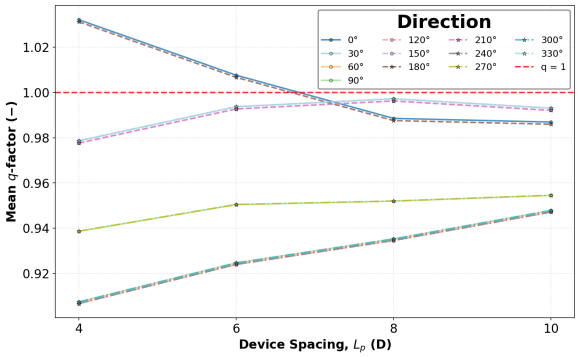
Only the results for irregular waves active control for small and big PA are shown here. The rest can be found in Appendix D for brevity.

**Regular waves passive control:** The variation of the mean $M$-factor with number of devices and spacing is shown in Figure D.16.

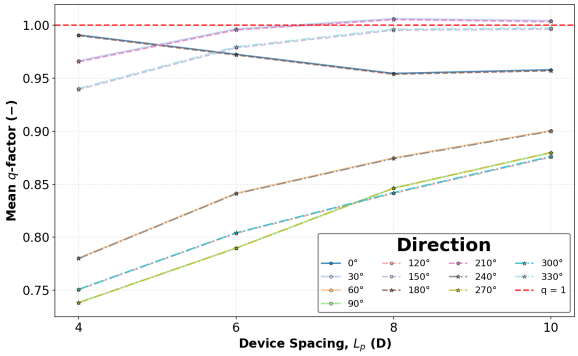
For mixed arrays composed of PAs and flaps operating under regular waves with passive control, the mean $M$-factor exhibits a clear dependence on wave direction and a secondary sensitivity to the number of devices, with distinct differences between small- and large-PA configurations. For both mixed array scales, aligned wave directions (0° and 180°) consistently yield $M$-factors well above unity across all array sizes, typically increasing from $N_t = 2$ to intermediate farms ($N_t = 4$–$7$) before saturating for larger arrays.

The mean $M$-factor for 180° is generally higher than 0° suggesting the radiated fields from the PAs are more beneficial for the flaps than the other way around. Moderately oblique directions (30°–60° and 150°–210°) also maintain $M > 1$, but large-PA mixed arrays exhibit noticeably greater variability with increasing $N_t$, reflecting their stronger radiated-wave interactions. Near-off-axis directions (120°, 240°, and 300°) remain clustered close to unity for both configurations, indicating limited cumulative interaction effects as the array grows.

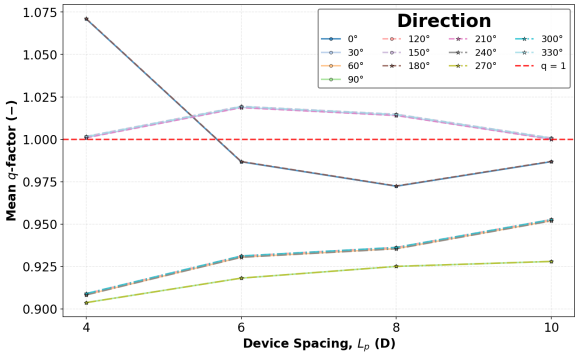
In contrast, transverse directions (90° and 270°) consistently produce $M$-factors well below unity, with a mild degradation as $N_t$ increases, particularly for large-PA arrays due to lack of participation from the flaps. Overall, while both mixed configurations preserve constructive interactions with increasing array size, small-PA mixed arrays display more stable and robust behaviour, whereas large-PA mixed arrays require greater care in farm scaling to avoid interference-driven losses.




(a) Small PA mono: Number of devices – 2, staggered configuration

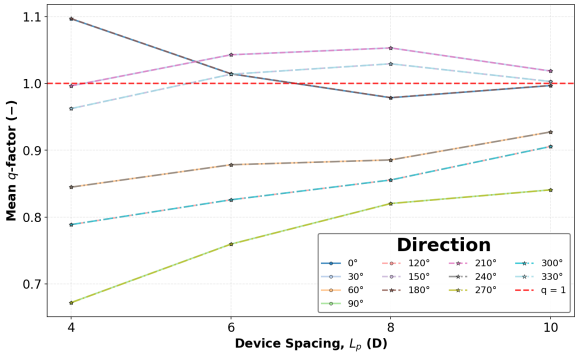



(b) Small PA mono: Number of devices – 10, staggered configuration

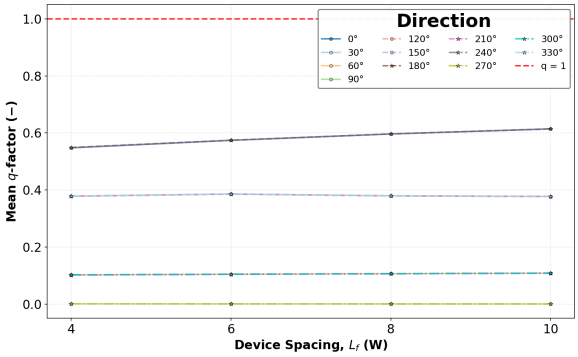



(c) Big PA mono: Number of devices – 2, staggered configuration

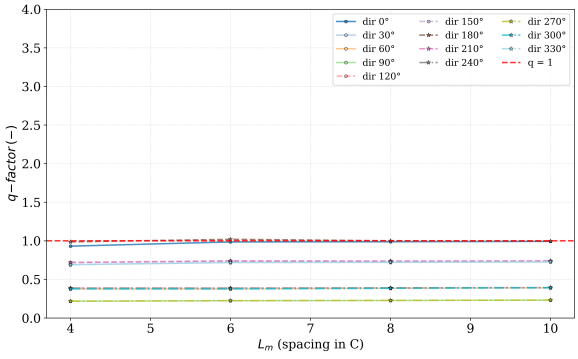
Figure 3.20.: Variation of mean $q$-factor (averaged over $T = 3$–$12$ s) with spacing for mono and mixed arrays under irregular waves with active control. The number of devices and array configuration for each case are indicated in the subcaptions.




(d) Big PA mono: Number of devices – 10, staggered configuration

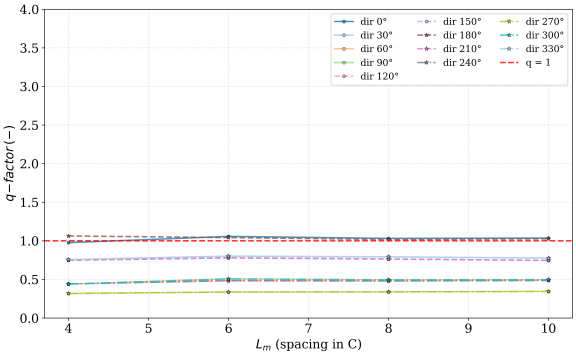



(e) Flap mono: Number of devices – 7, staggered configuration




(f) Mixed (small PA + flap): Number of devices – 7, staggered configuration

Figure 3.20.: (continued).




(g) Mixed (big PA + flap): Number of devices – 7, staggered configuration

Figure 3.20.: (continued).

With respect to inter-device spacing, the mean $M$-factor for both mixed array scales shows only moderate sensitivity over the range $L_m = 4C$–$10C$, with wave direction remaining the dominant factor. For aligned and moderately oblique directions, $M$ remains above unity for all spacings, with large-PA mixed arrays often exhibiting a shallow maximum at intermediate separations ($6C$–$8C$), reflecting an optimal balance between constructive coupling and reduced radiated-wave interference.

Small-PA mixed arrays, by contrast, show weaker spacing dependence, with $M$-factors remaining relatively uniform across the full spacing range. Near-off-axis directions cluster around unity for both configurations, while transverse directions persistently yield the lowest $M$-factors with only marginal recovery at intermediate spacings. In summary, spacing plays a secondary role compared to wave direction for mixed arrays, with small-PA configurations exhibiting greater insensitivity to layout density, and large-PA configurations benefiting most from moderate separations to control their stronger hydrodynamic interactions.

**Regular waves active control:** The variation of the mean $M$-factor with number of devices and spacing is shown in Figure D.17.

Under regular-wave conditions with active control, the mean $M$-factor for mixed arrays of point absorbers (PAs) and flaps exhibits a clear dependence on wave direction and a secondary sensitivity to the number of devices, with distinct differences between small- and large-PA configurations. For both array scales, aligned wave directions (0° and 180°) consistently yield $M$-factors well above unity across all values of $N_t$, indicating sustained constructive interactions as the farm grows.

In small-PA mixed arrays, the increase in $M$ from $N_t = 2$ to intermediate sizes ($N_t = 4$–$7$) is modest and quickly plateaus for larger farms, demonstrating that active control effectively limits the accumulation of radiated-wave interactions and leads to early saturation of array effects. Moderately oblique directions (30°–60° and 150°–210°) similarly maintain $M > 1$ with minimal sensitivity to array size.

In contrast, large-PA mixed arrays show more pronounced, and occasionally non-monotonic, variations with $N_t$, reflecting their larger hydrodynamic footprint and stronger cumulative interactions even under active control. Near-off-axis directions (120°, 240°, and 300°) remain clustered close to unity for both configurations, while transverse directions (90° and 270°) consistently yield the lowest $M$-factors, although with reduced variability compared to passive control. Overall, active control enhances robustness to array scaling for both configurations, but array-size effects remain more pronounced for large-PA mixed arrays than for small-PA ones.

With respect to inter-device spacing, the mean $M$-factor under active control exhibits a generally weak but directionally structured dependence for both small- and large-PA mixed arrays over the range $L_m = 4C$–$10C$. For aligned and moderately oblique wave directions, both configurations maintain $M$-factors above unity across all spacings, with only modest variations and shallow maxima typically observed at intermediate separations ($6C$–$8C$). This indicates that active control preserves constructive mixed-device interactions while limiting excessive radiated-wave interference as spacing increases.

Near-off-axis directions again cluster close to unity with no systematic spacing trend, while transverse directions consistently produce the lowest $M$-factors, remaining below unity even though active control leads to a shallower performance trough and occasional mild recovery at intermediate spacings. Comparing the two scales, small-PA mixed arrays exhibit a greater insensitivity to spacing, whereas large-PA mixed arrays display slightly stronger spacing-induced variability and benefit more noticeably from moderate separations that balance constructive interactions against residual interference effects.



**Irregular waves passive control:** The variation of the mean $M$-factor with number of devices and spacing is shown in Figure D.18.

Under irregular-wave conditions with passive control, the mean $M$-factor for mixed arrays of point absorbers (PAs) and flaps exhibits a clear dependence on wave direction and a secondary, scale-dependent sensitivity to the number of devices, with distinct differences between small- and large-PA configurations.

For small-PA mixed arrays, aligned wave directions (0° and 180°) consistently yield $M$-factors above unity for all array sizes, increasing modestly from $N_t = 2$ to intermediate farms ($N_t = 4$–$7$) before approaching saturation for larger arrays. Moderately oblique directions (30°–60° and 150°–210°) similarly remain close to or slightly above unity with only minor sensitivity to array growth, indicating that interaction effects tend to stabilise rather than accumulate under broadband forcing. Transverse directions (90° and 270°) yield the lowest $M$-factors, remaining below unity and showing a mild degradation with increasing $N_t$, while near-transverse off-axis directions (120°, 240°, and 300°) cluster close to unity with minimal variation, highlighting the stabilising role of the PAs.

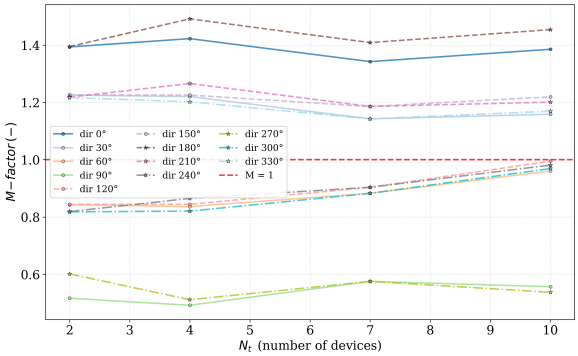
In contrast, mixed arrays with large PAs exhibit a more pronounced and often non-monotonic dependence on $N_t$, particularly for aligned and moderately oblique directions, reflecting their larger hydrodynamic footprint and stronger cumulative radiation effects. Overall, while both mixed configurations avoid the severe efficiency collapse observed in mono-flap arrays, large-PA mixed arrays display stronger array-size effects than small-PA mixed arrays, requiring greater care in farm scaling.

With respect to inter-device spacing, both small- and large-PA mixed arrays under irregular waves with passive control maintain average $M$-factors above unity across the full spacing range considered, confirming the inherent hydrodynamic advantage of mixed farms over mono-device configurations.

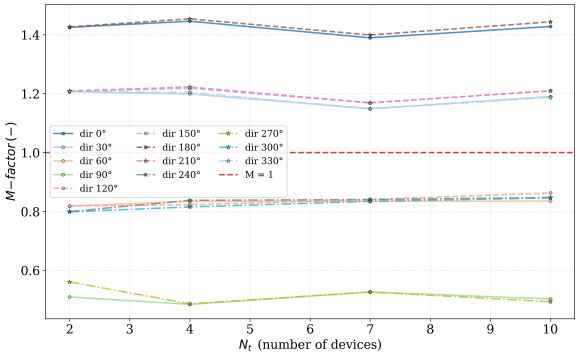
For small-PA mixed arrays, the highest $M$-factors occur at the tightest spacings ($\sim 4D$), where constructive interactions between the heaving PAs and pitching flaps are strongest, before gradually converging toward a stable plateau as spacing increases toward $10D$.

Large-PA mixed arrays show a similar qualitative trend, although the larger absorber footprint induces stronger local wave-field modifications at tight spacings, leading to greater variability in the interaction gains. As spacing increases, interaction effects diminish and the $M$-factor stabilises, yet remains above unity for both configurations, particularly in staggered layouts. Comparing the two scales, small-PA mixed arrays exhibit greater robustness to spacing variations, whereas large-PA mixed arrays benefit more noticeably from moderate separations that balance constructive coupling against interference effects.

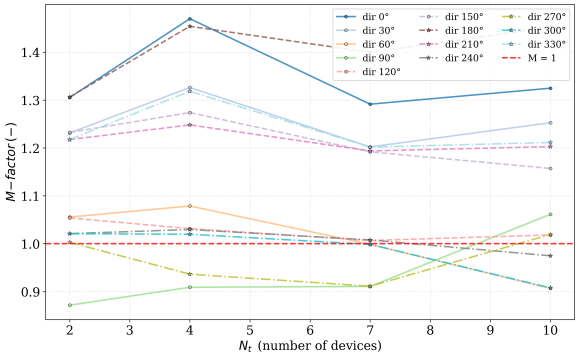
**Irregular waves active control:** The variation of the mean $M$-factor with number of devices and spacing is shown in Figure 3.21.




(a) Small PA–flap mixed: Spacing – 4$C$, staggered configuration

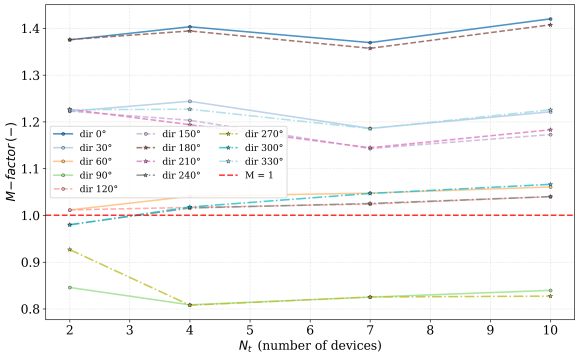



(b) Small PA–flap mixed: Spacing – 10$C$, staggered configuration

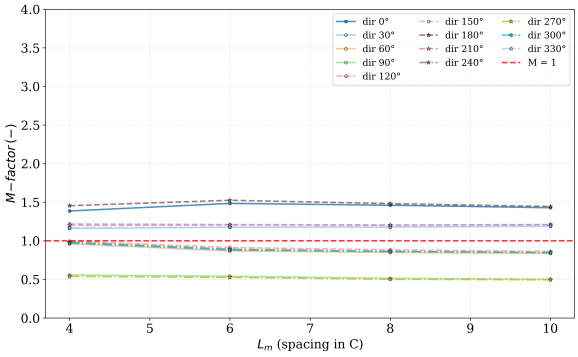



(c) Big PA–flap mixed: Spacing – 4$C$, staggered configuration

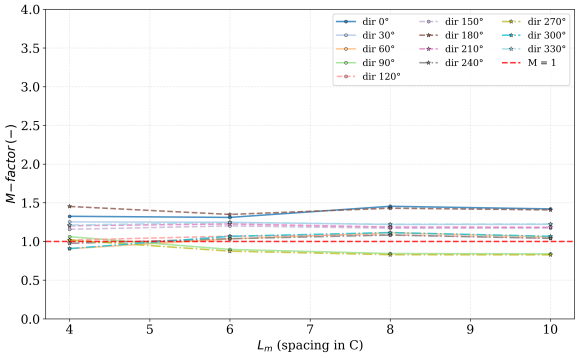
Figure 3.21.: Variation of the mean $M$-factor (averaged over $T = 3$–12 s) with number of devices and spacing for mixed arrays under irregular waves with active control. The number of devices/spacing and array configuration for each case are indicated in the subcaptions.




(d) Big PA–flap mixed: Spacing – 10$C$, staggered configuration




(e) Small PA–flap mixed: Number of devices – 10, staggered configuration




(f) Big PA–flap mixed: Number of devices – 10, staggered configuration

Figure 3.21.: (continued).

Under irregular-wave conditions with active control, the average $M$-factor for mixed arrays of PAs and flaps remains consistently above unity for all considered array sizes, confirming the strong hydrodynamic synergy enabled by control.

For mixed arrays with small PAs, the $M$-factor shows exceptional robustness with respect to the number of devices, typically remaining within a narrow band ($M \approx 1.1$–$1.3$) as the array scales from $N_b = 2$ to $N_b = 10$. This near-invariance indicates that active control effectively regulates inter-device interactions, preventing cumulative losses as additional bodies are introduced.

Mixed arrays with large PAs exhibit a similar qualitative behaviour, but with slightly higher peak efficiencies and a more noticeable, albeit mild, non-monotonic dependence on $N_b$. The larger hydrodynamic footprint of the big PAs leads to stronger radiated-wave interactions, which are largely mitigated—but not entirely eliminated—by active control. Consequently, small-PA mixed arrays offer more predictable and scalable performance, whereas large-PA mixed arrays can achieve higher efficiency gains provided that array growth is carefully managed.

When varying inter-device spacing, both small- and large-PA mixed arrays under active control maintain $M$-factors well above unity across the entire spacing range considered, demonstrating a clear advantage over mono-device farms.

For small-PA mixed arrays, the $M$-factor remains remarkably insensitive to spacing, with values typically between 1.15 and 1.25 from dense ($4D$) to sparse ($10D$) layouts, highlighting the ability of active control to suppress destructive interference and shadowing even in compact farms.

Large-PA mixed arrays display a stronger spacing dependence: tighter spacings tend to yield the highest $M$-factors by exploiting the substantial wave-field modification induced by the larger absorbers, while increasing separation leads to gradual saturation or slight reductions as interaction effects weaken. Comparing the two configurations, small-PA mixed arrays provide greater robustness to both spacing and layout variations, whereas large-PA mixed arrays deliver higher peak efficiencies at the cost of increased sensitivity to spatial arrangement.

### 3.7.7. Choosing the best configurations

To determine the optimal layout for detailed analysis, the performance of mixed arrays is evaluated using both $q$-factors and $M$-factors. While $q$-factors quantify array performance relative to isolated devices, $M$-factors normalize the power produced based on the distinct physical dimensions of the point absorbers (PAs) and flaps, providing a clearer comparison of hydrodynamic efficiency across mixed and mono-array types.

Only the results for irregular waves for small and big PA are shown here. The rest can be found in Appendix D for brevity.

Under regular wave conditions (see Figure D.19 and Figure D.20), the mixed configuration utilizing large PAs and flaps (5 each) in a staggered layout with active control is identified as the best overall configuration. While the small PA-flap mixed array shows a higher mean $M$ factor of 1.75, compared to the 1.66 (5% difference) achieved by the large PA-flap mixed array, the corresponding mean $q$-factor achieved by the larger PA-flap is 17% higher then the mean $q$-factor of 1.08 achieved by the small PA-flap mixed array. Furthermore, while multiple configurations achieve $q$ and $M$ values greater than 1 across 2 directions with $M$-factor greater than 1 for 10 directions, this specific large-scale mixed array provides the highest mean $M$-factor and thus the superior capture width efficiency as compared to other configurations.

In irregular waves (see Figure 3.22 and Figure 3.23), performance profiles are more varied, yet the 10-device staggered mixed array (large PA + flap) with passive control remains the preferred choice for comprehensive study, for similar reasoning to what was stated for the regular waves case. Within the large PA-flap mixed array cases, while configurations such as the 4 PA + 3 flap mixed array may yield slightly higher average $q$-factors in specific headings, the 10-device large-PA array achieves the highest average $M$-factor. Given that this configuration consistently outperforms mono-farms and demonstrates high hydrodynamic efficiency when accounting for device dimensions, it is

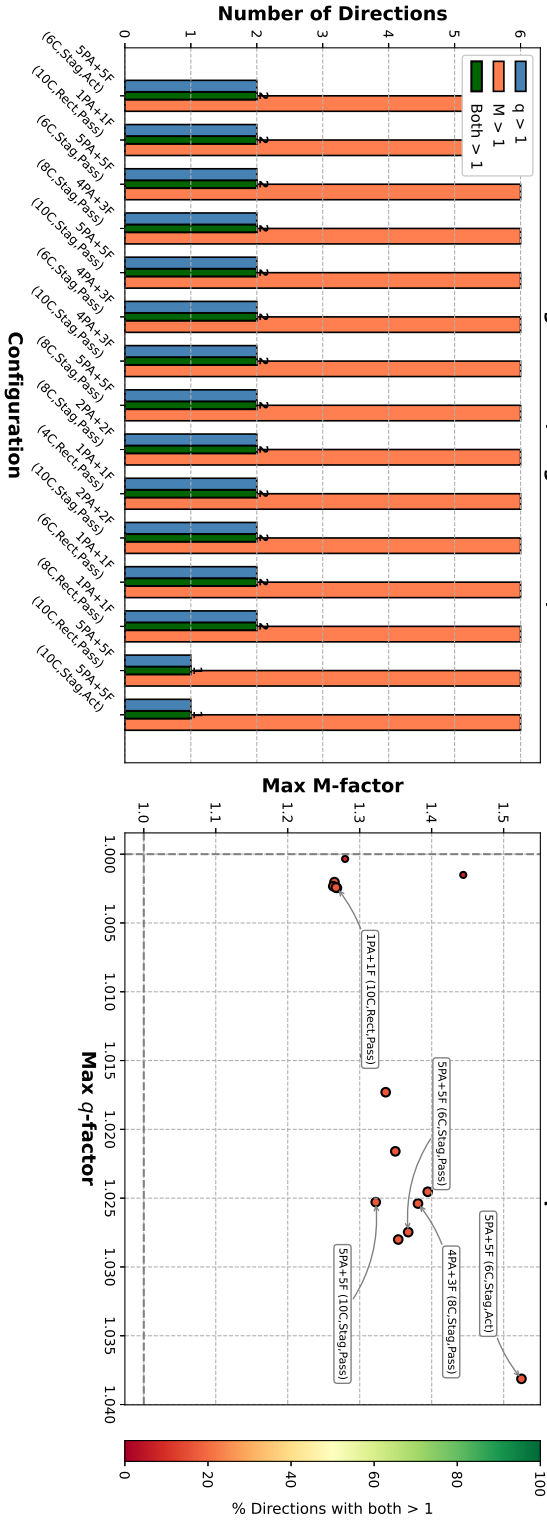



Figure 3.22.: Best-performing mixed array configuration for small point absorbers (PAs) combined with flaps under irregular wave conditions.

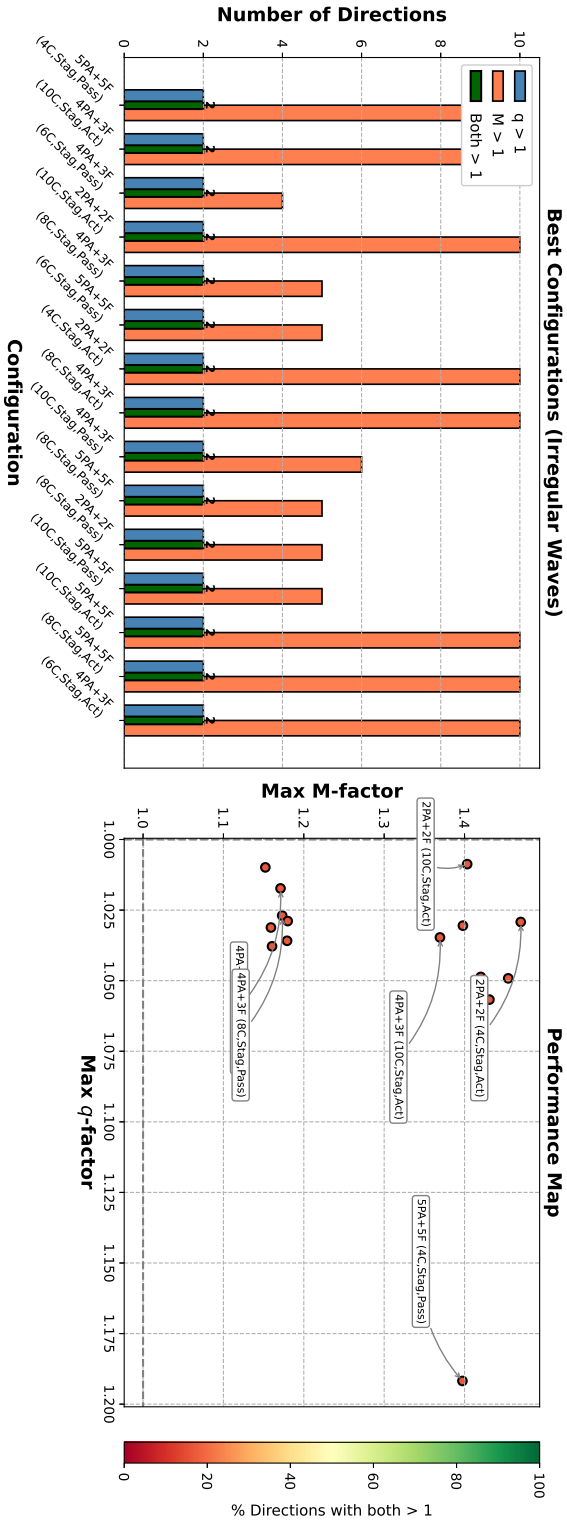



Figure 3.23.: Best-performing mixed array configuration for big point absorbers (PAs) combined with flaps under irregular wave conditions.

selected as the primary candidate for detailed analysis across both sea state conditions.

## 3.8. SUMMARY AND CONCLUSIONS

This chapter investigated the hydrodynamic performance of mono and mixed WEC arrays in shallow-water conditions representative of the Dutch nearshore environment. Mono arrays composed of PAs or flaps were compared against mixed PA–flap arrays using weakly non-linear frequency-domain modelling under passive and active control strategies.

Performance was evaluated using interaction-based ($q$-factor) and geometry-normalised ($M$-factor) metrics across variations in array size, spacing, layout, and incident wave direction. The results consistently show that mixed arrays are capable of exploiting complementary device dynamics, leading to enhanced hydrodynamic interactions and improved overall performance compared to mono-device farms under realistic directional and spectral conditions.

The primary advantage of mixed arrays lies in their ability to combine the strong, direction-dependent energy extraction of flaps with the more isotropic response of point absorbers. This synergy results in higher average $q$-factors than PA mono arrays and, in several configurations and certain directions, with performance mostly exceeding flap mono arrays.

Mixed arrays also exhibit greater directional robustness and reduced sensitivity to array size and spacing, maintaining stable performance as the number of devices increases. When assessed using the $M$-factor, mixed arrays frequently match or outperform mono farms on a per-unit-width basis, indicating that the observed gains are driven by genuine hydrodynamic interaction effects rather than device size alone.

However, mixed arrays also present some limitations. Their performance is more sensitive to configuration choices, with suboptimal layouts or unfavourable wave directions leading to partially destructive interactions. Under passive control, the performance advantage of mixed arrays over flap mono arrays is reduced particularly under irregular waves, indicating that advanced or coordinated control strategies are key to fully realising their potential.

In addition, mixed arrays introduce greater modelling and control complexity due to differences in device geometry, degrees of freedom, and motion constraints. Despite these challenges, the results demonstrate that, for shallow-water applications, mixed PA–flap arrays offer a robust and efficient alternative to mono-device farms when appropriately configured and controlled.

# 4

# ANALYSIS OF MIXED AND MONO ARRAYS IN DEEP WATERS

*To have what you have never had, you have to do what you have never done.*

Thomas Jefferson

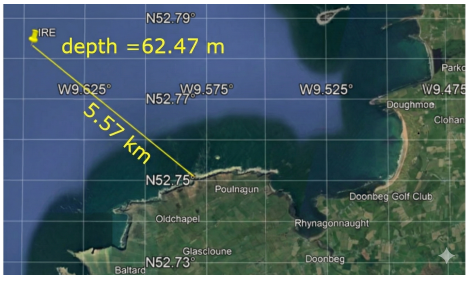
*The analysis presented in this chapter focuses on the hydrodynamics and performance comparison of mixed arrays, composed of Point Absorbers (PAs) and attenuators, against mono-device arrays in deep waters, considering a wave climate off the west coast of Ireland where highest wave occurrence is concentrated around $H_s = 1 - 1.5$ $m$ and $T_p = 9$ $s$. Using a weakly non-linear frequency-domain hydrodynamic model, device performance was systematically assessed across various farm sizes ($N_t = 2, 4, 7, 10$) and normalized spacings (4C to 10C), utilizing the q-factor (power gain) and M-factor (geometry-normalized efficiency) metrics. The study revealed that mono PA arrays were moderately destructive (mean q-factors below 0.96 in irregular waves), while mono attenuator arrays were highly directional, showing high constructive peaks (up to $q = 1.38$) but suffering from severe destructive troughs (down to $q = 0.60$) in irregular sea states. Critically, mixed arrays emerged as the most robust configuration, successfully blending these characteristics to retain high constructive potential (reaching $q_{max}$ up to 1.37) while the presence of PAs mitigated the deepest destructive troughs, leading to a more stable performance profile. Mixed arrays also demonstrated superior overall efficiency, reaching up to 30% more weighted capture width efficiency (M-factor) than mono-arrays. This efficiency advantage was found to be non-monotonic with size, suggesting an optimal intermediate array size around $N_t \approx 7$ where cooperative effects are maximized. Furthermore, in irregular waves, mixed arrays showed robust performance with only weak dependence on spacing across the 4D to 10D range, indicating greater layout flexibility. Based on consistency and superior average efficiency, the 5 PA + 5 attenuator mixed array was identified as the best-performing configuration.*

This chapter introduces the hydrodynamic modelling framework used to evaluate the performance of mono and mixed WEC arrays in deep-water conditions. Two wave energy converters are considered in this study. The first is the PA. The second is a two-body attenuator, inspired from the Mocean WEC [140]. The chapter begins by describing the wave climate and key modelling assumptions, followed by a detailed presentation of the weakly non-linear hydrodynamic models developed for both the PA and the flap, for single devices as well as array configurations. Similar to the analysis in shallow-water, the results first examine the global behaviour of mono and mixed arrays, before analysing the influence of incident wave direction, number of devices, and inter-device spacing. The chapter concludes by identifying the optimal mixed-array configuration for in-depth performance assessment.

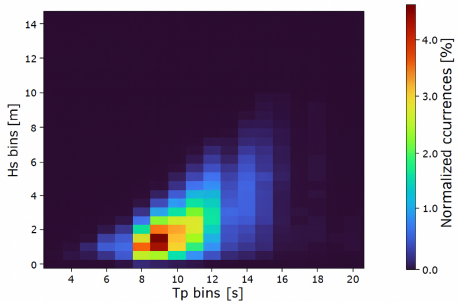
## 4.1. SCATTER DIAGRAM

The wave climate considered in this study corresponds to a location off the west coast of Ireland, at the latitude of Doonbeg. This region is exposed to long-period Atlantic swells and energetic winter storms. The coordinates and water depth of the selected site are provided in Figure 4.1a.

The corresponding scatter diagram is shown in Figure 4.1b. The site lies in a mid- to high-resource region, with the highest occurrence concentrated around $H_s = 1$–$1.5$ m and $T_p = 9$ s. The scatter diagram further indicates that, for a given significant wave height bin, the dominant contribution (approximately 20% of occurrences) is associated with $H_s = 1$–$1.5$ m. Therefore, this wave height range is adopted as the reference condition for analysing directional variations of the $q$-factor in section 4.6.




(a) Considered location at Lon −9.64°, Lat 52.78° off the coast of Ireland (taken from [153])




(b) Scatter diagram at Lon −9.64°, Lat 52.78° off the coast of Ireland (taken from [153])

Figure 4.1.: Selected offshore location and corresponding wave climate for the deep-water case off the coast of Ireland.

## 4.2. ASSUMPTIONS

Weakly non-linear, frequency-domain hydrodynamic models are used to simulate both single devices and arrays. This section summarises the key modelling assumptions adopted in the analysis.

### ASSUMING CYLINDRICAL SHAPE FOR THE PA

The point absorber (PA) in deep water is assumed to have a cylindrical geometry. Although this is not a common representation for commercially relevant devices, the choice is deliberate: it minimises the influence of strongly non-linear hydrostatic restoring and nonlinear Froude–Krylov (NLFK) forces, thereby ensuring that the weakly

non-linear framework remains suitable for predicting loads and absorbed power with reasonable accuracy.

#### SPACING OF THE WECS IN THE ARRAY

A minimum spacing of $4L$ is adopted, where $L$ is the characteristic dimension of the WEC within the array. This choice is motivated by two considerations: (a) to avoid direct physical interaction between devices in surge, and (b) because boundary element methods may yield inaccurate or overestimated interaction effects when inter-device gaps become small. In such cases, higher-order asymptotic corrections or more refined numerical treatments may be required [133, 134].

#### VISCOUS LOSSES

For regular waves, viscous drag is represented using the Lorentz linearisation approach. For the two-body attenuator device (based on the Mocean M100), previous work indicates that linear-model power estimates including viscous damping remain within approximately 10% accuracy for $H_s$ up to 2.5 m [140]. Since the present case study focuses on $H_s = 1.5$ m, the weakly non-linear framework is expected to provide reliable power estimates.

For irregular waves, a spectral-domain approach is adopted, consistent with the shallow-water analysis. This is appropriate for mid- to high-resource sea states for both PA devices [126] and attenuators [140]. Furthermore, following [140], the same viscous damping coefficient is applied across all degrees of freedom for the attenuator.



#### MOORINGS

Mooring forces are neglected in the hydrodynamic model, as both the PA and attenuator are assumed to be slack-moored (consistent with the Mocean device). Under this assumption, the influence of moorings on hydrodynamic response and absorbed power is expected to be negligible [131].

### 4.3. HYDRODYNAMIC MODEL IMPLEMENTED FOR THE SINGLE DEVICES

This section describes the hydrodynamic model used for the single PA and attenuator devices. The same modelling framework is subsequently extended to wave-energy arrays.

#### DEVICE DESCRIPTION

The PA geometry is modelled as a cylinder. Its mass and principal properties are chosen to be representative of the CorPower C4 device [124]. The corresponding geometric and mass properties are summarised in Table 4.1a.

The attenuator geometry is adapted from the Mocean M100 two-body attenuator [140]. While the original Mocean device is asymmetric, the geometry considered here assumes symmetric arms. The main geometric properties are listed in Table 4.1b (based on [140]). The mass properties are computed for the freely floating device, and the natural frequencies of both devices are determined from the listed properties and hydrodynamic coefficients.

The PA is constrained to operate only in heave. In contrast, the attenuator is modelled with four DOFs: surge, heave, pitch, and flex. Here, flex represents the relative rotational motion between the two arms and is the DOF through which the PTO extracts power [140].

The modelled DOFs for the attenuator are illustrated in Figure 4.2. The rigid-body modes (surge, heave, pitch) are shown along with the rear-arm pitch motion $\zeta_7$. If the forearm rotation about the device centre of gravity is represented by $\zeta_5$, then the flex DOF is defined as $\zeta_7 - \zeta_5$.

(a) Properties of the PA device

| Property | Value | Unit |
|---|---|---|
| Diameter | 9 | *m* |
| Weight | 60 | *T* |
| Draft | 5.4 | *m* |

(b) Properties of the attenuator device

| Property | Value | Unit |
|---|---|---|
| Length of each arm | 25 | *m* |
| Draft | 5 | *m* |
| Width (Middle) | 3.33 | *m* |
| Width (ends) | 7.56 | *m* |

Table 4.1.: Geometric and mass properties of the wave energy converters considered for the deep-water array configurations.

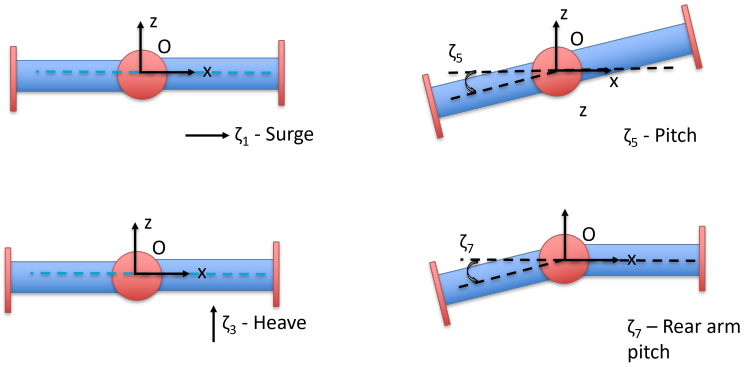



Figure 4.2.: DOFs of the attenuator device

### CONVERGENCE STUDY FOR THE MESH

A mesh convergence study was performed for both the PA and attenuator. The minimum panel size per device was estimated using $\lambda/6$ [43, 136], where $\lambda$ is the wavelength corresponding to the smallest period considered. Based on the scatter diagram, a minimum period of $T = 5$ s is adopted for both regular and irregular wave calculations. Under deep-water conditions, this yields a minimum required element size of approximately 39 m.

As in the shallow-water analysis, convergence was first assessed for single devices. A higher panel count was then selected for array simulations to better capture interaction effects, particularly at smaller spacings. Based on the single-device studies, 800 panels were sufficient for the PA hull and 821 panels for the attenuator hull. For array calculations (with 2–10 devices and a minimum spacing of 4 times the characteristic dimension), higher-resolution meshes were adopted: 1200 panels for the PA hull and 1212 panels per attenuator. Waterplane meshes were included for both devices to suppress irregular frequencies.

The final meshes used in all simulations based on convergence studies are shown in Figure 4.3 and Figure 4.4.

## 4.3.1. CALCULATION OF THE NATURAL FREQUENCY OF THE DEVICES

For the PA, the natural period is obtained in the same way as in the shallow-water analysis: by plotting the heave RAO against period and identifying the peak. The corresponding heave RAO is shown in Figure 4.5.

For the attenuator, a 4-DOF system is considered (see Figure 4.2), requiring the solution of four coupled equations. Two complementary approaches can be used to

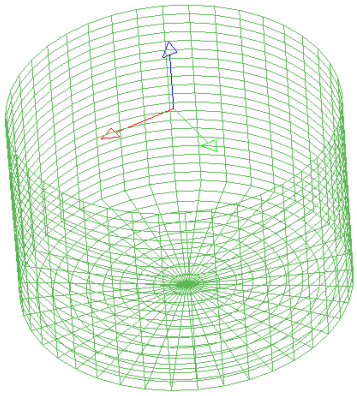


Figure 4.3.: Mesh for the PA with 1200 panels in the hull

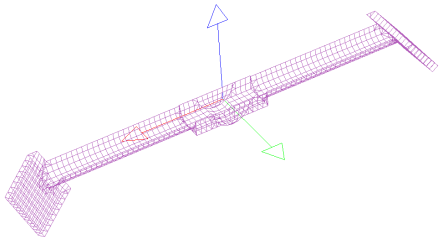


Figure 4.4.: Mesh for the attenuator with 1212 panels in the hull

identify natural frequencies: (a) plotting the determinant of the dynamic stiffness matrix versus period and identifying the zero crossings, and (b) plotting the RAOs for all DOFs obtained from the coupled system. The governing equations of motion are:

$$\left[-\omega_i^2\left(\mathbf{M}_d + \mathbf{M}_a(\omega_i)\right) + i\omega_i \mathbf{B}_a(\omega_i) + \mathbf{C}_h\right]\zeta(\omega_i) = \mathbf{F}_e(\omega_i) \tag{4.1}$$

Bold letter represents a matrix. Here $\mathbf{M}_d$ is the fully populated structural mass matrix and $\mathbf{M}_a(\omega_i)$ is the fully populated added-mass matrix. $\mathbf{B}_a(\omega_i)$ is the fully populated radiation-damping matrix, $\mathbf{C}_h$ is the fully populated hydrostatic stiffness matrix, $\mathbf{F}_e$ is the excitation force/moment vector, and $\zeta$ is the response vector. For an incident wave amplitude of 1 m, $\zeta$ represents the RAO vector. The derivation of the attenuator mass and stiffness matrices is provided in Appendix C.

Figure 4.6 shows the determinant of the dynamic stiffness matrix as a function of period. Three natural frequencies are evident: one dominated by surge, one by heave, and one associated with pitch/rear-arm pitch. Due to the symmetric configuration and $\zeta_7$ representing rear-arm pitch, it is expected that the pitch and rear-arm pitch modes align closely. To clarify the modal coupling, RAOs with and without radiation damping are compared in Figure 4.7. Clear coupling is observed between surge and pitch, and between heave, pitch, and rear-arm pitch. While the heave and pitch/rear-arm pitch peaks are only weakly affected by radiation damping, the surge peak shifts from 4.96 s to 5.35 s due to a surge damping ratio of approximately 2.2%.

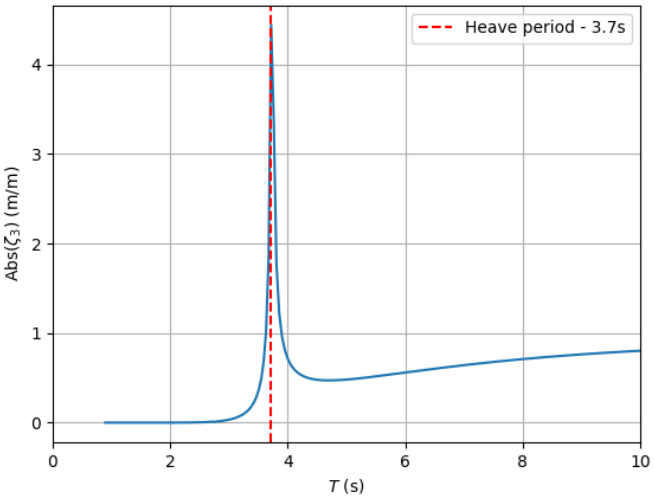



Figure 4.5.: RAO in heave for the cylinder PA

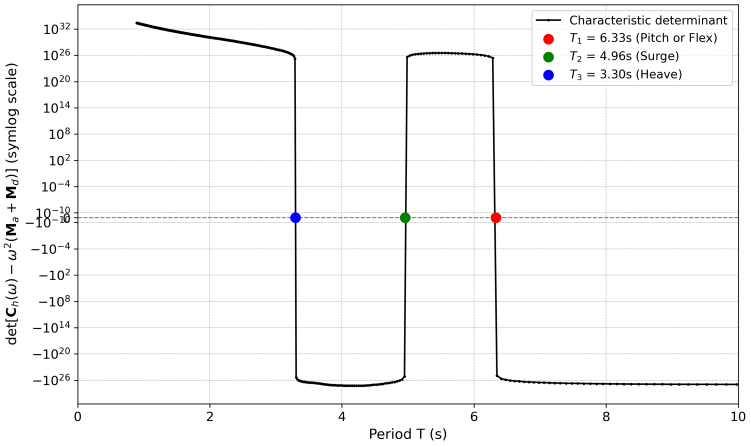



Figure 4.6.: Undamped determinant vs period for the attenuator

Frequency-dependent hydrodynamic coefficients and excitation forces are obtained using the frequency-domain BEM solver HAMS-MREL [54]. For the attenuator, the generalised-modes approach is employed following our previous work [104].

### 4.3.2. Incorporating control and viscous drag under regular waves - passive control strategy under no constraints

A passive control strategy, consistent with the shallow-water analysis, is adopted here. The procedure for computing the single-device response and absorbed power for the PA follows the same steps as in section 3.3.2.

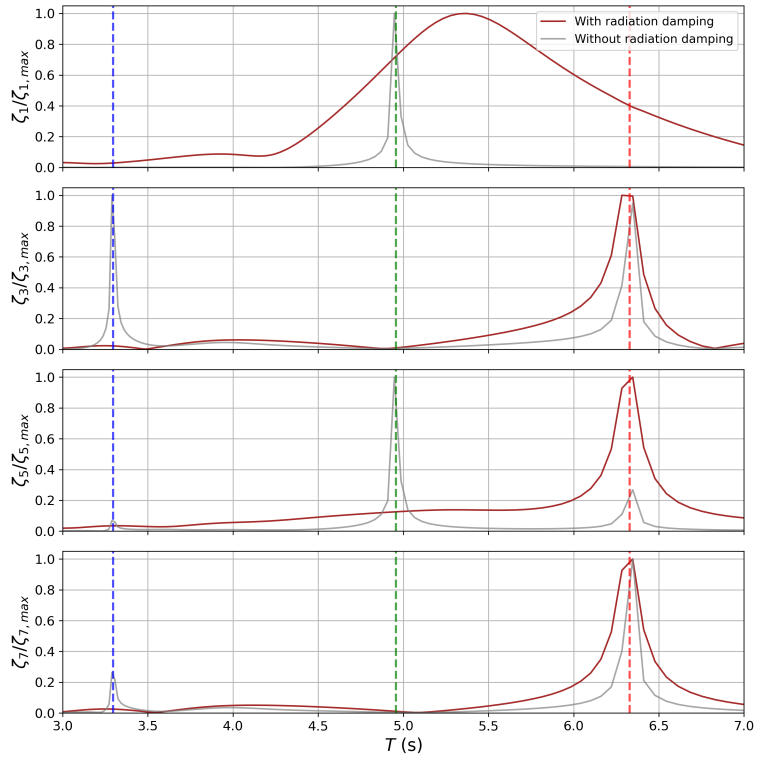



Figure 4.7.: Response with and without radiation damping for the attenuator

For the attenuator, the coupled equations of motion are solved to obtain the response:

$$\left[-\omega_i^2\left(\mathbf{M}_d + \mathbf{M}_a(\omega_i)\right) + i\omega_i\left(\mathbf{B}_a(\omega_i) + \mathbf{B}_{PTO} + \mathbf{B}_v\right) + \mathbf{C}_h\right]\zeta(\omega_i) = \mathbf{F}_e(\omega_i) \tag{4.2}$$

Here $\mathbf{B}_{PTO}(\omega_i)$ is the PTO damping matrix, defined as:

$$\mathbf{B}_{PTO}(\omega_i) = \begin{bmatrix} 0 & 0 & 0 & 0 \\ 0 & 0 & 0 & 0 \\ 0 & 0 & b_{PTO}(\omega_i) & -b_{PTO}(\omega_i) \\ 0 & 0 & -b_{PTO}(\omega_i) & b_{PTO}(\omega_i) \end{bmatrix} \tag{4.3}$$

where $b_{PTO}(\omega_i)$ is obtained via brute-force optimisation per frequency (details are provided later in section 4.6). $\mathbf{B}_v$ is the viscous damping matrix, assumed diagonal and based on a constant drag coefficient $C_D = 0.9$ following [140]. Differences in viscous contributions between DOFs arise from differences in projected drag areas, which are computed per DOF in Appendix C.

For the PA, the viscous drag coefficient is determined from the Keulegan–Carpenter number, yielding $C_D = 0.5$, consistent with the shallow-water analysis.

The absorbed power at each discrete frequency $\omega_i$ for the attenuator is computed as:

$$P(\omega_i) = \frac{1}{2} b_{PTO}(\omega_i)\omega_i^2 |\zeta_{7,i} - \zeta_{5,i}|^2 \tag{4.4}$$

To represent the uni-directional power delivered to the grid, a PTO conversion efficiency $\eta$ is applied. Efficiencies of 80–90% are achievable in PTO actuators [142, 143]; here $\eta = 0.9$ is assumed, giving the final power as $\eta P(\omega_i)$.

### 4.3.3. Incorporating control and viscous drag under irregular waves - passive control strategy under no constraints

For irregular waves, the procedure as utilized in the shallow-water analysis is applied to both the PA and attenuator, with one modification. The PTO damping coefficient is obtained via brute-force optimisation for each sea state (see section 4.6) and is kept constant throughout the iterative solution. Only the response-dependent damping contributions are iteratively updated.

## 4.4. Considered configurations



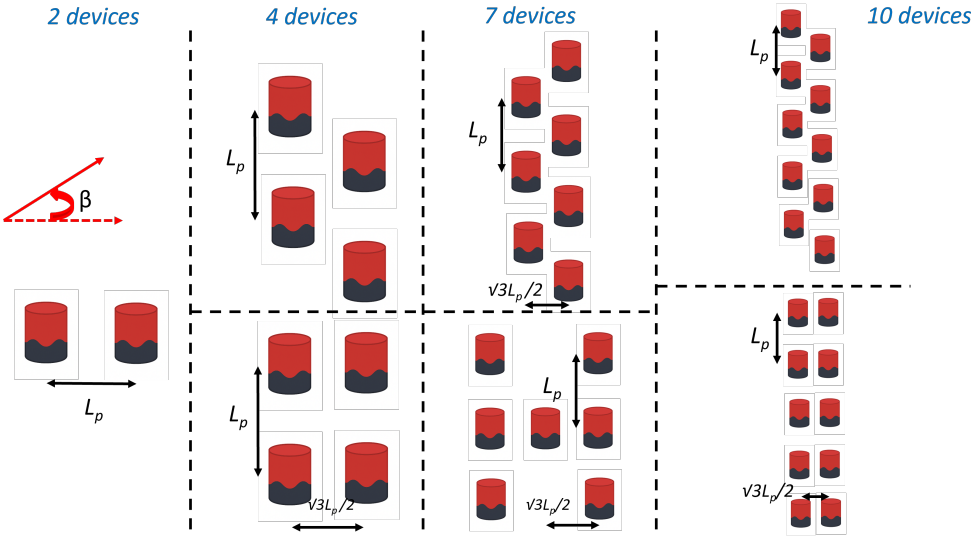



Figure 4.8.: PA configurations

The two mono and mixed array configurations are shown in Figure 4.8, Figure 4.9 and Figure 4.10. Across all three array types-point absorbers (PAs), attenuators, and mixed PA–attenuator farms-the configurations follow a consistent geometric logic based on array size (2, 4, 7, and 10 devices), layout, spacing, and directional exposure. For arrays with four or more devices, two layouts are considered: a rectangular configuration (bottom row in each panel) and a staggered configuration (top row). The rectangular layout places devices on a regular grid, whereas the staggered layout offsets alternate rows by half a spacing, producing a diamond-like packing.

All arrays are evaluated at four normalised spacings: $4C$, $6C$, $8C$, and $10C$, where $C$ denotes the characteristic device dimension (PA diameter $D$ for the PA array, attenuator length $L$ for the attenuator array, and an averaged characteristic dimension for the mixed case). This systematic spacing variation enables investigation of both near-field and far-field interaction effects across compact and more loosely spaced farms.

Each array is assessed for 12 incident wave directions, spaced at 30° intervals, covering the full 360° directional range. For the attenuator, 0° is defined as waves incident along the device length, i.e., waves strike the attenuator on its shorter side. This orientation is hydrodynamically important because attenuators exhibit strongly

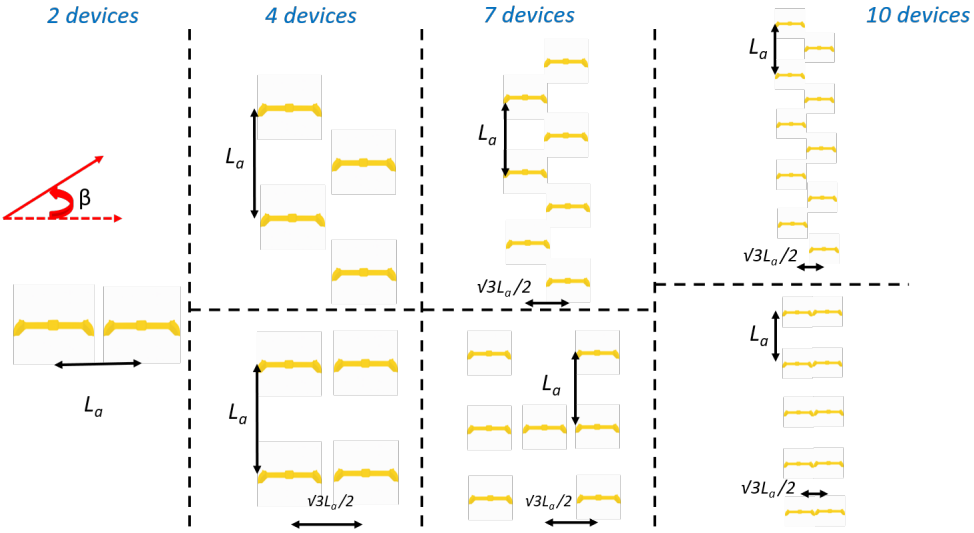



Figure 4.9.: Attenuator configurations

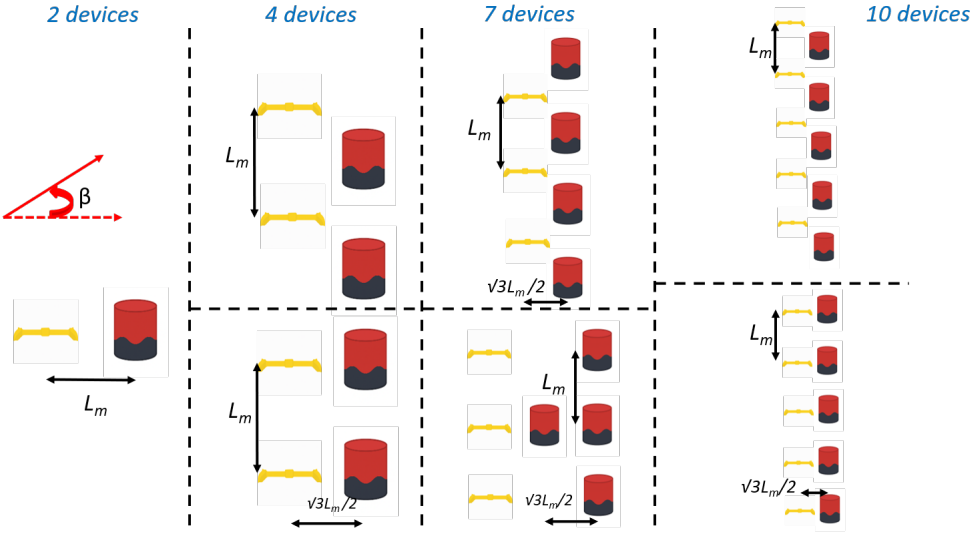



Figure 4.10.: Mixed configurations

direction-dependent excitation and radiation characteristics. In contrast, the single PA is axisymmetric in heave and is therefore directionally insensitive in isolation; however, in arrays, multi-body interactions still introduce direction-dependent power patterns. Mixed arrays combine these characteristics, with directional behaviour influenced both by the attenuator's orientation dependence and the PA's symmetry, leading to more asymmetric and, in some cases, more constructive interaction patterns than the mono-device farms.

The 2-device case provides the simplest interaction baseline and is useful for interpreting pairwise constructive and destructive interference. The 4-device arrays

extend this to first-order grid and staggered motifs, enabling cross-row interactions. The 7-device arrays represent an intermediate scale: the staggered layout forms a compact cluster around a central device, while the rectangular layout follows a denser multi-row pattern, capturing the transition from small to mid-scale farms. The 10-device arrays create elongated multi-row structures, where longer-range diffraction and radiation effects become more pronounced. Using consistent patterns across PA, attenuator, and mixed arrays allows direct comparison between device types and layouts, highlighting how geometry and orientation influence farm-level performance.

Considering all variations, a total of 3 (number of device counts) ×4 (number of spacings) ×12 (incident directions) ×2 (layouts) +4 × 12 (for the 2-device case) results in 336 cases per array type. Therefore, across the PA, attenuator, and mixed arrays, a total of 1008 cases are analysed.

## 4.5. HYDRODYNAMIC MODEL IMPLEMENTED FOR ARRAYS WITH PASSIVE CONTROL AND NO CONSTRAINTS



The weakly non-linear frequency-domain model developed for individual devices is extended to account for hydrodynamic interactions within wave farms. The multi-body equation of motion for a farm consisting of $m$ PA devices and $n$ attenuator devices at frequency $\omega_i$ is given by:

$$\left[-\omega_i^2\left(\mathbf{M}_{arr,d}+\mathbf{M}_{arr,a}(\omega_i)\right)+i\omega_i\left(\mathbf{B}_{arr,a}(\omega_i)+\mathbf{B}_{arr,\mathrm{PTO}}(\omega_i)+\mathbf{B}_{arr,v}\right)+\mathbf{C}_h\right]\boldsymbol{\zeta}_{arr}(\omega_i) = \mathbf{F}_{arr,e}(\omega_i), \tag{4.5}$$

where each term is now a matrix or vector describing the hydrodynamics of all devices in the array:

- $\mathbf{M}_{arr,d} \in \mathbb{R}^{(m+4n)\times(m+4n)}$ is the global structural mass matrix assembled by placing single-device mass matrices along the diagonal,
- $\mathbf{M}_{arr,a}(\omega_i) \in \mathbb{R}^{(m+4n)\times(m+4n)}$ is the fully populated added-mass matrix,
- $\mathbf{B}_{arr,a}(\omega_i) \in \mathbb{R}^{(m+4n)\times(m+4n)}$ is the fully populated radiation-damping matrix,
- $\mathbf{B}_{arr,\mathrm{PTO}}(\omega_i) \in \mathbb{R}^{(m+4n)\times(m+4n)}$ is the PTO-damping matrix,
- $\mathbf{B}_{arr,v} \in \mathbb{R}^{(m+4n)\times(m+4n)}$ is the diagonal linearised viscous-damping matrix,
- $\mathbf{C}_{arr,h} \in \mathbb{R}^{(m+4n)\times(m+4n)}$ is the global hydrostatic stiffness matrix assembled from single-device stiffness matrices along the diagonal,
- $\mathbf{F}_{arr,e}(\omega_i) \in \mathbb{R}^{(m+4n)\times 1}$ is the excitation force/moment vector,
- $\boldsymbol{\zeta}_{arr}(\omega_i) \in \mathbb{R}^{(m+4n)\times 1}$ is the response-amplitude (RAO) vector for all devices.

For an incident wave amplitude of 1 m, $\boldsymbol{\zeta}_{arr}(\omega_i)$ corresponds to the array RAO vector.

The PTO matrix $\mathbf{B}_{arr,\mathrm{PTO}}$ is constructed by placing the single-device PTO matrices along the diagonal of the global system. The PTO coefficients obtained from the single-device optimisation are directly applied in the array without re-optimising for inter-device interactions. This sub-optimal approach is adopted due to the increased complexity associated with multiple DOFs per attenuator device.

Viscous effects are incorporated following the same procedure used in the shallow-water array analysis.

For regular waves, the absorbed power of the array at frequency $\omega_i$ is computed as:

$$P_{\mathrm{arr}}(\omega_i) = \frac{1}{2}\eta\,\omega_i^2\,\boldsymbol{\zeta}^*(\omega_i)\,\mathbf{B}_{arr,\mathrm{PTO}}(\omega_i)\,\boldsymbol{\zeta}(\omega_i), \tag{4.6}$$

where * denotes the complex conjugate.

For irregular waves, the total absorbed power is obtained by spectral integration:

$$P_{\text{arr,irr}} = \int_0^\infty 2\,P_{arr}(\omega)\,S(\omega)\,d\omega, \tag{4.7}$$

where $P_{arr}(\omega)$ is the regular-wave array power and $S(\omega)$ is the wave spectral density.

## 4.6. RESULTS AND DISCUSSION

The same performance metrics, the $q$-factor and $M$-factor, are used to compare mono and mixed arrays and to identify the best-performing mixed-array configurations. This section explains the results from single devices to the array in terms of power production and the comparison metrics $q$-factor and $M$-factor.



### POWER ABSORPTION FROM THE SINGLE DEVICES

#### PA

Figure 4.11 shows the variation of the power absorbed by a single PA across a wide range of wave periods in both regular and irregular waves. For regular waves, the PTO coefficient was optimised per frequency following [139], whereas for irregular waves it was optimised per sea state, as described in the previous section. The PA exhibits a broadband response, with peak power absorption around 10 s and significant absorption over the period range from approximately 3 to 20 s.

Considering irregular waves, the absorbed power is lower overall, as the optimisation is performed over the full wave spectrum for each sea state. Additionally, viscous damping represented in the spectral domain becomes more dominant than the Lorentz linearisation–based damping used in regular-wave optimisation, further reducing the achievable power levels.

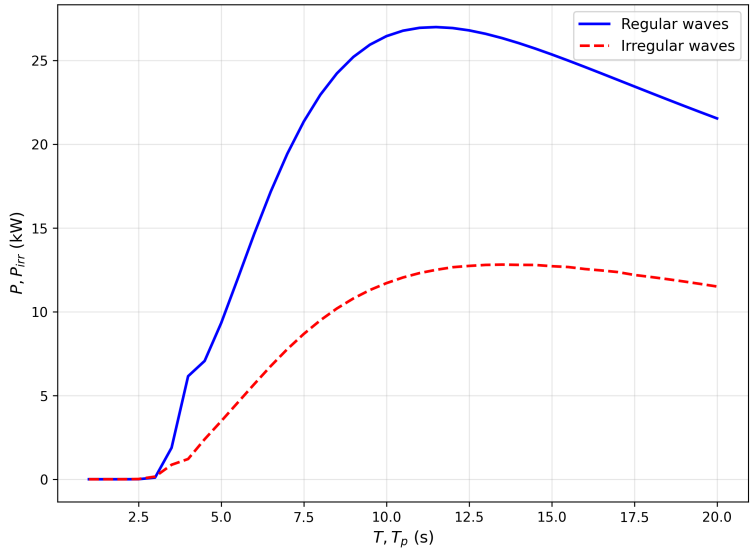



Figure 4.11.: Comparing power obtained in regular and irregular waves for the PA

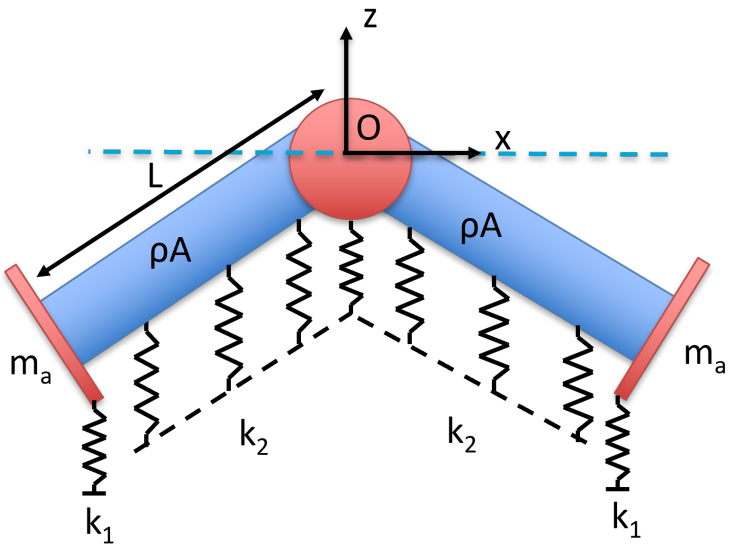



Figure 4.12.: Simplified modelling for obtaining the mass and stiffness matrices

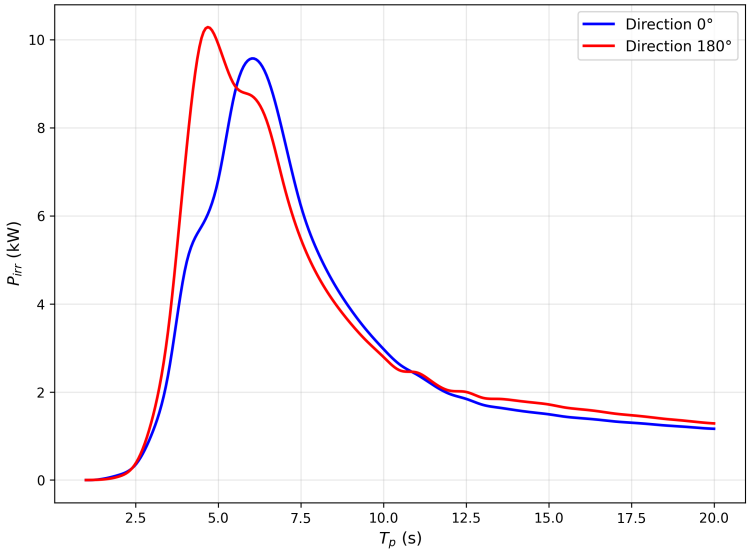



Figure 4.13.: Direction power absorbed by the attenuator in 0 and 180 °

### ATTENUATOR

In order to obtain the mass and stiffness matrices of the 4-DOF attenuator device, the Euler–Lagrange formulation was employed [154]. The full derivation is provided in Appendix C. For the purposes of this derivation, the attenuator was modelled in a simplified form, as shown in Figure 4.12, with two point masses at the ends of the device and distributed masses representing the arms. Hydrostatic stiffness, was modelled using point springs for the end masses and distributed springs along the arms.

While this simplified approach captures the global dynamic behaviour well, minor directional discrepancies arise. Consequently, when comparing the power absorbed in irregular waves at 0° and 180° (see Figure 4.13), slight differences are observed near the peak, even though the response would ideally be symmetric. At 0°, peak power occurs near the natural frequency of the heave DOF, whereas at 180° it aligns more closely with the surge natural frequency. These differences stem from the approximate estimation of the mass and stiffness matrices, DOF coupling, and the asymmetric contribution of the rear-arm pitch motion.

Despite this limitation, the overall absorbed power and its variation with period remain very similar between the two directions. Therefore, the results obtained for both single-device and array analyses remain reliable. For conservatism in the array analysis, the power corresponding to 180° incidence was used, as it yields slightly higher single-device power and therefore leads to lower (more conservative) estimates of the $q$- and $M$-factors.



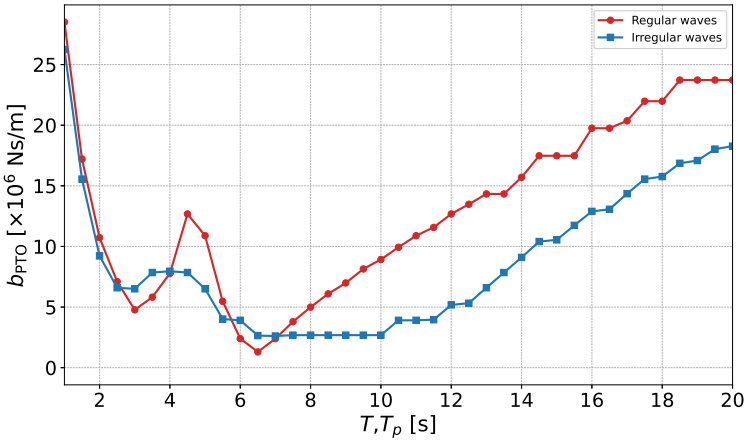



Figure 4.14.: $B_{PTO}$ for peak power vs $T, T_p$

To determine the PTO damping coefficient $b_{PTO}$ corresponding to peak power absorption, a brute-force optimisation was performed by varying $b_{PTO}$ and identifying the value that maximised absorbed power. Unlike the PA, which operates in a single DOF, this approach was chosen for the attenuator due to its 4-DOF dynamics and the dependence of the PTO on relative rotational motion between the two arms. The resulting variation of $b_{PTO}$ with wave period is shown in Figure 4.14. An example of the brute-force optimisation in irregular waves for $T_p = 7.5$ s and $H_s = 1.5$ m is shown in Figure 4.16.

The optimisation performed in irregular waves shifts the optimal PTO coefficient to lower values compared to regular waves, reflecting the spectral normalisation inherent to broadband excitation. This shift also explains why the absorbed power in irregular waves is generally lower than that in regular waves (see Figure 4.15).

Following the analysis of the single devices, we now move on to array analysis.

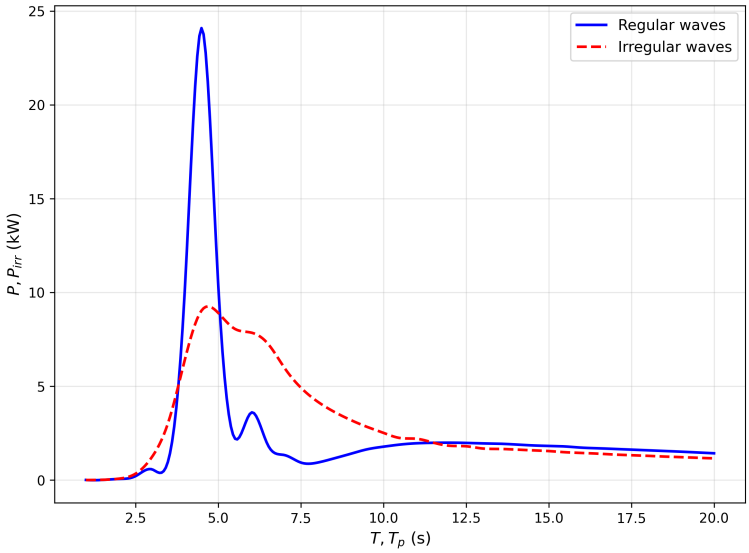



Figure 4.15.: Comparing power obtained in regular and irregular waves for the attenuator

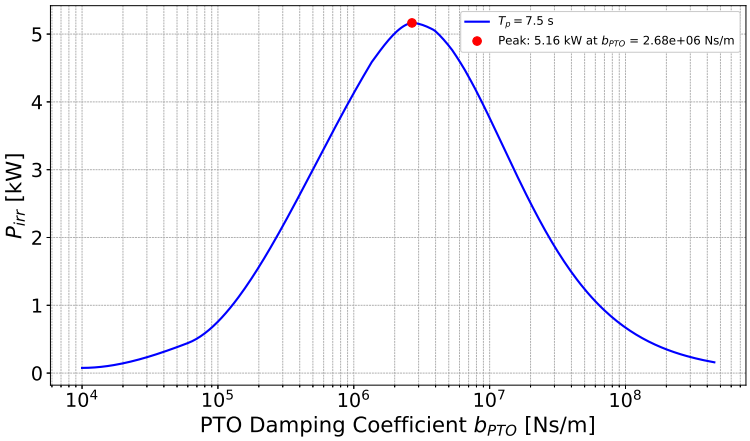



Figure 4.16.: Brute force optimization for $T_p$ = 7.5 s and $H_s$ = 1.5 m

### A GLOBAL VIEW OF THE ARRAY Q-FACTORS AND M-FACTORS

Only the results for irregular waves with passive control are shown here. The rest can be found in Appendix E for brevity.

Figure E.1 presents the variation of mean $q$-factors, averaged over the 5–15 s period range, for all mono and mixed array configurations under regular waves and passive control. Although this period range originates from the scatter diagram for irregular sea states, it is used here as a reference to assess array behaviour across the relevant operational bandwidth. Passive PTO damping values are taken from the frequency-by-frequency optimisation performed for the corresponding single devices.

The mono PA arrays, consisting of cylindrical, omni-directional devices constrained to heave motion, exhibit stable but mildly destructive behaviour, with $q$ typically between 0.90 and 0.97. This reflects the broadband absorption characteristics observed at the single-device level. In contrast, the mono attenuator arrays achieve substantially higher peak values (up to $q = 1.38$), owing to their multi-DOF operation (surge, heave, pitch, and flex), but their performance remains strongly directional. As a result, constructive behaviour is observed for some headings, while other directions remain destructive.

The mixed arrays successfully combine these characteristics. They retain the high constructive potential of the attenuators (reaching $q \approx 1.14$) while the presence of omni-directional PAs raises the lower bound of performance, bringing it closer to that of the mono PA arrays. This demonstrates the stabilising influence of PAs within mixed farms.



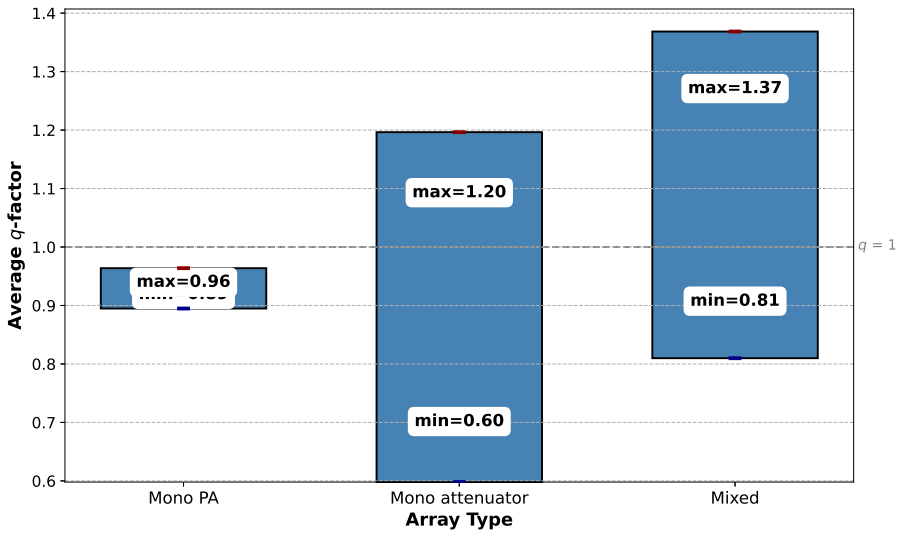



Figure 4.17.: Overall comparison of mono and mixed arrays consider mean q-factors under regular waves and passive control

In irregular waves (see Figure 4.17), PTO damping optimised per sea state is applied uniformly across all devices in the array. Under these conditions, array performance is strongly influenced by device bandwidth and directionality. Mono PA arrays remain consistently destructive ($q < 0.96$), while mono attenuator arrays display large variability ($q \in [0.60, 1.20]$), reflecting their sensitivity to spectral alignment and wave direction. The mixed arrays again emerge as the most robust configuration, reaching $q_{max} = 1.37$ and mitigating the deep destructive troughs observed in the pure attenuator arrays by combining broadband and directional response characteristics.

When looking at the $M$-factor in regular (see Figure E.3) and irregular waves (see Figure 4.19), mixed arrays generally show an $M$-factor greater than 1 indicating a higher

capture width ratio than the mono array. These are generally reaching as high as 30% more weighted capture width efficiency than the mono-arrays.

### 4.6.1. COMPARING MONO AND MIXED ARRAYS - DIRECTIONAL VARIATION

Only the results for irregular waves with passive control are shown here. The rest can be found in Appendix E for brevity.

As shown in Figure E.2, mono PA arrays exhibit an almost directionally invariant response, consistent with their omni-directional absorption characteristics. In contrast, mono attenuator arrays display pronounced directional dependence. Notably, higher $q$-factors are obtained for oblique wave incidence compared to head-on conditions, suggesting that constructive interactions between radiated and reflected wave fields are enhanced at these angles. The engagement of multiple DOFs further enables efficient excitation of flexural motion through multi-mode coupling.



Mixed arrays inherit features from both device types. The omni-directional response of the PA moderates extreme directional sensitivity, while the attenuator contributes periods of enhanced constructive behaviour. As a result, mixed arrays generally achieve $q$-factors that lie between those of the mono PA and mono attenuator arrays, while consistently outperforming the mono PA configuration.

The corresponding $M$-factor results (see Figure E.3) indicate that mixed arrays predominantly achieve $M > 1$, demonstrating superior efficiency when both absorbed power and device dimensions are considered. This trend persists in irregular waves (see Figure 4.19), where the benefits of broadband excitation further enhance mixed-array performance, particularly at oblique angles (30° and 60°), where $M$ reaches values up to approximately 1.3.

The directional behaviour becomes even more pronounced in irregular waves (see Figure 4.18), where the PTO parameters are optimised per sea state. This sea-state-based tuning broadens the effective response of both devices across the 5–15 s range, so the mean performance reflects the integrated interaction of radiated and diffracted wave fields over the spectrum rather than at a single representative period.

Consequently, the mono PA arrays remain largely directionally invariant but consistently destructive across headings, consistent with their omni-directional scattering and the smoothing effect of spectral averaging. In contrast, the mono attenuator arrays retain a clear directional signature: oblique headings tend to yield higher mean $q$-factors, while near-transverse directions (around 90° and 270°) remain comparatively weaker due to less effective excitation of the hinge-driven multi-DOF response.

Mixed arrays combine these characteristics, with the PAs mitigating the deepest directional troughs of the attenuator arrays and improving robustness, while the attenuators still provide periods of constructive interaction at favourable headings.

As a result, the mixed farms achieve mean $q$-factors that are closer to (and often exceed) unity over a larger set of headings than either mono configuration, indicating more reliable interaction gains under realistic broadband excitation. The corresponding $M$-factor trends (see Figure 4.19) reinforce this conclusion: mixed arrays predominantly yield $M > 1$ across directions, with the strongest efficiency gains occurring at oblique angles (e.g. 30°–60°) where geometry-normalised performance can approach $M \approx 1.3$.

### 4.6.2. VARIATION WITH THE NUMBER OF DEVICES

This section compares how the mean $q$-factor (averaged over $T = 5$–15 s) evolves as the farm size increases ($N_t = 2$–10) for the mono PA, mono attenuator, and mixed farms. For the 2-device case, the rectangular and staggered configurations are identical for the purposes of the results. For brevity, where typical trends exist over a number of spacings, only results for some spacings are shown.

Only the results for irregular waves with passive control are shown here. The rest can be found in Appendix E for brevity.

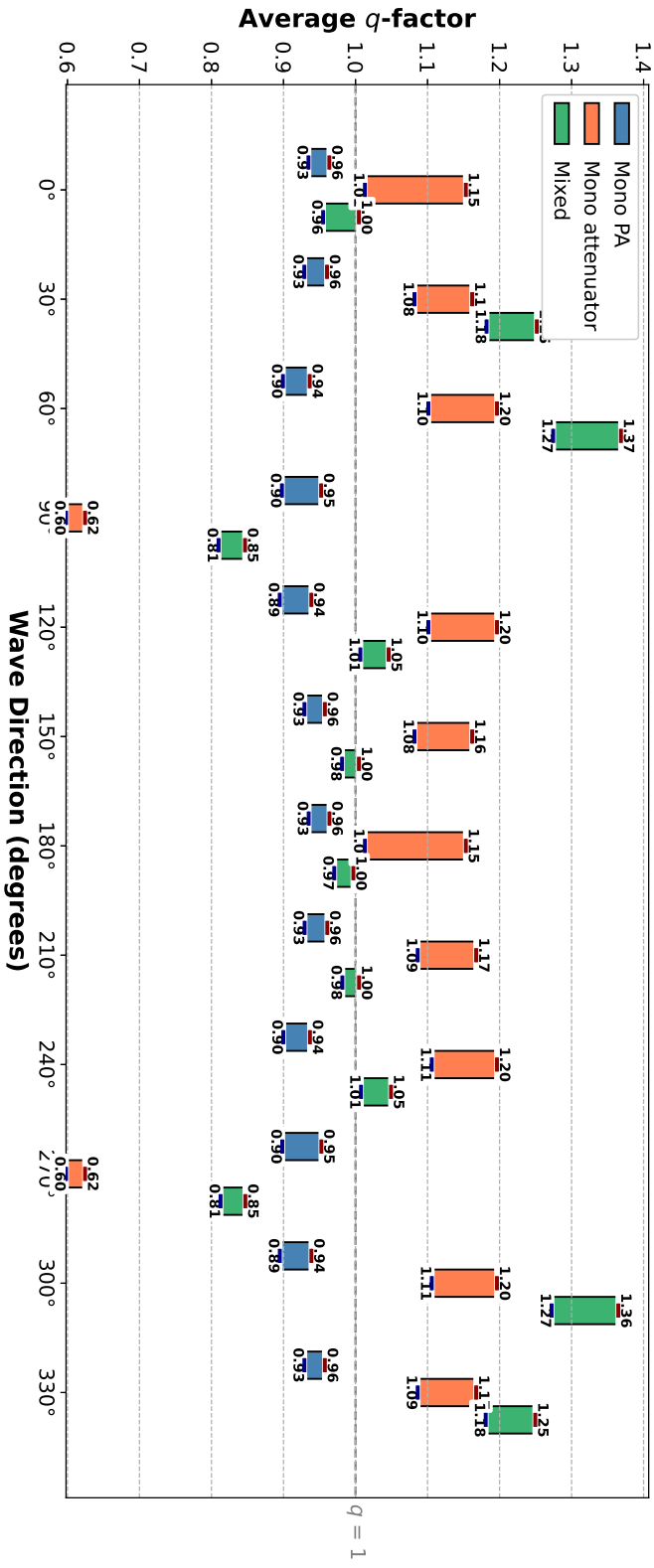



Figure 4.18.: Directional comparison of mono and mixed arrays considering mean q-factors under irregular waves and passive control

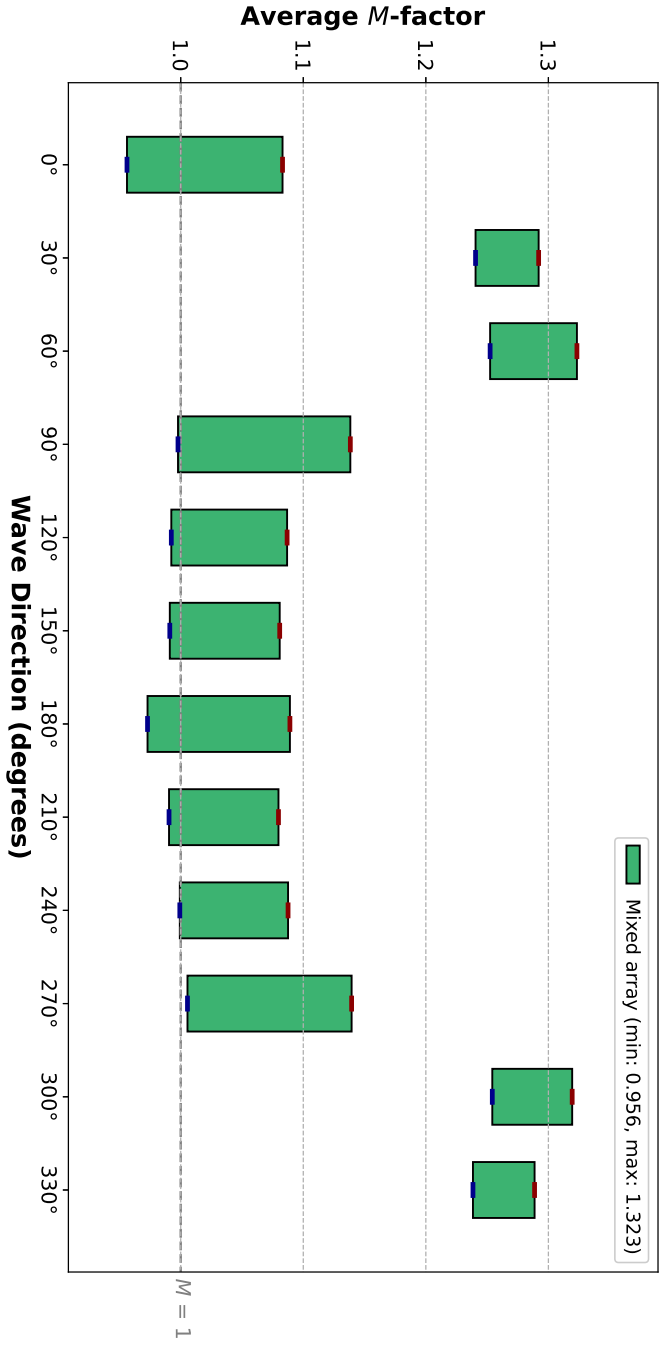



Figure 4.19.: Directional variation of the mean M-factor for mixed arrays in irregular waves

#### REGULAR WAVES: PASSIVE CONTROL

**PA arrays.** In regular waves, across spacings from 4$D$ to 10$D$, the cylindrical PA arrays exhibit mean $q$-factors in a narrow band slightly below unity (typically $q \approx 0.93$–$0.97$), indicating predominantly mild destructive interactions rather than strong array gains (see Figure E.4). Due to the omni-directional scattering of the PAs, the directional spread at a given configuration is small: head-on and following seas (0° and 180°) consistently sit at the upper end of the band, while oblique and beam headings (around 60°–120° and 240°–300°) are only a few percent lower. Overall, the PA arrays remain directionally robust, with no headings showing sharply different behaviour.

The dependence on the number of devices is similarly gentle. As $N_t$ increases from 2 to 10, most directions show gradual trends rather than abrupt changes: for many oblique headings the mean $q$ decreases monotonically with $N_t$, consistent with a slow strengthening of destructive interference as more radiating bodies are added. In contrast, axial directions such as 0° and 180° often display a shallow U-shaped pattern, with a slight dip at intermediate $N_t$ and a modest recovery for the largest arrays. Even for $N_t = 10$, the total variation relative to the 2-device case is only a few percent, suggesting that in regular waves the PA array effects saturate quickly with size.

Spacing and layout mainly modulate how strongly these weak trends appear. At 4$D$, coupling is strongest and the slope of $q$ versus $N_t$ is slightly steeper for the more destructive headings, particularly in the rectangular layout where alignment promotes more coherent shadowing. As spacing increases to 6$D$, 8$D$, and 10$D$, curves flatten and bunch together, indicating that the devices approach hydrodynamic independence. Staggered configurations systematically show slightly higher $q$ levels and reduced directional spread compared to rectangular ones. Overall, the regular-wave results confirm mild but persistent destructive interactions that depend weakly on both array size and spacing, while remaining broadly omni-directional.

**Attenuator arrays** The 4-DOF attenuator arrays (see Figure E.5) exhibit consistently constructive behaviour under regular waves for a wide range of headings. For all spacings from 4$D$ to 10$D$, mean $q$-factors exceed unity for most incidence angles, particularly between 120° and 330°, where wave excitation aligns favourably with the hinge motion. In these headings, the energy exchange between the bodies and the propagating wave field reinforces the response, producing $q$ in the range 1.30–1.35 with only weak dependence on $N_t$. This indicates strong hydrodynamic coupling and constructive interference typical of attenuator-type WECs in regular waves.

For headings at 0° and 180°, the arrays consistently show $q < 1$, reflecting less favourable excitation and slightly destructive interactions when waves propagate head on. Even in this sector, trends with $N_t$ remain smooth and relatively flat, implying that while destructive interference persists, it is not strongly sensitive to farm size. The destructive interactions worsen at perpendicular angles of 90 and 270° leading to the least performance which is expected, since that is the least favourable direction for the attenuator devices.

Overall, attenuator arrays show robust constructive interaction in regular waves driven primarily by geometry and hinge dynamics, with only moderate sensitivity to spacing or device number.

**Mixed arrays** For mixed farms under regular waves and passive control (see Figure E.6), the mean $q$-factor are seen to be destructive or constructive depending on the direction. The magnitude of the directional variability is smaller than in the mono attenuator arrays, suggesting that mixing device types slightly disrupts the coherence of wave patterns that would otherwise yield stronger constructive or destructive signatures with the mono-attenuators at certain angles. As $N_t$ increases from 2 to 10, only modest shifts in $q$ are observed, with small increases or decreases again directionally dependent.

This combined response reflects the fundamentally different radiation and scattering characteristics of the two devices: attenuators are strongly directional, whereas cylindrical PAs are largely omni-directional. When combined, their interference patterns

overlap coherently, to reduce directional sensitivity but also limits the magnitude of interaction-driven amplification. Relative to the mono arrays, mixed-array behaviour generally lies between the stable-but-destructive PA response and the highly directional yet constructive attenuator response, offering a more moderated directional dependence without pronounced regular-wave synergies under a single-period PTO tuning.

In regular waves, the $M$-factor for mixed arrays (see Figure E.7) shows a clear non-monotonic dependence on $N_t$ across all spacings ($4D$–$10D$) and both layouts. For most directions, $M$ is close to unity for small arrays ($N_t = 2$–$4$), increases to a pronounced maximum around $N_t = 7$ (with $M > 1$ for nearly all directions), and then decreases for $N_t = 10$, indicating an optimal intermediate array size where cooperative effects outweigh additional interference.

#### IRREGULAR WAVES: PASSIVE CONTROL



**PA arrays:** In irregular waves under passive control, the PA arrays show mean $q$-factors that remain consistently below unity across all spacings ($4D$–$10D$), indicating predominantly destructive interactions under broadband excitation (see Figure 4.20). The broader frequency content increases the likelihood of partial cancellations across the spectrum, resulting in mean $q$ typically between 0.90 and 0.96 for all headings and array sizes.

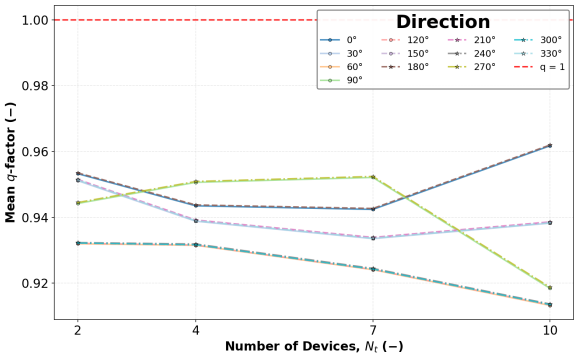
Spacing shows a clear but modest trend: at smaller spacings (e.g. $4D$), stronger coupling yields slightly larger directional spread and more pronounced destructive interference. As spacing increases to $6D$ and $8D$, curves converge; by $10D$, the band becomes narrow, consistent with near-independent behaviour. Staggered layouts remain less direction-sensitive than rectangular ones. With increasing $N_t$, array-aligned headings tend to reduce in $q$ due to cumulative shadowing across the rows, while oblique headings remain comparatively stable; these effects diminish as spacing approaches $10D$.

**Attenuator arrays** For the mono attenuator arrays in irregular waves (see Figure 4.21), a consistently constructive behaviour is observed across all spacings and device counts, with mean $q$-factors distinctly above unity for almost all incident-wave directions (see Figure 4.21). Since the PTO coefficient is optimised per sea state, the attenuator extracts energy effectively over a wider range of spectral components, enabling radiated and diffracted fields to interact more constructively within the array. As $N_t$ increases from 2 to 10, the mean $q$-factor typically remains between 1.05 and 1.20 depending on direction, indicating robust constructive interference under broadband excitation.

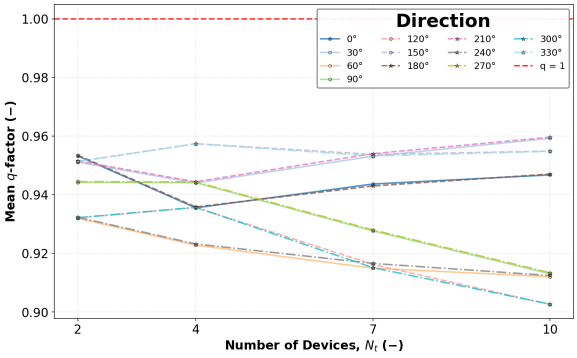
Trends with increasing array size remain smooth and do not show sharp transitions between constructive and destructive regimes. Constructive effects are already established for smaller arrays ($N_t = 2$–$4$), and persist as the array grows, reflecting favourable phasing supported by the multi-DOF response. Directional dependence remains present but modest unless the incident waves hits the array in the perpendicular direction, with oblique headings tending to yield slightly higher $q$ than head-on cases, consistent with more effective utilisation of coupled surge–heave–pitch dynamics under irregular sea states.

**Mixed arrays** In irregular waves, the mixed arrays change markedly compared to the regular-wave case: the mean $q$-factor now remains close to or exceeds unity across more directions and array sizes, indicating stronger constructive interactions under broadband excitation (see Figure 4.22). Peak values occur around oblique headings ($\sim 60°$ and $300°$), where $q$ reaches approximately 1.30–1.35 for all spacings from $4D$ to $10D$. This enhancement is driven by sea-state-based PTO tuning, which allows both device types to respond effectively across contributing spectral components; their distinct radiation patterns and natural periods promote coherence over a broader bandwidth.

Some directions remain weakly destructive, most notably near $90°$ and $270°$ where the attenuator contribution is reduced; even then, $q$ stays close around 0.8 and increases slightly with array size due to the PA contribution. Spacing effects remain limited across

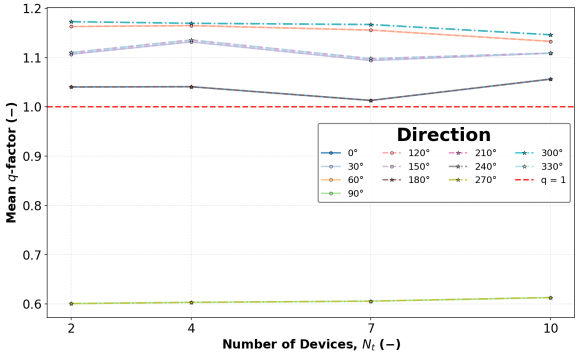



(a) Rectangular configuration

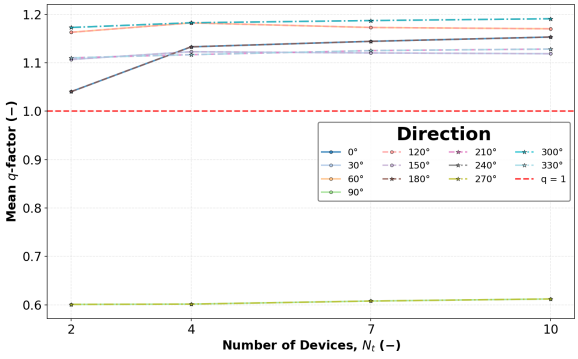



(b) Staggered configuration

Figure 4.20.: Variation of mean $q$-factors (averaged over $T = 5$–$15$ s) with the number of PAs in the farm for spacing $6D$ under irregular waves and passive control

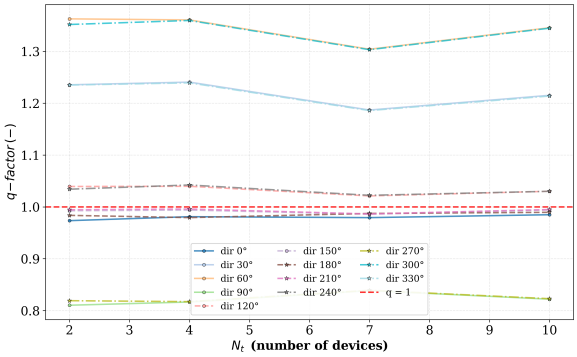



(a) Spacing 6$L$ and rectangular configuration

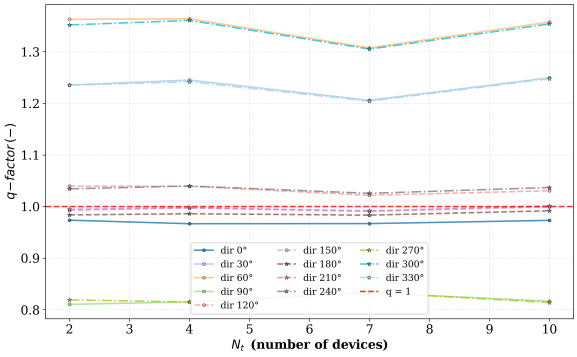



(b) Spacing 6$L$ and staggered configuration

Figure 4.21.: Variation of mean $q$-factors (averaged over $T = 5$–15 s) with the number of attenuators in the farm for spacing 6$L$ under irregular waves and passive control




(a) Spacing 6$D$ and rectangular configuration



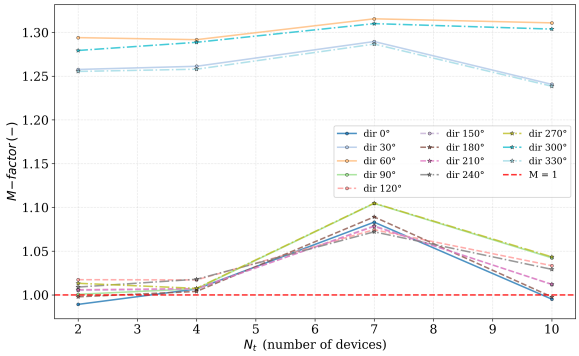

(b) Spacing 6$D$ and staggered configuration

Figure 4.22.: Variation of mean $q$-factors (averaged over $T = 5$–15 s) with the number of WECs in the mixed farm for spacing 6$C$ under irregular waves and passive control

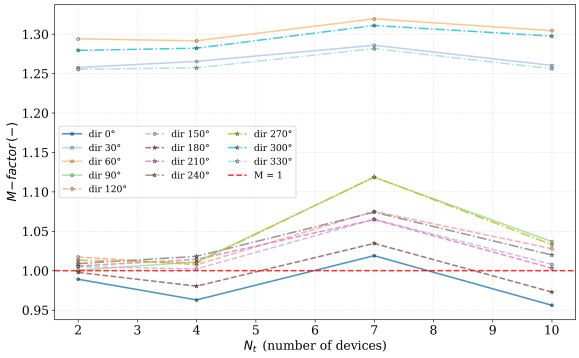
4*D*–10*D*, highlighting reduced sensitivity to geometric tuning in irregular seas. Relative to mono arrays, mixed arrays clearly outperform the mono PA arrays (predominantly destructive) and typically exceed the mono attenuator arrays across headings, indicating a synergistic combination of directional strength and broadband robustness.

In irregular waves, the mixed-array *M*-factor shows a consistent non-monotonic dependence on $N_t$ across spacings and layouts: near unity for $N_t = 2$–4, a maximum around $N_t \approx 7$, and a reduction at $N_t = 10$. This indicates an optimal intermediate size where mixed-device cooperative effects outweigh additional shadowing and partial cancellation under broadband forcing.






(a) Spacing 6*D* and rectangular configuration




(b) Spacing 6*D* and staggered configuration

Figure 4.23.: Variation of mean *M*-factors with the number of devices in the mixed farm for spacing 6*C* under irregular waves and passive control

### 4.6.3. VARIATION WITH SPACING

This section compares how the mean *q*-factor varies with inter-device spacing (4*D*–10*D*) for each farm type, grouped by sea state (regular vs irregular) and then by device composition (mono PA, mono attenuator, mixed). For brevity, where typical trends exist over a number of devices, only some results are shown.

Only the results for irregular waves with passive control are shown here. The rest can be found in Appendix E for brevity.

#### REGULAR WAVES: PASSIVE CONTROL

**PA arrays** The mean $q$-factor for mono PA arrays (see Figure E.8) shows weak sensitivity to spacing across all array sizes ($N_t = 2$–$10$). Increasing spacing from $4D$ to $10D$ produces only modest changes, with values remaining below unity, indicating that destructive interactions persist and are not fully alleviated by separation alone. For smaller arrays ($N_t = 2$ and 4), the variation is minimal; for larger arrays ($N_t = 7$ and 10), slight improvements may appear at intermediate spacings (often $6D$–$8D$), but they remain insufficient to yield constructive behaviour. Overall, increasing spacing alone does not drive PA farms into a consistently constructive regime under regular waves.

**Attenuator arrays** Under regular waves, mono attenuator arrays remain strongly direction-dependent across all spacings, reflecting the inherently directional response of the elongated multi-body device. Several directions consistently yield $q > 1$ (constructive interactions), while other headings remain destructive (see Figure E.9). With increasing device count, directional contrasts can become more pronounced, consistent with stronger scattering and radiation as the farm grows. However, across the tested range ($4D$–$10D$), spacing does not fundamentally change the dominant directional behaviour: array performance remains primarily governed by incidence direction and narrow-band tuning under regular-wave excitation.



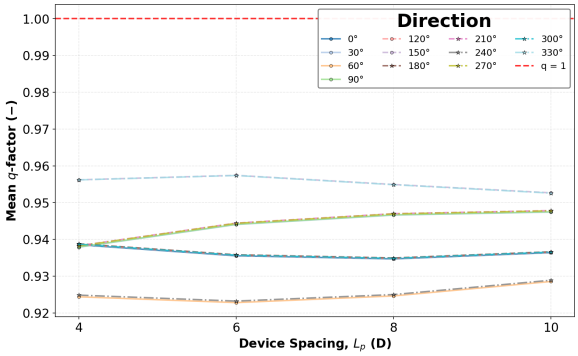
**Mixed arrays** For mixed arrays in regular waves, the dependence of mean $q$ on spacing ($4D$–$10D$) is generally smooth and weak across directions and array sizes (see Figure E.10). Compared to mono arrays, mixed farms do not exhibit sharp oscillatory trends with spacing, indicating that the presence of two device types mitigates strong near-field coherence. For several headings, slightly higher $q$ values appear at intermediate spacings ($6D$–$8D$), consistent with a balance between stronger coupling at small spacing and reduced interaction at wide spacing; however, these differences remain modest. Overall, mixed-array performance remains relatively robust to spacing in regular waves, but does not display pronounced constructive gains under passive, single-period tuning.

In regular waves, the mixed-array $M$-factor (see Figure E.11) remains close to unity across spacings and array sizes, with only modest deviations (slightly higher values often at intermediate spacings and larger arrays), indicating near-neutral geometry-normalized performance.

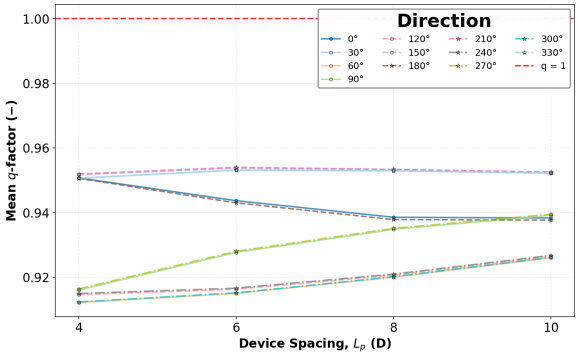
#### IRREGULAR WAVES: PASSIVE CONTROL

**PA arrays** For mono PA farms in irregular waves (see Figure 4.24), mean $q$ varies smoothly with increasing $q$-factors as the spacing increases. While the variation is small, the spacing of $10D$ provides the highest $q$-factors across multiple directions. Spacing sensitivity increases slightly with $N_t$, particularly for some oblique headings, but variations remain small, reinforcing that broadband averaging smooths stronger interaction signatures.

**Attenuator arrays** In irregular waves, mono attenuator arrays remain directionally dependent but exhibit smoother behaviour than in regular waves due to sea-state-based PTO tuning and a broader effective absorption bandwidth (see Figure 4.25). Several headings yield $q > 1$ across the investigated spacings, while less favourable headings remain closer to unity. Across $4D$–$10D$, spacing sensitivity is generally weak: interactions appear dominated more by directional excitation than by near-field spacing effects. Increasing device count does not systematically improve performance and can mildly reduce $q$ for some headings, consistent with persistent partial cancellations as the array grows.

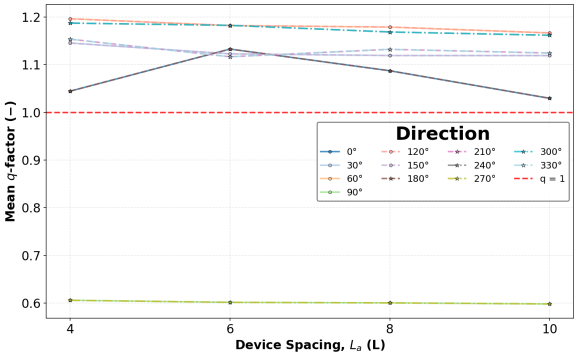



(a) 4 WEC array and staggered configuration

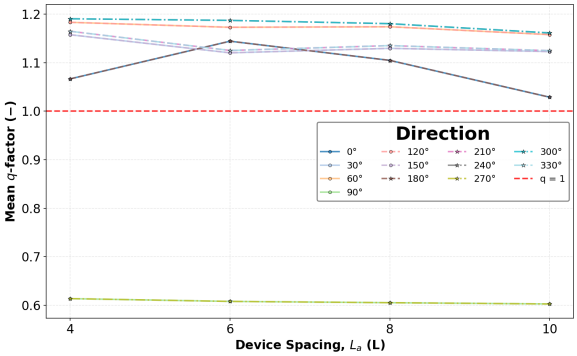



(b) 7 WEC array and staggered configuration

Figure 4.24.: Variation of mean $q$-factors (averaged over $T = 5$–$15$ s) with spacing for mono PA farms under irregular waves and passive control

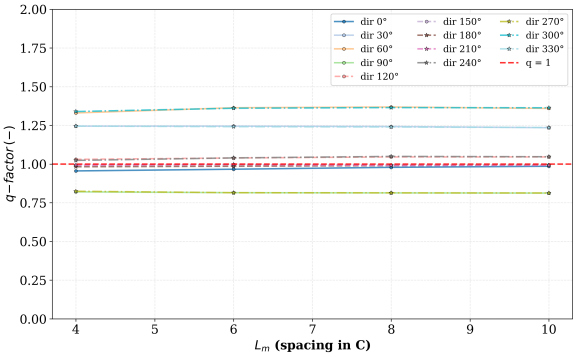



(a) 4 WEC array and staggered configuration

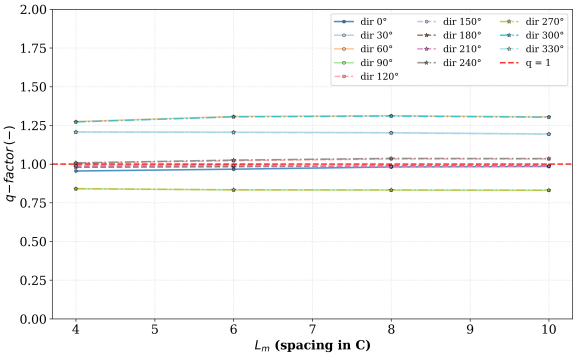



(b) 7 WEC array and staggered configuration

Figure 4.25.: Variation of mean $q$-factors (averaged over $T = 5$–$15$ s) with spacing for mono attenuator farms under irregular waves and passive control




(a) 4 WEC array and staggered configuration




(b) 7 WEC array and staggered configuration

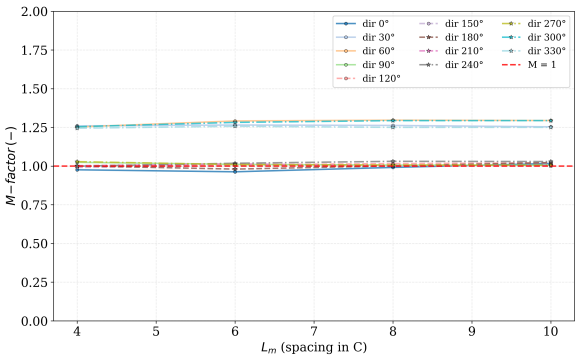
Figure 4.26.: Variation of mean $q$-factors (averaged over $T = 5$–$15$ s) with spacing for mixed farms under irregular waves and passive control

**Mixed arrays** For mixed arrays in irregular waves (see Figure 4.26), the average $q$-factor shows weak dependence on spacing across all array sizes and configurations. A mild increase in $q$ is often observed from tighter spacings ($4D$–$6D$) toward intermediate spacings (around $8D$), followed by a plateau toward $10D$, consistent with broadband averaging suppressing strong spacing-induced resonant effects. Directional spreading in irregular seas also reduces the spread across headings relative to regular-wave conditions. Overall, mixed arrays remain robust to spacing changes, offering layout flexibility without significant penalties.

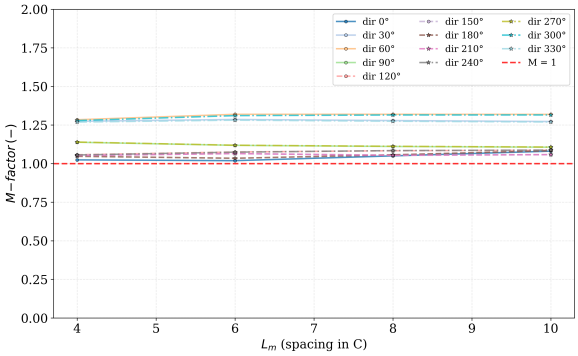
Compared to mono-device arrays under the same irregular-wave conditions, mixed arrays consistently demonstrate equal or slightly improved $q$-factor levels across the full spacing range. This improvement arises from complementary radiation and diffraction characteristics without introducing strong spacing sensitivity, highlighting the resilience of mixed farms in realistic sea states.

In irregular waves, the mixed-array $M$-factor remains consistently above unity across all spacings and array sizes, with only marginal spacing dependence. This indicates a robust geometry-normalized advantage from mixing devices under broadband excitation (see Figure 4.27).






(a) 4 WEC array and staggered configuration




(b) 7 WEC array and staggered configuration

Figure 4.27.: Variation of mean $M$-factors with spacing for mixed farms under irregular waves and passive control

### 4.6.4. CHOOSING THE BEST CONFIGURATIONS

Only the results for irregular waves with passive control are shown here. The rest can be found in Appendix E for brevity.

Based on the combined assessment of the $q$-factor and $M$-factor, the best-performing mixed array configurations are identified using both the number of directions for which the metrics exceed unity and their average values. The $q$-factor provides insight into the overall hydrodynamic interaction effects relative to isolated devices, while the $M$-factor additionally accounts for differences in device dimensions, enabling a fair comparison between mixed and mono arrays.

For regular waves (see Figure E.12), several configurations exhibit $q > 1$ and $M > 1$ across all considered directions. Among these, the mixed array consisting of 5 attenuators and 5 point absorbers in a staggered configuration stands out, as it achieves one of the highest average $q$-factors while simultaneously yielding the highest average $M$-factor. This indicates that the configuration not only benefits from constructive hydrodynamic interactions but also performs favourably when normalized for device size.

In irregular waves (see Figure 4.28), the performance trends are more clustered, with multiple configurations displaying comparable average $q$- and $M$-factors and maintaining $q > 1$ and $M > 1$ over a large number of directions. While the 4 PA + 3 attenuator configuration achieves the highest average $q$-factor, the larger mixed arrays, particularly the 5 PA + 5 attenuator configuration, yield the highest average $M$-factor and maintain robust performance across directions. Given its consistently strong performance under regular waves and its competitive behaviour under irregular conditions, the 5 PA + 5 attenuator mixed array is therefore also selected for detailed investigation in irregular wave conditions.

## 4.7. CONCLUSIONS

The analysis of mixed and mono arrays in deep waters concludes that mixed wave energy farms offer a more robust and stable performance profile compared to mono-device configurations. Mono point absorber (PA) arrays, consisting of omni-directional devices, generally exhibit stable but mildly destructive behaviour, with mean q-factors typically below 0.97 in regular waves and consistently below 0.96 in irregular waves. In contrast, mono attenuator arrays achieve substantially high constructive peaks (up to q = 1.38) in regular waves but are highly directional and prone to large variability, displaying deep destructive troughs (q down to 0.60) in irregular sea states.

The key finding is that mixed arrays successfully combine these characteristics: they leverage the high constructive potential of attenuators (reaching $q_{max}$ up to 1.37 in irregular waves) while the stabilizing influence of the PAs raises the lower bound of performance, effectively mitigating the deepest destructive troughs observed in pure attenuator arrays.

Beyond the raw power absorption quantified by the q-factor, mixed arrays also demonstrated superior overall efficiency as measured by the M-factor, reaching up to 30% more weighted capture width efficiency than mono-arrays. This superior geometry-normalized performance means that mixed arrays predominantly achieved $M > 1$ across tested directions in both regular and irregular waves. Furthermore, the performance of mixed arrays showed a non-monotonic dependence on farm size, indicating that an optimal intermediate array size exists around $N_t \approx 7$, where cooperative effects are maximized before additional interference reduces efficiency for larger farms ($N_t = 10$).

Critically, mixed arrays maintained robust performance with only weak dependence on spacing in irregular waves across the 4D to 10D range, suggesting layout flexibility in realistic sea states. Considering consistency across both metrics and wave conditions, the 5 PA + 5 attenuator mixed array was identified as the best-performing configuration, achieving one of the highest average q-factors and the highest average M-factor in irregular waves.

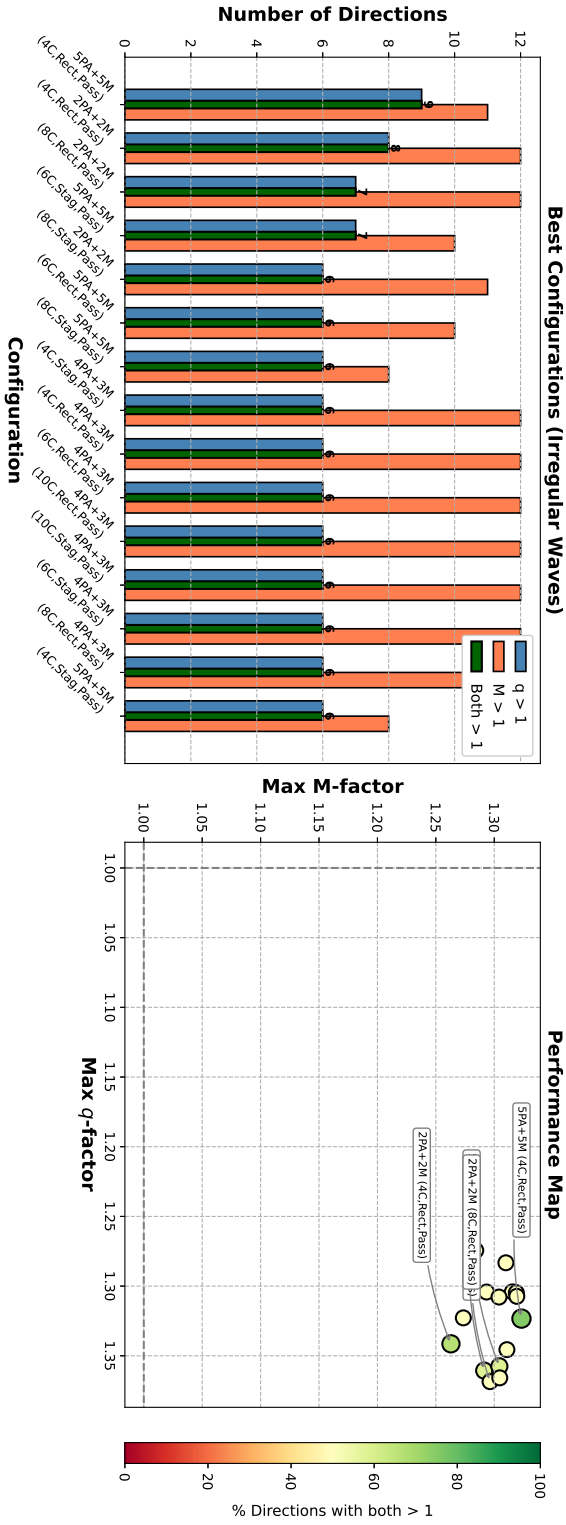



Figure 4.28.: Best performing mixed array configurations - irregular waves

# 5

# COMPARING THE HYDRODYNAMICS OF MIXED AND MONO-ARRAYS

*If you can't explain it simply, you don't understand it well enough*

Albert Einstein

*This chapter goes in depth into the hydrodynamics of mixed arrays in shallow and deep water, and how they compare to mono-arrays of these devices, for the best configurations selected in the previous chapters. The arrays are compared using the q- and M-factors as performance metrics, supported by detailed analyses of array geometry, device degrees of freedom, spacing relative to wavelength, and wave direction. The results demonstrate that mixed arrays exhibit a higher but inherently direction-dependent performance ceiling than mono-arrays, arising from complementary activation of device DOFs and geometry-driven hydrodynamic coupling. Selective representative cases are examined in detail to elucidate the underlying interaction mechanisms, using wave-field visualisation and device-level responses to distinguish between constructive and destructive interference regimes in both shallow and deep-water conditions.*

## 5.1. SHALLOW WATER - ANALYSIS IN REGULAR WAVES

This section provides further insights into the 10 device staggered configuration (5 large PAs + 5 flaps) with 10*C* spacing in regular waves and 4*C* spacing in irregular waves and how it behaves with respect to the mono PA and flap arrays. For brevity, the array natural frequencies and eigen vectors are only shown for the 10*C* spacing, since this is the best configuration considering regular waves.

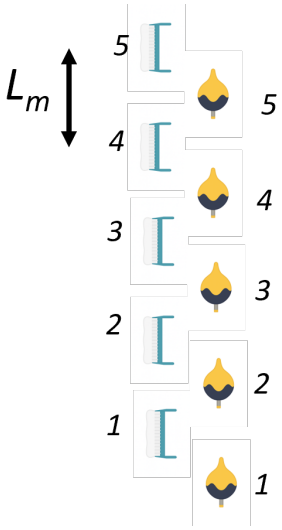



Figure 5.1.: 10 device mixed array with 5 large PAs and 5 flaps - Best configuration considering regular waves

The best configuration under regular waves is the 10 device array with 5 large PAs and 5 flaps (spacing of $L_m$ = 10 $C$ where $C$ = 15 m) with active control, shown in Figure 5.1. When considering both $q$ and $M$-factor, this configuration gave a $q$-factor >1 for 2 directions and $M$-factor > 1 for 10 directions showing its higher capture width efficiency across a range of directions.

### ARRAY NATURAL FREQUENCIES AND EIGEN VECTORS - UNDAMPED AND DAMPED

Knowing the natural frequencies of WEC arrays is essential for optimizing energy capture and informing control system design. When a WEC operates near resonance—where the incident wave frequency aligns with the device's natural frequency—power extraction is maximized. In arrays, hydrodynamic coupling through radiated and scattered waves shifts these natural frequencies from their isolated-device values, creating a set of coupled eigenmodes that depend on array layout, device spacing, and water depth. Accurate knowledge of these frequencies enables tuning of control strategies particularly active control to artificially match the dominant wave periods at a given site, guides array configuration decisions to achieve beneficial frequency broadbanding or avoid problematic resonance clustering, and identifies conditions where excessive motions could compromise structural integrity or mooring systems. For the purposes of this chapter, it also helps explain the behavior of the array, the coupling between devices and how the control strategy is influenced at these frequencies.

In order to obtain the undamped natural frequencies of the array and the corresponding eigen vectors, the eigen value problem is solved as:

$$\mathbf{C}_h\hat{\phi} = \lambda(\mathbf{M}_d + \mathbf{M}_a(\omega_i))\hat{\phi} \tag{5.1}$$

The values for which $\lambda = \omega_i^2$ will be the natural frequencies of the system. Since the array has 10 devices, with 1 DOF per device, 10 natural frequencies are expected for this system. The undamped natural frequencies for the mixed array are shown in Figure 5.2 The dots represent the frequencies at which $\lambda = \omega_i^2$. The natural period $T_n = 2\pi/\omega_n$, where $\omega_n$ is the natural frequency.

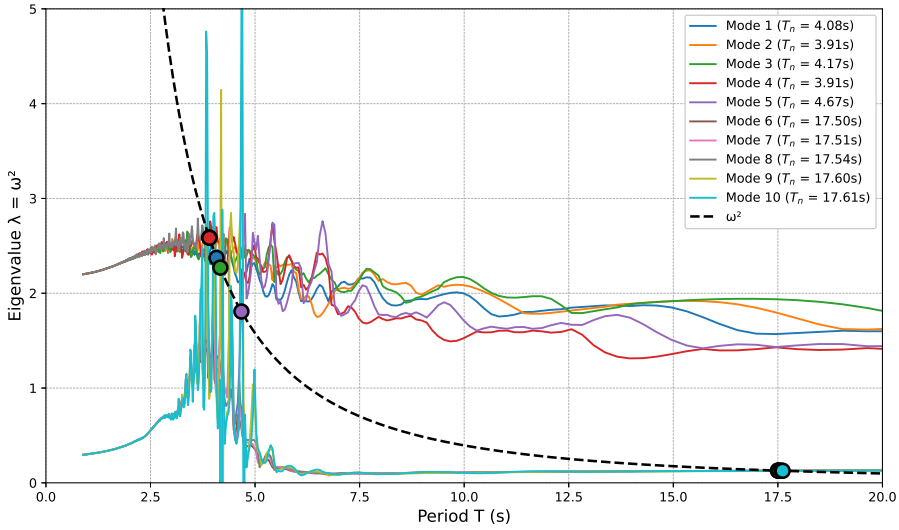



Figure 5.2.: Undamped natural frequency tracking

As seen in the figure, the first 5 modes are dominated by the PAs while the last 5 are dominated by the flaps. Two eigenvectors corresponding to the PA dominated and Flap dominated modes respectively are shown in Figure 5.3a and Figure 5.3b as an example. The first eigenmode at 4.67 s while dominanted by the PAs, also shows their coupling with the flaps arising due to the heave-pitch coupling while the second eigenmode is almost purely dominated by the flaps.

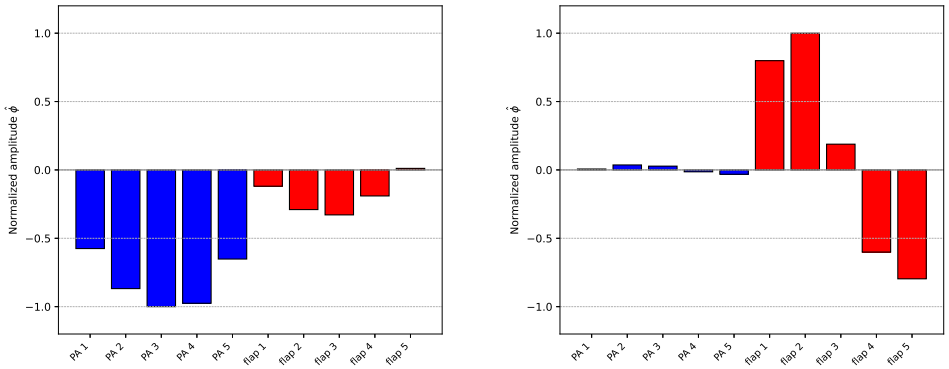
The coupling between the PAs and flaps can be observed clearly in Figure 5.3a, wherein at the natural period of 4.67 s, the hydrodynamic coupling of the added mass matrix introduces motions in the flaps as well.

Considering the same form as the undamped case:

$$[\mathbf{C_h} + i\omega_d \mathbf{B_\alpha}(\omega_i)]\,\hat{\phi} = \omega_d^2\,(\mathbf{M_d} + \mathbf{M_\alpha}(\omega_i))\,\hat{\phi} \tag{5.2}$$

This is a second order nonlinear eigenvalue problem for obtaining $\omega_d$. The solution requires an iterative procedure and is solved as following:

1. Solve the undamped problem to get initial estimate $\omega_d^{(0)} = \omega_n$
2. Construct the complex stiffness matrix: $\mathbf{C}^* = \mathbf{C_h} + i\omega_d^{(k)}\mathbf{B_\alpha}(\omega_i)$
3. Solve: $\mathbf{C}^*\phi = \lambda\,(\mathbf{M_d} + \mathbf{M_\alpha}(\omega_i))\,\phi$
4. Extract: $\omega_d^{(k+1)} = \sqrt{|\lambda|}$
5. Repeat until convergence




(a) Eigenmode corresponding to $T_n$ = 4.67 s (b) Eigenmode corresponding to $T_n$ = 17.51 s

Figure 5.3.: Undamped eigenmodes of the mixed array corresponding to selected natural periods

5

The eigenvalue $\lambda$ is complex: $\lambda = \lambda_r + i\lambda_i$
The damped natural frequency is then given as:

$$\omega_d = \sqrt{|\lambda|} = \sqrt{\sqrt{\lambda_r^2 + \lambda_i^2}} \tag{5.3}$$

$$T_d = \frac{2\pi}{\omega_d} \tag{5.4}$$

The damped natural frequencies and their comparison with the undamped frequencies are shown in Figure 5.4. It is observed that the radiation damping has little influence on the natural frequencies with a peak damping ratio for mode 4 of 15%.

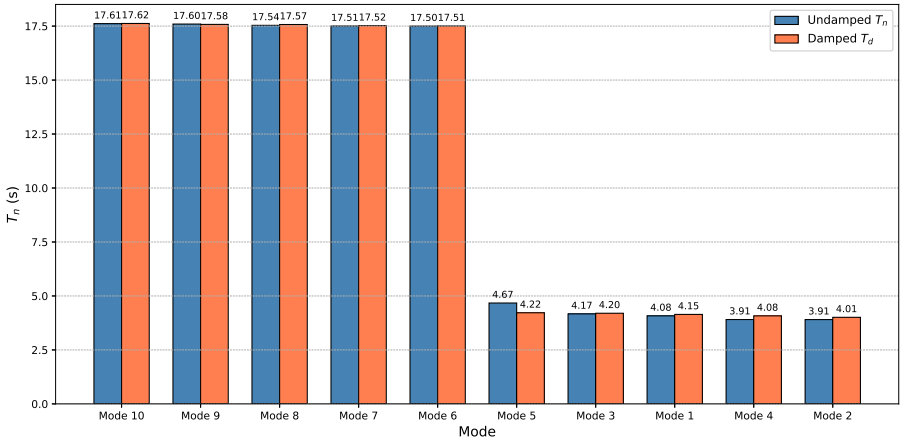



Figure 5.4.: Damped and undamped natural frequencies of the mixed array

Figure 5.5 shows the comparison of the range of natural frequencies of the PAs and flaps as obtained in mono and mixed arrays. The values for the single devices are also shown in dotted lines. Considering the undamped natural periods of both the PA and

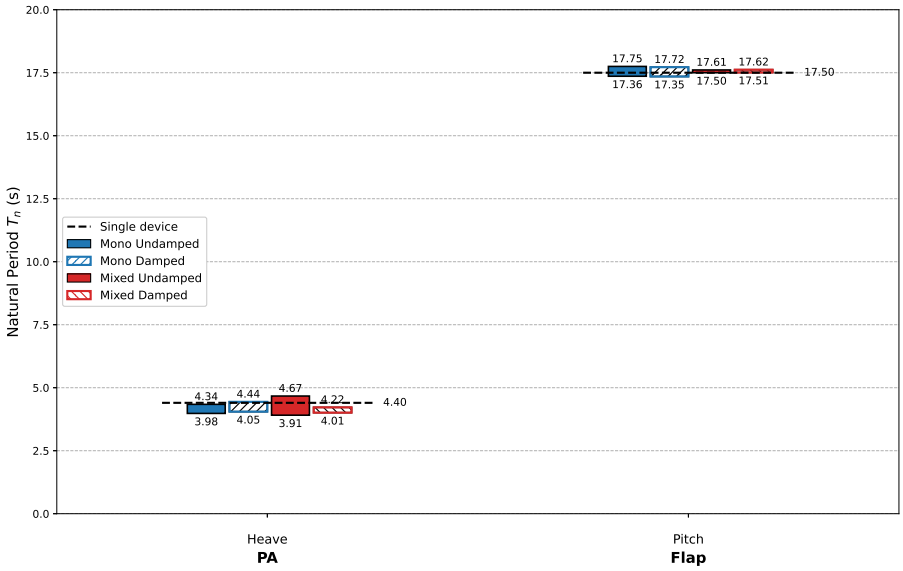



Figure 5.5.: Comparing the range of natural frequencies of PAs and flaps in mixed and mono arrays

flaps, the differences with the single device occur due to the hydrodynamic interactions between these devices in the mixed array. These are stronger for the PA as compared to the flap.

A simple way of understanding this is the added mass coupling strength, which is similar to the statistical correlation coefficient, and provides an estimate of how strong the coupling is. The closer the value is to 1 or greater than 1, the stronger the coupling of the PA-flap as compared to the PA-PA and flap-flap. The coupling strength is defined as:

$$\tilde{CS}_{ij} = \frac{A^{mix}_{PA \leftrightarrow Flap}(i,j)}{\sqrt{\bar{A}^{mix}_{PA} \cdot \bar{A}^{mix}_{Flap}}} \tag{5.5}$$

where $\bar{A}^{mix}_{PA}$ and $\bar{A}^{mix}_{Flap}$ are the mean absolute diagonal elements of the PA-PA and Flap-Flap blocks from the mixed array respectively, and the coupling strength is $\max_{i,j} |\tilde{A}_{ij}|$. This is for both the added mass and radiation damping terms. The coupling strength is a dimensionless diagnostic metric that quantifies the magnitude of hydrodynamic interaction between device types relative to their self-interaction: a value of $CS \approx 0.05$ indicates weak coupling where devices behave nearly independently, while $CS > 1$ indicates strong coupling where the motion of one device type significantly influences the hydrodynamic coefficients of the other. However, the coupling strength does not directly predict whether this interaction is beneficial or detrimental to power capture, as the actual performance impact depends on the sign of the coupling terms, the phase relationships between device motions, and the overall system dynamics—these effects are better captured by the percentage changes in RAO observed between mono-type and mixed arrays. But it can be beneficial to understand the strength of interaction between devices based on the quantity considered.

From Figure 5.6, It is observed that the coupling strength at 17.6 s which is closer to the flap's natural period is almost negligible (0.03) as compared to 4.7 s, where the coupling strength is more than 10 times higher at 0.39.

The difference in natural period spread between undamped and damped conditions

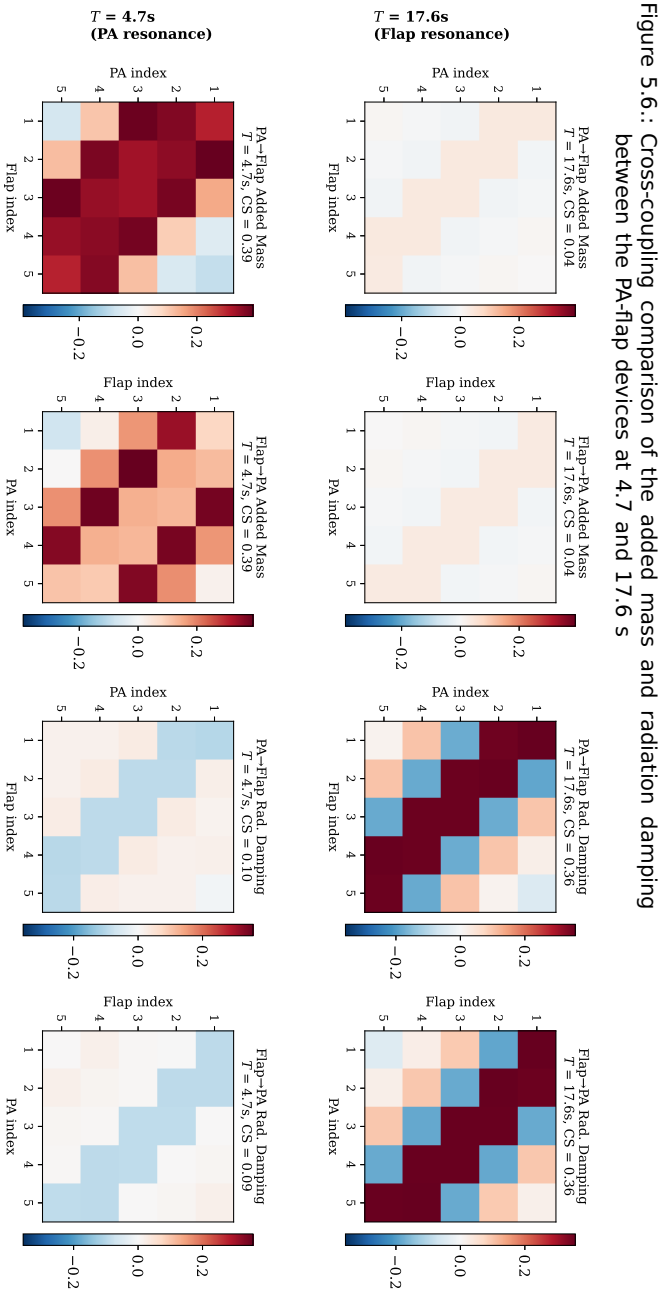



Figure 5.6.: Cross-coupling comparison of the added mass and radiation damping between the PA-flap devices at 4.7 and 17.6 s

can be explained by examining how added mass and radiation damping cross-coupling enter the eigenvalue problem. The characteristic equation for the coupled system is given by $\det\left[-\omega^2(\mathbf{M}_d + \mathbf{M}_a) + i\omega\mathbf{B}_a + \mathbf{C}_h\right] = 0$, where the added mass matrix $\mathbf{M}_a$ is multiplied by $\omega^2$ (real), while the radiation damping matrix $\mathbf{B}_a$ is multiplied by $i\omega$ (imaginary).

Consequently, cross-coupling in the added mass matrix primarily affects the natural frequencies of the coupled modes, whereas cross-coupling in the radiation damping matrix primarily affects the damping ratios without significantly altering the natural frequencies (unless the damping ratios are very high, greater than 20%).

At the $T = 4.7$ s (see Figure 5.6), the added mass cross-coupling is strong (coupling strength = 0.39) while the radiation damping cross-coupling is weak (coupling strength = 0.10). The strong added mass coupling creates distinct effective inertias for each PA mode, resulting in a large undamped period spread of 0.76 s. However, when damping is introduced, the weak radiation damping cross-coupling acts nearly uniformly on all modes, compressing the spread to 0.21 s.

In contrast, at $T = 17.6$ s (see Figure 5.6), the added mass cross-coupling is weak (0.04) while the radiation damping cross-coupling is strong (0.36). The weak added mass coupling results in a small undamped spread of 0.11 s, and despite the strong radiation damping cross-coupling, this spread remains unchanged when damping is included, as the radiation damping coupling affects only the modal damping characteristics rather than the natural frequencies.



### 5.1.1. PERFORMANCE BASED ON Q- AND M-FACTORS

The considered best mixed array in regular waves has mean $q > 1$ in 0 and 180° with the mean $M > 1$ for all directions except 90 and 270°, which is mainly due to the negligible contributions from the flaps in the array. To explain the hydrodynamics of mixed arrays further and how they pan out against the mono arrays, the direction 0° is selected and two periods are chosen, one where the mixed arrays performs the best while another where the mixed array performs the worst compared to the mono arrays. The $q$ for the mono/mixed and $M$-factor for the mixed array are shown in Figure 5.7. The period of 6 and 6.5 s are chosen for further analysis. At 6 s, the $q$ (1.6) and $M$-factor (2.25) for the mixed array are the best when compared to the mono arrays (0.75 for the flap and 0.6 for the large PA), while at 6.5 s, the mixed arrays perform worse than the mono arrays.

To understand this difference in the performance in detail, the hydrodynamic parameters, wave fields and spacing-to-wavelength ratios.

#### COMPARING HYDRODYNAMIC PARAMETERS

Table 5.1 presents the percent changes in key hydrodynamic parameters when comparing devices in the mixed array to their counterparts in the respective mono arrays for the two analysis periods. Table 5.2 summarises the radiation damping cross-coupling characteristics, which exhibit a critical sign reversal between the two periods.

The performance reversal between $T = 6.0$ s and $T = 6.5$ s arises from a combination of reinforcing hydrodynamic mechanisms that either enhance or suppress constructive device interactions.

At $T = 6.0$ s, the mixed array benefits from favorable wave-structure interactions across both device types. The Flap devices experience a mean percentage increase of 34% increase in excitation forces relative to the Flap mono array, driven by beneficial wave scattering from the neighboring PA devices. At the same time, the radiation damping cross-coupling between devices is predominantly positive, with a net contribution of $+6.43 \times 10^6 Ns$ for PA→Flap interactions and a majority of positive matrix elements (32 positive versus 18 negative; see Figure 5.8), indicating that radiated waves reinforce rather than oppose the motion of adjacent devices. The PA devices also exhibit an 11% reduction in added mass in the mixed configuration (see Table 5.1), shifting their dynamic response closer to resonance. Under active control, the associated increase

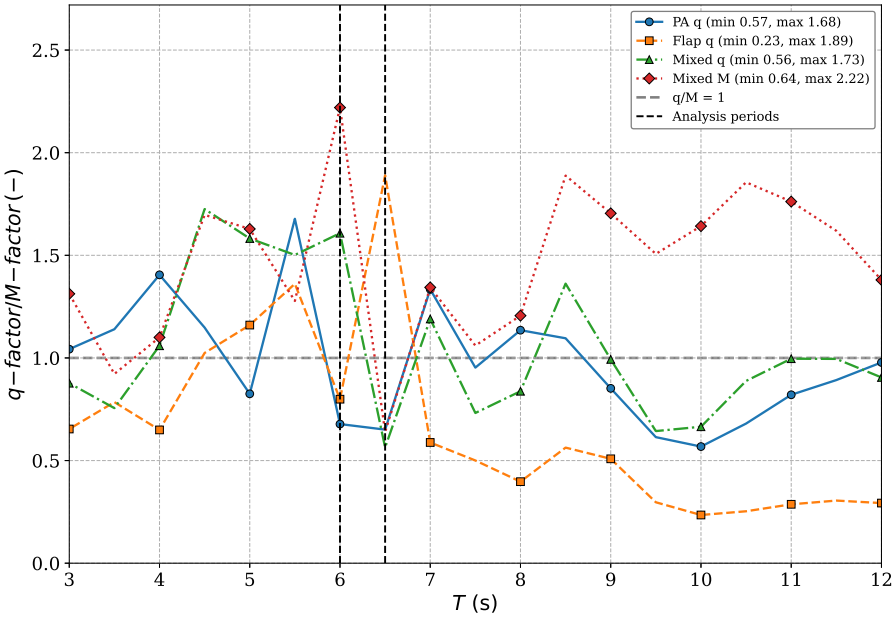



Figure 5.7.: $q$ and $M$-factor for the mono and mixed arrays with two analysis periods of $T = 6$ and 6.5 s

in radiation damping leads to a higher real part of the PTO for both the PA (6.2%) and the Flap (10.9%; see Table 5.1). Collectively, these effects result in a pronounced amplification of the PA response, with a 175% increase in heave RAO, while the Flap pitch RAO remains relatively unchanged (−7%; see Table 5.1).

Table 5.1.: Percent changes in hydrodynamic parameters: Mixed array vs Mono arrays. Positive values indicate an increase in the mixed array; negative values indicate a decrease.

| **Parameter** | $T = 6.0$ s | | $T = 6.5$ s | |
|---|---|---|---|---|
| | PA | Flap | PA | Flap |
| Excitation Force | +2.6% | **+34.1%** | **−23.6%** | **−15.6%** |
| Added Mass (diagonal) | −11.4% | +11.2% | −0.1% | −5.3% |
| Radiation Damping (diagonal) | +5.5% | +17.1% | −10.4% | +5.7% |
| PTO Damping (real part) | +6.2% | +10.9% | +0.0% | −5.3% |
| **RAO** | **+174.9%** | −7.3% | +34.8% | **−55.2%** |

In contrast, at $T = 6.5$ s the hydrodynamic interactions become unfavorable, leading to a marked deterioration in mixed-array performance. Excitation forces are substantially reduced for both device types in the mixed configuration, with decreases of 24% for the PA and 16% for the Flap, indicating adverse wave scattering at this period. Concurrently, the radiation damping cross-coupling switches sign, transitioning from predominantly positive at $T = 6.0$ s to predominantly negative at $T = 6.5$ s (see Figure 5.8), such that the radiated wave fields now oppose rather than support device motion. The resulting reduction in radiation damping leads to a lower real part of the PTO under active control, particularly for the PA (since in active control, the PTO damping is a linear factor of the

radiation damping). The most severe consequence is observed for the Flap devices, which exhibit a 55% reduction in pitch RAO relative to the mono array. This strong suppression of Flap motion dominates the overall response and constitutes the primary mechanism behind the underperformance of the mixed array at $T = 6.5$ s.

Table 5.2.: Radiation damping cross-coupling in the mixed array at $T = 6.0$ s and $T = 6.5$ s.

| **Parameter** | $T = 6.0$ s | $T = 6.5$ s |
|---|---|---|
| PA→Flap sum | $+6.43 \times 10^6$ Ns | $-2.08 \times 10^6$ Ns |
| Flap→PA sum | $+5.65 \times 10^6$ Ns | $-3.45 \times 10^6$ Ns |
| Sign distribution | 32 pos, 18 neg | 11 pos, 39 neg |
| **Interaction type** | **Constructive** | **Destructive** |

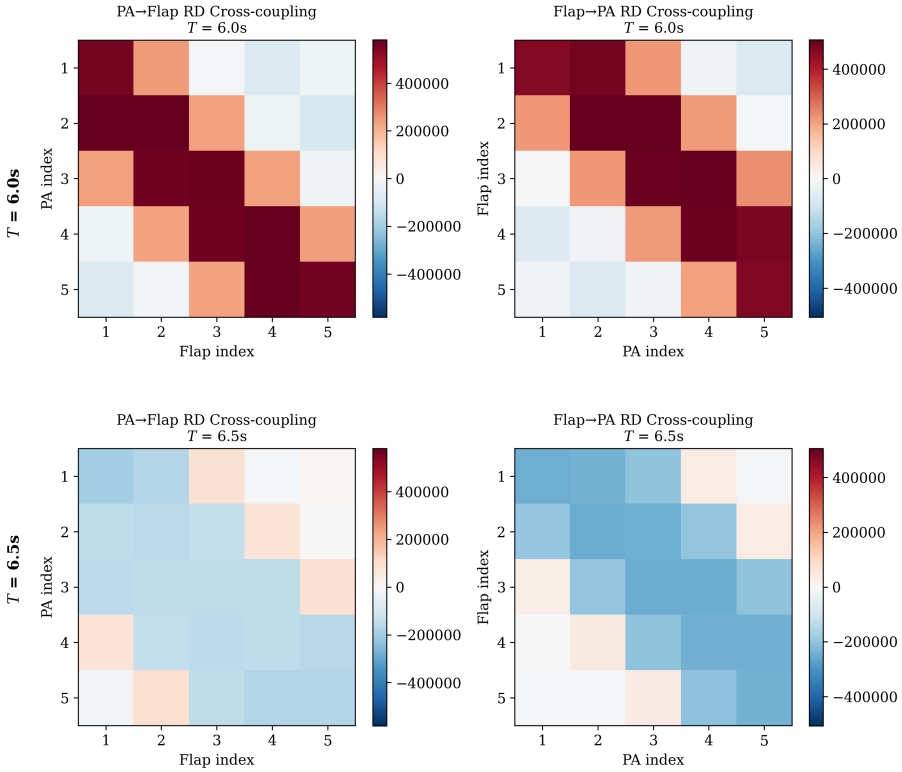



Figure 5.8.: Radiation damping cross-coupling matrices between PA and Flap devices in the mixed array. All units are in Ns. Top row: $T = 6.0$ s showing predominantly positive (red) values indicating constructive interaction. Bottom row: $T = 6.5$ s showing predominantly negative (blue) values indicating destructive interference.

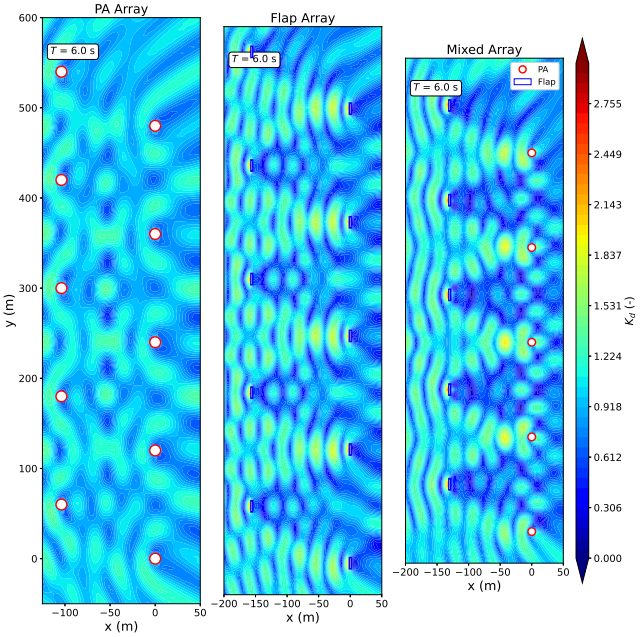



Figure 5.9.: Disturbance coefficient $K_d$ for mixed and mono arrays at $T = 6$s (The incoming wave direction is from left to right)

## WAVE FIELDS

The free-surface elevation wave fields are used to further elucidate the behaviour of the mono and mixed arrays at the two considered wave periods of 6 and 6.5 s.

Figure 5.9 presents the spatial distribution of the disturbance coefficient, defined as

$$K_d = \frac{|\eta_{\text{total}}|}{|\eta_{\text{inc}}|}, \tag{5.6}$$

for an incident wave period of 6 s, while Figure 5.10 shows the corresponding distribution at 6.5 s. Values of $K_d > 1$ indicate amplification of the incident wave due to constructive interference, whereas $K_d < 1$ denotes regions of destructive interaction. $\eta_{\text{total}}$ is the total free surface elevation combining both the diffraction and radiation free surface elevation with the RAOs, and $\eta_{\text{inc}}$ is the inclident wave field.

At $T = 6$ s (see Figure 5.9), a pronounced amplification is observed in the mixed arrays, particularly in front of the point absorbers (PAs), where $K_d$ reaches values of up to 2.1, corroborating the elevated RAO values reported in Table 5.1. The flaps within the mixed configuration also exhibit strong amplification, with peak values approaching 1.8. For the mono flap arrays, higher amplification is consistently observed in the rear row ($K_d \approx 1.8$) compared to the front row, where values remain closer to 1.5. In contrast, the PA mono arrays display the weakest amplification, with maximum $K_d$ values of approximately 1.2, and the resulting interference patterns remain largely localized in the immediate vicinity of the devices.

At $T = 6.5$ s (see Figure 5.10), the amplification pattern changes markedly. The mono flap arrays now exhibit the strongest response, with $K_d$ values reaching up to 2.7 in the rear flap row. In comparison, the mixed arrays behave more similarly to the PA mono arrays, with the rear PA row showing limited interaction and approaching near-independent behaviour. The PA mono array response remains largely unchanged

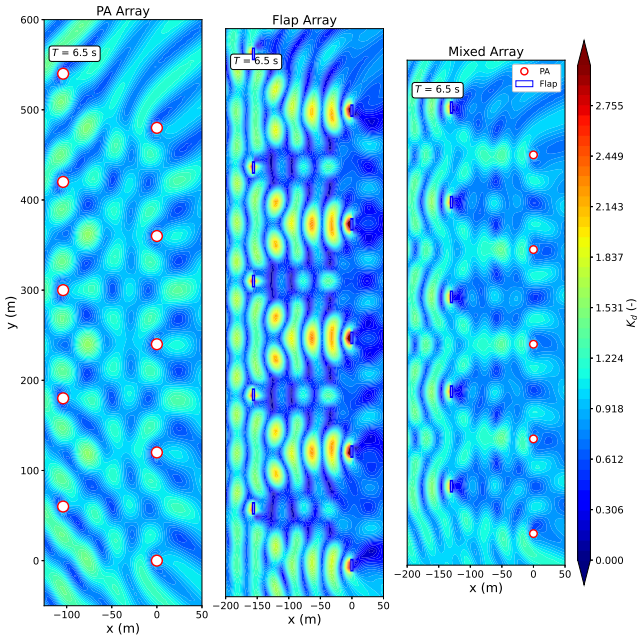



Figure 5.10.: Disturbance coefficient $K_d$ for mixed and mono arrays at $T = 6.5$s (The incoming wave direction is from left to right)

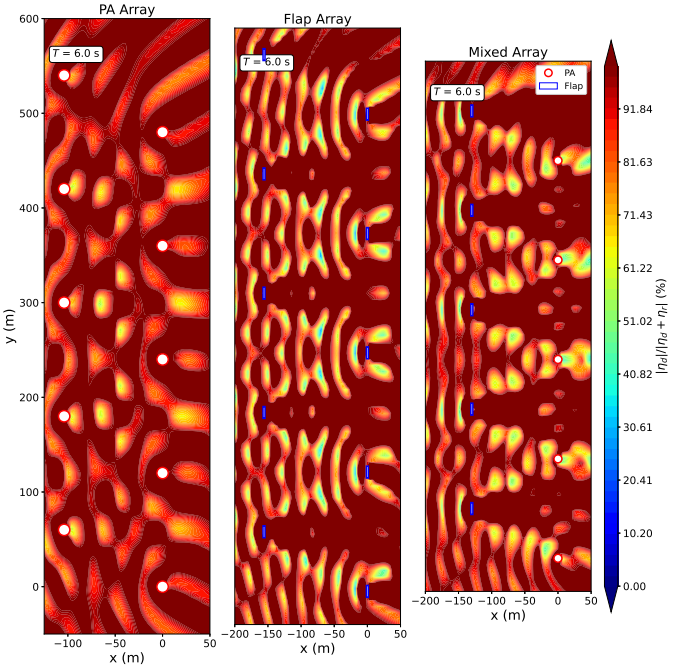
between $T = 6$ s and $T = 6.5$ s, consistent with the similar $q$-factor values observed at these two periods.

The relative performance of the mono and mixed WEC arrays can be further explained by comparing the device spacing to wavelength. For a water depth of $h = 14.5$ m, the dispersion relation yields wavelengths of $\lambda_w = 52.8$ m for $T = 6.0$ s and $\lambda_w = 60.0$ m for $T = 6.5$ s.

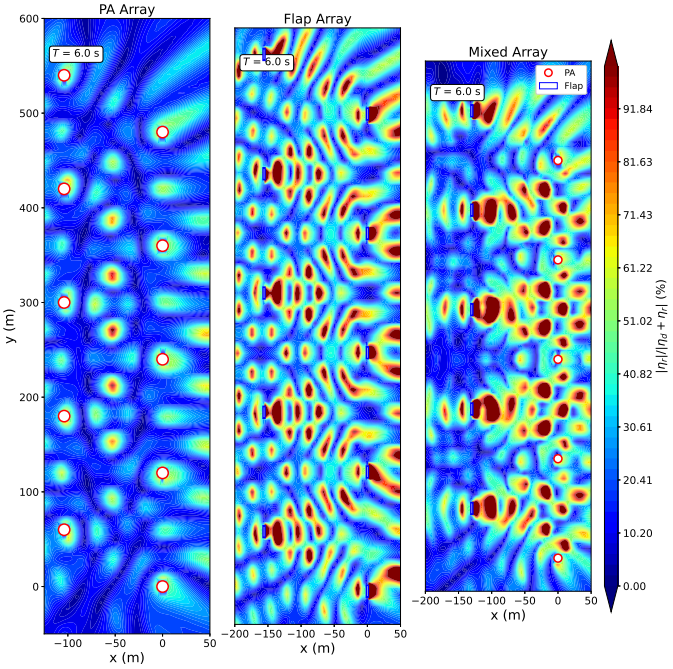
At $T = 6.5$ s, the flap array spacing ($L_\mathrm{f} = 180$ m $= 3.00\lambda_w$) and the PA array spacing ($L_\mathrm{p} = 120$ m $= 2.00\lambda_w$) correspond to exact integer multiples of the wavelength, promoting constructive interference between the radiated waves of neighbouring devices and enhancing wave–body interactions, as reflected by the elevated $K_d$ values. In contrast, the mixed array spacing ($L_\mathrm{m} = 150$ m $= 2.50\lambda_w$) represents a half-integer multiple, causing the radiated waves to arrive largely out of phase at adjacent devices, thereby inducing destructive interference and suppressing array performance.

At $T = 6.0$ s, the spacing-to-wavelength ratios shift accordingly. The mixed array spacing approaches a near-integer multiple ($L_\mathrm{m} = 2.84\lambda_w \approx 3\lambda_w$), favouring constructive interference, whereas the flap ($L_\mathrm{f} = 3.41\lambda_w$) and PA ($L_\mathrm{p} = 2.27\lambda_w$) mono arrays deviate from integer multiples, leading to reduced constructive array effects. This analysis highlights the strong sensitivity of WEC array hydrodynamic performance to the spacing-to-wavelength ratio, with integer multiples favouring constructive interference and enhanced energy capture, while half-integer multiples lead to destructive interference and diminished performance.

Finally, the differences in array performance observed at $T = 6$ s and $T = 6.5$ s are further corroborated by the diffraction and radiation percentage plots shown in Figure 5.11 and Figure 5.12, respectively. At $T = 6$ s, the PA mono arrays are predominantly diffraction-dominated, with radiation effects remaining largely localized around the individual devices. In contrast, the flap mono arrays exhibit comparatively stronger radiation contributions, although these remain confined to the vicinity of the

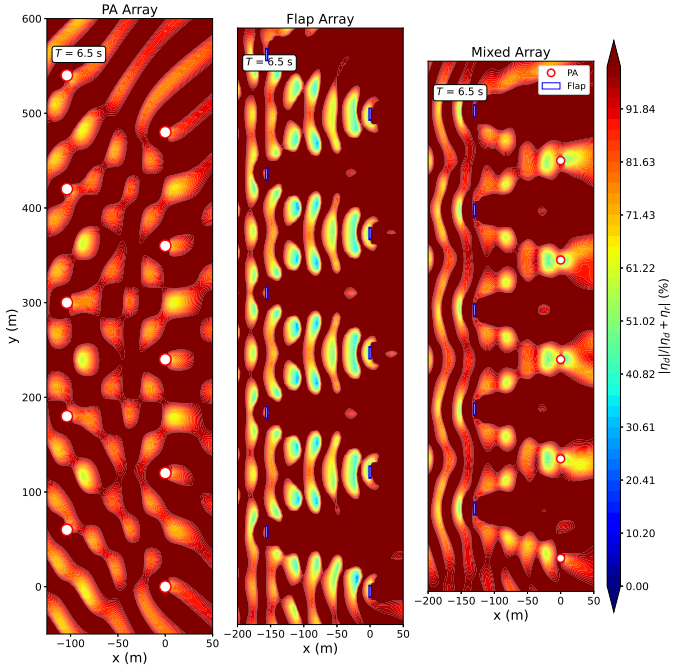



(a) Percentage diffraction in perturbed wave field

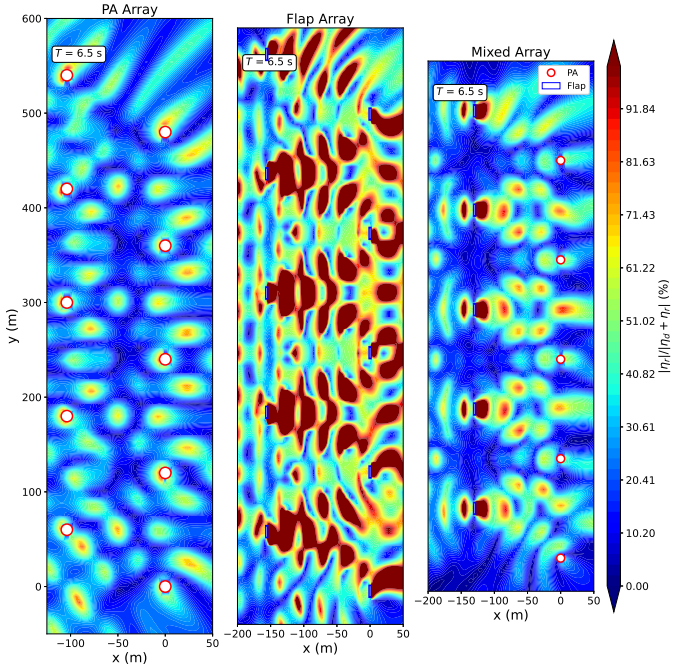



(b) Percentage radiation in perturbed wave field

Figure 5.11.: Percentage contributions of the diffraction and radiation to the perturbed wave field at $T$=6 s (The incoming wave direction is from left to right)




(a) Percentage diffraction in perturbed wave field




(b) Percentage radiation in perturbed wave field

Figure 5.12.: Percentage contributions of the diffraction and radiation to the perturbed wave field at $T = 6.5$ s (The incoming wave direction is from left to right)

flaps. Under these conditions, the mixed arrays perform favourably, as the radiation fields generated by the flaps interact constructively with those of the PAs, leading to enhanced collective behaviour. At $T = 6.5$ s, a distinct shift in the dominant mechanisms is observed. The PA mono arrays continue to display largely localized radiation effects, indicating limited inter-device interaction. The mixed arrays show an overall increase in radiation contributions; however, the flap mono arrays clearly dominate the response at this period, with the radiation field becoming both significantly stronger and more spatially extended. This enhanced radiation dominance is consistent with the increased constructive interference observed for the flap arrays at this wave period.

### COMPARING POWER FROM INDIVIDUAL DEVICES

The power absorption of the individual devices provides further insight into the array-level behaviour seen from the $q$ and $M$-factors. For the PA mono array (see Figure 5.13), the arrayed devices generally outperform the isolated PA over the period range between 5 and 8 s, indicating constructive hydrodynamic interactions over a relatively broad band.

In contrast, the flap mono array exhibits a narrower enhancement window, with improved performance relative to the isolated flap primarily at $T = 5$–$5.5$ s and again around $T = 6.5$ s (see Figure 5.14). Outside these intervals, destructive interference and unfavourable radiation interactions dominate, resulting in limited array-induced gains. These device-level trends are directly reflected in the corresponding array $q$-factors, confirming that mono arrays are inherently destructive in this case.



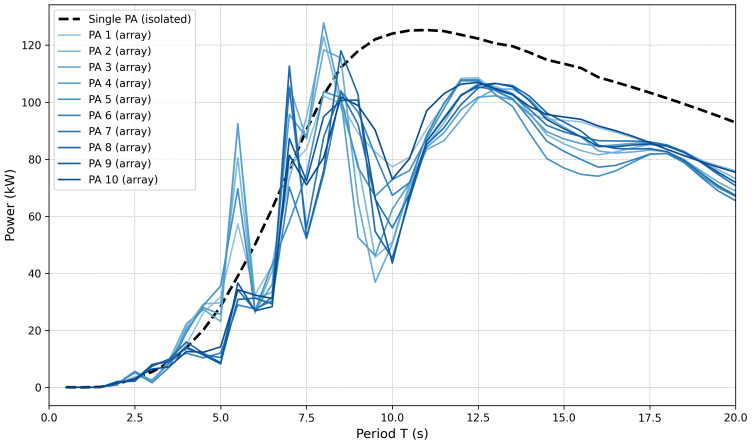



Figure 5.13.: Power absorption of individual devices in the mono PA array at 0° incident wave

The mixed arrays exhibit a markedly improved and complementary response (see Figure 5.15a and Figure 5.20b), arising from the different dynamic characteristics of the PA and flap devices. In this configuration, the PA devices generally absorb more power than the isolated PA over the period range of 4–6 s, where favourable scattering and positive radiation damping cross-coupling enhance the heave response of the PAs.

Conversely, the flap devices outperform their isolated counterparts over a substantially wider range spanning approximately 6.5–11 s, corresponding to periods where the flap pitch dynamics are dominant and less sensitive to adverse interactions. This staggered enhancement across periods leads to a complementary division of effective absorption between the two device types, such that when the performance of one device type begins to deteriorate, the other continues to contribute strongly. This is reflected directly

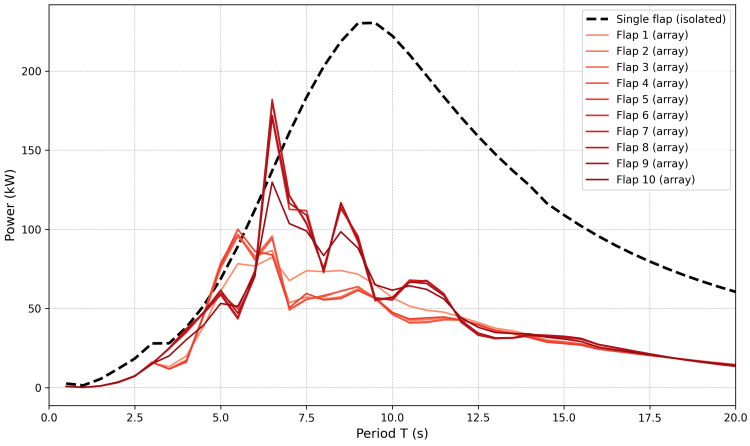



Figure 5.14.: Power absorption of individual devices in the mono flap array at 0° incident wave



in the *M*-factors, that shows the capture width efficiency greater than 1 for almost the entire considered range of 3-12 s.

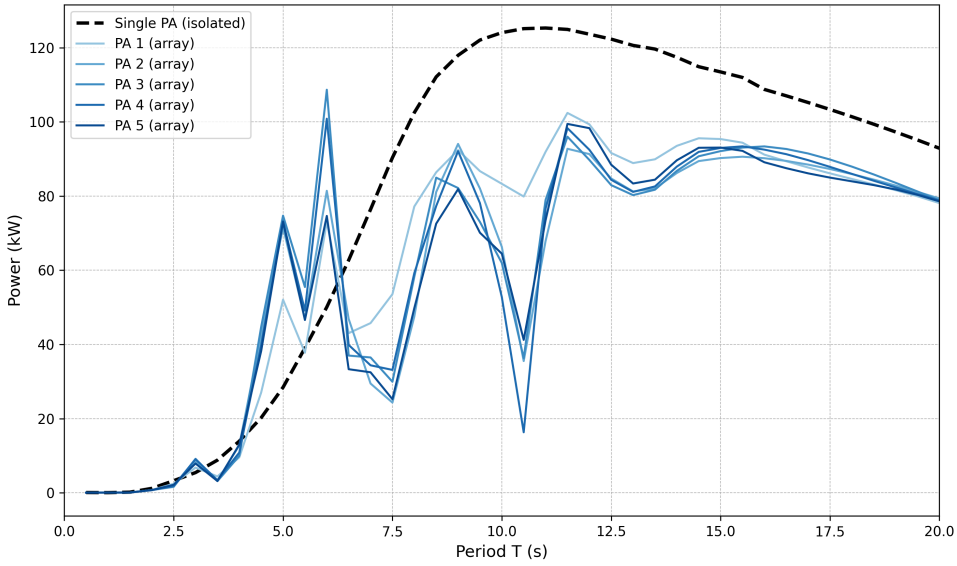
As a result, the mixed arrays achieve a significantly broader effective absorption bandwidth compared to either mono configuration. Importantly, the flaps within the mixed configuration consistently absorb substantially more power than those in the mono flap array across most of the analysed period range, highlighting the beneficial role of the PA devices in modifying the local wave field experienced by the flaps. A similar, though more period-dependent, improvement is observed for the PA devices relative to the mono PA array.

These findings demonstrate that the performance gains of the mixed arrays are not solely driven by peak enhancements at specific periods, but rather by a redistribution and extension of absorption efficiency across a wider range of wave conditions, which is particularly advantageous when integrated over realistic wave spectra.

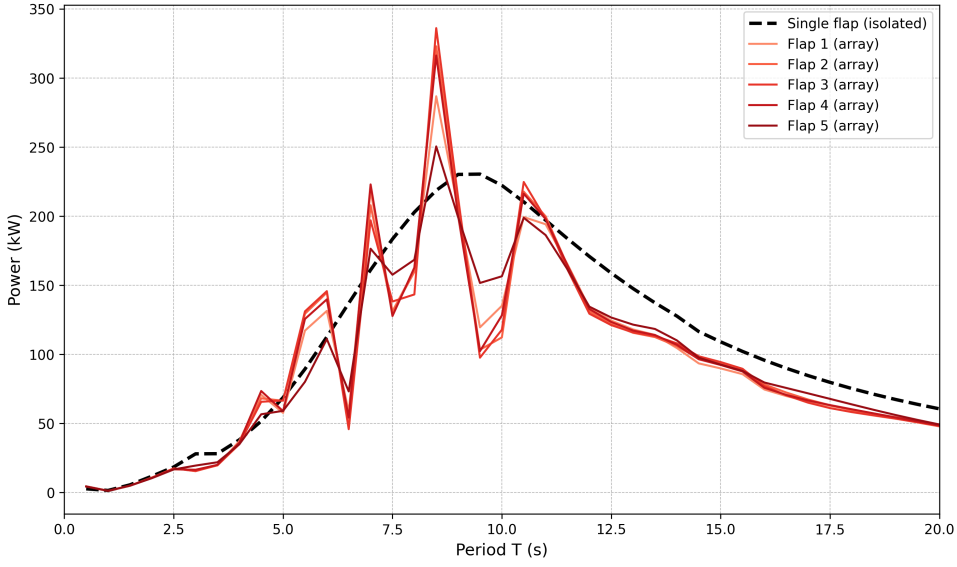
## 5.2. SHALLOW WATER - ANALYSIS IN IRREGULAR WAVES

This section provides further insights into the 10 device staggered configuration (5 PAs + 5 flaps) with 4*C* spacing under passive control and how it behaves with respect to the mono PA and flap arrays in irregular waves. This configuration was selected as the best shallow water mixed array configuration in irregular waves, giving a mean *q*-factor of 1.19 and a mean *M*-factor of 1.4 across the considered range of 3-12 s. This configuration also gave a mean *M*-factor greater than 1 for 10 directions out of 12.

Figure 5.16 presents the *q*- and *M*-factors for the mono and mixed arrays under head-on wave incidence (0°), where the mixed configuration exhibits its strongest performance. The PA mono array shows a moderate enhancement around its optimal response, with *q*-factors slightly exceeding unity in the range of $T_p \approx 3$–6 s before gradually decreasing at higher periods. The flap mono array exhibits a similar but weaker trend, with peak *q*-factors remaining close to unity. In contrast, the mixed array consistently outperforms both mono configurations across a broader range of wave periods, achieving a maximum *q*-factor of approximately 1.2. This enhancement is further reflected in the corresponding *M*-factor, which remains consistently above unity, indicating that the mixed array benefits from strong constructive hydrodynamic interactions compared to the mono. The clear separation between the mixed-array *q*- and *M*-factors and those of the mono arrays highlights the favourable coupling between PAs and flaps under head-on wave conditions, leading to superior collective performance.




(a) PA devices




(b) Flap devices

Figure 5.15.: Power absorption of individual devices in the mixed array at 0° incident wave

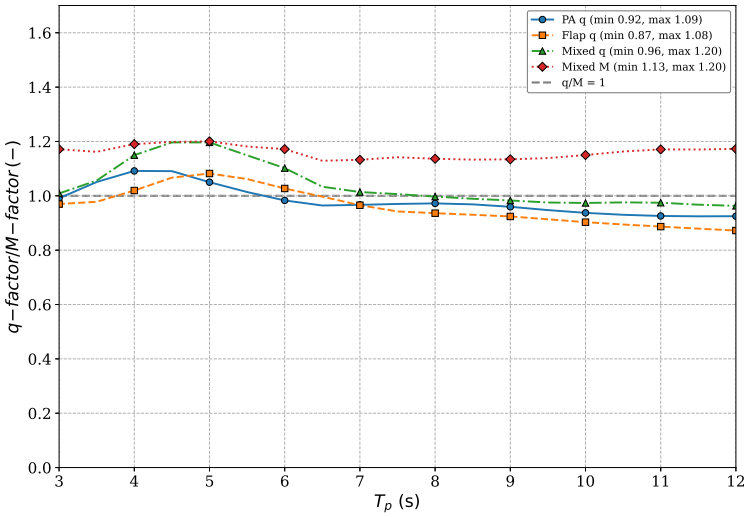



Figure 5.16.: $q$ factors for the mono and mixed arrays and $M$-factor for mixed arrays with passive control under irregular waves at incident angle of 0°

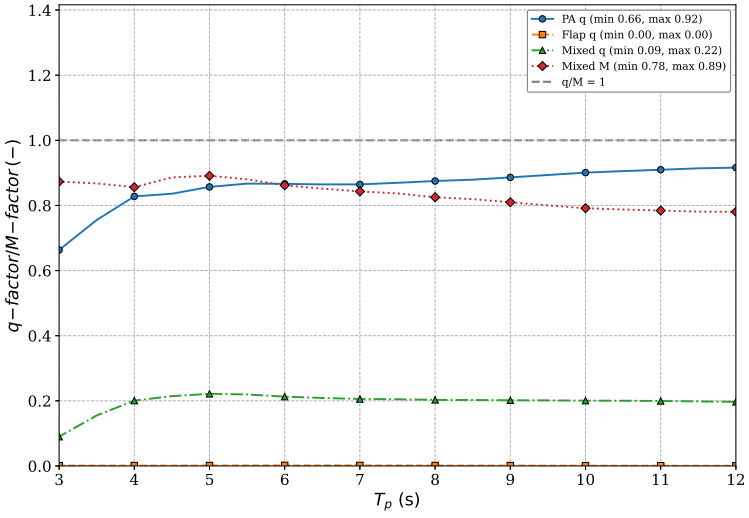



Figure 5.17.: $q$ factors for the mono and mixed arrays and $M$-factor for mixed arrays with passive control under irregular waves at incident angle of 90°

In contrast, Figure 5.17 shows the corresponding metrics for waves incident at 90°, representing the least favourable direction for the PA-flap mixed array. Under these conditions, the $q$-factors for all configurations remain below unity, indicating predominantly destructive interactions under irregular waves. The PA mono array performs much better than the flap mono array, which exhibits negligible power absorption across the entire period range since the wave is perperdicular to the longitudinal direction of the flap and unfavourable for pitch motion. The mixed array shows limited improvement over the mono flap configuration, with $q$-factors remaining significantly below unity and well separated from the corresponding $M$-factor, which also stays below one. This behaviour suggests weak and predominantly destructive hydrodynamic coupling when the wave direction is perpendicular to the primary array alignment. Overall, the strong contrast between the 0° and 90° cases underscores the pronounced directional dependence of mixed-array performance, with substantial gains achievable when the incident wave direction aligns favourably with the array geometry.

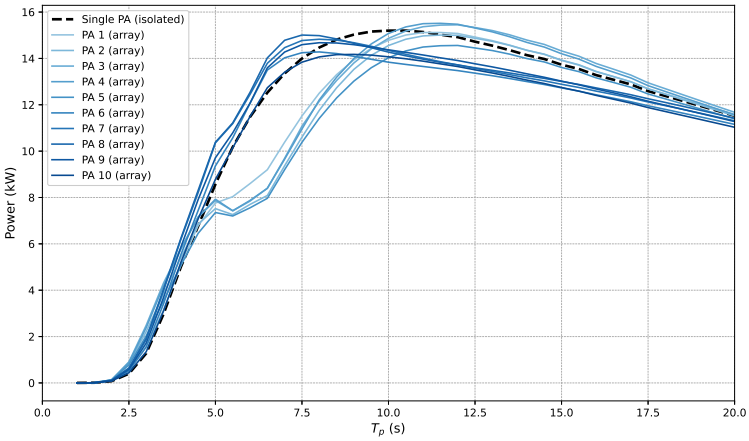



Figure 5.18.: Power absorption of individual devices in the mono PA array at 0° incident wave under passive control in irregular waves

The trends observed in the array-level $q$-factors at 0° can be directly linked to the power absorbed by the individual devices within the mono arrays. For the PA mono array (see Figure 5.18), the power absorbed by the arrayed PAs closely follows that of the isolated device, with modest deviations across the considered period range. Slight enhancements are observed in the intermediate period range ($T_p \approx 3$–$8$ s), where several arrayed PAs marginally outperform the isolated PA, corresponding to $q$-factors close to or slightly above unity. Outside this range, the individual PA power curves largely collapse onto the isolated response, reflecting weak hydrodynamic coupling and explaining the limited variation in the $q$-factor.

In contrast, the flap mono array (see Figure 5.19) exhibits a more pronounced reduction in individual device power relative to the isolated flap across almost all periods. Although localized enhancements are observed around the 5 to 6 s range, the arrayed flaps generally underperform the isolated device, leading to $q$-factors below unity and indicating predominantly destructive interactions within the mono flap configuration.

A markedly different behaviour emerges for the mixed arrays, where the enhanced $q$-factors are underpinned by clear gains in individual device power for both WEC types. For the PAs in the mixed configuration (see Figure 5.20a), most arrayed devices absorb more power than the isolated PA over the 3-5 s period range. Similarly, the flaps in the mixed array (see Figure 5.20b) exhibit substantially higher power absorption compared to the mono flap case, with many devices approaching or exceeding the isolated flap response over the 3-8 s range. The redistribution and amplification of power absorption

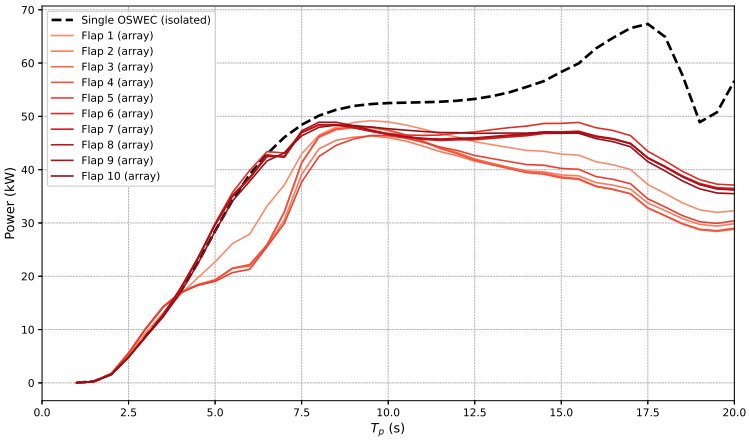



Figure 5.19.: Power absorption of individual devices in the mono flap array at 0° incident wave under passive control in irregular waves



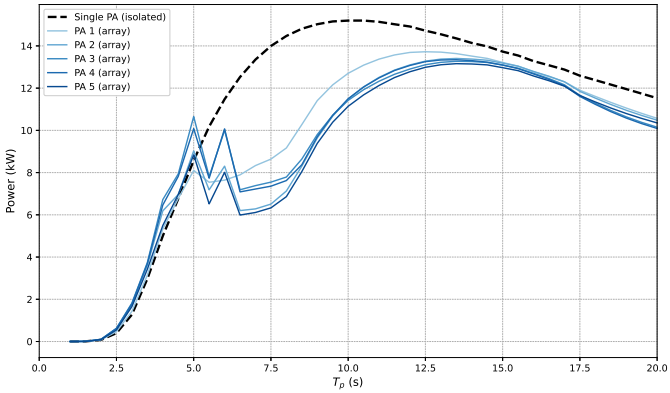
across individual devices in the mixed configuration demonstrates that the improved $q$-factors are not driven by isolated peak responses, but rather by coherent and complementary hydrodynamic interactions between PAs and flaps over a broad range of periods. This collective enhancement at the device level ultimately manifests as the superior array-level performance observed for the mixed farms.

For waves incident at 90°, the individual device power responses clearly explain the reduced $q$-factors observed for all array configurations. In the PA mono array (see Figure 5.21), the arrayed PAs consistently underperform relative to the isolated device across almost the entire period range. The reduction is particularly pronounced around the primary response peak, where the isolated PA exhibits its maximum power absorption while the arrayed devices show a systematic loss. This behaviour reflects predominantly destructive hydrodynamic interactions and shadowing effects under transverse wave incidence and is consistent with the $q$-factors remaining well below unity at 90°. For the flap mono array (see Figure 5.22), the effect is even more severe: the arrayed flaps absorb negligible power compared to the isolated flap due to the incident wave being perpendicular to the longitudinal direction of the flap.

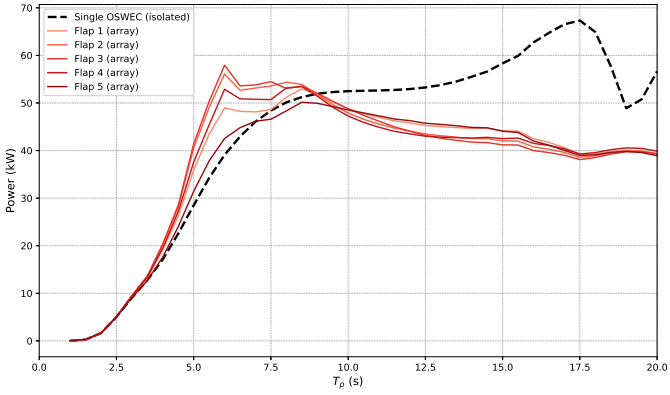
A similar trend is observed in the mixed arrays, where the limited array-level performance can again be traced back to the individual device responses. For the PAs in the mixed configuration (see Figure 5.23a), the arrayed devices absorb less power than the isolated PA across all considered periods, with no systematic enhancement evident. The flaps in the mixed array (see Figure 5.23b) likewise show very weak power absorption, comparable to or only marginally exceeding that of the mono flap array due to the interaction with the PA devices. This lack of individual-device enhancement explains why the mixed-array $q$-factors remain low at 90° and why the mixed configuration fails to provide any significant advantage over the mono arrays. Overall, the 90° case demonstrates that without favourable alignment between wave direction and array geometry, hydrodynamic coupling becomes predominantly destructive, suppressing individual device performance and, consequently, the overall array efficiency.

## 5.3. Deep water - Analysis in regular waves

This section provides further insights into the 10 device staggered configuration (5 PAs + 5 attenuators) with 6$C$ spacing and how it behaves with respect to the mono PA and attenuator arrays in regular waves.




(a) PA devices




(b) Flap devices

Figure 5.20.: Power absorption of individual devices in the mixed array at 0° incident wave with passive control under irregular waves

The best configuration under regular waves in deep waters is the 10 device array with 5 large PAs and 5 attenuators (spacing of $L_m = 6\ C$ where $C = 29.5$ m), shown in Figure 5.24. When considering both $q$ and $M$-factor, this configuration gave a $q$-factor >1 for 6 directions and $M$-factor > 1 for 8 directions showing its higher capture width efficiency across a range of directions.

### ARRAY NATURAL FREQUENCIES AND EIGEN VECTORS

Figure 5.25 presents the natural periods of the PA and attenuator devices in the mixed array. For the attenuator, the identified periods are associated with specific degrees of freedom (DOFs) based on the relative contributions of the individual DOFs within the corresponding eigenvectors, as well as their proximity to the natural periods of the isolated device.

Owing to the coupled nature of the system, a strict one-to-one assignment of each natural period to a single DOF is not always possible. Consequently, the DOF indicated in the legend reflects the dominant contribution inferred from both the eigenvector composition and the closeness of the natural period to that of the corresponding isolated-device DOF. With the PA, only two periods are shown in the legend due to

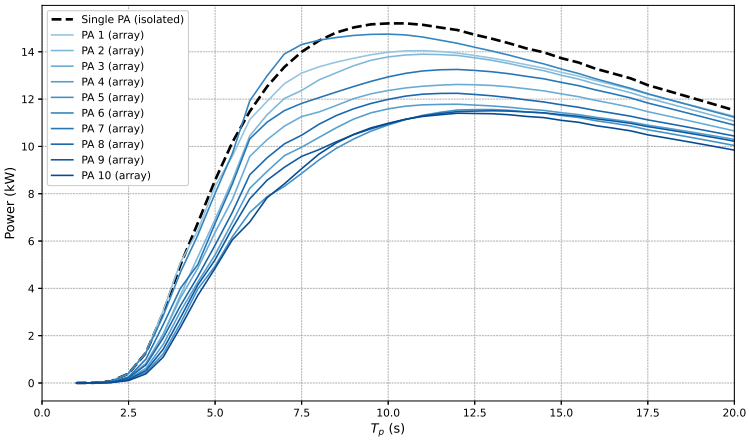



Figure 5.21.: Power absorption of individual devices in the mono PA array at 90° incident wave under passive control in irregular waves



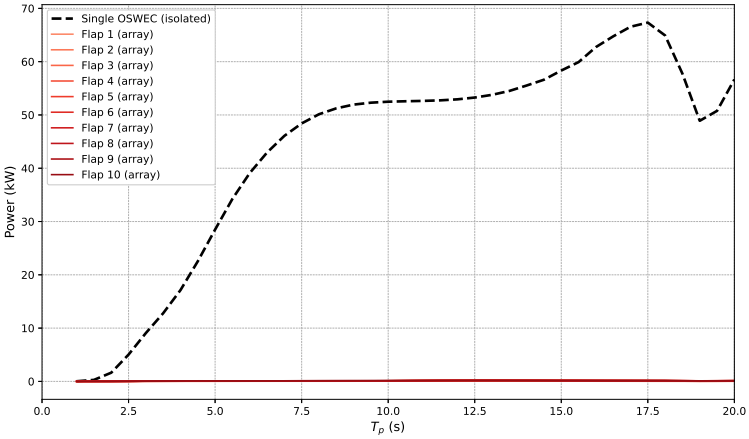
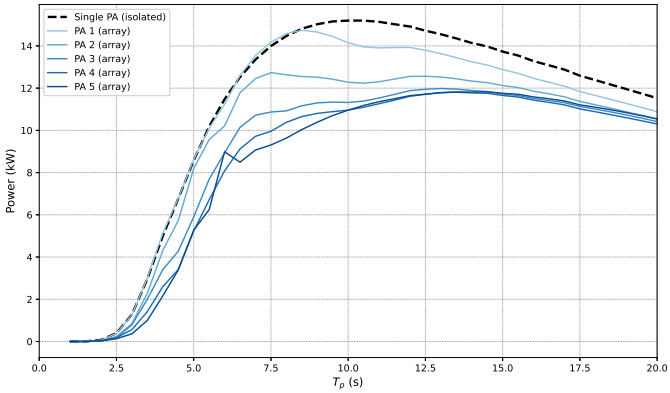



Figure 5.22.: Power absorption of individual devices in the mono flap array at 90° incident wave under passive control in irregular waves

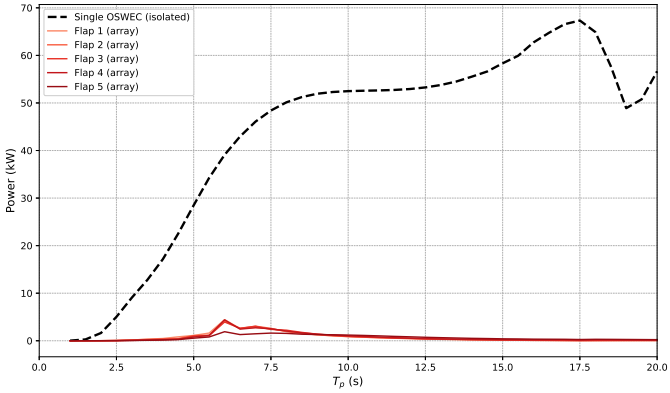
overlapping natural frequencies as well as closeness to the pitch/rear arm pitch natural period. Two eigen modes to understand this are shown in Figure 5.26.

At $T$= 3.94 s, the heave modes of the PA are active which is expected since this is close to the natural period of the isolated PA in heave. The coupling can be observed here, wherein the heave, pitch and rear arm pitch are also excited for the attenuators. Similarly, at $T$ = 7.88 s, heave modes in the attenuator are most dominant with the pitch and rear arm pitch modes also excited.

A limitation of the present frequency analysis arises primarily for the surge degree of freedom (DOF). In a freely floating attenuator, the hydrostatic stiffness associated with surge is zero, and both the diagonal and off-diagonal terms of the stiffness matrix corresponding to surge vanish. Consequently, the undamped surge mode corresponds to a rigid-body drift with $\lambda = 0$ and $\omega_n = 0$, and does not possess a natural period in the conventional sense.




(a) PA devices




(b) Flap devices

Figure 5.23.: Power absorption of individual devices in the mixed array at 90° incident wave with passive control under irregular waves

In the eigenvalue-tracking approach used here, natural frequencies are identified by locating intersections between the frequency-dependent eigenvalue curves $\lambda(\omega)$ and the line $\omega^2$. Since pure surge modes have $\lambda = 0$ for all frequencies, no such intersection occurs at any finite frequency, and these undamped surge modes are therefore absent from the results.

The surge-related periods that do appear in the undamped analysis are instead coupled modes, in which surge motion participates through hydrodynamic coupling via the mass and added-mass matrices. In these cases, the non-zero eigenvalue arises from coupling with other DOFs—such as heave, pitch, or rear arm pitch modes—that possess non-zero hydrostatic stiffness. While these coupled modes are correctly captured in the undamped analysis, their interpretation must account for the fact that surge itself does not provide a restoring mechanism.

The limitations become more pronounced when considering the damped natural frequencies. These are obtained by solving Equation 5.1. The damping ratio is then estimated using the perturbation-based approximation

$$\zeta \approx \frac{\mathrm{Im}(\lambda)}{2\,\mathrm{Re}(\lambda)},$$

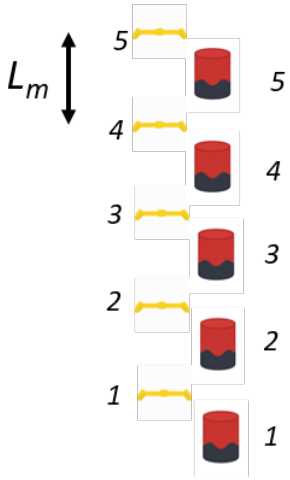



Figure 5.24.: 10 device mixed array with 5 large PAs and 5 attenuators - Best configuration considering regular waves



which assumes that the eigenvalue is dominated by the stiffness contribution, with damping acting as a small imaginary correction. This assumption is valid for DOFs with non-zero hydrostatic restoring forces, such as heave, pitch, and rear arm pitch.

However, for DOFs with zero hydrostatic stiffness—most such as surge, the real part of the eigenvalue approaches zero while the imaginary part remains finite. As a result, the computed damping ratio becomes unbounded, leading to physically meaningless values. In the present study, this manifested as damping ratios exceeding $\zeta > 100$ for surge-dominated modes. This behaviour reflects a fundamental modelling limitation rather than a physically overdamped response.

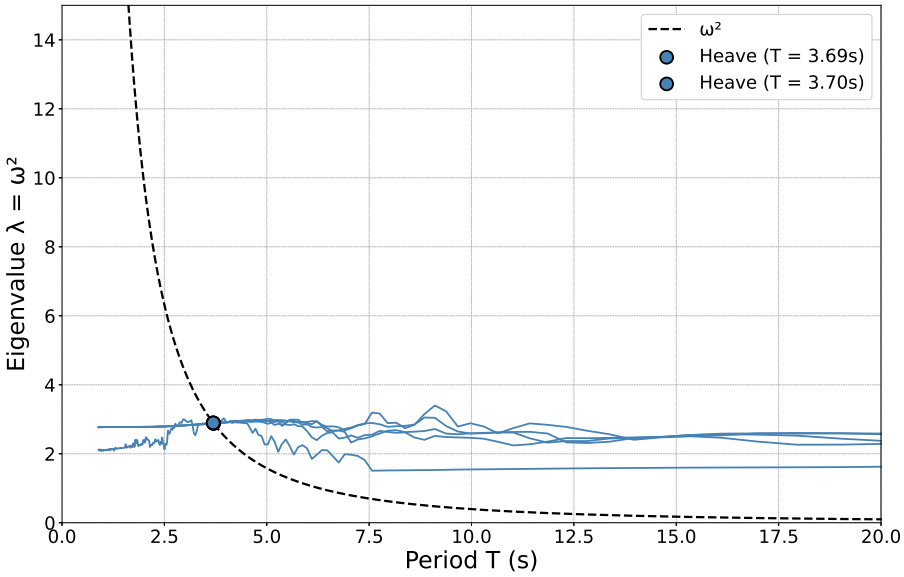
While the mooring stiffness is not included here since its influence on the power absorption is negligible particularly for slack moored WECs [131], introduction of mooring stiffness would provide a restoring force to the surge DOF, transforming it from a drift mode into a proper oscillatory mode.

A direct comparison of the range of natural periods across various DOF between mixed and mono arrays similar to the shallow water case is not performed here, since the interaction between the various DOFs, particularly within the same device, makes it very difficult to assess these ranges accurately.

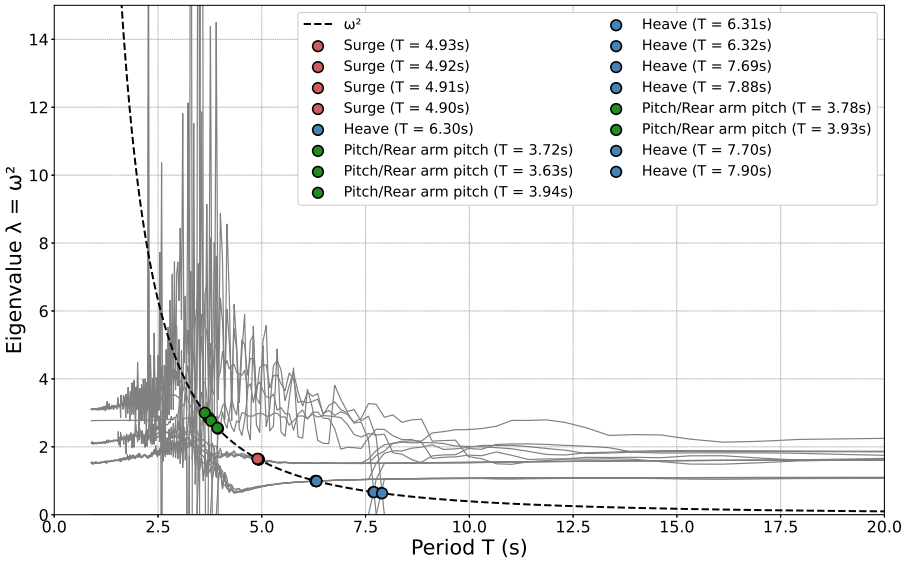
### 5.3.1. PERFORMANCE BASED ON Q- AND M-FACTORS

In regular waves, the attenuator mono arrays generally exhibit a higher mean $q$-factor across all wave directions when compared to both the mixed array and the PA mono array. However, when considering the mean $M$-factor, a different trend emerges: the mixed array consisting of 5 PAs and 5 attenuators at a spacing of $6C$ outperforms the mono arrays in 8 out of 12 the considered directions. This indicates that, despite lower average power production in terms of $q$, the mixed configuration benefits from favourable redistribution of absorbed power among its constituent devices, leading to superior capture width efficiency when assessed using the $M$-factor.

To further examine this behaviour, the head-on wave direction (0°) is considered in detail, focusing on analysis periods of $T = 5.5$ and 6 s. This is one of the directions where the average $M$-factor is greater than 1. At $T = 5.5$ s, the mixed array outperforms both mono configurations in terms of the $q$-factor, highlighting constructive hydrodynamic interactions between the PAs and attenuators. In contrast, at $T = 6$ s, the attenuator mono array exhibits the highest $q$-factor, surpassing both the mixed and PA



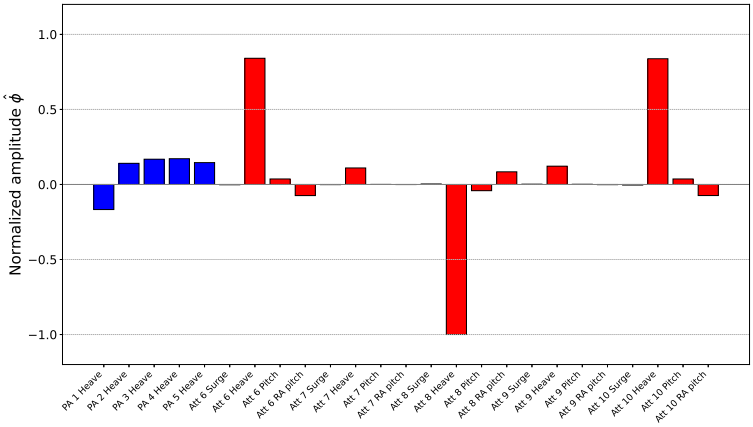

(a) PA natural frequency tracking



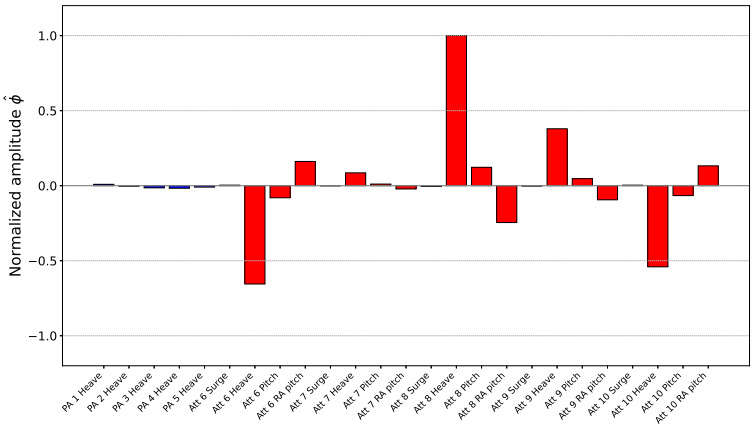

(b) Attenuator natural frequency tracking

Figure 5.25.: Natural frequency tracking for the mixed array

mono arrays. The corresponding variation in both $q$- and $M$-factors for this direction is illustrated in Figure 5.27.




(a) Array mode shape at the natural period $T = 3.94$ s




(b) Array mode shape at $T$=7.88 s

Figure 5.26.: Modes of the mixed array

### COMPARING HYDRODYNAMIC PARAMETERS

In order to understand the differences in the performance of the mono and mixed arrays between $T = 5.5$ s and 6 s, the comparison between the hydrodynamic parameters between the two arrays is considered. The mean percentage change in the hydrodynamic parameters for individual device from mono to mixed arrays is shown in Table 5.3.

At $T = 5.5$ s, the mixed array significantly outperforms the mono arrays, with both device types benefiting from the heterogeneous configuration. For PAs, the excitation force enhancement is substantial (+61.1%) while the radiation damping increase remains modest (+5.9%), indicating that PAs receive considerably more wave energy input due to constructive scattering from the attenuators without proportionally losing energy to radiation—yielding a +42.2% increase in PA RAO. Remarkably, the attenuators benefit even more dramatically: despite a relatively modest excitation enhancement (+7.6%), they experience a slight *reduction* in radiation damping (−1.5%), resulting in an exceptional +74.4% RAO gain. This asymmetric benefit arises because the PAs act as efficient scatterers that redirect wave energy toward the attenuators while

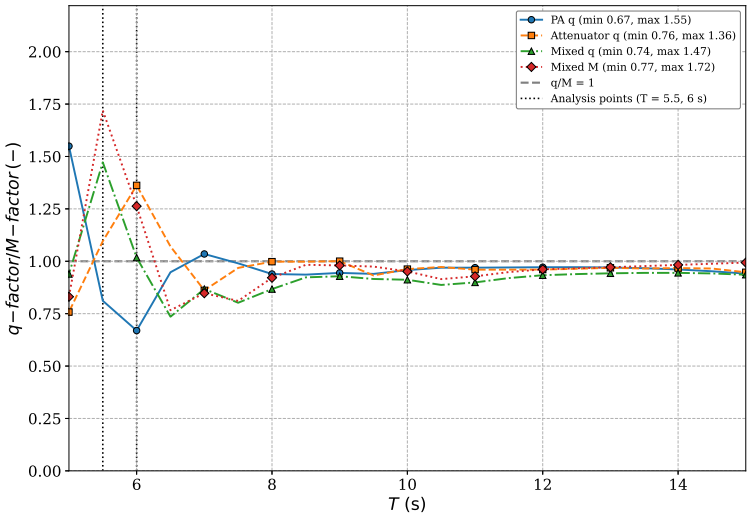



Figure 5.27.: $q$ factors for the mono and mixed arrays and $M$-factor for mixed arrays with passive control under regular waves at incident angle of 0°

simultaneously providing a partial radiation shield that reduces attenuator energy losses.

At $T = 6.0$ s, however, the underlying physics shifts unfavourably. The PA radiation damping increases dramatically (+16.4% compared to +5.9% at $T = 5.5$ s), and although excitation remains enhanced (+41.3%), a larger fraction of captured energy is radiated away rather than being available for power extraction, reducing the PA RAO gain to +18.7%. The attenuators fare even worse at this period: their excitation enhancement drops to just +4.0% while gaining minimal radiation damping benefit (−0.5%), resulting in a negligible +1.8% RAO improvement. The cross-coupling terms confirm this shift—radiation damping coupling strengths increase from 0.22–0.23 at $T = 5.5$ s to 0.24–0.26 at $T = 6.0$ s, establishing stronger energy transfer pathways between device types that erode the mixed array advantage.

Similar to the shallow water analysis, the coupling strength is used to understand the influence of the cross-coupling terms with respect to the diagonal terms. This is given by:

$$\mathrm{CS}_{\mathrm{PA}\to\mathrm{Att}} = \frac{\max|\mathbf{M}_{\mathrm{PA}\to\mathrm{Att}}|}{\sqrt{\overline{M}^{\mathrm{diag}}_{\mathrm{PA}} \cdot \overline{M}^{\mathrm{diag}}_{\mathrm{Att}}}} \tag{5.7}$$

where:

- $\mathbf{M}_{\mathrm{PA}\to\mathrm{Att}}$ is the off-diagonal cross-coupling block representing the influence of PA motion on Attenuator response (or vice versa for $\mathrm{CS}_{\mathrm{Att}\to\mathrm{PA}}$)
- $\overline{M}^{\mathrm{diag}}_{\mathrm{PA}} = \frac{1}{N_{\mathrm{PA}}} \sum_{i=1}^{N_{\mathrm{PA}}} |M^{\mathrm{PA}}_{ii}|$ is the mean of the absolute diagonal elements in the PA-PA block
- $\overline{M}^{\mathrm{diag}}_{\mathrm{Att}} = \frac{1}{N_{\mathrm{Att}}} \sum_{j=1}^{N_{\mathrm{Att}}} |M^{\mathrm{Att}}_{jj}|$ is the mean of the absolute diagonal elements in the Att-Att block
- $\mathbf{M}$ can represent either the added mass matrix $\mathbf{M}_a(\omega_i)$ or radiation damping matrix $\mathbf{B}_a(\omega_i)$

The cross-coupling heatmaps (see Figure 5.28) reveal that the radiation damping coupling from attenuators to PAs (Att → PA) generally exhibit stronger positive magnitudes at $T = 6.0$ s, indicating that attenuator motions induce larger damping forces on the PAs at this period.

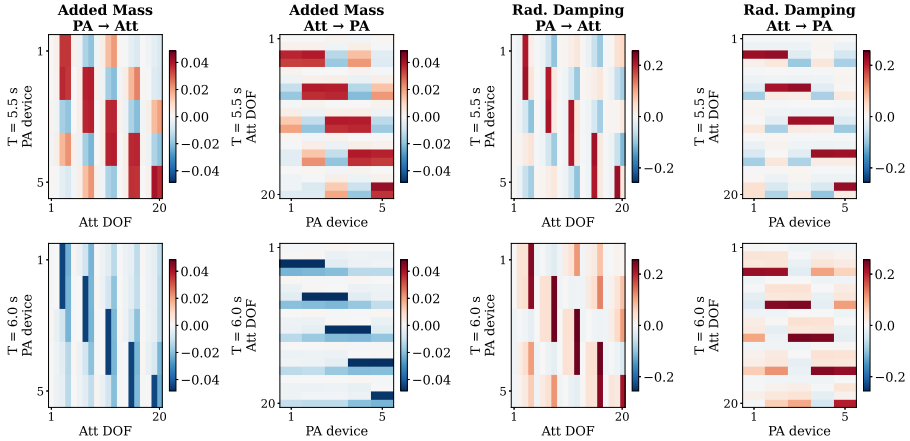



Figure 5.28.: Heatmaps for the cross-coupling strength for the added mass and radiation damping matrices for mono and mixed arrays for $T = 5.5$ and 6 s

In deep water, the wavelength follows the dispersion relation $\lambda_w = gT^2/2\pi$, giving $\lambda_w \approx 47.2$ m ($\lambda_w/2 \approx 23.6$ m) at $T = 5.5$ s and $\lambda_w \approx 56.2$ m ($\lambda_w/2 \approx 28.1$ m) at $T = 6.0$ s. These wavelengths have important implications for each device type. For the attenuators, optimal energy capture occurs when half the wavelength matches the arm length ($\approx 25$ m), enabling the device to span a full wave crest-to-trough differential. At $T = 5.5$ s, $\lambda_w/2 \approx 23.6$ m is very close to this optimal condition, whereas at $T = 6.0$ s, $\lambda_w/2 \approx 28.1$ m slightly exceeds it. For the point absorbers, efficient operation requires $\lambda_w \gg D$, where $D \approx 9$ m is the device diameter. Both periods satisfy this criterion ($\lambda_w/D \approx 5.2$ and 6.2, respectively), confirming that the PAs operate within the point absorber regime.

Table 5.3.: Percentage changes in hydrodynamic parameters: Mixed array vs Mono arrays (Deep Water, $\theta = 0°$). Positive values indicate an increase in the mixed array; negative values indicate a decrease.

| **Parameter** | $T = 5.5$ s | | $T = 6.0$ s | |
|---|---|---|---|---|
| | PA | Att | PA | Att |
| Excitation Force | +**61.1**% | +**9.6**% | +41.3% | +4.0% |
| Added Mass (diagonal) | −1.6% | +1.1% | +1.0% | +0.7% |
| Rad. Damping (diagonal) | +5.9% | −1.5% | +16.4% | −0.5% |
| **RAO** | +**42.2**% | +**74.4**% | +18.7% | +1.8% |

At $T = 5.5$ s, the attenuators operate near their optimal wavelength condition as seen in their RAOs, and the array spacing produces constructive interference in the excitation field reaching the PAs without proportionally increasing radiative coupling. At $T = 6.0$ s, the longer wavelength shifts the attenuators away from their optimal condition while strengthening the radiative coupling between device types, thereby reducing the net benefit of the mixed configuration. The attenuator mono array performs well at $T = 6.0$ s because, despite moving away from the optimal $\lambda/2$ condition, attenuators still respond

effectively to longer-period waves. In the mixed array, however, the attenuators lose energy through cross-coupling to the PAs, diminishing the overall array performance relative to the mono attenuator configuration.

### WAVE FIELDS

The disturbance coefficient $K_d = |\eta_{total}|/|\eta_{inc}|$ plots reveal distinct wave field characteristics that corroborate the hydrodynamic parameter analysis. At $T = 5.5$ s (see Figure 5.29a), the PA array exhibits pronounced hotspots (elevated $K_d$ values) immediately surrounding each device in the front row, indicating strong local wave amplification due to diffraction and radiation effects. The attenuator array displays a more distributed interference pattern with moderate amplification zones extending laterally from each device in the first row towards the devices in the second row.

Notably, in the mixed array configuration, the PAs in the second row exhibit substantially stronger hotspots compared to their mono-array counterparts, with $K_d$ values visibly exceeding those observed in the PA-only case. This amplified response directly corresponds to the +61.1% excitation force enhancement identified earlier, where constructive scattering from the attenuators concentrates wave energy at the PA locations.

The mixed array achieves superior performance at this period because the attenuators operate near their optimal condition ($\lambda/2 \approx 23.6$ m, close to the 25 m arm length) thus improving their response (+74%), thus generating strong scattered and radiated fields that constructively interfere at PA locations, while the modest radiation damping increase (+5.9%) allows PAs to efficiently convert this enhanced excitation into captured power rather than re-radiating it.

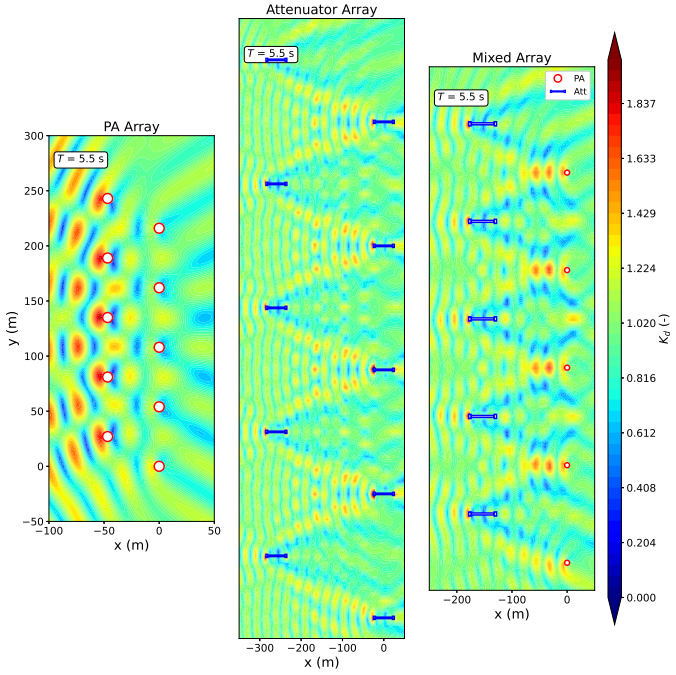
At $T = 6.0$ s, the wave field structure shifts noticeably, and the attenuator mono-array emerges as the best-performing configuration. The attenuator array produces reasonably coherent interference patterns with substantial $K_d$ amplification zones, benefiting from effective wave capture even as the wavelength ($\lambda_w/2 \approx 28.1$ m) slightly exceeds the optimal arm-length matching condition (still lower than $T = 5.5$ s as seen in the $q$-factor in Figure 5.27).

In contrast, the mixed array shows diminished PA hotspots and reduced contrast compared to $T = 5.5$ s. The longer wavelength strengthens radiative cross-coupling between device types (+16.4% radiation damping for PAs), causing energy absorbed by PAs to be partially transferred back to attenuator motions rather than being extracted by the PTO system.

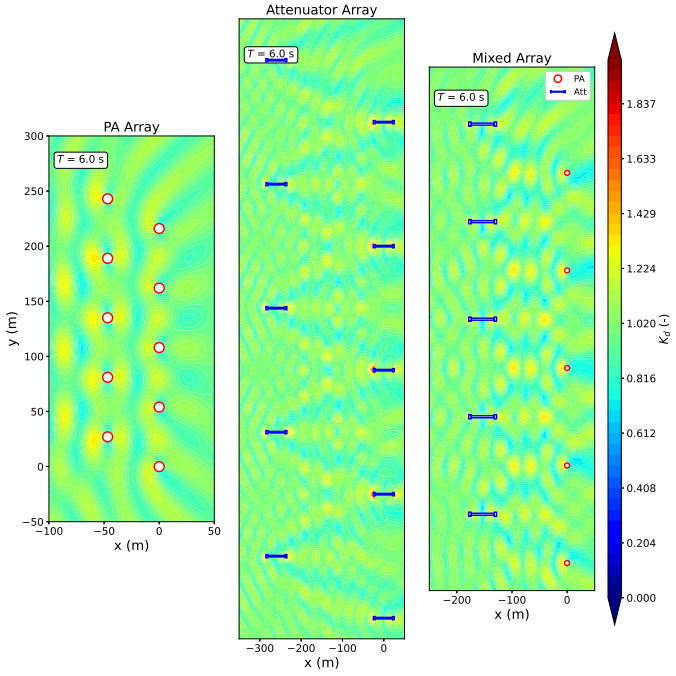
The attenuator mono-array outperforms the mixed configuration at this period because it avoids these inter-device energy losses entirely—each attenuator captures and converts wave energy independently without the parasitic coupling that penalises PAs in the mixed arrangement. The wake regions downstream of devices in the mixed array show altered shadowing patterns compared to the attenuator mono-array, visually confirming that the combined scattered field redistributes energy less favourably when cross-coupling effects dominate.

The decomposition into diffraction and radiation field percentages, computed as $|\eta_d|/|\eta_d+\eta_r|$ and $|\eta_r|/|\eta_d+\eta_r|$ respectively, provides direct visual evidence of the coupling mechanisms underlying these performance differences. At $T = 5.5$ s, the PA mono-array exhibits an almost uniformly diffraction-dominated wave field (exceeding 80% across the domain), with radiation contributions remaining localised to the immediate device vicinity. This indicates that PAs at this period operate primarily as scatterers rather than strong radiators, which is energetically favourable since diffraction represents wave-body interaction without energy loss.

The attenuator array displays more spatially varied patterns, with distinct radiation hotspots (40–60%) emanating from each device and interfering constructively between adjacent units. In the mixed array, the radiation field shows localised peaks near both device types, but crucially these hotspots remain spatially separated rather than forming connected corridors—the radiative coupling between PAs and attenuators has not yet established efficient energy transfer pathways, allowing each device type to retain its




(a) Disturbance coefficient $K_d$ for $T = 5.5$ s




(b) Disturbance coefficient $K_d$ for $T = 6.0$ s

Figure 5.29.: Comparison of the disturbance coefficient $K_d$ across the mono and mixed arrays for different wave periods under head-on wave conditions (The incoming wave direction is from left to right)

absorbed energy for PTO extraction.

At $T = 6.0$ s, the radiation percentage maps reveal a fundamentally different coupling regime. The PA mono-array remains diffraction-dominated, but the mixed array now exhibits pronounced radiation corridors extending between the PA column and the attenuator column. These elevated radiation percentage zones (50–70%) connecting the two device types visually manifest the strengthened cross-coupling identified in the radiation damping matrices. Energy radiated by oscillating PAs propagates toward the attenuators and vice versa, establishing parasitic transfer loops that reduce net power extraction.

The attenuator mono-array, by contrast, shows a more uniform diffraction-dominated field at this period, with radiation contributions confined to device-local regions. This spatial confinement indicates that attenuators operating slightly beyond their optimal wavelength condition radiate less aggressively, allowing them to function as efficient absorbers without significant inter-device radiative losses. The absence of cross-device-type coupling pathways in the mono-array configuration explains its superior performance at $T = 6.0$ s: each attenuator operates as an independent energy harvester without the energy redistribution penalties that afflict the mixed arrangement.

### COMPARING POWER FROM INDIVIDUAL DEVICES



The power comparison between the individual device types in the mono-arrays and mixed arrays further show what we have been discussing. At $T = 5.5$ s, the PA mono-array suffers from destructive interference (Fig. 5.32), with an array-averaged power of 9.7 kW per device compared to 13.3 kW for an isolated PA—a 27% reduction. However, when placed in the mixed configuration alongside attenuators (Fig. 5.34a), PAs achieve 12.5 kW per device, representing a 28.9% improvement over the mono-array performance.

The attenuators benefit even more dramatically: in the mixed array they produce 9.4 kW per device (Fig. 5.34b), compared to just 2.7 kW in the mono-array (Fig. 5.33)—a 3.5× enhancement. This remarkable improvement directly correlates with the wave field observations: the $K_d$ plots show that attenuators in the mixed array experience elevated disturbance coefficients in regions where PA-scattered fields constructively superpose with the incident wave. The attenuator RAO enhancement and PA RAO enhancement identified in the hydrodynamic analysis manifest directly in these power outputs.

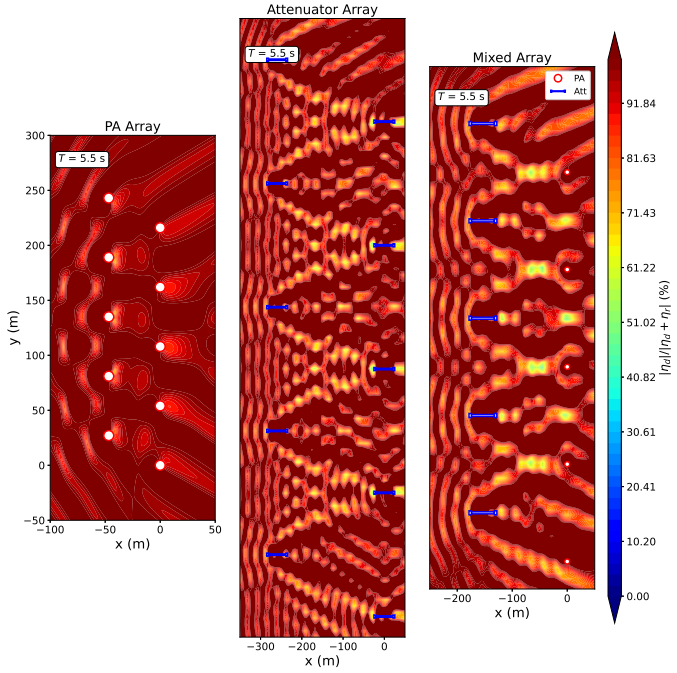
At $T = 6.0$ s, the mixed array advantage diminishes asymmetrically between device types. PAs in the mixed configuration still outperform their mono-array counterparts (13.2 kW vs 9.8 kW, a 34.7% improvement; compare Figs. 5.34a and 5.32), benefiting from continued excitation enhancement despite increased radiation damping .

However, the attenuators show a dramatically reduced benefit: 5.4 kW in the mixed array versus 4.9 kW in the mono-array (Figs. 5.34b and 5.33)—only a 10% improvement compared to 3.5× at $T = 5.5$ s. The longer wavelength ($\lambda_w = 56.2$ m) establishes efficient radiative coupling pathways where energy scattered by PAs toward attenuators is partially re-radiated back into the domain rather than being captured. The attenuator RAO enhancement drops from +74.4% at $T = 5.5$ s to just +1.8% at $T = 6.0$ s, confirming that the cross-coupling mechanism that benefited attenuators at shorter periods becomes neutral or slightly detrimental as wavelength increases beyond the optimal condition.

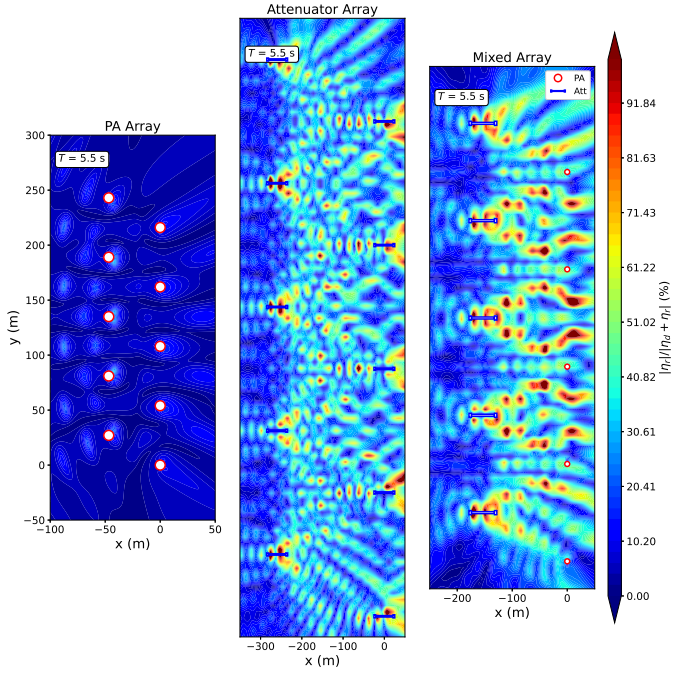
The high improvement in the attenuator RAO at $T = 5.5$ s compared to at 6 s is also why the $M$-factor at this period is so much higher, since the relative capture width for the attenuator is 50 m while for the PA, it is 9 m. Hence the enhancement in the power absorption for the attenuator has a much larger influence on the $M$-factor as compared to the PA.

## 5.4. DEEP WATER - ANALYSIS IN IRREGULAR WAVES

This section provides further insights into the 10 device rectangular configuration (5 PAs + 5 attenuators) with $4C$ spacing and how it behaves with respect to the mono PA and

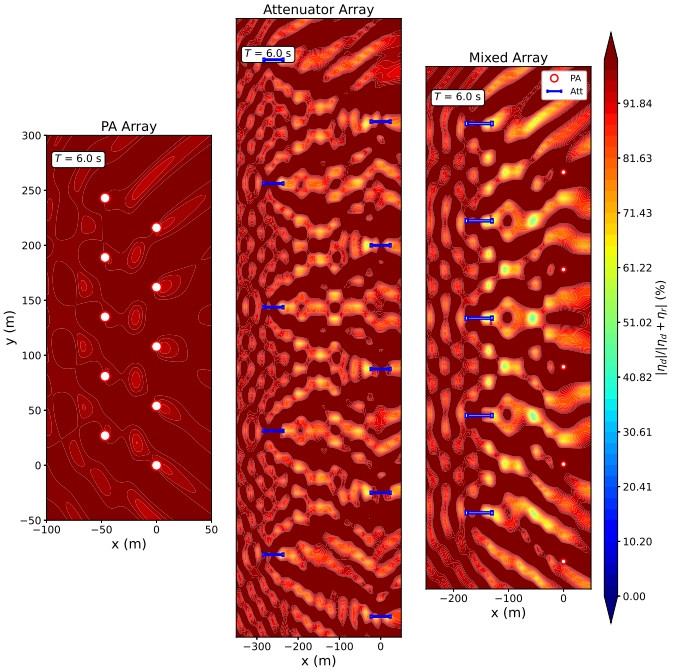



(a) Percentage diffraction in perturbed wave field

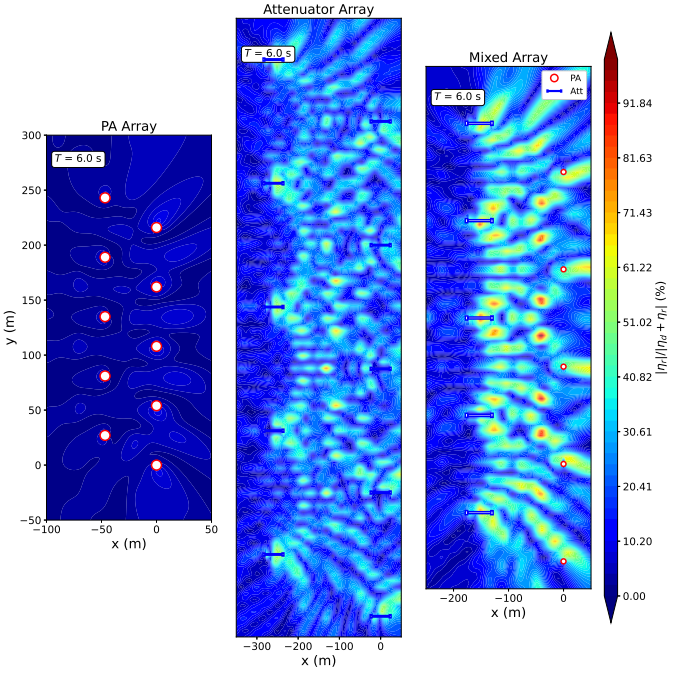



(b) Percentage radiation in perturbed wave field

Figure 5.30.: Percentage contributions of the diffraction and radiation to the perturbed wave field at $T$=5.5 s (The incoming wave direction is from left to right)




(a) Percentage diffraction in perturbed wave field




(b) Percentage radiation in perturbed wave field

Figure 5.31.: Percentage contributions of the diffraction and radiation to the perturbed wave field at $T$=6.0 s (The incoming wave direction is from left to right)

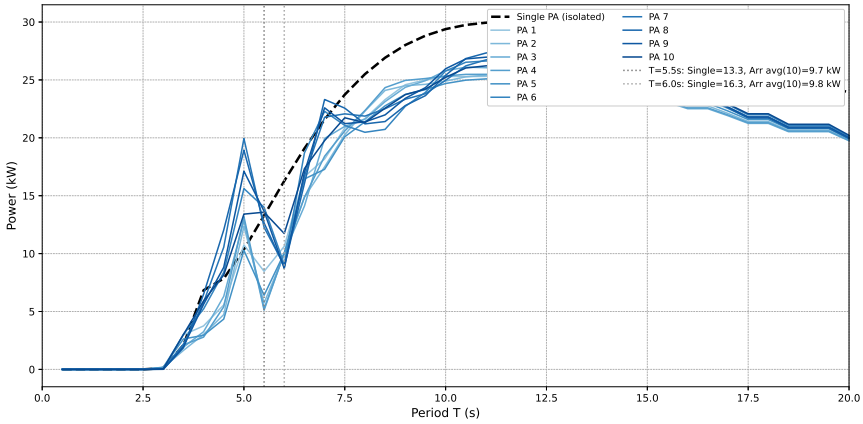



Figure 5.32.: Regular wave power output for the PA mono-array (10 devices) at $\theta = 0°$. Individual device power (coloured lines) compared against an isolated single PA (black dashed). Vertical dotted lines indicate $T = 5.5$ s and $T = 6.0$ s. The array-averaged power (9.7 kW at $T = 5.5$ s, 9.8 kW at $T = 6.0$ s) is significantly below the isolated device (13.3 kW and 16.3 kW respectively), indicating destructive hydrodynamic interference.



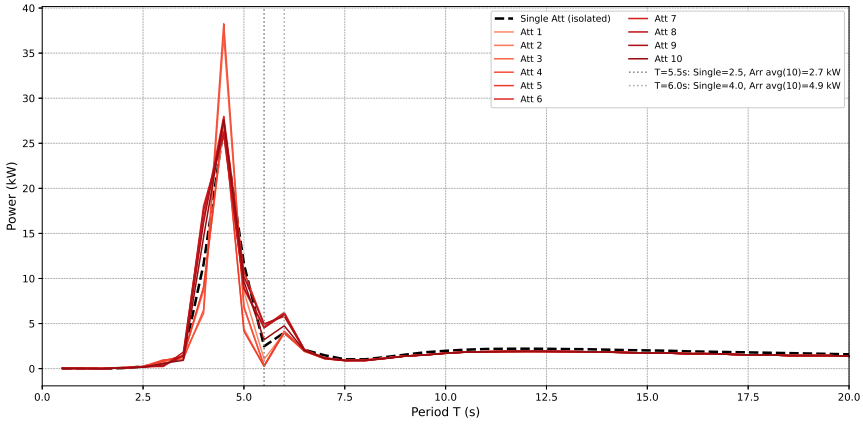
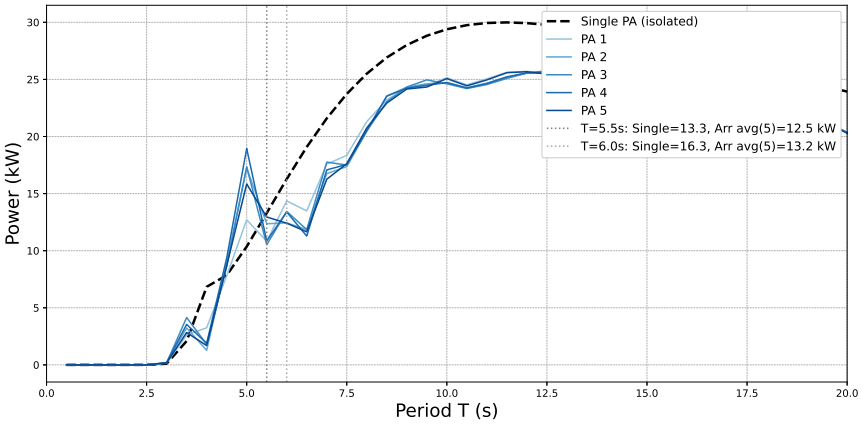
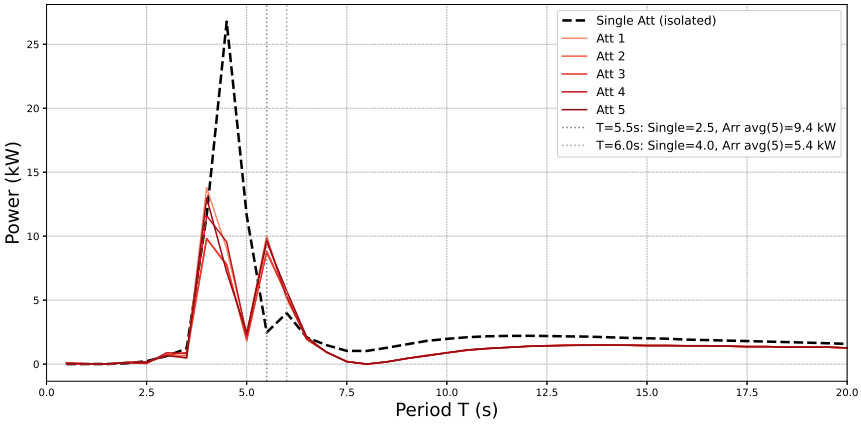



Figure 5.33.: Regular wave power output for the attenuator mono-array (10 devices) at $\theta = 0°$. Individual device power (coloured lines) compared against an isolated single attenuator (black dashed). The array-averaged power (2.7 kW at $T = 5.5$ s, 4.9 kW at $T = 6.0$ s) shows modest array interaction effects compared to the isolated device (2.5 kW and 4.0 kW respectively).




(a) PAs in mixed array (5 devices)




(b) Attenuators in mixed array (5 devices)

Figure 5.34.: Regular wave power output for devices within the mixed array configuration (5 PAs + 5 Attenuators) at $\theta = 0°$. (a) PAs achieve 12.5 kW at $T = 5.5$ s and 13.2 kW at $T = 6.0$ s, outperforming the mono-array (Fig. 5.32). (b) Attenuators achieve 9.4 kW at $T = 5.5$ s—a 3.5× enhancement over the mono-array (Fig. 5.33)—but only 5.4 kW at $T = 6.0$ s, indicating period-dependent synergy between device types.

attenuator arrays in irregular waves.

### PERFORMANCE BASED ON Q- AND M-FACTORS

This configuration was obtained as the best configuration in irregular waves with mean $q$ and $M$-factor greater than 1 for 9 directions. Here the results from two directions are selected which show symmetric behavior for the mono arrays, but asymmetric for the mixed arrays - 0 and 180°.

The $q$-factor and $M$-factor comparison between $\theta = 0°$ and $\theta = 180°$ for irregular waves (Figs. 5.35a and 5.35b) reveals a fundamental asymmetry in mixed array performance that is absent in mono-arrays. For this analysis, the PTO damping coefficient is optimised for each isolated device per sea state and subsequently applied to the corresponding devices within the array, ensuring a consistent baseline for comparing array interaction effects.

The PA and attenuator mono-arrays exhibit near-perfect directional symmetry, with $q$-factor differences below 0.05% between head-on and following sea conditions. The PA mono-array remains marginally destructive across all peak periods ($q \approx 0.95$–$0.99$), while the attenuator mono-array maintains constructive interactions throughout the $T_p = 5$–$15$ s range ($q \approx 1.01$–$1.20$).

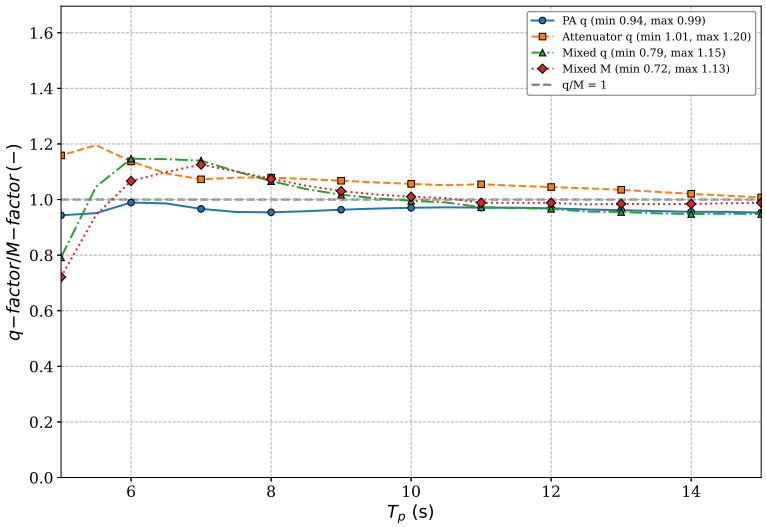
In contrast, the mixed array displays pronounced directional dependence: at $\theta = 0°$, constructive effects ($q > 1$) persist from $T_p = 5.5$ s to 9.5 s, whereas at $\theta = 180°$ this constructive range contracts to $T_p = 5.0$–$7.5$ s. The peak mixed array $q$-factor of 1.147 occurs at $T_p = 6.0$ s for $\theta = 0°$, representing a 15.9% improvement over the PA mono-array and marginally exceeding the attenuator mono-array by 0.8%. This directional sensitivity arises because the order in which waves encounter the different device types fundamentally alters the scattering and radiation coupling pathways—at $\theta = 0°$, the PA column acts as an initial diffractor that redirects wave energy toward the attenuator column under favourable phase conditions.

The $M$-factor, which normalises performance by the capture width ratio and thus accounts for the substantial dimensional differences between PAs (diameter $D = 9$ m) and attenuators (width $L = 50$ m), further amplifies this directional contrast. At $\theta = 0°$ and $T_p = 6$–$7$ s, the $M$-factor exceeds unity, indicating that the mixed array achieves higher hydrodynamic efficiency per unit characteristic length than the weighted average of both mono-farms operating independently. This efficiency gain vanishes at $\theta = 180°$, where the $M$-factor remains close to or below unity across most periods. The physical interpretation connects directly to the wave field analysis: at $\theta = 0°$, the diffraction-dominated fields generated by the front-row devices constructively enhance excitation forces on the rear-row devices without establishing significant radiative losses.

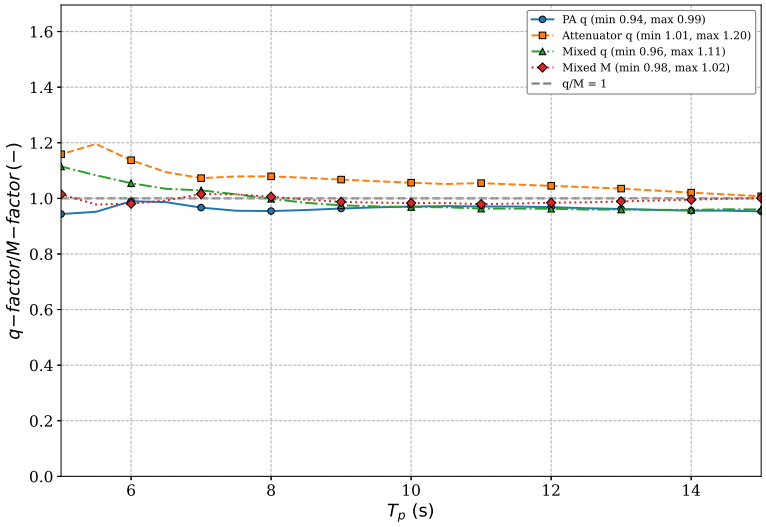
Conversely, at $\theta = 180°$, the reversed device ordering creates less favourable phase relationships, and the scattered fields from the PA devices interfere destructively with the incident wave at the trailing device locations. These findings underscore that mixed array orientation relative to the dominant wave direction is a critical design parameter—optimal siting can exploit the directional asymmetry to maximise energy capture, while suboptimal orientation may negate the synergistic benefits that mixed configurations offer over conventional mono-farms.

### COMPARING POWER FROM INDIVIDUAL DEVICES

The individual device power outputs (Figs. 5.36–5.38) provide physical insight into the $q$-factor and $M$-factor trends observed in Fig. 5.35. In the PA mono-array (Fig. 5.36a), total array power increases from 48.3 kW at $T_p = 5.5$ s to 126.2 kW at $T_p = 10$ s, yet the array-averaged power per device consistently falls below the isolated PA output, yielding $q < 1$ across all periods. This destructive interference arises from PA-PA hydrodynamic coupling, where devices in shadowed positions experience reduced wave excitation. Conversely, the attenuator mono-array (Fig. 5.36b) exhibits the opposite spectral trend—total power decreases from 107.1 kW at $T_p = 5.5$ s to 29.5 kW at $T_p = 10$ s—while maintaining $q > 1$ throughout the period range due to constructive attenuator-attenuator interactions.

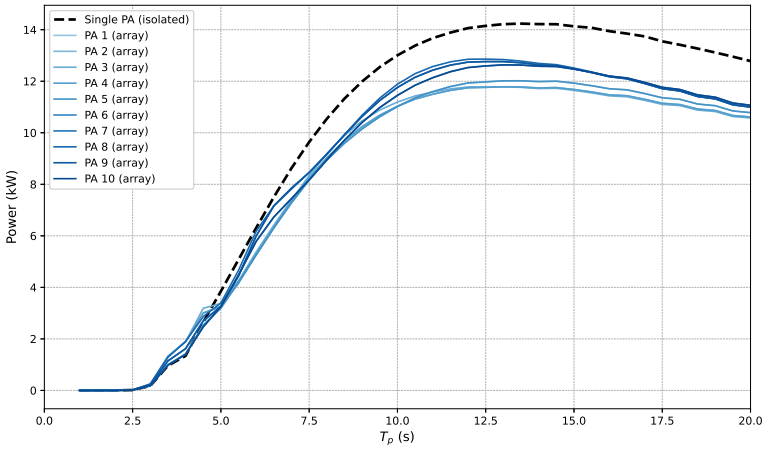



(a) $\theta = 0°$ (head-on sea)

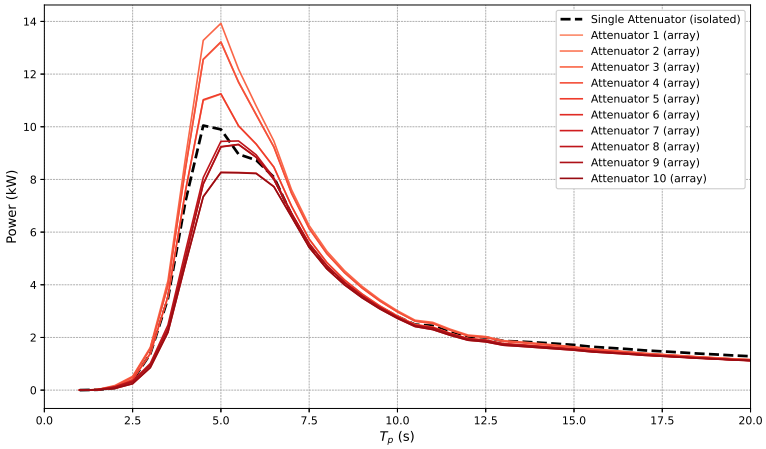



(b) $\theta = 180°$ (following sea)

Figure 5.35.: Comparison of $q$-factors for PA mono-array, attenuator mono-array, mixed array, and $M$-factor for the mixed array under irregular waves ($H_s = 1.5$ m). PTO damping is optimised for isolated devices per sea state and applied to array configurations. (a) At $\theta = 0°$, the mixed array achieves constructive interactions ($q > 1$) over $T_p = 5.5$–$9.5$ s with peak $q = 1.147$ at $T_p = 6.0$ s. (b) At $\theta = 180°$, the constructive range contracts to $T_p = 5.0$–$7.5$ s, demonstrating significant directional asymmetry in mixed array performance. The mono-arrays (PA and attenuator) show identical $q$-factors at both directions, confirming their directional symmetry. The horizontal dashed line indicates $q/M = 1$.

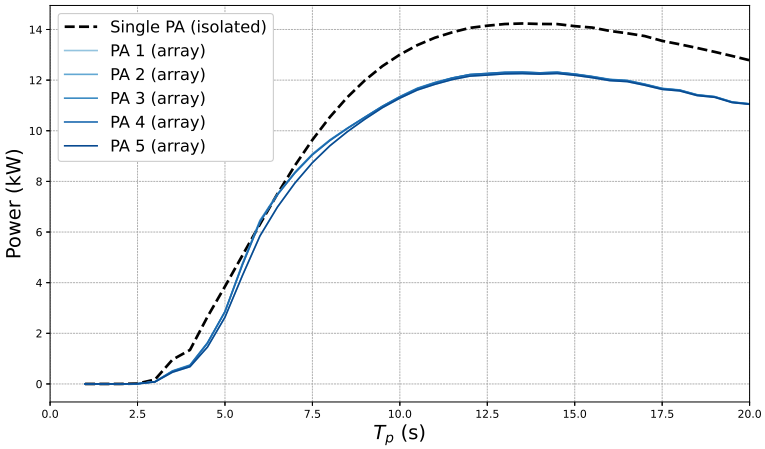



(a) PA mono-array (10 devices)

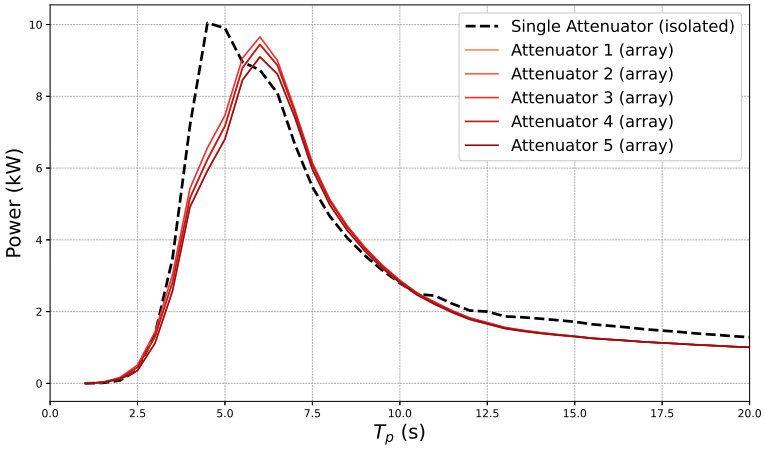



(b) Attenuator mono-array (10 devices)

Figure 5.36.: Individual device power output in mono-arrays under irregular waves ($H_s = 1.5$ m). PTO damping is optimised for each isolated device per sea state. (a) PA mono-array shows increasing power with peak period, with array-averaged performance below the isolated device ($q < 1$) indicating destructive interference. (b) Attenuator mono-array shows decreasing power with peak period, with array-averaged performance exceeding the isolated device ($q > 1$) indicating constructive interference. Note: Attenuator mono-array exhibits directional symmetry; the $\theta = 180°$ plot is representative of both head-on and following sea conditions.

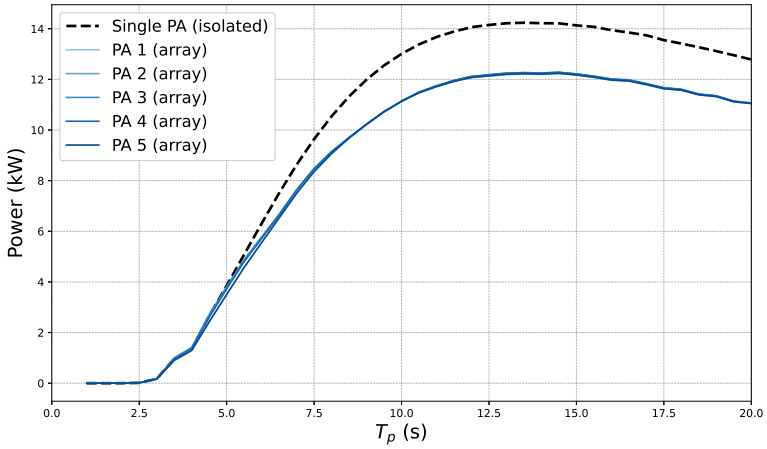



(a) PAs in mixed array (5 devices)

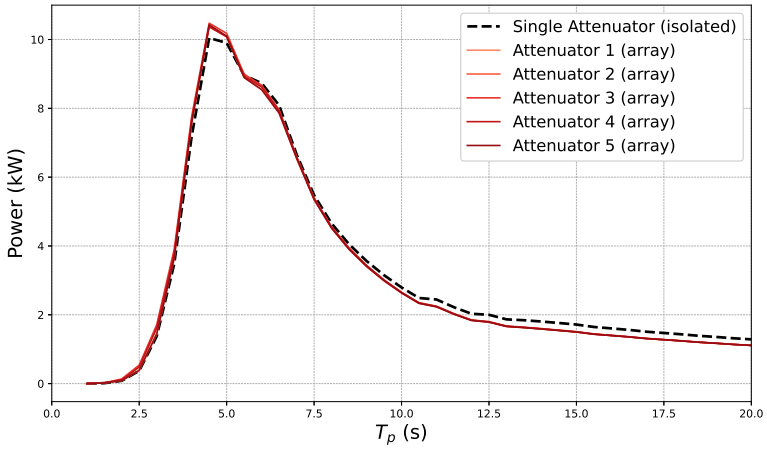



(b) Attenuators in mixed array (5 devices)

Figure 5.37.: Individual device power output in the mixed array at $\theta = 0°$ under irregular waves ($H_s = 1.5$ m). (a) PAs in the mixed configuration show enhanced performance compared to the PA mono-array, benefiting from scattered fields generated by neighbouring attenuators. (b) Attenuators in the mixed configuration maintain constructive interactions, particularly at shorter peak periods where PA-generated diffraction fields concentrate wave energy at attenuator locations.




(a) PAs in mixed array (5 devices)




(b) Attenuators in mixed array (5 devices)

Figure 5.38.: Individual device power output in the mixed array at $\theta = 180°$ under irregular waves ($H_s = 1.5$ m). Compared to $\theta = 0°$ (Fig. 5.37), the reversed wave approach direction alters the scattering dynamics, resulting in reduced constructive effects and a narrower range of peak periods with $q > 1$.

Crucially, the mixed array $q$-factor is defined relative to *isolated* devices: $q_{mixed} = P_{mixed}/(m \cdot P_{PA} + n \cdot P_{Att})$. Thus, $q_{mixed} > 1$ indicates that the total mixed array power exceeds what five isolated PAs and five isolated attenuators would produce independently—this does not require PAs to exhibit constructive self-interactions, but rather that the heterogeneous PA-attenuator cross-interactions are sufficiently beneficial to overcome the baseline.

The mixed array power distributions at $\theta = 0°$ (Fig. 5.37) and $\theta = 180°$ (Fig. 5.38) reveal how these cross-device-type interactions generate the observed $q$-factor enhancement. At $\theta = 0°$, the total mixed array power reaches 86.2 kW at $T_p = 6.0$ s, yielding $q = 1.147$. This value exceeds the attenuator mono-array $q$-factor (1.137) despite containing only five attenuators instead of ten, because the PAs in the mixed configuration benefit from attenuator-scattered fields that enhance their excitation forces—the same mechanism identified in the regular wave analysis where PA excitation increased by +41–61% in the mixed array. The PAs thus contribute positively not through constructive PA-PA interactions (which remain absent), but through favourable PA-attenuator coupling that allows them to capture energy from the modified wave field.

At $\theta = 180°$, the total power drops to 79.3 kW at $T_p = 6.0$ s ($q = 1.055$), representing an 8% reduction compared to $\theta = 0°$. The reversed wave direction disrupts the favourable scattering geometry: attenuators now encounter the incident wave first, and their scattered fields reach the PAs with less constructive phase alignment. This directional dependence directly manifests in the $M$-factor, which exceeds unity at $\theta = 0°$ (superior capture width ratio) but approaches unity at $\theta = 180°$, underscoring that realising the full potential of mixed WEC farms requires optimising array orientation relative to the dominant wave climate.



## 5.5. Limitations of the $q$- and $M$ factors

Before consolidating the findings of this chapter, it is worth acknowledging that the $q$- and $M$-factors used throughout this analysis, while informative, do have some drawbacks when it comes to array performance.

- The $q$- and $M$-factors characterise array performance in hydrodynamic and geometry-normalised terms, respectively, but neither reflects the cost of deploying and operating the array. Assessing economic feasibility therefore requires a dedicated techno-economic analysis.
- The $q$- and $M$-factors inherit the limitations of PTO tuning: a well-tuned isolated device sets a high baseline that can deflate $q$ and $M$ when the in-array devices are tuned without accounting for inter-device interactions.
- Similarly, the $q$- and $M$-factors do not account for the suitability of the device design itself (geometry, natural frequency, DOFs) for the target site, even though this is a primary determinant of absolute energy yield.
- Other factors such as spatial footprint, mooring loads, fatigue damage, and survivability cannot be derived from $q$ and $M$-factors

## 5.6. Conclusions

This chapter examined the hydrodynamic behaviour of mixed wave energy converter (WEC) arrays relative to mono-type arrays in both shallow and deep water conditions, using the $q$-factor and $M$-factor as primary performance metrics. The analysis combined regular and irregular wave conditions with detailed investigations of hydrodynamic coupling, wave-field characteristics, and device-level power absorption. Together, these results provide a physically consistent explanation of when and why mixed arrays outperform conventional mono arrays.

In shallow water under regular waves, mixed arrays composed of large PAs and flaps exhibit a higher, but strongly direction- and period-dependent, performance ceiling than

mono arrays. For the best-performing configuration (10 devices, 5 PAs + 5 flaps, spacing $L_m = 10C$), the mixed array achieved $q > 1$ in two directions and $M > 1$ in 10 out of 12 directions. At head-on wave incidence and a wave period of $T = 6.0$ s, the mixed array reached a peak $q$-factor of approximately 1.6 and an $M$-factor of 2.25, significantly exceeding the performance of the PA mono array ($q \approx 0.6$) and the flap mono array ($q \approx 0.75$). These gains coincide with coherent and spatially extended wave-field amplification, where the disturbance coefficient $K_d$ reaches values of approximately 2.1 in front of the PA row and up to 1.8 around the flaps, indicating strong constructive interference between radiated and diffracted wave components.

The physical origin of this enhancement lies in favourable hydrodynamic cross-coupling and phase alignment of the radiated wave fields. At $T = 6.0$ s, radiation damping cross-coupling between device types is predominantly constructive, with summed PA→Flap and Flap→PA contributions of $+6.43 \times 10^6$ Ns and $+5.65 \times 10^6$ Ns, respectively, and 32 out of 50 coupling terms being positive. As a result, the PA heave RAO increases by approximately 175%, flap excitation forces increase by 34%, and the mixed array generates a coherent downstream wave field that reinforces collective device motion.

In contrast, at $T = 6.5$ s the mixed-array spacing corresponds to a half-integer multiple of the wavelength ($L_m \approx 2.5\lambda$), leading to widespread destructive interference in the wave field. The radiation damping cross-coupling reverses sign (only 11 positive versus 39 negative terms), excitation forces decrease by 24% for the PA and 16% for the flap, and the flap pitch RAO is reduced by approximately 55%. The associated wave fields exhibit alternating regions of amplification and attenuation, and the mixed array behaves similarly to the PA mono array, while the mono flap array dominates the response with $K_d$ values reaching up to 2.7 in the rear row. These results demonstrate that wave-field coherence, governed primarily by the spacing-to-wavelength ratio, is a driver for both the gains and losses observed in mixed arrays.

Under irregular waves in shallow water with passive control, the same physical mechanisms remain operative, although their effects are spectrally smoothed. The selected mixed configuration (10 devices, $L_m = 4C$) attains a mean $q$-factor of 1.19 and a mean $M$-factor of 1.4 over the $T_p = 3$–$12$ s range, with $M > 1$ in 10 out of 12 directions. For head-on wave incidence, the mixed array consistently produces broader and more spatially coherent wave fields than either mono configuration, yielding $q$-factors approaching 1.2 across a wide range of peak periods.

In contrast, for waves incident at 90°, array performance deteriorates markedly. The point absorbers in both the mono and mixed arrays underperform relative to the isolated device due to predominantly destructive interactions. For the flap, this incidence angle leads to negligible excitation and almost no power absorption in the mono array. In the mixed configuration, however, hydrodynamic interaction with the PAs induces small but non-zero flap motions, allowing limited power absorption to persist even under these unfavourable conditions.

In deep water under regular waves, mixed arrays composed of PAs and attenuators display a different balance between peak power capture and spatial efficiency. While attenuator mono arrays generally achieve higher mean $q$-factors, the mixed array (10 devices, 5 PAs + 5 attenuators, spacing $L_m = 6C$) attains $M > 1$ in 8 out of 12 directions. This behaviour is reflected in the wave fields, where the mixed array generates more evenly distributed radiation patterns than either mono configuration. Although the resulting local amplification is weaker than that of the attenuator mono array, the mixed configuration redistributes absorbed energy more effectively across devices and directions, leading to superior capture width efficiency. This highlights that, in deep water, mixed arrays primarily benefit from enhanced spatial utilisation of the wave field rather than from maximising peak amplification at specific locations.

Across all cases, device-level power absorption confirms that mixed arrays benefit from complementary dynamics. PAs contribute strongly at shorter periods (typically 4–6 s), while flaps and attenuators dominate at longer periods (approximately 6.5–11 s). This staggered absorption leads to a broader effective bandwidth, which is reflected in spatially extended and coherent wave fields and results in sustained $M$-factors greater than unity over a wide range of conditions.

Overall, this chapter demonstrates that mixed WEC arrays can significantly outperform mono arrays by generating coherent, spatially extended wave fields that promote constructive hydrodynamic coupling and collective behaviour. However, these same coupling mechanisms can also induce severe performance penalties when array geometry or wave direction disrupts wave-field coherence. The results underline the necessity of directionally aware layout design and provide the physical foundation for the techno-economic analyses presented in the subsequent chapter, where the hydrodynamic gains identified here are translated into array-level spatial footprint and LCOE implications.

# 6

# ECONOMICS OF WAVE ENERGY ARRAYS

*Measure what is measurable, and make measurable what is not so*

Galileo Galilei


## ABSTRACT

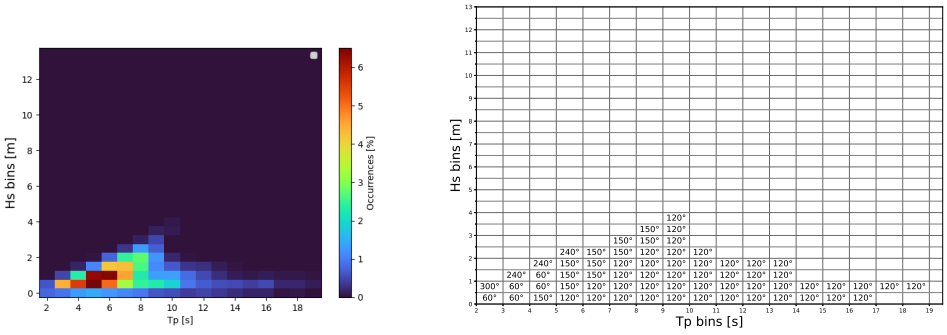
*This chapter presents a techno-economic comparison of mono and mixed wave energy converter (WEC) arrays in shallow- and deep-water environments. Depth-dependent cost assumptions are considered with array-level performance obtained from multibody hydrodynamic interaction analyses in HAMS-MREL. Device-level power matrices are employed exclusively to characterise the performance of individual devices and to establish rated power constraints. In contrast, array-level energy production is evaluated by explicitly accounting for hydrodynamic interactions between devices as well as wave-directional effects. Results show that array-level capacity factors are generally lower than single-device values, particularly for directional converters, yet mixed arrays consistently achieve capacity factors comparable to the best-performing mono-arrays. In shallow waters, mixed wave energy converter arrays occupy a favourable intermediate regime, achieving substantially higher packing densities than PA mono-arrays while maintaining markedly lower LCOE than flap-only configurations, thereby offering a particularly attractive solution under spatial constraints. In deep-water deployments, where space limitations are less critical and installation costs dominate, mixed arrays outperform attenuator and PA mono-arrays in terms of LCOE while simultaneously reducing the required array footprint. Overall, the results demonstrate that mixed WEC arrays constitute a robust and economically competitive deployment strategy, effectively balancing energy production, cost, and spatial efficiency at the array scale.*

Three representative cases are considered to examine the economic performance of mono and mixed arrays: two deployed in shallow water and the other in deep water. The two cases for shallow water considers devices operating in active and passive control. The same wave energy converter devices used in the preceding analyses are adopted here to ensure consistency in the economic assessment across array configurations.

## 6.1. SCATTER DIAGRAM AND DOMINANT DIRECTION PLOT IN SHALLOW AND DEEP WATERS

Figure 6.1a presents the scatter diagram adopted for the shallow-water analysis, which has previously been used to evaluate the performance of mono and mixed arrays comprising small and large PAs and oscillating flaps. To complement this, Figure 6.1b illustrates the dominant wave direction associated with each sea state in the same scatter diagram based on the scatter diagram.

For each hourly time series, WAVEWATCH III which was used to create the ECHOWAVE dataset [155] obtains the peak direction. Based on all the occurrences for a given sea state, the most recurring direction is selected as the dominant direction for that sea state. These reflect the data from 1991-2021 and are utilized to calculate the Annual Energy Production (AEP) from single devices and arrays, providing the capacity factor.



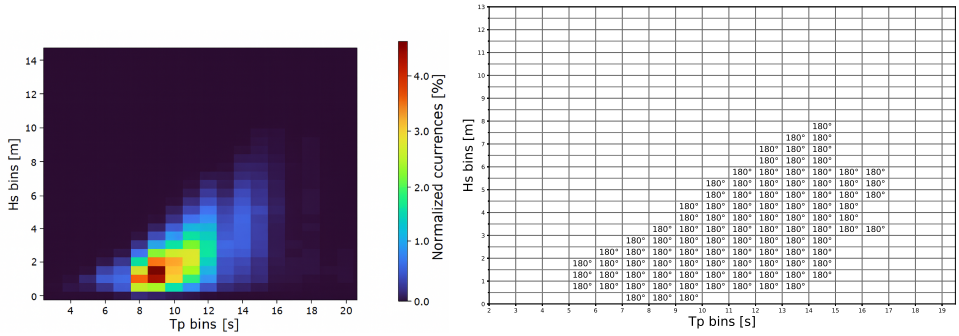

(a) (b)

Figure 6.1.: Scatter diagram and dominant direction plot in shallow water (Lat 53.6°, Lon 6.3° - Netherlands)

Figure 6.2a and Figure 6.2b show the scatter diagram and dominant wave direction plot for the deep water. It should be noted, that for the single sea state, the power matrix is created only for the most dominant direction so as to obtain conservative estimations of the capacity factors (only applies to the flap and attenuator). For the arrays however, these are utilized to obtain the realistic power estimation for the considered locations. The distribution of occurrences per direction based on the scatter diagram are shown in Table 6.1.

Table 6.1.: Wave direction distribution for deep and shallow water sites

| Direction (°) | Deep Water (%) | Shallow Water (%) |
|---|---|---|
| 60 | 0.06 | 15.20 |
| 120 | 0.00 | 44.41 |
| 180 | 99.94 | 38.75 |
| 240 | 0.00 | 1.18 |
| 300 | 0.00 | 0.46 |




(a) (b)

Figure 6.2.: Scatter diagram and dominant direction plot in deep water (Lon -9.64°, Lat 52.78° - Ireland)

## 6.2. Cost and performance evaluation of single devices

WEC cost assumptions in this study follow the depth-based classification and economic framework adopted in [14], where capital and operational costs are primarily linked to the deployment environment rather than device geometry alone.

Shallow-water deployments (0–20 m depth) benefit from reduced installation complexity, shorter export distances, and improved accessibility, leading to lower capital and operational expenditures. Intermediate and farshore deployments (50-150 m depth) are associated with increased costs due to deep-water mooring systems, dynamic power cables, harsher environmental loading, and more complex offshore installation and maintenance operations. Accordingly, shallow devices are characterised by baseline CAPEX values of approximately 3 M€/MW with fixed OPEX of 5% of CAPEX per year, whereas farshore devices are characterised by higher baseline CAPEX values of approximately 4.5–5 M€/MW and OPEX of 5–10% per year depending on the device. These costs represent TRL 6-7 WECs not benefitting from economics of scale.

Within this framework, six WEC device archetypes are considered across passive and active control strategies: a shallow-water flap, two shallow-water PA variants (12 m dia big PA for passive control and 6 m dia small PA with active control), a farshore PA, and a farshore attenuator.

For shallow-water deployments, both passive and active control strategies are analysed to quantify the economic implications of advanced control implementation through the differences in power production. The flap-type device directly follows the shallow-water baseline assumptions, as it is bottom-mounted and does not require moorings or dynamic electrical connections; this holds for both passive and active control variants.

The shallow-water PAs, being deployed in the same depth range, remain floating devices and therefore require mooring systems and dynamic cabling; their CAPEX is therefore assumed at an intermediate value of 3 M€/MW, and retaining the shallow-water fixed OPEX rate of 5% per year.

For farshore deployments, only passive control is considered. The attenuator represents the reference farshore device class and follows the farshore baseline assumptions of CAPEX of 5 M€/MW and OPEX of 10%. For the farshore PA, a slightly lower CAPEX of 4.5 M€/MW is assumed with OPEX of 5%, reflecting reduced deep-water mooring lines and dynamic export cable requirements compared to the attenuator.

This approach maintains consistency with the underlying energy-system modelling assumptions used in [14] while allowing clear differentiation between device types, deployment environments, and control strategies. The cost assumptions are summarised in Table 6.2.

While the shallow-water point absorber costs are not explicitly defined in [14], the intermediate CAPEX values adopted here reflect the presence of mooring systems

Table 6.2.: Cost assumptions for the WEC device types used in this study.

| Device | Deployment class | Control | CAPEX (M€/MW) | CAPEX (€/kW) | Fixed OPEX (% of CAPEX/yr) |
|---|---|---|---|---|---|
| Flap | Shallow | Passive/Active | 3.0 | 3000 | 5% |
| PA (Big) | Shallow | Passive | 3.5 | 3500 | 5% |
| PA (Small) | Shallow | Active | 3.0 | 3500 | 5% |
| PA | Farshore | Passive | 4.5 | 4500 | 5% |
| Attenuator | Farshore | Passive | 5.0 | 5000 | 10% |

and dynamic cabling absent in bottom-mounted devices, while retaining the reduced installation and maintenance advantages associated with shallow-water deployment. Notably, the CAPEX assumptions for active and passive control variants are kept identical, as the primary cost driver remains the deployment environment and device infrastructure with the control being considered directly in the rated power of the device.

### SINGLE DEVICE POWER AND ECONOMICS

The power matrices for the six considered devices are shown in Figure 6.3. The rated power for any WEC is usually driven by the geometry of the WEC and limited by the depth condition and PTO limits. The PTO limits are expressed through force and displacement constraints to ensure the safety of the device including the PTO.

When considering passive control methodolgy, no constraint is imposed and while a displacement constraint is imposed in the active control methodology, there is no limit on the PTO force. Therefore, to ensure that these limits are considered, the rated power for the single devices is capped to the $99^{th}$ percentile of the maximum power obtained from the power matrix (uncapped) considering the scatter diagram for the corresponding location.

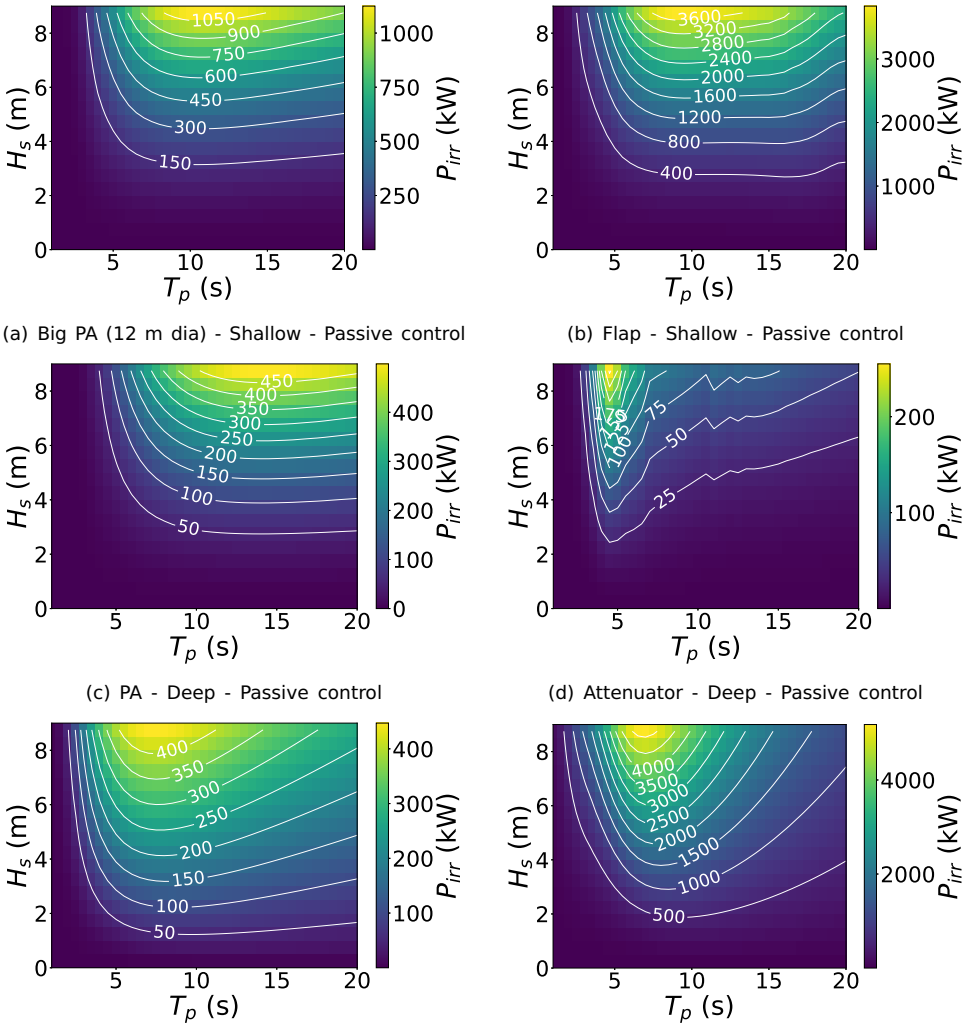
These values are thus set as hard limits to obtain the Capacity Factor (CF), AEP and LCOE from both the single devices and arrays. The rated power for the single devices are summarized in Table 6.3. While power capping does not explicitly constrain PTO force or displacement, it provides a practical means of accounting for rated capacity limits in the power calculation [144]. For the single devices such as flaps and attenuators, the power matrix and rated power are calculated based on the most dominant direction to keep the CF, AEP and LCOE conservative. This also results in lower q-factors for the flap and attenuator when doing array analyses later.

Table 6.3.: Rated power output for single WEC devices

| Device | Site | Control | $P_{rated}$ (kW) |
|---|---|---|---|
| PA (9m) | Deep | Passive | 300 |
| Attenuator | Deep | Passive | 50 |
| Big PA (12m) | Shallow | Passive | 150 |
| Flap | Shallow | Passive | 550 |
| Small PA (6m) | Shallow | Active | 150 |
| Flap | Shallow | Active | 1200 |

Based on the rated power, the CAPEX, OPEX and total costs of the single devices can be estimated. Furthermore, using the scatter diagram and power matrices, the AEP and LCOE can be estimated.

The Levelized Cost of Energy (LCOE) was estimated using the Capital Recovery Factor (CRF) method, which annualizes the capital expenditure over the project lifetime. While discounted cash-flow formulations are preferred for transparent technology benchmarking, the Capital Recovery Factor (CRF) approach is frequently adopted in large-scale energy system models, such as PyPSA-Eur-MREL, to compute the Total Annualised Cost (TAC) and optimise investment decisions across integrated European




(a) Big PA (12 m dia) - Shallow - Passive control

(b) Flap - Shallow - Passive control

(c) PA - Deep - Passive control

(d) Attenuator - Deep - Passive control

(e) Small PA (6 m dia) - Shallow - Active control

(f) Flap - Shallow - Active control

Figure 6.3.: Power matrices of single devices (Cutoff at $H_s$ = 9 m and no capping)

power systems [14, 16]. The CRF is calculated as:

$$\mathrm{CRF} = \frac{r(1+r)^n}{(1+r)^n - 1} \tag{6.1}$$

where $r$ is the discount rate and $n$ is the project duration in years. For this analysis, a discount rate of $r = 5\%$ and a project lifetime of $n = 20$ years were assumed, yielding a CRF of 0.0802. The LCOE is then computed as:

$$\mathrm{LCOE} = \frac{(\mathrm{CAPEX} \times \mathrm{CRF}) + \mathrm{OPEX}}{\mathrm{AEP}} \tag{6.2}$$

where CAPEX is the capital expenditure (€), OPEX is the annual operational expenditure

(€/year), and AEP is the annual energy production (MWh/year). The OPEX was estimated as 5% of CAPEX for all single devices. All cost estimates are based on 2021 values.

Table 6.4.: Cost and performance summary for single WEC devices

| Device | Site | Control | CAPEX (M€) | OPEX (M€) | Total (M€) | AEP (MWh) | CF (%) | LCOE (€/MWh) |
|---|---|---|---|---|---|---|---|---|
| PA (9m) | Deep | Passive | 1.34 | 0.07 | 1.41 | 465 | 18.0 | 496 |
| Attenuator | Deep | Passive | 0.23 | 0.03 | 0.26 | 79 | 19.0 | 540 |
| Big PA (12m) | Shallow | Passive | 0.54 | 0.03 | 0.57 | 247 | 18.2 | 286 |
| Flap | Shallow | Passive | 1.60 | 0.09 | 1.69 | 858 | 18.2 | 245 |
| Small PA (6m) | Shallow | Active | 0.46 | 0.02 | 0.48 | 395 | 29.3 | 152 |
| Flap | Shallow | Active | 3.51 | 0.18 | 3.69 | 2078 | 20.3 | 220 |

Table 6.4 presents the cost and performance metrics for single WEC devices across both sites and control strategies. A notable comparison can be made between the small PA (6 m diameter) with active control and the large PA (12 m diameter) with passive control, both operating at the same rated power of 150 kW.

Despite its smaller physical dimensions, the actively controlled PA achieves a significantly higher capacity factor (29.3% versus 18.2%) due to the enhanced power absorption enabled by active control. This translates to a 60% increase in AEP (395 MWh versus 247 MWh) while simultaneously reducing CAPEX by 15% (0.46 M€ versus 0.54 M€), as the smaller device requires less structural material for the same power rating. The combined effect yields an LCOE of 152 €/MWh for the small actively controlled PA, representing a 47% reduction compared to the larger passive device (286 €/MWh).

A similar trend is observed for the flap device, where active control increases the rated capacity from 550 kW to 1200 kW. While this results in substantially higher CAPEX (3.51 M€ versus 1.60 M€) and OPEX (0.18 M€ versus 0.09 M€), the AEP increases by a factor of 2.4 (2078 MWh versus 858 MWh). The capacity factor also improves modestly from 18.2% to 20.3%. Consequently, the actively controlled flap achieves a lower LCOE of 220 €/MWh compared to 245 €/MWh for the passive case, demonstrating that the additional investment in active control infrastructure is economically justified by the disproportionate gains in energy production.

The deep water devices exhibit considerably higher LCOE values compared to their shallow water counterparts, with the PA (9 m) and Attenuator reaching 496 €/MWh and 540 €/MWh, respectively.

This increase is attributable to several factors inherent to deep water deployments: longer mooring lines and more complex station-keeping systems, extended submarine cable lengths to shore, increased installation costs due to greater water depths, and higher operational expenditure associated with reduced accessibility for maintenance operations.

## 6.3. PRACTICAL CONSIDERATIONS FOR CHOOSING ARRAYS

To enable a meaningful economic comparison between mono and mixed wave energy converter (WEC) arrays composed of devices with substantially different rated powers, the total installed array capacity is adopted as the baseline metric.

For deep-water arrays, a target capacity of 1 MW is selected, reflecting the relatively high rated power of far-offshore devices. In shallow waters, larger disparities exist between device ratings. Arrays including the actively controlled flap (1200 kW) and the small point absorber (PA, 150 kW) therefore adopt a higher reference capacity of 5 MW for both mono and mixed configurations. For shallow-water arrays under passive control, where the Big PA (150 kW) and flap (550 kW) have more comparable ratings, a lower target capacity of 2 MW is selected. All capacities are consistent with realistic wave energy array sizing reported in the literature.

The levelised cost of energy (LCOE) is a usual benchmark for assessing wave energy project viability. In shallow waters (0–20 m depth), WECs generally achieve more

competitive LCOE values due to reduced exposure to extreme wave events, enabling lighter structural designs and lower capital expenditure (CAPEX) [14]. In contrast, deep-water deployments (50–150 m depth) are associated with substantially higher LCOE values, driven by CAPEX requirements of approximately €5 million/MW to ensure survivability under 100-year return-period wave conditions and the use of specialised offshore installation and maintenance vessels [156, 157].

Alongside LCOE, the spatial footprint of a wave energy array represents an important benchmark, as it is directly linked to array packing density and associated "area strain" on the marine environment and is often overlooked [156]. In deep-water regions, spatial constraints are generally less restrictive reducing the conflicts with other maritime users and minimising nearshore visual intrusion and public opposition [14].

Consequently, spatial footprint plays a secondary role in deep-water array comparisons. By contrast, shallow and nearshore environments face intense competition from commercial fisheries, shipping routes, and recreational activities. Packing densities should be limited making spatial footprint a key determinant of site feasibility and project permitting [156]. Accordingly, comparisons of mono and mixed arrays in shallow waters consider both LCOE and spatial footprint, whereas deep-water comparisons prioritise LCOE.

In addition to economic and spatial considerations, two practical constraints govern array layout. The first is the minimum hydrodynamic spacing required to ensure the accuracy of boundary element method (BEM) analyses, taken here as four times the characteristic dimension of the WEC. The second relates to maintenance accessibility, requiring sufficient clearance for service vessels to manoeuvre between devices. Maintenance operations typically employ multicat vessels with lengths between 10 and 40 m [158–160]. Vessels shorter than 20 m are commonly used in shallow waters, while deep-water operations generally require vessels of at least 20 m. Representative vessel lengths of 15 m (shallow) and 20 m (deep) are therefore assumed.

Maritime safety standards further recommend navigable lanes to accommodate the vessel's tactical diameter, defined as the space needed to execute a 180-degree emergency turn, which typically exceeds four times the vessel length [161]. This results in minimum inter-device spacings of around 60 m in shallow waters and around 80 m in deep waters, which are enforced across all array configurations considered.



## 6.4. Description of the array configurations

Three array cases are considered in the economic assessment: Array shallow small, Array shallow big, and Array deep. For each case, three configurations are evaluated, comprising two mono arrays and one mixed array. The target capacity, installed capacity, number of devices, and inter-device spacing for each configuration are summarised in Table 6.5. It should be noted that when considering these arrays, Optimization is not performed based on the location and economies of scale are not considered.

Table 6.5.: Target capacity, installed capacity, number of devices, and inter-device spacing for the mono and mixed array configurations considered in the economic assessment.

| Case | Configuration | Target cap. (MW) | Installed cap. (MW) | $N_{PA}$ | $N_{fl}$ | $N_{att}$ | Spacing (m) |
|---|---|---|---|---|---|---|---|
| Array shallow small | PA mono | 2.0 | 2.10 | 34 | 0 | 0 | 60 (10$D$) |
| Array shallow small | Flap mono | 2.0 | 2.20 | 0 | 5 | 0 | 72 (4$L$) |
| Array shallow small | Mixed | 2.0 | 2.10 | 2 | 4 | 0 | 60 (5$C$) |
| Array shallow big | PA mono | 5.0 | 5.10 | 14 | 0 | 0 | 60 (5$D$) |
| Array shallow big | Flap mono | 5.0 | 6.00 | 0 | 4 | 0 | 72 (4$L$) |
| Array shallow big | Mixed | 5.0 | 5.10 | 3 | 3 | 0 | 60 (4$L$) |
| Array deep | PA mono | 1.0 | 1.20 | 4 | 0 | 0 | 81 (9$D$) |
| Array deep | Attenuator mono | 1.0 | 1.00 | 0 | 0 | 20 | 200 (4$L$) |
| Array deep | Mixed | 1.0 | 1.00 | 3 | 0 | 2 | 118 (4$C$) |

For all mono and mixed configurations, a staggered layout is selected. This choice is motivated by its ability to minimise direct wave shadowing between neighbouring

WECs, thereby reducing systematic downstream energy losses and promoting a more uniform excitation of devices across the array. This behaviour has also been observed consistently in the previous hydrodynamic analyses for both shallow- and deep-water mono and mixed arrays (chapter 5 and chapter 4), across variations in the number of devices and inter-device spacing.

For both the shallow small and shallow big point absorber (PA) arrays, it is observed from the shallow-water hydrodynamic analyses presented earlier that increasing inter-device spacing generally leads to an improvement in the mean array interaction factor ($q$-factor). Specifically, increasing the spacing from approximately $4D$ to $10D$ resulted in typical increases in the mean $q$-factor from about 0.85 to 0.95. While this trend indicates progressively weaker hydrodynamic interaction at larger spacings, the associated gains in performance remain relatively modest.

In contrast, increasing the inter-device spacing leads to a substantial increase in the spatial footprint, defined here as the total plan-view area occupied by the array, $A_{arr}$. This increase in occupied area results in a pronounced reduction in packing density, defined as the installed capacity per unit area. Consequently, the marginal improvement in $q$-factor obtained at larger spacings does not compensate for the significant loss in spatial efficiency.

Based on this trade-off, the inter-device spacing for all configurations is fixed at the minimum practical distance, approximately $4D$ (or the equivalent characteristic length for non-axisymmetric devices), subject to marine safety, vessel access, and maintenance requirements. This choice represents a balanced compromise between acceptable hydrodynamic interaction, operational feasibility, and efficient use of marine space.

The layouts, inter-device spacings, and spatial footprints, expressed as the total array area $A_{arr}$, associated with each configuration are illustrated in Figure 6.4–Figure 6.6.

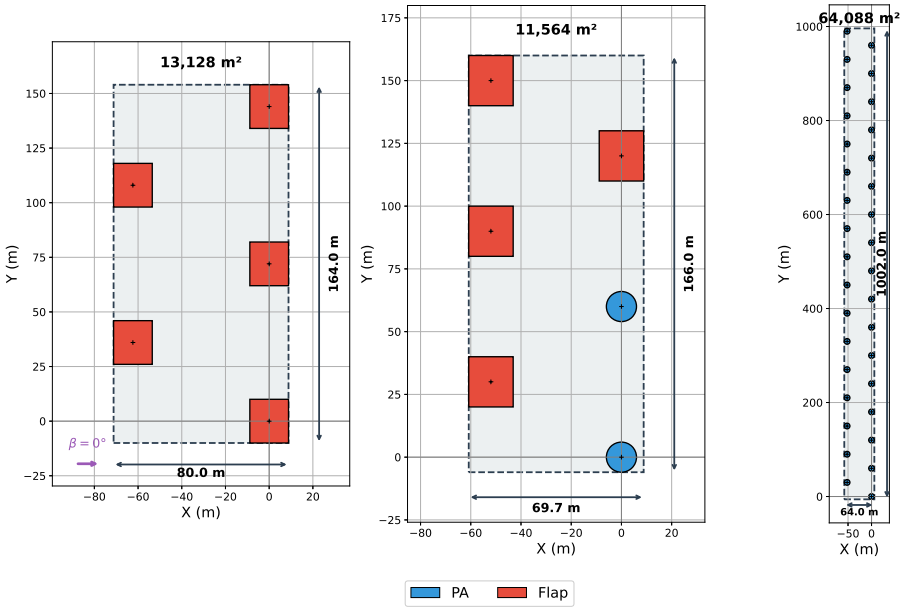



Figure 6.4.: Array shallow small layouts for the mono and mixed configurations, showing the footprint polygons used to determine the total array area $A_{arr}$.

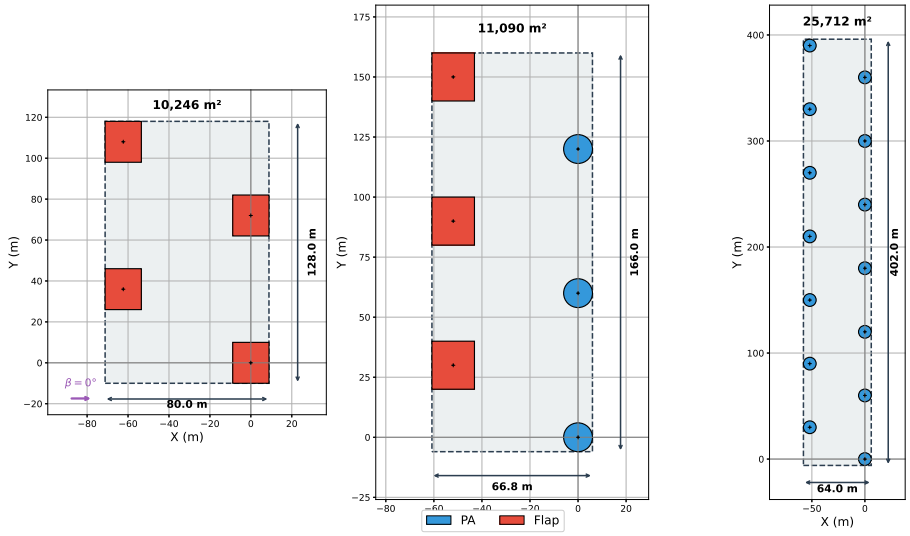



Figure 6.5.: Array shallow big layouts for the mono and mixed configurations, showing the footprint polygons used to determine the total array area $A_{arr}$.

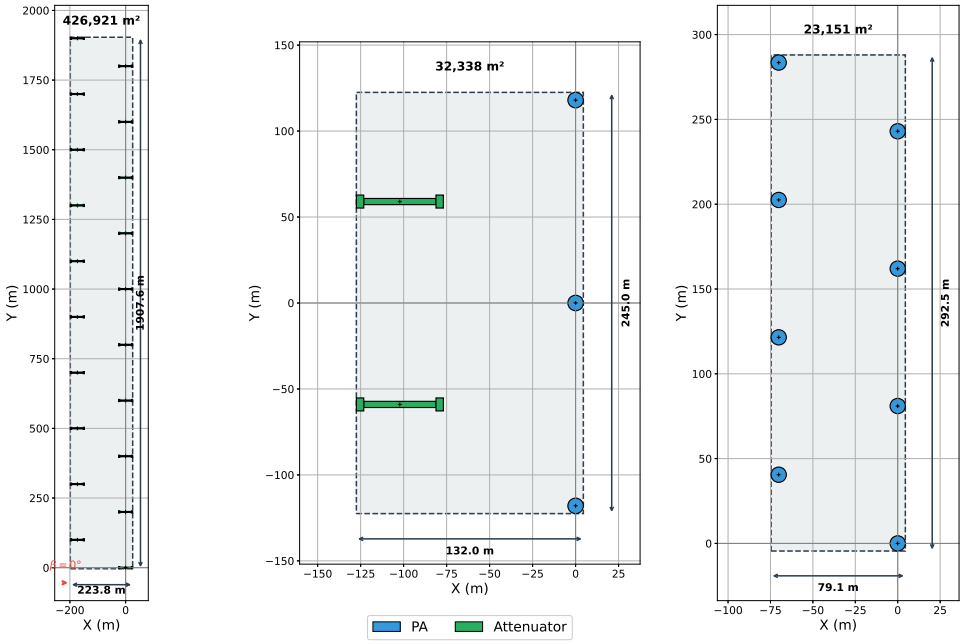



Figure 6.6.: Array deep layouts for the mono and mixed configurations, showing the footprint polygons used to determine the total array area $A_{arr}$.

## 6.5. WAVE ARRAY ECONOMICS

Here, the spatial footprint refers to the total plan-view area occupied by the array, $A_{arr}$, whereas the packing density provides a direct measure of spatial efficiency by relating the installed capacity to the occupied area.

The spatial footprint (see Table 6.6) comparison reveals clear and systematic differences between mono and mixed array configurations across all three cases. In the shallow small case, the mixed array occupies a substantially smaller area than the PA mono-array while maintaining a comparable installed capacity, resulting in a significantly higher packing density.

Although the flap mono-array achieves the highest packing density due to its compact layout, this comes at the expense of a markedly higher LCOE. In contrast, the mixed configuration provides a balanced compromise, combining high spatial efficiency with improved economic performance relative to the flap mono-array.

A similar pattern is observed in the shallow big case. Both the flap mono-array and the mixed array exhibit packing densities that are substantially higher than that of the PA mono-array. However, the mixed configuration closely approaches the spatial efficiency of the flap mono-array while avoiding the large footprint and reduced space utilisation associated with the PA-only layout. These results indicate that, in shallow water, mixed arrays consistently reduce the total occupied area relative to the least spatially efficient mono-array, while maintaining greater flexibility in technology selection.

Table 6.6.: Spatial footprint and packing density of the mono and mixed array configurations. The spatial footprint is defined as the total array area $A_{arr}$, while the packing density is defined as the installed capacity per unit area.

| Case | Config. | $P_{inst}$ (MW) | $A_{arr}$ (km$^2$) | Packing density (MW/km$^2$) |
|---|---|---|---|---|
| Array shallow small | PA mono | 2.10 | 0.025713 | 81 |
| Array shallow small | Flap mono | 2.20 | 0.010352 | 212 |
| Array shallow small | Mixed | 2.10 | 0.011204 | 187 |
| Array shallow big | PA mono | 5.10 | 0.064088 | 79 |
| Array shallow big | Flap mono | 6.00 | 0.013128 | 457 |
| Array shallow big | Mixed | 5.10 | 0.011842 | 431 |
| Array deep | PA mono | 1.20 | 0.014587 | 83 |
| Array deep | Attenuator mono | 1.00 | 0.426921 | 3 |
| Array deep | Mixed | 1.00 | 0.032338 | 31 |

The contrast is most pronounced in the deep-water case. The attenuator mono-array occupies an order-of-magnitude larger area than the PA mono-array, reflecting the elongated geometry and operational spacing requirements of attenuator devices. The mixed array, by contrast, achieves a substantial reduction in spatial footprint relative to the attenuator mono-array, resulting in a significantly improved packing density. This demonstrates that mixed arrays can effectively mitigate the spatial penalties associated with directional devices in deep water.

When comparing array-level performance to the corresponding single-device metrics, a general reduction in CF is observed for most array configurations (see Table 6.7 and Table 6.4). This reduction is more pronounced for directional wave energy converters, such as flaps and attenuators, than for point absorbers. The primary reason for this behaviour is that the rated power used at the array level is derived from the dominant-direction power matrix of the single device. Consequently, wave directions deviating from the dominant direction contribute less effectively to power production at the array level, leading to reduced effective capacity factors and, in turn, higher LCOE values for directional devices when deployed in arrays.

A comparison between mono and mixed arrays shows that mixed configurations generally achieve CFs that are comparable to, or only marginally lower than, those of the best-performing mono-arrays, while offering substantial advantages in terms of spatial footprint and overall economic performance. In shallow water, mixed arrays

Table 6.7.: Capacity factor (CF), annual energy production (AEP), and CRF-based LCOE for the mono and mixed array configurations (Note: In deep waters, a discount rate of 7%, between attenuator and PA, is utilized since the 10 % is mainly for attenuator type of devices due to additional moorings while the 5% is used for PA devices due to comparatively lesser mooring systems and dynamic cabling)

| Case | Config. | CF (%) | AEP (MWh/yr) | Total (CRF) (M€) | LCOE (CRF) (€/MWh) |
|---|---|---|---|---|---|
| Array shallow small | PA mono | 17.90 | 3266.00 | 0.8447 | 258.64 |
| Array shallow small | Flap mono | 9.09 | 1733.00 | 0.8399 | 484.65 |
| Array shallow small | Mixed | 10.24 | 1900.00 | 0.8109 | 426.80 |
| Array shallow big | PA mono | 26.95 | 12415.00 | 2.0371 | 164.08 |
| Array shallow big | Flap mono | 6.83 | 3601.25 | 2.2870 | 635.07 |
| Array shallow big | Mixed | 8.04 | 3587.00 | 1.9495 | 543.48 |
| Array deep | PA mono | 16.58 | 1746.00 | 0.9241 | 529.29 |
| Array deep | Attenuator mono | 19.00 | 1664.00 | 0.8489 | 510.18 |
| Array deep | Mixed | 16.80 | 1466.00 | 0.6485 | 442.37 |

exhibit lower capacity factors than PA mono-arrays but significantly outperform flap mono-arrays in terms of LCOE, owing to their improved packing density and more balanced utilisation of device types. In deep water, the mixed array achieves a slightly lower capacity factor than the attenuator mono-array, yet benefits from a much smaller array area and a lower total cost with CRF, resulting in a reduced LCOE.

Figure 6.7 further illustrates the trade-off between packing density and LCOE for shallow-water configurations. From a system-level perspective, the objective for array deployment is not to minimise LCOE or maximise packing density independently, but to achieve the lowest possible LCOE while maintaining a high degree of spatial efficiency. This combined criterion is particularly important in shallow-water environments, where marine space is limited and spatial constraints strongly influence project feasibility.

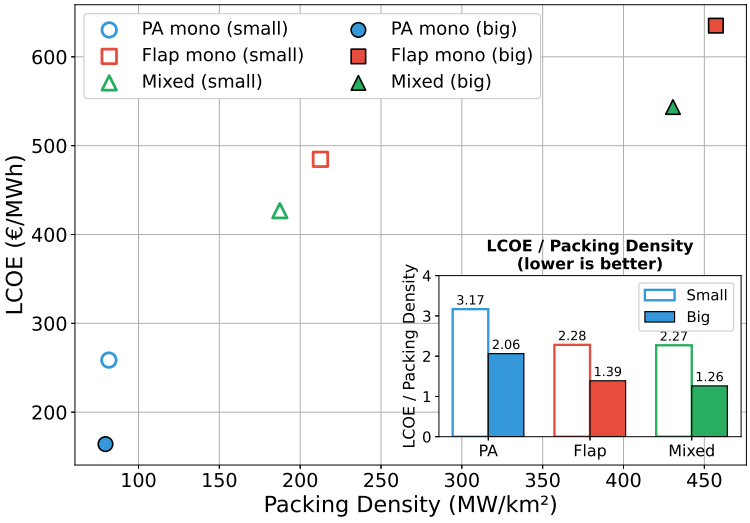



Figure 6.7.: LCOE versus packing density for shallow-water WEC array configurations. Hollow markers represent small arrays and filled markers represent large arrays. The inset bar chart shows the Figure of Merit (FoM = Packing Density / LCOE), where higher values indicate better combined cost- and space-efficiency.

Under this combined performance perspective, mixed arrays consistently outperform mono-array configurations. While PA mono-arrays achieve relatively low LCOE values, they do so at comparatively low packing densities. Conversely, flap mono-arrays offer very high packing densities but suffer from prohibitively high LCOE values. Mixed arrays occupy a favourable intermediate regime, combining substantially higher packing densities than PA mono-arrays with significantly lower LCOE than flap mono-arrays. As a result, mixed arrays provide the most robust and balanced solution when both economic performance and spatial efficiency are considered simultaneously.

As an example, if we consider the Shallow big case, the PA mono has a packing density of 79 MW/km$^2$ with an LCOE of 164 €/MWh. If we deploy the flap mono array with the same packing density, then its LCOE would be 110 €/MWh and that of the mixed arrays would be 99 €/MWh making it the cheapest array considering the same packing density.

In deep water, the relative importance of these metrics shifts. Given the greater availability of marine space and the dominance of offshore installation and structural costs, LCOE becomes the primary performance driver, with packing density playing a secondary role. Even under this criterion, mixed arrays continue to demonstrate clear advantages. Although mixed configurations do not necessarily maximise packing density, they consistently achieve lower LCOE values than attenuator mono-arrays while maintaining a substantially reduced spatial footprint. This reinforces the conclusion that mixed arrays offer a superior deployment strategy across both shallow- and deep-water environments.

## 6.6. CONCLUSIONS



This chapter presented a quantitative techno-economic comparison of mono and mixed wave energy converter (WEC) arrays deployed in shallow- and deep-water environments, explicitly accounting for multibody hydrodynamic interactions, directional wave climates, and depth-dependent cost assumptions. Array-level performance was evaluated using HAMS-MREL, while device-level power matrices were employed solely to define rated power constraints and ensure consistency between single-device and array-level assessments.

Across all configurations, array-level capacity factors were generally lower than those of isolated devices, with reductions typically ranging between 5 and 15 percentage points depending on device type and deployment depth. This reduction was most pronounced for directional devices, such as flaps and attenuators. In addition to hydrodynamic interaction effects, this behaviour is partly attributable to the adopted power evaluation methodology: for single directional devices, power matrices and rated power were derived considering only the dominant wave direction to obtain conservative performance estimates, whereas at the array level, energy production was computed by accounting for contributions from all wave directions in the scatter diagram. As a result, wave components deviating from the dominant direction contribute less effectively to power production at the array level, leading to a further reduction in the effective capacity factor for directional devices.

In shallow-water deployments, spatial footprint emerged as a key determinant of economic viability. PA mono-arrays achieved relatively low LCOE values, amounting to approximately 259 €/MWh for the shallow small case and 164 €/MWh for the shallow big case, but required large occupied areas, resulting in low packing densities of around 81 and 79 MW/km$^2$, respectively. In contrast, flap mono-arrays attained very high packing densities, reaching up to 457 MW/km$^2$, but at the expense of substantially higher LCOE values, exceeding 480 €/MWh for the shallow small case and 630 €/MWh for the shallow big case.

Mixed arrays consistently occupied a favourable intermediate regime. For the shallow small case, the mixed configuration achieved a packing density of 187 MW/km$^2$, more than double that of the PA mono-array, while maintaining a significantly lower LCOE of about 427 €/MWh compared to the flap mono-array. A similar trend was observed in the shallow big case, where the mixed array reached a packing density of 431 MW/km$^2$ with

an LCOE of approximately 543 €/MWh, closely approaching the spatial efficiency of the flap mono-array while avoiding its extreme cost penalty.

Crucially, when comparisons are performed at an equivalent spatial footprint or packing density, mixed arrays demonstrate a clear economic advantage. For the shallow big case, fixing the packing density to that of the PA mono-array at approximately 79 MW/km$^2$ results in an estimated LCOE of about 110 €/MWh for the flap mono-array, while the mixed array achieves an even lower LCOE of approximately 99 €/MWh. This illustrates that the apparent cost disadvantage of directional devices in shallow water is largely driven by spatial inefficiency rather than intrinsic energy performance, and that mixed arrays provide the most cost-effective solution under identical spatial constraints.

In deep-water environments, the relative importance of spatial footprint diminishes due to greater space availability, while LCOE becomes the dominant performance metric. The attenuator mono-array achieved an LCOE of around 510 €/MWh but required a very large footprint of approximately 0.43 km$^2$, corresponding to a packing density of only 3 MW/km$^2$. By contrast, the mixed array reduced the occupied area by more than an order of magnitude to about 0.03 km$^2$, increased the packing density to roughly 31 MW/km$^2$, and achieved a substantially lower LCOE of approximately 442 €/MWh, despite a slightly lower capacity factor. This demonstrates that mixed arrays can effectively mitigate the spatial penalties associated with elongated and highly directional devices while improving overall economic performance.

Overall, the findings confirm that mixed wave energy arrays represent a robust and economically competitive deployment strategy across both shallow- and deep-water environments. By leveraging complementary device characteristics and explicitly accounting for multibody hydrodynamic interactions and directional wave effects at the array level, mixed arrays enable a balanced trade-off between energy production, cost, and spatial efficiency. These results highlight the importance of array-level optimisation in realistic techno-economic assessments and demonstrate that moving beyond mono-technology deployments can yield substantial benefits for future wave energy farms.

# 7

# CONCLUSIONS

This thesis investigated the hydrodynamic interactions, performance characteristics, and techno-economic viability of mixed wave energy converter (WEC) arrays in comparison with mono-device arrays. By developing a robust numerical framework and applying it to both shallow- and deep-water environments, the research demonstrated that mixed arrays provide a viable pathway toward enhanced robustness, improved spatial efficiency, and increased economic competitiveness. The main conclusions drawn from this work are synthesised below.

To enable the efficient analysis of large-scale WEC arrays, the HAMS-MREL solver was developed as a multi-body extension of the open-source HAMS Boundary Integral Equation Method solver. The numerical framework demonstrated strong accuracy and robustness when benchmarked against reference solutions, achieving mean square errors in wave field predictions below 2% and hydrodynamic coefficient deviations typically within 5%. The implementation of extended BIE successfully suppressed irregular frequencies, while the generalised modes formulation accurately captured the dynamics of constrained devices such as bottom-mounted flaps. By exploiting global symmetry and OpenMP parallelisation, HAMS-MREL achieved speed-up factors of up to 47.2 relative to serial simulations, establishing it as a scalable and computationally efficient tool for dense array analysis and optimisation.

The hydrodynamic behaviour of mixed arrays composed of PAs and oscillating flaps in shallow water revealed distinct advantages over mono-device configurations. Using interaction-based ($q$-factor) and geometry-normalised ($M$-factor) performance metrics, the analysis showed that mixed arrays effectively exploit the complementary dynamics of the constituent devices. While mono-flap arrays exhibited strong directionality and PA mono arrays showed largely isotropic responses, mixed arrays successfully combined these characteristics to achieve higher average geometry-normalised performance. The strongest synergetic effects were observed for specific configurations in which heterogeneous hydrodynamic interactions exceeded the summed performance of individual devices, resulting in stable and robust behaviour as array size increased.

In deep-water depths, mixed arrays comprising PAs and attenuators were found to outperform mono-device arrays in terms of robustness and overall efficiency. Mono-attenuator arrays exhibited highly directional behaviour, achieving strong constructive interference for favourable wave headings but suffering severe performance degradation under unfavourable incidence angles. The inclusion of PAs in mixed arrays mitigated these deep destructive troughs while preserving the constructive potential of the attenuators. An optimal intermediate array size was identified, at which cooperative hydrodynamic effects were maximised. At this configuration, mixed arrays achieved weighted capture width efficiencies up to 30% higher than those of the corresponding mono arrays.

Detailed hydrodynamic analysis provided insight into the physical mechanisms underpinning the enhanced performance of mixed arrays. In shallow water, performance gains were primarily driven by coherent spatial interactions, with radiation damping cross-coupling terms becoming predominantly positive at specific wave periods. In deep water, PAs acted as effective wave scatterers, redirecting incident wave energy toward attenuators and

modifying the local wave field. This mechanism smoothed the spectral response of the array and prevented the performance collapse observed in mono-attenuator arrays under perpendicular wave incidence, thereby ensuring more consistent power production across a wider range of wave headings.

The techno-economic assessment confirmed that the hydrodynamic advantages of mixed arrays translate directly into economic benefits. In shallow water, mixed arrays occupied a favourable intermediate regime, achieving substantially higher packing densities than PA mono arrays while maintaining significantly lower LCOE than flap mono arrays. Considering the same packing density, it is shown that mixed arrays have much lower LCOE than both mono arrays. In deep water, where installation and infrastructure costs dominate, mixed arrays achieved lower LCOE than both attenuator and point-absorber mono arrays, while simultaneously reducing the required spatial footprint. Overall, mixed arrays effectively mitigated the high spatial penalty associated with PA mono arrays and the high cost penalty of flap and attenuator mono arrays, offering a balanced solution in terms of energy production, cost efficiency, and spatial utilisation.

In summary, this thesis demonstrates that integrating multiple WEC technologies within a single wave farm is not only hydrodynamically advantageous, through enhanced constructive interference and improved robustness, but also economically competitive. Mixed arrays therefore represent a promising and flexible deployment strategy for future wave energy developments.

## 7.1. LIMITATIONS AND FUTURE WORK

Despite the comprehensive scope of this study, several limitations remain and motivate directions for future research:

- When considering extreme sea states, the currently implemented weakly non-linear frequency domain formulation might not be applicable. In order to more accurately capture the transient and strongly non-linear effects at these sea states, a time-domain model is required. Future work should therefore incorporate time-domain simulations to assess survivability, control performance, and fatigue loading in mixed arrays.

- For single flap and attenuator devices, performance is currently evaluated only for the dominant wave direction. Extending this directional treatment consistently to array-level assessments, including both $q$- and $M$-factors, would provide less conservative and more representative performance estimates.

- The present PTO models, under both passive and active control, do not impose explicit force limits, which become increasingly important at higher sea states. In the techno-economic analysis, power capping is currently used as an indirect proxy for force limitation. Incorporating direct force constraints within the control formulation would improve physical realism and predictive accuracy.

- The techno-economic assessment relies on representative cost models and does not explicitly account for site-specific installation conditions, maintenance logistics, or electrical infrastructure constraints. Further refinement of the economic framework, including uncertainty quantification and integration with spatial planning tools, would enable more realistic deployment assessments.

- For the attenuator device, only passive control strategies were considered. Investigating active control for attenuators would provide valuable insight into their interaction mechanisms and potential performance gains within mono and mixed arrays.

- The estimation of the mass and stiffness matrices for the attenuator can be further improved by considering the full geometric representation of the mesh or by enforcing symmetry in the flexible degrees of freedom. This would help resolve the observed discrepancies in absorbed power between 0° and 180° wave incidence.

- Including mooring stiffness in surge for the attenuator would enable more accurate prediction of surge-related eigenmodes during eigenfrequency analysis.
- For active control strategies, explicitly accounting for the energy expended in real time, including reverse energy flow and PTO actuator efficiency, would allow for a more complete assessment of net power absorption and control effectiveness.
- The current study does not consider array-level optimisation with respect to device number, spacing, or site location. Incorporating array optimisation would provide deeper insight into the relative effectiveness of mixed and mono arrays and further strengthen the techno-economic analysis.
- Finally, while this thesis focuses on a limited set of device combinations, the mixed-array concept is inherently general and applicable to a wider range of WEC technologies. Future studies should explore alternative device pairings, adaptive array layouts, and the co-optimisation of control strategies and array geometry to further enhance array-level performance and economic viability.

# BIBLIOGRAPHY


[1] *UN Nations - Global Issues - Population*. Accessed on May 28, 2023. 2022. url: https://www.un.org/en/global-issues/population.

[2] UNFCCC Momentum for Change. *Eco Wave Power: Generating Clean Energy From the Ocean*. https://unfccc.int/climate-action/momentum-for-change/women-for-results/eco-wave-power. Accessed: 2026-01-22. 2019.

[3] P. Balitsky. "A Numerical Investigation of the Array Effects of Wave Energy Converters With a Realistic Power Take-off System Utilizing a Coupled Model Suite". PhD thesis. Ghent University, July 2019.

[4] I. A. Hernández-Robles, X. González-Ramírez, J. A. Gómez-Gutiérrez, and J. M. Ramirez. "Wave power assessment for electricity generation with powerbouy system by wave motion emulation modelling". In: *Sustainable Energy Technologies and Assessments* 43 (2021), p. 100962. issn: 2213-1388. doi: https://doi.org/10.1016/j.seta.2020.100962. url: https://www.sciencedirect.com/science/article/pii/S2213138820313904.

[5] T. Chakraborty. "A MCDM-NBO Approach for Selection of Installation Location for Wave Energy Power Plants". In: *Application of Geographical Information Systems and Soft Computation Techniques in Water and Water Based Renewable Energy Problems*. Ed. by M. Majumder. Singapore: Springer Singapore, 2018, pp. 121–140.

[6] *Tsunamis behave as shallow-water waves*. Accessed: 2023-25-08. 2017. url: https://www.geological-digressions.com/tsunamis-behave-as-shallow-water-waves/.

[7] K. Gunn and C. Stock-Williams. "Quantifying the global wave power resource". In: *Renewable Energy* 44 (2012), pp. 296–304. issn: 0960-1481. doi: https://doi.org/10.1016/j.renene.2012.01.101. url: https://www.sciencedirect.com/science/article/pii/S0960148112001310.

[8] C. Guedes Soares, J. Bhattacharjee, M. Tello Ruiz, and L. Pietra. "Review and classification of wave energy converters". In: *Maritime Engineering and Technology* (Nov. 2012), pp. 585–594. doi: 10.1201/b12726-82.

[9] F.-X. Faÿ, E. Robles, M. Marcos, E. Aldaiturriaga, and E. F. Camacho. "Sea trial results of a predictive algorithm at the Mutriku Wave power plant and controllers assessment based on a detailed plant model". In: *Renewable Energy* 146 (2020), pp. 1725–1745. issn: 0960-1481. doi: https://doi.org/10.1016/j.renene.2019.07.129. url: https://www.sciencedirect.com/science/article/pii/S0960148119311498.

[10] SBM Offshore. *Sea trial in the Principality of Monaco announced for SBM Offshore's innovative S3® Wave Energy Converter*. https://www.sbmoffshore.com/newsroom/sea-trial-principality-monaco-announced-sbm-offshores-innovative-s3r-wave/. Accessed: 2025-01-23. 2019.

[11] *Corpower*. 2024. url: https://corpowerocean.com/corpack/.

[12] G. Lavidas and K. Blok. "Shifting wave energy perceptions: The case for wave energy converter (WEC) feasibility at milder resources". In: *Renewable Energy* 170 (2021), pp. 1143–1155. issn: 0960-1481. doi: https://doi.org/10.1016/j.renene.2021.02.041. url: https://www.sciencedirect.com/science/article/pii/S0960148121002093.

[13] S. Astariz and G. Iglesias. “The economics of wave energy: A review”. In: *Renewable and Sustainable Energy Reviews* 45 (2015), pp. 397–408. issn: 1364-0321. doi: https://doi.org/10.1016/j.rser.2015.01.061. url: https://www.sciencedirect.com/science/article/pii/S1364032115000714.

[14] G. Lavidas, L. Mezilis, M. Alday, H. Baki, J. Tan, A. Jain, T. Engelfried, and **V. Raghavan**. “Marine renewables in energy systems: Impacts of climate data, generators, energy policies, opportunities, and untapped potential for 100% decarbonised systems”. In: *Energy* 336 (2025), p. 138359. issn: 0360-5442. doi: 10.1016/j.energy.2025.138359.

[15] G. Dalton, R. Alcorn, and T. Lewis. “Case study feasibility analysis of the Pelamis wave energy convertor in Ireland, Portugal and North America”. In: *Renewable Energy* 35.2 (2010), pp. 443–455. issn: 0960-1481. doi: https://doi.org/10.1016/j.renene.2009.07.003. url: https://www.sciencedirect.com/science/article/pii/S0960148109002948.

[16] G. Allan, M. Gilmartin, P. McGregor, and K. Swales. “Levelised costs of Wave and Tidal energy in the UK: Cost competitiveness and the importance of “banded” Renewables Obligation Certificates”. In: *Energy Policy* 39.1 (2011), pp. 23–39. issn: 0301-4215. doi: https://doi.org/10.1016/j.enpol.2010.08.029. url: https://www.sciencedirect.com/science/article/pii/S0301421510006440.

[17] J. Bru, T. S. Seland, J. Dai, and Z. Jiang. “Life cycle cost analysis of an offshore floating photovoltaic concept in the North Sea”. In: *Renewable Energy* 249 (2025), p. 122981. issn: 0960-1481. doi: https://doi.org/10.1016/j.renene.2025.122981. url: https://www.sciencedirect.com/science/article/pii/S0960148125006433.

[18] S. Foteinis. “Wave energy converters in low energy seas: Current state and opportunities”. In: *Renewable and Sustainable Energy Reviews* 162 (2022), p. 112448. issn: 1364-0321. doi: https://doi.org/10.1016/j.rser.2022.112448. url: https://www.sciencedirect.com/science/article/pii/S1364032122003549.

[19] B. Guo and J. Ringwood. “A review of wave energy technology from a research and commercial perspective”. In: *Renewable Power Generation, IET* 15 (Oct. 2021), pp. 3065–. doi: 10.1049/rpg2.12302.

[20] *AW WaveRoller*. 2024. url: https://aw-energy.com/utility-scale-power/.

[21] *HiWave-5 project*. 2025. url: https://www.hiwave-5.eu/about-us/.

[22] *ONDEP project*. 2024. url: https://www.ondep-wave.eu/.

[23] J. Falnes and P. McIver. “Surface wave interactions with systems of oscillating bodies and pressure distributions”. In: *Applied Ocean Research* 7.4 (1985), pp. 225–234. issn: 0141-1187. doi: https://doi.org/10.1016/0141-1187(85)90029-X. url: https://www.sciencedirect.com/science/article/pii/014111878590029X.

[24] S. Mavrakos. “Hydrodynamic coefficients for groups of interacting vertical axisymmetric bodies”. In: *Ocean Engineering* 18.5 (1991), pp. 485–515. issn: 0029-8018. doi: https://doi.org/10.1016/0029-8018(91)90027-N. url: https://www.sciencedirect.com/science/article/pii/002980189190

[25] J. Falnes and J. Todalshaug. “Heaving buoys, point absorbers and arrays”. In: *Philosophical transactions. Series A, Mathematical, physical, and engineering sciences* 370 (Jan. 2012), pp. 246–77. doi: 10.1098/rsta.2011.0249.

7

[26] H. Wolgamot, P. Taylor, and R. Eatock Taylor. “The interaction factor and directionality in wave energy arrays”. In: *Ocean Engineering* 47 (2012), pp. 65–73. issn: 0029-8018. doi: https://doi.org/10.1016/j.oceaneng.2012.03.017. url: https://www.sciencedirect.com/science/article/pii/S0029801812001138.

[27] J. C. McNatt, V. Venugopal, and D. Forehand. “A novel method for deriving the diffraction transfer matrix and its application to multi-body interactions in water waves”. In: *Ocean Engineering* 94 (2015), pp. 173–185. issn: 0029-8018. doi: https://doi.org/10.1016/j.oceaneng.2014.11.029. url: https://www.sciencedirect.com/science/article/pii/S0029801814004417.

[28] G. Tokić and D. K. Yue. “Hydrodynamics of large wave energy converter arrays with random configuration variations”. In: *Journal of Fluid Mechanics* 923 (2021), R1. doi: 10.1017/jfm.2021.584.

[29] T. Vervaet, V. Stratigaki, F. Ferri, L. De Beule, H. Claerbout, B. De Witte, M. Vantorre, and P. Troch. “Experimental Modelling of an Isolated WECfarm Real-Time Controllable Heaving Point Absorber Wave Energy Converter”. In: *Journal of Marine Science and Engineering* 10.10 (2022). issn: 2077-1312. doi: 10.3390/jmse10101480. url: https://www.mdpi.com/2077-1312/10/10/1480.

[30] S.-H. Yang, J. W. Ringsberg, and E. Johnson. “Wave energy converters in array configurations—Influence of interaction effects on the power performance and fatigue of mooring lines”. In: *Ocean Engineering* 211 (2020), p. 107294. issn: 0029-8018. doi: https://doi.org/10.1016/j.oceaneng.2020.107294. url: https://www.sciencedirect.com/science/article/pii/S002980182030337

[31] B. Borgarino, A. Babarit, and P. Ferrant. “Impact of wave interactions effects on energy absorption in large arrays of wave energy converters”. In: *Ocean Engineering* 41 (2012), pp. 79–88. issn: 0029-8018. doi: https://doi.org/10.1016/j.oceaneng.2011.12.025. url: https://www.sciencedirect.com/science/article/pii/S0029801812000054.

[32] M. Penalba, I. Touzón, J. Lopez-Mendia, and V. Nava. “A numerical study on the hydrodynamic impact of device slenderness and array size in wave energy farms in realistic wave climates”. In: *Ocean Engineering* 142 (2017), pp. 224–232. issn: 0029-8018. doi: https://doi.org/10.1016/j.oceaneng.2017.06.047. url: https://www.sciencedirect.com/science/article/pii/S0029801817303517.

[33] R. J. Bergillos, C. Rodriguez-Delgado, J. Allen, and G. Iglesias. “Wave energy converter configuration in dual wave farms”. In: *Ocean Engineering* 178 (2019), pp. 204–214. issn: 0029-8018. doi: https://doi.org/10.1016/j.oceaneng.2019.03.001. url: https://www.sciencedirect.com/science/article/pii/S0029801819300939.

[34] *Wave Energy Farm Assessment in Real Wave Climates: The North Sea*. Vol. Volume 7: Ocean Renewable Energy. International Conference on Offshore Mechanics and Arctic Engineering. June 2024, V007T09A062. doi: 10.1115/OMAE2024-120946. eprint: https://asmedigitalcollection.asme.org/OMAE/proceedings-pdf/OMAE2024/87851/V007T09A062/7361960/v007t09a062-omae2024-120946.pdf. url: https://doi.org/10.1115/OMAE2024-120946.

[35] S. Bozzi, M. Giassi, A. Moreno Miquel, A. Antonini, F. Bizzozero, G. Gruosso, R. Archetti, and G. Passoni. “Wave energy farm design in real wave climates: the Italian offshore”. In: *Energy* 122 (2017), pp. 378–389. issn: 0360-5442. doi: https://doi.org/10.1016/j.energy.2017.01.094. url: https://www.sciencedirect.com/science/article/pii/S0360544217301019.

[36] B. Child and V. Venugopal. “Optimal configurations of wave energy device arrays”. In: *Ocean Engineering* 37.16 (2010), pp. 1402–1417. issn: 0029-8018. doi: https://doi.org/10.1016/j.oceaneng.2010.06.010. url: https://www.sciencedirect.com/science/article/pii/S0029801810001447.

[37] Y. Peña-Sanchez, D. García-Violini, M. Penalba, A. Zarketa-Astigarraga, F. Ferri, V. Nava, and J. V. Ringwood. “Control co-design for wave energy farms: Optimisation of array layout and mooring configuration in a realistic wave climate”. In: *Renewable Energy* 227 (2024), p. 120506. issn: 0960-1481. doi: https://doi.org/10.1016/j.renene.2024.120506. url: https://www.sciencedirect.com/science/article/pii/S0960148124005718.

[38] M. Giassi and M. Göteman. “Layout design of wave energy parks by a genetic algorithm”. In: *Ocean Engineering* 154 (2018), pp. 252–261. issn: 0029-8018. doi: https://doi.org/10.1016/j.oceaneng.2018.01.096. url: https://www.sciencedirect.com/science/article/pii/S0029801818301045.

[39] M. Göteman, J. Engström, M. Eriksson, and J. Isberg. “Optimizing wave energy parks with over 1000 interacting point-absorbers using an approximate analytical method”. In: *International Journal of Marine Energy* 10 (2015), pp. 113–126. issn: 2214-1669. doi: https://doi.org/10.1016/j.ijome.2015.02.001. url: https://www.sciencedirect.com/science/article/pii/S2214166915000

[40] J. Engström, M. Eriksson, M. Göteman, J. Isberg, and M. Leijon. “Performance of large arrays of point absorbing direct-driven wave energy converters”. In: *Journal of Applied Physics* 114.20 (Nov. 2013), p. 204502. issn: 0021-8979. doi: 10.1063/1.4833241. eprint: https://pubs.aip.org/aip/jap/article-pdf/doi/10.1063/1.4833241/13681152/204502_1_online.pdf. url: https://doi.org/10.1063/1.4833241.

[41] N. Faedo, Y. Peña-Sanchez, E. Pasta, G. Papini, F. D. Mosquera, and F. Ferri. “SWELL: An open-access experimental dataset for arrays of wave energy conversion systems”. In: *Renewable Energy* 212 (2023), pp. 699–716. issn: 0960-1481. doi: https://doi.org/10.1016/j.renene.2023.05.069. url: https://www.sciencedirect.com/science/article/pii/S0960148123006924.

[42] P. Balitsky, N. Quartier, G. Verao Fernandez, V. Stratigaki, and P. Troch. “Analyzing the Near-Field Effects and the Power Production of an Array of Heaving Cylindrical WECs and OSWECs Using a Coupled Hydrodynamic-PTO Model”. In: *Energies* 11.12 (2018). issn: 1996-1073. doi: 10.3390/en11123489. url: https://www.mdpi.com/1996-1073/11/12/3489.

[43] Z. Y. Tay and V. Venugopal. “Hydrodynamic interactions of oscillating wave surge converters in an array under random sea state”. In: *Ocean Engineering* 145 (2017), pp. 382–394. issn: 0029-8018. doi: https://doi.org/10.1016/j.oceaneng.2017.09.012. url: https://www.sciencedirect.com/science/article/pii/S0029801817305310.

[44] J. C. McNatt, A. Porter, and K. Ruehl. “Comparison of Numerical Methods for Modeling the Wave Field Effects Generated by Individual Wave Energy Converters and Multiple Converter Wave Farms”. In: *Journal of Marine Science and Engineering* 8.3 (2020). issn: 2077-1312. doi: 10.3390/jmse8030168. url: https://www.mdpi.com/2077-1312/8/3/168.

[45] S. Zheng, Y. Zhang, and G. Iglesias. “Power capture performance of hybrid wave farms combining different wave energy conversion technologies: The H-factor”. In: *Energy* 204 (2020), p. 117920. issn: 0360-5442. doi: https://doi.org/10.1016/j.energy.2020.117920. url: https://www.sciencedirect.com/science/article/pii/S0360544220310276.

[46] M. Göteman. “Wave energy parks with point-absorbers of different dimensions”. In: *Journal of Fluids and Structures* 74 (2017), pp. 142–157. issn: 0889-9746. doi: https://doi.org/10.1016/j.jfluidstructs.2017.07.012. url: https://www.sciencedirect.com/science/article/pii/S0889974617301627.

[47] A. M. Ermakov, Z. A. Ali, K. Mahmoodi, O. Mason, and J. V. Ringwood. “Optimisation of heterogeneous wave energy converter arrays: A control co-design strategy”. In: *Renewable Energy* 244 (2025), p. 122637. issn: 0960-1481. doi: https://doi.org/10.1016/j.renene.2025.122637. url: https://www.sciencedirect.com/science/article/pii/S096014812500299X.

[48] H. Abdulkadir and O. Abdelkhalik. “Optimization of heterogeneous arrays of wave energy converters”. In: *Ocean Engineering* 272 (2023), p. 113818. issn: 0029-8018. doi: https://doi.org/10.1016/j.oceaneng.2023.113818. url: https://www.sciencedirect.com/science/article/pii/S002980182300202

[49] H. Kagemoto and D. K. P. Yue. “Interactions among multiple three-dimensional bodies in water waves: an exact algebraic method”. In: *Journal of Fluid Mechanics* 166 (1986), pp. 189–209. doi: 10.1017/S0022112086000101.

[50] E. Renzi and F. Dias. “Relations for a periodic array of flap-type wave energy converters”. In: *Applied Ocean Research* 39 (2013), pp. 31–39. issn: 0141-1187. doi: https://doi.org/10.1016/j.apor.2012.09.002. url: https://www.sciencedirect.com/science/article/pii/S0141118712000764.

[51] P. Ricci. “Chapter 3 - Time-Domain Models”. In: *Numerical Modelling of Wave Energy Converters*. Ed. by M. Folley. Academic Press, 2016, pp. 31–66. isbn: 978-0-12-803210-7. doi: https://doi.org/10.1016/B978-0-12-803210-7.00003-7. url: https://www.sciencedirect.com/science/article/pii/B9780128032107000037.

[52] C. Beels, P. Troch, G. De Backer, M. Vantorre, and J. De Rouck. “Numerical implementation and sensitivity analysis of a wave energy converter in a time-dependent mild-slope equation model”. In: *Coastal Engineering* 57.5 (2010), pp. 471–492. issn: 0378-3839. doi: https://doi.org/10.1016/j.coastaleng.2009.11.003. url: https://www.sciencedirect.com/science/article/pii/S0378383909001823.

[53] L. Huang, Y. Li, D. Benites-Munoz, C. Windt, A. Feichtner, S. Tavakoli, J. Davidson, R. Paredes, T. Quintuna, E. Ransley, M. Colombo, M. Li, P. Cardiff, and G. Tabor. “A Review on the Modelling of Wave–Structure Interactions Based on OpenFOAM”. In: *OpenFOAM Journal* 2 (Aug. 2022), pp. 116–142. doi: 10.51560/ofj.v2.65. url: https://journal.openfoam.com/index.php/ofj/article/view/65.

[54] **V.Raghavan**, E.Loukogeorgaki, N.Mantadakis, A. Metrikine, and G.Lavidas. “HAMS-MREL, a new open source multiple body solver for marine renewable energies: Model description, application and validation”. In: *Renewable Energy* 237 (2024), p. 121577. issn: 0960-1481. doi: https://doi.org/10.1016/j.renene.2024.121577.

[55] M. Alves. “Chapter 2 - Frequency-Domain Models”. In: *Numerical Modelling of Wave Energy Converters*. Ed. by M. Folley. Academic Press, 2016, pp. 11–30. isbn: 978-0-12-803210-7. doi: https://doi.org/10.1016/B978-0-12-803210-7.00002-5. url: https://www.sciencedirect.com/science/article/pii/B9780128032107000025.

[56] **V.Raghavan**, I.Simonetti, A. Metrikine, G.Lavidas, and L.Cappietti. “A new numerical modelling framework for fixed oscillating water column wave energy conversion device combining BEM and CFD methods: Validation with experiments”. In: *Ocean Engineering* 301 (2024), p. 117543. issn: 0029-8018. doi: https://doi.org/10.1016/j.oceaneng.2024.117543.

[57] C.-H. Lee and J. N. Newman. “Computation of wave effects using the panel method”. In: 2003. url: https://api.semanticscholar.org/CorpusID:17331425.

[58] DNV-GL. *WADAM - SESAM User Manual*. English. Version 9.3. DNV GL. 2018. 73 pp.

[59] ORCINA. *OrcaWave v11.4e*. English. Version 11.4e. Orcina Ltd. 2023.

[60] B. Veritas. *Hydrostar Hydrodynamic Solver*. https://marine-offshore.bureauveritas.com/hydrostar-software-powerful-hydrodynamic. [Online; accessed 12-December-2024]. 2024.

[61] *ANSYS. Ansys AQWA v14.5 2012*. Accessed on May 28, 2023. 2012. url: https://www.ansys.com/products/structures/ansys-mechanical.

[62] *Hydrodynamic Analysis of Different Configurations of the M4 Wave Energy Converter System Using OREGEN*. Vol. Volume 7: Ocean Renewable Energy. International Conference on Offshore Mechanics and Arctic Engineering. June 2024, V007T09A066. doi: 10.1115/OMAE2024-123824. eprint: https://asmedigitalcollection.asme.org/OMAE/proceedings-pdf/OMAE2024/87851/V007T09A066/7361926/v007t09a066-omae2024-123824.pdf. url: https://doi.org/10.1115/OMAE2024-123824.

[63] F. P. Chau and R. E. Taylor. “Second-order wave diffraction by a vertical cylinder”. In: *Journal of Fluid Mechanics* 240 (1992), pp. 571–599. doi: 10.1017/S0022112092000211.

[64] L. Sun, P. Stansby, J. Zang, E. Moreno, and P. Taylor. “Linear diffraction analysis for optimisation of the three-float multi-mode wave energy converter M4 in regular waves including small arrays”. In: *Journal of Ocean Engineering and Marine Energy* 2 (2016), pp. 429–438. doi: https://doi.org/10.1007/s40722-016-0059-1.

[65] H. Wolgamot, R. Eatock Taylor, and P. Taylor. “Effects of second-order hydrodynamics on the efficiency of a wave energy array”. In: *International Journal of Marine Energy* 15 (2016). Selected Papers from the European Wave and Tidal Energy Conference 2015, Nante, France, pp. 85–99. issn: 2214-1669. doi: https://doi.org/10.1016/j.ijome.2016.04.005. url: https://www.sciencedirect.com/science/article/pii/S2214166916300170.

[66] *Software Framework to Accelerate BEM Linear Wave Load Program Using OpenMP (OREGEN-BEM)*. Vol. All Days. International Ocean and Polar Engineering Conference. June 2023, ISOPE-I-23–323. eprint: https://onepetro.org/ISOPEIOPEC/proceedings-pdf/ISOPE23/All-ISOPE23/ISOPE-I-23-323/3165579/isope-i-23-323.pdf.

[67] Y. Liu, S. Yoshida, C. Hu, M. Sueyoshi, L. Sun, J. Gao, P. Cong, and G. He. “A reliable open-source package for performance evaluation of floating renewable energy systems in coastal and offshore regions”. In: *Energy Conversion and Management* 174 (2018), pp. 516–536. issn: 0196-8904. doi: https://doi.org/10.1016/j.enconman.2018.08.012. url: https://www.sciencedirect.com/science/article/pii/S0196890418308562.

[68] G. Li, P. Stansby, and S. Draycott. “General formulation for floating body with elastic mooring in irregular waves: A hybrid linear and nonlinear framework and validation”. In: *Marine Structures* 96 (2024), p. 103623. issn: 0951-8339. doi: https://doi.org/10.1016/j.marstruc.2024.103623. url: https://www.sciencedirect.com/science/article/pii/S0951833924000510.

[69] A. Babarit and G. Delhommeau. “Theoretical and numerical aspects of the open source BEM solver NEMOH”. In: *11th European Wave and Tidal Energy Conference (EWTEC2015)*. Proceedings of the 11th European Wave and Tidal Energy Conference. Nantes, France, Sept. 2015. url: https://hal.science/hal-01198800.

[70] P. Balitsky, G. Verao Fernandez, V. Stratigaki, and P. Troch. “Coupling Methodology for Modelling the Near-Field and Far-Field Effects of a Wave Energy Converter”. In: June 2017. doi: 10.1115/OMAE2017-61892.

[71] G. Verao Fernandez, P. Balitsky, V. Stratigaki, and P. Troch. “Coupling Methodology for Studying the Far Field Effects of Wave Energy Converter Arrays over a Varying Bathymetry”. In: *Energies* 11.11 (2018). issn: 1996-1073. doi: 10.3390/en11112899. url: https://www.mdpi.com/1996-1073/11/11/2899.

[72] H. Mankle, Y.-H. Yu, and B. DuPont. “WEC-Sim Array Development and Experimental Comparison Study”. In: *National Renewable Energy Laboratory* (2019). url: https://www.nrel.gov/docs/fy20osti/74083.pdf.

[73] Verao Fernandez, Gael and Balitsky, Philip and Stratigaki, Vicky and Troch, Peter. “Validation of a coupling methodology for numerical modelling of near and far field effects of Wave Energy Converter arrays using the MILDwave and NEMOH models, based on the WECwakes experimental database”. eng. In: *Book of Abstracts Special Publication 80*. Bredene, Belgium, 2018, 124–125.

[74] S. D. Chowdhury, R. D. L. Cruz, T. V. Huynh, B. Winship, and R. Manasseh. “Computation of power from an array of wave energy converters using a boundary element method”. In: (Jan. 2016).

[75] T. Verbrugghe, V. Stratigaki, P. Troch, R. Rabussier, and A. Kortenhaus. “A Comparison Study of a Generic Coupling Methodology for Modeling Wake Effects of Wave Energy Converter Arrays”. In: *Energies* 10.11 (2017). issn: 1996-1073. doi: 10.3390/en10111697. url: https://www.mdpi.com/1996-1073/10/11/1697.

[76] R. Kurnia and G. Ducrozet. “NEMOH: Open-source boundary element solver for computation of first- and second-order hydrodynamic loads in the frequency domain”. In: *Computer Physics Communications* 292 (2023), p. 108885. issn: 0010-4655. doi: https://doi.org/10.1016/j.cpc.2023.108885. url: https://www.sciencedirect.com/science/article/pii/S0010465523002308.

[77] T. Kelly, I. Zabala, Y. Peña-Sanchez, M. Penalba, J. V. Ringwood, J. C. Henriques, and J. M. Blanco. “A post-processing technique for removing ‘irregular frequencies’ and other issues in the results from BEM solvers”. In: *International Marine Energy Journal* 5.1 (June 2022), pp. 123–131. doi: 10.36688/imej.5.123-131. url: https://marineenergyjournal.org/imej/article/view/114.

[78] S. Marburg and S. Amini. “Cat’s eye radiation with boundary elements: Comparative study on treatment of irregular frequencies”. In: *Journal of Computational Acoustics* 13 (Mar. 2005). doi: 10.1142/S0218396X05002566.

[79] Y. Liu. “HAMS: A Frequency-Domain Preprocessor for Wave-Structure Interactions—Theory, Development, and Application”. In: *Journal of Marine Science and Engineering* 7.3 (2019). issn: 2077-1312. doi: 10.3390/jmse7030081. url: https://www.mdpi.com/2077-1312/7/3/81.

[80] W. Sheng, E. Tapoglou, X. Ma, C. Taylor, R. Dorrell, D. Parsons, and G. Aggidis. “Hydrodynamic studies of floating structures: Comparison of wave-structure interaction modelling”. In: *Ocean Engineering* 249 (2022). issn: 0029-8018. doi: https://doi.org/10.1016/j.oceaneng.2022.110878. url: https://www.sciencedirect.com/science/article/pii/S0029801822003183.

[81] M. Penalba, T. Kelly, and J. Ringwood. “Using NEMOH for Modelling Wave Energy Converters: A Comparative Study with WAMIT”. In: Aug. 2017.

[82] M. Ancellin and F. Dias. “Capytaine: a Python-based linear potential flow solver”. In: *Journal of Open Source Software* 4 (2019), p. 1341. doi: 10.21105/joss.01341.

[83] *Application of Irregular Frequency Removal Feature in Capytaine for Anode Cage Installation Over a Monopile Wind Turbine*. Vol. Volume 5A: Ocean Engineering. International Conference on Offshore Mechanics and Arctic Engineering. June 2024, V05AT06A063. doi: 10.1115/OMAE2024-126801. eprint: https://asmedigitalcollection.asme.org/OMAE/proceedings-pdf/OMAE2024/87820/V05AT06A063/7360876/v05at06a063-omae2024-126801.pdf. url: https://doi.org/10.1115/OMAE2024-126801.

[84] N. Quartier, T. Vervaet, G. V. Fernandez, J. M. Domínguez, A. J. Crespo, V. Stratigaki, and P. Troch. "High-fidelity numerical modelling of a two-WEC array with accurate implementation of the PTO system and control strategy using DualSPHysics". In: *Energy* 296 (2024), p. 130888. issn: 0360-5442. doi: https://doi.org/10.1016/j.energy.2024.130888. url: https://www.sciencedirect.com/science/article/pii/S0360544224006601.

[85] T. Vervaet, N. Quartier, E. Carpintero Moreno, G. Verao Fernandez, F. Ferri, V. Stratigaki, and P. Troch. "System identification and centralised causal impedance matching control of a row of two heaving point absorber wave energy converters". In: *Ocean Engineering* 309 (2024), p. 118399. issn: 0029-8018. doi: https://doi.org/10.1016/j.oceaneng.2024.118399. url: https://www.sciencedirect.com/science/article/pii/S0029801824017372.

[86] **V. Raghavan**, G. Lavidas, and A. Metrikine. "Comparing Open-Source BEM solvers for analysing wave energy converters". In: *Journal of Physics: Conference Series* 2647.7 (June 2024), p. 072002. doi: 10.1088/1742-6596/2647/7/072002. url: https://dx.doi.org/10.1088/1742-6596/2647/7/072002.

[87] E. Uzunoglu, Y. Liu, and C. G. Soares. "Performance of the open-source potential flow solver HAMS in estimating the hydrodynamic properties of a floating wind turbine". In: CRC Press, Oct. 2022, pp. 619–627. doi: 10.1201/9781003360773-70. url: https://www.taylorfrancis.com/chapters/edit/10.1201/9781003360773-70.

[88] Y. Guo, Y.-H. Yu, J. van Rij, and N. Tom. "Inclusion of Structural Flexibility in Design Load Analysis for Wave Energy Converters". In: Jan. 2018.

[89] J. van Rij, Y.-H. Yu, and Y. Guo. "Structural Loads Analysis for Wave Energy Converters". In: 2017, V010T09A023. doi: 10.1115/OMAE2017-62139.

[90] H. Liang, H. Wu, and F. Noblesse. "Validation of a global approximation for wave diffraction-radiation in deep water". In: *Applied Ocean Research* 74 (2018), pp. 80–86. issn: 0141-1187. doi: https://doi.org/10.1016/j.apor.2018.02.025. url: https://www.sciencedirect.com/science/article/pii/S0141118718300075.

[91] M. Kashiwagi, K. Endo, and H. Yamaguchi. "Wave drift forces and moments on two ships arranged side by side in waves". In: *Ocean Engineering* 32.5 (2005), pp. 529–555. issn: 0029-8018. doi: https://doi.org/10.1016/j.oceaneng.2004.09.005. url: https://www.sciencedirect.com/science/article/pii/S0029801804002252.

[92] T. Matsui, K. Kato, and T. Shirai. "A hybrid integral equation method for diffraction and radiation of water waves by three-dimensional bodies". In: *Computational Mechanics* 2 (1987), pp. 119–135. doi: https://doi.org/10.1007/BF00282134. url: https://doi-org.tudelft.idm.oclc.org/10.1007/BF00282134.

[93] F. Chau. "The Second Order Velocity Potential for Diffraction of Waves by Fixed Offshore Structures." PhD thesis. University College London, 1989.

[94] J. Newman. "Wave effects on deformable bodies". In: *Applied Ocean Research* 16.1 (1994), pp. 47–59. issn: 0141-1187. doi: https://doi.org/10.1016/0141-1187(94)90013-2. url: https://www.sciencedirect.com/science/article/pii/0141118794900132.

[95] G. Sismani and E. Loukogeorgaki. “Frequency-based investigation of a floating wave energy converter system with multiple flaps”. In: *Applied Mathematical Modelling* 84 (2020), pp. 522–535. issn: 0307-904X. doi: https://doi.org/10.1016/j.apm.2020.04.013. url: https://www.sciencedirect.com/science/article/pii/S0307904X20302067.

[96] **V.Raghavan**, A. Metrikine, and G. Lavidas. “Theory and validation of the new features in BIEM solver HAMS-MREL”. In: *Journal of Ocean Engineering and Marine Energy* (2025). issn: 2198-6452. doi: 10.1007/s40722-025-00431-8.

[97] F. Fàbregas Flavià, C. McNatt, F. Rongère, A. Babarit, and A. Clément. “A numerical tool for the frequency domain simulation of large arrays of identical floating bodies in waves”. In: *Ocean Engineering* 148 (2018), pp. 299–311. issn: 0029-8018. doi: https://doi.org/10.1016/j.oceaneng.2017.11.026. url: https://www.sciencedirect.com/science/article/pii/S0029801817306935.

[98] Y. Liu, H. Liang, M. Kashiwagi, and P. Cong. “Alternative approaches of evaluating Diffraction Transfer Matrix and Radiation Characteristics using the hybrid source-dipole formulation”. In: *Applied Ocean Research* 114 (2021), p. 102769. issn: 0141-1187. doi: https://doi.org/10.1016/j.apor.2021.102769. url: https://www.sciencedirect.com/science/article/pii/S0141118721002455.

[99] J. N. Newman. *Marine Hydrodynamics*. The MIT Press, Aug. 1977. isbn: 9780262280617. doi: 10.7551/mitpress/4443.001.0001. url: https://doi.org/10.7551/mitpress/4443.001.0001.

[100] C. H. Lee and J. N. Newman. *WAMIT User Manual, Versions 6.4, 6.4PC, 6.3S, 6.3S-PC*. English. Version 6.4, 6.4PC, 6.3S, 6.3S-PC. WAMIT, Inc. 343 pp.

[101] G. Wu. “The interaction of water waves with a group of submerged spheres”. In: *Applied Ocean Research* 17.3 (1995), pp. 165–184. issn: 0141-1187. doi: https://doi.org/10.1016/0141-1187(95)00010-0. url: https://www.sciencedirect.com/science/article/pii/0141118795000100.

[102] R. C. Thorne. “Multipole expansions in the theory of surface waves”. In: *Mathematical Proceedings of the Cambridge Philosophical Society* 49.4 (1953), pp. 707–716. doi: 10.1017/S0305004100028905.

[103] J. Van ’T Hoff. “Hydrodynamic modelling of the oscillating wave surge converter”. PhD thesis. Queens University Belfast, 2009.

[104] **V. Raghavan**, A. Metrikine, G. Lavidas, T. Islam, and V. Venugopal. “Extension of HAMS with the generalized modes approach”. In: *Innovations in Renewable Energies Offshore*. Ed. by C. Soares and S. Wang. Proceedings of the 6th International Conference on Renewable Energies Offshore, RENEW 2024. CRC Press / Balkema - Taylor and Francis Group, 2024, pp. 193–199. isbn: 9781032905570. doi: 10.1201/9781003558859-22.

[105] J. N. Newman. “Algorithms for the free-surface Green function”. In: *Journal of Engineering Mathematics* 19 (1985), pp. 57–67. issn: 1573-2703. doi: https://doi.org/10.1007/BF00055041. url: https://link.springer.com/article/10.1007/BF00055041#article-info.

[106] X. Ping, H. Wang, Q. Li, X. Yin, X. Wang, and C. li. “A Discussion on the Solution of Linear Systems Appeared in Gradient Coil Optimization with the Finite Element Method”. In: *Applied Magnetic Resonance* 51 (Apr. 2020). doi: 10.1007/s00723-020-01189-y.

[107] D. Kisacik, V. Stratigaki, M. Wu, L. Cappietti, I. Simonetti, P. Troch, A. Crespo, C. Altomare, J. Domínguez, M. Hall, M. Gómez-Gesteira, R. B. Canelas, and P. Stansby. "Efficiency and Survivability of a Floating Oscillating Water Column Wave Energy Converter Moored to the Seabed: An Overview of the EsflOWC MaRINET2 Database". In: *Water* 12.4 (2020). issn: 2073-4441. url: https://www.mdpi.com/2073-4441/12/4/992.

[108] **V. Raghavan**, A. Esposito, and L. Cappietti. "VALIDATION OF BEM SOLVER NEMOH WITH EXPERIMENTS ON A BOX OWC DEVICE". In: *Experiment and Numerical Validation Report NBEMB_01, LABIMA, University of Florence* (2022).

[109] B. Le Méhauté. "An Introduction to Hydrodynamics and Water Waves". In: *Springer* (1976). doi: https://doi.org/10.1007/978-3-642-85567-2.

[110] **V. Raghavan**, I. Simonetti, G. Lavidas, and L. Cappietti. "Numerical modelling of a box-type and bottom-detached oscillating water column wave energy conversion device: a comparison with experimental data and between BEM and CFD numerical modelling". In: *Proceedings of the European Wave and Tidal Energy Conference* 15 (2023). doi: 10.36688/ewtec-2023-142. url: https://submissions.ewtec.org/proc-ewtec/article/view/142.

[111] I. Simonetti and L. Cappietti. "Hydraulic performance of oscillating water column structures as anti-reflection devices to reduce harbour agitation". In: *Coastal Engineering* 165 (2021), p. 103837. issn: 0378-3839. doi: https://doi.org/10.1016/j.coastaleng.2020.103837. url: https://www.sciencedirect.com/science/article/pii/S0378383920305238.

[112] W. Sheng, R. Alcorn, and A. Lewis. "Assessment of primary energy conversions of oscillating water columns. I. Hydrodynamic analysis". In: *Renewable and Sustainable Energy* 6 (2014). doi: https://doi.org/10.1063/1.4896850. url: https://aip.scitation.org/doi/10.1063/1.4896850.

[113] A. Sarmento, L. Gato, and A. de O. Falcão. "Turbine-controlled wave energy absorption by oscillating water column devices". In: *Ocean Engineering* 17.5 (1990), pp. 481–497. issn: 0029-8018. doi: https://doi.org/10.1016/0029-8018(90)90040-D. url: https://www.sciencedirect.com/science/article/pii/002980189090040D.

[114] B. N. Fox, R. P. Gomes, and L. M. Gato. "Analysis of oscillating-water-column wave energy converter configurations for integration into caisson breakwaters". In: *Applied Energy* 295 (2021), p. 117023. issn: 0306-2619. doi: https://doi.org/10.1016/j.apenergy.2021.117023. url: https://www.sciencedirect.com/science/article/pii/S0306261921004876.

[115] W. Sheng and G. Aggidis. *Fundamentals of Wave Energy Conversions: The Dynamics of the Wave-Structure Interactions and Wave Energy Optimisation*. Eliva press, 2022, pp. 234–235. isbn: 978-9994982769. url: https://www.elivapress.com/en/book/book-3680559883/.

[116] K. Belibassakis, A. Magkouris, and E. Rusu. "A BEM for the Hydrodynamic Analysis of Oscillating Water Column Systems in Variable Bathymetry". In: *Energies* 13.13 (2020). issn: 1996-1073. doi: 10.3390/en13133403. url: https://www.mdpi.com/1996-1073/13/13/3403.

[117] A. Asiikkis, **V.Raghavan**, D. E. Grigoriadis, A. Metrikine, G. Lavidas, and A. Vakis. "Experimental validation of time domain simulations with HAMS-MREL and comparative analysis of linear and weakly nonlinear models for dense WEC arrays". In: *Ocean Engineering* 341 (2025), p. 122553. issn: 0029-8018. doi: 10.1016/j.oceaneng.2025.122553.

[118] M. Lawson, Y.-H. Yu, K. Ruehl, C. Michelen, and N. Tom. *WEC-Sim Wave Energy Converter Simulator*. NREL Data Catalog. Last updated December 18, 2024. Golden, CO, USA, 2016. doi: 10.7799/1887272.

[119] M. Lawson, Y.-H. Yu, K. Ruehl, C. Michelen, and N. Tom. *WEC-Sim Wave Energy Converter Simulator*. NREL Data Catalog. Last updated: December 18, 2024. Golden, CO, 2016. doi: 10.7799/1887272. url: https://doi.org/10.7799/1887272.

[120] *Development of PTO-Sim: A Power Performance Module for the Open-Source Wave Energy Converter Code WEC-Sim*. Vol. Volume 9: Ocean Renewable Energy. International Conference on Offshore Mechanics and Arctic Engineering. May 2015, V009T09A032. doi: 10.1115/OMAE2015-42074. eprint: https://asmedigitalcollection.asme.org/OMAE/proceedings-pdf/OMAE2015/56574/V009T09A032/4435057/v009t09a032-omae2015-42074.pdf. url: https://doi.org/10.1115/OMAE2015-42074.

[121] G. Lavidas and H. Polinder. "Wave energy in the Netherlands: Past, present and future perspectives". English. In: *Proceedings of the 13th European Wave Energy and Tidal Conference (EWTEC 2019)*. EWTEC, 2019. url: https://ewtec.org/conferences/ewtec-2019/.

[122] G. Lavidas and H. Polinder. "North Sea Wave Database (NSWD) and the Need for Reliable Resource Data: A 38 Year Database for Metocean and Wave Energy Assessments". In: *Atmosphere* 10.9 (2019). issn: 2073-4433. doi: 10.3390/atmos10090551. url: https://www.mdpi.com/2073-4433/10/9/551.

[123] G. Lavidas and M. Alday Gonzalez. *Wave Energy Assessment | North Sea Wave Database: Dutch-Wave And Tidal Energy ResourceS*. English. Delft University of Technology, Faculteit Civiele Techniek en Geowetenschappen, 2022.

[124] X. Shao, J. W. Ringsberg, H.-D. Yao, U. R. S. L. Gowda, H. N. Khedkar, and J. H. Todalshaug. "Hydrodynamic Interactions and Enhanced Energy Harnessing amongst Many WEC Units in Large-Size Wave Parks". In: *Journal of Marine Science and Engineering* 12.5 (2024). issn: 2077-1312. url: https://www.mdpi.com/2077-1312/12/5/730.

[125] B. Le Méhauté. *An Introduction to Hydrodynamics and Water Waves*. 1st ed. Springer Study Edition. Springer Berlin, Heidelberg, 1976, p. 323. isbn: 978-3-642-85567-2. doi: 10.1007/978-3-642-85567-2.

[126] L. S. P. da Silva, B. S. Cazzolato, N. Y. Sergiienko, B. Ding, H. M. Morishita, and C. P. Pesce. "Statistical linearization of the Morison's equation applied to wave energy converters". In: *Journal of Ocean Engineering and Marine Energy* 6.2 (2020), pp. 157–169. issn: 2198-6452. doi: 10.1007/s40722-020-00165-9. url: https://doi.org/10.1007/s40722-020-00165-9.

[127] G. Giorgi and J. V. Ringwood. "Nonlinear Froude-Krylov and viscous drag representations for wave energy converters in the computation/fidelity continuum". In: *Ocean Engineering* 141 (2017), pp. 164–175. issn: 0029-8018. doi: https://doi.org/10.1016/j.oceaneng.2017.06.030. url: https://www.sciencedirect.com/science/article/pii/S0029801817303256.

[128] Y. Gu, B. Ding, N. Y. Sergiienko, B. S. Cazzolato, and G. Giorgi. "The effects of predominant nonlinear hydrodynamics on the power absorption performance of a heaving point absorber adopting linear control principles". In: *Ocean Engineering* 325 (2025), p. 120774. issn: 0029-8018. doi: https://doi.org/10.1016/j.oceaneng.2025.120774. url: https://www.sciencedirect.com/science/article/pii/S0029801825004895.

[129] J. Tan and G. Lavidas. "A modified spectral-domain model for nonlinear hydrostatic restoring force of heaving wave energy converters". In: *Ocean Engineering* 309 (2024), p. 118581. issn: 0029-8018. doi: https://doi.org/10.1016/j.oceaneng.2024.118581. url: https://www.sciencedirect.com/science/article/pii/S002980182401919X.

[130] K. Nielsen. *Numerical Modelling of Wave Energy Converters*. Tech. rep. OES Task 10 Report. Paris, France: International Energy Agency – Ocean Energy Systems (IEA-OES), Sept. 2024. url: https://www.ocean-energy-systems.org.

[131] A. Babarit, J. Hals, M. Muliawan, A. Kurniawan, T. Moan, and J. Krokstad. “Numerical benchmarking study of a selection of wave energy converters”. In: *Renewable Energy* 41 (2012), pp. 44–63. issn: 0960-1481. doi: https://doi.org/10.1016/j.renene.2011.10.002. url: https://www.sciencedirect.com/science/article/pii/S0960148111005672.

[132] J. Meyer, C. Windt, P. Sinn, and A. Hildebrandt. “On the mooring methodology of heaving point absorber arrays”. In: *Ocean Engineering* 281 (2023), p. 114659. issn: 0029-8018. doi: https://doi.org/10.1016/j.oceaneng.2023.114659. url: https://www.sciencedirect.com/science/article/pii/S0029801823010430.

[133] J. N. Newman. “Wave Effects on Multiple Bodies”. In: 2001.

[134] M. Chen, H. Guo, R. Wang, R. Tao, and N. Cheng. “Effects of Gap Resonance on the Hydrodynamics and Dynamics of a Multi-Module Floating System with Narrow Gaps”. In: *Journal of Marine Science and Engineering* 9.11 (2021). issn: 2077-1312. doi: 10.3390/jmse9111256. url: https://www.mdpi.com/2077-1312/9/11/1256.

[135] P. Laporte Weywada. “D1.1 Advanced Wave-Structure Interaction Model – Theory and User Manual”. In: *Zenodo* (2018). doi: https://doi.org/10.5281/zenodo.2562765.

[136] H. Jafaryeganeh, J. M. Rodrigues, and C. Guedes Soares. “Influence of mesh refinement on the motions predicted by a panel code”. In: Oct. 2014, pp. 1029–1038. isbn: 978-1-138-02727-5. doi: 10.13140/2.1.5191.9363.

[137] S. MARBURG. “SIX BOUNDARY ELEMENTS PER WAVELENGTH: IS THAT ENOUGH?” In: *Journal of Computational Acoustics* 10.01 (2002), pp. 25–51. doi: 10.1142/S0218396X02001401. eprint: https://doi.org/10.1142/S0218396X02001401
url: https://doi.org/10.1142/S0218396X02001401.

[138] D. Ning, X. Su, M. Zhao, and B. Teng. “Numerical study of resonance induced by wave action on multiple rectangular boxes with narrow gaps”. In: *Acta Oceanologica Sinica* 34.5 (2015), pp. 92–102. issn: 1869-1099. doi: 10.1007/s13131-015-0672-1. url: https://doi.org/10.1007/s13131-015-0672-1.

[139] *Optimum Reactive Control and Control by Latching of a Wave-Absorbing Semisubmerged Heaving Sphere*. Vol. 21st International Conference on Offshore Mechanics and Arctic Engineering, Volume 4. International Conference on Offshore Mechanics and Arctic Engineering. June 2002, pp. 415–423. doi: 10.1115/OMAE2002-28172. eprint: https://asmedigitalcollection.asme.org/OMAE/proceedings-pdf/OMAE2002/36142/415/4545242/415_1.pdf.
url: https://doi.org/10.1115/OMAE2002-28172.

[140] J. McNatt and C. Retzler. “The performance of the Mocean M100 wave energy converter described through numerical and physical modelling”. In: *International Marine Energy Journal* 3 (May 2020), pp. 11–19. doi: 10.36688/imej.3.11-19.

[141] J. Todalshaug, A. Babarit, J. Krokstad, M. J. Muliawan, A. Kurniawan, and T. Moan. *The NumWEC project. Numerical estimation of energy delivery from a selection of wave energy converters – final report*. Apr. 2015. doi: 10.13140/RG.2.1.3807.8885.

[142] *Optimising Reactive Control in Non-Ideal Efficiency Wave Energy Converters*. Vol. Volume 9A: Ocean Renewable Energy. International Conference on Offshore Mechanics and Arctic Engineering. June 2014, V09AT09A002. doi: 10.1115/OMAE2014-23005. eprint: https://asmedigitalcollection.asme.org/OMAE/proceedings-pdf/OMAE2014/45530/V09AT09A002/4432200/v09at09a002omae2014-23005.pdf. url: https://doi.org/10.1115/OMAE2014-23005.

[143] R. Genest, F. Bonnefoy, A. H. Clément, and A. Babarit. “Effect of non-ideal power take-off on the energy absorption of a reactively controlled one degree of freedom wave energy converter”. In: *Applied Ocean Research* 48 (2014), pp. 236–243. issn: 0141-1187. doi: https://doi.org/10.1016/j.apor.2014.09.001. url: https://www.sciencedirect.com/science/article/pii/S0141118714000893.

[144] M.Alday, **V.Raghavan**, and G.Lavidas. “Effects of wave spectrum representation on power production estimations from point absorbers”. In: *Applied Ocean Research* 161 (2025), p. 104626. issn: 0141-1187. doi: https://doi.org/10.1016/j.apor.2025.104626.

[145] O. M. Mazzaretto, M. Menéndez, and H. Lobeto. “A global evaluation of the JONSWAP spectra suitability on coastal areas”. In: *Ocean Engineering* 266 (2022), p. 112756. issn: 0029-8018. doi: https://doi.org/10.1016/j.oceaneng.2022.112756. url: https://www.sciencedirect.com/science/article/pii/S002980182202039X.

[146] J. Tan, W. Tao, A. J. Laguna, H. Polinder, Y. Xing, and S. Miedema. “A spectral-domain wave-to-wire model of wave energy converters”. In: *Applied Ocean Research* 138 (2023), p. 103650. issn: 0141-1187. doi: https://doi.org/10.1016/j.apor.2023.103650. url: https://www.sciencedirect.com/science/article/pii/S0141118723001918.

[147] M. Folley and T. Whittaker. “Spectral modelling of wave energy converters”. In: *Coastal Engineering* 57.10 (2010), pp. 892–897. issn: 0378-3839. doi: https://doi.org/10.1016/j.coastaleng.2010.05.007. url: https://www.sciencedirect.com/science/article/pii/S0378383910000700.

[148] J. Tan. “Improving the Techno-Economic Performance of Wave Energy Converters: From the Perspective of Systematic Sizing”. English. Dissertation (TU Delft). Delft University of Technology, 2022. isbn: 978-94-6458-745-6. doi: 10.4233/uuid:de50235b-1d2a-43f3-bcfa-1dd5f570ab5a.

[149] F. Fusco and J. V. Ringwood. “A Simple and Effective Real-Time Controller for Wave Energy Converters”. In: *IEEE Transactions on Sustainable Energy* 4.1 (2013), pp. 21–30. doi: 10.1109/TSTE.2012.2196717.

[150] J. Falnes and A. Kurniawan. *Ocean Waves and Oscillating Systems: Linear Interactions Including Wave-Energy Extraction*. Vol. 8. Cambridge University Press, 2020.

[151] F. Fusco and J. V. Ringwood. “Short-Term Wave Forecasting for Real-Time Control of Wave Energy Converters”. In: *IEEE Transactions on Sustainable Energy* 1.2 (2010), pp. 99–106. doi: 10.1109/TSTE.2010.2047414.

[152] J. Falnes. “Radiation impedance matrix and optimum power absorption for interacting oscillators in surface waves”. In: *Applied Ocean Research* 2.2 (1980), pp. 75–80. issn: 0141-1187. doi: https://doi.org/10.1016/0141-1187(80)90032-2. url: https://www.sciencedirect.com/science/article/pii/0141118780900322.

[153] *Improving the Wave Energy Production Using Multi-Size WEC Arrays With Passive Control*. Vol. Volume 7: Ocean Renewable Energy. International Conference on Offshore Mechanics and Arctic Engineering. June 2024, V007T09A065. doi: 10.1115/OMAE2024-123655. eprint: https://asmedigitalcollection.asme.org/OMAE/proceedings-pdf/OMAE2024/87851/V007T09A065/7361505/v007t09a065-omae2024-123655.pdf. url: https://doi.org/10.1115/OMAE2024-123655.

[154] J. T. Katsikadelis. “Chapter Two - Preliminary Mathematical Knowledge”. In: *The Boundary Element Method for Engineers and Scientists (Second Edition)*. Ed. by J. T. Katsikadelis. Second Edition. Oxford: Academic Press, 2016, pp. 13–33. isbn: 978-0-12-804493-3. doi: https://doi.org/10.1016/B978-0-12-804493-3.00002-3. url: https://www.sciencedirect.com/science/article/pii/B9780128044933000023.

[155] M. Alday and G. Lavidas. “The ECHOWAVE Hindcast: A 30-years high resolution database for wave energy applications in North Atlantic European waters”. In: *Renewable Energy* 236 (2024), p. 121391. issn: 0960-1481. doi: https://doi.org/10.1016/j.renene.2024.121391. url: https://www.sciencedirect.com/science/article/pii/S0960148124014599.

[156] G. Dalton, G. Allan, N. Beaumont, A. Georgakaki, N. Hacking, T. Hooper, S. Kerr, A. M. O’Hagan, K. Reilly, P. Ricci, W. Sheng, and T. Stallard. “Economic and socio-economic assessment methods for ocean renewable energy: Public and private perspectives”. In: *Renewable and Sustainable Energy Reviews* 45 (2015), pp. 850–878. issn: 1364-0321. doi: https://doi.org/10.1016/j.rser.2015.01.068. url: https://www.sciencedirect.com/science/article/pii/S1364032115000787.

[157] D. Magagna and A. Uihlein. “Ocean energy development in Europe: Current status and future perspectives”. In: *International Journal of Marine Energy* 11 (2015), pp. 84–104. issn: 2214-1669. doi: https://doi.org/10.1016/j.ijome.2015.05.001. url: https://www.sciencedirect.com/science/article/pii/S2214166915000181.

[158] Herman Senior BV. *Multicat Auxilia (Damen 3515) Product Sheet*. Tech. rep. Length: 34.65 m. Heavy-duty vessel for offshore wind support and heavy lifting. Herman Senior, 2019. url: https://hermansr.com/multicat-auxilia/.

[159] Damen Shipyards Group. *Modular Multi Cat 1205 Product Sheet*. Tech. rep. Length: 12.75m. Optimized for dredging support and inland maintenance. Damen Shipyards, 2024. url: https://www.damen.com/vessels/workboats/multicats/multi-cat-2712.

[160] Offshore Wind Biz. “MarineCo Orders Damen Multi Cat 2712”. In: *Offshore Wind News* (Dec. 2014). Details the first contract for the 27-meter variant for offshore wind service. url: https://www.offshorewind.biz/2014/12/31/marineco-orders-damen-multi-cat-2712/.

[161] H.-Z. Hsu. “Safety Domain Measurement for Vessels in an Overtaking Situation”. In: *International Journal of e-Navigation and Maritime Economy* 1 (2014), pp. 29–38. issn: 2405-5352. doi: https://doi.org/10.1016/j.enavi.2014.12.004. url: https://www.sciencedirect.com/science/article/pii/S2405535214000059.

[162] M. Rosati, J. Henriques, and J. Ringwood. “Oscillating-water-column wave energy converters: A critical review of numerical modelling and control”. In: *Energy Conversion and Management: X* 16 (2022), p. 100322. issn: 2590-1745. doi: https://doi.org/10.1016/j.ecmx.2022.100322. url: https://www.sciencedirect.com/science/article/pii/S2590174522001453.

[163] W. Sheng, R. Alcorn, and A. Lewis. “Assessment of primary energy conversions of oscillating water columns. I. Hydrodynamic analysis”. In: *Journal of Renewable and Sustainable Energy* 6.5 (Sept. 2014). 053113. issn: 1941-7012. doi: 10.1063/1.4896850. eprint: https://pubs.aip.org/aip/jrse/article-pdf/doi/10.1063/1.4896850/14729925/053113_1_online.pdf. url: https://doi.org/10.1063/1.4896850.

[164] M. Penalba, T. Kelly, and J. Ringwood. “Using NEMOH for Modelling Wave Energy Converters: A Comparative Study with WAMIT”. In: *12th European Wave and Tidal Energy Conference (EWTEC)*. 2017. url: https://mural.maynoothuniversity.ie/12466/.

[165] A. Cotten and D. Forehand. “Optimisation of a novel, sloped module, multibody wave energy converter, using an efficient modelling technique”. In: *Renewable Energy* 162 (2020), pp. 727–742. issn: 0960-1481. doi: https://doi.org/10.1016/j.renene.2020.07.091. url: https://www.sciencedirect.com/science/article/pii/S0960148120311678.

[166] **V. Raghavan** and G. Lavidas. “Mixed Wave Energy arrays, re-thinking wave array configurations:a economics based approach”. In: *Renewable Energy* (2026). ***Under Review***.

[167] **V. Raghavan**, A. Metrikine, and G. Lavidas. “Mixed Wave Energy arrays, re-thinking wave array configurations:a hydrodynamics based approach”. In: *Renewable Energy* (2026). ***Under Review***.

[168] T. Engelfried, M. Alday, **V. Raghavan**, and G. Lavidas. “Geospatial analysis of the life cycle global warming impacts from marine renewables”. In: *Renewable and Sustainable Energy Reviews* 226 (2026), p. 116338. issn: 1364-0321. doi: https://doi.org/10.1016/j.rser.2025.116338. url: https://www.sciencedirect.com/science/article/pii/S1364032125010111.

[169] **V. Raghavan**, A. Cotten, A. Metrikine, and G. Lavidas. “Assessing the Performance of Arrays of Two-Body Hinged Attenuator WECs”. In: *Proceedings of the ASME International Ocean Offshore and Arctic Engineering Conference (OMAE 2026)*. ***Accepted***. Tokyo, Japan, June 2026, OMAE2026–183627.

[170] **V. Raghavan**, A. Metrikine, and G. Lavidas. “Exploring the Hydrodynamics of Mixed Wave Energy Farms”. In: *Proceedings of the European Wave and Tidal Energy Conference (EWTEC 2025)*. Vol. 16. Sept. 2025, Paper 699. doi: 10.36688/ewtec-2025-699. url: https://doi.org/10.36688/ewtec-2025-699.

[171] **V. Raghavan**, A. Metrikine, and G. Lavidas. “Additional Features in HAMS-MREL: A New Open-Source BIEM Solver for Offshore Energy Applications”. In: *Proceedings of the European Wave and Tidal Energy Conference (EWTEC 2025)*. Vol. 16. Sept. 2025, Paper 700. doi: 10.36688/ewtec-2025-700. url: https://doi.org/10.36688/ewtec-2025-700.

[172] M. Alday, **V. Raghavan**, and G. Lavidas. “Influence of the Wave Spectrum Representation on Production Estimations From Point Absorbers WEC Farms”. In: *Proceedings of the European Wave and Tidal Energy Conference (EWTEC 2025)*. Vol. 16. Sept. 2025, Paper 752. doi: 10.36688/ewtec-2025-752. url: https://doi.org/10.36688/ewtec-2025-752.

[173] M. Alday, **V. Raghavan**, and G. Lavidas. “Representing Wave Energy Converters in the SWAN Model With Varying Transmission Coefficients Across Frequencies”. In: *Proceedings of the European Wave and Tidal Energy Conference (EWTEC 2025)*. Vol. 16. Sept. 2025, Paper 866. doi: 10.36688/ewtec-2025-866. url: https://doi.org/10.36688/ewtec-2025-866.

[174] A. Jain, J. Tan, **V. Raghavan**, and G. Lavidas. “A Study on Wave Energy Converter Arrays Using Data-Driven Polynomial Chaos Expansion”. In: *Proceedings of the European Wave and Tidal Energy Conference (EWTEC 2025)*. Vol. 16. Sept. 2025, Paper 984. url: https://publications.evolvingcities.org/proc-ewtec/article/view/984.

[175] G. M. Alday, **V. Raghavan**, and G. Lavidas. “Improving the Wave Energy Production Using Multi-Size WEC Arrays With Passive Control”. In: *Proceedings of the International Conference on Offshore Mechanics and Arctic Engineering (OMAE 2024)*. Vol. 7. Ocean Renewable Energy. June 2024, V007T09A065. doi: 10.1115/OMAE2024-123655. url: https://doi.org/10.1115/OMAE2024-123655.

[176] **V. Raghavan**, G. M. Alday, A. Metrikine, and G. Lavidas. “Wave Energy Farm Assessment in Real Wave Climates: The North Sea”. In: *Proceedings of the International Conference on Offshore Mechanics and Arctic Engineering (OMAE 2024)*. Vol. 7. Ocean Renewable Energy. June 2024, V007T09A062. doi: 10.1115/OMAE2024-120946. url: https://doi.org/10.1115/OMAE2024-120946.

[177] M. Alday, **V. Raghavan**, and G. Lavidas. “Analysis of the North Atlantic offshore energy flux from different reanalysis and hindcasts”. In: *Proceedings of the European Wave and Tidal Energy Conference*. Vol. 15. European Wave and Tidal Energy Conference, 2023. doi: 10.36688/ewtec-2023-140. url: https://submissions.ewtec.org/proc-ewtec/article/view/140.

[178] **V. Raghavan**, G. Lavidas, A. Metrikine, N. Mantadakis, and E. Loukogeorgaki. “A comparative study on BEM solvers for Wave Energy Converters”. In: CRC Press, Oct. 2022, pp. 441–447. doi: 10.1201/9781003360773-50. url: https://www.taylorfrancis.com/books/9781003360773/chapters/10.1201/9781003360773-50.

# A

# ADDITIONAL VALIDATION CASES FOR HAMS-MREL

Two cases in addition to the Case 1 and 2 in chapter 2 are shown here. These are taking from [54].

## A.1. CASE 1 - THREE SEMI-SUBMERGED CYLINDERS COMPARED WITH SEMI-ANALYTICAL SOLUTIONS AND WAMIT

The case is taken from the work by Mavrakos [24], which provides a solution for the hydrodynamic coefficients based on a semi-analytical method. The work focuses on obtaining the hydrodynamic coefficients (added mass and radiation damping) from the different combination of axisymmetric bodies. Here the cylindrical case is considered.

The radiation problem is solved using an semi-analytical method that combines single body hydrodynamic characteristics with the multiple scattering approach to account for the interaction phenomena. By superimposing various orders of radiated/scattered waves emanating from one body oscillating in the vicinity of the others, the velocity potential is derived for each body within the multi-component system. This methodology is applicable for any number of axisymmetric bodies with any geometrical arrangement, provided the vertical projections of any two bodies not overlap.

The three semi-immersed floating cylinder problem is shown in Figure A.1. The mesh used for this case in both HAMS-MREL and WAMIT is shown in Figure A.2. The properties selected for the three-cylinder case have been shown in Table A.1. The number of panels were based on a convergence study that was carried out as part of the research.

The results comparing the added mass in surge and pitch-surge for cylinder 1 is shown in Figure A.3a and Figure A.3b. HAMS-MREL is very close to the semi-analytical solution and WAMIT for $\nu a < 1.5$. Beyond that, small differences are observed between HAMS-MREL and WAMIT. The results comparing the radiation damping in surge and pitch-surge for cylinder 1 is shown in Figure A.3c and Figure A.3d respectively. The results for the surge added mass and radiation damping for cylinder 2 are plotted in Figure A.4a and Figure A.4b respectively. A trend similar to cylinder 1 is observed.

Table A.1.: Properties used for the simulation in HAMS-MREL and WAMIT for Case 1

| Property | Unit | Value |
|---|---|---|
| Diameter, $D$ | $m$ | 6 |
| Spacing, $L$ | $m$ | 15 |
| Water Depth, $h$ | $m$ | 120 |
| Draft, $H$ | $m$ | 10.95 |
| Angle of incidence, $\beta$ | *degrees* | 0 |

A

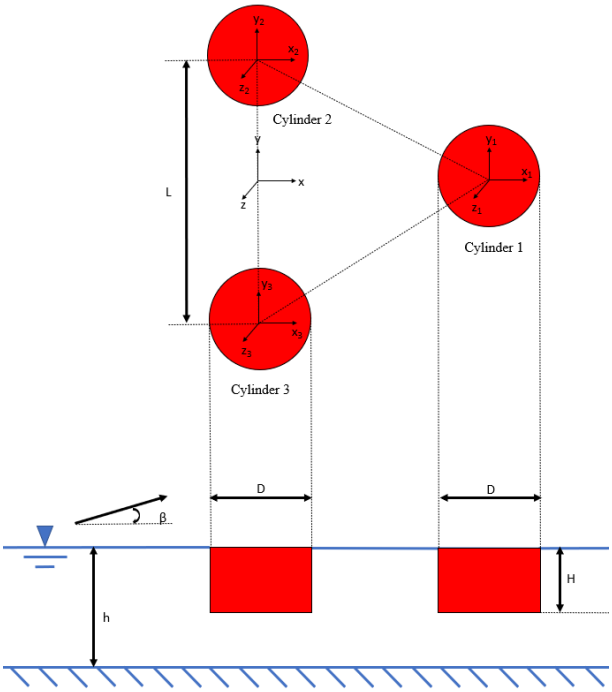



Figure A.1.: Three semi-immersed floating cylinders

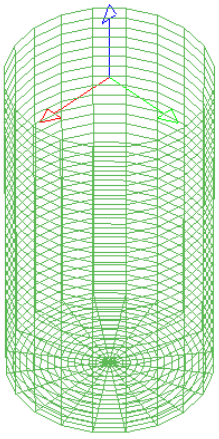
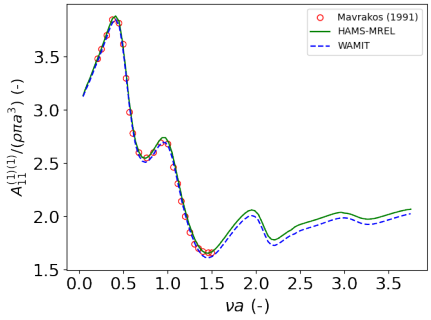
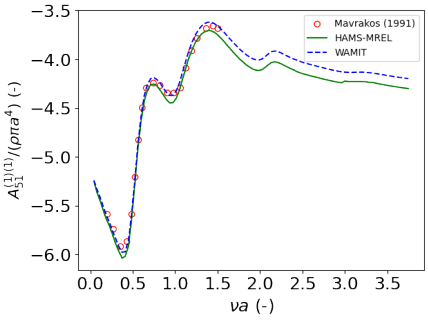


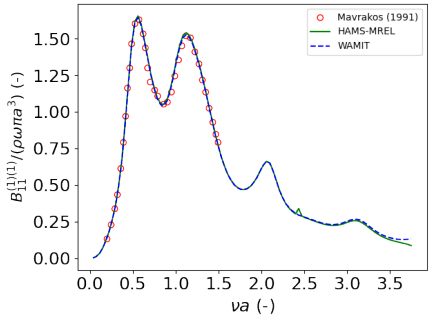
Figure A.2.: Cylindrical mesh with 900 panels used in Case 1



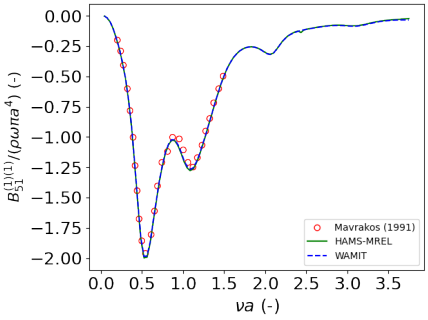

(a) Added mass in surge




(b) Added mass in pitch-surge

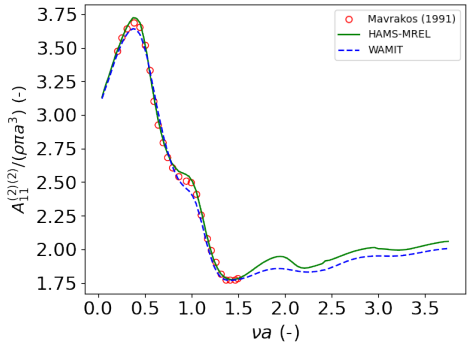



(c) Radiation damping in surge

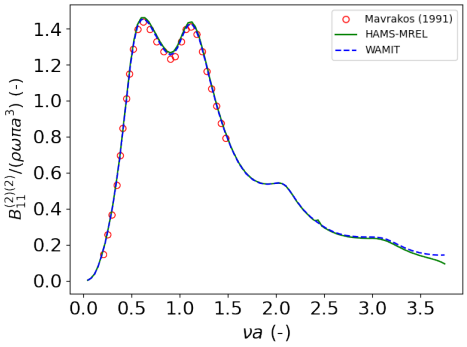



(d) Radiation damping in pitch-surge

Figure A.3.: Hydrodynamic coefficients for surge and pitch-surge for Cylinder 1




(a) Added mass in surge




(b) Radiation damping in surge

Figure A.4.: Hydrodynamic coefficients for surge cylinder 2

A

## A.2. CASE 2 - FLOATING OWC COMPARED WITH SEMI-ANALYTICAL SOLUTIONS AND WAMIT

This case is that of a floating OWC.

Most literature showing modelling approaches for OWCs with BIEM utilize WAMIT as the BIEM solver, particularly when doing experimental validations. To this extent, WAMIT is also the most developed BIEM solver for OWCs as it offers the ability to model the OWC in two different ways. The first method models an imaginary piston above the internal water column as a thin massless disk in combination with generalized degrees of freedom that can use all 6 modes [162] (usually heave is only used). This method utilizes dipole panels to model the thin disk, which also requires a high resolution for the mesh. However, since only the disk is modelled with dipole panels, the computational effort is reasonable. The second method models the hull of the OWC and an imaginary piston in a two-body system, where the length of the piston is varied so as to replace part of the water column [163]. This is particularly useful when the water column moves only in heave.

The second method is adopted here for modelling the floating OWC in HAMS-MREL since it does not have the feature of generalized degrees of freedom for modelling the massless disk. An inter-model comparison is performed with WAMIT. The case from the work of Penalba et al. [164] has been considered wherein a simplified version of the Sparbuoy is modelled. The length of the imaginary piston is chosen to be equal to the length of the column based on the work of Sheng et al [163] since this better captures the hydrodynamics of the OWC system including the added mass at infinite frequency, which becomes essential when performing time domain analysis of the OWC system.

It has been shown in the work of Sheng [163], that considering different lengths of the piston will result in different added masses due in heaving. However, the total mass, which is equal to the sum of the mass of the piston (which is the mass of the water column replaced by the piston from the free surface to the length of the water column) and the added mass due to the heaving piston, are approximately constant over all considered piston lengths. Therefore, the combination of added mass and mass of the piston in HAMS-MREL, as obtained from the second method, is compared here with the added mass obtained with the generalized modes case (first method) and two-body method (second method) as obtained from WAMIT. These comparisons are shown assuming motion only in heaving.

The meshes for the two considered cases are shown in Fig. A.6a and Fig. A.6b. When modelling the OWC with the generalized modes, the internal column surface mesh is modelled as part of the hull mesh. The properties of the model are specified in Table. A.2. The number of panels used for the two-body case was based on a convergence study conducted as part of this research. The results for the total mass (added mass + mass of piston) is shown in Fig. A.7 and the radiation damping is shown in Fig. A.8. As seen, the results match perfectly between the two codes validating this extension of HAMS-MREL for obtaining a solution with overlapping panels.

Table A.2.: Properties used for the simulation in HAMS-MREL and WAMIT for Case 2

| Property | Unit | Value |
|---|---|---|
| Inner Radius, $r_1$ | *m* | 2 |
| Outer Radius, $r_2$ | *m* | 3 |
| Water Depth, $h$ | *m* | Infinite |
| Draft, $H$ | *m* | 10 |
| Angle of incidence, $\beta$ | *degrees* | 0 |

### A.2.1. COMPUTATIONAL RESOURCES COMPARING HAMS-MREL AND WAMIT

This section focuses on comparing the computation time between WAMIT and HAMS-MREL for the two cases considered.

Comparison is done between WAMIT and HAMS-MREL in terms of the analysis time for the considered four cases. The analyses were carried out in a 4 core, 8 GB RAM PC with a Intel Core i5-4440 CPU processor (3.10 GHz). The computation times for the analyses

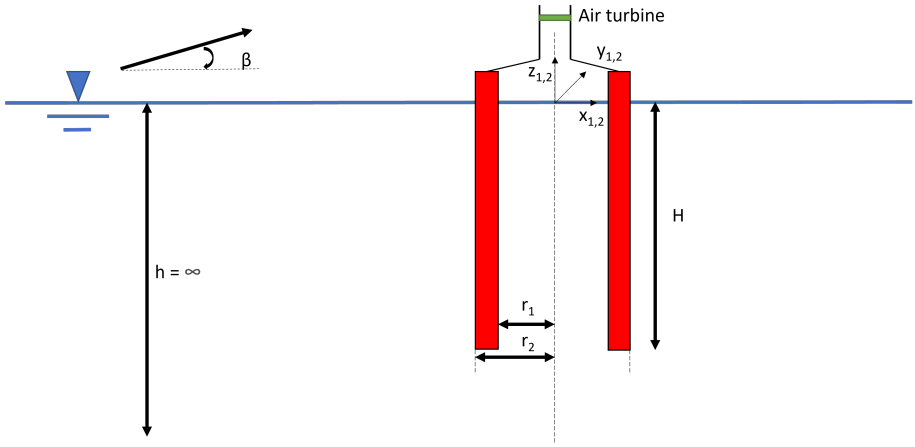
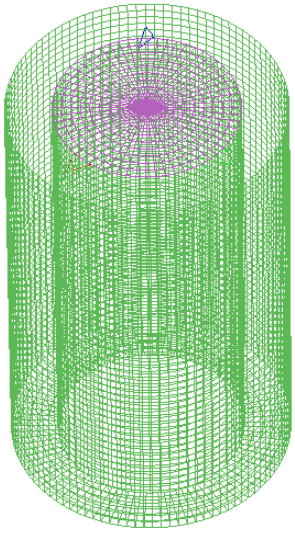
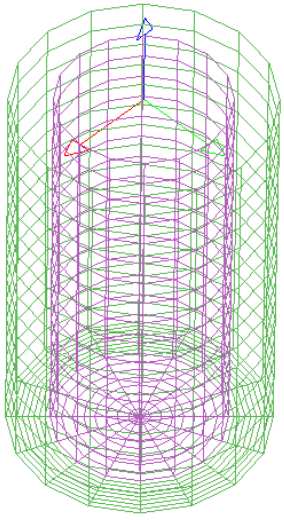



Figure A.5.: Floating OWC



(a) Thin massless disk representation of the piston using a generalized heave mode. Thin disk (purple) and hull of OWC (green). Total of 2275 panels across the entire model.



(b) Two-body representation of the Sparbuoy OWC, where the piston is modelled over the length of the internal water column. Internal water surface (purple) and hull of OWC (green). 640 panels for the hull and 384 panels for the internal water column.

Figure A.6.: Numerical representations of the Sparbuoy floating OWC considered in this study.

A

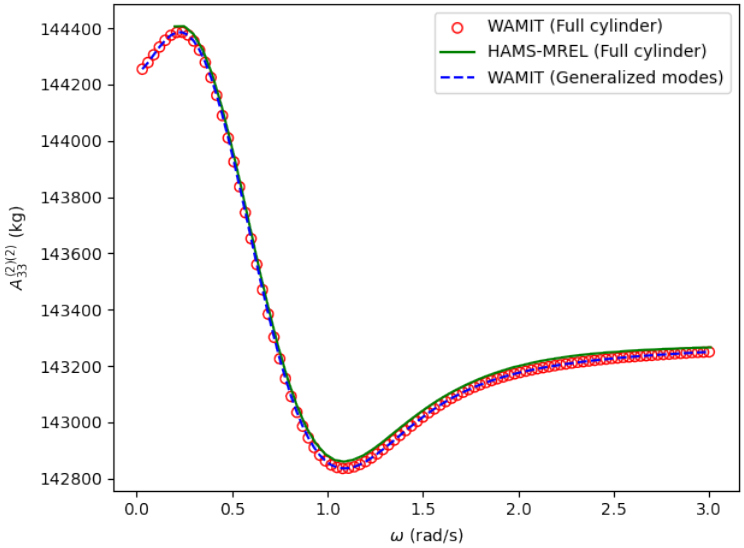



Figure A.7.: Total mass (Mass of piston + Added mass) in heaving for the internal free surface

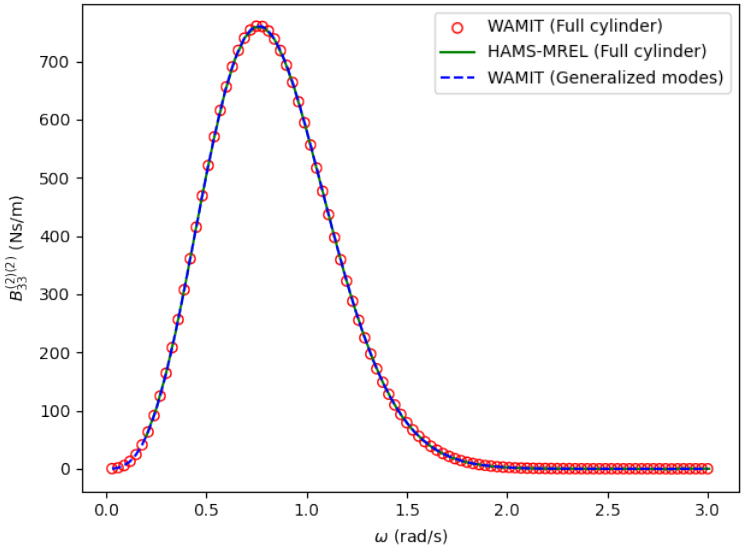



Figure A.8.: Radiation damping in heaving for the internal free surface

are shown in Table. A.3. Since WAMIT v6.1 was used for these analyses, no parallelization was available in WAMIT. Accordingly, for this comparison, no parallelization was used in HAMS-MREL.

Table A.3.: Simulation times for the 4 cases with HAMS-MREL and WAMIT (Time in min)

| Case | $N_p^T$ | $N_\omega$ | WAMIT | HAMS-MREL |
|---|---|---|---|---|
| Case 1 | 2700 | 100 | 65.45 | 716.67 |
| Case 2 | 1024 | 202 | 18.5 | 4.16 |

In Table A.3, $N_p^T$ is the total number of panels and $N_\omega$ is the number of frequencies used in the analysis. From Table. A.3, it can be observed that for the considered infinite depth case (Case 4), HAMS-MREL is more than 4 times faster than WAMIT, whereas for the considered finite depth case (Case 1), it is 11 times slower than WAMIT. HAMS-MREL does employ parallelization, which can speed up the calculations. This feature was added in WAMIT for v7 or higher [80].

# B

# FLAP - BIEM SHAPE FUNCTION, ROTATIONAL INERTIA AND VISCOUS DAMPING COEFFICIENT

## B.1. IMPLEMENTATION OF THE GENERALIZED MODES TO OBTAIN THE SHAPE FUNCTIONS

In this section, the implementation of the generalized modes is explained based on the work of [94]. This work considering the flap geometry from [103] has been published as [104]. The provided derivation is a generic one for flap type converters.

### B.1.1. BODY BOUNDARY CONDITION FOR THE FIRST ORDER BOUNDARY VALUE PROBLEM

The body boundary condition in the BIEM formulation can be expressed as a general expression:

$$\frac{\partial \varphi_j}{\partial n} = \mathbf{S_j}.\mathbf{n} \tag{B.1}$$

where $S_j$ is a 3D vector shape function with cartesian components $u_j, v_j, w_j$ and $\mathbf{n} = (n_x, n_y, n_z)$ is the normal vector projecting from the body towards the fluid [94]. For the rigid body translational degrees of freedom ($j$ = 1,2,3), the shape function is unit vector in the corresponding direction, and for the rigid body rotations (j=4,5,6), $\mathbf{S_j} = \mathbf{S_{j-3}} \times \mathbf{r}$, where $\mathbf{r}$ is the lever arm vector with respect to a rotation center[94, 95].

The projection of the normal vector can be written in general as:

$$\mathbf{S_j}.\mathbf{n} = u_j n_x + v_j n_j + w_j n_z \tag{B.2}$$

Therefore, by deriving this vector shape function for any additional mode/degree of freedom, the radiation and diffraction problem can also be solved considering this degree of freedom in HAMS/HAMS-MREL. The vector shape function can represent general mode shapes corresponding to structural deflections, the motions of the interior free surfaces inside moonpools, or multiple bodies with constraints [57].

### B.1.2. DERIVATION OF THE SHAPE FUNCTION FOR A FLAP

The geometry is shown in Figure B.1. The flap top combines two geometries, a upper triangular box and a lower triangular box, while the flap bottom, which is rigidly fixed to the sea bottom, is composed of a rectangular box. The hinge is located at $L_s$ from the free surface. The water depth is $d$ m, thus the hinge being at 2 m above the sea bottom.

$XYZ$ is the global coordinate system. $xyz$ is the local coordinate system located at the top of the flap and coincides with the global coordinate system, $x_d y_d z_d$ is the deformed coordinate system due to the flap's unit rotation $\theta$. The flap is aligned such that the width ($W$) is along the $Y$ axis. The surface of the flap is discretized into panels.

The global position vector $\mathbf{U_f} = (U_{f,x}, U_{f,y}, U_{f,z})$ of a random panel can be obtained based on the work of [95] and is given as:

$$U_{f,x} = -L_s \sin\theta + X\cos\theta + Z\sin\theta, \tag{B.3a}$$
$$U_{f,y} = Y, \tag{B.3b}$$
$$U_{f,z} = -L_s(1-\cos\theta) - X\sin\theta + Z\cos\theta. \tag{B.3c}$$

Here $X, Y, Z$ can be directly utilized as it aligns with $x, y, z$. The position vector of the hinge $\mathbf{U_h}$ is given as:

$$\mathbf{U_h} = (0, 0, -L_s) \tag{B.4}$$

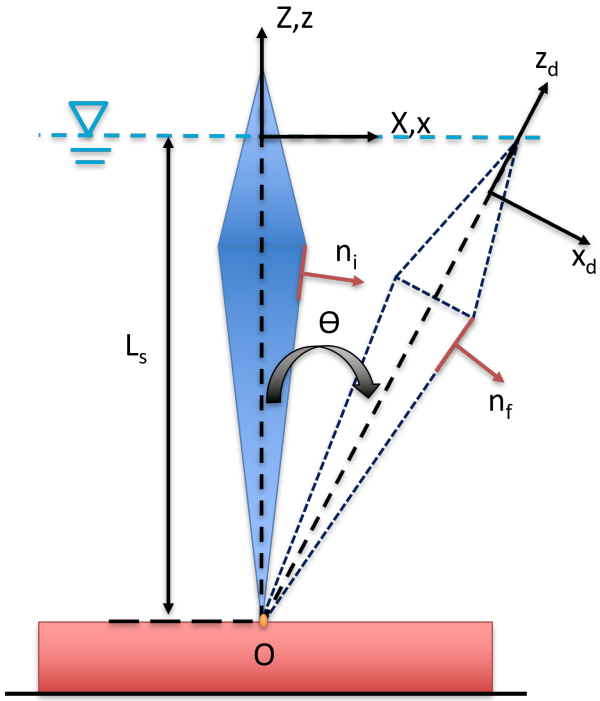



Figure B.1.: Schematic representation of rotation of the flap

Since we want to use the pitch rotation of the rigid flap top about the hinge, the lever arm vector $\mathbf{r}$ needs to be derived which is given as:

$$\mathbf{r} = \mathbf{U_f} - \mathbf{U_h} \tag{B.5}$$

with $\mathbf{r} = (r_x, r_y, r_z)$ where

$$r_x = -L_s sin\theta + Xcos\theta + Zsin\theta \tag{B.6a}$$
$$r_y = Y \tag{B.6b}$$
$$r_z = L_s cos\theta - Xsin\theta + Zcos\theta \tag{B.6c}$$

The normal vector for the considered panel in the deformed state is given as:

$$\mathbf{n_f} = (n_{i,x}cos\theta + n_{i,z}sin\theta, n_{i,y}, -n_{i,x}sin\theta + n_{i,z}cos\theta) \tag{B.7}$$

where $\mathbf{n_i} = (n_{i,x}, n_{i,y}, n_{i,z})$ is the normal vector of the considered panel in the undeformed state. The normal vector for the rigid body rotation for the pitch about the hinge can then be obtained as the $y$ component of the cross product $\mathbf{r} \times \mathbf{n_f}$ (since the pitching occurs about the y-axis), which is obtained as:



$$n_{7,top} = n_{i,x}(L_s + Z) + n_{i,z}(-X) \tag{B.8}$$

From this the shape function for the additional degree of freedom/mode shape for the flap top can be obtained as:

$$\mathbf{S_{7,top}} = (L_s + Z, 0, -X) \tag{B.9}$$

Since the flap bottom is stationary, the shape function for the bottom is a null vector.

$$\mathbf{S_{7,bottom}} = (0, 0, 0) \tag{B.10}$$

Using this as the body boundary condition for the additional pitch motion about the hinge, the radiation and diffraction problems can be solved to obtain the hydrodynamic coefficients and excitation forces.

## B.2. Derivation of the moment of inertia of the flap

The rotational moment of inertia of the flap is required for the inertial term in the equation of motion.

### Geometry and mass distribution

The flap cross-section consists of two triangles A (top) and B (bottom) joined at the base of width $t$ (see Figure B.2). Heights: $L_{s1}$ (top triangle), $L_{s2}$ (bottom triangle), total height $L_s = L_{s1} + L_{s2}$.

Assuming uniform areal density (mass proportional to area):

$$L_s = L_{s1} + L_{s2}, \qquad m = m_A + m_B, \qquad m_A = \frac{L_{s1}}{L_s}\, m, \qquad m_B = \frac{L_{s2}}{L_s}\, m.$$

### Centroid distances

Measured from the bottom reference axis $x_3$:

$$\Delta x_A = L_{s2} + \frac{L_{s1}}{3}, \qquad \Delta x_B = \frac{2L_{s2}}{3}.$$

### Centroidal second moments

For a triangle (about centroidal axes parallel to its base/width):

$$I'_{x_1x_1} = \frac{m_A L_{s1}^2}{18}, \qquad I'_{x_2x_2} = \frac{m_B L_{s2}^2}{18}, \qquad I'_{zz} = \frac{m_A t^2}{18} + \frac{m_B t^2}{18} = \frac{mt^2}{18}.$$

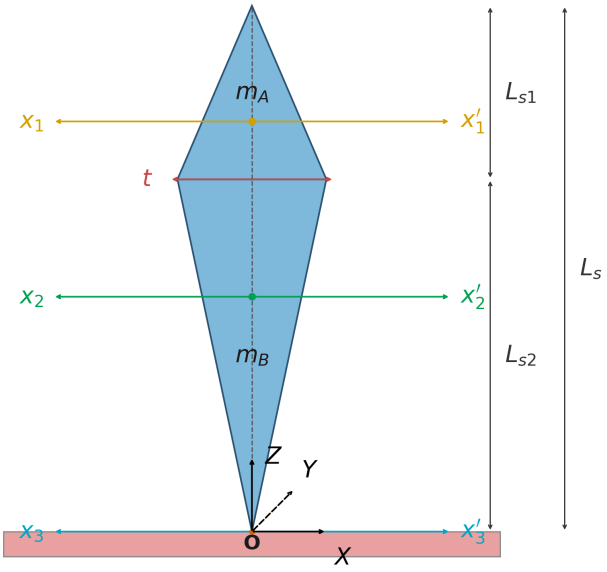



Figure B.2.: Cross-section of the flap

### PARALLEL-AXIS THEOREM

Shifting to the bottom axis $x_3$:

$$\begin{aligned} I'_{x_3x_3} &= I'_{x_1x_1} + m_A(\Delta x_A)^2 + I'_{x_2x_2} + m_B(\Delta x_B)^2 \\ &= \frac{m_A L_{s1}^2}{18} + m_A\left(L_{s2} + \frac{L_{s1}}{3}\right)^2 + \frac{m_B L_{s2}^2}{18} + m_B\left(\frac{2L_{s2}}{3}\right)^2 \\ &= m_A\left(\frac{L_{s1}^2}{6} + L_{s2}^2 + \frac{2L_{s1}L_{s2}}{3}\right) + m_B\left(\frac{L_{s2}^2}{2}\right). \end{aligned} \tag{B.11}$$

### IN-PLANE TRANSVERSE MOMENT OF INERTIA

Using the same triangle formula for width $t$:

$$\begin{aligned} I'_{yy} &= I'_{x_3x_3} + \frac{m_A t^2}{18} + \frac{m_B t^2}{18} \\ &= m_A\left(\frac{L_{s1}^2}{6} + L_{s2}^2 + \frac{2L_{s1}L_{s2}}{3} + \frac{t^2}{18}\right) + m_B\left(\frac{L_{s2}^2}{2} + \frac{t^2}{18}\right) \\ &= m_A\left(\frac{3L_{s1}^2 + 18L_{s2}^2 + 12L_{s1}L_{s2} + t^2}{18}\right) + m_B\left(\frac{9L_{s2}^2 + t^2}{18}\right). \end{aligned} \tag{B.12}$$

### FINAL EXPRESSION IN TERMS OF TOTAL MASS

Substituting $m_A = \frac{L_{s1}}{L_s} m$ and $m_B = \frac{L_{s2}}{L_s} m$:

$$I'_{yy} = \frac{m}{18L_s}\left[L_{s1}\left(3L_{s1}^2 + 18L_{s2}^2 + 12L_{s1}L_{s2} + t^2\right) + L_{s2}\left(9L_{s2}^2 + t^2\right)\right], \tag{B.13}$$

(B.14)

For the flap inspired by waveroller, $L_{s1} = 3.5$ m, $L_{s2} = 7.1$ m and $t = 3$ m.

## B.3. DERIVATION OF THE LINEARIZED VISCOUS DAMPING COEFFICIENT FOR THE FLAP

The linearized viscous damping coefficient is used for the regular wave analysis in both shallow and deep waters as well as the starting point for the iterative procedure considering passive control for the irregular wave analysis. When considering the flap in pitch motion, the viscous moment needs to be estimated to account for the drag.

Considering the flap oscillating in pitch about a hinge at point O (bottom apex). The flap has:

- Total height: $L_s = L_{s1} + L_{s2}$
- Width (along the $Y$ axis): $W$ (constant)
- Pitch angle: $\theta(t)$, angular velocity: $\dot{\theta}(t)$

The drag force depends on the projected area normal to the flow direction, when considering translational degrees of freedom. When considering the pitch moment, this is obtained considering the moment of area projected in $X$ and $Z$ directions. Since the flap is symmetric about the $Z$ (see Figure B.2), the moments due to the opposite side cancel each other out. Therefore, the the viscous moments depends on the projection of the area along $X$ which is the area $W \times L_s$.

For a differential strip of length $dz$ at height $z$ with projected width $W$, the drag force is given as:

$$dF_D = \frac{1}{2}\rho C_D W |v(z)| v(z) dz$$

where:

- $\rho$ = water density
- $C_D$ = drag coefficient
- $W$ = projected width (constant along height)
- $v(z) = z\dot{\theta}$ = local velocity at height $z$

The moment contribution from each element about the hinge is:

$$dM_D = z \cdot dF_D = \frac{1}{2}\rho C_D W z |z\dot{\theta}| (z\dot{\theta}) dz$$

Considering positive rotation in the counter-clockwise direction (Figure B.1), the moment is:

$$dM_D = \frac{1}{2}\rho C_D W z^3 \dot{\theta}^2 dz$$

Integrating over the full height $L_s$:

$$M_D = \frac{1}{2}\rho C_D W \dot{\theta}^2 \int_0^{L_s} z^3 dz$$

$$M_D = \frac{1}{2}\rho C_D W \dot{\theta}^2 \cdot \frac{L_s^4}{4}$$

finally giving

$$M_D = \frac{\rho C_D W L_s^4}{8} |\dot{\theta}|\dot{\theta} = C_{NL} |\dot{\theta}|\dot{\theta}$$

where the nonlinear damping coefficient is:

$$C_{NL} = \frac{\rho C_D W L_s^4}{8}$$

The linearization of quadratic damping $|\dot{\theta}|\dot{\theta}$ uses energy equivalence over one cycle. This results in the linearized damping coefficient relating moment and rotation (similar to [147] and [140]):

$$b_v = \frac{8}{3\pi} C_{NL}$$

which finally gives:

$$b_v = \frac{\rho C_D W L_s^4 \omega}{3\pi}$$

# C

# ATTENUATOR - DERIVING THE MASS, STIFFNESS AND VISCOUS DAMPING MATRICES

## C.1. DERIVING THE MASS AND STIFFNESS MATRICES

In order to derive the mass and stiffness matrices for the attenuator, the Euler-Lagrange formulation is utilized [154]. The attenuator is simplified into a combination of two point masses at either ends of the devices, and two rigid rods that connect the point masses to the centre of the attenuator representing the arms of the attenuator, where the hinge is present. The schematic is shown in Figure C.1.

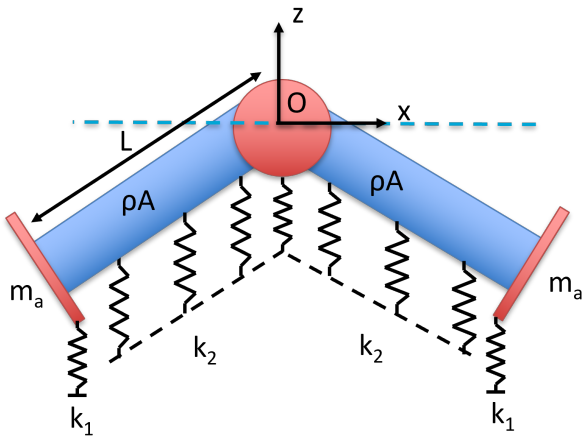



Figure C.1.: Schematic representation of the attenuator to determine mass and stiffness matrices

- a rear arm occupying $x \in [-L, 0]$,
- a front arm occupying $x \in [0, L]$.

Other properties are as follows:

- uniform line mass $\rho A$ along both arms,
- point masses $m_a$ located at $x = \pm L$,

- a vertical distributed stiffness $k_2$ acting along both arms representing the stiffness of the fluid,
- vertical point springs of stiffness $k_1$ at $x = \pm L$ representing the stiffness of the fluid with respect to the point masses.

Due to the symmetry of the structure, the Centre Of Gravity (COG) is located at $x = 0$. All motions are assumed to be small, which is in line with BIEM. The system has four generalized coordinates based on the four degrees of freedom considered

$$\boldsymbol{\zeta} = \begin{bmatrix} \zeta_1 \\ \zeta_3 \\ \zeta_5 \\ \zeta_7 \end{bmatrix},$$

where

- $\zeta_1$ is the surge (horizontal translation of the COG),
- $\zeta_3$ is the heave (vertical translation of the COG),
- $\zeta_5$ is the global pitch rotation about the COG,
- $\zeta_7$ is a front-arm flex rotation acting only on the front arm $x \in [0, L]$.

Both rotations $\zeta_5$ and $\zeta_7$ are defined as clockwise positive. The DOFs are shown in Figure C.2

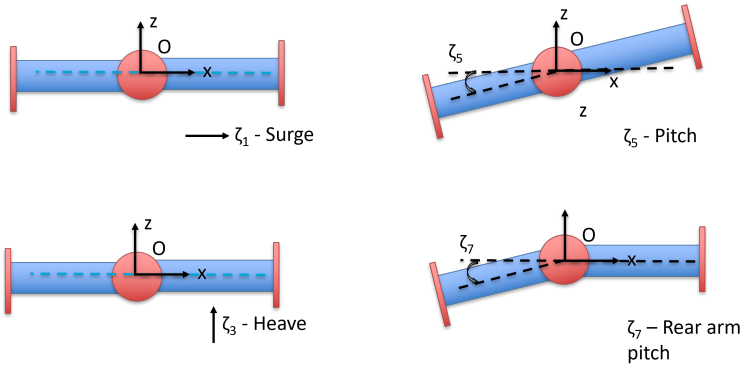



Figure C.2.: DOFs of the attenuator

### C.1.1. KINEMATICS

Only vertical motion contributes to the potential energy of the springs and to the vertical component of kinetic energy. The vertical displacement field for any $x$ is defined as:

$$w(x) = \zeta_3 + x\,\zeta_5 + H_r(x)\,x\,\zeta_7, \tag{C.1}$$

where $H_r(x)$ is an indicator function selecting the rear arm:

$$H_r(x) = \begin{cases} 1, & x \in [-L, 0], \\ 0, & x \in (0, L]. \end{cases}$$

Hence,

$$w(x) = \begin{cases} \zeta_3 + x(\zeta_5 + \zeta_7), & x \in [-L, 0], \\ \zeta_3 + x\zeta_5, & x \in [0, L]. \end{cases}$$

The corresponding vertical velocity field is

$$\dot{w}(x) = \dot{\zeta}_3 + x\dot{\zeta}_5 + H_r(x)\, x\dot{\zeta}_7. \tag{C.2}$$

At the endpoints,

$$w(-L) = \zeta_3 - L\zeta_5 - L\zeta_7, \qquad w(+L) = \zeta_3 + L\zeta_5.$$



### C.1.2. KINETIC ENERGY

The total kinetic energy consists of horizontal and vertical motion:

$$T = T_{\mathrm{h}} + T_{\mathrm{v}}.$$

The horizontal contribution is

$$T_{\mathrm{h}} = \frac{1}{2} M_t \dot{\zeta}_1^2, \qquad M_t = 2\rho AL + 2m_a.$$

The vertical kinetic energy is given by

$$T_{\mathrm{v}} = \frac{1}{2} \int_{-L}^{L} \rho A\, \dot{w}(x)^2\, dx + \frac{1}{2} m_a \dot{w}(-L)^2 + \frac{1}{2} m_a \dot{w}(+L)^2.$$

### C.1.3. POTENTIAL ENERGY

The total potential energy consists of distributed and point-spring contributions:

$$V = \frac{1}{2} \int_{-L}^{L} k_2\, w(x)^2\, dx + \frac{1}{2} k_1 w(-L)^2 + \frac{1}{2} k_1 w(+L)^2.$$

### C.1.4. EULER–LAGRANGE FORMULATION

The equations of motion are obtained by applying the Euler–Lagrange equations to the Lagrangian

$$\mathcal{L} = T - V.$$

For each generalised coordinate $\zeta_i$, the Euler–Lagrange equation reads

$$\frac{d}{dt}\left(\frac{\partial \mathcal{L}}{\partial \dot{\zeta}_i}\right) - \frac{\partial \mathcal{L}}{\partial \zeta_i} = Q_i, \tag{C.3}$$

where $Q_i$ denotes the generalised non-conservative force. Since the goal here is to obtain the mass and stiffness matrices, $Q_i$ can be ignored. By applying the Euler–Lagrange formulation, the terms corresponding to the displacements and velocities in the four derived equations of motion can be used to obtain the mass and stiffness matrices.

### C.1.5. MASS AND STIFFNESS MATRICES

Obtaining the terms corresponding to the velocities of the four generalized coordinates, the mass matrix can be obtained as:

$$\mathbf{M} = \begin{bmatrix} M_t & 0 & 0 & 0 \\ 0 & M_t & 0 & S_{\text{rear}} \\ 0 & 0 & I_{\text{full}} & I_{\text{rear}} \\ 0 & S_{\text{rear}} & I_{\text{rear}} & I_{\text{rear}} \end{bmatrix}. \tag{C.4}$$

where

$$I_{\text{full}} = \frac{2}{3}\rho A L^3 + 2m_a L^2, \tag{C.5}$$

$$I_{\text{rear}} = \frac{1}{3}\rho A L^3 + m_a L^2, \tag{C.6}$$

$$S_{\text{rear}} = \frac{1}{2}\rho A L^2 + m_a L, \tag{C.7}$$

and corresponding to the displacements/rotations, the stiffness matrix can be obtained as:

$$\mathbf{K} = \begin{bmatrix} 0 & 0 & 0 & 0 \\ 0 & 2k_2L + 2k_1 & 0 & \frac{1}{2}k_2L^2 + k_1L \\ 0 & 0 & \frac{2}{3}k_2L^3 + 2k_1L^2 & \frac{1}{3}k_2L^3 + k_1L^2 \\ 0 & \frac{1}{2}k_2L^2 + k_1L & \frac{1}{3}k_2L^3 + k_1L^2 & \frac{1}{3}k_2L^3 + k_1L^2 \end{bmatrix}. \tag{C.8}$$

For calculating the mass $m_a$, area $A$ and stiffnesses $k$ and $k_1$, the hydrostatic functions in HAMS/HAMS-MREL were utilized.

When considering the mass and stiffness matrices of the attenuator, the geometry is simplified so as to accelerate the calculation of these matrices. Slight deviations are observed in the power produced by the attenuator when considering the incident wave direction of 0° and 180°, which could be due to these simplifications. These can be improved further in the future by utilizing the elements in the mesh directly using methods similar to the one shown in [165].

## C.2. DERIVING THE VISCOUS DAMPING COEFFICIENT MATRIX

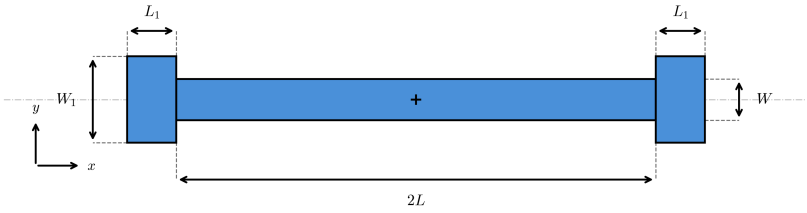



Figure C.3.: Top view attenuator

For the viscous damping coefficient matrix of the attenuator, a diagonal matrix is assumed, with the viscous damping coefficients per DOF. The linear viscous damping coefficient matrix can be written as:

$$\mathbf{B_v} = \begin{bmatrix} \frac{4}{3\pi}\rho C_D A_1 & 0 & 0 & 0 \\ 0 & \frac{4}{3\pi}\rho C_D A_3 & 0 & 0 \\ 0 & 0 & \frac{4}{3\pi}\rho C_D J_5 & 0 \\ 0 & 0 & 0 & \frac{4}{3\pi}\rho C_D J_7 \end{bmatrix}. \tag{C.9}$$

where $A_1$ and $A_3$ are the projected areas in surge and heave, while $J_5$ and $J_7$ are the second moment of the area about the COG for the pitch and rear arm pitch respectively. The projected areas in surge and heave are obtained using RHINO due to the complicated nature of the mesh. For the pitch and rear-arm pitch, the same methodology as the flap was utilized. The pitch and rear-arm pitch have contributions due to the normals in $x$ and $z$. Since the geometry is symmetric about the $z$ axis, the contributions due to the normals in $x$ cancel out. There only the normals in $z$ contribute. The attenuator geometry from the top shown in Figure C.3.

Using the same integration procedure as adopted for the flap, the second moment of the areas can be obtained as:

$$J_5 = \frac{WL^4}{2} + \frac{W_1(L+L_1)^4 - W_1L^4}{2} \tag{C.10}$$

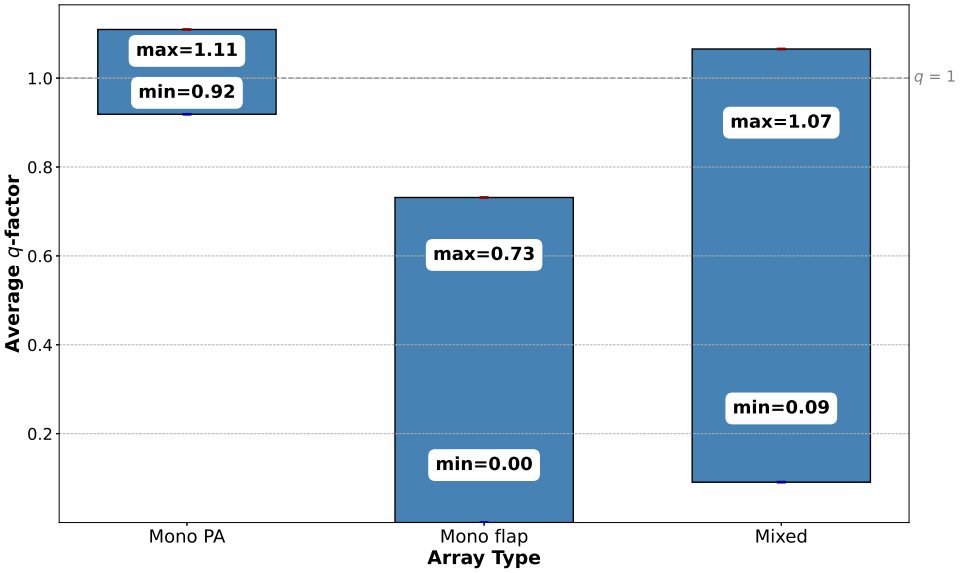
and

$$J_7 = \frac{WL^4}{4} + \frac{W_1(L+L_1)^4 - W_1L^4}{4} \tag{C.11}$$

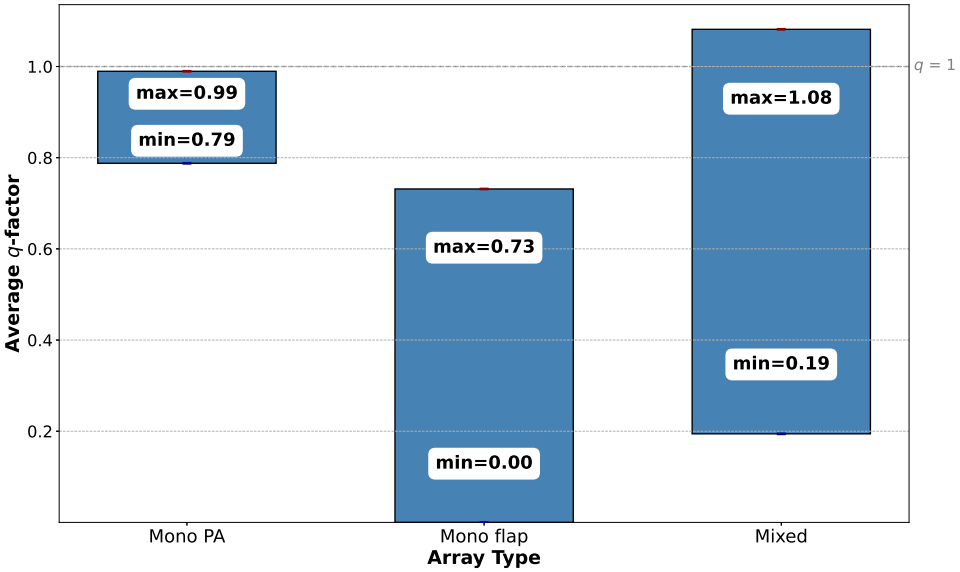
# D

# ADDITIONAL RESULTS FOR SHALLOW-WATER MIXED ARRAYS

This appendix contains the figures from the results of the shallow-water mixed-array study that were omitted from the main text for brevity. For each case, only the irregular waves with active control results are kept in the main chapter; the corresponding regular-passive, regular-active and irregular-passive results are gathered here. All figures use the same naming, labels and format as in the main chapter, so the cross-references in the main text resolve directly to the figures in this appendix.

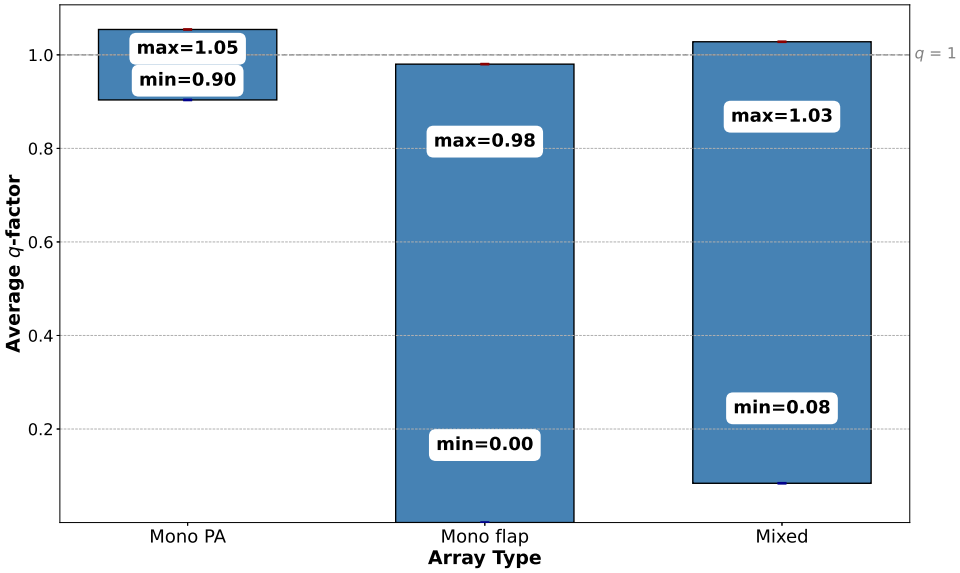



(a) Small PA

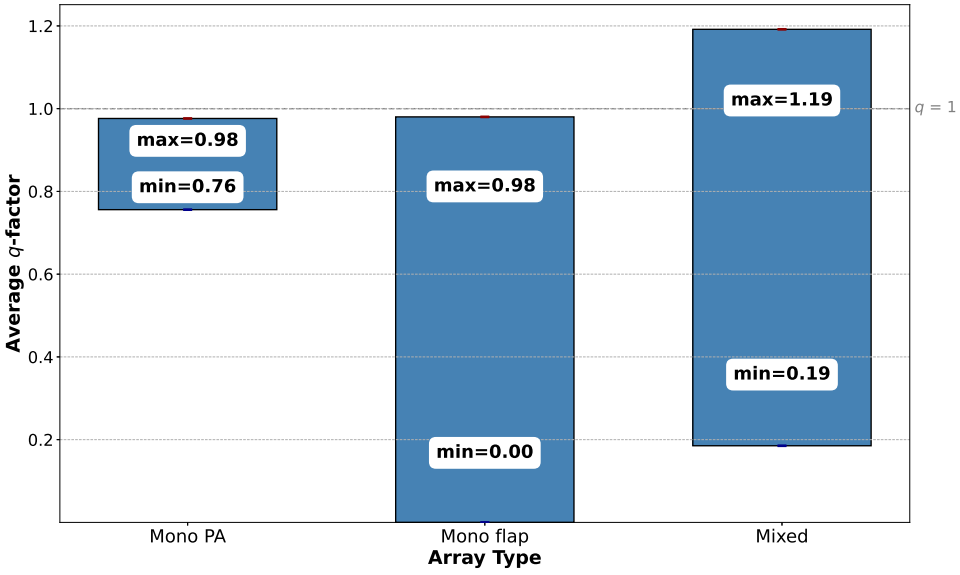



(b) Large PA

Figure D.1.: Overall comparison of mono and mixed arrays considering mean $q$-factors under regular waves and passive control, shown for mixed arrays using (a) a small PA and (b) a large PA.

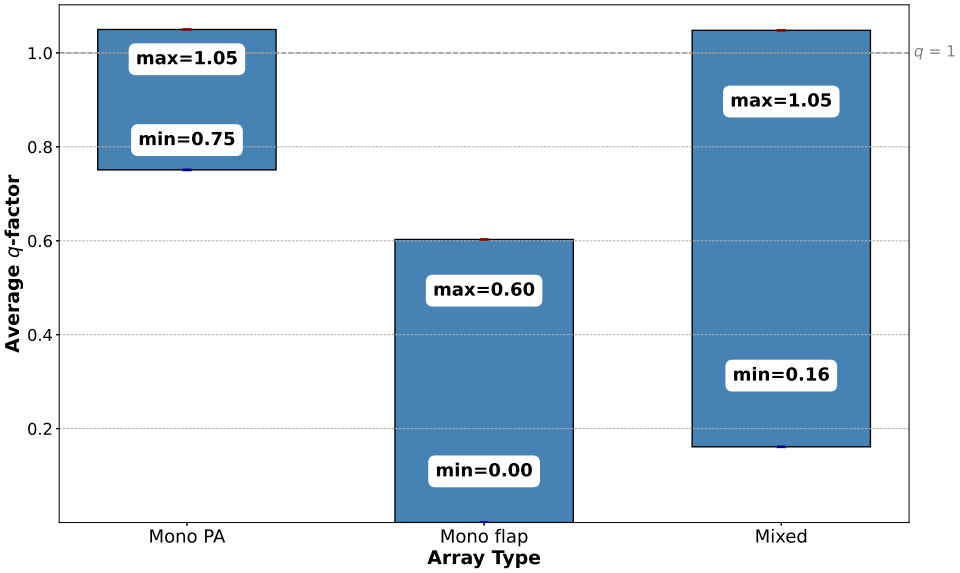



(a) Small PA

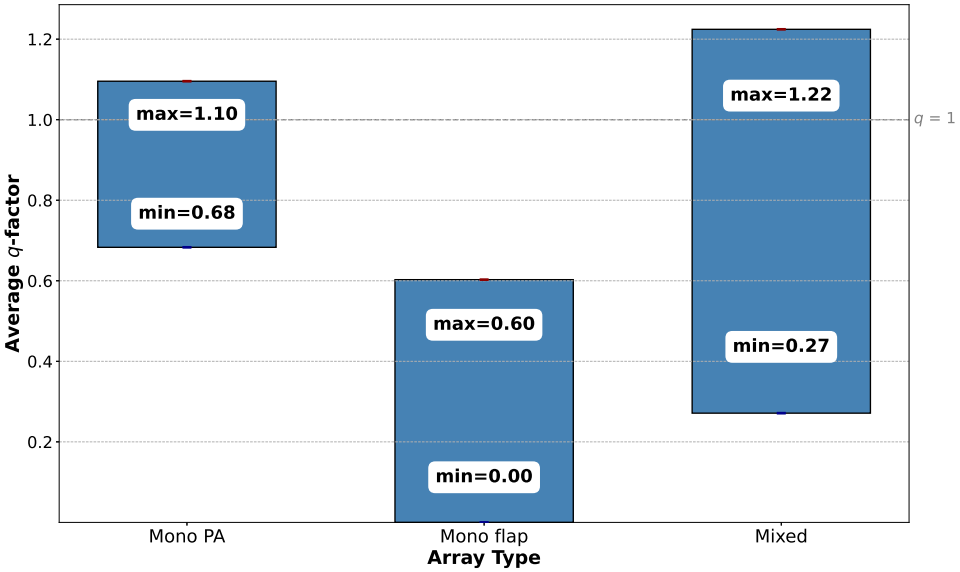



(b) Large PA

Figure D.2.: Overall comparison of mono and mixed arrays considering mean $q$-factors under irregular waves and passive control, shown for mixed arrays using (a) a small PA and (b) a large PA.




(a) Small PA




(b) Large PA

Figure D.3.: Overall comparison of mono and mixed arrays considering mean $q$-factors under regular waves and active control, shown for mixed arrays using (a) a small PA and (b) a large PA.

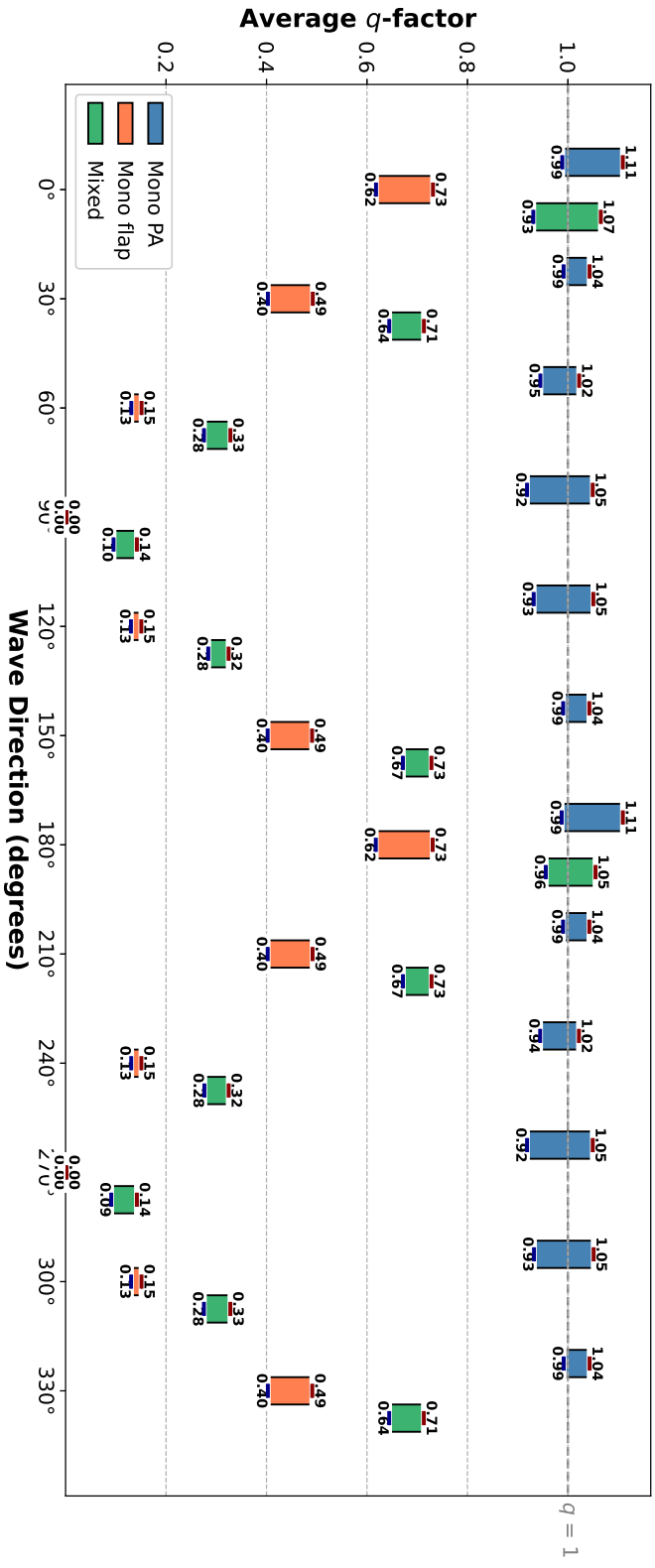



Figure D.4.: Directional comparison of mono and mixed arrays under regular waves and passive control: small PA.

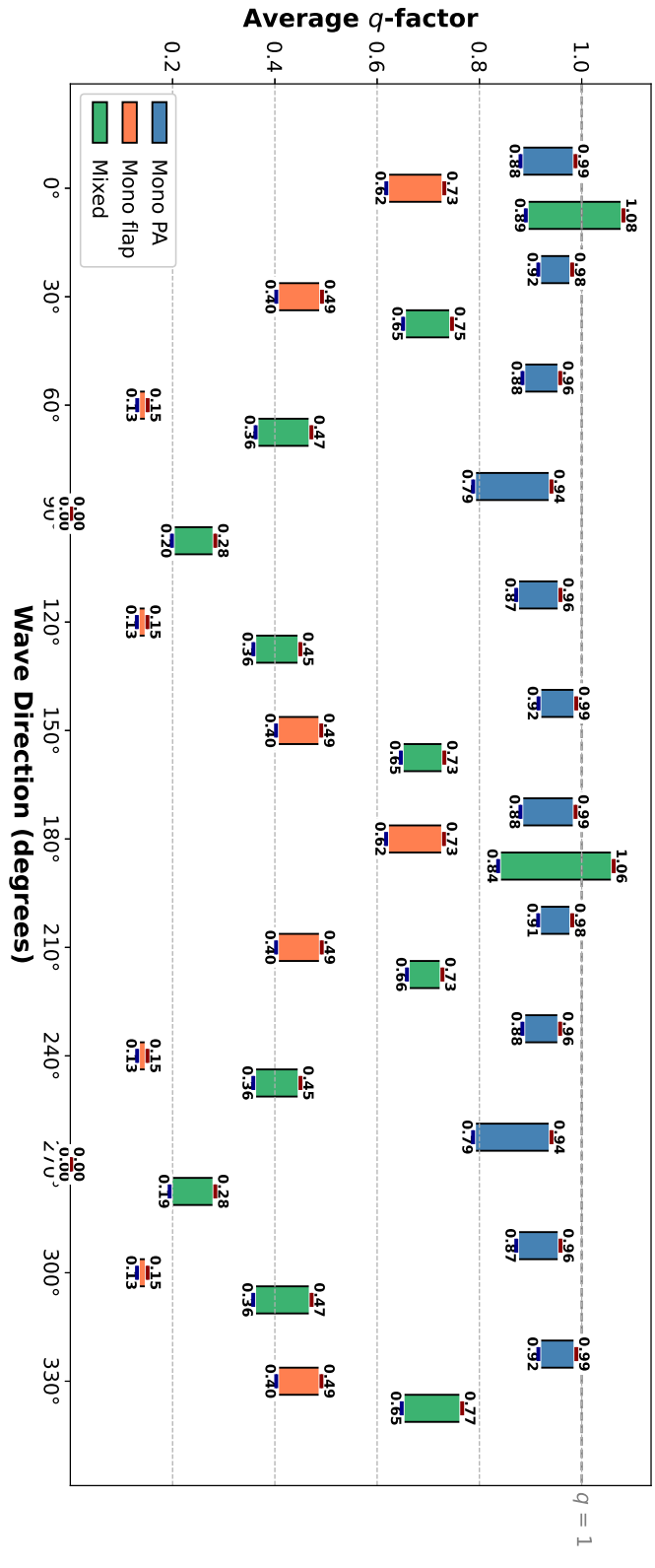



Figure D.5.: Directional comparison of mono and mixed arrays under regular waves and passive control: large PA.

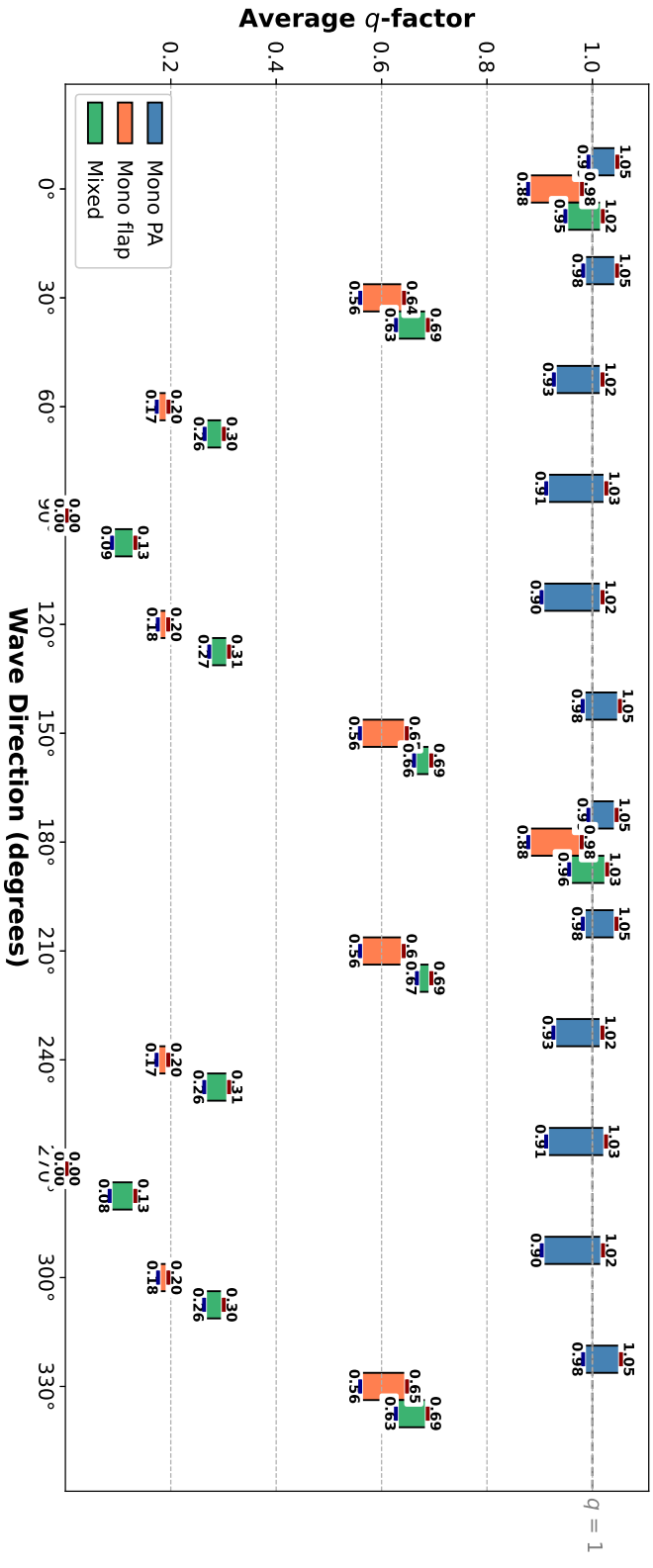



Figure D.6.: Directional comparison of mono and mixed arrays under irregular waves and passive control: small PA.

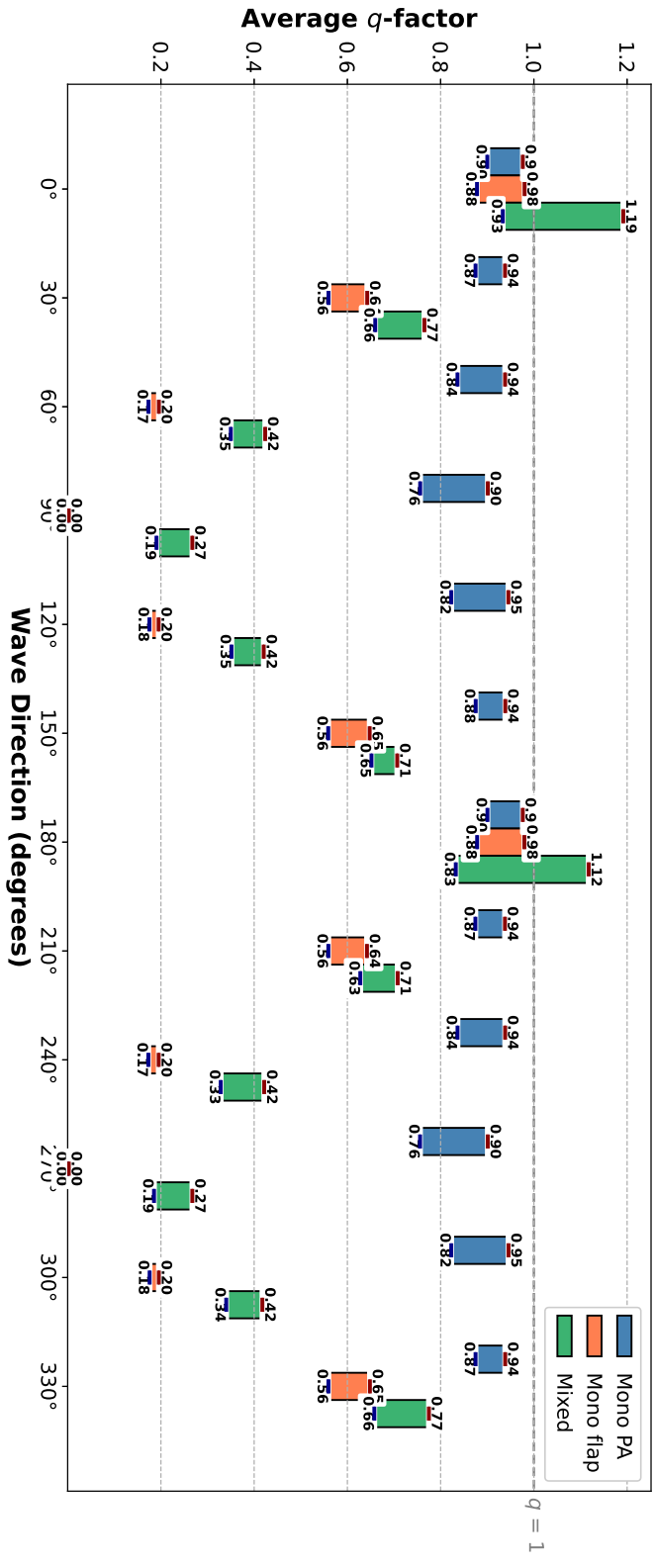



Figure D.7.: Directional comparison of mono and mixed arrays under irregular waves and passive control: large PA.

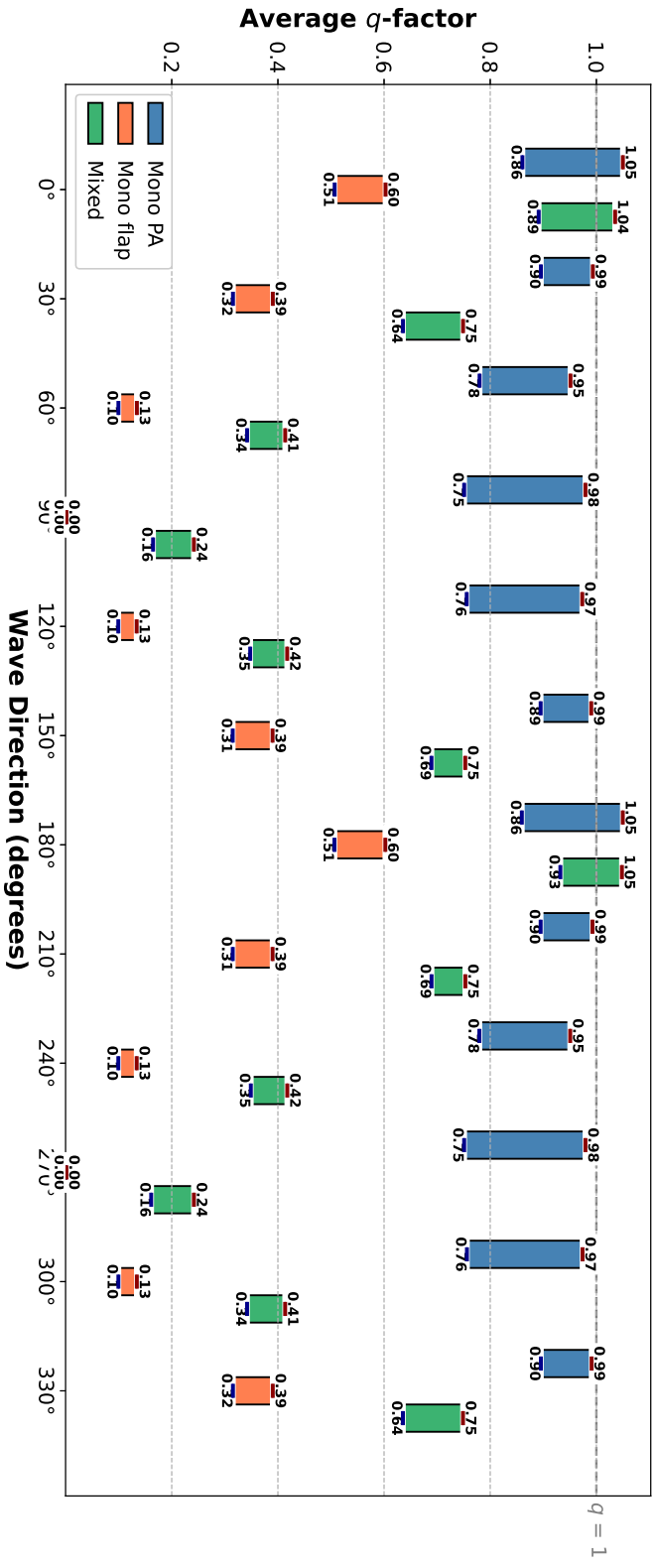



Figure D.8.: Directional comparison of mono and mixed arrays under regular waves and active control: small PA.

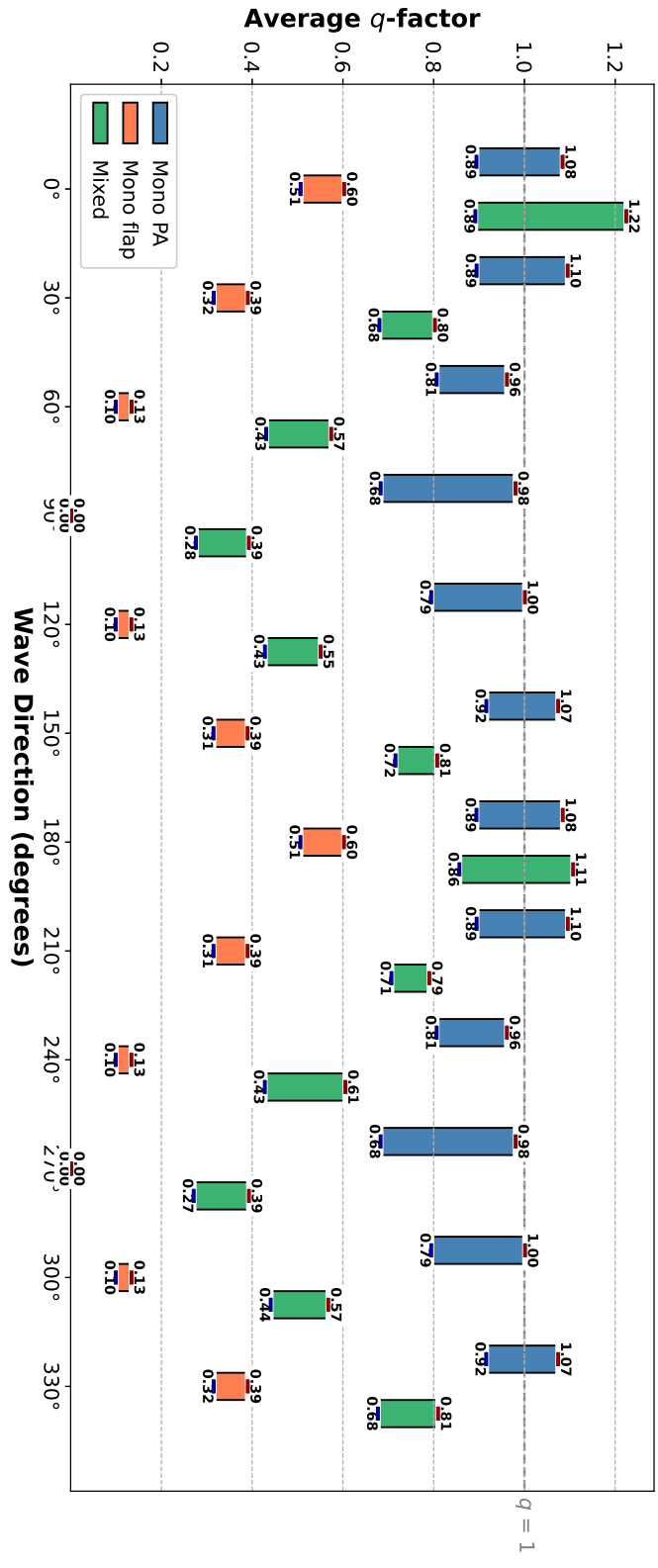
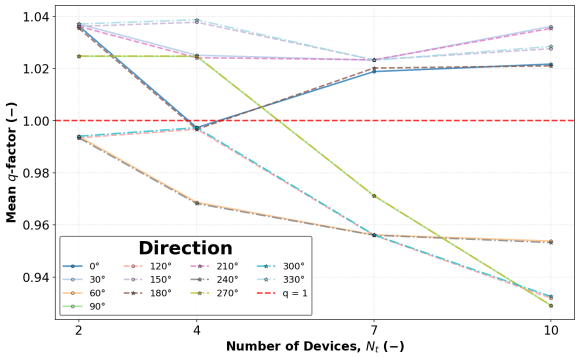
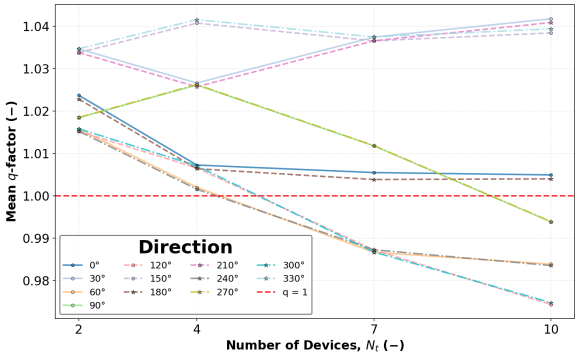


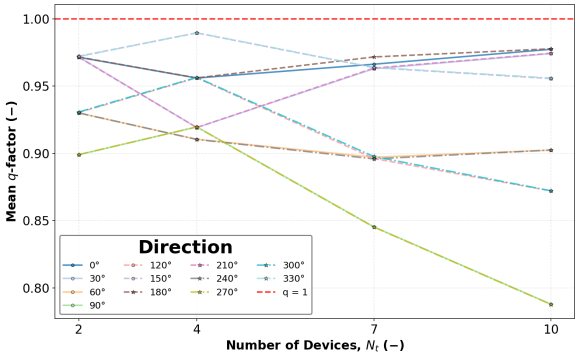

Figure D.9.: Directional comparison of mono and mixed arrays under regular waves and active control: large PA.




(a) Small PA mono: spacing 4$D$, staggered configuration

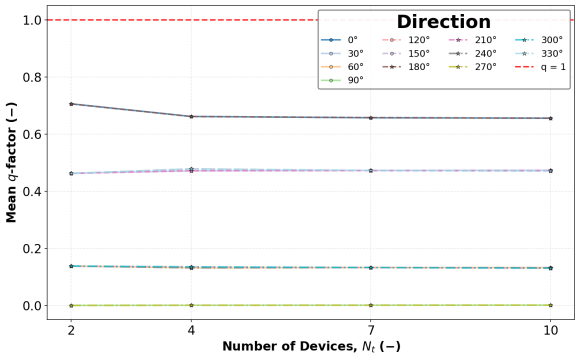



(b) Small PA mono: spacing 10$D$, staggered configuration

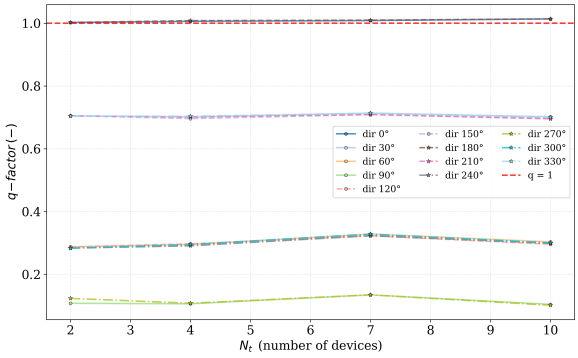



(c) Big PA mono: spacing 4$D$, staggered configuration

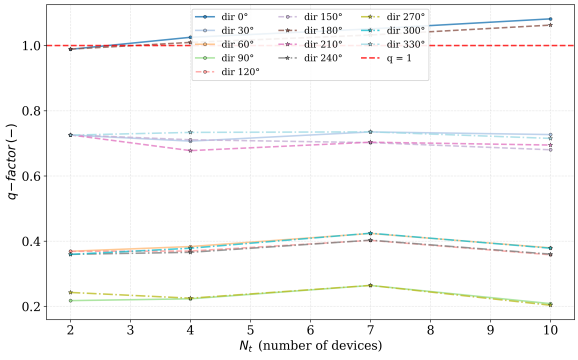
Figure D.10.: Variation of mean $q$-factor (averaged over $T = 3$–12 s) with the number of devices $N_b$ for mono and mixed arrays under regular waves with passive control. Spacing and configuration for each case are indicated in the subcaptions.




(d) Flap mono: spacing 6$D$, staggered configuration

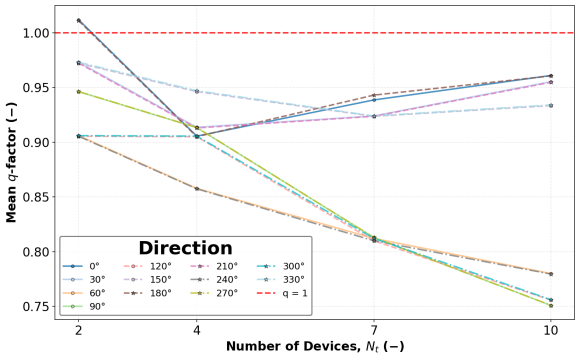



(e) Mixed (small PA + flap): spacing 8$D$, staggered configuration

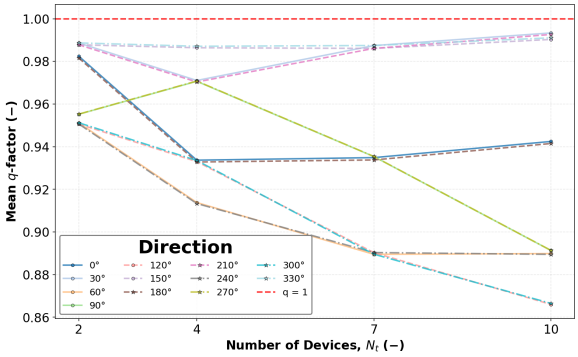



(f) Mixed (big PA + flap): spacing 8$D$, staggered configuration

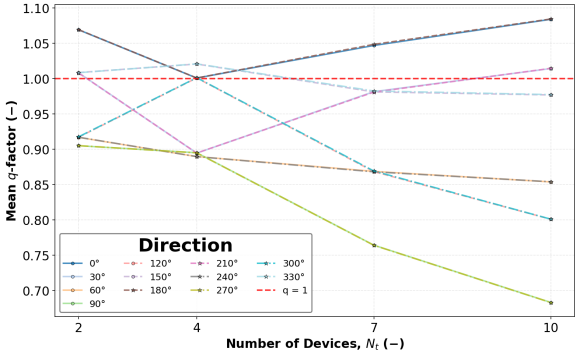
Figure D.10.: (continued).




(a) Small PA mono: spacing 4$D$, staggered configuration

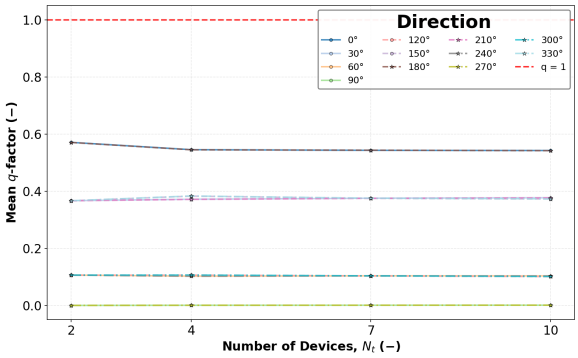



(b) Small PA mono: spacing 10$D$, staggered configuration

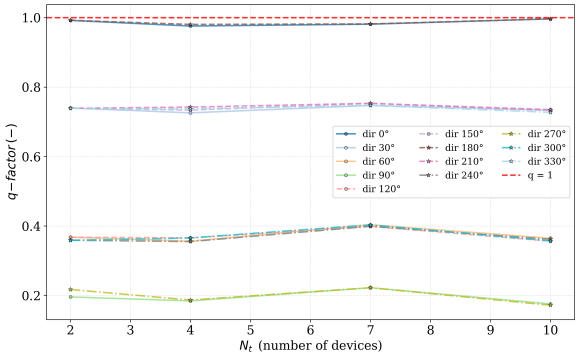



(c) Big PA mono: spacing 4$D$, staggered configuration

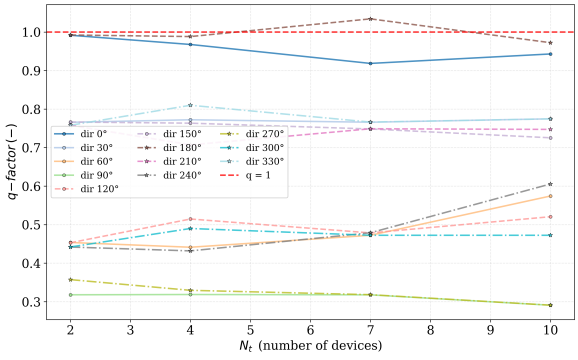
Figure D.11.: Variation of mean $q$-factor (averaged over $T = 3$–12 s) with the number of devices $N_b$ for mono and mixed arrays under regular waves with active control. Spacing and configuration for each case are indicated in the subcaptions.




(d) Flap mono: spacing 6$D$, staggered configuration

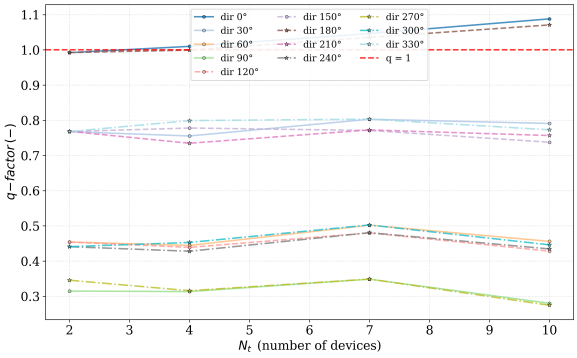



(e) Mixed (small PA + flap): spacing 8$D$, staggered configuration



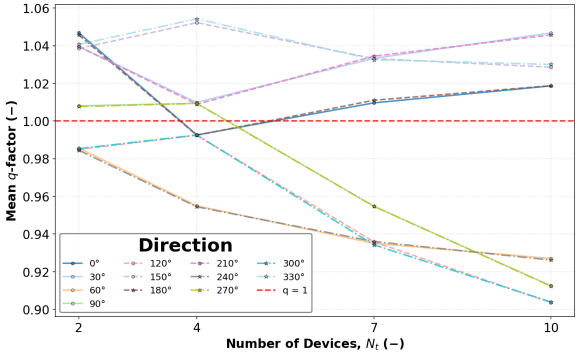

(f) Mixed (big PA + flap): spacing 4$D$, staggered configuration

Figure D.11.: (continued).

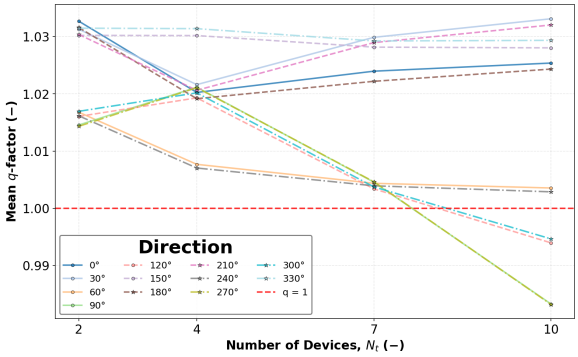



(g) Mixed (big PA + flap): spacing 8$D$, staggered configuration

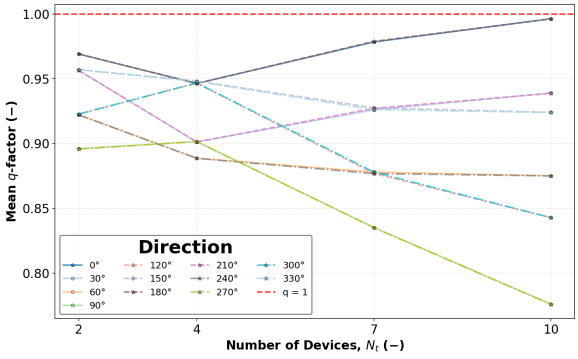
Figure D.11.: (continued).




(a) Small PA mono: spacing 4$D$, staggered configuration

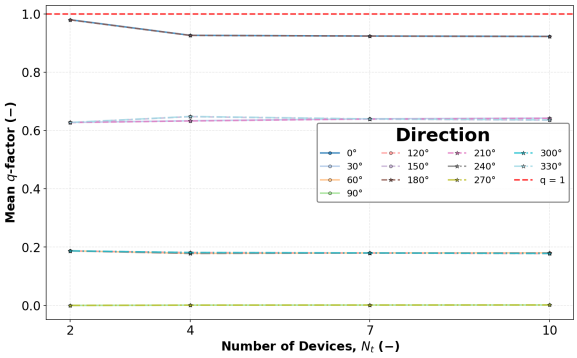



(b) Small PA mono: spacing 10$D$, staggered configuration

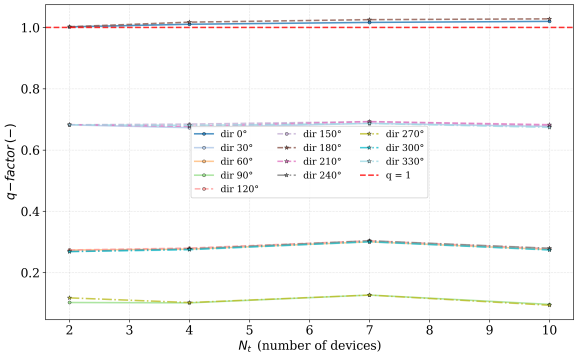



(c) Big PA mono: spacing 4$D$, staggered configuration

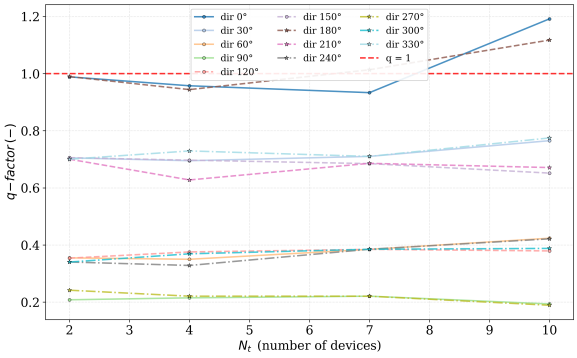
Figure D.12.: Variation of mean $q$-factor (averaged over $T$ = 3–12 s) with the number of devices $N_b$ for mono and mixed arrays under irregular waves with passive control. Spacing and configuration for each case are indicated in the subcaptions.




(d) Flap mono: spacing 6$D$, staggered configuration



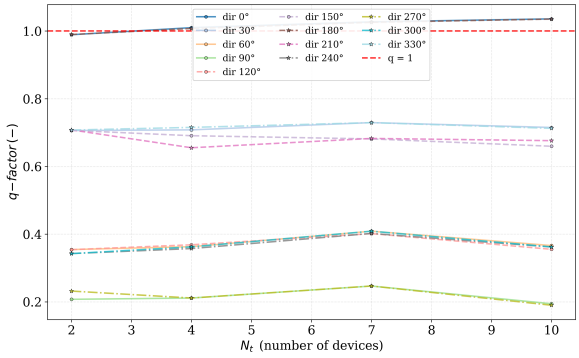

(e) Mixed (small PA + flap): spacing 8$D$, staggered configuration




(f) Mixed (big PA + flap): spacing 4$D$, staggered configuration

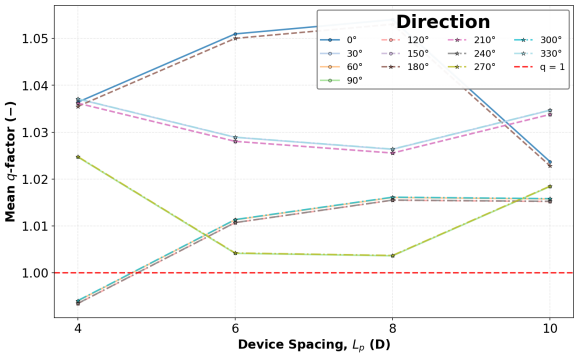
Figure D.12.: (continued).

D

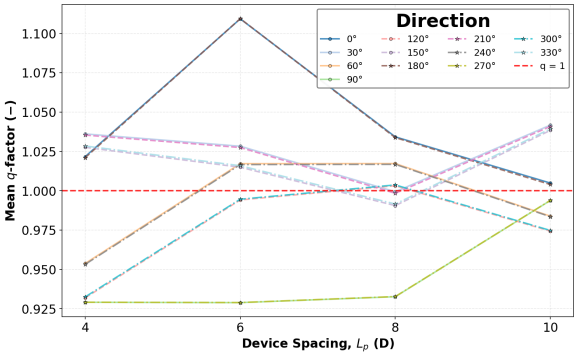



(g) Mixed (big PA + flap): spacing 8$D$, staggered configuration

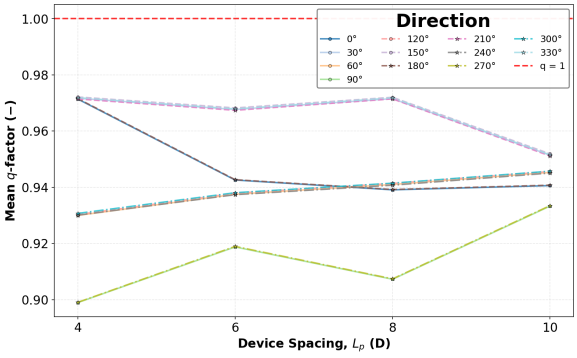
Figure D.12.: (continued).




(a) Small PA mono: Number of devices - 2, staggered configuration

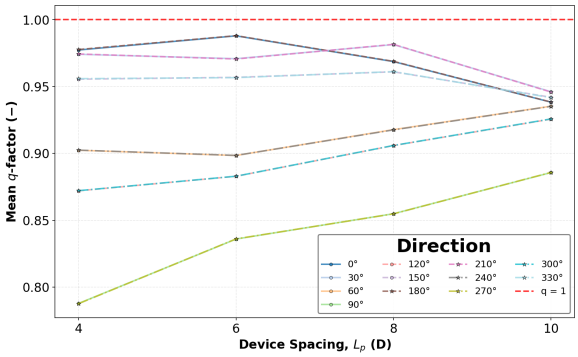



(b) Small PA mono: Number of devices - 10, staggered configuration

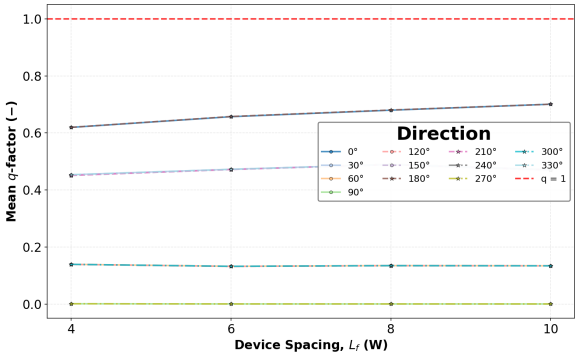



(c) Big PA mono: Number of devices - 2, staggered configuration

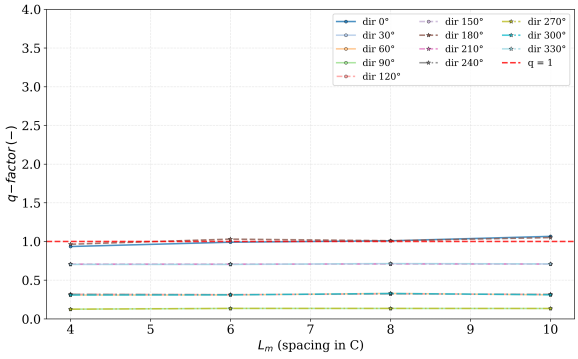
Figure D.13.: Variation of mean $q$-factor (averaged over $T$ = 3–12 s) with the spacing for mono and mixed arrays under regular waves with passive control. Number of devices and configuration for each case are indicated in the subcaptions.




(d) Big PA mono: Number of devices - 10, staggered configuration

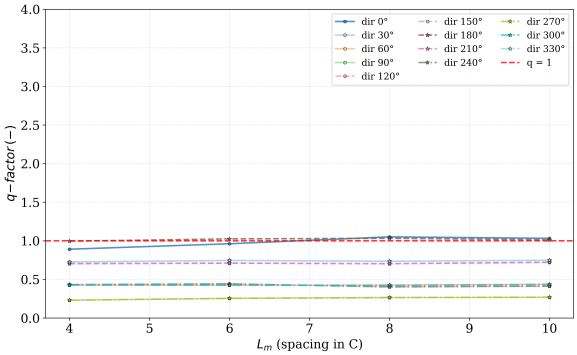



(e) Flap mono: Number of devices - 7, staggered configuration



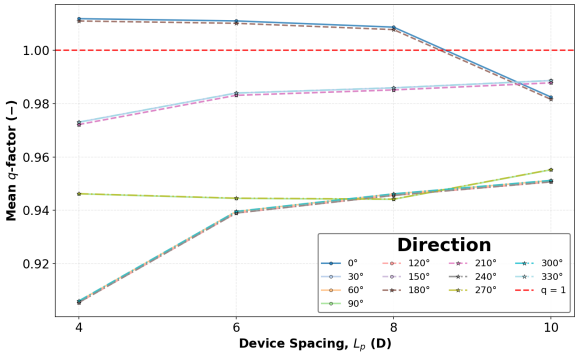

(f) Mixed (small PA + flap): Number of devices - 7, staggered configuration

Figure D.13.: (continued).

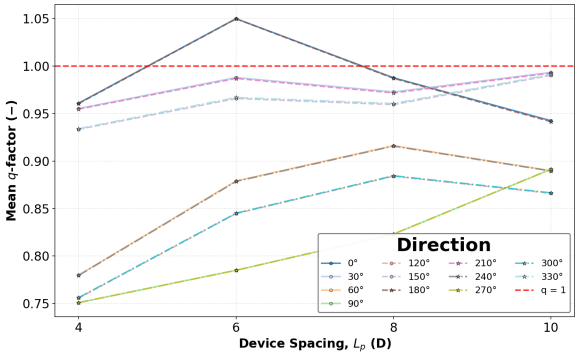



(g) Mixed (big PA + flap): Number of devices - 7, staggered configuration

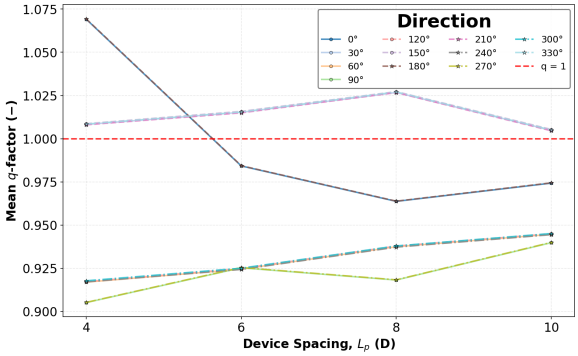
Figure D.13.: (continued).




(a) Small PA mono: Number of devices – 2, staggered configuration

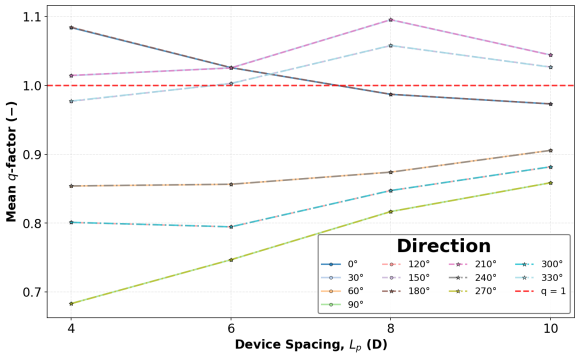



(b) Small PA mono: Number of devices – 10, staggered configuration

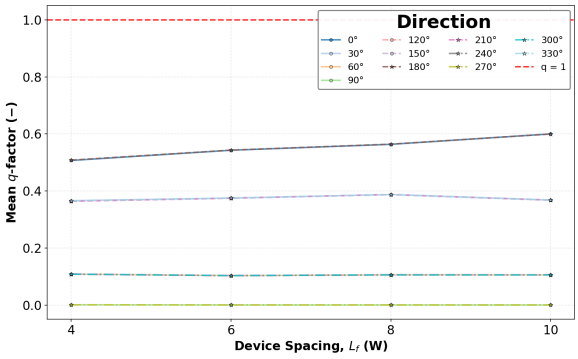



(c) Big PA mono: Number of devices – 2, staggered configuration

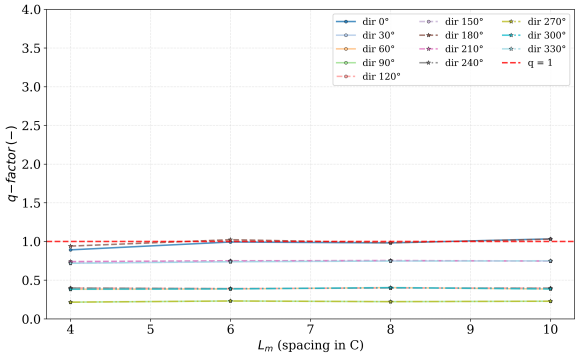
Figure D.14.: Variation of mean $q$-factor (averaged over $T = 3$–$12$ s) with spacing for mono and mixed arrays under regular waves with active control. The number of devices and array configuration for each case are indicated in the subcaptions.




(d) Big PA mono: Number of devices – 10, staggered configuration

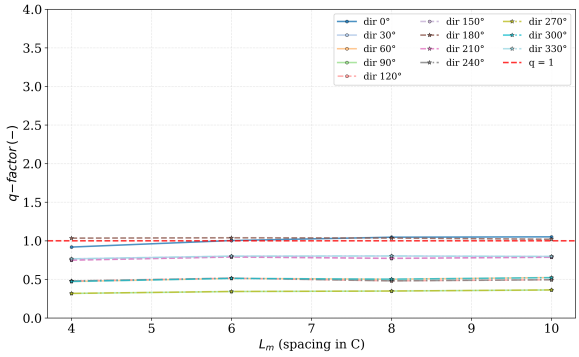



(e) Flap mono: Number of devices – 7, staggered configuration



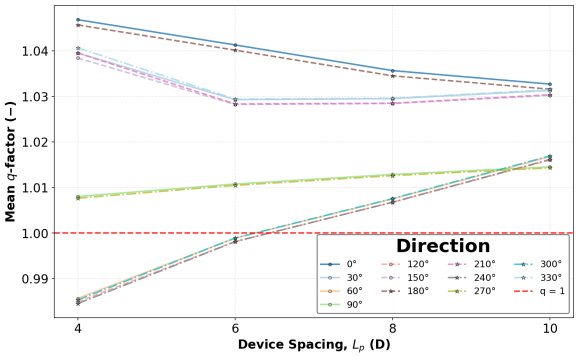

(f) Mixed (small PA + flap): Number of devices – 7, staggered configuration

Figure D.14.: (continued).

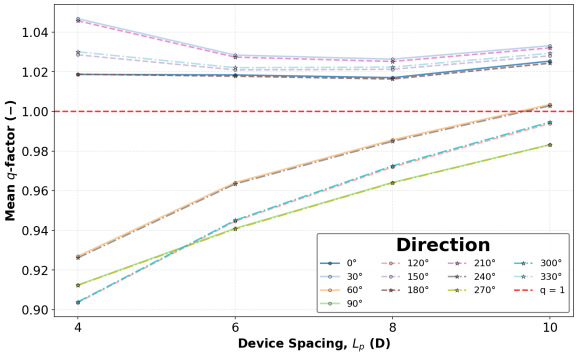



(g) Mixed (big PA + flap): Number of devices – 7, staggered configuration

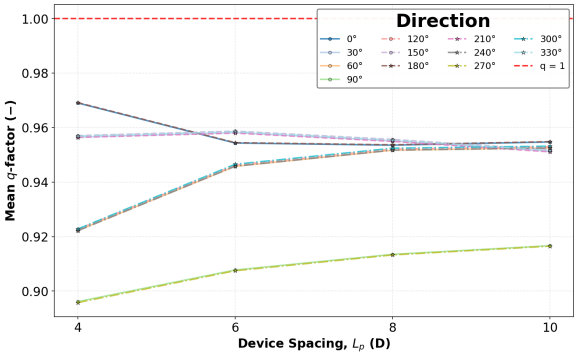
Figure D.14.: (continued).




(a) Small PA mono: Number of devices – 2, staggered configuration

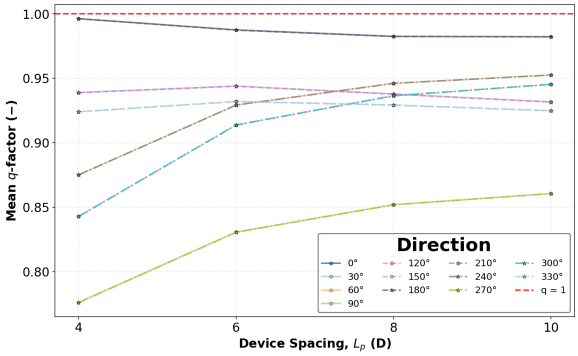



(b) Small PA mono: Number of devices – 10, staggered configuration

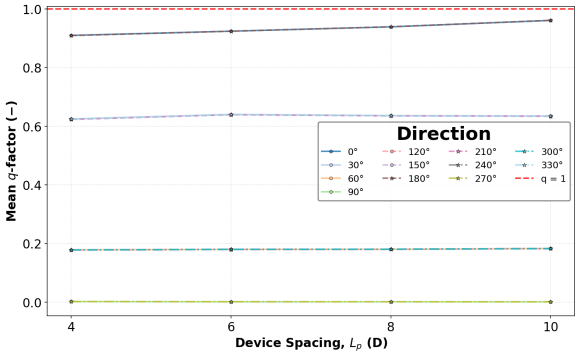



(c) Big PA mono: Number of devices – 2, staggered configuration

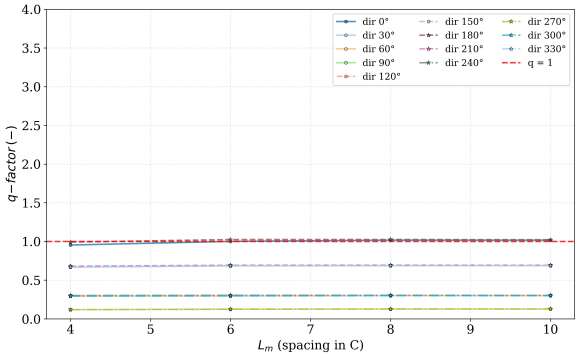
Figure D.15.: Variation of mean $q$-factor (averaged over $T = 3$–$12$ s) with spacing for mono and mixed arrays under irregular waves with passive control. The number of devices and array configuration for each case are indicated in the subcaptions.




(d) Big PA mono: Number of devices – 10, staggered configuration

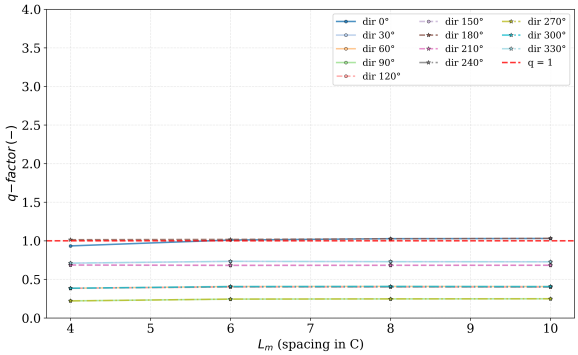



(e) Flap mono: Number of devices – 7, staggered configuration



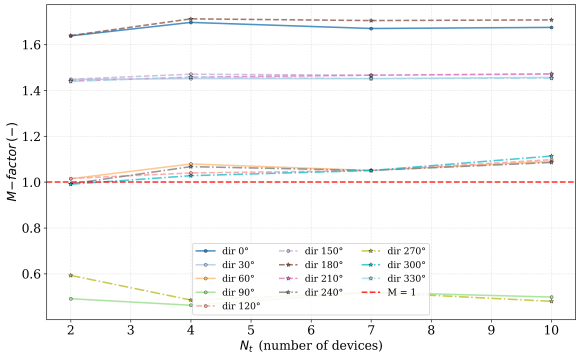

(f) Mixed (small PA + flap): Number of devices – 7, staggered configuration

Figure D.15.: (continued).

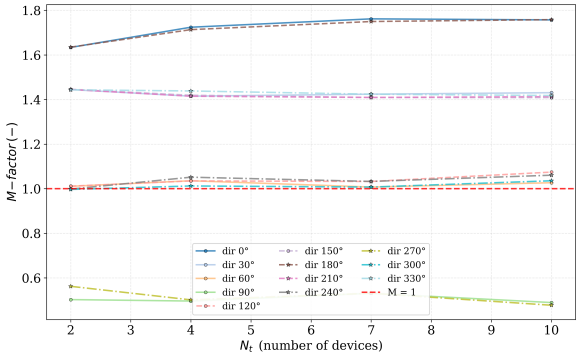



(g) Mixed (big PA + flap): Number of devices – 7, staggered configuration

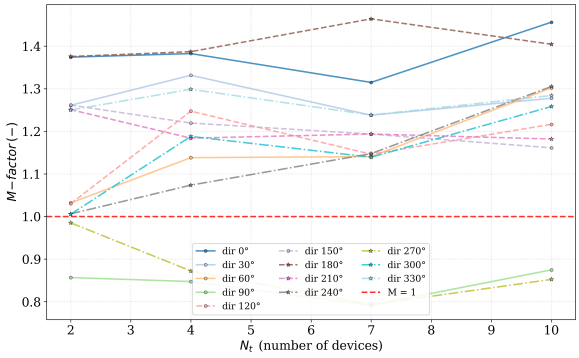
Figure D.15.: (continued).




(a) Small PA-flap mixed: Spacing – 4$C$, staggered configuration

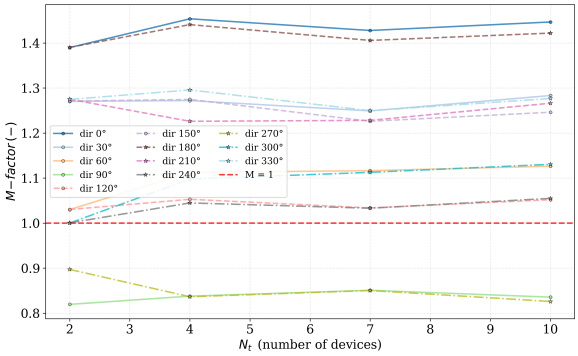



(b) Small PA-flap mixed: Spacing – 10$C$, staggered configuration

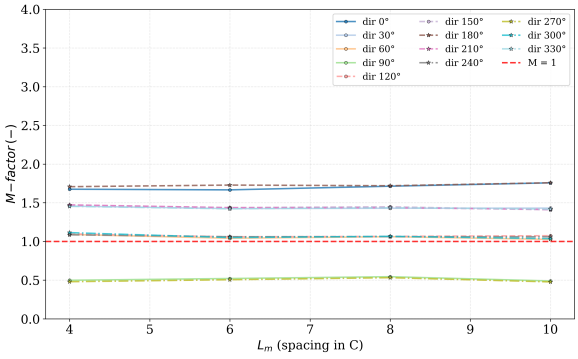



(c) Big PA-flap mixed: Spacing – 4$C$, staggered configuration

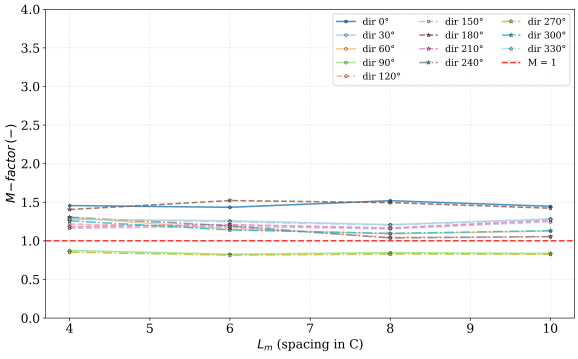
Figure D.16.: Variation of mean $M$-factor (averaged over $T$ = 3–12 s) with number of devices and spacing for mixed arrays under regular waves with passive control. The number of devices/spacing and array configuration for each case are indicated in the subcaptions.




(d) Big PA-flap mixed: Spacing – 10$C$, staggered configuration

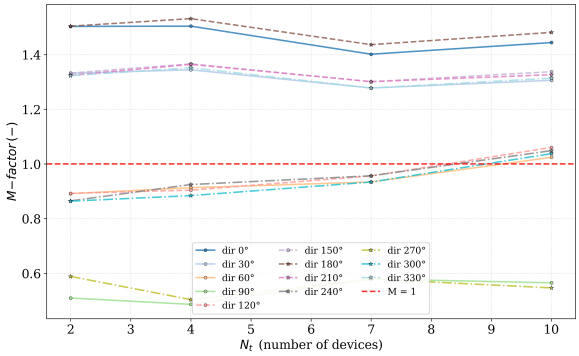



(e) Small PA-flap mixed: number of devices – 10, staggered configuration

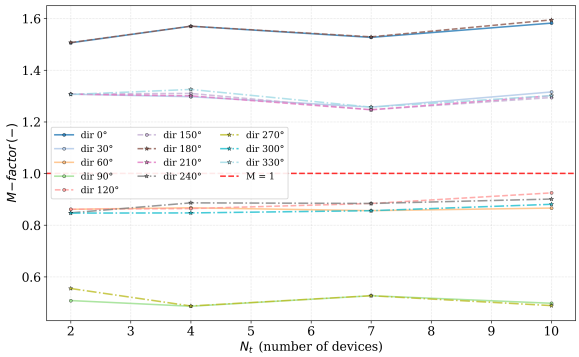



(f) Big PA-flap mixed: number of devices – 10, staggered configuration

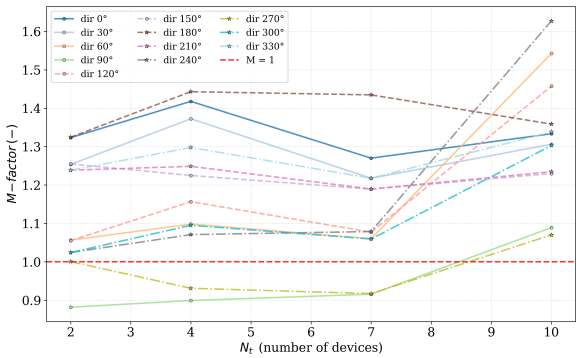
Figure D.16.: (continued).




(a) Small PA–flap mixed: Spacing – 4$C$, staggered configuration

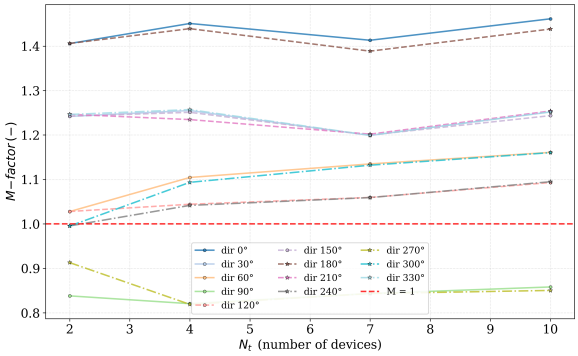



(b) Small PA–flap mixed: Spacing – 10$C$, staggered configuration

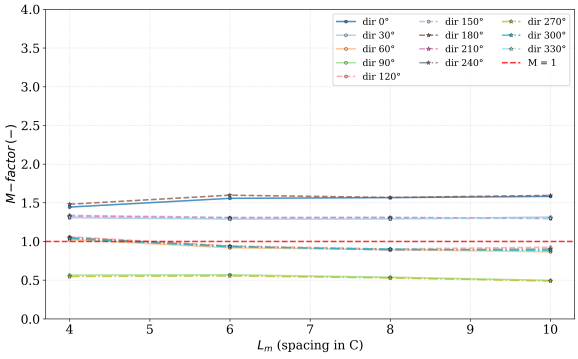



(c) Big PA–flap mixed: Spacing – 4$C$, staggered configuration

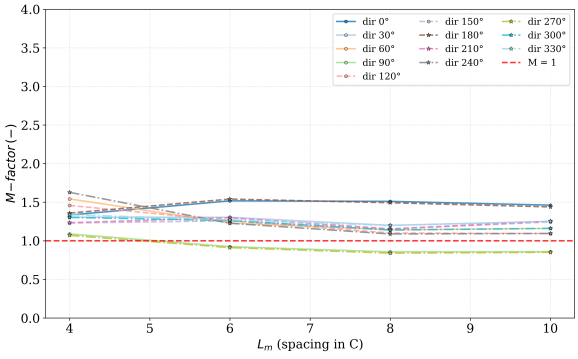
Figure D.17.: Variation of the mean $M$-factor (averaged over $T$ = 3–12 s) with number of devices and spacing for mixed arrays under regular waves with active control. The number of devices/spacing and array configuration for each case are indicated in the subcaptions.




(d) Big PA–flap mixed: Spacing – 10$C$, staggered configuration

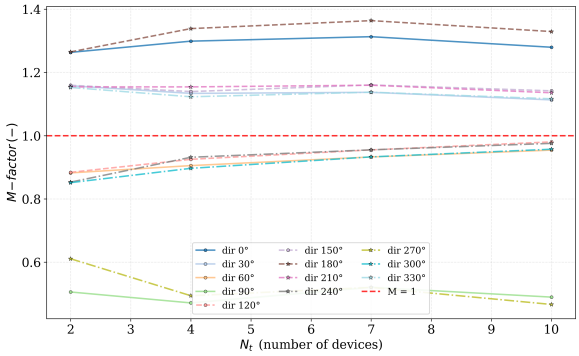



(e) Small PA–flap mixed: Number of devices – 10, staggered configuration

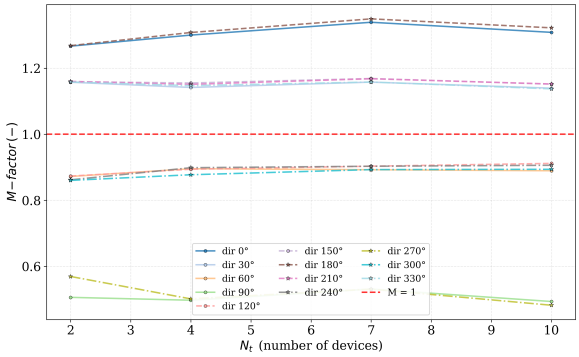



(f) Big PA–flap mixed: Number of devices – 10, staggered configuration

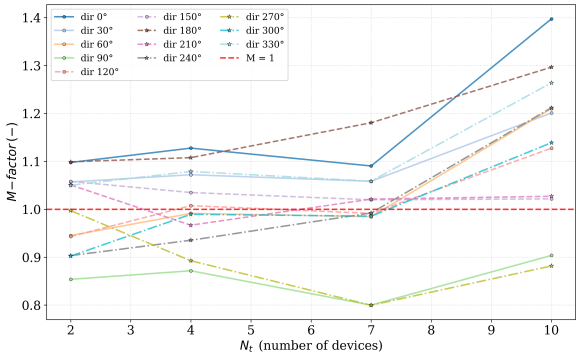
Figure D.17.: (continued).




(a) Small PA–flap mixed: Spacing – 4$C$, staggered configuration

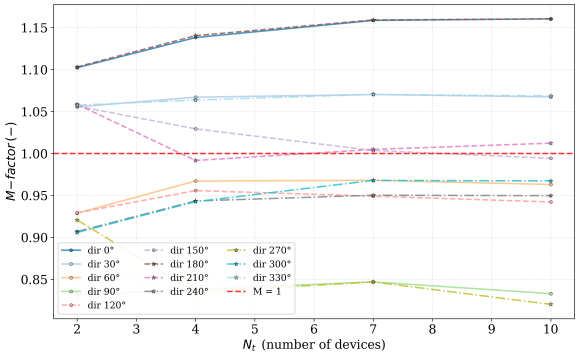



(b) Small PA–flap mixed: Spacing – 10$C$, staggered configuration

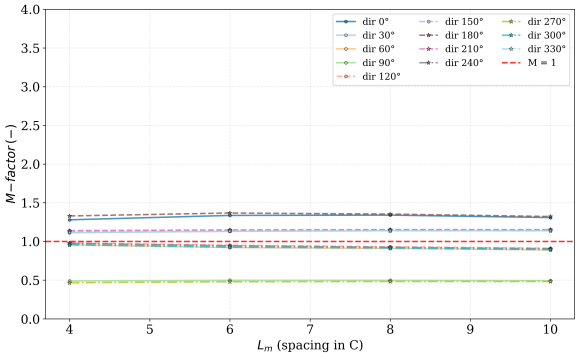



(c) Big PA–flap mixed: Spacing – 4$C$, staggered configuration

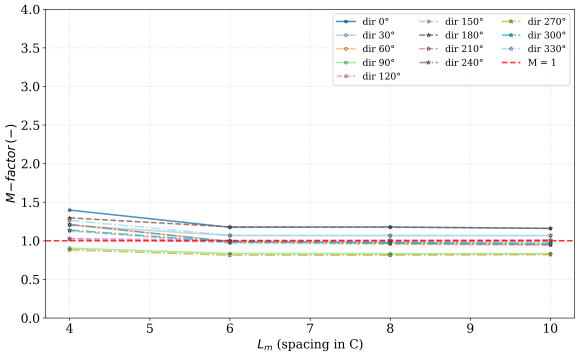
Figure D.18.: Variation of the mean $M$-factor (averaged over $T$ = 3–12 s) with number of devices and spacing for mixed arrays under irregular waves with passive control. The number of devices/spacing and array configuration for each case are indicated in the subcaptions.




(d) Big PA–flap mixed: Spacing – 10$C$, staggered configuration




(e) Small PA–flap mixed: Number of devices – 10, staggered configuration




(f) Big PA–flap mixed: Number of devices – 10, staggered configuration

Figure D.18.: (continued).

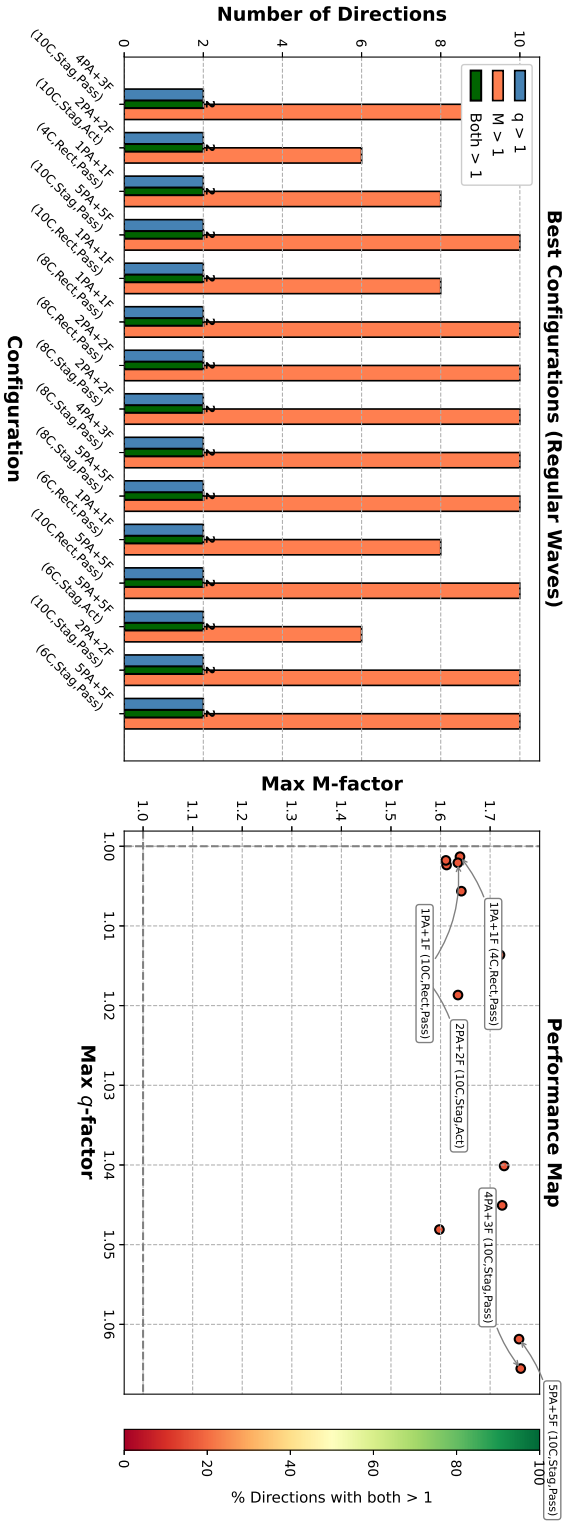



Figure D.19.: Best-performing mixed array configuration for small point absorbers (PAs) combined with flaps under regular wave conditions.

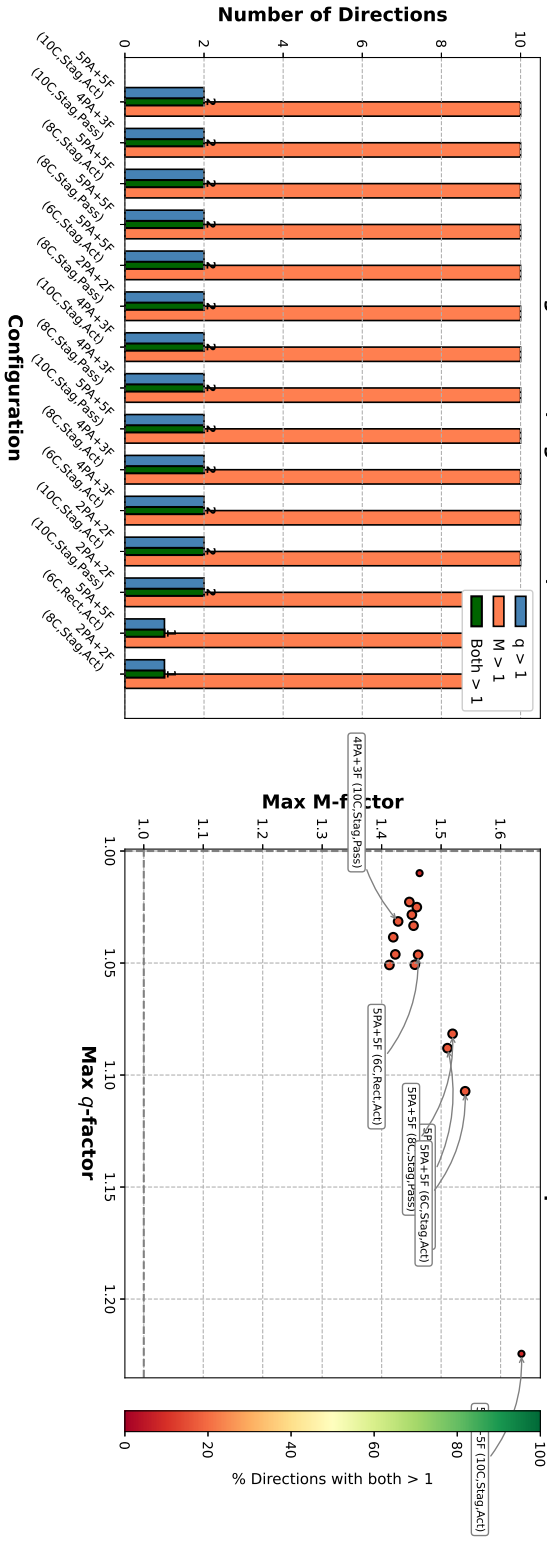



Figure D.20.: Best-performing mixed array configuration for big point absorbers (PAs) combined with flaps under regular wave conditions.

# E

# ADDITIONAL RESULTS FOR DEEP-WATER MIXED ARRAYS

This appendix contains the figures from the results of the deep-water mixed-array study that were omitted from the main text for brevity. For each case, only the irregular waves with passive control results are kept in the main chapter; the corresponding regular-wave passive-control results are gathered here. All figures use the same naming, labels and format as in the main chapter, so the cross-references in the main text resolve directly to the figures in this appendix.

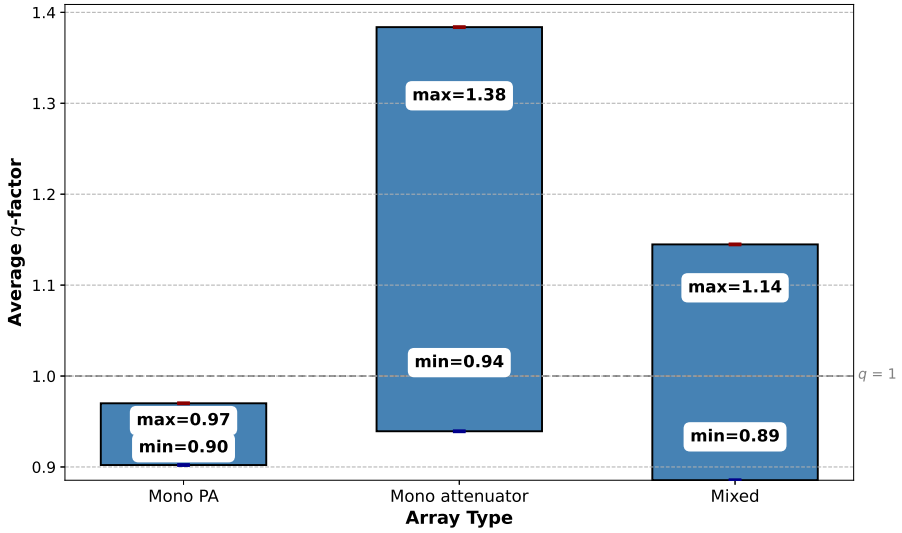



Figure E.1.: Overall comparison of mono and mixed arrays consider mean q-factors under regular waves and passive control

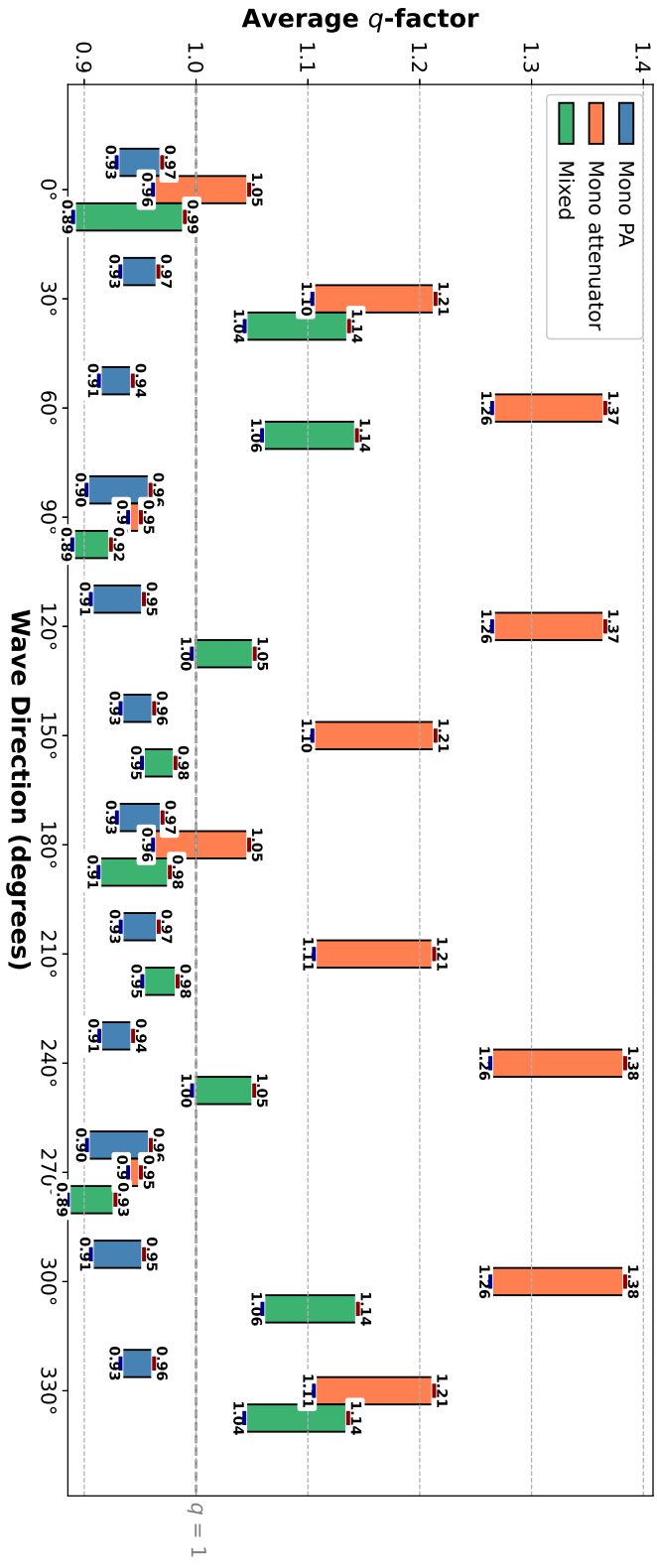



Figure E.2.: Directional comparison of mono and mixed arrays considering mean q-factors under regular waves and passive control

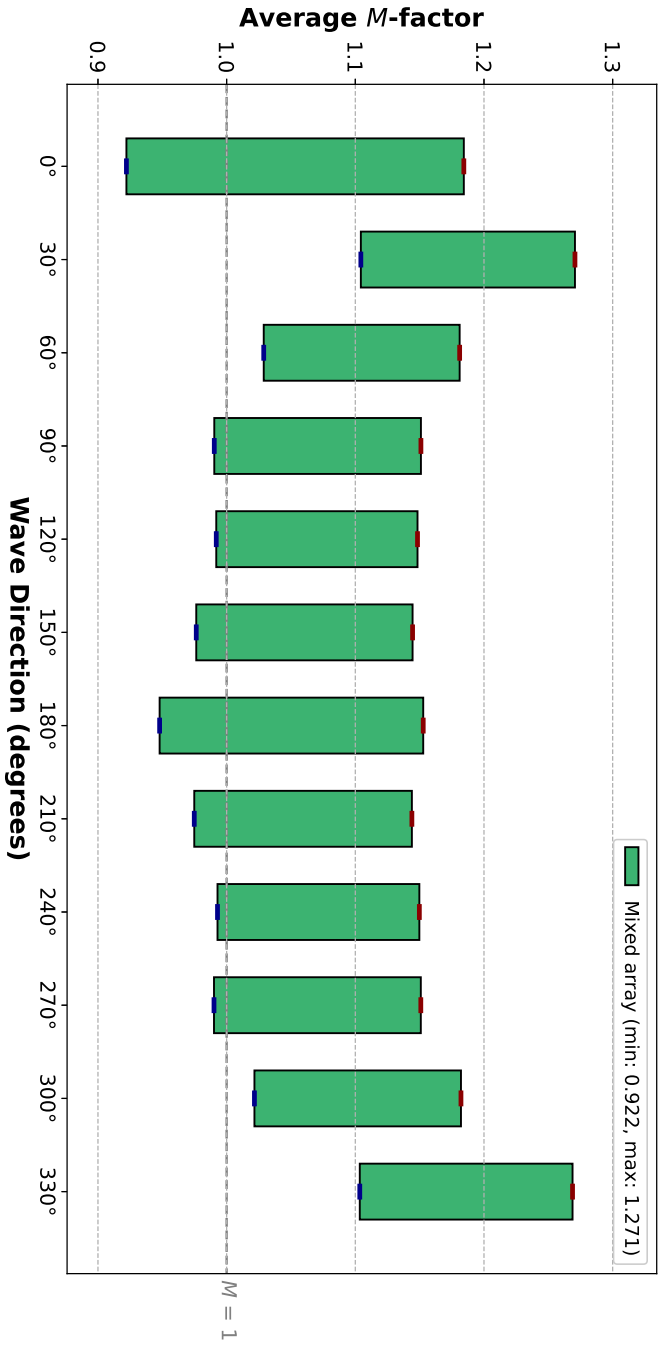
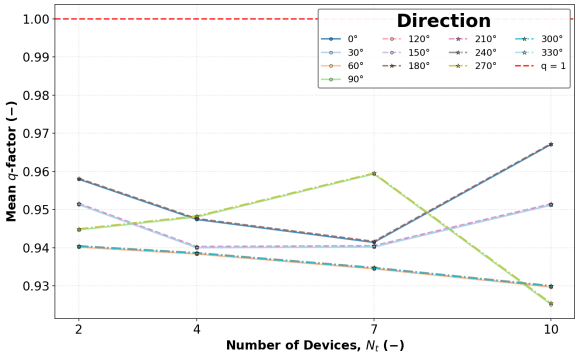
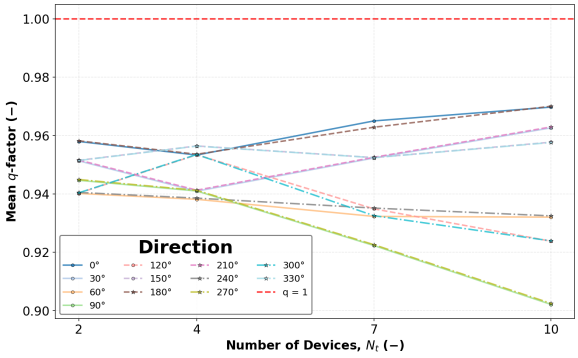



Figure E.3.: Directional variation of the mean M-factor for mixed arrays in regular waves

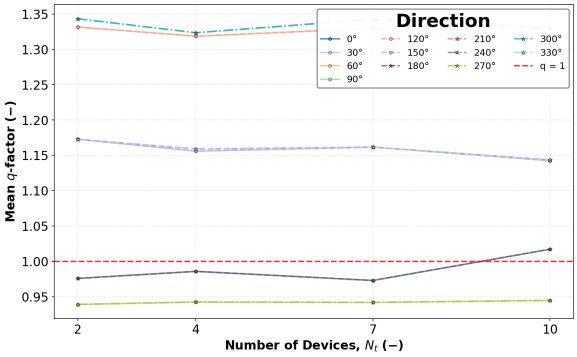



(a) Rectangular configuration

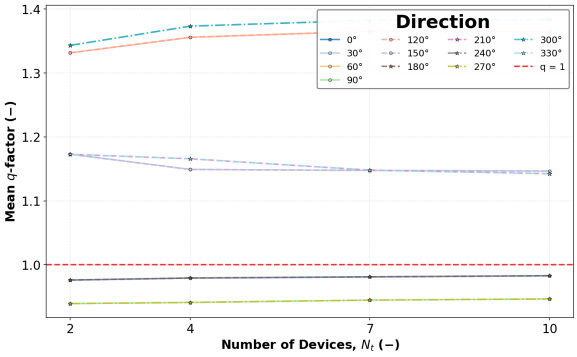



(b) Staggered configuration

Figure E.4.: Variation of mean $q$-factors (averaged over $T = 5$–$15$ s) with the number of PAs in the farm across $6D$ under regular waves and passive control

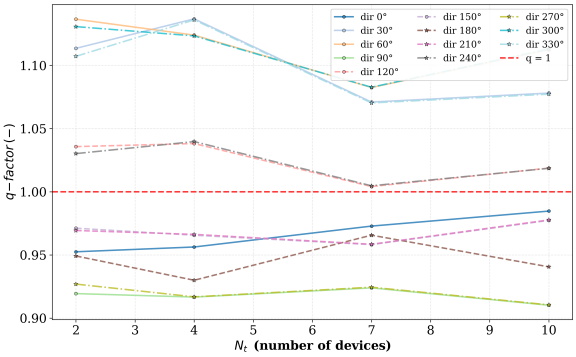



(a) Rectangular configuration

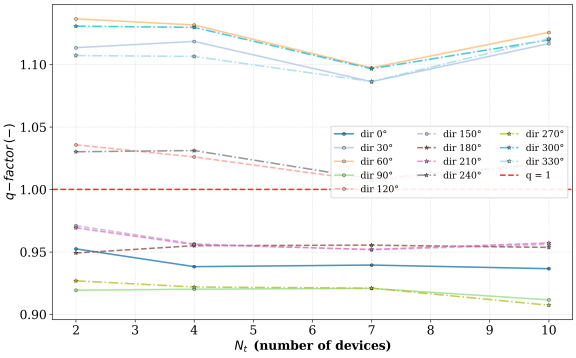



(b) Staggered configuration

Figure E.5.: Variation of mean $q$-factors (averaged over $T$ = 5–15 s) with the number of attenuators in the farm for spacing $6L$ under regular waves and passive control

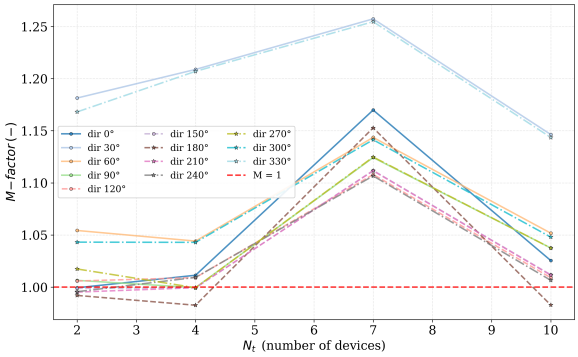



(a) Rectangular configuration

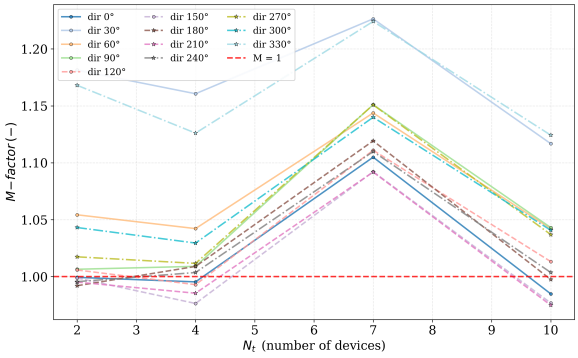



(b) Staggered configuration

Figure E.6.: Variation of mean $q$-factors (averaged over $T$ = 5–15 s) with the number of WECs in the mixed farm for spacing $6C$ under regular waves and passive control

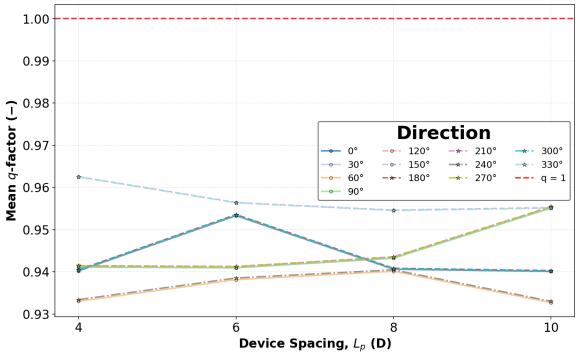



(a) Rectangular configuration

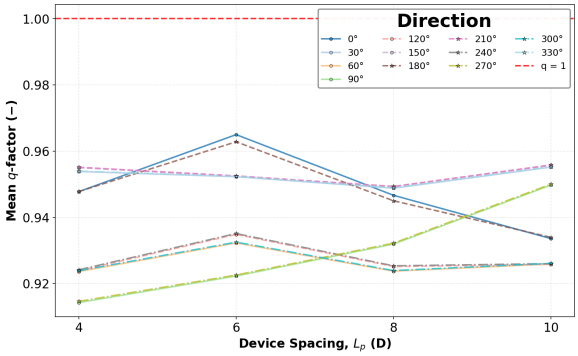



(b) Staggered configuration

Figure E.7.: Variation of mean *M*-factors with the number of devices in the mixed farm for spacing 6*C* under regular waves and passive control

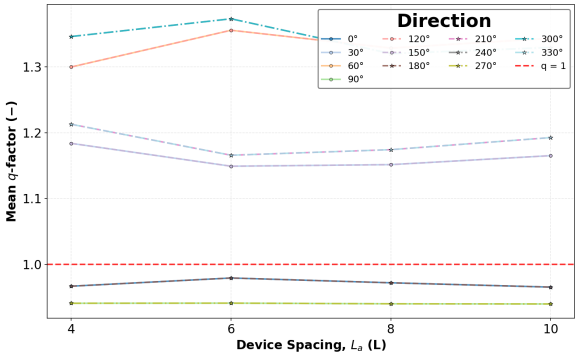



(a) 4 WEC array and staggered configuration

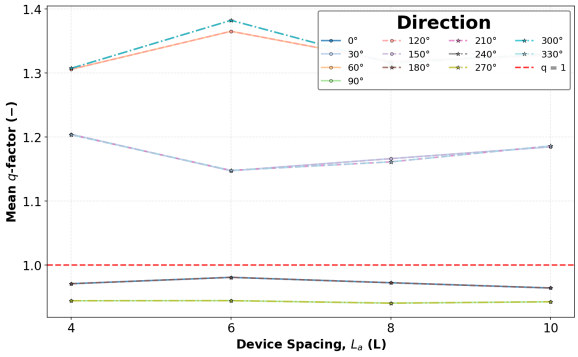



(b) 7 WEC array and staggered configuration

Figure E.8.: Variation of mean $q$-factors (averaged over $T = 5$–$15$ s) with spacing for mono PA farms under regular waves and passive control

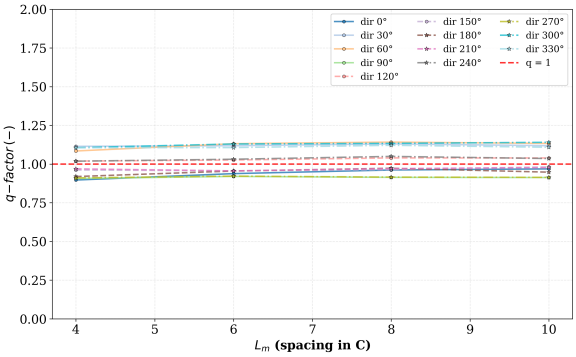



(a) 4 WEC array and staggered configuration

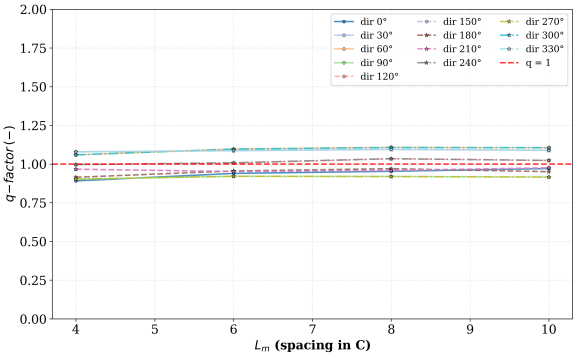



(b) 7 WEC array and staggered configuration

Figure E.9.: Variation of mean $q$-factors (averaged over $T = 5$–$15$ s) with spacing for mono attenuator farms under regular waves and passive control

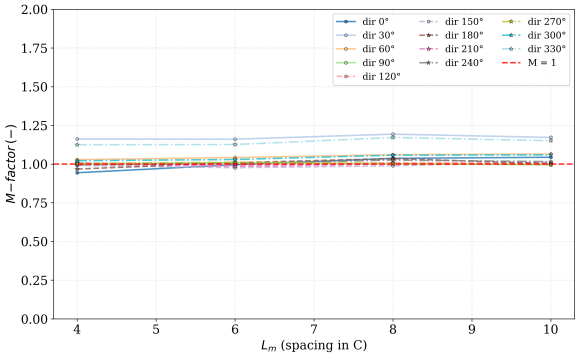



(a) 4 WEC array and staggered configuration

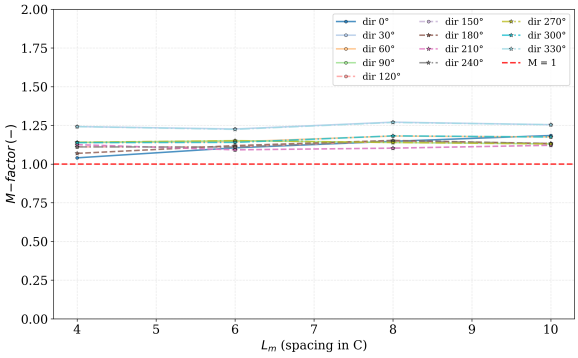



(b) 7 WEC array and staggered configuration

Figure E.10.: Variation of mean $q$-factors (averaged over $T = 5$–$15$ s) with spacing for mixed farms under regular waves and passive control




(a) 4 WEC array and staggered configuration




(b) 7 WEC array and staggered configuration

Figure E.11.: Variation of mean *M*-factors with spacing for mixed farms under regular waves and passive control

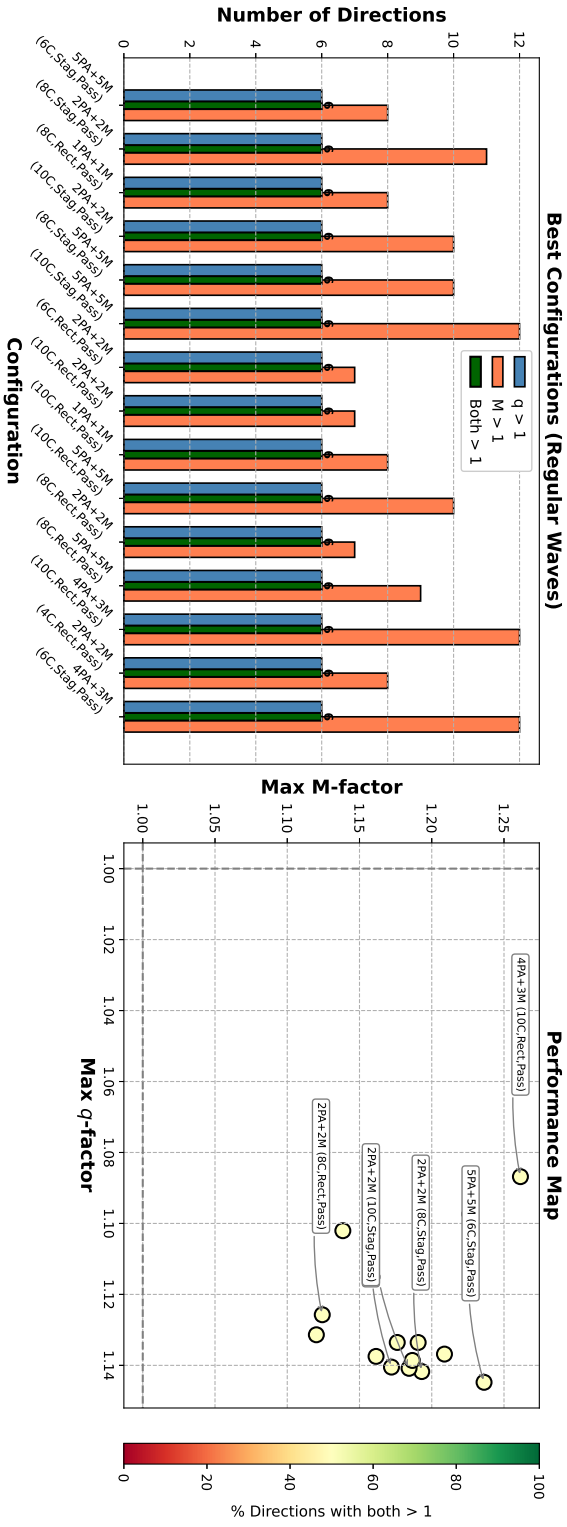



Figure E.12.: Best performing mixed array configurations - regular waves

# ACKNOWLEDGEMENTS

This PhD journey has been intense, demanding, and deeply rewarding. It is without doubt the most challenging goal I have set for myself, and I am grateful to finally see the light at the end of the tunnel. Although the path has been long and far from linear, I would not have reached this point without the support of many people. I would therefore like to take a moment to express my sincere gratitude.

First and foremost, I would like to thank George and Andrei for selecting me for this position and for being critical, committed supervisors. I have gained far more from your guidance than I ever expected.

George, I have always admired your patience in discussing ideas and your willingness to make time whenever I needed it, regardless of the situation. You looked out for me not only professionally, but also on a personal level, for which I am deeply thankful. Your extensive knowledge and wisdom will stay with me for many years to come.

Andrei, I have admired your capabilities as a teacher ever since I took your course Structural Dynamics. From that point on, through my MSc thesis and now during my PhD, you have continued to evolve as a teacher and mentor from whom I still learn a great deal. Your strong focus on the physics of the problem has been an invaluable source of learning, helping me develop a clearer sense of which questions truly matter and how to approach my work with deeper understanding.

To Eva and Nikos, this marked my first research collaboration during the course of my PhD, as well as my first trip to Greece. Eva, thank you for helping me build a solid understanding of the fundamentals of multi-body interactions in BIEM. Your guidance at an early stage of my PhD was invaluable.

Nikos, thank you for collaborating with me on this work and for the friendship that grew during my visit. I will always remember the endless frappés (refilled throughout the day) and truly appreciate you showing me around Thessaloniki and Halkidiki. I wish you the very best with your PhD defense and hope you have a fruitful and meaningful tenure in the army.

To Lorenzo, Irene, and Andrea, thank you for taking the time to help me understand oscillating water columns from both experimental and numerical perspectives. My collaboration in Florence remains one of the most memorable experiences of my PhD.

To Sharath san and Takeshi san, thank you for hosting me in Japan for the IPOEYR programme. Although the programme lasted only a week, it was a wonderful combination of knowledge sharing, cultural exchange, and social interaction. I sincerely hope you continue to organise this initiative for many years to come.

To Alessandro and Hayo, thank you for your critical feedback during my Go/No Go assessment, which helped me better shape and refine my research goals going forward. To Jørgen, Markel, Timothy and Matthieu, thank you for your kindness and for taking the time to answer my questions on BIEM and control modelling for WECs.

To Yingyi, the developer of the single-body HAMS solver, thank you for your patience and for answering my questions when I was first exploring HAMS. Although HAMS-MREL has evolved significantly since I began working on it, it would not have been possible without the original HAMS code that you so generously developed with clarity and efficiency.

To Alfred, what started as a meeting to discuss the modelling of an attenuator in HAMS-MREL over two years ago eventually led to a collaborative publication on attenuator arrays. Thank you for your patience, time, and insightful feedback. You consistently provided in-depth examples to explain complex concepts, which I deeply appreciated. I hope this collaboration continues for many years to come.

To Venki and Touhidul, thank you for being wonderful hosts in Edinburgh, and for sharing your knowledge and hospitality during my stay. To Tian, Soumarup, and Mridu, thank you as well for your help and warmth during my time in Edinburgh.

To all the MSc students I had the privilege of working with during your thesis projects — Sung, Shilu, Julie, Zekai, and Raymond—I hope you enjoyed working on these topics as much as I did. I am grateful for the opportunity to have been your supervisor and to support you as you developed into researchers during your MSc studies. It is wonderful to see all of you doing so well, and I wish you every success in your future endeavours.

To the INORE group, of which I have been a part for the past two years, although it has often been challenging to find time to meet in person, I am truly grateful to belong to such a diverse and motivated community actively contributing to offshore renewable energy. In every meeting I attend, I can feel the passion within this group, and it continually motivates me to keep working in this field.

To the team at SURF and DelftBlue, who are responsible to the supercomputers utilized for running the simulations in research, I extend my heartfelt gratitude. Without your support, these simulations and results would not have been possible in the given time.

To the Marine Renewable Energies Lab (MREL) — Matias, Jian, Avni, Lefteris, Tabea, Harish, Felix, and many more—thank you for your support on both a professional and personal level. The collaborations and interactions I have shared with all of you are memories I will cherish for the rest of my life. To the visiting researchers I had the pleasure of interacting with — Konstantinos, Manuel, Guilia, Sarah, and Chen—it was a pleasure getting to know you, and I hope we can collaborate again in the future. To my fellow members of the PhD council—Lisa, Valeria, and Fatemeh — thank you for your understanding and support in helping strengthen the PhD community at TU Delft and for contributing to initiatives that will continue for years to come. To my current and former colleagues in Offshore Engineering—Thanasis, Jan, Shagun, Jithu, Andrei, Panagiota, Peter, Vagelis, Rens, Yaxi, Timo, Ina, and many others—I wish you all the very best for the future.

To my friends — Vasu, Meeneesh, Maadhangi, Shivaani, Fabian, Shwetha, Karthik, Linda and many others — thank you for always checking in on me and for the many joyful moments we shared along the way. These memories mean a great deal to me, and I hope to have you in my life for a long time to come.

To my family — Appa, Amma, and my sister Rohini — your encouragement, support, enthusiasm, and love throughout this journey have been extraordinary. You have been my constant source of strength, even from afar, and your belief in me never wavered during the most challenging moments of this PhD. Thank you for pushing me not only to persevere academically, but also to reflect, grow, and become a better person. Every milestone I reached was made possible by the values, resilience, and curiosity you instilled in me long before this journey began. I hope I can continue to make you proud in everything I do for the rest of my life.

To uncle, aunty, and Satya—thank you for being a constant source of encouragement, support, and positivity. I am truly proud to have you as part of our family and deeply grateful for your care. Your belief in me and your kind words have meant a lot, and I value the warmth you bring into my life.

And finally, to my wife Durga, although you entered my life midway through this PhD, it feels as though I have known you all my life. I could never have imagined how much richer my life would become with you by my side. Your constant support, encouragement, and unwavering strength during the most critical phase of my PhD are more than I could ever have hoped for. While we have had our ups and downs over the past two years, I am incredibly proud of your patience and resilience in standing beside me through a journey you never anticipated for yourself. You have helped me grow as a human being and I hope to keep becoming a better man and to keep making you proud.

*Vaibhav Raghavan*
*May, 2026*

# LIST OF PUBLICATIONS, AWARDS AND OPEN-SOURCE CONTRIBUTIONS

## JOURNAL PUBLICATIONS

9. **V. Raghavan** and G. Lavidas. "Mixed Wave Energy arrays, re-thinking wave array configurations:a economics based approach". In: *Renewable Energy* (2026). ***Under Review***

8. **V. Raghavan**, A. Metrikine, and G. Lavidas. "Mixed Wave Energy arrays, re-thinking wave array configurations:a hydrodynamics based approach". In: *Renewable Energy* (2026). ***Under Review***

7. **V.Raghavan**, A. Metrikine, and G. Lavidas. "Theory and validation of the new features in BIEM solver HAMS-MREL". in: *Journal of Ocean Engineering and Marine Energy* (2025). issn: 2198-6452. doi: 10.1007/s40722-025-00431-8

6. T. Engelfried, M. Alday, **V. Raghavan**, and G. Lavidas. "Geospatial analysis of the life cycle global warming impacts from marine renewables". In: *Renewable and Sustainable Energy Reviews* 226 (2026), p. 116338. issn: 1364-0321. doi: https://doi.org/10.1016/j.rser.2025.116338. url: https://www.sciencedirect.com/science/article/pii/S1364032125010111

5. G. Lavidas, L. Mezilis, M. Alday, H. Baki, J. Tan, A. Jain, T. Engelfried, and **V. Raghavan**. "Marine renewables in energy systems: Impacts of climate data, generators, energy policies, opportunities, and untapped potential for 100% decarbonised systems". In: *Energy* 336 (2025), p. 138359. issn: 0360-5442. doi: 10.1016/j.energy.2025.138359

4. A. Asiikkis, **V.Raghavan**, D. E. Grigoriadis, A. Metrikine, G. Lavidas, and A. Vakis. "Experimental validation of time domain simulations with HAMS-MREL and comparative analysis of linear and weakly nonlinear models for dense WEC arrays". In: *Ocean Engineering* 341 (2025), p. 122553. issn: 0029-8018. doi: 10.1016/j.oceaneng.2025.122553

3. M.Alday, **V.Raghavan**, and G.Lavidas. "Effects of wave spectrum representation on power production estimations from point absorbers". In: *Applied Ocean Research* 161 (2025), p. 104626. issn: 0141-1187. doi: https://doi.org/10.1016/j.apor.2025.104626

2. **V.Raghavan**, E.Loukogeorgaki, N.Mantadakis, A. Metrikine, and G.Lavidas. "HAMS-MREL, a new open source multiple body solver for marine renewable energies: Model description, application and validation". In: *Renewable Energy* 237 (2024), p. 121577. issn: 0960-1481. doi: https://doi.org/10.1016/j.renene.2024.121577

1. **V.Raghavan**, I.Simonetti, A. Metrikine, G.Lavidas, and L.Cappietti. "A new numerical modelling framework for fixed oscillating water column wave energy conversion device combining BEM and CFD methods: Validation with experiments". In: *Ocean Engineering* 301 (2024), p. 117543. issn: 0029-8018. doi: https://doi.org/10.1016/j.oceaneng.2024.117543

## CONFERENCE PUBLICATIONS

13. **V. Raghavan**, A. Cotten, A. Metrikine, and G. Lavidas. “Assessing the Performance of Arrays of Two-Body Hinged Attenuator WECs”. In: *Proceedings of the ASME International Ocean Offshore and Arctic Engineering Conference (OMAE 2026)*. ***Accepted***. Tokyo, Japan, June 2026, OMAE2026–183627

12. **V. Raghavan**, A. Metrikine, and G. Lavidas. “Exploring the Hydrodynamics of Mixed Wave Energy Farms”. In: *Proceedings of the European Wave and Tidal Energy Conference (EWTEC 2025)*. Vol. 16. Sept. 2025, Paper 699. doi: 10.36688/ewtec-2025-699. url: https://doi.org/10.36688/ewtec-2025-699

11. **V. Raghavan**, A. Metrikine, and G. Lavidas. “Additional Features in HAMS-MREL: A New Open-Source BIEM Solver for Offshore Energy Applications”. In: *Proceedings of the European Wave and Tidal Energy Conference (EWTEC 2025)*. Vol. 16. Sept. 2025, Paper 700. doi: 10.36688/ewtec-2025-700. url: https://doi.org/10.36688/ewtec-2025-700

10. M. Alday, **V. Raghavan**, and G. Lavidas. “Influence of the Wave Spectrum Representation on Production Estimations From Point Absorbers WEC Farms”. In: *Proceedings of the European Wave and Tidal Energy Conference (EWTEC 2025)*. Vol. 16. Sept. 2025, Paper 752. doi: 10.36688/ewtec-2025-752. url: https://doi.org/10.36688/ewtec-2025-752

9. M. Alday, **V. Raghavan**, and G. Lavidas. “Representing Wave Energy Converters in the SWAN Model With Varying Transmission Coefficients Across Frequencies”. In: *Proceedings of the European Wave and Tidal Energy Conference (EWTEC 2025)*. Vol. 16. Sept. 2025, Paper 866. doi: 10.36688/ewtec-2025-866. url: https://doi.org/10.36688/ewtec-2025-866

8. A. Jain, J. Tan, **V. Raghavan**, and G. Lavidas. “A Study on Wave Energy Converter Arrays Using Data-Driven Polynomial Chaos Expansion”. In: *Proceedings of the European Wave and Tidal Energy Conference (EWTEC 2025)*. Vol. 16. Sept. 2025, Paper 984. url: https://publications.evolvingcities.org/proc-ewtec/article/view/984

7. **V. Raghavan**, A. Metrikine, G. Lavidas, T. Islam, and V. Venugopal. “Extension of HAMS with the generalized modes approach”. In: *Innovations in Renewable Energies Offshore*. Ed. by C. Soares and S. Wang. Proceedings of the 6th International Conference on Renewable Energies Offshore, RENEW 2024. CRC Press / Balkema - Taylor and Francis Group, 2024, pp. 193–199. isbn: 9781032905570. doi: 10.1201/9781003558859-22

6. G. M. Alday, **V. Raghavan**, and G. Lavidas. “Improving the Wave Energy Production Using Multi-Size WEC Arrays With Passive Control”. In: *Proceedings of the International Conference on Offshore Mechanics and Arctic Engineering (OMAE 2024)*. Vol. 7. Ocean Renewable Energy. June 2024, V007T09A065. doi: 10.1115/OMAE2024-123655. url: https://doi.org/10.1115/OMAE2024-123655

5. **V. Raghavan**, G. M. Alday, A. Metrikine, and G. Lavidas. “Wave Energy Farm Assessment in Real Wave Climates: The North Sea”. In: *Proceedings of the International Conference on Offshore Mechanics and Arctic Engineering (OMAE 2024)*. Vol. 7. Ocean Renewable Energy. June 2024, V007T09A062. doi: 10.1115/OMAE2024-120946. url: https://doi.org/10.1115/OMAE2024-120946

4. M. Alday, **V. Raghavan**, and G. Lavidas. “Analysis of the North Atlantic offshore energy flux from different reanalysis and hindcasts”. In: *Proceedings of the European Wave and Tidal Energy Conference*. Vol. 15. European Wave and Tidal Energy Conference, 2023. doi: 10.36688/ewtec-2023-140. url: https://submissions.ewtec.org/proc-ewtec/article/view/140

3. **V. Raghavan**, I. Simonetti, G. Lavidas, and L. Cappietti. “Numerical modelling of a box-type and bottom-detached oscillating water column wave energy conversion device: a comparison with experimental data and between BEM and CFD numerical modelling”. In: *Proceedings of the European Wave and Tidal Energy Conference* 15 (2023). doi: 10.36688/ewtec-2023-142. url: https://submissions.ewtec.org/proc-ewtec/article/view/142

2. **V. Raghavan**, G. Lavidas, and A. Metrikine. “Comparing Open-Source BEM solvers for analysing wave energy converters”. In: *Journal of Physics: Conference Series* 2647.7 (June 2024), p. 072002. doi: 10.1088/1742-6596/2647/7/072002. url: https://dx.doi.org/10.1088/1742-6596/2647/7/072002

1. **V. Raghavan**, G. Lavidas, A. Metrikine, N. Mantadakis, and E. Loukogeorgaki. “A comparative study on BEM solvers for Wave Energy Converters”. In: CRC Press, Oct. 2022, pp. 441–447. doi: 10.1201/9781003360773-50. url: https://www.taylorfrancis.com/books/9781003360773/chapters/10.1201/9781003360773-50

## AWARDS

- 2022 - WECANET personal grant for visiting fellowship at Aristotle university, Thessaloniki
- 2023 and 2024 - ’Young Researcher’ award as part of the IPOEYR, at Institute of Ocean Energy Saga University, for research in state-of-the-art topics in Offshore wind/wave/tidal/floating solar etc.
- 2023 - INORE grant for international collaboration with the University of Edinburgh
- 2025 - DCC grant/support for 10 months for improving HAMS-MREL

## OPEN-SOURCE CONTRIBUTIONS

- HAMS-MREL (Open-source BIEM solver) - published in 4TU.ResearchData - DOI: 10.4121/1ba9ae9a-c1d5-4886-ada8-33072e4dff7d.v2
  - Personal Github repository: https://github.com/vaibhavraghavan/HAMS-MREL
  - MREL lab Github repository: https://github.com/Marine-Renewable-Energies-Lab/HAMS-MREL

# CURRICULUM VITæ

## Vaibhav Raghavan

25-10-1992 Born in New Delhi, India

### ACADEMIC EXPERIENCE

2010–2014 Bachelor of Technology
*Civil Engineering*
Faculty of Civil Engineering
Amrita Vishwavidyapeetham
Coimbatore, India

2015–2017 Master of Science
*Structural Engineering (Structural Mechanics)*
Section of Offshore Engineering
Faculty of Civil Engineering and Geosciences
Delft University of Technology
Delft, Netherlands

2022–2026 Doctoral Researcher
*Mixed wave energy arrays: Going beyond the status quo*
Section of Offshore Engineering
Faculty of Civil Engineering and Geosciences
Delft University of Technology
Delft, Netherlands

2026–present Postdoctoral Researcher
Section of Offshore Engineering
Faculty of Civil Engineering and Geosciences
Delft University of Technology
Delft, Netherlands

### WORK EXPERIENCE

2017–2021 Structural Engineer/Software Developer
Advanced Technology and Research
Royal Haskoning DHV
Rotterdam, Netherlands